

POLITECNICO DI TORINO
Repository ISTITUZIONALE

Aeronautics and Astronautics, AIDAA XXVII International Congress

Original

Aeronautics and Astronautics, AIDAA XXVII International Congress / De Rosa, S.; Petrolo, M.; Zaccariotto, M.. - (2023).

Availability:

This version is available at: 11583/2983591 since: 2023-11-04T12:45:18Z

Publisher:

Materials Research Forum LLC

Published

DOI:

Terms of use:

This article is made available under terms and conditions as specified in the corresponding bibliographic description in the repository

Publisher copyright

(Article begins on next page)

hybrid training. The most interesting results related to the hybrid training, for which 30 intact images and 30 damaged images were selected, equally divided between numerical and experimental. In this case we were unable to obtain an accuracy higher than 83.3% in the training validation phase; thus, we have not been able to predict the behavior of this network. It was decided to test it anyway and evaluate the results. This condition was also analyzed because we wanted to simulate a situation in which few experimental data were obtained and, therefore, it was necessary to thicken the latter with data obtained numerically. Surprising results were provided by the hybrid network, trained with mixed signals. In fact, overall, it is the network that has shown a higher recognition rate. These results confirmed the high potential that characterizes the hybrid training obtained by combining validated experimental and numerical data.

Real Classification	undamaged	117	5
	damaged	1	204
		undamaged	damaged
		Predicted Classification	

Fig. 4. Results obtained by the Net trained on “hybrid” results

References

- [1] Ranasinghe K., Sabatini R., Gardi A., Bijjahalli S., Kapoor R., Fahey T., Thangavel K. Advances in Integrated System Health Management for mission-essential and safety-critical aerospace applications. Progress in Aerospace Sciences. Volume 128. 2022. <https://doi.org/10.1016/j.paerosci.2021.100758>
- [2] Memmolo, V.; Maio, L.; Boffa, N.D.; Monaco, E.; Ricci, F. Damage detection tomography based on guided waves in composite structures using a distributed sensor network. Opt. Eng. 2015, 55, 011007. <https://doi.org/10.1117/1.OE.55.1.011007>
- [3] E. Monaco, N.D. Boffa, F. Ricci, L. Maio, V. Memmolo, Guided waves for structural health monitoring in composites: a review and implementation strategies, Progress in Aerospace Sciences, Volume 129, 2022. <https://doi.org/10.1016/j.paerosci.2021.100790>
- [4] Mahindra Rautela, J. Senthilnath, Jochen Moll, Srinivasan Gopalakrishnan, Combined two-level damage identification strategy using ultrasonic guided waves and physical knowledge assisted machine learning, Ultrasonics, Volume 115, 2021. <https://doi.org/10.1016/j.ultras.2021.106451>
- [5] E. Monaco, N. D. Boffa, F. Ricci, M. Rautela, M. Cinque, Simulation of waves propagation into composites thin shells by FEM methodologies for training of deep neural networks aimed at damage reconstruction, Spie Smart Structures/NDE - Health Monitoring of Structural and Biological Systems XV Conference - March 2021. <https://doi.org/10.1117/12.2583572>
- [6] Rautela M., Gopalakrishnan S., Monaco E. “Unsupervised deep learning-based delamination detection in aerospace composite panels” – Spie Smart Structures/NDE - Health Monitoring of Structural and Biological Systems XV Conference - March 2021. <https://doi.org/10.1117/12.2582993>

Deployment of a CubeSat radiative surface through an autonomous torsional SMA actuator

Filippo Carnier^{1,a*}, Alberto Riccardo Donati^{1,b}, Elena Villa^{2,c},
Daniela Rigamonti^{1,d} Paolo Bettini^{1,e}

¹ Dept. of Aerospace Science and Technology, Politecnico di Milano, Via La Masa 34, 20156 Milano, Italy

² Consiglio Nazionale delle Ricerche Istituto per l'Energetica e le Interfasi (CNR IENI), Unità Operativa di Supporto di Lecco, Corso Promessi Sposi, 29, 23900 Lecco, Italy

^afilippo.carnier@mail.polimi.it, ^balbertoriccardo.donati@mail.polimi.it, ^celena.villa@cnr.it,
^ddaniela.rigamonti@polimi.it, ^epaolo.bettini@polimi.it

Keywords: Torsional Shape Memory Alloys, CubeSats, Deployable Radiator, Thermal Control

Abstract. This study aims to provide a proof of concept concerning the integration of an "S" shaped SMA tube into the thermal circuit of a 12U CubeSat. The torsion-based actuator utilizes the heat from the circulating fluid accumulated inside the satellite to enable the deployment of a radiator panel through the manifestation of the shape memory effect in the material, facilitating heat dissipation via radiation.

Introduction

CubeSats have proven over time to be a viable alternative to conventional systems, performing the same scientific operations in a considerably smaller volume. Despite their many innovative aspects, the miniaturization of this class of satellites still presents several challenges to overcome. In particular, integrating hardware components in such limited space restricts design flexibility and poses specific issues in developing adequate thermal control systems due to constrained power supplies.

A commonly adopted strategy for thermal management involves deploying radiator panels to dissipate heat generated by the system's internal components via radiation in the space environment. Among the various deployment mechanism solutions, using shape memory alloy actuators could represent a revolutionary choice.

SMA can lead to very convenient devices with a significant reduction in mechanical complexity and size and better reliability of the actuation system, providing an excellent technological opportunity to replace conventional electric, pneumatic or hydraulic actuators across all sectors, especially in the space segment [1].

The following work aims to develop a torsional SMA tubular actuator to be integrated on a 12U CubeSat's thermal fluid loop circuit in order to deploy a radiator panel, thus maintaining the satellite's internal environment within the appropriate temperature ranges. The torsional behavior of SMA actuators is not widely discussed in the literature and presents critical aspects that still require further investigation, such as cycling stability, a crucial property for optimal integration into a space system.

Concept description

In the proposed solution, the actuator exhibits an S-shaped tubular morphology [2] which enables the integration of the SMA into a closed-loop liquid circuit, allowing for thermal control operations and panel actuation to coexist within the same element, significantly reducing system complexity. In this approach, the mechanism governing the SMA activation is the same fluid flowing inside



the circuit, which experiences localized heating within the satellite due to heat dissipation from internal components and external thermal loads. Through convective heat exchange, the tube, initially deformed in torsion in the martensitic phase with the panel fully closed, generates adequate torque as the SME unfolds, ensuring a 90-degree opening of the radiator element. As the deformation imposed on the tube's central section recovers, the end embedded within the panel is compelled to rotate rigidly, subsequently facilitating the panel's movement (Figure 1).

After the first recovery of the memorized form, neither the return to the low temperature (even below M_f) nor subsequent heating can induce further variations in the shape, until a deformation provided by an external element is set again. Since the actuator is required to operate cyclically depending on the satellite's thermal demands, a rearming strategy must be implemented (for instance, the rearming element can be represented by a torsional spring).

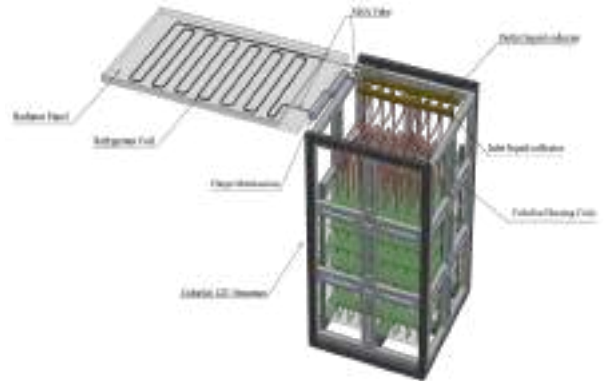


Fig. 1: Concept proposed

Manufacturing and thermomechanical characterization of the SMA actuator

The prototype design process began with the production of various actuator samples using unprocessed tubes made of NiTi alloy. Starting from the unprocessed material purchased, which has an outer diameter of 3 mm, a thickness of 0.24 mm, and pseudoelastic properties, it was necessary to implement heat treatments in order to obtain the desired shape and modify the characteristic temperatures set to achieve shape memory properties. Thermal treatments result in the generation of numerous precipitates inside the material, compromising the maximum performance that the actuator can provide. Therefore, for future developments, it will be necessary to employ tubes that already exhibit characteristic temperatures suitable for the final application. The tube is firstly inserted into a mold, designed in accordance with the geometry to be imposed on the material, followed by a two-phase furnace heating: a) preheating the tube to a temperature of 565°C and b) maintaining a constant temperature at that level for 45 minutes.

To assess transformation temperatures and behavior, DSC tests have been conducted on a single sample. The results reveal that M_f , M_s , A_s , and A_f are -11.99°C, 20.98°C, 20.43°C, and 43.35°C, respectively.

Rotary recovery tests have also been performed to gain a clear understanding of the actuator's performance, particularly in terms of the material's deformation state recovery capacity. The residual rotation detected at the end of each cycle is related to the vertical distance between the initial and final points of the hysteresis curve, indicating a deformation that the material will not be able to recover. This distance increases as the torsional load applied to the tube increases. For torque values greater than 0.07 Nm, the formation of a non-negligible residual deformation was detected.

Cycling tests have been performed to assess the number of cycles after which a complete recovery of the imposed deformation is no longer guaranteed, due to a permanent modification of the crystalline microstructure of the alloy. The tests were conducted with an applied load of $T=0.0655$ Nm, as the rotary recovery data indicate that this value represents the minimum load required to impose a 90° rotation on the material in the martensitic phase.

From the cycling tests, it was concluded that after 70 cycles, the material starts to exhibit a destabilization of performance. These results are extremely promising when compared to those of linear actuators with a high degree of precipitates within the matrix, in which the destabilization of shape memory properties emerges after a few cycles.

Prototype design and fabrication

A conceptual mockup has been designed (Figure 2) and constructed to evaluate the feasibility of the proposed solution through experimental tests conducted in a terrestrial environment, simulating only the internal heating within the CubeSat. Consequently, no rearming mechanism has been implemented. As a result, after each opening process, the system must be cooled inside refrigerators and manually rearmed.

The prototype features a liquid fluid loop integrated into a fixed frame, with dimensions identical to those of a 12U CubeSat structure, and a 3D printed frame free to rotate, representing the radiator panel. The actuator is housed inside a hinge mechanism necessary to ensure the alignment of the tube to the desired axis of rotation for the panel deployment and its connection to the fixed frame.



Fig. 2: Experimental mockup

The hinge mechanism is composed of two elements, one intended to be attached to the fixed frame and the other to the mobile frame, both capable of rotating with respect to each other.

The two components are then forced to rotate relative to each other by 90° thereby generating a torsional stress state in the central section of the tube and thus preloading it in order to mount the panel in a closed configuration. Subsequently, each element is connected to the corresponding frame, and finally, the support element for the panel is inserted and mounted onto the panel itself. The liquid fluid loop consists of two copper serpentine, each one connected to an end of the actuator, positioned respectively inside the CubeSat structure and the panel. The circulation of the liquid is mediated by a micropump, in turn, connected to the serpentine via PTFE flexible hoses that close the loop.

Test results

A test of the prototype was conducted to demonstrate the functionality of the design. The test started with the prototype at room temperature with the SMA tube already in the armed configuration (i.e., panel closed). The circulating liquid was heated at the internal coil within the fixed frame using an electric resistance wire, wrapped upstream of the actuator's inlet section, powered to dissipate 400W due to the Joule effect.

The entire process was monitored by a FLIR

infrared thermal camera and two thermocouples, positioned at the inlet and outlet sections of the tube. The angles reached were measured using a graduated scale located beneath the panel.

The heating proved to be adequate, allowing the tube to reach temperatures suitable for complete austenitization of the alloy. As a result, the panel achieved a rotation of 85° in 155 seconds from the time the current supply was turned on, as shown in figure 4. The inability to reach a fully open position (i.e, 90° of rotation) is related to the thermal treatments the material underwent. These treatments lead to the formation of precipitates, which compromise the macroscopic recovery of the imposed deformation state

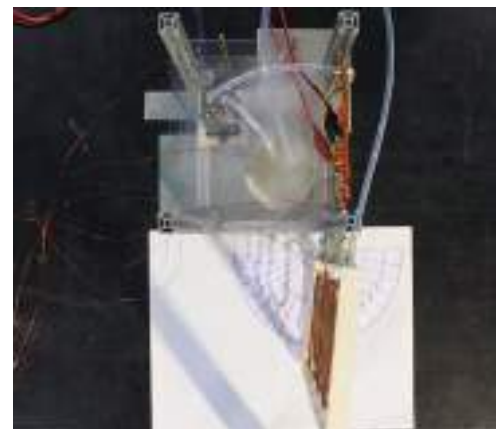


Fig. 3: Final angle reached

during the development of the shape memory effect at the material level.

Conclusions

The presented work aims to provide a proof of concept on the feasibility of developing a torsional tubular SMA actuator, which is activated by the internal circulation of a fluid heated to an appropriate temperature. The goal is to integrate this actuator into a 12U CubeSat's thermal fluid loop circuit for the purpose of deploying a radiator panel to 90° angle of rotation.

The fabrication process started with the production of various actuator samples using precursor tubes for stents, made of NiTi alloy, due to the purchasing easiness. The outer diameter of these tubes is 3 mm and the wall thickness is 0.24 mm. Since these precursor tubes exhibited pseudoelastic behavior, it was deemed necessary to implement thermal treatments in order to obtain the desired morphology and shape memory features. Torsion tests demonstrated that significant rotations could be achieved at low strain/stress levels, highlighting the suitability of this approach for the 90-degree deployment of a radiating panel on a small satellite. Moreover, cycling tests revealed that, despite the high degree of precipitates within the matrix, the material's stability is ensured for approximately 70 cycles. This result is particularly noteworthy, as it is well known that linear SMA actuators with high precipitate content tend to become unstable much earlier. Consequently, it has been shown that the choice to implement a torsion-based actuation system can be considered highly valid. Subsequently, a prototype was designed and developed to assess the feasibility of employing the actuator in a real satellite operational context. The system was then tested in a terrestrial environment, yielding highly interesting results, as the panel reached an angle of 85° within a relatively short time. The incomplete achievement of the desired rotation can be attributed to the high concentration of precipitates in the actuator, which compromises its maximum attainable performance. Nevertheless, these results are extremely promising, as, even with this non-optimal material, a comprehensive feasibility study of the system to be developed was provided, demonstrating a solid foundation for reliability.

Acknowledgments Authors would like to acknowledge gratefully ASI for the support under the collaboration agreement with Politecnico di Milano n.2018-5-HH.0 of the framework agreement n.2016-27-H.0

References

- [1] Lagoudas D.C and Dimitris C. Shape Memory Alloy: modeling and engineering applications. Springer, 2008.
- [2] D Rigamonti, P Bettini, L Di Landro, and G Sala. Development of a smart hinge based on shape memory alloys for space applications. In 25th Conference of the Italian Association of Aeronautics and Astronautics (AIDAA 2019), pages 1719–1742. AIDAA, 2019.

Development of an FBG-based hinge moment measuring system for wind tunnel testing

A. Taraborrelli^{1,a}, A. Gurioli^{2,b}, P. De Fidelibus^{2,c}, E. Casciaro^{1,d},
M. Boffadossi^{1,e}, P. Bettini^{1,f}

¹Department of Aerospace Science and Technologies, Politecnico di Milano, via La Masa 34,
20156, Milano (MI), Italy

²Air Vehicle Technologies, Wind Tunnel Testing, Leonardo Aircraft Division, via ing. Paolo
Foresio 1, 21040, Venegono Superiore (VA), Italy

^aalessandro.taraborrelli@mail.polimi.it, ^balessandro.gurioli@leonardocompany.com,

^cparide.defidelibus@leonardocompany.com, ^demanuele.casciaro@polimi.it,

^emaurizio.boffadossi@polimi.it, ^fpaolo.bettini@polimi.it

Keywords: Additive Manufacturing, Fiber Bragg Gratings, Wind Tunnel Testing, Hinge Moment

Abstract. This paper presents the development and implementation of a hinge moment measuring system for wind tunnel tests based on Fiber Bragg Grating (FBG) sensors. These sensors, which are drawn directly into optical fibers, are capable of measuring strain and temperature variations and represent a precious addition to the aeronautical industry thanks to their peculiar characteristics, including high accuracy, low invasivity, embeddability and electromagnetic immunity. In detail, the development of the system exploits a combination of Fused Deposition Modeling technology and FemtoSecond® Gratings to design and create an independent, deformable structure in which a set of FBGs could be embedded within internal curved channels obtained during the 3D-printing process. This involved a complete re-design of the interface between the stabilizer and the elevator of a horizontal tail model. The material used for producing the structure is ULTEM 9085™, which made the development of the system particularly cost-effective and efficient. The paper also describes the installation of the FBGs, including the design of the channels, the selection of a glue, its injection technique and the following calibration procedure. Finally, the component is tested in the wind tunnel facility of Leonardo Aircraft Division in Venegono (VA, Italy), and the obtained results for some elevator's deflections are presented.

Introduction

Wind tunnel testing is a well-established discipline in Engineering, which, side-by-side with modern computational fluid dynamics, is used for the analysis of the behaviour and performance of aircrafts, cars, buildings and more during their design phase. In wind tunnel activities, the main focus is on measuring forces and moments, and for static measurements, this is typically done by relying on strain gauges. However, strain gauges still show many disadvantages, including inertial effects, high invasivity and susceptibility to electromagnetic interference among the others [1]. Optical fiber sensors represent a promising alternative to strain gauges, thank to their peculiar characteristics such as high sensitivity, faster response time, low invasivity and immunity to electromagnetic interference [2]. Furthermore, these sensors can be directly integrated into structures both during and after their manufacturing process, as demonstrated by S. Pinto [3], who successfully installed them in a component through internal, straight channels directly created during a 3D printing sequence. This paper describes the design and testing of an optical fiber-based hinge moment measuring system for the elevator of a wind tunnel aircraft model's horizontal tail. Since these measurements are highly critical and challenging to obtain by using traditional



strain gauges sensors, especially because of the size constraints imposed by the component, the activity presented in this work focused on developing a system based on a minimally invasive technology. To do this, a complete re-design of the interface between the stabilizer and the elevator of the model was carried out, in order to integrate between them an independent, deformable structure capable of hosting several Fiber Bragg Gratings (FBGs) within internal curved passages obtained through the Fused Deposition Modeling (FDM) technique. The making of this work was made possible thank to Leonardo Company's Aircraft Division in Venegono (VA, Italy), with special recognition to the Wind Tunnel Department. The Company's printer, specifically the Stratasys Fortus® 400mc, was used to build the component with the ULTEM™ 9085 material, which guarantees excellent physical and mechanical properties for high-demand and special applications.

Design

The design of the intermediate deformable structure, shown in Fig. 1 and 2, is the result of an accurate trade-off between the overall structural stiffness of the assembly and the deformability of the sensitive sections. This was achieved by performing several Finite Element Analysis on the component, which were carried out by imposing a set of hinge moments corresponding to the expected loads for the experimental conditions under exam. The final design presents two deformable trusses per each measuring station (4 in total), since the idea was to keep a back-up channel which could have been useful in case of problems related to the adjacent one.



Figure 1: 3D-view of the deformable structure's design (without channels)

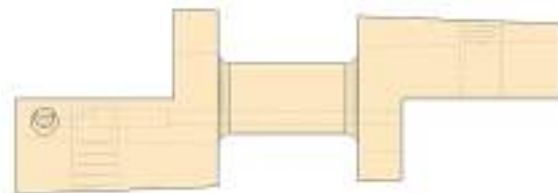


Figure 2: View from the wing root with detail of the system of channels

Manufacturing of the Internal Channels and Sensors' Installation

The design of the internal channels in the structure had to meet several requirements, including the presence of turns, conjunction points and areas with varying radius, as well as the compatibility with the size constraints of the structure and the printing resolution of the Fortus® 400mc. Several tests were conducted until finding out an optimum pattern and diameter for the passages. Small sinks were included in the design at the conjunction areas between the channels, to prevent the printer from depositing excessive material that could potentially obstruct the passages. Fig. 3 shows the intended position of five polyimide-coated Femto-Second gratings (in blue) inside the channels. To fix and secure the sensors in each measuring station, M-Bond 600 Adhesive by Micro Measurements was chosen and used, since it resulted compatible with ULTEM and guaranteed an optimal viscosity for the application, as well as a high performance for stress analyses. A compatible blue dye was added to the adhesive to make the procedure visible through the material. The mixture was inserted into the channels through the sinks with a 0.6 mm rounded-head nozzle, halting the injection as soon as it was observed to come out from the end of the channel on the interface side with the elevator. The component was then left for curing under heat lamps for 5 hours at 55°C.

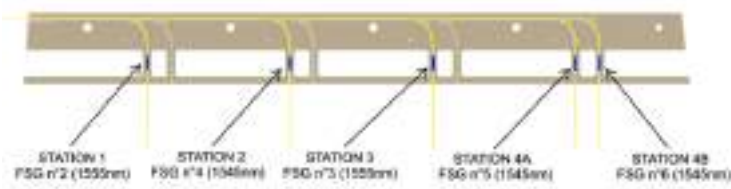


Figure 3: Designated position for each embedded sensor



Figure 4: Injection of the glue

Calibration

The calibration of the system of sensors was performed by using the specialized equipment of the company. The deformable structure was secured to the other components with five screws per side, tightened with a torque wrench to guarantee the repeatability of the constraint after each installation. Five holes were drilled on a dummy elevator at 10 mm behind the hinge axis. Each hole was loaded singularly and then in combination with others to accurately reproduce a set of calibration hinge moments on the elevator, chosen in accordance with the expected loads during testing. A first-order calibration vector, which links the signals to the loads, was calculated by performing a regression between the vector of all applied hinge moments and the matrix containing the measured wavelength variations from all the sensors. The sensor embedded in station 4B (Fig.3) was excluded from this calculation as it was damaged during the installation and the output signals resulted altered with respect to the expected one.

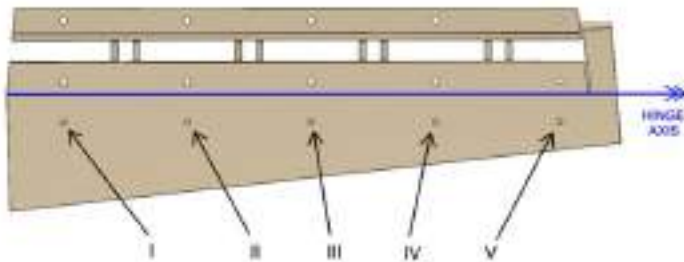


Figure 5: Calibration points on the elevator



Figure 6: Detail of the final product

Results

Since FBGs are sensible to both mechanical and thermal deformation, the model was accurately designed in a way that the temperature-related wavelength shifts during testing resulted to be significantly smaller than the mechanical ones. Despite that, the effect of temperature oscillations during testing was not considered negligible, and it was decided to perform a thermal calibration of the sensors directly in the wind tunnel environment, by investigating their response during a heating cycle in relation to the data provided by a thermocouple installed inside the fuselage of the model. Temperature variations were also reduced by limiting the duration of each test, conducting them in a continuous sweep mode in pitch, with an α -sweep rate of $0.5^\circ/\text{s}$. The campaign involved installing the full horizontal tail assembly on the corresponding aircraft model (Fig. 7) and testing three different elevator deflections δ of 0° , $+12.5^\circ$ and -12.5° at wind speeds of 40 and 50 m/s. The tests were repeated several times to assess the level of repeatability of the measurements.

The averaged results for the examined conditions, normalized with respect to the maximum tested α and the maximum measured hinge moment, are presented in Fig. 8, 9 and 10.



Figure 7: Full assembly mounted on the model

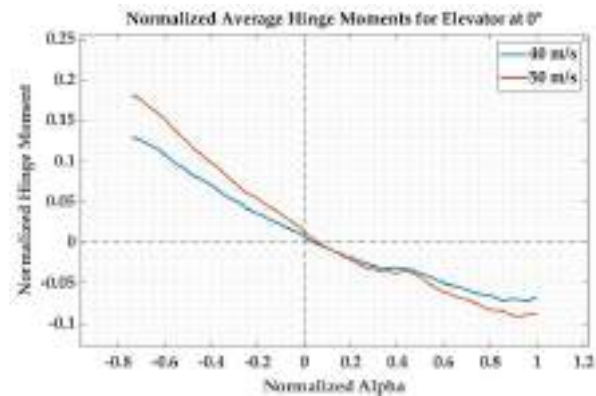


Figure 8: Results for non-deflected elevator

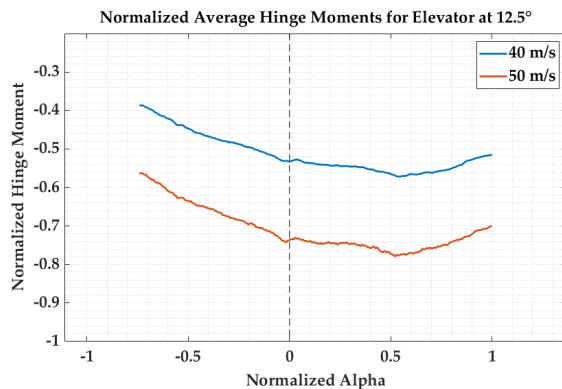


Figure 9: Results for +12.5° elevator deflection

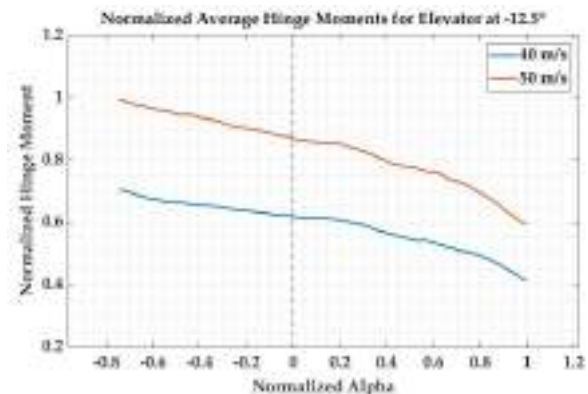


Figure 10: Results for -12.5° elevator deflection

Conclusion and future improvements

This work proves how the production of a wind tunnel model's component with embedded optical fiber sensors is possible with a low-invasive and re-usable solution and can produce successful results which otherwise could not be achieved with conventional measurement systems. In fact, the collected measurements resulted compatible with the expected ones, indicating that the experimental setup and procedures were appropriately designed and executed. However, to extend the application range of the component and allow for testing at higher wind speeds, it should be stiffened, for example by increasing the size of the deformable stations. Future developments should also explore other additive manufacturing techniques, including metallic 3D-printing, to improve the durability of the component and to overcome the structural limitations related to the use of polymeric materials. Finally, the back-up configuration proposed in this work could be exploited to include, for each station, an unconstrained sensor for compensation of temperature effects. All these upgrades clearly have the potential to improve the performance of the system.

References

- [1] C. Tropea, A. Yarin, J. Foss, "Springer Handbook of Experimental Fluid Mechanics" (2007). DOI: <https://doi.org/10.1007/978-3-540-30299-5>
- [2] A. Kersey, M.A Davis, H.J. Patrick, M. Leblanc, K. Koo, C.G. Askins, M. Putnam, E. Friebele, "Fiber Grating Sensors", Journal of Lightwave Technology (1997) vol. 15, issue 8, pp. 1442 – 1463. DOI: <https://doi.org/10.1109/50.618377>
- [3] S. Pinto, "Development and testing of optical fiber based monitoring systems for a wind tunnel application", Politecnico Di Milano, URL: <http://hdl.handle.net/10589/148372>

Buckling and post-buckling response of curved, composite, stiffened panels under combined loads including pressurization

Luisa Boni^{1,a*}, Daniele Fanteria^{1,b*}, Tommaso Lucchesi¹

¹Department of Civil and Industrial Engineering – Aerospace division, University of Pisa, via G. Caruso, 8, Pisa, Italy

^aluisa.boni@unipi.it, ^bdaniele.fanteria@unipi.it

Keywords: Post-Buckling, Curved Composite Stiffened Panel, Finite Element Analysis, Combined Loads

Abstract. In recent years, metal stiffened shells for aerospace applications have been gradually replaced by composite shells, which are widely used in fuselage, tail, and wing structures due to their advantageous properties. Under operating conditions, stiffened panels are subjected to different types of loads, combined in various ways, which can lead to instability. Like their metallic counterparts, allowing post-buckling within the operational envelope could lead to significant weight reductions for composite structures, but unlike the metal case, their response in this state is not fully understood and the potential of composites is not fully exploited. In this context, the main objective of the present work is to investigate the buckling and post-buckling behavior of composite curved panels subjected to combined loads. The buckling behavior of a representative stiffened curved panel has been simulated by non-linear finite element analyses, from the simplest pure compression and pure shear cases to the final analysis of the panel subjected to pressurization, shear, and compression simultaneously. The results of this study quantify the reduction of the critical compression and shear loads due to their simultaneous action, as well as the effect of the pressurization load, which was generally beneficial, but remarkably so in the case of pure shear.

Introduction

Over the years, the use of composite materials has gradually increased, reaching levels of up to 50% of the structural weight of new generation aircraft such as the Airbus A350 or Boeing B787. In this context, metal stiffened shells, either flat or curved, have been replaced by their composite counterparts. Regardless of their constituent materials, stiffened panels must withstand a variety of complex loading conditions, any of which could cause the panel to buckle. Therefore, it is of paramount importance to establish methods that can effectively predict the structural behavior of composite panels beyond the first occurrence of instability in order to exploit their post-buckling capabilities. In the present work, the Finite Element Method (FEM) has been chosen as the main analysis tool. Indeed, the FEM has proven to be a valuable tool for investigating the structural response of stiffened panels [1].

Particular attention has been paid to the realistic modelling of geometry, loading and boundary conditions, avoiding the oversimplifications commonly found in the literature. The commercial software ABAQUS 2022 [2] was used to perform all the FE analyses. The modelling and simulation strategies are preliminarily validated on a metal panel whose data are available in the literature, as well as experimental and numerical results detailing its critical and post-critical behavior.

For this the lower fuselage panel studied by Rouse et alii in [3] was selected. Considerable effort has been made to apply realistic boundary conditions to the panel under analysis to avoid the D - BOX modelling used in [3] but not described in detail. The reference metal panel model was loaded with pure compression only. A composite version of the panel was then developed to investigate its stability under combined loading.

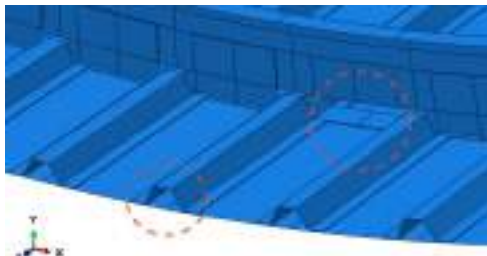


Reference panel and development of the composite version

The reference panel is made of aluminium alloy and consists of a curved skin stiffened by fifteen hat-section stringers and four zee-section frames. An aluminium tear strip is bonded to the skin underneath all the stiffening elements. While the stringers are attached directly to the skin, the frames are attached to the skin by shear clips and to the stringers by tension ties.

Quadrilateral, 4-node, stress/displacement shell elements with reduced integration and a large strain formulation (S4R) [2] were used to model all panel components. The tear strip was modelled implicitly by increasing the thickness of the skin under the stiffening elements and the connections between adjacent members were modelled using TIE constraints.

The eigenvectors provided by a preliminary linear buckling analysis were assigned as initial imperfections to a non-linear analysis to determine the pure compression buckling load of the structure. The loading and Boundary Conditions (BC) were assigned according to a typical experimental setup: one of the curved edges was fixed and the other was compressed by a concentrated axial force applied to the reference node, which shares its d.o.f. with all edge nodes. The analysis yielded a buckling load substantially in agreement with that reported in [3], thus qualifying the metal model as a reference to develop of the composite version.



	Ply n.	CPT [mm]	Stacking sequence
Skin	14	1.75	[+45/-45/90/+45/-45/0/0] _s
Stringer	16	2	[+45/-45/90/+45/-45/0/90/0] _s
Frame	48	6	[+45/-45/90/+45/-45/0/90/0] _{3s}
Shear Clip	32	4	[+45/-45/90/+45/-45/0/90/0] _{2s}

Fig. 1 – Composite panel architecture and layup.

The composite panel has “omega” section stringers (15 as a reference, with the same spacing) as shown in Fig. 1. The attached flanges of adjacent stringers are extended to form a pad-up under the shear clips (see Fig. 1). The width of the shear clips has been increased while maintaining sufficient clearance for the stringers to pass through ('mouse holes'); the tension straps have been eliminated. All components are thin laminates of carbon-epoxy prepreg and have a symmetrical and balanced stacking sequence to avoid couplings (see Fig. 1).

Tab. 1 – Stiffness properties of the composite panel compared to the reference.

	Skin				Stringer	
Material	AA Alloy	CFRP		Material	AA Alloy	CFRP
Thick. [mm]	1.6	1.75		Cross section	Hat	"Omega"
Esten. Stiff. [kN/mm]	Et/(1-v²)	A11	A22	Cross Sect. Area [mm²]	249.5	248.8 (-0.3%)
	131.2	109.4 (-16.6%)	77.6 (-40.9%)	Axial Stiff. (EA) [kN]	17895	12560 (-29.8%)
Flex. Stiff. [kN*mm]	Et³/12(1-v²)	D11	D22	Bend. Stiff. (EIyy) [kNm²]	2.61	1.34 (-48.7%)
	28.0	16.4 (-41.4%)	25.2 (-10.0%)			

The composite stringers are designed to have the same cross-sectional area as their metallic counterparts, and the composite skin has a thickness comparable to the metallic reference.

The frames and shear clips were dimensioned to carry the combined loads without causing instability problems. The stiffness properties of the composite panel are shown in Tab. 1. Overall, the reference panel has stiffer elements than the composite panel.

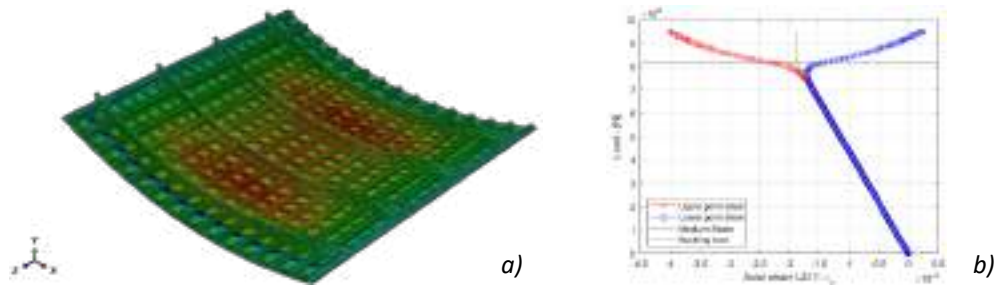


Fig. 2 – Compression buckling: radial displacement a) and load-strain diagram b)

The analyses on the composite panel were carried out using a mean element size close to that used for the reference panel, which was selected through a sensitivity analysis. Despite the lower stiffness, the compression buckling load of the composite panel is 820 kN (deformed shape in Fig. 2), significantly higher than that of the metal panel (570 kN).

The composite design was then frozen and used for all subsequent analyses.

Compression and Shear Buckling

The same procedure as for compression was used to calculate shear buckling: the eigenmodes of the linear analyses were used to perturb the geometry in the non-linear analyses. Again, using an experimental setup as a reference to enforce BC, one curved edge was fixed and the other was loaded by a pure torque (acting around the axis of the cylinder defined by the skin).

The strain analysis confirmed that the structure had been subjected to pure shear, as the longitudinal and transverse strains were zero prior to the instability, which manifested itself with skin buckles following patterns like those of metal panels. The skin between the stiffeners develops diagonal buckles at an angle of about 30° , as shown in Fig. 3a.

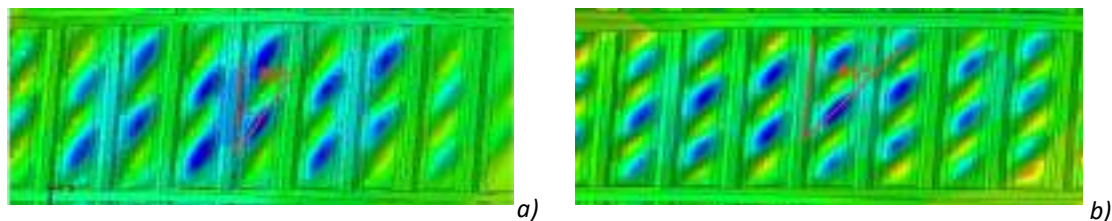


Fig.3 - Waves orientation for a) pure shear and b) shear and compression

The post-buckling configuration and stress state meet the *Incomplete Diagonal Tension Theory* formulated by Khun [4], widely accepted as the reference theory about shear buckling. The effect of restrained warping was also investigated and a strong reduction in buckling torque, quantifiable to about 50%, was found when warping is allowed. Eventually, an analysis was then carried out under the simultaneous action of compression and shear, with restrained warping. The effect of the compression is to increase the effectiveness of the shear loads in inducing the diagonal tension field; this synergy reduces the combined buckling load by about 40% with respect to the compression alone. Furthermore, in accordance with the reference theory, the angle of inclination of the buckles increased up to 45° , as shown in Fig. 3b.

The Effects of Pressurisation

The pressure was applied in advance to obtain realistic conditions: the radial displacement was left free, the symmetry is imposed along straight edges and the longitudinal stress that occurs in the real fuselage is introduced as an imposed displacement, evaluated through an ad hoc analysis.

In a second step, an increasing external compressive or shear load was applied to reach the buckling condition and to study the behavior of the panel in the post-buckling regime. The results

of these analyses show that pressurization increases the buckling load significantly - 1540 KN vs. 821 KN for compression only (more than 85% increase) - or even remarkably: 3110 KNm vs. 1430 KNm for shear only (more than 115% increase).

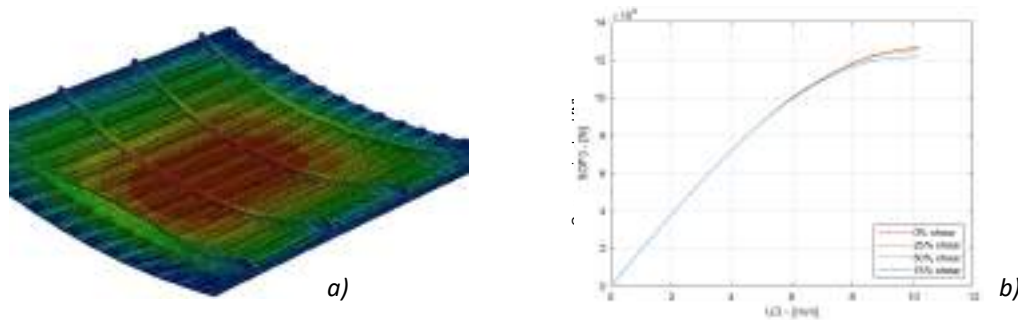


Fig.4 – Simultaneous application of pressurization, compression, and shear: a) Radial displacement, b) Longitudinal load-displacement curve.

Finally, some compression analyses were carried out at a given level of pressurisation with a constant shear load applied (increasing percentages of the pure shear buckling load were considered). For each value of the shear load, the deformed shape shown in Figure 4a is very different from those relevant to individual load cases (see Figures 2 and 3). The influence of the different shear levels on the longitudinal load-displacement curve is shown in Figure 4b. The buckling load is insensitive to the shear that slightly affects the post-buckling phase.

Conclusions

The study allowed the development of buckling and post-buckling modelling and analysis strategies under single and combined loading. Results relevant representative stiffened composite curved panel show that the buckling and post-buckling behavior in shear is consistent with the incomplete diagonal tension theory developed for metal structures.

The reduction in buckling load under simultaneous compression and shear loads is quantified and the effect of pressurisation is evaluated. Pressurisation is found to be remarkably beneficial in the case of pure compression; when shear is also present, it slightly affects the post-buckling phase, while the buckling load remains the same.

References

- [1] L. Boni, D. Fanteria, and A. Lanciotti, Post-buckling behaviour of flat stiffened composite panels: Experiments vs. analysis, *Composite Structures*. (2012), pp. 3421 – 3433.
<https://doi.org/10.1016/j.compstruct.2012.06.005>
- [2] ABAQUS 2022 User's Manual, Dassault Systèmes Simulia Corp., Providence, USA (2022).
- [3] M. Rouse, R. Young, and R. Gehrki, Structural stability of a stiffened aluminum fuselage panel subjected to combined mechanical and internal pressure loads, 44th AIAA/ASME/ASCE/AHS/ASC Structures, Structural Dynamics, and Materials Conference. (2003).
<https://doi.org/10.2514/6.2003-1423>
- [4] P. Kuhn, J.P. Peterson, and L.R. Levin, A summary of diagonal tension Part I: methods of analysis, NACA TN 2661. (1952).

MOST Project

Insights on state of the art and perspectives of XR for human machine interfaces in advanced air mobility and urban air mobility

Sandhya Santhosh^{1,a *}, Francesca DeCrescenzo¹, Millene Gomes Araujo¹,
Marzia Corsi¹, Sara Bagassi¹, Fabrizio Lamberti², Filippo Gabriele Praticò²,
Domenico Accardo³, Claudia Conte³, Francesco De Nola⁴, Marco Bazzani⁴,
Joyce Adriano Losi⁵

¹Department of Industrial Engineering, University of Bologna, Italy

²Department of Control and Computer Engineering, Polytechnic of Turin, Italy

³Department of Industrial Engineering, University of Naples Federico II, Italy

⁴Teoresi Group, Italy

⁵Accenture

* sandhya.santhosh2@unibo.it

Keywords: Urban Air Mobility, Advanced Air Mobility, Unmanned Aerial Systems, Immersive Technologies, Extended Reality, Human Machine Interfaces, U-Space

Abstract. With technological innovation and advancements, especially in autonomy, battery and digitization, the future of air transport and mobility is transiting towards a broader spectrum of Advanced Air Mobility (AAM) and Urban Air Mobility (UAM). UAM envisions safer, faster, and more sustainable air mobility for smarter cities and urban environments including passenger transport and goods delivery. Nevertheless, this concept is still considered extremely breakthrough and several technological and operational aspects are mostly undefined. In this context, a comprehensive approach to AAM/UAM may be to adapt cutting-edge technologies in developing sustainable framework and Human-Machine Interfaces (HMIs) in order to realize the challenges, benefits, and conditions of such transport system in advance for future safer, more reliable and globally approved operations. One of the technologies that can contribute to accelerate advancements through human centred simulating UAM processes and operations is XR (eXtended Reality). This paper presents the early steps of a multidisciplinary study performed under the framework of PNRR (Piano Nazionale di Ripresa e Resilienza) and MOST (Centro Nazionale Mobilità Sostenibile) project in analyzing the perspectives of XR based HMIs for UAM paradigm and potential AAM/UAM use case scenarios that can be simulated with XR in view of attaining efficient and effective future solutions. Furthermore, the work introduces the state-of-the-art overview on XR facilitated UAM applications and considers prospective potential use cases that can be developed through PNRR research study in demonstrating XR as an enabling technology in promising areas of the UAM framework.

Introduction

Air mobility, also referred to as AAM or UAM, has emerged as a transformative concept in the realm of transportation, offering new possibilities for efficient and sustainable movement of people and goods. According to the studies performed in the framework of the Italian AAM Strategic Plan, the global AAM market is expected to grow at a 20-25% rate from 2021 to 2030, reaching an estimated value of around USD 38-55 billion per year [1]. A significant interest is paid to its implementation in the context of urban environments where UAM represents a promising vision for the future of transportation of goods and passengers, aiming at providing efficient and sustainable aerial transportation solutions within urban areas [1][2]. According to Tojal et al.,



UAM is a mobility concept for urban areas that makes use of any kind of mainly Unmanned Aerial Systems (UASs) to perform any type of mission that is operated in the Very Low Level (VLL) airspace aiming at improving the welfare of individuals and organizations [3]. Thanks to technological advancements in UAM in conjunction with advanced materials, aircraft architecture, enhanced battery capacity, digitalisation of air traffic management etc., the commercial exploitations of such mobility system is expected to become a reality in Europe within 3 to 5 years [4]. However, the actual implementation of UAM comes with numerous challenges. The safe integration of UAM vehicles into urban airspace, the development of infrastructures such as vertiports and changing stations, regulatory frameworks, public acceptance, and efficient operations are among key considerations (as highlighted in Fig.1)[5][6]. These challenges necessitate a multidisciplinary approach that involves collaboration between industry stakeholders, policymakers, urban planners, aviation authorities, and technology innovators [7]. Therefore, attention has been increasing towards contemplating innovative technologies in simulating and developing advanced human-machine interfaces (HMIs) through human and user-centred approaches for future UAM scenarios and foreseeing the challenges in order to find efficient and effective solutions and support regulatory processes.

Immersive media comprising Virtual Reality (VR), Augmented Reality (AR), and Mixed Reality (MR) are amongst the currently fastest growing and promising tools for such innovative HMIs. These, also commonly referred to with the umbrella term XR, enable the users to experience immersive and interactive environments, and have been proven to enhance design validations, reduce training costs, enhance user engagement, improve communication and collaboration with seamless data access etc.[8], [9],[10],[11]. Through a comprehensive analysis of existing literature, case studies, and industry developments, the present work aims to provide insights into the current state of UAM scenarios and explores the potential role of XR-based HMIs and simulations. By understanding the complexity of UAM, we can better appreciate the significant impact it may have on urban transportation and facilitate its successful integration into our cities.

Related work on XR-based HMIs and Simulations for UAM

It is recognized that in the realm of the digital transformation of processes and the 4.0 industrial revolution, XR technologies have paved the way to advanced HMIs acting as a bridge connecting the gap between humans and machines [13]. Revenue in AR and VR market worldwide is expected to show an annual growth rate (CAGR 2023-2027) of 40.12%, resulting in a projected market volume of US\$9.10bn by 2027 [14]. It is evident that XR and UAM are together rapidly growing markets. Besides this aspect it must be considered that the integration of XR-based HMIs and simulations for UAM presents numerous benefits. It facilitates the design and evaluation of user-centric interfaces that consider human factors, ergonomics, and cognitive workload in highly automated environments. Furthermore, XR-based simulations enable stakeholders to assess the feasibility and performance of UAM systems, optimize operational procedures and identify potential safety risks.



Fig. 1. Overview of XR simulation themes for UAM: (1) Types of UAM (2) Top concerns highlighted by EASA (3) Potential UAM themes for XR applications.

To this regard, we have performed a preliminary study on collecting a selection of the existing works in the field of XR-based UAM and categorised them into 3 different perspectives: Market, Scientific, and Industrial research (see Table 1).

Table 1. Selection of previous works relevant for this study

	Reference	Forecasts		
Market Perspective	[1]	Global AAM/UAM market research forecasts a growth of CAGR at 20/25% from 2021 to 2030		
	[14]	AR and VR market worldwide is expected to show an annual growth rate (CAGR 2023-2027) of 40.12%		
		UAM Mission Scenarios	Description	XR technology
Scientific Perspective	[15]	Collaborative Decision Making	3D map rendering with planes, runways and waypoints demonstrating air traffic scenarios	AR
	[16]	Simulation of Workspace	Taking off and landing a quadcopter	VR, CAVE
	[17]	System integration and testing	Urban Traffic Management, UAS operations	HMI, AR, CAVE
	[18][19][20]	Public/ Social Acceptance	Auditory and Visual perception of drones, acceptance of Air taxis	AR, VR
	[21][22]	Virtual Prototyping and Design	Urban Airport Infrastructure design, Air taxi cabin	VR, MR
Industry Perspective	[24][25]	Visualization of Airspace data	CLARITY: HMD for Air traffic control -Drone Control with intuitive gestures	MR, VR AR
	[23][26][27]	Training and Simulation	-Real-time Tower and Apron Control Research Simulator (NARSIM) -Pilot training program for eVTOL -eVTOL Flight Simulator	Simulator, AR, AI, VR, MR, MR
	[28][29]	Simulation	Drone Simulator	AR-to-gamepad interface

Conclusion

UAM is an emerging transport system with dedicated services that integrate aerial unmanned platforms for passengers and goods transport in urban environment. As UAM progresses, there is a growing need for advanced HMIs and simulations to enhance the design, operation, and ensure safety of these complex systems. With advent growth towards automation, technologies such as XR offers innovative solutions for creating immersive environments and interactive experiences for future UAM scenarios. In this context, this paper highlights a literature study on XR-based HMIs and simulations to support UAM services. We classified the information into three perspectives of scientific, industrial and market in view of highlighting the main areas of XR-based HMIs and simulations for future UAM scenarios. It has been observed that the literature identifies the key aspects relating to the fields of virtual prototyping, design, training, simulation, human

factors evaluation, airspace visualization, collaborative decision making, system integration and testing, public engagement, and education/marketing.

Acknowledgments

This study was carried out within the MOST – Sustainable Mobility National Research Center and received funding from the European Union Next-Generation EU (PIANO NAZIONALE DI RIPRESA E RESILIENZA (PNRR) – MISSIONE 4 COMPONENTE 2, INVESTIMENTO 1.4 – D.D. 1033 17/06/2022, CN000000023). This manuscript reflects only the authors' views and opinions, neither the European Union nor the European Commission can be considered responsible for them.

References

- [1] AAM National Strategic Plan (2021-2030) for the development of Advanced Air Mobility in Italy, www.enac.gov.it
- [2] White Paper on Urban Air Mobility and Sustainable development, <https://www.asd-europe.org> (2023).
- [3] M. Tojal, H. Hesselink, A. Fransoy, E. Ventas, V. Gordo, Y. Xu, Analysis of the definition of Urban Air Mobility –how its attributes impact on the development of the concept, *Transportation Research Procedia*, Volume 59, 2021, Pages 3-13, ISSN 2352-1465. <https://doi.org/10.1016/j.trpro.2021.11.091>
- [4] EASA Urban Air Mobility <https://www.easa.europa.eu/en/domains/urban-air-mobility-uam>
- [5] Bauranov, A., & Rakas, J. (2021). Designing airspace for urban air mobility: A review of concepts and approaches. *Progress in Aerospace Sciences*, 125, p.100726. <https://doi.org/10.1016/j.paerosci.2021.100726>
- [6] Schweiger, K. and Preis, L., 2022. Urban Air Mobility: Systematic Review of Scientific Publications and Regulations for Vertiport Design and Operations. *Drones*, 6(7), p.179. <https://doi.org/10.3390/drones6070179>
- [7] Full report <https://www.easa.europa.eu/sites/default/files/dfu/uam-full-report.pdf>
- [8] Santhosh, S., De Crescenzo, F. and Vitolo, B., 2022. Defining the potential of extended reality tools for implementing co-creation of user oriented products and systems. In *Design Tools and Methods in Industrial Engineering II: ADM 2021*, September 9–10, 2021, Rome, Italy (pp. 165-174). Springer International Publishing. https://doi.org/10.1007/978-3-030-91234-5_17
- [9] Bagassi, S., De Crescenzo, F., Piastra, S., Persiani, C. A., Ellejmi, M., Groskreutz, A. R., & Higuera, J. (2020). Human-in-the-loop evaluation of an augmented reality based interface for the airport control tower. *Computers in Industry*, 123, 103291. <https://doi.org/10.1016/j.compind.2020.103291>
- [10] Praticò, F. G., & Lamberti, F. (2021). Towards the adoption of virtual reality training systems for the self-tuition of industrial robot operators: A case study at KUKA. *Computers in Industry*, 129, 103446. <https://doi.org/10.1016/j.compind.2021.103446>
- [11] Sikorski, B., Leoncini, P., & Luongo, C. (2020). A glasses-based holographic tabletop for collaborative monitoring of aerial missions. In *Augmented Reality, Virtual Reality, and Computer Graphics: 7th Int.Conf., AVR 2020, Lecce, Italy, September 7–10, 2020, Proceedings, Part I* 7 (pp. 343-360). Springer International Publishing. https://doi.org/10.1007/978-3-030-58465-8_26
- [12] <https://www.easa.europa.eu/en/light/topics/vertiports-urban-environment>
- [13] <https://www.agendadigitale.eu/industry-4-0/hmi-cose-ladvanced-human-machine-interfaces-e-perche-e-utile-per-lindustria-4-0/>, Accessed on 22/05/2023.
- [14] <https://www.statista.com/>

- [15] Malich T., Hanakova L., Socha V., Van den Bergh S., Serlova M., Socha L., Stojic S., Kraus J. Use of virtual and Augmented Reality in design of software for airspace (2019) ICMT 2019 - 7th International Conference on Military Technologies, Proceedings, art. no. 8870030. <https://doi.org/10.1109/MILTECHS.2019.8870030>
- [16] Marayong, P., Shankar, P., Wei, J., Nguyen, H., Strybel, T. Z., & Battiste, V. (2020, March). Urban Air Mobility System Testbed using CAVE Virtual Reality Environment. In 2020 IEEE Aerospace Conference (pp. 1-7). IEEE. <https://doi.org/10.1109/AERO47225.2020.9172534>
- [17] Dao, Q. V., Homola, J., Cencetti, M., Mercer, J., & Martin, L. (2019, August). A Research Platform for Urban Air Mobility (UAM) and UAS Traffic Management (UTM) Concepts and Application. In International Conference on Human Interaction & Emerging Technologies (IHET 2019) (No. ARC-E-DAA-TN68588).
- [18] Aalmoes, R., & Sieben, N. (2021, March). Noise and visual perception of Urban Air Mobility vehicles. In Delft International Conference on Urban Air Mobility (DICUAM), virtual.
- [19] Stolz, Maria and Tim Laudien. "Assessing Social Acceptance of Urban Air Mobility using Virtual Reality." 2022 IEEE/AIAA 41st Digital Avionics Systems Conference (DASC) (2022): 1-9. <https://doi.org/10.1109/DASC55683.2022.9925775>
- [20] Janotta, F. & Hogreve, J (2021). Acceptance of AirTaxis – Empirical insights following a flight in virtual reality. <https://doi.org/10.31219/osf.io/m62yd>
- [21] Stewart Birrell, William Payre, Katie Zdanowicz, Paul Herriotts, Urban air mobility infrastructure design: Using virtual reality to capture user experience within the world's first urban airport, Applied Ergonomics, Volume 105, 2022, 103843, ISSN 0003-6870. <https://doi.org/10.1016/j.apergo.2022.103843>
- [22] T. Laudien, J. M. Ernst and B. Isabella Schuchardt, "Implementing a Customizable Air Taxi Simulator with a Video-See-Through Head-Mounted Display – A Comparison of Different Mixed reality Approaches," 2022 IEEE/AIAA 41st Digital Avionics Systems Conference (DASC), Portsmouth, VA, USA, 2022, pp. 1-10. <https://doi.org/10.1109/DASC55683.2022.9925870>
- [23] <https://aurora-uam.eu/#summary>
- [24] <https://360.world/clairity/#:~:text=The%20CLAIRITY%20system%20takes%20the,unique%20HMD%20and%20camera%20solutions.>
- [25] Konstantoudakis K, Christaki K, Tsiakmakis D, Sainidis D, Albanis G, Dimou A, Daras P. Drone Control in AR: An Intuitive System for Single-Handed Gesture Control, Drone Tracking, and Contextualized Camera Feed Visualization in Augmented Reality. Drones. 2022 Feb 10;6(2):43. <https://doi.org/10.3390/drones6020043>
- [26] <https://www.volocopter.com/newsroom/cae-and-volocopter-partner-to-create-global-air-taxi-pilot-workforce/>
- [27] <https://flyelite.com/evtol/>
- [28] <https://www.geospatialworld.net/news/worlds-first-augmented-reality-drone-flight-simulator-app-launched-epson/>
- [29] <https://www.dji.com/it/simulator/info>

Electric conversion of a general aviation aircraft: a case study

Sergio Bagarello^{1,2,a}, Ivano Benedetti^{1,2,b*}

¹ Department of Engineering, Università degli Studi di Palermo, Viale delle Scienze, Edificio 8, 90128 Palermo, Italy

² Sustainable Mobility Center - Centro Nazionale per la Mobilità Sostenibile – MOST – Italy

^a sergio.bagarello@unipa.it, ^b ivano.benedetti@unipa.it

Keywords: Aircraft Electric Conversion, Electric Propulsion, Electric General Aviation, Aircraft Conceptual Design

Abstract. This study analyses the process required to convert a conventional, air-breathing, piston-powered, General Aviation (GA) airplane to fully electric propulsion. The work is configured as a feasibility study for such modifications with the intent of setting a path for similar electric conversion programs on GA airplanes. The motivation behind industries' interest in alternative propulsion is examined and a full comprehension of the characteristics of the plane in question is achieved through the acquisition of transversal knowledge, examining the aircraft both from the engineering and real-world user points of view. Electric motor, batteries, auxiliary systems and implementation considerations were all made in accordance with regulatory authorities' requirements, with the purpose of making the project to comply with EASA CS Part 23. The present work analyses the performances expected from the electric plane and compares them with the standard aircraft evaluating the project's pros and cons. Considerations regarding typical mission profiles show how the electric powerplant will allow the airplane to outperform his conventional counterpart in terms of rate of climb, pollutant emission reduction, noise levels and operating costs. Such gains are however counterbalanced by the detriment of range and endurance performances, which might be deemed acceptable considering the specific plane's intended use. The study shows how, even though close integration in electric GA aircrafts is desirable since the first stages of conceptual design, piston-to-electric conversions are possible and may indeed contribute to mitigate aviation climate impact.

Introduction

In recent years, the themes of sustainability and low/zero-emissions propulsion have assumed great relevance in aviation. Aviation represents a crucial asset and the only way to transport people and goods across the world within a day. In 2016, the sector drove \$2.7 trillion in economic activity and supported 65.5 million jobs, which made up 3.6% of the global gross domestic product (GDP) [1]. However, the destructive environmental consequences of aviation are undeniable. Although flying makes up only 3.5% of total human-induced carbon emissions, it is one of the most challenging to decarbonize [1]. In the interest of sustaining policies like the MEA (More Electric Aircrafts) [2], a feasible path might consist in converting established, well-known, conventional airplanes to electric power via a process that makes the new project an interesting alternative with respect to the gas-powered counterpart, cutting the costs of designing a new plane from scratch. This study therefore analyzes the process needed to replace the propulsive system of a conventional internal combustion engine airplane with a state-of-the-art electric motor and the associated batteries for the new aircraft to be used *as a trainer and semi-acrobatic General Aviation plane*.

Conversion Process

Requirements. Considering the current state of the technology, flight time represents one of the major limitations in electrical aircraft's capability. Therefore, the logical target market for electric



aircraft would be identified by applications for which flight time and range are not as decisive as they are in commercial aviation. Student pilots normally train in flights of about one hour. Anything more is generally considered counterproductive according to most flight instructors, so flight training represents a perfect target application [3]. The aircraft chosen as case study is the *SOCATA Tampico TB-9*, a French-made, all-metal, low-wing, four-seater, single engine aircraft in use in numerous flight schools [4]. It is well-known for its straightforward approach, forgiving aerodynamics characteristics and robust build.

Batteries mass. The sizing process needs to evaluate the batteries total mass m_b [kg]. Given the required run-time endurance E [s], the mass of the batteries can be computed as

$$m_b = \frac{P_{sh} E}{E_{sb} \eta_{bzs}} \quad (1)$$

where P_{sh} is the required shaft power during run-time [kW], E_{sb} is the battery specific energy [J/kg] and η_{bzs} represents the total system efficiency from battery to motor output shaft.

A safer and more conservative approach considers the power used equal to 120 kW, the maximum rated power that the selected motor can deliver, and the required batteries mass is found to be 387 kg. However, a more detailed analysis of the mission in hand, whose features are retrieved from the aircraft flight manual [5], requires the knowledge of the expected power levels during all flight operations, which resulted in $m_b = 346.3$ kg. For the sake of the study, the more conservative value has been considered.

Powerplant installation. The conventional aircraft is equipped with a four-cylinders, direct drive air-cooled Lycoming O-320-D2A engine capable of producing 160 hp at 2700 rpm. It is connected to the frontal bulkhead via a steel engine support structure, easily modifiable to account for the different form factors of the two powerplants [6]. After a careful market survey, the more suitable engine for the conversion is found to be the Safran ENGINEUS™ in the 120 kW configuration.

Energy is provided by state-of-the-art lithium-sulfur batteries produced by Sion Power with a specific energy of 500 Wh/kg. The cathode is made of sulfur and a conductive material while the anode is made of lithium or a lithium-alloy. The reaction between lithium and sulfur is highly energetic, which leads to a high energy density in the battery.

In the conversion process, the main constraint is the need to comply with the Maximum Take-Off Weight (MTOW) of the standard model. EASA's Supplemental Type Certificate specifications allow a 5% deviation from the initial MTOW of the plane after the modifications, which will therefore be retained as a requirement. The weight check – Table 1 – shows how the removal of the internal combustion engine, of the tanks and fuel system, of fuel and of the rear bench and passengers leaves enough mass available for the installation of the motor, batteries, and auxiliary systems even in the most demanding configuration of 120 kW continuous P_{sh} . The payload reduction is clearly another cost of the conversion, but it is deemed acceptable considering the prospective use of the converted airplane as a GA trainer.

Centre of gravity preservation. Trim, stability, and structural considerations require that the new powerplant is integrated preserving the allowed CG envelope. The main components placement for the considered aircraft is schematized in Fig.1. The necessary checks are performed using the aircraft standard Mass and Balance modulus [7] as a reference – Table 2 – and verifying that in even in the most demanding configuration (two people plus baggage) the Center of Gravity stays inside its nominal envelope, Fig.1.

Table 1: Weight analysis for the converted aircraft.

TB-9 Maximum Take-Off Weight		1060 Kg	Total of Removed items
Removed items	Engine	120 Kg	- 448.76 Kg
	Tanks and fuel lines	45 Kg	
	AVGAS100LL	113.76 Kg	
	Rear passengers	170 Kg	
Added items	Electric motor	45 Kg	+442 Kg
	Batteries	387 Kg	
	Cables and Insulation	10 Kg	
Electric TB-9 Take-Off Weight		1053 Kg	Total of Added items

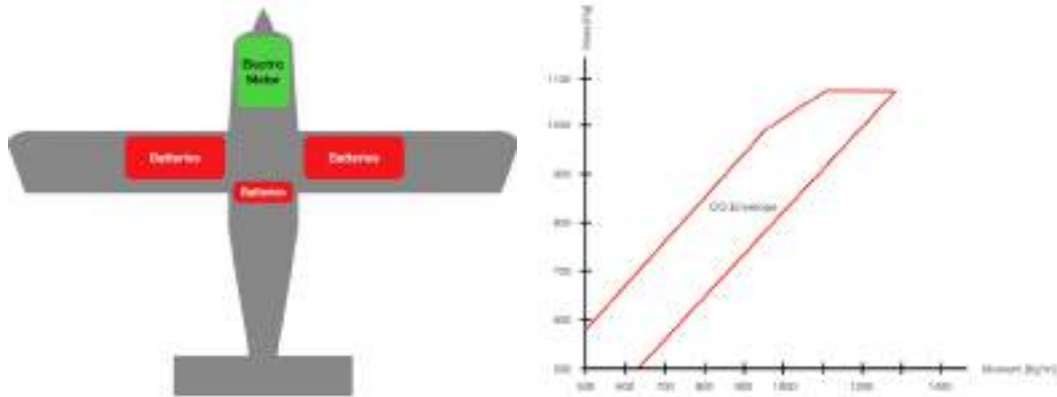


Figure 1: Components placement (left) and center of gravity envelope (right) for the converted aircraft.

Table 2: mass and balance check.

	Weight [kg]	Arm [m]	Moment [Kgm]
Aircraft	808	0.965	779.72
Pilot and co-pilot	170	1.155	196.35
Baggage	65	2.035	132.275
TOTAL	1043		1108.345

Performance evaluation. In conventional engines, the volumetric efficiency decreases significantly with altitude: electric engines, on the contrary, are not susceptible to altitude variations in terms of power output. The limiting factor in terms of ceiling of the electrified airplane is related to air density decreases through propeller and lifting surfaces. With the implementation of electric technology, at 80 KIAS, the rate of climb achievable, and more importantly, sustainable for a longer time, will be given by

$$V_V = \frac{\eta_p P_{sh}}{W} - \frac{V}{(L/D)} \quad (2)$$

where V is the flight speed, η_p is the propeller efficiency, W the aircraft weight [N] and $\frac{L}{D}$ is the lift-to-drag ratio. For the case in hand, Eq.(2) provides $V_V = 1212$ ft/min.

Range is strongly affected by the limitations of the employed technology: in the case in hand the usable run-time endurance will be limited to 60 min for normal operations plus sufficient energy supply to sustain a holding pattern of 30 min. The theoretical range can be estimated as

$$R = \frac{E_{sb} \eta_{bzs} \eta_p}{g} \left(\frac{m_b}{m} \right) \left(\frac{L}{D} \right) \quad (3)$$

where m_b/m is the battery mass fraction. For the considered case Eq.(3) provides $R = 353$ km. Operating costs significantly benefit from the electric conversion and, considering the price of electricity at the time of the development of the study of €0.35/kWh, 20% savings per flight-hour are estimated with respect to AVGAS operations, see Table 4.

Table 4: Performance analysis for the converted aircraft.

Theoretical Range	–55.7%
Endurance	–68.75%
Payload	–43%
Climb rate	+61.6%
Cost per flight hour	–20%
Emissions	–100%

Summary

The electric conversion of a GA trainer aircraft has been assessed. Although range and endurance are heavily affected by the limitations of the current battery technology, as expected, the other performances remain acceptable or are even enhanced and the overall platform may be profitably employed in applications where range and endurance are not the main concern, as in the considered case of training aircraft. While the platform emissions are certainly reduced, overall emission reductions depend on the *green quality* of the energy sources employed for battery recharging.

Acknowledgements

The authors acknowledge the support of the Sustainable Mobility Center (Centro Nazionale per la Mobilità Sostenibile - CNMS) under Grant CN00000023 CUP B73C22000760001.

References

- [1] Kousoulidou M, Lonza L, European Aviation Environmental Report 2016. EASA, EEA, EUROCONTROL; JRC99523, 2016
- [2] Brelje, BJ, Martins, JRRA, Electric, hybrid, and turboelectric fixed-wing aircraft: A review of concepts, models, and design approaches. *Progress in Aerospace Sciences*, 104, 1-19, 2019. <https://doi.org/10.1016/j.paerosci.2018.06.004>
- [3] Raymer, D., *Aircraft design: a conceptual approach*, American Institute of Aeronautics and Astronautics, 2012. <https://doi.org/10.2514/4.869112>
- [4] GlobalAir.com, “Socata Tampico TB-9“, GlobalAir, <https://www.globalair.com/aircraft-for-sale/specifications?specid=523>, 2023
- [5] AeroClub Palermo DTO Flying School, *Manuale di impiego – Velivolo Socata TB-9*, Palermo (PA), 90137 Italy, 2019
- [6] Lycoming Engines, *O-320 Series Operator’s Manual*, Williamsport, PA 17701 USA, 2006
- [7] AeroClub Palermo DTO Flying School, *Modulo di caricamento e centraggio – Velivolo Socata TB-9, Modello CO5, Ed.1*, Palermo (PA), 90137 Italy, 2019

Aerodynamic design of advanced rear end for large passenger aircraft

Salvatore Corcione^{1,a*}, Vincenzo Cusati^{1,b} and Fabrizio Nicolosi^{1,c}

¹ Industrial Engineering Department, University of Naples Federico II, Via Claudio 21, 80125, Naples, Italy

^asalvatore.corcione@unina.it, ^bvincenzo.cusati@unina.it, ^cfabrnico@unina.it

Keywords: Aircraft Design, Forward Swept Tailplane, Leading Edge eXtension, Aerodynamics

Abstract. This paper focuses on the aerodynamic design of an advanced rear end concept for a large passenger aircraft, such as the Airbus A320. The aim was to reduce the size of the horizontal tailplane to minimize the aerodynamic drawbacks related to longitudinal stability and control requirements. This reduction would lead to improved aircraft performance by reducing fuel burn and rear-end weight. Assuming the same position of the aerodynamic center of the horizontal tailplane of a conventional aircraft, the results of this investigation showed that the required stabilizing performance of the tail could be achieved with a smaller tail surface. A reduction of 6% in tail planform area was achieved by leveraging the unique aerodynamic characteristics of a forward-swept tail, combined with the implementation of a leading-edge extension device. The reduced wetted area and the lower weight of the horizontal empennage could result in fuel savings of 100 to 120 kg of fuel per 1,000 km. This is equivalent to approximately 1.0 to 1.2% for the specific aircraft category being considered.

Introduction

Advancements in design and improvements in empennage efficiency and effectiveness have the potential to enhance aircraft performance by reducing fuel burn and weight through reductions in tail-plane size. The penalties associated with meeting both longitudinal and directional stability and control requirements constitute a significant portion of the total aircraft drag. Loads acting on aircraft tails contribute to the overall induced drag, compressibility, profile drag, structural weight, and maximum lift capability of the aircraft. The empennage of a typical Large Passenger Aircraft accounts for one-fifth to one-fourth of the total lifting surface and 3% up to 6% of the maximum take-off weight. It contributes 5% to 8% to the total trimmed drag in cruise conditions [1].

The simplest unconventional solution is represented by the Vee-tail [2,3]. This solution is sometimes used in remotely piloted aircraft and has also been implemented in mass-produced manned aircraft, such as the Beechcraft Bonanza M35. However, the results of the NEFA [4] project concluded that although a Vee-tail configuration offered performance improvements due to its reduced wetted area, the added complexity and additional system did not result in any weight or cost benefits over a conventional empennage. A comprehensive study on advanced rear-end configurations was recently conducted in the EU-funded project NACRE [5] demonstrated that these configurations could offer advantages in terms of reducing empennage drag, but not in terms of weight.

To further advance the implementation of rear-end concepts that effectively reduce drag and weight, the utilization of a forward-swept horizontal tailplane could represent a viable way.

The adoption of a forward-swept tailplane enables a structural configuration in which the connection of the horizontal tail to the rear end does not require a structural opening in a region of the fuselage that is heavily affected by structural loads [6]. By removing the structural opening at the rear end, the weight of the fuselage can be reduced. This solution also reduces fuselage deformations, resulting in a more efficient horizontal stabilizer surface [6].



Transonic aircraft wings typically have a positive sweepback. The main reason is linked to the aircraft encountering a vertical gust during its flight. In the case of positive sweepback, the bending deformation decreases the local angle of attack, resulting in a natural reduction of aerodynamic loads. In the case of a wing with a negative sweep angle, the effect is reversed. As a result, static divergence may occur, leading to structural failure. Forward-swept wings are capable of withstanding significantly higher gust loads compared to wings with positive sweepback, making them heavier. Despite this drawback, several studies have explored the potential of utilizing the aerodynamic advantages of a forward-swept wing [7,8] propose a solution to mitigate the coupling between flexional and torsional deformation by using aeroelastic tailoring techniques. In terms of structural sizing, aeroelasticity is less demanding for wings with a relatively low aspect ratio. Thus, in the case of horizontal tails, introducing negative sweep angles could be a viable solution to improve the performance of the rear-end and empennage.

Forward-swept lifting surfaces offer several aerodynamic advantages over conventional sweepback designs. For a given leading edge sweep angle, forward-swept wings exhibit a shock-sweep angle that is five degrees higher than that of aft-swept wings [9]. Therefore, the implementation of a forward-swept design requires a smaller leading edge sweep angle compared to a positively swept-back configuration with an equivalent sweep angle at the quarter chord line. Moreover, in a forward-swept wing, the airflow moves from the root to the tip, resulting in higher stall angles [10], increasing the maximum aerodynamic forces or reducing the tailplane area can yield the same maximum force, potentially leading to a decrease in drag and weight.

This paper deals with the aerodynamic design of an advanced rear-end configuration carried out within the EU-funded project named IMPACT [11]. The aim is to optimize the rear-end of the fuselage and empennage of large passenger aircraft to reduce drag, weight, and fuel burn. The investigation focuses on minimizing the surface area of the horizontal tailplane by utilizing the unique characteristics of a forward-swept lifting surface, which is further enhanced by passive leading edge extension devices.

Advanced Rear End Aerodynamic design

To fully catch the peculiar aerodynamic features, high-fidelity CFD RANS calculation were required. The high-fidelity analysis was performed using the commercial software STARCCM+. Details of the numerical model setup are reported Table 1, whereas Figure 1 shows a comprehensive overview of the fluid domain and the application of boundary conditions. The investigation started by comparing the reference isolated tailplane geometries: a conventional tail (HTP) and a reference forward-swept arrangement. Table 2 summarizes the main design parameters. Results clearly indicate that the isolated forward-swept tail arrangement effectively wash in the aerodynamic loads. Thanks to this peculiar behavior, the FSHTP exhibits better aerodynamic performance in terms of lift curve slope and maximum achievable negative lift coefficient, as indicated by the chart of Figure 2. This means that an aerodynamically equivalent forward-swept tail would require a smaller area to reach the same aircraft stability and control characteristics.

Since an additional component must be added, this element can be designed to enhance the lifting capacity of the tail. In this respect, the additional element would be a leading-edge extension device (LEX).

Table 1 Numerical setup and mesh characteristics for high-fidelity CFD analysis

Parameter	Value
Domain span	$16 b_H/2$
Domain height	$30 b_H/2$
Domain length	$100 b_H/2$
Mesh type	unstructured polyhedral
On body minimum surface size	0.0042 (m)
On body target surface size	0.035 (m)
Number of volume cells	11 183 156
Number of prism layers	25
First cell wall distance	$1e^{-6}$ (m)
Turbulence model	SST $\kappa-\omega$
Flow model	Compressible
Inflow boundary condition	Free stream
Outflow boundary condition	Pressure outlet
Number of iterations	5000
Mach number	0.2
Flight altitude	sea level

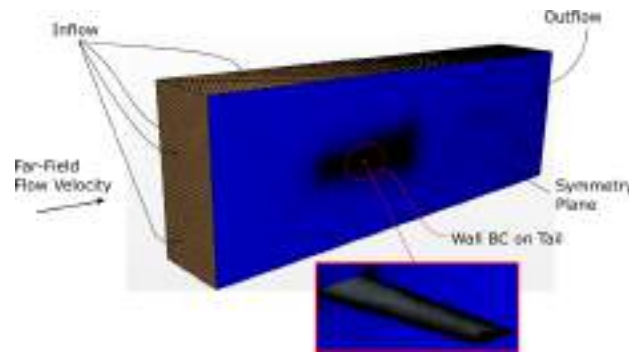


Figure 1 Fluid domain and boundary conditions using STAR-CCM+.

Table 2 Reference geometries, HTP and FSHTP.

	HTP	FSHTP
Sweep angle	32 deg	-15 deg
S_H	31.36 m ²	31.36 m ²
$b_H/2$	6.723 m	6.723 m
Taper Ratio	0.36	0.715
Aspect Ratio	5.765	5.765

Unfortunately, these advantages are lost when considering the fuselage-tail configuration. The forward-swept tail arrangement exhibits significant separation at the junction with the fuselage. This reflects on the lifting capabilities, as shown in Figure 3.

To design an effective advanced rear end that incorporates a forward-swept tailplane, an additional component must be introduced to prevent significant flow separation at the junction of the fuselage.

Leading Edge eXtensions (LEX) are aerodynamic features found on some aircraft, typically fighter jets. LEX refers to the forward extensions of the wing root area, usually in a triangular or trapezoidal shape. They are located at the junction between the wing and the fuselage. The primary purpose of LEX is to improve the aircraft's high angle-of-attack performance and enhance its manoeuvrability.

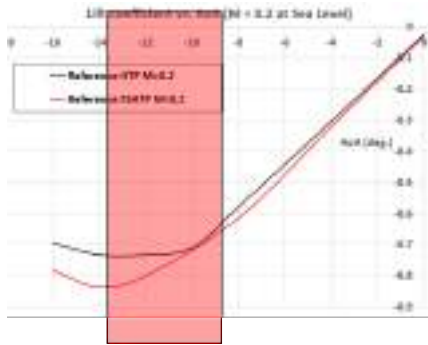


Figure 2 Comparison of the lift coefficient curves for conventional HTP and FSHTP configurations.

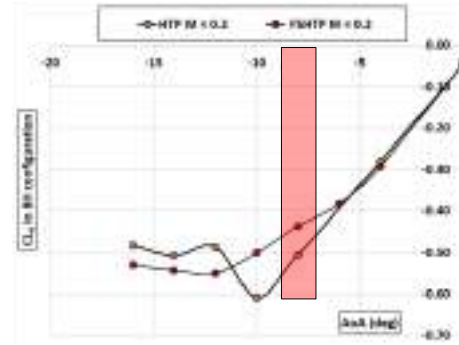


Figure 3 Comparison of the lift coefficient curves for HTP and FSHTP (body and horizontal tailplane).

By performing a Design of Experiment about several forward-swept tailplanes and LEX designs, see Figure 4, the best solution has been identified. As shown by the results of Figure 5, the maximum lift capabilities of the horizontal empennage can significantly be improved by introducing a forward-swept tailplane enhanced by a LEX device. The optimum solution (see the solid grey line in Figure 5), provides for a tailplane area which is 6% lower than the reference tails (see Table 3) giving a maximum negative lift coefficient which is approximatively 20% higher than the reference conventional tailplane.

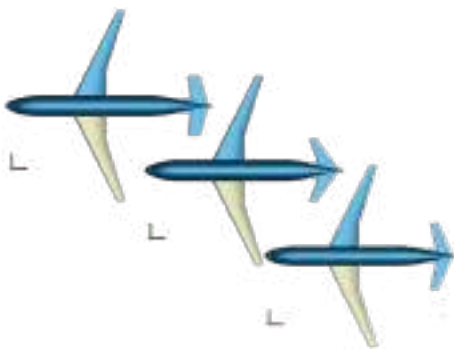


Figure 4 Some configurations investigated in the DoE execution.

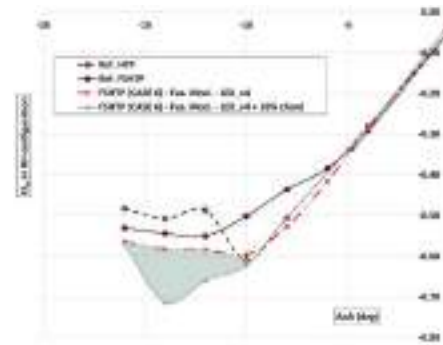


Figure 5 Lift coefficient curves for reference HTP, FSHTP and best FSHTP enhanced by a LEX device (in body and horizontal tailplane arrangement).

Table 3 Geometric parameters, reference HTP, FSHTP and Optimised FSHTP and LEX.

	HTP	FSHTP	Optimised FSHTP+LEX
Sweep angle	32 deg	-15 deg	-10 deg
S_H	31.36 m ²	31.36 m ²	29.45 m ²
b_H/2	6.723 m	6.723 m	6.723 m
Taper Ratio	0.36	0.715	0.620
Aspect Ratio	5.765	5.765	6.103
(C_{LEX}+C_{rootH})/C_{rootH}	---	---	1.804
b_{LEX}/b_H	---	---	0.217

References

- [1] Anderson, J.D., Aircraft Performance and Design, WCB McGraw-Hill, Boston, MA, USA, 1999
- [2] Sánchez-Carmona, A. and Cuerno-Rejado, C. and García-Hernández, L., Unconventional tail configurations for transport aircraft, Progress in Flight Physics 9 (2017) 127-148.
<https://doi.org/10.1051/eucass/2016090127>
- [3] Sánchez-Carmona, A. and Cuerno-Rejado, C., Vee-tail conceptual design criteria for commercial transport aeroplanes, Chinese Journal of Aeronautics 32 (2019) 595-610. Chinese Journal of Aeronautics. <https://doi.org/10.1016/j.cja.2018.06.012>
- [4] CleanSky, New empennage for aircraft (NEFA), <https://cordis.europa.eu/project/id/G4RD-CT-2002-00864>
- [5] Frota, J. and Nicholls, K. and Müller, M. and Gall, P.E. and Loerke, J. and Macgregor, K. and Schmollgruber, P. and Russell, J. and Hepperle, M. and Dron, S. and Plötner, K. and Gallant, G., Final Activity Report. New Aircraft Concept Research (NACRE), NACRE Consortium: Blagnac, France (2010). <https://cordis.europa.eu/project/id/516068/reporting>
- [6] Llamas Sandin, R.C. and Luque Buzo, M., Aircraft Horizontal Stabilizer Surface, Google Patents (2010) US 2010/0148000 A1. <https://patents.google.com/patent/US20100148000A1/en>
- [7] Seitz, A. and Kruse, M. and Wunderlich, T. and Bold, J. and Heinrich, L., The DLR Project LamAiR: Design of a NLF Forward Swept Wing for Short and Medium Range Transport Application, 29th AIAA Applied Aerodynamics Conference (2012).
<https://doi.org/10.2514/6.2011-3526>
- [8] Seitz, A. and Hübner, A. and Risse, K., The DLR TuLam project: design of a short and medium range transport aircraft with forward swept NLF wing, CEAS Aeronautical Journal 11 (2020) 449-459. <https://doi.org/10.2514/6.2011-3526>
- [9] Roskam, J. and Lan, C.T.E., Airplane Aerodynamics and Performance, DARcorporation, Lawrence, Kansas 66044, USA, 1999
- [10] Bertin, J.J. and Cummings, R.M., Aerodynamics for Engineers, Pearson Education International, Upper Saddle River, NJ, 2009
- [11] Aircraft advanced rear end and eMpennage oPtimisaAtion enhanced by anti-iCe coaTings and devices (IMPACT), GA no. 885052. <https://www.impact-cleansky-project.eu/>

Towards multidisciplinary design optimization of next-generation green aircraft

Luca Pustina^{1,a*}, Matteo Blandino^{1,b}, Pietro Paolo Ciottoli^{1,c} and Franco Mastroddi^{1,d}

¹Department of Mechanical and Aerospace Engineering, Sapienza University of Rome, Via Eudossiana 18, 00184 Rome, Italy

^aluca.pustina@uniroma1.it, ^bmatteo.blandino@uniroma1.it, ^cpietropaulo.ciottoli@uniroma1.it, ^dfranco.mastroddi@uniroma1.it

Keywords: Green Aircraft, Multi-Disciplinary Optimization, Reduced Order Model

Abstract. Reducing greenhouse gas emissions is one of the most important challenges of the next future. The aviation industry faces increasing pressure to reduce its environmental footprint and improve its sustainability. This work is framed within the Italian national project “MOST- Spoke 1 - AIR MOBILITY - WP5,” which studies innovative solutions for next-generation green aircraft. This paper proposes a multidisciplinary design optimization (MDO) framework for the design of new-generation green aircraft. Several propulsion solutions are analyzed, including fully electric and hydrogen fuel cells. The Multidisciplinary Design Optimization (MDO) framework considers several disciplines, including aerodynamics, structures, flight dynamics, propulsion, cost analysis, and life-cycle analysis for facing at the best the design challenge of next-generation green aircraft.

Introduction

For developing new-generation green aircraft, it is important to consider the interactions between the system's disciplines. Through early resolution of the multidisciplinary optimization (MDO) problem using state-of-the-art computational analysis tools, it is possible to enhance the design while concurrently minimizing the time and cost associated with the design cycle. In the realm of developing next-generation environmentally friendly aircraft, while the Maximum Take Off Mass (MTOM) remains a conventional optimization objective due to its strong correlation with the overall lifecycle cost of the aircraft, it is crucial to conduct a thorough-life cycle analysis and establish a metric for assessing the aircraft's overall environmental sustainability. Accurately modeling new-generation environmentally friendly propulsion systems and establishing a merit function for comparing the environmental friendliness of aircraft, such as the total equivalent CO₂, is crucial. In addition to traditional disciplines like aerodynamics, structures, and flight dynamics, green propulsion system modeling and life cycle analysis are essential, even in early design stages. This study provides an overview of physical-based models for structural analysis, aerodynamics, green propulsion systems, and life cycle analysis for preliminary design. Moreover, a Multi-Disciplinary Optimization (MDO) architecture is presented, including considerations of Design Variables (DVs), constraints, and objective functions.

Structural modeling

Structural models are essential for optimizing aircraft performance, efficiency, and safety. They must withstand different loads and conditions while being lightweight to maximize range, payload capacity, and minimize operating costs. Various low fidelity structural models are used for aircraft optimization, such as analytical beam models. Beam models efficiently represent elongated components like wings, fuselages, and tails, considering bending, shear, torsion and axial loads. They provide insights into stress distribution, deflections, and dynamic response, assuming linear



elasticity, small deflection theory, and homogeneous materials. Beam models are valuable for preliminary design, concept exploration, and rapid evaluation of structural configurations. However, with enhancements in computational capabilities, Finite Element Models (FEM) have gained popularity in aircraft optimization due to their versatility and accuracy. Moreover, FEM allows for a more detailed analysis of complex geometries. It is particularly beneficial for innovative aircraft configurations such as, for example, the blended wing body, and truss braced wings. In this work, a FEM model of the entire aircraft is generated using an in-house code called FUROR (Framework for aUtomatic geneRatiOn of aeRoelastic models) based on the input of assigned set of design variables. FUROR utilizes the open-source geometric library OpenCasCade to automatically generate the wing boxes and fuselage geometries, and the open-source code GMSH for automatic FEM grid generation. The generation of the aircraft FE model involves three steps. First, the aircraft geometry is defined based on main standard geometrical characteristics such as wingspan, dihedral, sweep, chord, and fuselage length (see Fig. 1). Additionally, the geometry of the main structural components, including wing spars, ribs, and stringers, is also defined. In the second step, a hybrid structured-unstructured FEM mesh is generated using GMSH. Finally, the complete FE aircraft model is generated, where the beam sections and shell thickness of the FEM model are defined in a standard Nastran input file. Furthermore, during this phase, the connections between the wings and the fuselage are established using a simplified approach that is compatible with the early design stage. Additionally, FUROR has the capability to generate the aerodynamic wing model, which will be discussed in detail in the following section.



Fig. 1: Generation of FE aircraft models with different main standard geometrical characteristics. In grey a standard regional aircraft, in blue an increased wingspan design and in red an increased wing sweep design.

Aerodynamic modeling

Aerodynamic modeling is crucial in the preliminary design for evaluating forces and mission performance. Various models exist with different accuracy and computational cost. Simplified physical-based aerodynamics models such as strip theory, doublet lattice, or vortex lattice methods are crucial in the field. Strip theory divides the wing into sections, evaluating the local angle of attack for each. Lookup tables determine each segment's lift and drag coefficients and the corresponding aerodynamic forces. A correction factor is applied for three-dimensional effects, and the Theodorsen method can be used for unsteady aeroelastic dynamic analyses. Strip theory enables the estimation of aerodynamic efficiency with drag estimation, also approximately incorporating viscous effects. However, strip theory lacks accuracy in estimating three-dimensional effects and wing interactions because simple analytical models are typically used in such cases. In preliminary design, the doublet lattice method is commonly employed as a three-dimensional model. It offers enhanced accuracy in lift evaluation, making it suitable for aeroelastic analysis and accounting for finite wake effects. In the FUROR software, both the strip theory approach and the doublet lattice method are available.

Propulsion Modeling

The proposed model for the propulsive system is based upon the work of De Vries et al. [1]. Authors aimed to propose a simple method for evaluating the benefits and technological needs of integrating a secondary energy source (batteries or fuel cells) with the primary thermal source (fuel) in the redesign of an existing aircraft. In this method, the various configurations are characterized by the supplied power ratio, which represents the ratio between the power output from the batteries and the total power output, taking into account the electric subsystem and the fuel. The proposed method combines constraint analysis, mission analysis, and subsequent aircraft mass estimation. The first step involves a classical constraint analysis that aims to meet all mission requirements by utilizing an aircraft propulsive power constraint diagram.

From this diagram [1], a specific design point is selected based on the power-to-weight ratio (P_p/W_{TO}) and wing loading (W_{TO}/S). Then, the next step consists of quasi-stationary mission analysis to size the aircraft in energy terms, having chosen a first attempt MTOM. A simplified mission profile is selected, consisting of different flight phases. Various authors [2,3] have derived analytical formulas similar to the Breguet equation or modified it for hybrid aircraft, but these formulas depend on the aircraft configuration, and there is no universally optimal choice. The presented design method explores different approaches for using battery and fuel in specific flight phases. The energy requirements from both fuel and battery sources are integrated over the entire mission duration. In the final phase, the aircraft's masses are estimated, including energy sources and propulsion system components. From these mass estimates and the mass outcomes of the structure subsystem, MTOM is derived, which corresponds to the energy required by the two energy sources to complete the mission. The last two steps of the method are iterated until the MTOM value of two consecutive iterations converges below a certain chosen tolerance. Lastly, a basic life cycle analysis should be conducted to estimate the total CO₂ emissions. This analysis considers not only fuel emissions from gas turbine engines but also battery discharge for hybrid/full-electric aircraft, as well as the production and transportation of aircraft components. This approach ensures a fair comparison among the proposed configurations.

Multidisciplinary Design Optimization

The initial stage of aircraft design involves establishing the Top-Level Aircraft Requirements, e.g., desired overall performance, capabilities, and main characteristics of the aircraft. Traditionally, the optimization objective has focused on the Maximum Take Off Mass (MTOM) due to its close relationship with the overall lifecycle cost of the aircraft. A thorough life cycle analysis is crucial in developing eco-friendly aircraft to evaluate overall environmental sustainability. After defining the objective functions, the next step involves selecting the DVs and determining their ranges. Both structural and shape variables must be employed. Structural variables primarily focus on minimizing weight, while shape variables contribute to the optimization of aerodynamics which is of the utmost importance for the propulsion design to the evaluation of the energy requirements. Finally, to fully address the MDO problem, constraints need to be defined. This includes considering mission constraints such as range and altitude, conducting a stress assessment for extreme maneuver load cases to ensure aircraft safety, and incorporating constraints directly related to the propulsion system such as take-off distance and the estimated specific energy for the batteries and fuel cells that will be introduced in the weight estimation process. The design space can be systematically investigated by an optimizer (a possible choice is the Multi Objective Genetic Algorithm) to uncover the Pareto front of the selected objective functions (MTOM and total equivalent CO₂). When the complete multidisciplinary analysis (MDA) is executed for every set of DVs, the MDO framework is referred to as Multi-Disciplinary Feasible (MDF) architecture [4]. This ensures the feasibility of each discipline for every set of DVs. The MDA involves conducting a trim and static structural analysis for various extreme maneuver load cases, followed by an aeroelastic analysis to ensure sufficient aeroelastic damping during maximum aircraft speed

conditions (see Fig. 2). Additionally, the constraint and mission analysis are carried out to estimate the required battery pack (or fuel cells) mass necessary to accomplish the TLARs. Finally, the life cycle analysis is performed. To handle interdependencies among disciplines, an iterative approach is used, ensuring convergence of the MDA by matching the disciplines' output copy with the final output.

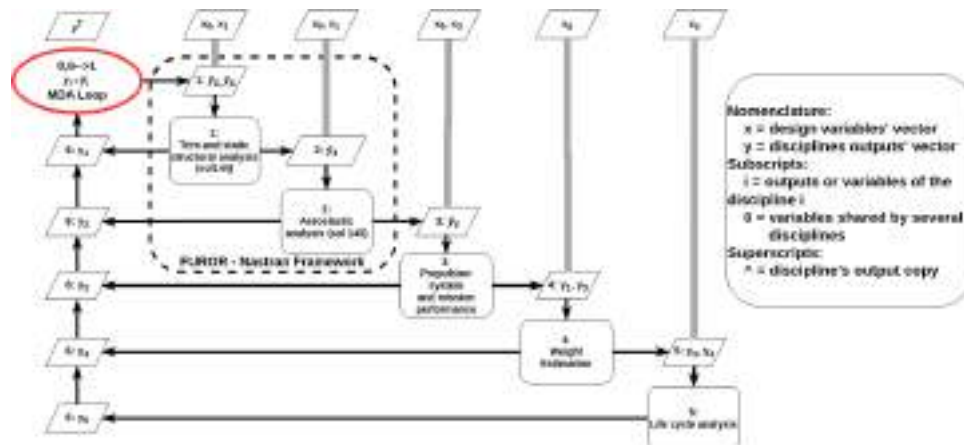


Fig. 2: Multi-Disciplinary Analysis Extended Design Structure Matrix [4]

Conclusions

This work presents an MDO architecture for advanced green aircraft, outlining the objective function, constraints, and design variables. Additionally, it describes the reduced order models (ROMs) for each discipline with appropriate fidelity for early design. The subsequent phases involve implementing the proposed MDO framework and conducting optimization on a reference regional aircraft, exploring various propulsion systems and innovative configurations (e.g., blended wing body, truss braced wing).

Acknowledgements

This work is part of the research activity developed by the authors within the framework of the “PNRR” CN4 MOST (Mobilità sostenibile): SPOKE 1 (Air Mobility), WP5: “Multidisciplinary design optimization and innovative solutions for next generation green aircraft with demonstrator”.

References

- [1] De Vries R., Brown M., and Vos R. Preliminary sizing method for hybrid-electric distributed propulsion aircraft. *Journal of Aircraft*, pages 2172–2188, 2019.
<https://doi.org/10.2514/1.C035388>
- [2] Voskuil M., van Bogaert J., and Rao A. G. Analysis and design of hybrid electric regional turboprop aircraft. *CEAS Aeronautical Journal*, Vol. 9, pages 15–25, 2018.
<https://doi.org/10.1007/s13272-017-0272-1>
- [3] Wroblewski G. E. and Ansell P. J. A bréguet range equation for hybrid-electric jet aircraft sizing and analysis. *AIAA Propulsion and Energy 2020 Forum*, pages 1–24, 2020.
- [4] Martins, Joaquim RRA, and Andrew B. Lambe. "Multidisciplinary design optimization: a survey of architectures." *AIAA journal* 51.9 (2013): 2049-2075.
<https://doi.org/10.2514/1.J051895>

Improvements in on-board systems design for advanced sustainable air mobility

Claudia Conte^{1,a*} and Domenico Accardo^{1,b}

¹Department of Industrial Engineering, University of Naples Federico II, Italy

^aclaudia.conte2@unina.it, ^bdomenico.accardo@unina.it

Keywords: Model Based Systems Engineering, Embedded Systems, Unmanned Aerial Systems, U-Space

Abstract. This paper describes the activity proposed in the context of National Center for Sustainable Mobility (CN MOST) for designing an advanced core Guidance, Navigation, and Control system together with an effective on-board systems configuration for sustainable air mobility. A Model Based Systems Engineering strategy is adopted to support the design and development phases. The introduction of new sustainability objectives and the U-Space services to support the integration of unmanned air vehicles in the traditional Air Traffic Management drives the need of a full redesign of on-board systems that must be interfaced with different air platform categories. High performance processing units are considered for embedded systems, including but not limited to machine learning based, image processing and data fusion algorithms for advanced navigation. Three use-cases are presented as reference platform and mission types for validating the proposed systems configuration, specifically unmanned electric Vertical Take Off and Landing aircraft, fully electric general aviation aircraft, and hybrid-electric regional aircraft.

Introduction

The worldwide effort to increase technological improvement towards more sustainable air mobility is focusing on advanced propulsion systems, effective route planning, efficient airframe design and high-performance on-board Guidance, Navigation, and Control (GN&C) solutions [1-4]. Moreover, an innovative redesign of on-board equipment and systems is needed to meet new requirements and guarantee high safety levels according to the rapid changes of Air Traffic Management (ATM) that will include manned and unmanned vehicles with different specifications [5].

The need to integrate the so-called Unmanned Aerial Systems (UASs) with the existing traditional aviation is the focus of several programs [6]. The European response to this need has been implemented thanks to the definition of U-Space [7] for operations at Very Low Level (VLL) airspace in the context of the UAS Traffic Management (UTM). The definition of standard services - such as contingency management, traffic information, identification, collision avoidance, tracking - that allow to safely manage several vehicles with different tasks drives the design and development of specific on-board equipment with an increasing level of autonomy. Modular on-board systems configurations [8] can support the development of core enabling modules that can be designed for a wide range of vehicles also thanks to the use of low-cost Commercial Off The Shelf (COTS) processing units [9].

This paper aims at presenting an overview of the design activity focused on on-board systems configuration in the context of integrated ATM/UTM environment. Modular configurations are investigated to adapt innovative features of core GN&C systems to different air vehicles also assessing specific risk analysis evaluations for strategical and tactical mission management.



Overview of On-board Systems Design

The rapid evolution of air traffic requirements carries out the design and development of advanced on-board systems that must meet new mission profiles. Data fusion algorithms, Machine Learning based methods and modular configurations are the main drivers for innovative enabling technologies that support new generation air vehicles in complex environments.

A groundbreaking approach that follows all the design and development phases by using an advanced implementation method for systems modeling will support the adoption of advanced hardware and software components as well as effective real-time processing algorithms, such as the Model Based Systems Engineering (MBSE). The International Council On Systems Engineering (INCOSE) is developing several initiatives in the field of MBSE [10]. The National Aeronautics and Space Administration (NASA) started the MBSE Pathfinder in space topics [11]. The European Space Agency (ESA) founded the MB4SE and OSMOSE groups to introduce the MBSE concept [12].

The main aim of the proposed activity is the design of an advanced core GN&C system that can be adapted to different types of air vehicles and interfaced with the under development services of the integrated ATM/UTM. The general workflow description is reported in Fig.1 by following an MBSE approach [13] that helps to reduce the risk of unexpected redesign issues.

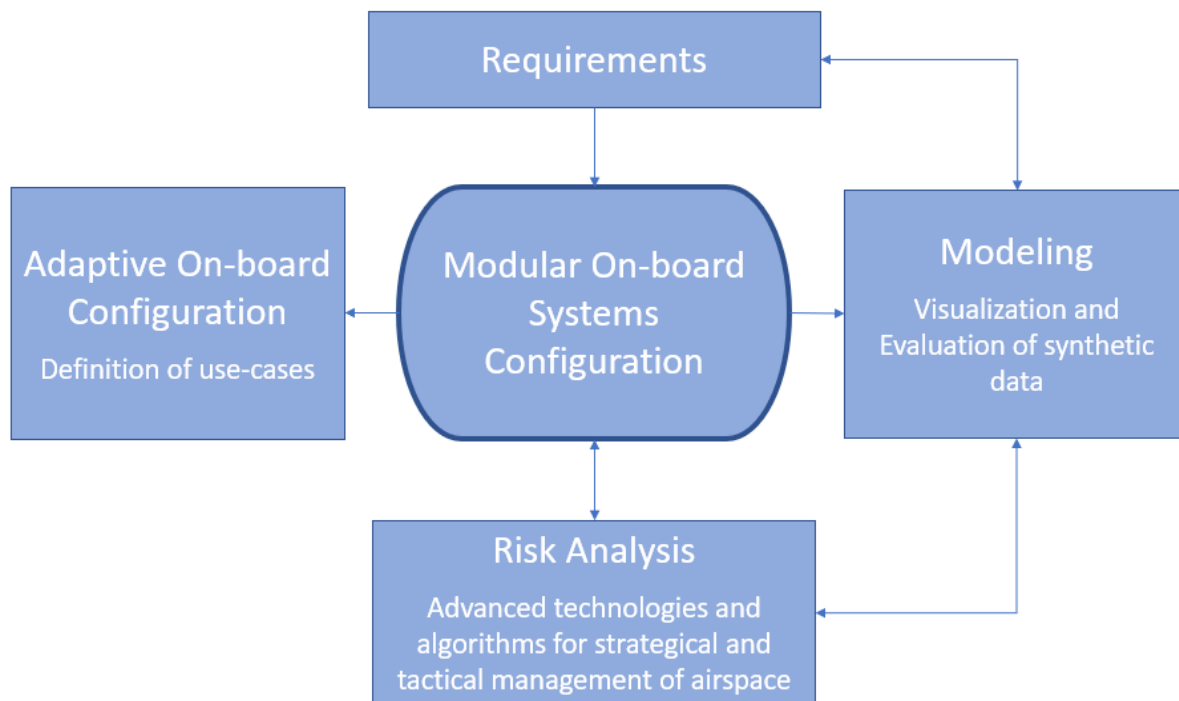


Fig. 1. Schematic description of the workflow for the proposed on-board systems design.

The requirements definition involves the selection of possible stakeholders and the regulatory framework analysis. Specific user needs must be highlighted, such as business goals, safety and security issues, and typical mission profiles must be identified. A model-based design strategy helps the development of a modular configuration and thanks to the evaluation and visualization in dedicated Human Machine Interfaces (HMIs) of synthetic output data, a risk analysis of the designed aerial system can be carried out to safely manage the mission at both strategical and tactical levels. The development of specific systems models allows to refine the initial requirements and associate each requirement to the related system module. Ad hoc use cases must

be designed to validate the identified requirements and test the developed modular configuration in different scenarios.

Definition of Use Cases

The preliminary analysis of requirements for the proposed design solution involves the identification of reference platforms and missions. The aerial vehicles that are included in the analysis are: i) unmanned electric Vertical Take Off and Landing (eVTOL) aircraft, such as [14], ii) fully electric general aviation aircraft, such as [15], and iii) hybrid electric regional aircraft, such as [16].

The unmanned eVTOL platform is involved in the context of Smart Cities [17] for Urban Air Mobility (UAM) purposes. Typical mission profiles include package delivery and air-taxi operations.

The fully electric general aviation aircraft is one of the reference platforms for fully electric propulsion as well as electric on-board systems implementation. Personal transport and dedicated professional applications, such as surveillance and mapping are some relevant missions.

The hybrid electric regional aircraft involves the challenge of developing more electric on-board systems configuration for medium haul routes. The main designed task is related to commercial aviation transport with less than 100 seats also considering high efficiency sustainability features.

The mentioned platforms are the reference case study for the design of an adaptive on-board system configuration, identifying the core modules and enabling technologies to meet the developing requirements of air mobility.

Conclusion

This paper describes an overview of on-board design activity carried out in integrated manned and unmanned aviation with new needs and services. The development of proper design strategies for on-board systems helps address the increasing complexity level. During the activity, the on-board systems design can be carried out according to an MBSE strategy to manage more complex implementations. The main expected advantages of the proposed strategy include the rapid integration in the digital environment, the assessment of inter-modules interactions, the increase of overall system reliability level and the reduction of commercial implementation.

Acknowledgments

This study was carried out within the National Center for Sustainable Mobility (Centro Nazionale per la Mobilità Sostenibile CN MOST CN00000023 - PNRR - M4C2 Inv. 1.4). This manuscript reflects only the authors' views and opinions, neither the European Union nor the European Commission can be considered responsible for them.

References

- [1] A. H. Epstein, S. M. O'Flarity, Considerations for Reducing Aviation's CO₂ with Aircraft Electric Propulsion, *Journal of Propulsion and Power*, AIAA, 2019, vol 35:3, pp. 572-582, <https://doi.org/10.2514/1.B37015>
- [2] V. Grewe, A. Gangoli Rao, T. Grönstedt, et al., Evaluating the climate impact of aviation emission scenarios towards the Paris agreement including COVID-19 effects, *Nature Communications*, 2021, 12, 3841, <https://doi.org/10.1038/s41467-021-24091-y>
- [3] D. Eisenhut, N. Moebs, E. Windels, D. Bergmann, I. Geiß, R. Reis, A. Strohmayr, Aircraft Requirements for Sustainable Regional Aviation, *Aerospace*, 2021, 8, 61. <https://doi.org/10.3390/aerospace8030061>

- [4] N. Avogadro, M. Cattaneo, S. Paleari, R. Redondi, Replacing short-medium haul intra-European flights with high-speed rail: Impact on CO2 emissions and regional accessibility, *Transport Policy*, 2021, vol. 14, pp. 25-39, <https://doi.org/10.1016/j.tranpol.2021.08.014>
- [5] Information on <https://www.sesarju.eu/newsroom/brochures-publications/state-harmonisation>
- [6] Information on https://www.faa.gov/uas/research_development/traffic_management.
- [7] C. Barrado, M. Boyero, L. Brucculeri, G. Ferrara, A. Hately, P. Hullah, D. Martin-Marrero, E. Pastor, A.P. Rushton, A. Volkert, U-Space Concept of Operations: A Key Enabler for Opening Airspace to Emerging Low-Altitude Operations, *Aerospace*, 2020, 7, 24. <https://doi.org/10.3390/aerospace7030024>
- [8] R. Nouacer, M. Hussein, H. Espinoza, Y. Ouhammou, M. Ladeira, R. Castiñeira, Towards a framework of key technologies for drones, *Microprocessors and Microsystems*, 2020, vol. 77, <https://doi.org/10.1016/j.micpro.2020.103142>.
- [9] C. Conte, G. de Alteriis, G. Rufino and D. Accardo, An Innovative Process-Based Mission Management System for Unmanned Vehicles, 2020, IEEE 7th International Workshop on Metrology for AeroSpace (MetroAeroSpace), 2020, pp. 377-381, <https://doi.org/10.1109/MetroAeroSpace48742.2020.9160121>
- [10] Information on <https://www.incose.org/incose-member-resources/working-groups/transformational/mbse-initiative>.
- [11] Information on <https://ntrs.nasa.gov/citations/20170009110>
- [12] Information on <https://technology.esa.int/page/MBSE>
- [13] Information on <https://www.mathworks.com/solutions/model-based-systems-engineering.html>
- [14] Information on <https://flyingbasket.com/fb3>
- [15] Information on <https://www.nasa.gov/specials/X57/>
- [16] Information on <https://www.clean-aviation.eu/hybrid-electric-regional-aircraft>
- [17] Information on <https://www.easa.europa.eu/en/domains/urban-air-mobility-uam>

Recent developments about hybrid propelled aircraft: a short review

L.M. Cardone^{1*a}, S. De Rosa^{1b}, G. Petrone^{1c}, F. Franco^{1d}, C.S. Greco^{1e}

¹ Department of Industrial Engineering, Università di Napoli Federico II, Via Claudio 21, 80125, Napoli, Italia

^aluigimaria.cardone@unina.it, ^bsergio.derosa@unina.it, ^cgiuseppe.petrone@unina.it,
^dfrancesco.franco@unina.it, ^ecarlosalvatore.greco@unina.it

Keywords: Hybrid Propulsion Systems, Fuel Cell, Electric Aircraft

Abstract. Over the last decades, the rapid growth of the consumption of fossil fuel has generated an increased need for energy sustainability. The negative impact on the environment and now, as a global society, the dependence on fossil fuel have been questioned. For contrasting these adverse effects, NASA calls on the aeronautic industry to reduce aircraft fuel burn by 70% by 2025 in their N+3 concepts. Following high-profile government and industry studies, electric aircraft propulsion has emerged as an important research topic, this includes all-electric, hybrid electric, and turbo-electric architectures. The paper overviews the recent state-of-art about the innovative propulsion systems exploring the operating logic, their technological requirements, the ongoing research, and development in all the components necessary to make this technological change a feasible option for the future of passenger flight. It will be also reported the existing commercial products, prototypes, demonstrators for having a precise picture of the situation.

Introduction

Over the last decades, the economization of transportation has generated a sharp increase in fossil fuel consumption, causing a considerable increase in pollutant emissions. This increase in CO₂ emissions has prompted major industry companies and research institutions to develop new propulsion technologies for the aviation sector that are more efficient and have a reduced environmental impact. The new strong requirements about the emission pushed the academic and industrial researchers to investigate a new and sustainable type of engines for aerospace sector. Following the outcomes of these research Electric Propulsion Systems (EPS) and Hybrid Electric Propulsion System (HEPS) received a great emphasis and they have emerged as an important research topic and possible solution to satisfy the requirements imposed by NASA. In the next sections, the various innovative propulsion systems, identified in literature, will be discussed, labeling their advantages, disadvantages, and relative fields of application in relation to the type of aircraft that can accommodate them. Then the demonstrators will be reported that have been realized. In the end conclusion will be drawn.

Innovative Propulsion Systems

This section reports the main innovative propulsion systems identified in the literature. All the systems will briefly be introduced highlighting its advantages and disadvantages.

Sustainable Aviation Fuel SAF

Sustainable Aviation Fuel (SAF) can be defined as alternative fuel to conventional fossil-based jet fuel that is produced from either biological or non-biological sources. These fuels belong to the drop-in fuels class, characterized by having the same chemical and physical characteristics of the fuels used in aviation. This is a key aspect of its possible success because it allows the manufacturers do not make substantial modifications to the aircraft. The International Civil Aviation Organization (ICAO) reported that it would be physically possible to meet 100% of

demand by 2050, which corresponds to a 63% reduction in emissions. So, it seems that SAF is a simple way to reduce CO₂ emission but there are also some disadvantages as the highly cost of production, that could be reduced only with a combination of policy incentives, capital investments, and time [1].

All Electric Propulsion Systems

All-electric aircraft configuration is the simplest of all the electric architectures in terms of layout, the power source, in this category is the rechargeable battery, connected directly to an electric motor through a power management system that drives a propeller. Globally this system is characterized by an higher efficiency compares with the classical propulsion system (83% vs 25% of the classical propulsion system). This category of aircraft has many advantages, including zero-local-emission, low noise, and operating cost reduction. The most critical disadvantage of this category of aircraft is the battery storage technology that has not achieved sufficient maturity to cover the same distances as jet fuel-driven aircraft [2].

An evolution of the classical battery storage system are the Fuel Cells propulsion system. This system is composed by three main components: the Fuel Cell, the hydrogen storage tank (gaseous or liquid), and a buffer battery. This category of aircraft is characterized by a much lower Maximum Take Off Weight (MTOW), as battery weight is almost eliminated, compared to an analogue battery storage aircraft and a similar refueling times and weights, comparable to the classical propulsion systems present on the market today. These systems are characterized by a great versatility since they do not require pre-storage of energy in batteries, but they only need to store a quantity of hydrogen required to accomplish the proposed mission. There are different types of F-Cells, a clever way to classified them is by the type of electrolyte used, the most common one used in the transport industry are the Proton Exchange Membrane (PEM) characterized by a low temperature of exercise, simplicity of manufacturing, reliability, and the competitive cost of production [3].

Hybrid-Electric Propulsion Systems HEPs

The implementation of full-electric propulsion systems, for classes of aircraft other than simple demonstrators, is critical because the technology of energy storage in batteries, as well as the realization of the various components associated with the distribution of energy on the aircraft, is still unsuitable for their realization, especially considering the deadlines imposed by the European Union. Instead, a more viable route is to go and complement the classical turbojet/turboprop systems with electric machines thus evaluating an additional propulsive methodology known as Hybrid Systems. This category includes 3 possible configurations examined: Hybrid Series configuration, Hybrid Parallel configuration, and Hybrid Series/Parallel configuration [4].

In a Series Hybrid configuration, the Electric Motor (EM) is the only component which drives the propeller, without any gearbox, this implies that the Internal Combustion Engine (ICE) can run always at its optimal regime. Due to this condition, fuel efficiency can remain high, and its lifespan can be lengthened. Another advantage is the flexibility of choosing the ICE location due to its the mechanical decoupling. The series configuration suffers of many disadvantages, such as massive power loss due the conversion system and an high cost of the components that have to be sizing to maximum power require during the mission.

In the Parallel Hybrid configuration type of system, the propeller is driven by both ICE and EM. From this configuration, multiply advantages are achieved. The most important advantage is that small ICE and small EM can be selected because all the main components of the system do not need to be sized to cope with maximum power requirements. Also, this configuration has some disadvantages, the main one is that it needs an efficiency energy management strategy, because it

must optimize the power contribution of the ICE and the EM, to make them always work under the most efficient conditions.

The last analyzed configuration is the Hybrid Series–Parallel system. It is a mixture of two architectures show before, the main part of this configuration is the planetary gearbox at which the propulsion components, such as propellers, engine, EM, and generator, are connected to it. All the advantages and disadvantages of this system belong to the power-split part. The main advantage of using this device is that all the engine, ICE and EM, work in their maximum efficiency region. Despite this important advantage this type of system suffers of a constate dissipation rate due to the permanent connection between the part. These configurations are the most used architectures in aerospace and automotive sectors. Among them, the series configuration enables the engine to operate at its ideal operating condition, but as cited before, its system efficiency is relatively low since large power losses exist in the energy conversion. The series–parallel is the most functional, but the most complicated configuration out of the three architectures. It is the least popular configuration concerning aircraft application due to high complexity. it can therefore be inferred that, given current levels of technology, the parallel hybrid configuration appears to be the most versatile.

Flight Demonstrators

The attention is now focused on the attempts made by universities and research institutions in moving from purely theoretical models to prototypes able to fly, all the models have been classified according to their geometrical dimensions. With this parameter three categories are identified: small, medium, and large scale. The small scale is convenient for demonstrating the feasibility of the hybrid electric technology, several attempts were made by industries and research group, the most interested one is the Drone develop by Harris Aerial which use a fuel cell system with a small high-pressure tank of Hydrogen [5].

The medium scale is interesting because there is the opportunity to ensure the transportation of people. The most innovative flying configuration is the conversion kit installed on an ATR 72 proposed by ZeroAvia [6]. The last class of aircraft is the most critical one due to the technological limit of the component available. One interesting possible configuration is the one proposed by ZEROe program developed by Airbus which use two hybrid-hydrogen turboprop engines installed on an A350 [7].

So, the small/mid-scale sector, both academic and industrial institutes presented the flying or flying-capable demos. Furthermore, the studies of large hybrid aircrafts are still at the stage of concept designs and analysis due to the limitation of electrical and other technologies.

In Figure 1, it is interesting to observe that there is an area, indicated with the red square, are confined most of the different configurations before cited. It is evident that the maximum distance that can be covered is about 350 nm (648 km) while as far as the transport of passengers is concerned from the datasheets it has been found that these aircraft carry at most 4 people.

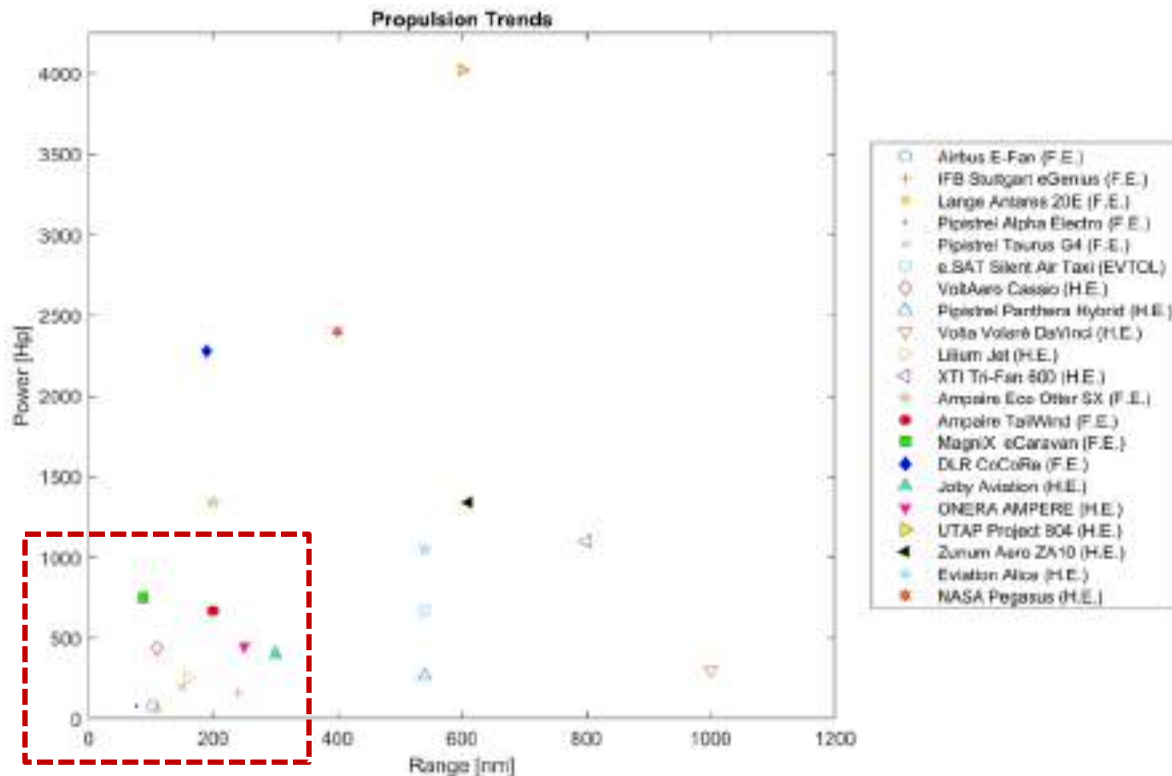


Figure 1 Propulsion Trends (F.E.: Full Electric; H.E.: Hybrid Electric)

Conclusion

The main purpose of this work is to quickly present the actual state of the art of new propulsion systems potentially adaptable to current aircraft configurations to achieve the CO₂ emission reduction targets set in 2050.

Without further technological development of batteries, it can be concluded that:

- Full-electric aircraft are implementable at most to the General Aviation category.
- Series/Parallel hybrid systems and fuel cells, characterized by a greater flexibility can be applied on a large scale of aircraft guaranteeing a partial abatement of CO₂.
- The main route remains SAF as they are solutions that can ideally be applied immediately since they do not require any modifications in the aircraft.

All the data reported in this short paper comes from a full paper under review [8].

Acknowledgments

This study was carried out within the MOST – Sustainable Mobility National Research Center and received funding from the European Union Next-Generation EU (PIANO NAZIONALE DI RIPRESA E RESILIENZA (PNRR) – MISSIONE 4 COMPONENTE 2, INVESTIMENTO 1.4 – D.D. 1033 17/06/2022, CN00000023). This manuscript reflects only the authors' views and opinions, neither the European Union nor the European Commission can be considered responsible for them.

References

- [1] Ng, K.S., Farooq, D., Yang, A., 2021. Global biorenewable development strategies for sustainable aviation fuel production. *Renew. Sustain. Energy Rev.* 150, 111502. <https://doi.org/10.1016/j.rser.2021.111502>
- [2] Brelje, B.J., Martins, J.R.R.A., 2019. Electric, hybrid, and turboelectric fixed-wing aircraft: A review of concepts, models, and design approaches. *Prog. Aerosp. Sci.* 104, 1–19. <https://doi.org/10.1016/j.paerosci.2018.06.004>

- [3] Olabi, A.G., et alii, 2021. Fuel cell application in the automotive industry and future perspective. *Energy* 214, 118955. <https://doi.org/10.1016/j.energy.2020.118955>
- [4] Singh, K.V., Bansal, H.O., Singh, D., 2019. A comprehensive review on hybrid electric vehicles: architectures and components. *J. Mod. Transp.* 27, 77–107. <https://doi.org/10.1007/s40534-019-0184-3>
- [5] Harris Aerial, 2023. Carrier H6 Hybrid. <https://www.harrisaerial.com/carrier-h6-hybrid-drone/>
- [6] ZeroAvia, 2022. ZA2000 2-5MW modular hydrogen-electric powertrain for 40-80 seat regional turboprops by 2027. <https://zeroavia.com>
- [7] AIRBUS, 2022. ZEROe :Towards the world's first hydrogen-powered commercial aircraft, <https://www.airbus.com/en/innovation/low-carbon-aviation/hydrogen/zeroe#:~:text=In%202022%2C%20we%20launched%20our,combustion%20propulsion%20system%20by%202025>
- [8] Cardone L. M., et alii, 2023. Review of the Recent Developments about the Hybrid Propelled Aircraft, submitted to *Aerotecnica Missili e Spazio*, under review.

Refined structural theories for dynamic and fatigue analyses of structure subjected to random excitations

Matteo Filippi^{1,a,*}, Elisa Tortorelli^{1,b}, Marco Petrolo^{1,c} and Erasmo Carrera^{1,d}

¹Department of Mechanical and Aerospace Engineering, Politecnico di Torino, Turin, Italy, 10129

^amatteo.filippi@polito.it, ^belisa.tortorelli@polito.it, ^cmarco.petrolo@polito.it,

^derasmo.carrera@polito.it

Keywords: Random Excitation, Refined Structural Model

Abstract. This paper presents the application of low- and high-fidelity finite beam elements to analyze the dynamic response of aerospace structures subjected to random excitations. The refined structural models are developed with the Carrera Unified Formulation (CUF), enabling arbitrary finite element solutions to be easily generated. The solution scheme uses power spectral densities and the modal reduction strategy to reduce the computational burden. The response of an aluminum box beam is studied and compared with a solution obtained by a commercial code. Considering the root-mean-square value of the axial stress, an estimation of the fatigue life of the structure is obtained.

Introduction

Fatigue is one of the prevalent causes of failure in structural and mechanical components. To correctly estimate the fatigue life of an element, it is essential to evaluate the stress distribution as accurately as possible. Time and frequency domain analyses can be employed to characterize the fatigue performance of a structure. In particular, the frequency domain approach is preferred thanks to its lower computational cost than direct integrations of the governing equation in the time domain. [1-2]. In particular, the Power Spectral Density (PSD) method is commonly used in structural dynamics and random vibration analysis [3]. The Finite Element (FE) method is a flexible and powerful tool for determining displacement and stress spectra. Previous works mostly adopted finite elements based on classical and first-order shear deformation theories [4-5]. While these kinematics expansions are suitable for various structural problems, they may not hold valid assumptions for other applications, such as laminated and thin-walled structures. Two- and three-dimensional (3D) FE formulations can be employed to address their limitations, but they often lead to a significant increase in computational costs. This study proposes an alternative approach by utilizing high-order finite beam elements. These elements provide an accurate and computationally efficient solution for predicting structural responses to random excitations. The Carrera Unified Formulation (CUF) enables the automatic implementation of various kinematic models through a recursive notation. Specifically, the response of a clamped-free box beam is given in terms of PSD and root-mean-square (RMS) of displacements and stresses, and a fatigue life prediction is provided given the value of RMS of axial stress.

One-dimensional finite elements

The one-dimensional (1D) model adopted in this work is based on the Carrera Unified Formulation (CUF). According to the CUF, the 3D displacement field of a solid beam with main dimension along the y-axis, can be expressed as a generic expansion of the generalized displacements $u_\tau(y, t)$:

$$\mathbf{u}(x, y, z, t) = \mathbf{F}_\tau(x, z) \mathbf{N}_i(y) \mathbf{u}_\tau(y, t), \quad \tau = 1, 2, \dots, M \text{ and } i = 1, \dots, n_{sn} \quad (1)$$

In this equation, M represents the number of terms used in the expansion, while nsn represents the number of structural nodes of a single Finite Element (FE). Repeated subscripts indicate summation, $N_i(y)$ refers to the 1D FE shape functions, and $F_\tau(x, z)$ represents arbitrary functions on the cross-section. In this study, we adopt the Taylor (TE) and Lagrange (LE) expansion classes as polynomial bases. By introducing the Principle of Virtual Displacement (PVD) $\delta L_{int} = \delta L_{ext}$, it is possible to derive finite element matrices and vectors by assembling the so-called *Fundamental Nuclei*. These nuclei are the invariant of the methodology.

Theory of random response and fatigue life prediction

Using the Fourier transform of the equation of motion, it is possible to obtain the equation in frequency domain:

$$\mathbf{q}_k(\omega) = [-\omega^2 \mathbf{M} + i\omega \mathbf{C} + \mathbf{K}]^{-1} \mathbf{F}_k^* \quad i = \sqrt{-1} \quad (3)$$

Where \mathbf{q}_k is the column vector that collects the degrees of freedom (DOF) of the FE model, k is an arbitrary non-null generalized coordinate, \mathbf{F}_k^* is the generalized force vector in frequency domain and it has only one non-null term (equal to 1).

To reduce the computational cost, it is a common practice to employ a modal reduction strategy. The Power Spectral Density (PSD) function of a signal gives an indication of the average power contained in particular frequencies and the root mean square (RMS) represents the square root of the area below PSD curve. Given the input PSD function of the load \mathbf{S}_F , the output PSD of the three-dimensional displacement \mathbf{S}_u and the stress \mathbf{S}_σ components at various frequencies (ω) are obtained:

$$\begin{aligned} \mathbf{S}_{u_i}(\omega) &= \bar{\mathbf{H}}_{u_i}(\omega) \mathbf{S}_F(\omega) \mathbf{H}_{u_i}^T(\omega) & i &= 1, 2, 3 \\ \mathbf{S}_{\sigma_j}(\omega) &= \bar{\mathbf{H}}_{\sigma_j}(\omega) \mathbf{S}_F(\omega) \mathbf{H}_{\sigma_j}^T(\omega) & j &= 1, \dots, 6 \end{aligned} \quad (4)$$

where $\bar{\mathbf{H}}(\omega)$ and $\mathbf{H}^T(\omega)$ are the complex conjugate and the transpose of the transfer function and it can be computed with the FE method by performing as many frequencies response analysis as of the non-null terms (\mathbf{nnz}) in the generalized force vector \mathbf{F} :

$$\mathbf{H}_{q_k}(\omega) = [\mathbf{q}_{k_1} \quad \mathbf{q}_{k_2} \quad \dots \quad \mathbf{q}_{k_L}] \quad k = 1, \dots, \mathbf{nnz} \quad L = 1, \dots, fs \quad (5)$$

where \mathbf{q} is derived from Eq. (3) and fs is the number of frequency steps. In this work, the structure is subjected to white noise excitations, thus the PSD of this type of noise is constant.

Numerical results

The numerical example refers to a clamped-free box beam made of aluminum alloy with $E = 71.7$ GPa, $G = 27.6$ GPa, $\nu = 0.3$, $\rho = 2700 \text{ kgm}^{-3}$ and dimensions $L = 2.00$ m, $h = 0.05$ m, $b = 0.25$ m, $t = 0.01$ m. The beam is subjected to three-point loads (1 N) as shown in Figure 1.

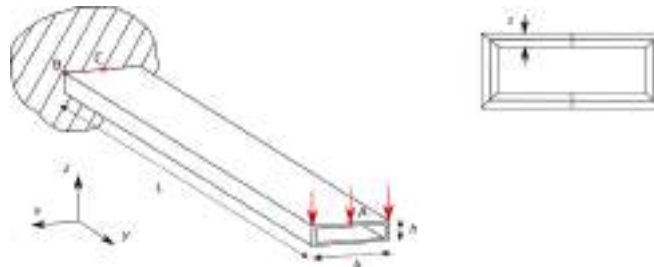


Figure 1. Boundary conditions and geometry of the clamped-free box beam subjected to clipped white noise. Scheme of the cross-section.

The structure was discretized using ten cubic beam elements. The first ten natural frequencies of the structure (Table 2) and the mass participation (Figure 2) were evaluated by conducting a normal mode analysis. The results have been obtained with the 12-LE9 model consisting of two Lagrange-type bi-quadratic elements for each lateral edge and four for the top and bottom surfaces. In the following analyses, forty modes were employed.

Table 1. First six natural frequencies obtained with NASTAN and CUF-FEM approach.

12-LE9	NASTRAN
13.90	13.88
56.13	56.17
84.03	83.09
178.68	170.8
223.17	216.08
324.78	324.67
406.34	378.13
461.23	424.19
613.37	539.52
629.52	563.01

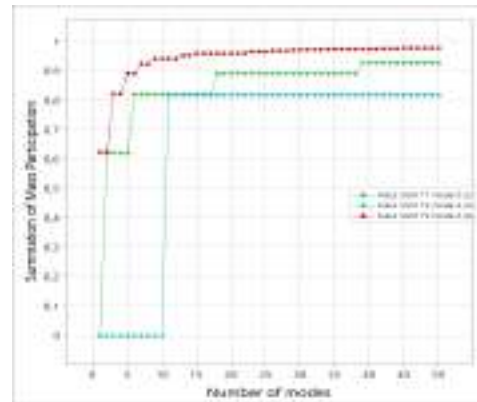


Figure 2. Mass participation versus number of modes of the box beam response.

Figure 3 shows point A's vertical displacement PSD and point C's axial stress PSD. In Figure 4, the distribution along the thickness corresponding to Point C of the root mean square of the axial stress is shown. Statistically speaking, the RMS stress value represents the 1σ value and will be experienced 68.3% of the time. A 2σ will be experienced 27.1% of the time, and a 3σ will be experienced 4.33%. These values represent 99.73% of the stresses the beam will experience at point C. Using Miner's cumulative damage $R_n = \frac{n_1}{N_1} + \frac{n_2}{N_2} + \frac{n_3}{N_3}$, it possible to obtained n , which is the number of cycles to fail: $1 = \frac{0.6831n}{N_1} + \frac{0.271n}{N_2} + \frac{0.0433n}{N_3}$. If the beam is vibrating at a frequency of 13.9 Hz (first natural frequency), then it will take approximately 2769 hours to fail. The results show that the 1D CUF approach is a valuable alternative to the common the 3D approach used by commercial codes.

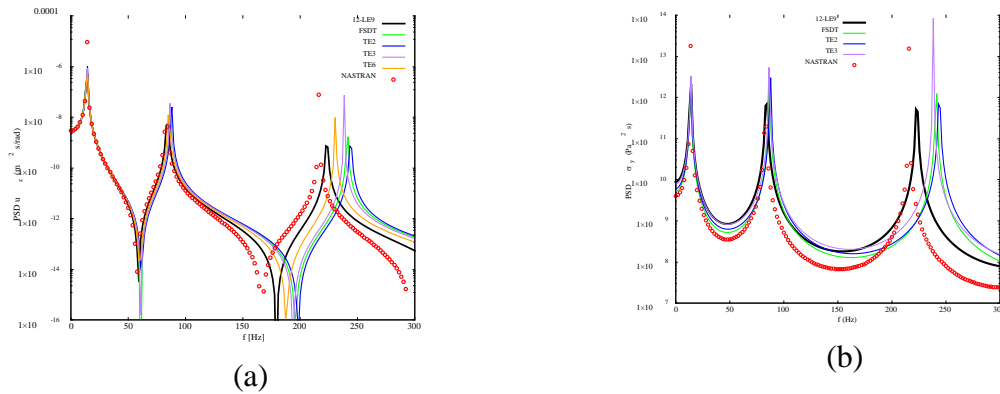
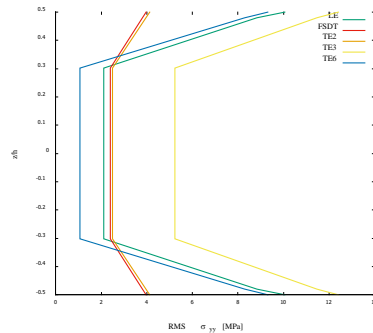


Figure 3. PSD of: (a) vertical displacement of point A, (b) axial stress of point B.



	1 RMS	2 RMS	3 RMS
S	10.06	20.12	30.18
N	4.3E10	1.8E8	7.6E6

Figure 4. RMS distributions of the axial stress along the thickness. On the right, a table with values taken from a fatigue curve of aluminium. For a given stress in [MPa], the number of cycles needed to cause failure is given.

Acknowledgments

This study was carried out within the MOST – Sustainable Mobility National Research Center and received funding from the European Union Next-Generation EU (PIANO NAZIONALE DI RIPRESA E RESILIENZA (PNRR) – MISSIONE 4 COMPONENTE 2, INVESTIMENTO 1.4 – D.D. 1033 17/06/2022, CN00000023). This manuscript reflects only the authors' views and opinions, neither the European Union nor the European Commission can be considered responsible for them.

References

- [1] Muñiz-Calvente M. A comparative review of time- and frequency-domain methods for fatigue damage assessment. *International Journal of Fatigue*, 163, 107069 (2022). <https://doi.org/10.1016/j.ijfatigue.2022.107069>
- [2] Halfpenny, A. A frequency domain approach for fatigue life estimation from finite element analysis. *Key Engineering Materials*, 167, pp 401-410 (1999). <https://doi.org/10.4028/www.scientific.net/KEM.167-168.401>
- [3] Rafiee R., Sharifi P. Stochastic failure analysis of composite pipes subjected to random excitation. *Construction and Building Materials*, 224, pp 950-961 (2019). <https://doi.org/10.1016/j.conbuildmat.2019.07.107>
- [4] Olson M. D., A consistent finite element method for random response problems. *Computers & Structures*, 2, pp 163-180 (1972). [https://doi.org/10.1016/0045-7949\(72\)90026-0](https://doi.org/10.1016/0045-7949(72)90026-0)
- [5] Dey, S. S., Finite element method for random response of structures due to stochastic excitation, *Computer Methods in Applied Mechanics and Engineering*, Vol. 20, No. 2, pp. 173–194 (1979). [https://doi.org/10.1016/0045-7825\(79\)90016-1](https://doi.org/10.1016/0045-7825(79)90016-1)

Satellite and Space Systems

Facility for validating technologies for the autonomous space rendezvous and docking to uncooperative targets

M. Sabatini^{1,a,*}, G.B. Palmerini^{1,b}, P. Gasbarri^{1,c}, F. Angeletti^{1,d}

¹Scuola di Ingegneria Aerospaziale, Sapienza University of Rome, Via Salaria 851 Rome

^amarco.sabatini@uniroma1.it, ^bgiovanni.palmerini@uniroma1.it, ^cpaolo.gasbarri@uniroma1.it,

^dfederica.angeletti@uniroma1.it

Keywords: Autonomous Proximity Operations; Relative Navigation; Free-Floating Platforms

Abstract. We present the latest advancements in the air-bearing facility installed at La Sapienza's GN Lab in the School of Aerospace Engineering. This facility has been utilized in recent times to validate robust control laws for simultaneous attitude control and vibration active damping. The instrumentation and testbed have been restructured and enhanced to enable simulations of close proximity operations. Relative pose determination, accomplished through visual navigation as either an auxiliary or standalone system, is the first building block. Leveraging the acquired knowledge, optimal guidance and control algorithms can be tested for contactless operations (e.g. on-orbit inspection), as well as berthing and docking tasks.

Introduction

Rendezvous and docking maneuvers have been successfully performed since the early days of spaceflight, but still pose challenges due to the increasing complexity of the mission scenario. From the early missions that required a human pilot, the goal of autonomous operations has already been achieved with notable examples in the ISS cargo resupply.

The current state of the art in proximity operations still involves some form of cooperation between the maneuvering satellite (the Chaser) and the Target satellite in the form of aids to relative navigation or in the form of mechanical interfaces to facilitate the docking phase. In either case, the Target satellite is usually controlled and fully operational. Much research is being done to extend these operations to a larger class of objects that are noncooperative and uncontrolled. Applications range from debris removal (see [1]) to orbital maintenance operations to repair or extend the operational life of a satellite.

Several missions have been developed to demonstrate the technology required for rendezvous and proximity operations (see the AVANTI demonstration [2] or the ELSA -D mission [3]).

A fundamental step in increasing the TRL of the required technologies is to conduct ground experiments to validate the components in a laboratory environment (typically TRL 4/5). For example, the work in [4] focuses on experimental verification by implementing and comparing real-time guidance algorithms on the Floating Spacecraft Simulator (FSS) testbed; a similar air-bearing testbed is used in [5] to validate the effectiveness of relative pose measurement systems. Various experimental approaches (e.g., using drones) can be used to test guidance and navigation subsystems (see [6]).

One of the most critical technologies to consolidate for successful close-proximity operations is the ability of an active spacecraft to accurately estimate its relative position and attitude (pose) with respect to an active/inactive Target (see [7]).

At the Guidance and Navigation Laboratory (GN Lab) of the School of Aerospace Engineering at La Sapienza, University of Rome, we have developed over the last decade a test bed consisting of a free-floating platform that can maneuver in a frictionless environment thanks to ON-OFF thrusters. The test bed, now in its second stage of development, has been used in the recent past to



validate the active robust control system for attitude control of large flexible satellites as part of an ESA ITT study.

This paper shows the current equipment of the facility, consisting of two free-floating platforms (with a fleet to be expanded in the near future), a very accurate external measurement system (providing position and attitude measurements of the platforms with an accuracy of 0.1 mm and 0.01 degrees, respectively), and large screens for the projection of simulated orbital views that are changed in real time according to the motion of the platform.

With this configuration, it is now possible to validate critical short-range subsystems, such as visual navigation to determine the position of an uncooperative target in difficult lighting conditions and with limited computing power. Different algorithms can be tested for long-range (in which case a simple angle algorithm can be used) and short-range scenarios (feature-based algorithms or AI techniques are viable options). Maneuvers based on this information can eventually lead to docking, a phase where experimental validation of the behavior of the mechanisms and platforms during contact dynamics in a reactionless environment is critical. Successful validation of the critical aspects of GNC in a laboratory environment will pave the way for the realization of space-based enablers using microsatellites.

The first platform: early development of PINOCCHIO

The GN Lab has been developing a free-floating platform since 2012 (see [8]). In its first version, the platform, named PINOCCHIO (Platform Integrating Navigation and Orbital Control Capabilities Hosting Intelligence Onboard), was a 10-kg class platform, that utilized low-pressure air (10 atm) stored in an onboard tank for generating a thin film of air removing the friction between the air-bearings and the working table. It incorporated a second onboard tank supplying eight nozzles, serving as cold gas thrusters to enable horizontal movement and rotation around the vertical axis (yaw). Originally, a glass table (Fig. 1 - left) was used, but it was later upgraded to a black granite table due to its improved dimensional stability and operational workspace. PINOCCHIO operated autonomously, with its onboard computer managing all functions. The modular architecture allowed for the integration of various avionics components, including accelerometers, gyros, cameras, and lab star sensors, to instrument the guidance and control systems for both position and attitude. The platform's bus, which closely resembled the size and mass properties of a real microsatellite, proved instrumental in numerous studies conducted by the Sapienza team in recent years, as referenced in [9][10][11]. These studies encompassed areas such as rendezvous and docking guidance, optical navigation, and combined control of the platform's attitude during robotic arm motion (as depicted in Fig. 1). Additionally, the team explored the effects of flexibility in attitude control resulting from elastic appendages.

The need to further investigate the research field of attitude control of very large and flexible satellites using a multi-input multi-output control with attitude and elastic sensors and actuators, in the framework of the ESA ITT EXPRO-PLUS project “ACACLAS” (Advanced Collocated Active Control of Large Antenna Structures), called for the design, realization and characterization of a new platform to increase the performance and the capabilities of the test rig.



Fig. 1 The first version of the floating platform (left) and one of the experiments focused on the use of space robotic manipulators (right)

The second platform: a special focus on attitude control of highly flexible satellites

A new platform has been developed to enhance the performance of the initial platform in several aspects:

- (a) Increasing the bus rigidity
- (b) Extending the duration of experiments
- (c) Including a dedicated electronics module for the payload
- (d) Equipping the test rig with a high-accuracy metrology system.

The floating platform's structure has been completely redesigned using an Aluminum alloy (UNI 6060). It has overall dimensions of 300 mm × 350 mm × 480 mm (height) and consists of three compartments, which can be expanded due to its modular design, catering to specific purposes. The lower compartment houses the pneumatic system, while the second floor (300 mm × 350 mm × 100 mm) accommodates the electronics, including sensors, microcontrollers, power supplies, and wiring (see Fig. 2 - left). To achieve the required long experiment duration, a high-pressure tank with an operational pressure of 200 atm is used (see Fig. 2 - right). The third floor provides additional modules for specific missions. Currently, it houses the electronics required to control flexible appendages, such as solar panels and antennas (see Fig. 3 - left). These structures can be easily attached when experiments necessitate active control of flexible appendages. In such cases, a smaller, more precise working table is utilized since attitude maneuvers are typically the main focus (see Fig. 3 - right).

For accurate measurements of the structure's attitude and elastic displacement, a VICON system is employed. This technique utilizes retroreflective markers that are tracked by six infrared cameras. A detailed characterization of the platform can be found in reference [13], demonstrating navigation accuracy below 100 μm for position and 0.003 deg for attitude.



Fig. 2 The new version of the floating platform (left) with the high-pressure systems for air-bearings and thrusters (right).



Fig. 3 Electronics compartment (left) used for vibration sensing and control of the highly flexible appendages (right).

A testbed for autonomous rendezvous and docking

The two platforms and the external metrology system have been now repurposed at the scope of testing guidance, control and, more specifically, optical navigation for the determination of the relative pose of a Chaser satellite with respect to a Target satellites. Active electro-optics systems can be used and tested, showing a promising performance (see [12]); these systems can be aided or partially substituted by vision systems (monocular or stereovision). For a hardware-in-the-loop test, the orbital environment should be reconstructed also from a visual point of view. To achieve this, an array of screens has been arranged to project realistic potential background images (Fig. 4 - left depicts the currently installed first screen). This allows the Chaser satellite's acquired image to include not only relevant Target satellite features but also various potential sources of visual disturbance, such as Earth landscapes, clouds, or stars (see Fig. 4 - right). Additionally, a lamp simulating the sun's position can be used to account for the constraint of avoiding blinding of the Chaser's cameras.



Fig. 4 First installed white screen with the two floating platforms (left) and a snapshot acquired by the navigation systems on board the Chaser satellite (right).

The onboard navigation systems provide relative pose measurements that must be validated thanks to benchmark metrology systems. The VICON system already mentioned in the previous section is a powerful mean in this sense. The inertial position of both platforms can be computed in real-time with a maximum frequency of 300 Hz, and with an accuracy which is much better than what achievable with the onboard systems. Fig. 5 reports an example of the visualization and the stream of data available with such a system, where each platform is identified by a different pattern of reflective markers.

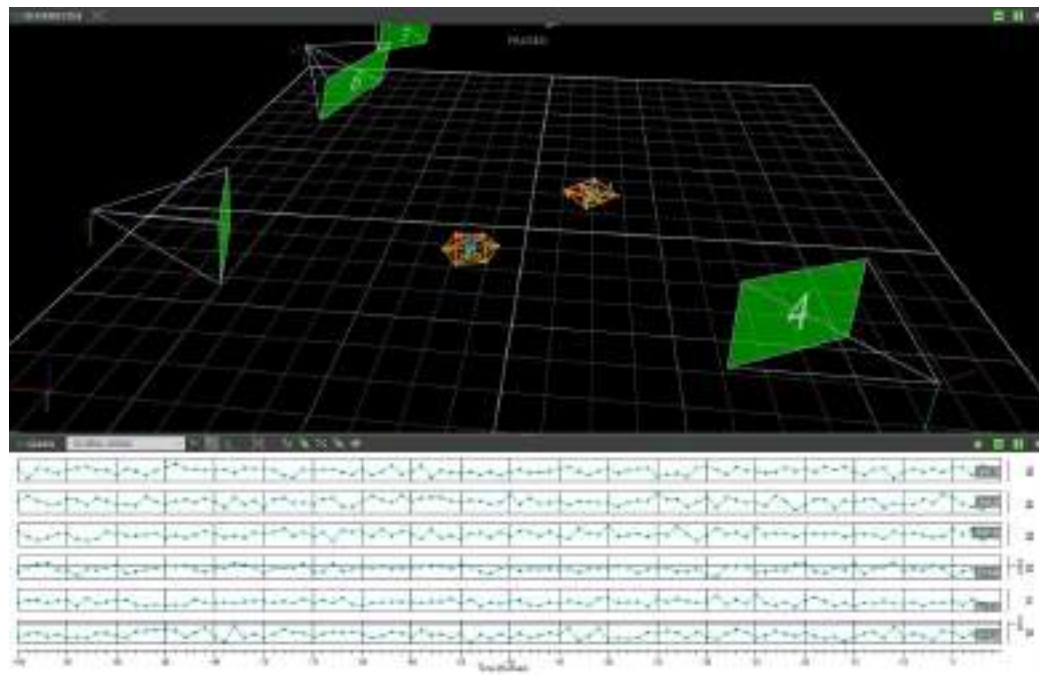


Fig. 5 Chaser and Target platforms acquired by the external metrology system

This set up can be used not only for visual based navigation, but also for testing range finders (LIDAR or radio frequency) and systems emulating differential GPS measurements. Relative pose determination is one of the building blocks of the autonomous rendezvous and docking operations. While it can be also tested using robotic arms (see [14]), with the air-bearing approach also the guidance and control algorithms can be tested in closed loop, including the contact forces and the post contact dynamics which are among the most difficult phases to simulate. The position and

attitude control of the single platforms are accurate enough (see Fig. 6 for an example of an attitude slew maneuvers of 30 deg, with stationary error of 0.1 deg) to allow for a complete docking, including the validation of the performance of mechanical hardware.

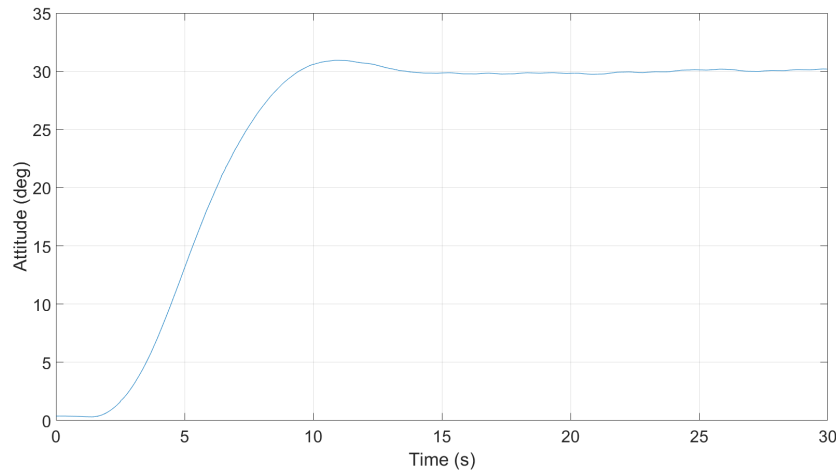


Fig. 6 Example of an attitude slew maneuver

Conclusions

We have showcased the key features and performance of an experimental testbed that has played a crucial role in validating attitude control algorithms for highly flexible spacecraft. Currently, we are expanding its capabilities to facilitate testing of space proximity operations, specifically focusing on control and relative navigation. We encourage the academic community to explore this platform for validating and testing various building blocks of the autonomous formation flying guidance, navigation, and control architecture, in the framework of future fruitful collaborations.

References

- [1] C. Bonnal, J.-M. Ruault, M.-C. Desjean, "Active debris removal: Recent progress and current trends" *Acta Astronautica* 85 (2013) pp. 51–60. <https://doi.org/10.1016/j.actaastro.2012.11.009>
- [2] G. Gaias and J.-S. Ardaens, "Flight Demonstration of Autonomous Noncooperative Rendezvous in Low Earth Orbit", *Journal Of Guidance, Control, And Dynamics* Vol. 41, No. 6, June 2018. <https://doi.org/10.2514/1.G003239>
- [3] J. Forshaw, S. Iizuka, C. Blackerby, and N. Okada, "ELSA-d – A novel end-of-life debris removal mission: mission overview, CONOPS, and launch preparations", *First Int'l. Orbital Debris Conf.* (2019)
- [4] R. Zappulla II, H. Park, J. Virgili-Llop and M. Romano, "Experiments on Autonomous Spacecraft Rendezvous and Docking Using an Adaptive Artificial Potential Field Approach", *AAS* 16-459
- [5] Z. Wei, H. Wen, H. Hu, D. Jin, "Ground experiment on rendezvous and docking with aspinning target using multistage control strategy" *Aerospace Science and Technology* 104 (2020) 105967. <https://doi.org/10.1016/j.ast.2020.105967>
- [6] T. Mahendrakar et al., "Autonomous Rendezvous with Non-Cooperative Target Objects with Swarm Chasers And Observers", *AAS* 23-423
- [7] R. Opromolla, G. Fasano, G. Rufino, M. Grassi, "A review of cooperative and uncooperative spacecraft pose determination techniques for close-proximity operations", *Progress in Aerospace Sciences* 93 (2017) 53–72. <https://doi.org/10.1016/j.paerosci.2017.07.001>

- [8] M. Sabatini, M. Farnocchia, G. Palmerini, “Design and Tests of a Frictionless 2D Platform for Studying Space Navigation and Control Subsystems”, paper7.1406, IEEE Aerospace Conference 2012, BigSky, Montana, USA. <https://doi.org/10.1109/AERO.2012.6187259>
- [9] M. Sabatini, G. B. Palmerini, P. Gasbarri, “Synergetic approach in attitude control of very flexible satellites by means of thrusters and PZT devices”, Aerospace Science and Technology, Volume 96, 2020. <https://doi.org/10.1016/j.ast.2019.105541>
- [10] M. Sabatini, P. Gasbarri, G. B. Palmerini, Coordinated control of a space manipulator tested by means of an air bearing free floating platform, Acta Astronautica, Volume 139, October 2017, Pages 296-305. <https://doi.org/10.1016/j.actaastro.2017.07.015>
- [11] M. Sabatini, G. B. Palmerini, P. Gasbarri, “A Testbed For Visual Based Navigation And Control During Space Rendezvous Operations”, Acta Astronautica, Volume 117, 1 December 2015, Pages 184-196. <https://doi.org/10.1016/j.actaastro.2015.07.026>
- [12] A. Nocerino et al., "Experimental validation of inertia parameters and attitude estimation of uncooperative space targets using solid state LIDAR", Article in press, <https://doi.org/10.1016/j.actaastro.2023.02.010>
- [13] M. Sabatini, P. Gasbarri, G. B. Palmerini, “Design, realization and characterization of a free-floating platform for flexible satellite control experiments”, Acta Astronautica, 2023, in press. <https://doi.org/10.1016/j.actaastro.2023.05.007>
- [14] R. Volpe et al., “Testing and Validation of an Image-Based, Pose and Shape Reconstruction Algorithm for Didymos Mission”, Aerotec. Missili Spaz. 99, 17–32 (2020). <https://doi.org/10.1007/s42496-020-00034-6>

Simulation of in-space fragmentation events

Lorenzo Olivieri^{1,a,*}, Cinzia Giacomuzzo^{1,b}, Stefano Lopresti^{1,c} and
Alessandro Francesconi^{2,d}

¹ CISAS “G. Colombo”, University of Padova, Via Venezia 15, 35131 Padova, Italy

² DII/CISAS, University of Padova, Via Venezia 1, 35131 Padova, Italy

^alorenzo.olivieri@unipd.it, ^bcinzia.giacomuzzo@unipd.it, ^cstefano.lopresti@unipd.it,

^dalessandro.francesconi@unipd.it

Keywords: Space Debris, Fragmentation, Break-Up, Numerical Simulations

Abstract. In the next years the space debris population is expected to progressively grow due to in-space collisions and break-up events; in addition, anti-satellite tests can further affect the debris environment by generating large clouds of fragments. The simulation of these events allows identifying the main parameters affecting fragmentation and generating statistically accurate populations of generated debris, both above and below detection thresholds for ground-based observatories. Such information can be employed to improve current fragmentation models and to reproduce historical events to better understand their influence on the non-detectable space debris population. In addition, numerical simulation can also be employed to identify the most critical object to be removed to reduce the risk of irreversible orbit pollution. In this paper, the simulation of historical in-orbit fragmentation events is discussed and the generated debris populations are presented. The presented case-studies include the COSMOS-IRIDIUM collision, the COSMOS 1408 anti-satellite test, the 2022-151B CZ-6A in-orbit break-up, and a potential collision of ENVISAT with a spent rocket stage; for these events, results are presented in terms of cumulative fragments distributions and debris orbital distributions.

Introduction

The increasing number of objects resident in Earth orbits is leading the debris environment dangerously close to the Kessler Syndrome, i.e. to a condition of self-sustained cascade impacts and break-ups that would strongly reduce the access and exploitation of near-Earth space [1]. Mitigation techniques and strategies to reduce the hazard of space debris are under evaluation by the scientific community and the main stakeholders [2]; however, it is still crucial to understand the physical processes involved in spacecraft collisions and fragmentations. Data on spacecraft breakup can be acquired by the observation of in-space fragmentation events [3-4], the execution of ground tests [5-6], and the performing of numerical simulations [7-8].

In this context, the University of Padova has developed the Collision Simulation Tool Solver (CSTS) to numerically evaluate in-space fragmentation events [9-10]. In the tool (see Fig. 1), the colliding bodies are modelled with a mesh of Macroscopic Elements (MEs) that represent the main parts of the satellite; structural links connect them forming a system-level net. In case of collision, the involved MEs are subjected to fragmentation, while structural damage can be transmitted through the links; this approach can be propagated through a cascade effect representative of the object fragmentation, allowing the simulation of complex collision scenarios and producing statistically accurate results.

In this work, the CSTS is employed to replicate three fragmentation events observed in orbit and the potential breakup of ENVISAT due to the collision with a spent rocket stage. For each case, a brief description of the model and the main simulation results are presented.



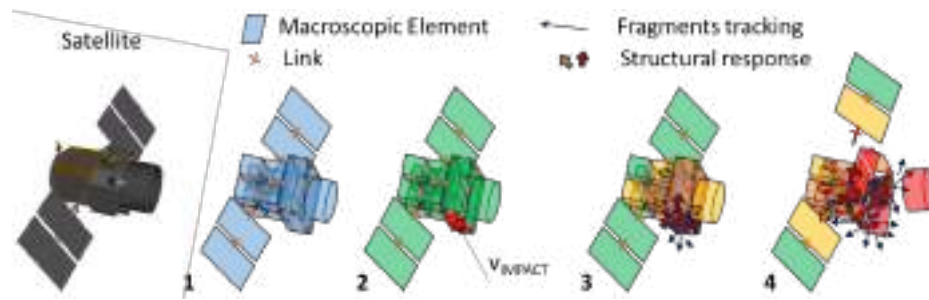


Fig. 1: CSTS modelling with MEs and links and simulation logic with cascade effect

In-space fragmentation case studies

1. COSMOS-IRIDIUM collision

This event, dating back to 2009, was the first collision between two intact spacecraft, the active IRIIDIUM 33 and the defunct COSMOS 2251. In CSTS, two simulations replicating a central and a glancing impact have been performed. Fig. 2 shows the geometrical models for both cases and the obtained results in terms of cumulative characteristic length distribution; the glancing impact data (yellow) is clearly in accordance with the NASA SBM model.

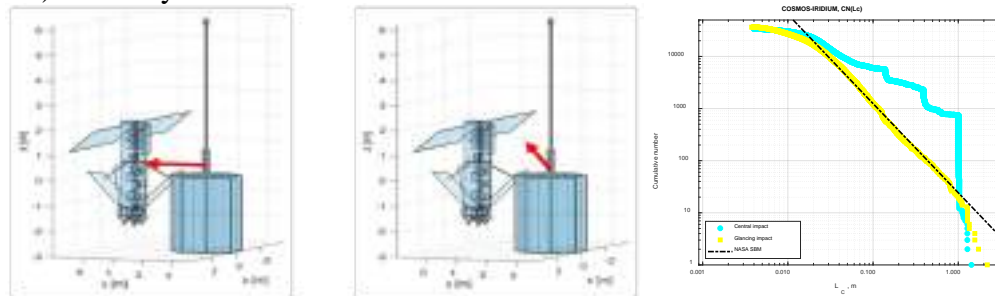


Fig. 2: COSMOS-IRIDIUM geometrical models for central (left) and glancing (centre) impacts and generated fragments cumulative distributions (right)

The Gabbard diagram in Fig. 3 compares CSTS data with the observed fragments for COSMOS 2251. Again, it is possible to notice an accordance between numerical data and observations.

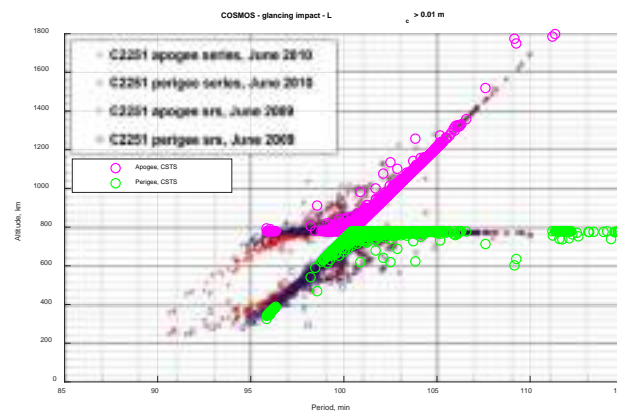


Fig. 3: Comparison of observed and simulated fragments (glancing impact) on the Gabbard diagram for COSMOS 2251 debris cloud

2. COSMOS 1408 anti-satellite test

In November 2021 a Russian anti-satellite test led to the break-up of the defunct COSMOS 1408 satellite. For this case, only partial information on the spacecraft and the kinetic impactor were available; the accuracy of CSTS model (see Fig. 4, left) is therefore limited, leading to an underestimation of the fragments cumulative number (in red in Fig. 4, center) with respect to observations (blue line) and NASA SBM model (black lines). However, as visible in the Gabbard

diagram (Fig. 4, right), the orbital distribution of generated fragments is still in accordance with observations.

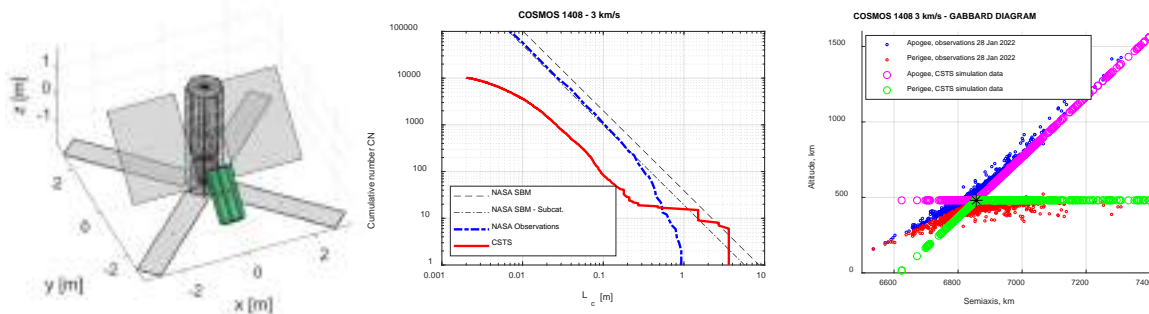


Fig. 4: geometrical model of COSMOS 1408, in gray, and the kinetic impactor, green (left); generated fragments cumulative distributions (center) and Gabbard diagram (left)

3. 2022-151B CZ-6A in-orbit break-up

In November 2022, the second stage of the CZ-6A fragmented after releasing its payload. This event was replicated with a dedicated CSTS simulation (Fig. 5), estimating the explosion of a tank. A total of more than 500 fragments were obtained by the simulation; numerical data are still compatible with the orbital distribution of observed fragments (Fig. 5).

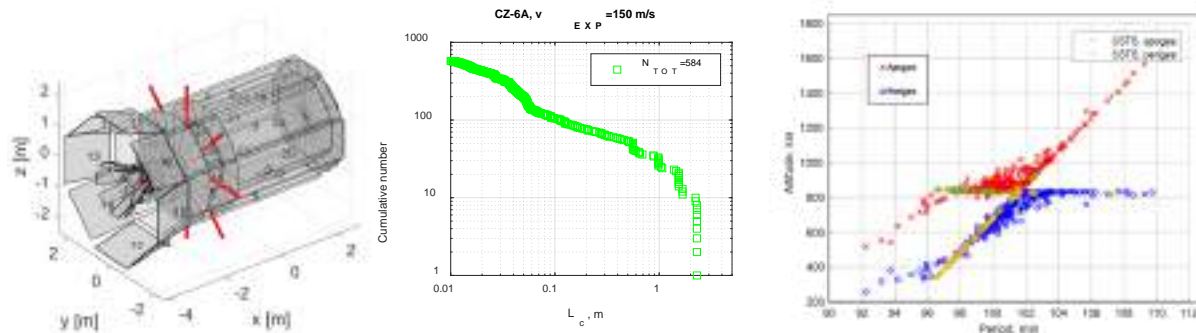


Fig. 5: CZ-6A geometrical model (left), generated fragments cumulative distributions (centre), and comparison of observed and simulated fragments on the Gabbard diagram (right)

4. Potential collision of ENVISAT with a spent rocket stage

Last, this potential collision scenario evaluated an impact of ENVISAT with a spent rocket stage (Fig. 6, left) at two different velocities, respectively of 1 km/s and 10 km/s. With CSTS it is possible to obtain the cumulative distributions reported in Fig. 6, right. As expected, the 10 km/s scenario generates more fragments due to the higher energy of the event, with about 100,000 fragments larger than 5 mm. The obtained distribution is below the estimation of this event performed by the NASA SBM; however, this breakup would strongly affect the already crowded 800 km sun-synchronous orbit currently occupied by ENVISAT.

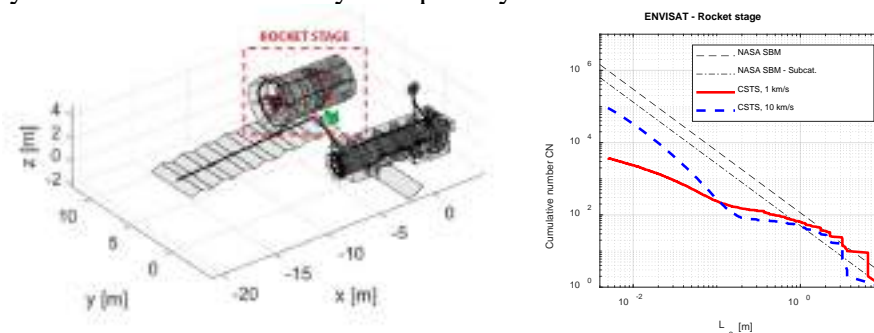


Fig. 6: ENVISAT Vs. rocket stage impact geometrical models (left) and generated fragments cumulative distributions (right)

Conclusions

This paper presented four simulation cases for in-space break-up events. It is shown that CSTS is capable to replicate complex fragmentation scenarios, providing statistically accurate results. These data will be employed to evaluate the effect of break-ups in the evolution of the non-detectable debris population and to assess the correlated risks.

Acknowledgements

The CSTS software was developed in the framework of ESA contracts No. 4000119143/16/NL/BJ/zk “Numerical simulations for spacecraft catastrophic disruption analysis” and No. 4000133656/20/D/SR, “Exploiting numerical modelling for the characterisation of collision break-ups; the COSMOS-IRIDIUM collision was modelled in the framework of the aforementioned ESA contract 4000133656/20/D/SR. The other simulations were performed in the framework of ASI-INAF Agreement “Supporto alle attività IADC e validazione pre-operativa per SST (N. 2020-6-HH.0)”.

References

- [1] Kessler, D. J., and Cour-Palais, B. G. "Collision frequency of artificial satellites: The creation of a debris belt." *Journal of Geophysical Research: Space Physics* 83.A6 (1978): 2637-2646. <https://doi.org/10.1029/JA083iA06p02637>
- [2] Yakovlev, M. (2005, August). The “IADC Space Debris Mitigation Guidelines” and supporting documents. In 4th European Conference on Space Debris (Vol. 587, pp. 591-597).
- [3] Krag, H., et al. "A 1 cm space debris impact onto the sentinel-1a solar array." *Acta Astronautica* 137 (2017): 434-443. <https://doi.org/10.1016/j.actaastro.2017.05.010>
- [4] Kelso, T. S. "Analysis of the iridium 33 cosmos 2251 collision." (2009).
- [5] Hanada, T., Liou, J. C., Nakajima, T., & Stansbery, E. (2009). Outcome of recent satellite impact experiments. *Advances in Space Research*, 44(5), 558-567. <https://doi.org/10.1016/j.asr.2009.04.016>
- [6] Olivieri, L., Smocovich, P. A., Giacomuzzo, C., & Francesconi, A. (2022). Characterization of the fragments generated by a Picosatellite impact experiment. *International Journal of Impact Engineering*, 168, 104313. <https://doi.org/10.1016/j.ijimpeng.2022.104313>
- [7] McKnight, D., Maher, R., and Nagl, L.. "Fragmentation Algorithms for Strategic and Theater Targets (FASTT) Empirical Breakup Model, Ver 3.0." DNA-TR-94-104, December (1994).
- [8] Sorge, M. E. "Satellite fragmentation modeling with IMPACT." AIAA/AAS Astrodynamics Specialist Conference and Exhibit. 2008. <https://doi.org/10.2514/6.2008-6265>
- [9] Francesconi, A., et al. "CST: A new semi-empirical tool for simulating spacecraft collisions in orbit." *Acta Astronautica* 160 (2019): 195-205. <https://doi.org/10.1016/j.actaastro.2019.04.035>
- [10] Olivieri L., et al. “Simulations of satellites mock-up fragmentation.” *Acta Astronautica*, accepted on February 25th, 2023. <https://doi.org/10.1016/j.actaastro.2023.02.036>

Scientific activity of Sapienza University of Rome aerospace systems laboratory on the study of lunar regolith simulants, focusing on their effect on the microwave fields propagation

Andrea Delfini^{1,a}, Roberto Pastore^{1,b*}, Fabio Santoni^{1,c}, Michele Lustrino^{2,d} and Mario Marchetti^{3,e}

¹Department of Astronautical, Electric and Energy Engineering, Sapienza University of Rome, Via Eudossiana 18, 00184 Rome, Italy

²Department of Earth Science, Sapienza University of Rome, P.le Aldo Moro 5, 00185 Rome, Italy

³AIDAA, Via Salaria 851, 00100 Rome, Italy

^aandrea.delfini@uniroma1.it, ^broberto.pastore@uniroma1.it, ^cfabio.santoni@uniroma1.it,

^dmichele.lustrino@uniroma1.it, ^emarchettimario335@gmail.com

Keywords: Lunar Regolith, Moon Surface Absorption, Electromagnetic Microwave Propagation

Abstract. The forthcoming space missions aiming at developing new habits on the Moon and into deep space are opening new challenges for materials scientists in enabling in-situ efficient systems and subsystems. During the last decades, Space Agencies programs of long-term missions addressed to the future Moon colonization moved the aerospace research interest toward the knowledge of how the lunar conditions could represent scientific and technological tasks to be tackled, to deal with such a big challenge. Among very many matters, a still open question is to understand how proper the lunar environment would be for TLC systems daily used on Earth, or whether it should be necessary to establish different stable systems on the Moon by finding alternative solutions with respect to the Earth conventional technologies. This paper introduces the scientific activity developed during recent years at the Aerospace Systems Laboratory of Sapienza University of Rome, concerning the study of lunar regolith with focus on its effect on the microwave fields propagation. The research addresses such task by simulating several representative Moon environmental conditions, reproducing well defined chemical/physical background in terms of atmospheric parameters and soil compositions, as from the available literature data, and analyzing the microwave propagation characteristics to design efficiently mobile TLC systems operating on the Moon. With the further objective of considering regolith as main routine resource for drawing up systems and facilities constituting lunar living structures, the analysis of regolith-microwave interaction is thus focused on two specific paths, such as building airtight structures by means of ISRU methodologies and the EM compatibility (EMC) analysis of simulated lunar environment & TLC systems design. This work can be thus considered as linked to the forthcoming projects aimed at enhancing the research community knowledge about the Moon environment, by assessing scientific background and establishing technological processes for lunar TLC systems development.

Introduction

The required degree of technical innovation will allow to achieve scientific outcomes of huge impact and industrial fallout, taking into account the utmost interest for the Moon occurring nowadays. It has to be stressed that Long Term Evolution (LTE)/4G technology promises to revolutionize lunar surface communications by delivering reliable, high data rates while containing power, size and cost. Communications will be a crucial component for NASA's Artemis program,

which will establish a sustainable presence on the Moon by the end of the decade. Deploying the first LTE/4G communications system in space will pave the way towards sustainable human presence on the lunar surface: the network, in fact, will provide critical communication capabilities for many different data transmission applications, including vital command and control functions, remote control of lunar rovers, real-time navigation and streaming of high definition video. These communication applications are all vital to long-term mission on the lunar surface, since reliable, resilient and high-capacity communications networks will be key for supporting a sustainable human presence on the Moon. The same LTE technologies that have met the world's mobile data and voice needs for the last decade are well suited to provide mission critical and state-of-the-art connectivity and communications capabilities for any future space expedition. Commercial off-the-shelf communications technologies, particularly the standards-based fourth generation cellular technology, are mature, proven reliable and robust, easily deployable, and scalable. NASA plans to leverage these innovations for its Artemis program, which will establish sustainable operations on the Moon by the end of the decade in preparation for an expedition to Mars. Thus, the presented research aims at lay down useful guidelines to deploy advanced TLC technologies in the most extreme environments, in order to validate the solution's performance and technology readiness level, and further optimize it for future terrestrial and space applications.

Work Summary

The scientific activity developed during recent years at the Aerospace Systems Laboratory (LSA – “Sapienza” University of Rome) concerned the study of lunar regolith, focusing on its effect on the microwave fields propagation. The research addresses such task by carrying out a full experimental characterization performed by simulating several representative Moon environmental conditions – i.e., by reproducing well defined chemical/physical background in terms of atmospheric parameters and soil compositions, as from the available literature data – and analyzing the microwave propagation characteristics in order to design efficiently mobile telecommunications systems operating on the Moon. With the further objective of considering regolith as main routine resource for drawing up systems and facilities constituting lunar living structures, the analysis of regolith-microwave interaction is thus focused on two specific paths:

- Building airtight structures by means of ISRU methodologies: the study is framed within the field of EM characterization of hybrid materials for space application currently carried out at LSA laboratories, focusing on the properties of several typologies of regolith-based bulk materials in terms of microwave reflection, absorption and transmission properties, in order to assess the basic conditions for remote operations.
- EM compatibility (EMC) analysis of simulated lunar environment & TLC systems design: the open question of understanding how the Moon environment would be fit for communications systems daily used on Earth, or whether it should be necessary to establish alternative solutions, is carried out by means of advanced facilities available at LSA laboratories, by reproducing fully constrained chemical/physical background conditions in terms of atmospheric and soil compositions, and analyzing the free space EM field propagation characteristics within lunar simulated environment.

The proposed study considers various types of lunar regolith reproduced on the basis of literature findings (see data in [1-3]). The base material used is dark powder of volcanic origin (Black Pyroclastite), which is enriched with the inclusion of various weight percentages of Ilmenite, in order to make it more similar to the regolith found on the surface of the basaltic lunar seas (main components: Ilmenite, Iron and Titanium Oxide). In order to obtain samples as much as possible responsive to the reality, the percentage of Titanium Oxide present in the Ilmenite sand is set as a parameter, and the correspondent percentage in weight of Ilmenite is added to the pyroclastic sand by mechanical mixing.

The electromagnetic experimental characterization is performed by means of a reverberation chamber (RC), due to the intrinsic capability provided by such experimental equipment to perform electromagnetic compatibility (EMC) tests with high level of accuracy. The facility adopted is the ‘Space Environment Simulator’ (SAS) of the Aerospace Systems Laboratory (LSA) available @ DIAEE – Sapienza University of Rome, which is a cylindrical vacuum chamber (volume around 5m^3) adapted to perform microwave characterization in conditions of chaotic EM propagation (see Fig.1, [4-6]). Basically, by using a reverberation chamber the knowledge of the absorbed power allows to retrieve the as-called absorption cross section (ACS) of the object under investigation. The inner SAS atmosphere is controlled in terms of vacuum level, temperature and percentage of humidity. In particular, the latter environmental parameter influence on materials ACS is investigated by exploring conditions of ultra-high vacuum, medium-low pressure, standard and increasingly moistened air, in order to discriminate the microwave absorption effects not due to lunar simulants intrinsic characteristics [7]. A representative result of the experimental characterization of the reverberation environment adopted is reported in Fig.2, where the measurements of the quality factor of the RC for different atmosphere conditions – i.e., max vacuum ‘blank’ level ($\sim 10^{-5}$ mbar), low pressure ($\sim 10^{-3}$ mbar) CO_2 filled and standard air – and the corresponding absorbing cross section (evaluated as discrepancy against the reference) are plotted over the microwave broadband considered. The influence of the partial presence of humidity in air is appreciable, especially at increasing frequency, giving evidence of the power absorbing effectiveness due to dipolar rotation resonances of the water vapor molecules in the EM range under investigation [8,9].



Fig.1. Inner view of the reverberation chamber for microwave characterization arranged by adapting the Space Environment Simulator of the Aerospace Systems Laboratory @ DIAEE – Sapienza Univ. of Rome.

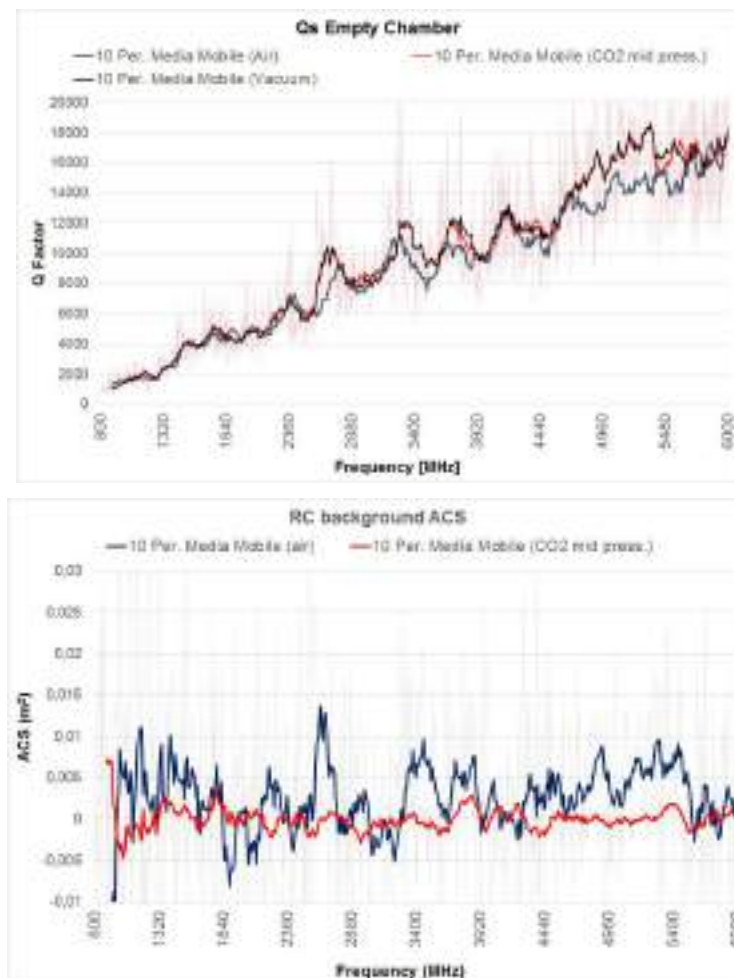


Fig.2. SAS chamber's quality factors and environments ACS measurements.

References

- [1] D. S. McKay et al., Lunar Regolith in Lunar Sourcebook A User's Guide to the Moon, Cambridge University Press, 1991, 346.
- [2] Y. Qian et al., Young lunar mare basalts in the Chang'e-5 sample return region, northern Oceanus Procellarum, Earth and Planetary Science Letters 555 (2021) 116702.
<https://doi.org/10.1016/j.epsl.2020.116702>
- [3] D. P. Moriarty III et al., The search for lunar mantle rocks exposed on the surface of the Moon, Nature Communications 12 (2021), 4659. <https://doi.org/10.1038/s41467-021-24626-3>
- [4] D. Micheli, F. Santoni, A. Giusti, A. Delfini, R. Pastore, A. Vricella, M. Albano, L. Arena, F. Piergentili, M. Marchetti, Electromagnetic absorption properties of spacecraft and space debris, Acta Astronaut. 133 (2017) 128-135. <https://doi.org/10.1016/j.actaastro.2017.01.015>
- [5] D. Micheli, A. Delfini, R. Pastore, M. Marchetti, R. Diana, G. Gradoni, Absorption cross section of building materials at mm wavelength in a reverberation chamber, Meas. Sci. Technol. 28 (2017) 024001. <https://doi.org/10.1088/1361-6501/aa53a1>
- [6] D. Micheli, A. Delfini, F. Piergentili, et al., Measurement of Martian Soil Electromagnetic Absorption Cross Section from 800 MHz to 6 GHz for future Mars Cellular Telecommunication systems, 2022 IEEE 9th International Workshop on Metrology for AeroSpace, MetroAeroSpace

2022 - Proceedings, Pages 219-224.

<https://doi.org/10.1109/MetroAeroSpace54187.2022.9855901>

[7] Z. Wei, Moisture in tunnel influenced to transmission features of electromagnetic wave, Coal Science and technology 31 (2003) 39-41.

[8] T. Meissner, F. J. Wentz, The complex dielectric constant of pure and sea water from microwave satellite observations, IEEE T. Geosci. Remote 42 (2004) 1836-1849.

<https://doi.org/10.1109/TGRS.2004.831888>

[9] M. Zribi, A. Le Morvan, N. Baghdadi N, Dielectric constant modelling with soil–air composition and its effect on SAR radar signal backscattered over soil surface, Sensors 8 (2008) 6810-6824. <https://doi.org/10.3390/s8116810>

The new transmitting antenna for BIRALES

G. Bianchi^{1,a}, S. Mariotti^{1,b}, M.F. Montaruli^{2,c*}, P. Di Lizia^{2,d}, M. Massari^{2,e},
M.A. De Luca^{2,f}, R. Demuru^{3,g}, G. Sangaletti^{3,h}, L. Mesiano^{3,i}, I. Boreanaz^{3,l}

¹ Istituto Nazionale di Astrofisica, Via P. Gobetti 101, 40129, Bologna, Italy

² Politecnico di Milano, Department of Aerospace Science and Technology, Via G. La Masa 34, 20156, Milan, Italy

³ SELT Aerospace & Defense, Viale delle Industrie 13/22, 20020, Arese (MI), Italy

^agermano.bianchi@inaf.it, ^bsergio.mariotti@inaf.it, ^cmarcofelice.montaruli@polimi.it,
^dpierluigi.dilizia@polimi.it, ^emauro.massari@polimi.it, ^fmariaalessandra.deluca@polimi.it,
^griccardo.demuru@selt-sistemi.com, ^hgiovanni.sangaletti@selt-sistemi.com,
ⁱluca.mesiano@selt-sistemi.com, ^livan.boreanaz@selt-sistemi.com

Keywords: Space Debris, EUSST, Radar, Emitter

Abstract. In the last decades the increasing Resident Space Objects (RSOs) population is fostering many Space Surveillance and Tracking (SST) initiatives, which are currently based on the use of ground sensors. These can be distinguished in optical, laser and radar and categorized in tracking and survey sensors. In particular, the survey radars allow to determine the orbit of both catalogued and uncatalogued objects. Italy contributes to the European SST (EUSST) activities with the Bistatic RADAR for LEO Survey (BIRALES), whose transmitter is the Radio Frequency Transmitter (TRF), located at the Italian Joint Test Range of Salto di Quirra in Sardinia, and whose receiver is a portion of the Northern Cross Radio Telescope, located at the Medicina Radio Astronomical Station, near Bologna. The current sensor configuration is undergoing an upgrade process, including the receiver field of view extension and a new transmitter station. The purpose of the work is to present the new transmitting antenna of BIRALES, showing its technological progress and the potential for the monitoring of space debris. The final objective is to produce a high technological radar to improve the performance of the EUSST sensors network. In particular, the aim is to increase both the number of detectable objects and the sensitivity to detect fragments of a few centimetres up to an altitude of 2,000 km, with a remarkable improvement of orbit determination procedures and quality. The transmitting antenna has been designed to be very flexible for any type of observations, modifying its parameters depending on the observation needs and according to the service to offer (monitoring of fragments, re-entry or for collision avoidance). The work presents the system architecture and the transmitting antenna structure, and the performance are assessed through numerical simulations.

Introduction

Due to the growing complexity of the orbital environment, space-based assets are increasingly at risk of collision with other operational spacecraft or debris [1] [2]. At the same time, objects may re-enter the Earth's atmosphere and cause damage on the ground [3]. To address these concerns, the Space Surveillance and Tracking (SST) Consortium was established by the European Parliament and the Council in 2015. The EUSST system comprises a network of ground-based sensors aimed at surveying and tracking space objects, together with processing capabilities aiming at providing data, information and services [4].

BIRALES belongs to EUSST network, and this article focuses on the description of the transmitter and the final architecture of BIRALES, showing its capabilities.



BIRALES architecture

BIRALES is a bi-static radar [5] [6] [7] which uses the North-South branch of the Northern Cross radio telescope (Fig. 1) located in Medicina (BO) as receiving antenna (RX).



Fig. 1 BIRALES receiving antenna.



Fig. 2 BIRALES current (black) and future baseline (red).

The transmitting one is currently a parabolic dish located in Sardinia with a baseline of about 580 km. A new transmitter (TX), which will guarantee further performance increases, is under construction and will be installed closer to the receiver, forming a 250 km baseline. The new TX has been designed to work perfectly coupled with the RX and aligned as much as possible at the same terrestrial meridian of the RX, in order to maximize the overlap of the two antenna beams. The location identified for the transmitting antenna is 250 km southerly, as reported in the Fig. 2. The reduced baseline will also grant an increase in sensitivity. The receiving antenna has a collective area of about 11,000 m², and it is composed by 64 parallel parabolic cylindrical reflectors with 256 receivers installed on the focal lines (4 receivers per focal line).

Two types of observations are foreseen [8]: survey mode, for catalogue updating, observation of uncontrolled re-entry of large objects and monitoring to avoid collisions, and high-sensitivity mode, to observe fragmentations events and detect small objects (down to a few centimetres). The new TX is designed to adjust the Field of View (FoV) and gain according to the specific observation requested. In survey mode, the 64 cylindrical reflectors of the Northern Cross are collected in 8 groups of 8 cylinders, regularly spaced in elevation in order to obtain a coverage of the sky of about 45 deg in the N-S direction (each individual group of 8 antennas has a FoV of about 7x7 deg). Simultaneously, the TX is switched to the survey configuration mode, in order to have the same irradiated sky area of 7x45 deg (Fig. 3).

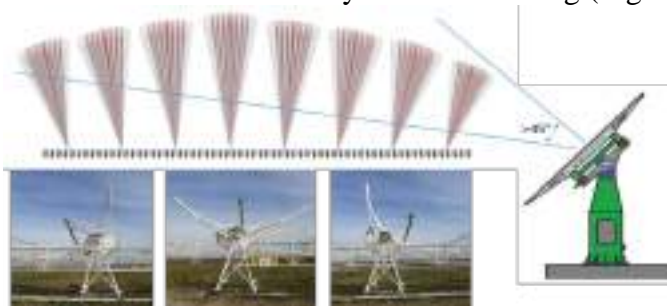


Fig. 3 BIRALES in survey configuration mode.

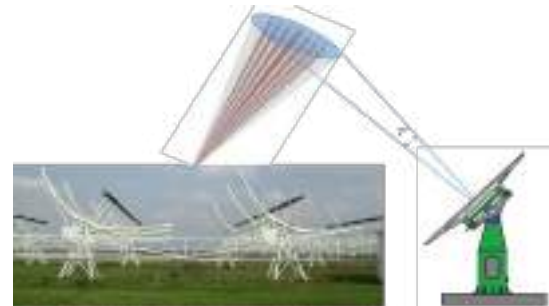


Fig. 4 BIRALES in high sensitivity mode.

In the high-sensitivity mode, the 64 cylindrical parabolic reflectors of the Northern Cross are pointed at the same declination to increase the antenna gain. At the same time, the transmitting antenna is switched to the high-sensitivity mode, increasing the gain and reducing the beam width at 7 deg (Fig. 4).

The selected architecture for the transmitting antenna is a patch array architecture (Fig. 5), composed of two sub-arrays which can be controlled to different beam apertures based on search and tracking operations (Fig. 6). The narrow beam sub-array is composed by a matrix of 8x4

antenna elements; each antenna element of the narrow beam array can sustain more than 312.5W in continuous wave (CW) mode. The wide beam sub-array is composed of a matrix of 1x8 antenna elements; each antenna element of the wide beam array can sustain more than 1.25KW of CW power. Considering the very demanding functional requirement for BIRALES, the antenna arrays and elements have been designed to optimize power factors, reflections, lobes, beam directivity and performance. The Antenna Control Unit (ACU) is installed on a two-axes pedestal able to tilt and rotate the antenna on azimuth and elevation axes. The implementation of a two-axes pedestal allows to relocate antenna beams and redirect monitoring and tracking waveforms to different sky areas (Fig. 7).

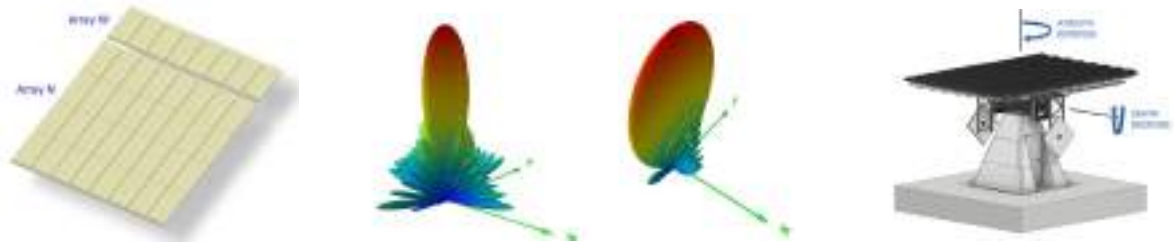


Fig. 5 Transmitting patch array antenna. Fig. 6 narrow (left) and wide (right) beams. Fig. 7 Transmitting antenna.

The new transmitting antenna will be fed by a power amplifier, able to provide an RF power up to 10 kW. Since the power amplifier is intended to operate continuously (24/7) in automatic and remote mode, the design needs to take into account the robustness and some redundancy criteria. The power amplifier will operate with two different modulations: continuous wave (CW) and pulse compression chirp modulation.

Radar performance

A simulation is carried out to evaluate the performance of the new configuration. In particular, it is fundamental to assess the importance of setting the transmitter station along the same meridian as the receiver one. To this purpose, the catalogue maintenance capability is examined in two configurations: the first configuration involves no misalignment (0 deg) between the transmitter and receiver meridians, while the second configuration introduces a misalignment of 0.2 deg between them. For both cases, a baseline of 250 km is considered. The study is conducted through the SpaceCraft and Objects Observation Planning (SCOOP) software, which, given a space objects catalogue, an analysis time window and the stations composing a survey sensor (like the ones involved in a bistatic radar), computes the observable transit. The space object catalogue is generally provided through the Two-Line Elements (TLEs), automatically downloaded from Spacetrack website, of the targets required by the user.

The simulation regards an analysis time window ranging from 00:00:00 of March 20th to 23:59:59 of March 26th, 2023 (according to a UTC time coordinate). The receiver station is considered pointed towards the zenith direction, with a FoV of 7x45 deg (7 deg in azimuth and 45 deg in elevation), that is in the survey operational mode. Both the transmitting stations are evaluated considering a 7x45 deg FoV, and three North pointing elevations are investigated: 45 deg, 60 deg and 75 deg. Results are shown in Table I and Table II, for the 0 deg and 0.2 deg offset from the receiver station meridian respectively. In particular, the number of detected objects, the number of transit and the median detection duration are reported.

Focusing on Table I it is possible to observe that the higher the pointing elevation, the larger the number of both detected objects and transits. Comparing Table I and Table II results, it is possible to observe that a 0.2 deg longitude offset with respect to the receiver meridian deteriorates the detection rate, that is the contribution to space objects catalogue maintenance.

*Tab.I 0 deg offset case.
offset case.*

Pointing elevation	Number of objects	Number of transits	Median duration
45 deg	738	1147	7.1 s
60 deg	968	1889	5.5 s
75 deg	985	2040	4.8 s

Tab.II 0.2 deg

Pointing elevation	Number of objects	Number of transits	Median duration
45 deg	722	1104	7.4 s
60 deg	788	1321	6.6 s
75 deg	739	1221	6.4 s

Conclusions

This article describes the transmitter architecture of BIRALES. Numerical simulations highlighted that placing the transmitter station along the same meridian as the receiver one would represent a remarkable plus in terms of contribution to the building-up and maintenance of the space objects catalogue.

Acknowledgement

The research activities described in this paper were performed within the European Commission Framework Programme H2020 “SST Space Surveillance and Tracking” contracts N. 952852 (2-3SST2018-20).

References

- [1] A. De Vittori et al., "Low-Thrust Collision Avoidance Maneuver Optimization", Journal of Guidance, Control, and Dynamics, 45(10), 1815-1829, 2022. <https://doi.org/10.2514/1.G006630>
- [2] A. Muciaccia, et al., "Observation and Analysis of Cosmos 1408 Fragmentation." INTERNATIONAL ASTRONAUTICAL CONGRESS: IAC PROCEEDINGS. 2022.
- [3] R. Cipollone, et al., "A Re-Entry Analysis Software Module for Space Surveillance and Tracking Operations." INTERNATIONAL ASTRONAUTICAL CONGRESS: IAC PROCEEDINGS. 2022.
- [4] M.F. Montaruli, et al., "A software suite for orbit determination in Space Surveillance and Tracking applications." 9th European Conference for Aerospace Sciences (EUCASS 2022). 2022.
- [5] G. Bianchi et al., "A new concept of bi-static radar for space debris detection and monitoring", 1st International Conference on Electrical, Computer, Communications and Mechatronics Engineering (ICECCME), 2021, pp. 1-6. <https://doi.org/10.1109/ICECCME52200.2021.9590991>
- [6] G. Bianchi, et al. "Exploration of an innovative ranging method for bistatic radar, applied in LEO Space Debris surveying and tracking." Proceedings of the International Astronautical Congress, IAC. 2020.
- [7] M.F. Montaruli, L. Facchini, P. Di Lizia, M. Massari, G. Pupillo, G. Bianchi, G. Naldi, "Adaptive track estimation on a radar array system for space surveillance", Acta Astronautica, 2022, ISSN 0094-5765. <https://doi.org/10.1016/j.actaastro.2022.05.051>
- [8] G. Bianchi et al., "A New Concept of Transmitting Antenna on Bi-Static Radar for Space Debris Monitoring", 2nd International Conference on Electrical, Computer, Communications and Mechatronics Engineering (ICECCME), 2022. <https://doi.org/10.1109/ICECCME55909.2022.9988566>

Continuous empowering with laser power transmission technologies for ISRU moon assets: CIRA approach

Maria Chiara Noviello^{1,a *}, Nunzia Favaloro^{1,b}

¹Italian Aerospace Research Centre (CIRA), Via Maiorise, 81043, Capua, CE (Italy)

Space Exploration Technologies Laboratory

^am.noviello@cira.it, ^bn.favaloro@cira.it

Keywords: ISRU, LPT, Moon, Exploration

Abstract. Due to the potential possibility of changing the dynamics of the New Space Economy, In-Situ Resource Utilization (ISRU) is acquiring more and more importance within the Space Exploration scenario. Indeed, the closest space missions will return humans to the Moon, while planning the long-term stay. This aspect opens the way to the need for employment and processing of local resources, with the aim of reducing the dependence on Earth-based resources, also ensuring the financial sustainability of the space exploration programs. ISRU technologies will demand for energy values likely to be in the Megawatt range and, eventually, at Gigawatt levels, to be ensured in the harsh hazardous environmental conditions of the celestial bodies (e.g. Moon, Mars, Near Earth Asteroids). This work, performed by the CIRA TEES Laboratory, provides the CIRA approach to the feasibility study concerning the Laser Power Transmission (LPT) technologies for Moon assets empowering. The aim is to evaluate whether LPT can be a potentially efficient solution for continuous power delivery from an orbiting source device, considering long-distance wireless employments and severe environmental conditions, to drive ISRU Moon assets (habitats, rovers, local industrial plants, conveyance facilities, et cetera). For the purpose of this study, starting from the space mission identification, an increasing complexity multi-step approach was properly conceived by CIRA to design the dedicated LPT system responding to the evaluated mission requirements.

ISRU: CIRA LPT Model & Approach

The term ISRU (In-Situ Resource Utilization) refers to the use and processing of local resources directly found on the Moon, or other planetary bodies, to obtain raw materials supporting robotic and/or human space exploration missions. ISRU technologies aim at creating products or services fundamental for lunar and Mars long-term stays, also reducing the need for continuous resupply from the Earth, [1], with an unavoidable huge impact on the dynamics of the New Space Economy.

In general terms, the ISRU domain relies on three key concepts: identification (prospecting for recoverability), processing (mining, extraction, beneficiation) and use of local (natural and artificial) resources. Each concept will imply dedicated technologies, systems and capability development involving various technical disciplines, [2]. More in detail, local resources account for the ones recoverable on extra-terrestrial bodies.

This paper deals with the problem of the Moon ISRU assets' continuous power delivery. Indeed, for the lunar case, the severe environmental conditions of the surface, combined with the long periods of darkness due to its day-night cycle, make the energy supply a pivotal issue. Several approaches have recently been considered to store and provide energy to the surface of the Moon by means of ISRU (In-Situ Resource Utilization) technology, [3]. Among the various potential solutions identified in literature, the CIRA TEES laboratory is deepening the one based on the solar power caught by dedicated satellites (Solar Power Satellites, SPS) in proper orbits, equipped with a laser system, capable of generating a power laser beam driven for long distances to activate

Moon assets (rovers, habitats, infrastructures, etc.). From now on, the overall system this work refers to will be designated as LPT (Laser Power Transmission) system, portrayed in Figure 1.

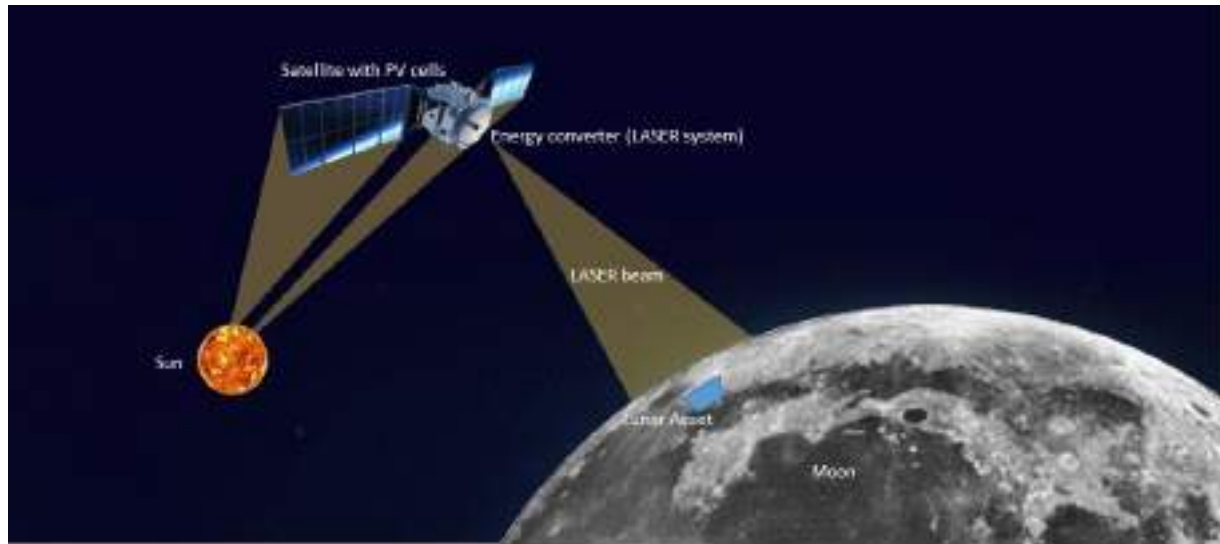


Figure 1 - Space Laser Power Transmission System Overview for Moon Assets Empowering

The space system, this work refers to, has been intended as promising in order to empower Moon assets in a continuous manner. Figure 2 reports a block schematization of the previous Figure 1, helpful to understand the here described work.

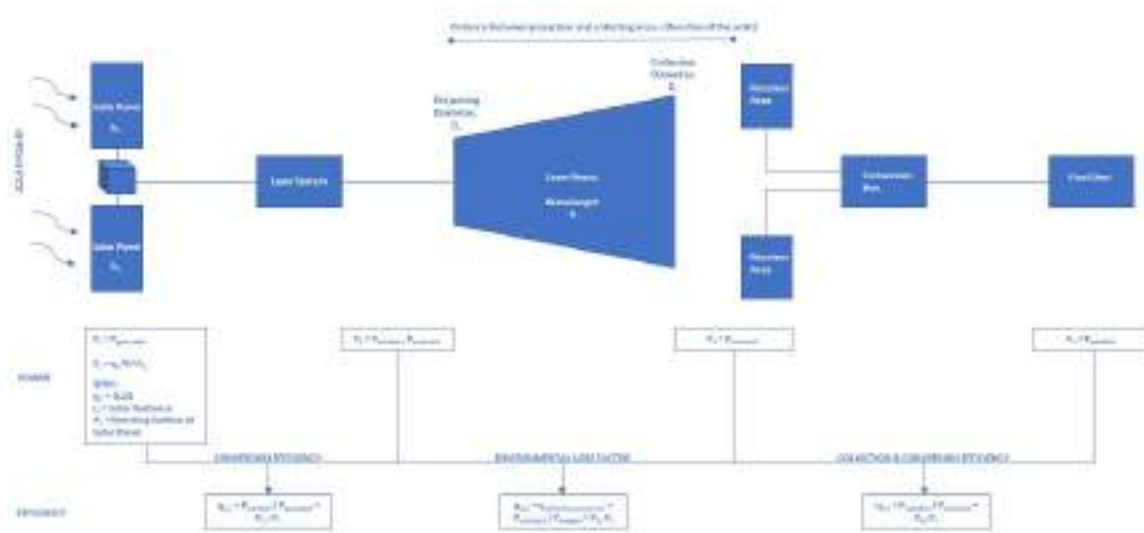


Figure 2 - CIRA LPT Preliminary Model Block Schematization

In particular, the overall system is composed by:

- One/more satellite/s, equipped with photovoltaic solar panels to catch the Sun power (the choice of the orbit is not the actual objective of this study);
- A laser system, using solar energy to generate a laser power beam;
- A laser power collecting station, with a proper receiving area;
- A conversion box, capable of converting the laser power beam into electrical energy to activate:
- A final user, which functioning needs to be guaranteed by the overall system.

Precisely, CIRA is now performing an accurate study to assess such a complex topic in terms of feasibility of the conceived system process. Thus, a multi-step dedicated approach has been developed: the main phases are depicted in Figure 3, with a focus on the Step 2.

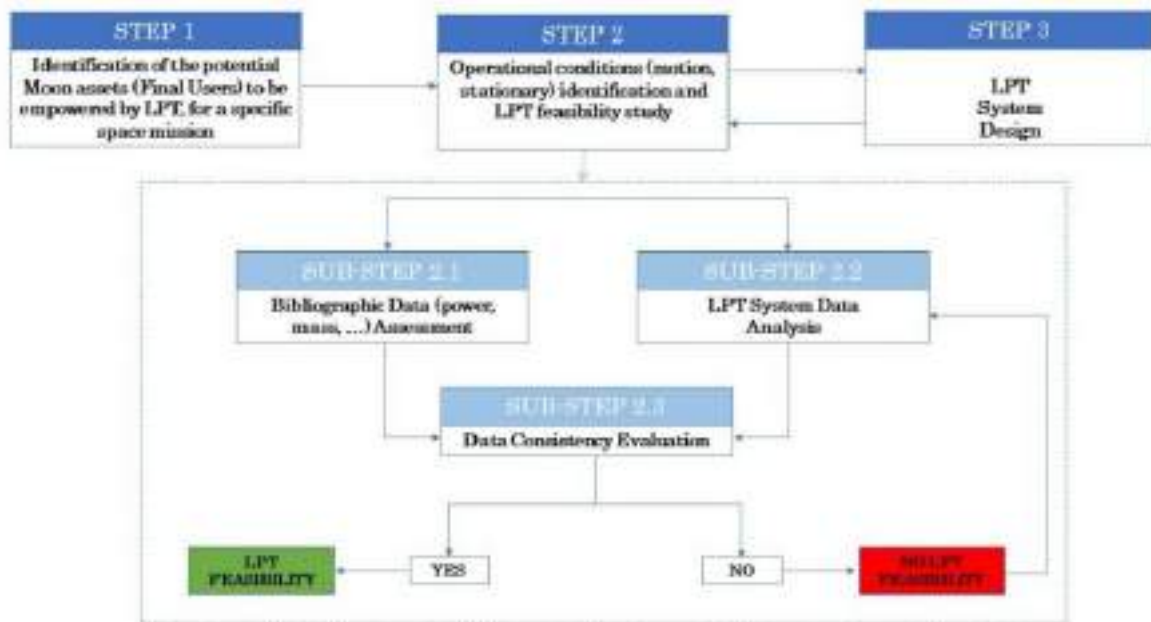


Figure 3 - LPT feasibility study for IRSU applications: the CIRA Approach

A first brief description of the conceived three steps is herein provided, while the Section 2 contains a more detailed characterization of the STEP 2, core of this work:

- STEP 1: dealing with the identification of the potential IRSU Moon assets to be empowered by means of an LPT system, for a given space mission. The Global Exploration Roadmap (GER, [6]) has been used in support of this stage to screen the possible final users of the LPT system, mentioning rovers, (for mobility, transportation, image acquisition, data measurement), landers (crew, cargo, robotic), habitats (pressurized, mono- or multi-module), industrial plants (for production and processing of materials), extraction instruments/equipment (bucket-wheel, auger/drill, scoop, pneumatic excavator), comminution instruments/equipment (size crushing, sorting), et cetera.
- STEP 2: among the final users, deriving from the Step 1, the rover has been chosen as the model to develop the preliminary LPT feasibility study in this stage. In particular, the Step 2 has been further exploded into three sub-steps:
 - ✓ SUB-STEP 2.1: after schematizing the possible operative conditions for the chosen systems (rovers), this sub-step collects literature power and mass data of (already dismissed/currently working) rovers for Moon and Mars exploration, also accounting instruments (magnetometers, spectrometers, etc.), cameras and actuators. An example of some collected data is reported in Table 1, for the Intrepid lunar rover, [4].

Table 1 - Collected mass and power data for Intrepid rover at system and sub-system level

		Operational Condition	Mass [Kg]	Power [W]	Reference
System	Intrepid Rover (Moon)	Driving Mode	371,00	239,00	Table 3-3, [4]
Sub-System	Instruments	Stationary Mode	11,50	16,00	Table 1-3, [4]
	Cameras		8,50	14,00	
	Actuators		48,31	60,00	Mass, Appendix D, [4]; Power, Table 3-2, [4]

- ✓ SUB-STEP 2.2: LPT system data analysis, by means of the implementation of analysis loops to process data resulting from the sub-step 2.1, [5], to be confronted with into the:
- ✓ SUB-STEP 2.3: dealing with the consistency assessment of the values deriving from the previous sub-steps.
- STEP 3: not object of the present work, regarding the LPT system design and optimization of design parameters, [7].

Operational Conditions Identification and LPT Feasibility Study: Focus on The Step 2

As before mentioned, the real core of this work is the Step 2, herein described more in detail.

At first, a collection of data from literature was indispensable to have an overview of the power and mass values related to still working/already dismissed Moon rover systems. Those values have been then used as key elements to drive the following two approaches, namely the direct and the reverse ones. In particular, referring to the preliminary model block scheme reported in Figure 2, the Table 2 summarizes the input and output parameters considered in both cases.

Table 2 - Direct and Reverse Approaches Input and Output Parameters for preliminary LPT Data System Analysis

Direct Approach		Reverse Approach	
Input Parameters	Ordered Output Parameters	Input Parameters	Ordered Output Parameters
η_0 , Solar Panel Efficiency	P_1 , Generated Power	P_4 , Final User Available Power	$\eta_{3,2}$, Collecting Conversion Efficiency
I_R , Solar Radiance	P_2 , Emitted Power	D_p , Projecting Beam Diameter	P_3 , Collected Power
A_1 , Emitting Surface of Solar Panels	$\eta_{3,2}$, Collecting Conversion Efficiency	D_c , Collected Beam Diameter	P_2 , Emitted Power
$\eta_{2,1}$, Laser system Conversion Efficiency	P_3 , Collected Power	r , Relative Distance Emitter - Receiver	P_1 , Generated Power
D_p , Projecting Beam Diameter	P_4 , Final User Available Power	λ , Power Beam Wavelength	A_1 , Emitting Surface of Solar Panels
D_c , Collected Beam Diameter		η_0 , Solar Panel Efficiency	
r , Relative Distance Emitter - Receiver		I_R , Solar Radiance	
λ , Power Beam Wavelength		$\eta_{2,1}$, Laser system Conversion Efficiency	
$\eta_{4,3}$, Final User Conversion Efficiency		$\eta_{4,3}$, Final User Conversion Efficiency	

Thanks to the direct approach, a sensitivity analysis of P_4 (Power Available for systems) as a function of A_1 (Solar Panel Area) has been carried out. Figure 4 reports the linear trend (based on the preliminary LPT system model) of $P_4 = P_4(A_1)$, by using Nd:YAG laser for Moon applications ($\eta_{3,2}$ resulted equal to 1, according with the lack of a consistent atmosphere).

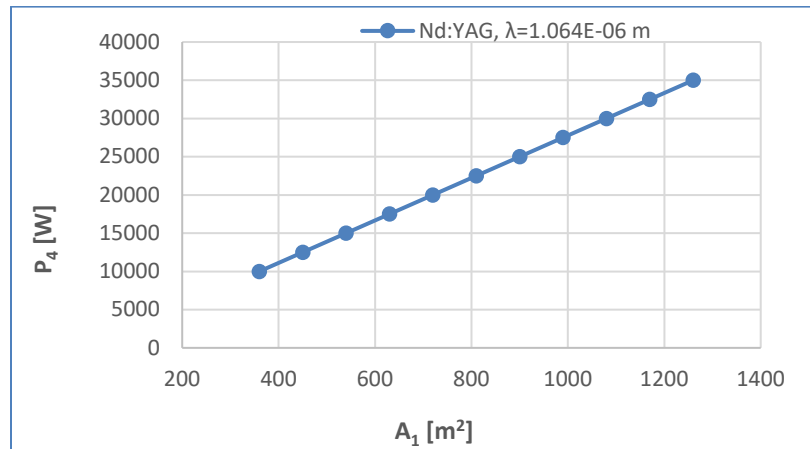


Figure 4 - Lunar Final User Power as a function of Satellite Solar Panel Area, $P_4=P_4(A_1)$

Conclusions

Referring to the challenge of the continuous empowering of Moon ISRU assets, the CIRA TEES laboratory developed a multi-step approach to conduct a preliminary feasibility study of a Solar Laser Power Transmission System for the power delivery across long distances, starting from an orbiting satellite.

At the current state, interesting results have been achieved in terms of the trend of the identified final user (rover system) available power as a function of the solar photovoltaic panels emitting area (/s, if more satellites will be considered in a more advanced system). The next step of this work will account the optimization of design parameters, such as the satellite orbit selection.

References

- [1] M. Baldry, N. Gurieff, D. F. Keogh, “Imagining Sustainable Human Ecosystems with Power-to-x in-situ Resource Utilisation Technology”, 4 November 2022. <https://doi.org/10.20944/preprints202111.0508.v1>
- [2] In-Situ Resource Utilization Gap Assessment Report, International Space Exploration Coordination Group (ISECG), NASA, 2021
- [3] M. F. Palos, P. Serra, S. Fereres, K. Stephenson, R. Gonzales-Cinca, “Lunar ISRU energy storage and electricity generation”, Acta Astronautica Journal, Volume 170, May 2020, Pages 412-420. <https://doi.org/10.1016/j.actaastro.2020.02.005>
- [4] NASA Intrepid Planetary Mission Concept Study Report, 2020
- [5] C. Cugnet, E. Sein, A. Celeste, L. Summerer, “Solar Power Satellites For Space Exploration And Applications”. November 2004
- [6] Global Exploration Roadmap, GER, ISECG (globalspaceexploration.org), Posted on 23 May, 2023
- [7] N. Favaloro et al., “Enabling Technologies for Space Exploration Missions: the CIRA-TEDS Program Roadmap Perspective”, Aerotecnica Missili & Spazio, Springer Nature, June 2023. <https://doi.org/10.1007/s42496-023-00159-4>

Preliminary design of a CubeSat in loose formation with ICEYE-X16 for plastic litter detection

Francesca Pelliccia^{1,a*}, Raffaele Minichini¹, Maria Salvato¹, Salvatore Barone¹,
Salvatore Dario dell'Aquila¹, Vincenzo Esposito¹, Marco Madonna¹,
Andrea Mazzeo¹, Ilaria Salerno¹, Antimo Verde¹, Marco Grasso¹,
Antonio Gigantino¹, Alfredo Renga¹

¹Università degli Studi di Napoli Federico II, Dipartimento di Ingegneria Industriale, Piazzale
Tecchio 80, 80125, Napoli, Italy

^afrancesca.pelliccia2@studenti.unina.it

Keywords: Plastic Detection from Space, Multispectral/SAR Database, CubeSat Mission

Abstract. Every year, more than 14 million metric tons of plastic are estimated to enter rivers, lakes, and seas [1], becoming one of the main sources of pollution with significant economic and ecological impact on sensitive habitats, welfare, and vulnerable, endangered species. In this context, keeping track of plastic litter hot-spots and their evolution in time - both in open sea and coastal areas - becomes of fundamental importance. Plastic detection from space is at an early stage and, although some interesting capabilities have been demonstrated by multi-spectral imagery, hyperspectral sensing, and GNSS reflectometry, such technologies do not yet allow for the operational detection and monitoring of plastic from space on a global scale, with sufficient temporal and spatial coverage. The characteristics of Synthetic Aperture Radar (SAR) imagery would represent a keystone to realize almost continuous global monitoring of plastic litter at sea, but robust and reliable approaches for SAR-based plastic detection at sea are not available. The main problem is the lack of a large and assessed dataset to train and test new procedures and methods (e.g., deep learning) on large scales. Starting from this point, CROSSEYE (Combined in pendulum Remote Observation cubeSat System for icEYE) mission is presented with the objective to generate a wide dataset of multi-spectral and SAR images collected at the same time over the same areas. Plastic detection in multi-spectral images is mature enough to be used as a ground truth to cue SAR-based algorithms that autonomously perform the same task. CROSSEYE exploits a pre-existing SAR satellite belonging to ICEYE constellation - ICEYE-X16 - and completes it with an additional multi-spectral camera equipped on a 6U CubeSat. The results coming from the preliminary design of CROSSEYE demonstrate the feasibility of a mission capable of detecting plastic debris from space by using state-of-the-art technologies.

Introduction

The primary objective of this mission is to validate an innovative measurement principle of combining acquisitions from different sensors, specifically electro-optical (EO) and radar systems. By leveraging the respective strengths of these technologies, namely the all-weather and all-time capabilities of radars and the spectral analysis capabilities of EO sensors, the aim is to detect plastic pollution floating in open sea (20 km or more from the coast) [2]. To achieve this, the mission will gather a comprehensive dataset of multi-spectral and synthetic aperture radar (SAR) images collected simultaneously (within four hours) over the same areas. The detection of plastic in the multi-spectral images will serve as a cue for SAR-based algorithms to perform the same task [3]. Furthermore, CROSSEYE will demonstrate how the aforementioned measurement principle can be enabled by means of a simple low-cost platform, both exploiting and enhancing the capabilities of other missions already in orbit. The mission will raise awareness of marine plastic litter among



the general public, governments, and related organizations, stimulating interest in the topic and attracting investments towards finding solutions. These objectives are aligned with the United Nations Sustainable Development Goals (SDGs) 6 [4] and 14 [5] addressing clean water, sanitation, conservation and sustainable use of marine resources.

Payload

Electro-optical pushbroom scanners have a long history of successful implementation in space applications, often relying on readily available Commercial Off-The-Shelf (COTS) components. However, the requirements of the CROSSEYE mission pose a challenge in finding off-the-shelf sensors that can meet the mission criteria while being compatible with a 6U CubeSat standard platform in terms of mass and sizes. For plastic debris detection, a 20 m ground resolution is needed [6] as well as a wide spectral range from VNIR to SWIR bands. In particular, [6] and [7] report how the computation of certain indexes might aid the detection of floating debris: the Floating Debris Index (FDI), the Normalized Difference Vegetation Index (NDVI), and the Floating Algae Index (FAI). To calculate these indexes, the payload will need to detect several bands inspired from the Sentinel-2 Multi-Spectral Instrument (MSI) - B2, B3, B4, B6, B8, B11 [8]. Consequently, a custom multispectral pushbroom scanner (Table 1) is specifically designed to meet the needs of the mission. To accommodate the different wavelength ranges, two separate detectors are necessary as the technology employed for Visible and NIR wavelengths (VNIR) differs from that required for SWIR (Short-Wave InfraRed) wavelengths. To address CubeSat size limitations, the camera utilizes a single focal plane, where the two mentioned detectors share the same optic scheme rather than having separate pushbroom designs. Special band-pass filters are necessary for the detectors to effectively sense the specific bands listed before.

Table 1 - Pushbroom scanner main specifications

		VNIR	SWIR
Telescope parameters	Focal length [mm]	400	400
	Aperture [mm]	96.0	96.0
	F/#	4.17	4.17
	FOV across track [deg]	1.76	2.20
	Swath width [km]	16.0	20.0
	Ground sampling distance [m]	15.6	9.80
	MTF @ 32.5 lin/mm	0.66	0.66
Focal plane parameters	Number of pixel (H x V)	1024 x 25	2048 x 1
	Pixel size [μm]	12 x 12	7.5 x 7.5
	Number of bands	5	1
	Pixel depth [bits per pixel]	8	8
Mission parameters	Altitude [km]	520	
	Ground resolution [m]	20.0	
	Target frequency [lin/mm]	32.5	
Sizing parameters	Mass [kg]	4.09	
	Volume [mm ³]	1.59e+06 (< 2U)	
	Data rate [Mbps]	473	
	Power consumption (Standby-On) [W]	1.00-35.0 W	

Orbit design - pendulum formation

CROSSEYE mission concept is developed around the notion of pendulum configuration, a particular type of loose formation flying, also known as parallel orbits formation. CROSSEYE CubeSat flies at a safe distance from ICEYE-X16, without affecting, limiting, or altering its

functionalities. The goal is to have CROSSEYE S/C as deputy and to have the chief role covered by ICEYE-X16 S/C, an X-band SAR satellite launched in January 2022. The orbital parameters of the chief satellite are reported in Table 2.

Table 2 - ICEYE X-16 orbital parameters

Altitude [km]	Inclination [deg]	LTAN	Eccentricity	AOP [deg]
525	97.485	10:00 PM	0.0011925	67.3522

According to the chosen configuration, CROSSEYE S/C orbit is defined in relation to the orbital parameters of ICEYE-X16 S/C: the formation is achieved by separating the orbits of the two spacecrafts in terms of Right Ascension of the Ascending Node (RAAN) Ω and true anomaly v . $\Delta\Omega$ and Δv are determined from geometrical considerations (Fig. 1), where R_B is the Slant Range at boresight, α is the angle between CROSSEYE S/C and ICEYE-X16 S/C nadiral direction of observation, q is the aperture angle of ICEYE-X16 SAR. Given the risk of collision, especially when flying where the orbits cross - at poles -, CROSSEYE S/C and ICEYE-X16 S/C are separated in eccentricity, too [9]. The pendulum formation parameters are listed in Table 3; the CROSSEYE S/C orbital parameters are derived (Table 4). The orbit is defined as SSO, and the Argument of Perigee (AOP) is chosen to make the orbit of CROSSEYE S/C frozen [10].

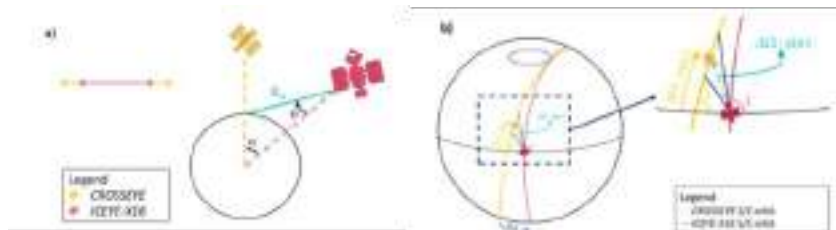


Fig. 1 - a) CROSSEYE and ICEYE-X16 relative observation geometry; b) Pendulum configuration: geometry

Table 3 - Pendulum formation parameters

$\Delta\Omega$ [deg]	Δv [deg]	Δe
1.7263	-0.22488	-1.2149 e-04

Table 4 - CROSSEYE S/C orbital parameters

Altitude [km]	Inclination [deg]	LTAN	Eccentricity	AOP [deg]
525	97.485	10:00 PM	0.0010710	90

Space Segment

Other than the payload, CROSSEYE S/C consists of an attitude determination and control subsystem (ADCS), an on-board data-handling subsystem, an on-board software, a communication subsystem, an electric power subsystem (EPS), a passive thermal control subsystem (TCS), a chemical propulsion subsystem. A GNSS receiver is mounted on the platform to obtain accurate position and velocity measurements. ADCS guarantees Nadir pointing during observations with a minimum accuracy of 1% of the FOV of the equipped EO payload. As attitude control, a three-axis stabilized strategy is adopted by pairing reaction wheels with magnetorquers. Concerning the EPS, triple junction GaAs solar cells are selected for the solar arrays and Lithium-Polymer are chosen for the batteries. TCS consists of a thermal coating formed by a mixture of aluminium and white paint. Considering the significant data rate of the payload, TT&C subsystem is composed of an X-band antenna and a diplexer interfacing with an X-band transceiver. As for the propulsion subsystem, thrusters use an ammonium dinitramide-based *green* monopropellant, in line with the sustainable nature of the mission. Except for the payload, all the components of the subsystems are COTS and easily integrable with each other, resulting in a standard 6U CubeSat

architecture compliant with the CubeSat Design Specifications [11]. CROSSEYE space segment communicates with its ground segment. This relies on 11 of the 17 active Leaf Space network ground stations placed at middle latitudes all around the world.

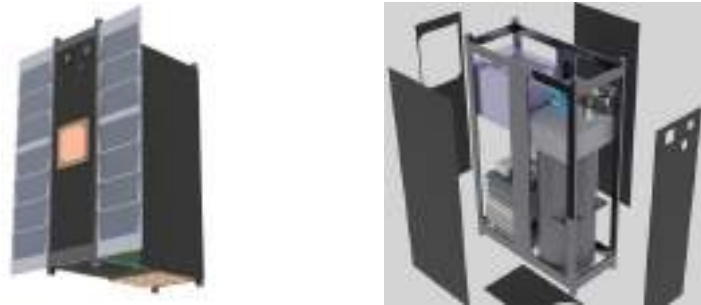


Fig. 2 - CROSSEYE platform CAD model and exploded view

Conclusions and further development

An incremental strategy can be implemented for CROSSEYE mission: by limiting the initial expenditure to a single CubeSat mission, this can be replaced or augmented with future missions of the same type to widen the quantity and quality of collected data. The design here proposed is easily adaptable to other SAR-equipped platforms that, mutatis mutandis, will have the capability to build a database that is tailored to fit the customer's demands (i.e., wildfire, coastal erosion, plastics). In general, the capabilities of CubeSat-related technologies are expected to improve in coming years: the combination of miniaturization challenges, and the potential for future technological advancements create an exciting prospect for the CROSSEYE mission. Else than technicalities, the mission will set the stage for significant contribution to plastic litter detection from space, promoting sustainability and furthering the understanding of Earth's ecosystem.

References

- [1] Information on <https://www.iucn.org/resources/issues-brief/marine-plastic-pollution>
- [2] Information on https://www.un.org/Depts/los/convention_agreements/texts/unclos/part2.htm
- [3] Savastano S. et al., A First Approach to the Automatic Detection of Marine Litter in SAR Images Using Artificial Intelligence, IEEE International Geoscience and Remote Sensing Symposium IGARSS (2021) 8704-8707. <https://doi.org/10.1109/IGARSS47720.2021.9737038>
- [4] Information on <https://sdgs.un.org/goals/goal6>
- [5] Information on <https://sdgs.un.org/goals/goal14>
- [6] Biermann L. et al., Finding Plastic Patches in Coastal Waters using Optical Satellite Data, Sci Rep 10, 5364 (2020). <https://doi.org/10.1038/s41598-020-62298-z>
- [7] Hu C., A novel ocean color index to detect floating algae in the global oceans", Remote Sensing of Environment 113 (2009) 2118-2129. <https://doi.org/10.1016/j.rse.2009.05.012>
- [8] Morales - Caselles C. et al., An inshore-offshore sorting system revealed from global classification of ocean litter, Nature Sustainability 4 (2021) 484-493. <https://doi.org/10.1038/s41893-021-00720-8>
- [9] D'Errico M. et al., Relative Trajectory Design, Distributed Space Missions for Earth System Monitoring. Space Technology Library 31 (2019).
- [10] Fasano G., Space Flight Dynamics lectures University of Naples Federico II (2022).
- [11] The CubeSat Program, CubeSat Design Specification (1U - 12U) - Revision 14.1 (2022).

A revisited and general Kane's formulation applied to very flexible multibody spacecraft

D.P. Madonna^{1,a}, P. Gasbarri^{2,b}, M. Pontani^{3,c}, F. Gennari^{4,d},
L. Scialanga^{4,e} and A. Marchetti^{4,f}

¹Department of Mechanical and Aerospace Engineering, Sapienza University of Rome, via Eudossiana 18, 00184 Rome, Italy

²School of Aerospace Engineering, Sapienza University of Rome, via Salaria 851, 00138 Rome, Italy

³Department of Astronautical, Electrical, and Energy Engineering, Sapienza University of Rome, via Salaria 851, 00138 Rome, Italy

⁴Thales Alenia Space Italia, via Saccomuro 24, 00131 Rome, Italy

^adavidpaolo.madonna@uniroma1.it, ^bpaolo.gasbarri@uniroma1.it, ^cmauro.pontani@uniroma1.it,
^dfabrizio.gennari@thalesaleniaspace.com, ^eluigi.scialanga@thalesaleniaspace.com,
^fandrea.marchetti@thalesaleniaspace.com

Keywords: Multibody Spacecraft Dynamics, Kane's Method, Flexible Spacecraft

Abstract. Current space missions require predicting the spacecraft dynamics with considerable reliability. Among the various components of a spacecraft, subsystems like payload, structures, and power depend heavily on the dynamic behavior of the satellite during its operational life. Therefore, to ensure that the results obtained through numerical simulations correspond to the actual behavior, an accurate dynamical model must be developed. In this context, an implementation of Kane's method is presented to derive the dynamical equations of a spacecraft composed of both rigid and flexible bodies connected via joints in tree topology. Starting from the kinematics of two generic interconnected bodies, a systematic approach is derived and the recursive structure of the equations is investigated. The Kane's formulation allows a relatively simple derivation of the equation of motion while obtaining the minimum set of differential equations, which implies lower computational time. On the other hand, this formulation excludes reaction forces and torques from the dynamical equations. Nevertheless, in this work a strategy to compute them a posteriori without further numerical integrations is presented. Flexibility is introduced through the standard modal decomposition technique, so that modal shapes obtained by FEA software can be directly utilized to characterize the elastic motion of the flexible bodies. A spacecraft composed of a rigid bus and several flexible appendages is modeled and numerical simulations point out that this systematic method is very effective for this illustrative example.

Introduction

The advanced level of technology in space missions and the substantial economic investment they require necessitate a high level of predictability in all aspects of the mission. The performance of critical subsystems, such as the payload, structures, and power subsystem, is directly influenced by the dynamic behavior of the satellite throughout its operational lifetime. Therefore, it is crucial to develop an accurate dynamical model that ensures the correspondence between numerical simulations and the actual behavior of the satellite. While it may be acceptable in some cases to model the spacecraft as a single rigid body, typically it is necessary to consider the satellite as a multibody system comprising both rigid and flexible elements. Various approaches exist to derive the dynamical equations of a multibody system. However, in this work, Kane's formulation is exclusively adopted due to its distinct advantages in terms of both algebraic and computational



aspects [1]. A practical version of Kane's equation, as provided in [2], has been extended in this research to encompass spacecraft consisting of both flexible and rigid bodies. The outcome is a concise matrix formulation that is also compatible with the results of modal analysis obtained through a finite element code such as NASTRAN.

Kinematics

Before providing the general form of Kane's equation, it is necessary to outline the kinematic quantities of interest.

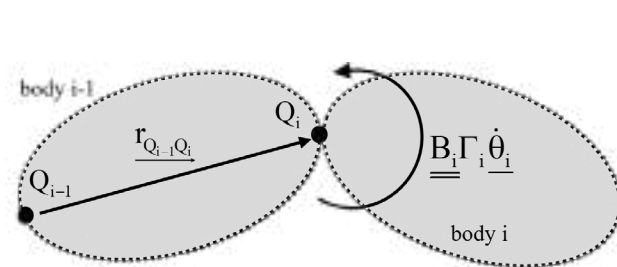


Fig. 1: two bodies connected via rotary joint

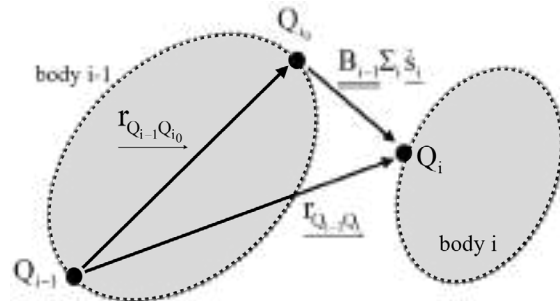


Fig. 2: two bodies connected via prismatic joint

Considering Figs. 1-2, the linear velocity of the connection point Q_i between two flexible bodies and the angular velocity of body i , both evaluated with respect to the inertial frame N , are

$$\text{rotary joint: } \begin{cases} \underline{N} \underline{v}^{Q_i} = \underline{N} \underline{v}^{Q_{i-1}} - \underline{B}_{i-1} \underline{r}_{Q_{i-1}Q_i}^J \underline{\omega}_{i-1} + \underline{B}_{i-1} \sum_{k=1}^{n_F} \underline{\Phi}_k^{(i-1)}(Q_i) \dot{q}_k \\ \underline{N} \underline{\omega}^{B_i} = \underline{N} \underline{\omega}^{B_{i-1}} + \underline{B}_i \Gamma_i \dot{\theta}_i \end{cases} \quad (1)$$

$$\text{prismatic joint: } \begin{cases} \underline{N} \underline{v}^{Q_i} = \underline{N} \underline{v}^{Q_{i-1}} - \underline{B}_{i-1} \underline{r}_{Q_{i-1}Q_i}^J \underline{\omega}_{i-1} + \underline{B}_{i-1} \sum_{k=1}^{n_F} \underline{\Phi}_k^{(i-1)}(Q_i) \dot{q}_k + \underline{B}_{i-1} \Sigma_i \dot{s}_i \\ \underline{N} \underline{\omega}^{B_i} = \underline{N} \underline{\omega}^{B_{i-1}} \end{cases} \quad (2)$$

where $\underline{\square}$ denotes an invariant physical vector, $\underline{\square}^J$ denotes the components of a vector, $\underline{B}_i = \begin{bmatrix} \underline{b}_1 & \underline{b}_2 & \underline{b}_3 \end{bmatrix}$ is the vectrix associated with the i -th body frame [3], superscript “ J ” denotes the skew matrix associated with a vector, Γ_i and Σ_i are the i -th rotary and prismatic “joint partial” respectively, i.e. the $3 \times n_j$ matrices (n_j is the number of degrees of freedom allowed by the joint) that, if post multiplied by the i -th joint velocity vector (angular $\dot{\theta}_i$ or linear \dot{s}_i), provide the relative velocity of the i -th body with respect to the $(i-1)$ -th body [2]. Moreover, following the standard modal decomposition approach [4], $\underline{\Phi}_k^{(i)}(P_i)$ is the k -th modal shape associated with the i -th body and evaluated in the generic point P_i of body i , while q_k is the k -th modal amplitude and n_F is the total number of elastic modes. For the sake of clarity, it is important to notice that $\underline{q} = [q_1 \ \cdots \ q_k \ \cdots \ q_{n_F}]$ contains the concatenation of the elastic modes of all the flexible bodies that compose the structure, so $\underline{\Phi}_k^{(i)}(P_i)$ is a zero vector when k corresponds to the elastic mode of a body different from the i -th one. The “Eulerian” velocities of Eqs. 1-2 are a function of the generalized velocities, i.e. the minimum-dimension set of velocities that completely describe the system dynamics. Considering a typical spacecraft topology and calling the bus “body 1”, the vector of generalized velocities shows the following structure:

$$\underline{u} = \begin{bmatrix} \underline{v}_{Q_1}^T & \underline{\omega}_1^T & \left\{ \dot{\underline{\theta}}_i^T \right\}_{N_{RJ}} & \left\{ \dot{\underline{s}}_i^T \right\}_{N_{PJ}} & \dot{q}_1 & \cdots & \dot{q}_{n_F} \end{bmatrix} \quad (3)$$

where \underline{v}_1 and $\underline{\omega}_1$ are the components of linear and angular velocity of the bus respectively (being the root body, Q_1 can be any point of body 1), written with respect to \underline{B}_1 ; the terms in parentheses refer to N_{RJ} revolute joints and N_{PJ} prismatic joints, respectively. To pass from generalized velocities to the Eulerian ones, it is necessary to introduce the partial velocity matrices, which play a crucial role in the Kane's formulation [5]. Specifically, the $3N_B \times 1$ vector (N_B is the number of bodies) containing the velocities of all points Q_i written with respect to \underline{B}_1 is obtained by pre-multiplying \underline{u} by the matrix of linear partial velocities V , while the angular velocities are provided by the use of the matrix of angular partial velocities Ω . Both V and Ω have dimensions $3N_B \times n$, where n is the total number of degrees of freedom of the structure. Each $3 \times n$ block is associated with a body, while each column is associated with a single degree of freedom of the system. Thanks to recursion, in Eqs. 1-2, it is possible to identify a repeating structure even in the partial velocities. Specifically, the i -th $3 \times n_{DOF}$ block shows the following structure:

$$V_i = \begin{bmatrix} \underline{R}_{i \leftarrow 1} & -\widetilde{\underline{R}}_{i \leftarrow 1} \underline{r}_{Q_1 Q_i}^{(1)} & \left\{ -\widetilde{\underline{R}}_{i \leftarrow j} \underline{r}_{Q_j Q_i}^{(j)} \Gamma_j \right\}_{N_{RJ}} & \left\{ \underline{R}_{i \leftarrow j} \Sigma_{j+1} \right\}_{N_{PJ}} & \left\{ \sum_{m=1}^{i-1} \underline{R}_{i \leftarrow m} \Phi_k^{(m)}(Q_{m+1}) \right\}_{n_F} \end{bmatrix} \quad (4)$$

$$\Omega_i = \begin{bmatrix} 0_{3 \times 3} & \underline{R}_{i \leftarrow 1} & \left\{ \underline{R}_{i \leftarrow j} \Gamma_j \right\}_{N_{RJ}} & 0_{3 \times n_{PJ}} & 0_{3 \times n_F} \end{bmatrix} \quad (5)$$

where $\underline{R}_{i \leftarrow j}$ is the rotation matrix from frame \underline{B}_j to frame \underline{B}_i , superscript (i) in vectors specifies the frame with respect the components are written to, j refers to the body downstream of the joint whose degrees of freedom are being considered, n_{PJ} is the total number of degrees of freedom associated with prismatic joints. Moreover, the last component in Eq. 4 needs the introduction of the concept of "kinematic chain" to be explained. The kinematic chain can be seen as a branch of the tree topology of the multibody spacecraft. Every kinematic chain starts from the root body (body 1) and branches out to one of the terminal bodies: the number of kinematic chains of a structure corresponds to the number of end bodies. Hence, the index m in the last term of Eq. 4 proceeds only along bodies belonging to the same kinematic chain. Furthermore, all the terms in parentheses of Eqs. 4-5 must be replaced by blocks of zeros (with consistent dimensions) if the two considered bodies do not belong to the same kinematic chain.

To complete the kinematic description, accelerations must be derived. In Kane's formulation, it is important to identify the terms of the accelerations that do not depend on the time derivative of the generalized velocities. These terms are called "remainder accelerations" and, with reference to the building blocks in Figs. 1-2, show the following structure:

$$RJ: \begin{cases} \underline{a}_i^{(R)} = \underline{R}_{i \leftarrow i-1} \underline{a}_{i-1}^{(R)} \Big|_{Q_i} \\ \underline{a}_i^{(R)} \Big|_{Q_{i+1}} = \underline{R}_{i \leftarrow i-1} \underline{a}_{i-1}^{(R)} \Big|_{Q_i} - \widetilde{\underline{r}}_{Q_i Q_{i+1}} \underline{\omega}_i^* - \widetilde{\underline{\omega}}_i \widetilde{\underline{r}}_{Q_i Q_{i+1}} \underline{\omega}_i + 2 \widetilde{\underline{\omega}}_i \sum_{k=1}^{n_F} \Phi_k^{(i)}(Q_{i+1}) \dot{q}_k \\ \underline{\alpha}_i^{(R)} = \underline{R}_{i \leftarrow i-1} \underline{\alpha}_{i-1}^{(R)} + \dot{\underline{\Gamma}}_i \dot{\underline{\theta}}_i + \widetilde{\underline{\omega}}_i \underline{\Gamma}_i \dot{\underline{\theta}}_i \end{cases} \quad (6)$$

$$PJ: \begin{cases} \underline{a}_i^{(R)} = \underline{R}_{i \leftarrow i-1} \underline{a}_{i-1}^{(R)} \Big|_{Q_i} \\ \underline{a}_i^{(R)} \Big|_{Q_{i+1}} = \underline{R}_{i \leftarrow i-1} \underline{a}_{i-1}^{(R)} \Big|_{Q_i} - \underline{r}_{Q_i Q_{i+1}}^* \underline{\omega}_i - \left(\dot{\underline{S}}_{i+1} \underline{s}_{i+1} + 2 \underline{\Sigma}_{i+1} \dot{\underline{s}}_{i+1} \right) \underline{\omega}_i \\ \quad - \underline{\omega}_i^T \underline{r}_{Q_i Q_{i+1}} \underline{\omega}_i + 2 \underline{\omega}_i^T \sum_{k=1}^{n_F} \underline{\Phi}_k^{(i)}(Q_{i+1}) \dot{q}_k + \dot{\underline{S}}_{i+1} \dot{\underline{s}}_{i+1} \\ \underline{\alpha}_i^{(R)} = \underline{R}_{i \leftarrow i-1} \underline{\alpha}_{i-1}^{(R)} \end{cases} \quad (7)$$

$$\underline{\omega}_i^* = \dot{\underline{R}}_{i \leftarrow i-1} \underline{\omega}_i + \sum_{m=2}^{i-1} \left(\dot{\underline{R}}_{i \leftarrow m} \underline{\Gamma}_m \dot{\underline{\theta}}_m + \underline{R}_{i \leftarrow m} \underline{\dot{\Gamma}}_m \dot{\underline{\theta}}_m \right) + \underline{\dot{\Gamma}}_i \dot{\underline{\theta}}_i \quad (8)$$

Actually, even in this case the structure must follow the scheme of kinematic chains: the passage from body $i-1$ to body i must be intended as a passage between two consecutive bodies on the same kinematic chain, not as a passage between two bodies with consecutive numeration. As for the last term of Eq. 4, the index m in Eq. 8 proceeds along the kinematic chains, not following the consecutive numeration.

Kane's equations

Applying the Kane's procedure to derive the dynamics of a multibody structure, the following expression is obtained:

$$\begin{aligned} & \left\langle \underline{V}^T \{ \underline{M} \underline{V} - \underline{S} \underline{\Omega} + \underline{B} \underline{\Delta} \} + \underline{\Omega}^T \{ \underline{S} \underline{V} - \underline{J} \underline{\Omega} + \underline{C} \underline{\Delta} \} + \underline{\Delta}^T \{ \underline{B}^T \underline{V}_F - \underline{C}^T \underline{\Omega}_F + \underline{Y} \underline{\Delta} \} \right\rangle \dot{\underline{u}} = \\ & = \underline{V}^T \{ -\underline{M} \underline{a}^{(R)} + \underline{S} \underline{\alpha}^{(R)} + [\underline{\tilde{\omega}} \underline{S} \underline{\omega}] - 2 [\underline{\tilde{\omega}} \underline{B}] \} + \underline{\Omega}^T \{ -\underline{S} \underline{a}^{(R)} - \underline{J} \underline{\alpha}^{(R)} - [\underline{\tilde{\omega}} \underline{J} \underline{\omega}] - 2 [\underline{N} \underline{\omega}] \} + \\ & + \underline{\Delta}^T \{ -\underline{B}^T \underline{a}_F^{(R)} - \underline{C}^T \underline{\alpha}_F^{(R)} + [\underline{\omega}^T \underline{L} \underline{\omega}] + 2 [\underline{\omega}^T \underline{d}] \} - \underline{K} \underline{q} - \underline{Z} \dot{\underline{q}} + \underline{\hat{f}} \end{aligned} \quad (9)$$

where $\underline{\Delta} = \begin{bmatrix} 0_{n_F \times n_R} & \underline{I}_{n_F \times n_F} \end{bmatrix}$, being n_R and n_F the rigid and flexible degrees of freedom respectively of the whole system, \underline{M} , \underline{S} and \underline{J} are matrices containing masses, static moments and inertia moments respectively, \underline{B} and \underline{C} are matrices containing translation and rotation modal participation factors respectively of all the flexible bodies of the structure; \underline{Y} is the modal mass matrix, $\underline{a}^{(R)}$ and $\underline{\alpha}^{(R)}$ are $3N_B \times 1$ vectors containing respectively linear and angular remainder accelerations of all the bodies, subscript F in vectors and matrices indicates that only rows associated with flexible bodies must be retained, $\underline{\omega}$ is the $3N_B \times 1$ vector containing the angular velocities of all the bodies, \underline{N} , \underline{L} and \underline{D} are three other modal integrals (in addition to \underline{B} , \underline{C} and \underline{G}), \underline{K} is the stiffness matrix, \underline{Z} is the damping matrix, $\underline{\hat{f}}$ is the vector containing the generalized active forces, i.e. the projection of external and interface forces and torques along the directions of partial velocities [5]. The structure of the terms appearing in Eq. 9 are reported in the Appendix.

Extraction of constraint reactions

The unavailability of constraint reactions is a significant limitation in Kane's formulation. However, for spacecraft with a tree topology configuration, it is possible to reconstruct the time histories of constraint reactions quite easily through a post-processing approach that relies on Newton/Euler equations, following the numerical integration of Kane's equations. In fact, unlike Kane's method, the Newton/Euler formulation for multibody structures incorporates constraint reactions in the state vector (however, this inclusion leads to longer computational times) [1, 6]. The procedure follows the subsequent steps: after the numerical solution of Kane's equations, one obtains $\underline{u}(t)$ and $\dot{\underline{u}}(t)$. Then, by utilizing the partial velocities and remainder accelerations, it is

possible to reconstruct the temporal profiles of velocities and accelerations for all bodies within the structure. As a result, the constraint reactions become the only unknowns in the Newton-Euler equations that can be resolved through a post-processing module. During this operation, a top-down approach is necessary, starting from the bodies at the end of the kinematic chains. This is because each of these bodies has only a single joint, and one can then proceed backward along the kinematic chain toward the root body. In the example of Fig. 4,

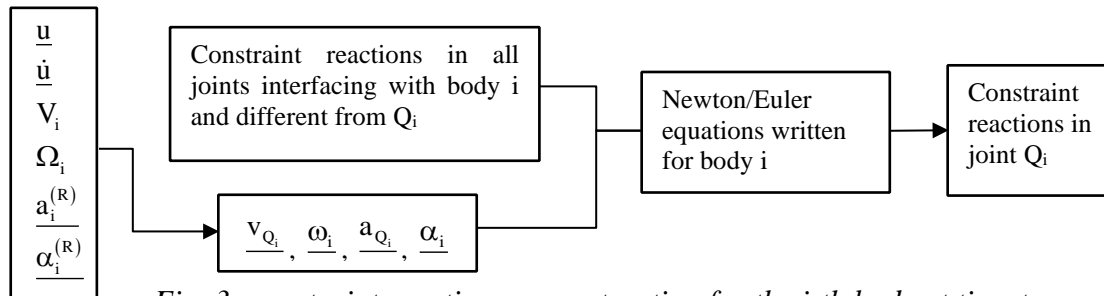


Fig. 3: constraint reactions reconstruction for the i -th body at time t

the constraint reactions must be computed first in joints Q_3 , Q_4 and Q_6 , and then in joints Q_2 and Q_5 . The order of computing reactions for joints with the same subordination ranking can be any.

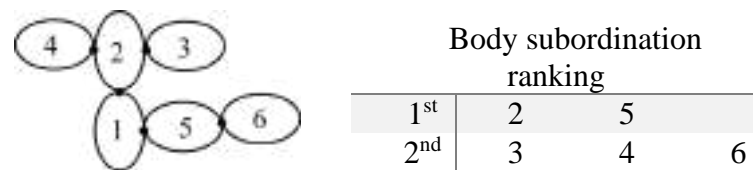


Fig. 4: example of top-down logic in deriving the constraint

Illustrative results

simulation

The presented formulation has been implemented in a numerical code to simulate the dynamic behavior of Explorer I, which is the same case studied in Reference [2]. The spacecraft consists of a cylindrical rigid bus and four appendages connected to the bus, as depicted in Figure 5. Similarly to the study in Reference [2], this investigation focuses on the spontaneous transition from a minor-axis to a major-axis spin caused by damping effects in the structure. However, there is a difference in the approach: while the analysis reported in [2] considered the appendages as rigid and introduced flexibility by incorporating a torsional spring-damper system at the interfaces between the appendages and the bus, in this work, the appendages are directly treated as flexible beams attached to the central the body of the spacecraft. Figure 6 illustrates the expected behavior of the bus angular velocity components, which exhibit the previously mentioned transition of the rotational behavior.

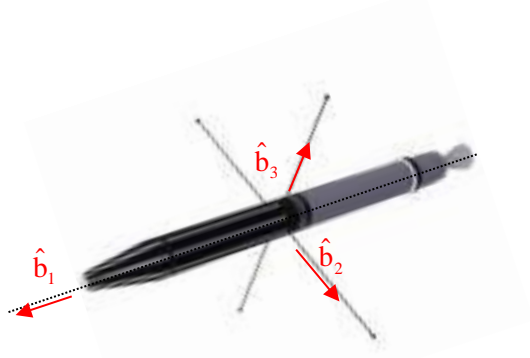


Fig. 5: sketch of the Explorer I [7]

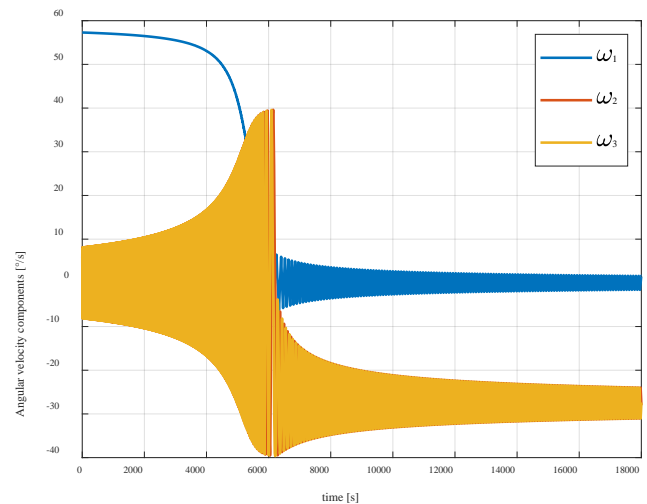


Fig. 6: time histories of the angular velocity components

Concluding remarks

A revised formulation of Kane's dynamical equations for a flexible multibody spacecraft is presented. By conducting a kinematic analysis, the expressions for partial velocities and remainder accelerations are derived, while emphasizing their recursive nature. The complete matrix formulation is provided, along with a proposed strategy for determining constraint reactions. Additionally, a numerical implementation of the formulation at hand is presented using the case of the Explorer I mission.

References

- [1] A. Pisculli, L. Felicetti, M. Sabatini, P. Gasbarri and G. B. Palmerini, "A Hybrid Formulation for Modelling Multibody Spacecraft", *Aerotecnica Missili & Spazio*, no. 94, pp. 91-101, 2015. <https://doi.org/10.1007/BF03404692>
- [2] E. T. Stoneking, "Implementation of Kane's Method for a Spacecraft", in *AIAA Guidance, Navigation, and Control (GNC) Conference*, Boston, 2013. <https://doi.org/10.2514/6.2013-4649>
- [3] P. C. Hughes, "Spacecraft Attitude Dynamics", Wiley, 1986. <https://doi.org/10.1017/S0001924000015578>
- [4] S. S. Rao, "Vibration of Continuous Systems", Wiley, 2007. <https://doi.org/10.1002/9780470117866>
- [5] C. M. Roithmayr and D. H. Hodges, "Dynamics: Theory and Application of Kane's Method", Cambridge, 2016. <https://doi.org/10.1115/1.4034731>
- [6] P. Santini and P. Gasbarri, "Dynamics of multibody systems in space environment; Lagrangian vs. Eulerian approach". *Acta Astronautica*, vol. 54, no. 1, pp. 1-24, 2004. [https://doi.org/10.1016/S0094-5765\(02\)00277-1](https://doi.org/10.1016/S0094-5765(02)00277-1)
- [7] "Explorer 1 - Overview", NASA JPL, [Online]. Available: <https://explorer1.jpl.nasa.gov/about/>.

APPENDIX

A1. mass distribution and modal integrals

In the following expressions, the index “j” indicates the body, while the indices “k” and “l” identify the elastic mode.

- $\underline{m}_j = \int_{B_j} dm$
- $\underline{b}_k^j = \int_{B_j} \underline{\Phi}_k^j dm$
- $\underline{s}_j = \int_{B_j} \underline{r}_{Q_j P_j} dm + \sum_{k=1}^{n_F} \underline{b}_k^j q_k$
- $\underline{c}_k^j = \int_{B_j} \underline{\widetilde{r}_{Q_j P_j}^j} \underline{\Phi}_k^j dm$
- $\underline{d}_{kl}^j = \int_{B_j} \underline{\widetilde{\Phi}_k^j} \underline{\Phi}_l^j dm$
- $\underline{g}_k^j = \underline{c}_k^j - \sum_{l=1}^{n_F} \underline{d}_{kl}^j q_k$
- $\underline{y}_k^j = \int_{B_j} \left(\underline{\Phi}_k^j \right)^2 dm$
- $\underline{N}_k^j = - \int_{B_j} \underline{\widetilde{\Phi}_k^j} \underline{\widetilde{r}_{Q_j P_j}^j} dm$
- $\underline{J}_j = - \int_{B_j} \underline{\widetilde{r}_{Q_j P_j}^j} \underline{\widetilde{r}_{Q_j P_j}^j} dm + \sum_{k=1}^{n_F} \left(\underline{N}_k^j + \underline{N}_k^{jT} \right) q_k$
- $\underline{L}_k^j = \underline{N}_k^j - \sum_{l=1}^{n_F} q_l \int_{B_j} \underline{\widetilde{\Phi}_l^j} \underline{\widetilde{\Phi}_k^j} dm$

A2. description of the terms of eq. 9

$$\begin{aligned}
 \underline{M} &= \begin{bmatrix} m_1 \underline{I}_{3 \times 3} & & 0 \\ & m_2 \underline{I}_{3 \times 3} & \\ & & \ddots \\ 0 & & & m_{N_B} \underline{I}_{3 \times 3} \end{bmatrix} & \underline{S} &= \begin{bmatrix} \underline{s}_1 & & 0 \\ \sim & \underline{s}_2 & \\ & \ddots & \\ 0 & & \sim & \underline{s}_{N_B} \end{bmatrix} & \underline{J} &= \begin{bmatrix} J_1 & & 0 \\ & J_2 & \\ & & \ddots \\ 0 & & & J_{N_B} \end{bmatrix} \\
 \underline{B} &= \begin{bmatrix} \underline{b}_1^1 & \underline{b}_2^1 & \cdots & \underline{b}_{n_F}^1 \\ \underline{b}_1^2 & \underline{b}_2^2 & \cdots & \underline{b}_{n_F}^2 \\ \vdots & \vdots & \vdots & \vdots \\ \underline{b}_1^{N_{B,F}} & \underline{b}_2^{N_{B,F}} & \cdots & \underline{b}_{n_F}^{N_{B,F}} \end{bmatrix} & \underline{C} &= \begin{bmatrix} \underline{c}_1^1 & \underline{c}_2^1 & \cdots & \underline{c}_{n_F}^1 \\ \underline{c}_1^2 & \underline{c}_2^2 & \cdots & \underline{c}_{n_F}^2 \\ \vdots & \vdots & \vdots & \vdots \\ \underline{c}_1^{N_{B,F}} & \underline{c}_2^{N_{B,F}} & \cdots & \underline{c}_{n_F}^{N_{B,F}} \end{bmatrix} & \underline{G} &= \begin{bmatrix} \underline{g}_1^1 & \underline{g}_2^1 & \cdots & \underline{g}_{n_F}^1 \\ \underline{g}_1^2 & \underline{g}_2^2 & \cdots & \underline{g}_{n_F}^2 \\ \vdots & \vdots & \vdots & \vdots \\ \underline{g}_1^{N_{B,F}} & \underline{g}_2^{N_{B,F}} & \cdots & \underline{g}_{n_F}^{N_{B,F}} \end{bmatrix}
 \end{aligned}$$

$$Y = \begin{bmatrix} Y^1 & & 0 \\ & Y^2 & \\ & & \ddots \\ 0 & & & Y^{N_{B,F}} \end{bmatrix} \quad \text{where } Y^j = \begin{bmatrix} y_1^j & & \\ & \ddots & \\ & & y_{n_{F,j}}^j \end{bmatrix}$$

$N_{B,F}$ is the number of flexible bodies in the multibody spacecraft
 $n_{F,j}$ is the number of elastic modes associated with the j-th body

$$[\tilde{\omega} S \omega] = \begin{bmatrix} \tilde{\omega}_1 s_1 \omega_1 \\ \tilde{\omega}_2 s_2 \omega_2 \\ \vdots \\ \tilde{\omega}_{N_B} s_{N_B} \omega_{N_B} \end{bmatrix} \quad [\tilde{\omega} B] = \begin{bmatrix} \tilde{\omega}_1 \sum_{k=1}^{n_F} b_k^1 \dot{q}_k \\ \tilde{\omega}_2 \sum_{k=1}^{n_F} b_k^2 \dot{q}_k \\ \vdots \\ \tilde{\omega}_{N_B} \sum_{k=1}^{n_F} b_k^{N_{B,F}} \dot{q}_k \end{bmatrix}$$

$$[\tilde{\omega} J \omega] = \begin{bmatrix} \tilde{\omega}_1 J_1 \omega_1 \\ \tilde{\omega}_2 J_2 \omega_2 \\ \vdots \\ \tilde{\omega}_{N_B} J_{N_B} \omega_{N_B} \end{bmatrix} \quad [N^T \omega] = \begin{bmatrix} \sum_{k=1}^{n_F} N_k^{1T} \dot{q}_k \omega_1 \\ \sum_{k=1}^{n_F} N_k^{2T} \dot{q}_k \omega_2 \\ \vdots \\ \sum_{k=1}^{n_F} N_k^{N_{B,F}T} \dot{q}_k \omega_{N_B} \end{bmatrix}$$

$$[\omega^T L \omega] = \begin{bmatrix} \sum_{j=1}^{N_{B,F}} \omega_j^T L_1^j \omega_j \\ \sum_{j=1}^{N_{B,F}} \omega_j^T L_2^j \omega_j \\ \vdots \\ \sum_{j=1}^{N_{B,F}} \omega_j^T L_{n_F}^j \omega_j \end{bmatrix} \quad [\omega^T d] = \begin{bmatrix} \sum_{j=1}^{N_{B,F}} \omega_j^T \left(\sum_{k=1}^{n_F} d_{1k}^j \dot{q}_k \right) \\ \sum_{j=1}^{N_{B,F}} \omega_j^T \left(\sum_{k=1}^{n_F} d_{2k}^j \dot{q}_k \right) \\ \vdots \\ \sum_{j=1}^{N_{B,F}} \omega_j^T \left(\sum_{k=1}^{n_F} d_{n_F k}^j \dot{q}_k \right) \end{bmatrix}$$

$$K = \begin{bmatrix} 0_{n_R \times n_R} & & & \\ & (\lambda_1)^2 & 0 & 0 \\ & 0 & \ddots & 0 \\ & 0 & 0 & (\lambda_{n_F})^2 \end{bmatrix} \quad Z = \begin{bmatrix} 0_{n_R \times n_R} & & & \\ & 2\zeta_1 \lambda_1 & 0 & 0 \\ & 0 & \ddots & 0 \\ & 0 & 0 & 2\zeta_{n_F} \lambda_{n_F} \end{bmatrix}$$

λ_k is the natural frequency of the k-th elastic mode
 ζ_k is the damping factor of the k-th mode

Concept and feasibility analysis of the Alba CubeSat mission

M. Mozzato^{1*}, S. Enzo¹, R. Lazzaro¹, M. Minato¹, G. Bemporad¹, D. Visentin¹,
F. Filippini¹, A. Dalla Via¹, A. Farina¹, E. Pilone¹, F. Basana², L. Olivieri²,
G. Colombatti³, A. Francesconi³

¹ University of Padova, Via 8 Febbraio, 2 - 35122 Padova, Italy

² CISAS G. Colombo, Via Venezia, 15 - 35131 Padova, Italy

³ DII/CISAS, Via Venezia, 1 - 35131 Padova, Italy

*monica.mozzato@studenti.unipd.it

Keywords: CubeSat; Feasibility Analysis, Debris, Fly Your Satellite! Design Booster

Abstract. Alba CubeSat is a 2U CubeSat which is being developed by a student team at the University of Padova. The Alba project aims to design, build, test, launch, and operate University of Padova's first student CubeSat, featuring four different payloads that aim to satisfy four independent objectives. The first goal is to collect data regarding the debris environment in LEO, the second goal is the study of the satellite vibrations, the third one is about CubeSat attitude determination through laser ranging technology and the fourth goal concerns satellite laser and quantum communication. The Alba CubeSat mission has been selected by ESA to join the Fly Your Satellite! Design Booster programme in December 2022. This paper presents the feasibility study of the Alba CubeSat mission reproduced in the framework of the "Space Systems Laboratory" class of M.Sc. in Aerospace Engineering at the University of Padova. In the beginning, a mission requirements definition was conducted. After that, the mission feasibility was considered, with preliminary requirements verification to assess the ability of the spacecraft to survive the space environment, including compliance with Debris Mitigation Guidelines, ground station visibility and minimum operative lifetime evaluation. The Alba mission sets a base for a better understanding of the space environment and its interaction with nanosatellites, and an improvement of the accuracy of debris models. Furthermore, this paper, describing the educational experience and the results achieved, will provide a useful example for future students' studies on CubeSat mission design.

Keywords: CubeSat; Feasibility Analysis, Debris, Fly Your Satellite! Design Booster

Introduction

One of the most common trends in the space sector is the evolution of CubeSats, micro satellites measuring just a few tens of centimeters in size. Their strength is not just the small dimensions and weight that guarantee a reduction of power consumption and costs, a CubeSat is also the perfect chance to sharpen the students' abilities and knowledge of the space industry. For that purpose, an accurate and comprehensive research of a CubeSat mission has been done by students, with a special focus on the requirements definition, starting with mission objectives. This activity has given the opportunity to face and address the issues and challenges of a space mission design. In the present work an alternative design of the 2U CubeSat mission of the student team Alba CubeSat of the University of Padova [1] is presented.

Students' work was aimed to define the requirements, based on which the commercial off-the-shelf (COTS) components have been selected for a preliminary design, while maintaining the original design of the four payloads. In addition, the students' team has identified and evaluated



the risks and the success criteria, and they have carried out a wide variety of simulations in order to perform a complete feasibility analysis.

Mission overview

Alba CubeSat is a project that aims to design, build, test, launch, and operate University of Padova's first student-built 2U CubeSat, which features four distinct payloads that seek to achieve four independent objectives. In particular, the derived mission requirements are:

1. to collect in-situ measurements of the sub-mm space debris environment in LEO;
2. to study the micro-vibration environment on the satellite throughout different mission phases;
3. to do orbit and attitude determination through laser ranging;
4. to investigate alternative systems for possible Satellite Quantum Communication applications on nanosatellites using active retro-reflectors.

Starting from these, the system requirements were defined according to the process shown in Figure 1. The identification of requirements is a milestone that is the basis of any design activity. In order to define the requirements, assumptions were made, such as the altitude and type of operative orbit, the launch vehicle that will carry the CubeSat and the launch date. The study of the micro-vibration sensor and active retro-reflectors is beyond the scope of this paper.

For every requirement identified, one or more of these verification methods were assigned: analysis, test, review of design and inspection. Throughout the analysis, each requirement was subjected to review, update and tailoring as the mission development progressed and different needs or constraints emerged.

Another critical activity was the identification of risks and success criteria. The students compiled a risk register, in which the level of risk was evaluated and mitigation actions were proposed. Since this is a student-designed CubeSat project, the majority of the success criteria were linked to an educational purpose.

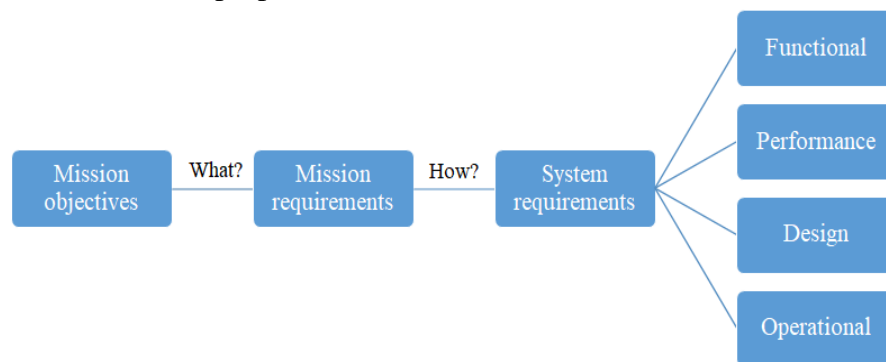


Figure 1: Logical scheme followed to identify requirements

Preliminary Analyses

An analysis of the possible target orbits has been performed considering the European Code of Conduct for space debris mitigation and the orbits commonly reached by other missions. A 500 km Sun-Synchronous Orbit (SSO) has been selected as the baseline for the mission. In order to be compatible with as many launches as possible, the LTAN has not been fixed. Therefore, the two extreme cases have been considered in the analyses, namely a worst hot case (WHC) scenario with an LTAN of 6AM (Dawn/Dusk), and a worst cold case (WCC) with an LTAN of 12AM (Noon/Midnight). The launch date has been assumed to be 30/03/2027 and the eccentricity of the orbit is 0.001.

With the chosen design (shown in the following section) mass budget and atmospheric reentry comply with ESA guidelines [2][3]. The thermal and power budgets have been calculated

considering two extreme cases for on-board activities. At this stage, four operational modes have been defined: safe, idle, communication and payload. The two worst cases scenarios are representative of a safe mode for the minimum power consumption, and a communication mode for the maximum. Ground station visibility has been taken into account for link and data budget.

Environmental analyses have been performed to ensure component compatibility with thermal ranges, radiation and atomic oxygen interactions. Systema, an Airbus software, has been used for thermal and radiation analyses. The radiation analysis shows the accumulated radiation dose over the one-year operational lifespan (Figure 2). The thermal analyses show that the internal components reached a maximum temperature of 45 °C and a minimum of 39 °C in the WHC (Figure 3). In the WCC scenario, internal temperature ranges from -10 °C to 20 °C.

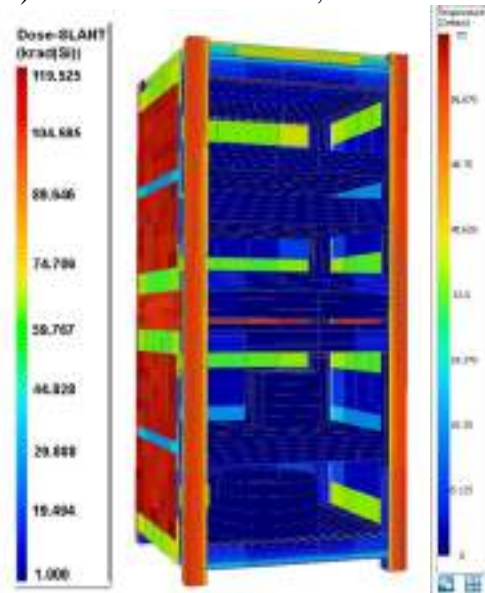


Figure 2: One-year cumulative radiation

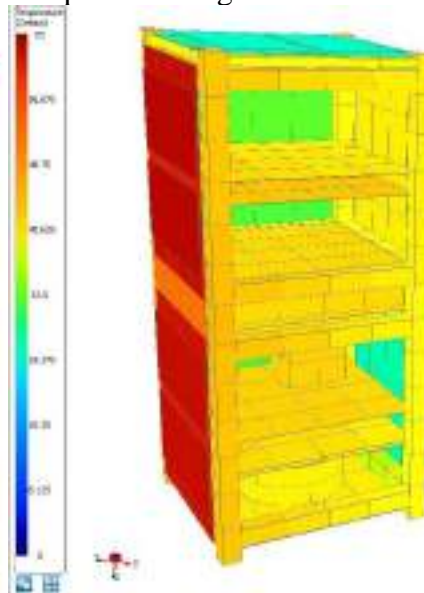


Figure 3: Component's temperature WHC

Subsystems and components selection

Component selection comes from the necessity to meet the requirements and system-level compatibility. After preliminary analyses, the following design choices have been made (Figure 4). Except the impact sensor, micro-vibration sensor and active retro-reflectors which are in-house developed, the other components are all COTS.

1. The four payloads are: the impact sensor which is a new system based on the technology demonstrator DRAGONS [4]; the laser ranging payload is composed by 6 CCRs with a 12.7 mm diameter; the micro-vibration sensor and the active retro-reflectors which are considered as black boxes with known specifications.
2. The 2U structure is made of an aluminum alloy (Al 6061) and is qualified according to ECSS-E-ST-10-03.
3. The ADCS is able to meet the three-axis stabilization pointing accuracy needed by the payloads ($\pm 20^\circ$ for each axis).
4. The power system includes: a 43 Wh battery pack and seven 1U solar panels.
5. Thermal management is based on passive conduction and radiation except for the battery pack which is equipped with a heater.
6. The OBC has been designed for space applications with limited resources. It fulfills the processing power, memory capacity, radiation tolerance and system-compatibility requirements.

7. The communication system comprehends a transceiver and an antenna. It is the most power-consuming subsystem during transmission, with a power consumption up to 3.3 W and an output power of 1 W.

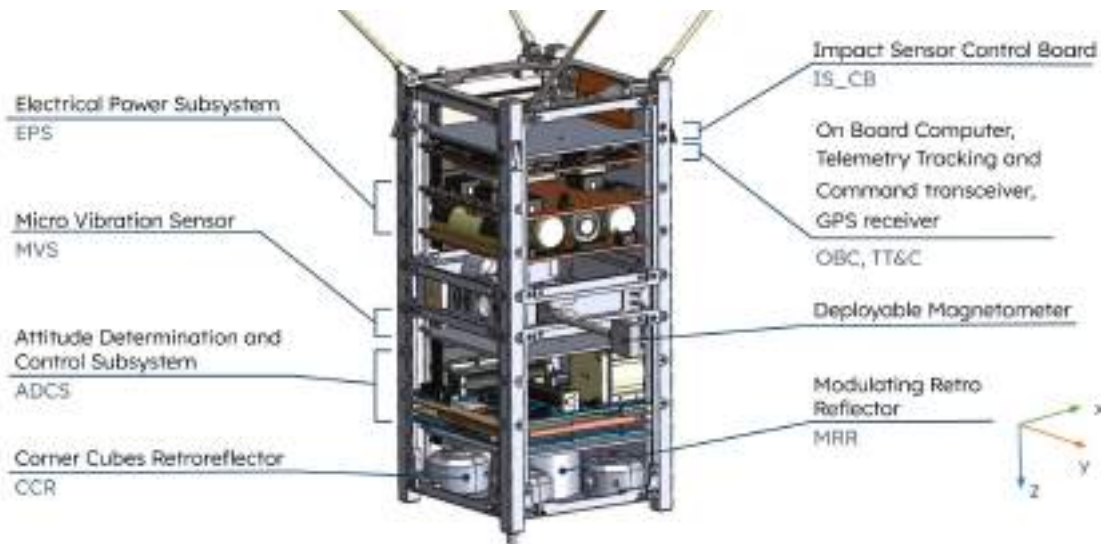


Figure 4: Internal components, solar panels have been removed

Conclusions

The successful development of this work involved several key tasks, including identifying requirements and their corresponding verification methods, identifying risks and find mitigation actions, designing and studying the functionality of two payloads (laser ranging and impact sensor), selecting appropriate commercial off-the-shelf (COTS) components for the subsystems, and conducting analyses to verify the specified requirements.

One of the critical points identified was the enclosure of all the components in a 2U, in particular the CCRs. Therefore, it is to be considered the development of a homemade structure for the CCRs to address this issue. Moreover, the power budget analysis revealed a potential insufficiency in power generation by the solar panels during the worst-case scenario (noon-midnight orbit). However, it is important to note that power consumption was likely overestimated.

The present work has contributed to enhancing students' understanding of how to conduct a feasibility study for a space mission. It also can serve as a useful reference, assisting anyone who is embarking on their first mission feasibility study.

References

- [1] Development of a multi-payload 2U CubeSat: the Alba project - F.Basana, A.A. Avram, F.Fontanot, L.Lion, A.Francesconi - 4th Symposium on Space Educational Activities - Barcelona, April 2022
- [2] European Space Agency - Margin Philosophy for Science Assessment Studies - Issue 1 - Revision 3 - 15/06/2012
- [3] ESSB-HB-U-002 - ESA Space Debris Mitigation WG. - ESA Space Debris Mitigation Compliance, Verification Guidelines - Issue 1 - 19/02/2015
- [4] LIOU, J.-C., et al. dragons-a micrometeoroid and orbital debris impact sensor. In: Nano-Satellite Symposium (NSAT). 2015

Space object identification and correlation through AI-aided light curve feature extraction

Chiara Bertolini^{1,a}, Riccardo Cipollone^{1,b*}, Andrea De Vittori^{1,c},
Pierluigi Di Lizia^{1,d}, Mauro Massari^{1,e}

¹ Department of Aerospace Science and Technology, Politecnico Di Milano, Via Giuseppe La
Masa 54 20156, Milano

^achiara.bertolini@polimi.it, ^briccardo.cipollone@polimi.it, ^candrea.devittori@polimi.it,
^dpierluigi.dilizia@polimi.it, ^emauro.massari@polimi.it

Keywords: Light Curves, Neural Networks, Correlation

Abstract. With the constant growth of objects in orbit, the monitoring and cataloging of space population is essential. Light curves obtained from ground stations support this point, providing valuable information about the observed objects. The idea of using them to identify an object through correlation with a catalogued reference takes hold from their wide availability. This article focuses on the development of a tool for the analysis and correlation of two light curves, ARIEL. This tool is built through neural networks and declined in three strategies, each with its own goal: ROGUE, LINDEN and SIERRA. The light curves were retrieved via the database managed by the Mini-MegaTORTORA observatory and filtered using the Savitzky-Golay filter.

Introduction

The near-Earth environment is getting more populated, as commercial applications become a substantial part of the space economy, increasing the risk of collisions and fragmentations [1]. To keep track of this expanding population and to assess the risk of in-orbit collision and fragmentation, space agencies deploy Space Surveillance and Tracking (SST) systems [2]. Ground-based stations allow to retrieve orbital data of human-made objects [3]. When dealing with optical telescopes, photometry analysis can be performed, and light curves are generated as a consequence. Light curves, which represent object brightness variations, provide information on orbit regime, tumbling motion, and spacecraft geometry, enabling characterization of observed objects.

In general, traditional estimation-based methods, like the so-called Light Curve Inversion, have been extensively used for the identification of space objects [4]. However, complex models have to be considered and the resulting analysis is computationally time-consuming. Consequently, the state of the art is now drifting to the use of machine learning with bespoke Convolutional Neural Networks (CNN) or Recursive Neural Networks (RNN) ensuring up to 90% prediction accuracy [5][6].

This project proposes a novel approach to light curve characterization through the Machine Learning based Light curve Analysis (ARIEL) tool. Raw light curves are recovered from the database managed by the Mini-MegaTORTORA (MMT-9) observatory [7] and then pre-processed, before being fed into three different neural networks (NN): ROGUE, LINDEN, and SIERRA.

Performance for these networks is then assessed using different datasets obtained by varying the number of spacecraft platforms.

Theoretical background

As mentioned above, light curves are recovered from shots acquired with optical telescopes. An example of the observatory is represented by MMT-9 system [6], which predisposes a constantly



updated database for human-made space objects. From that database, the main information recovered are the space object characteristics and corresponding light curves retrieved, each associated with a track ID and time-tag. The data are summarized in the following Table.

Table 1 – Data recovery from MMT-9 database

Data	Number of objects
Total number of objects recovered	6.314
Total number of light curves available	Over 150.000
Objects per category	
<i>Type of orbit</i>	LEO: 5.206; GEO: 174; Other: 934
<i>Attitude regime</i>	Periodic: 985; Aperiodic: 1550; Non variable: 3779
<i>Type of object</i>	Rocket bodies: 827; Debris: 839; Satellites: 4648

Before entering the NN, however, these raw light curves are pre-processed using the Savitzky-Golay filter [8], with smoothing properties particularly indicated for reducing high frequency noise. The outcome can be seen in Figure 1, where the grey signal is the raw light curve, while the red is the filtered one.

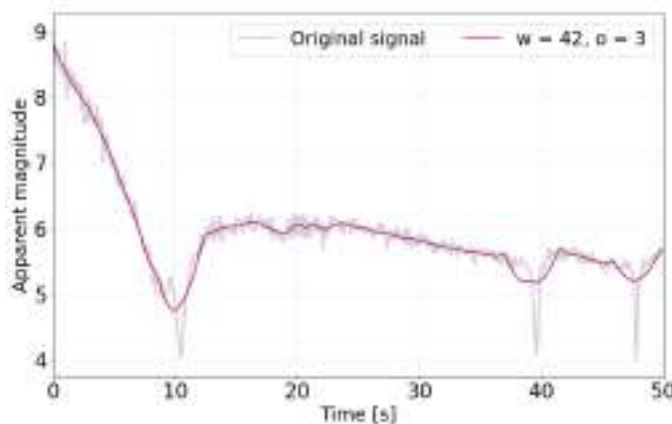


Figure 1 - Filtered light curve (cropped)

To assess the performances of the ARIEL networks, the focus was mainly on objects belonging to LEO or Low-Medium Orbit (LMO) regions, with periodic or aperiodic tumbling motion. The corresponding light curves have been filtered and stored in datasets, accompanied by the name and the type of object considered, i.e. Rocket body, Debris or Satellite. To avoid any bias towards a specific spacecraft, different platforms for each type are considered. For example, a dataset considers light curves belonging to

Iridium and NOAA objects, but both labeled as “Satellites” – as stated in the MMT-9 database. Two different sets have therefore been considered. First, the Nominal dataset represent nominal conditions of operation of ARIEL, meaning a limited number of platforms a first version featuring periodic objects only, and a following one including aperiodic too. Then, a Variability test assesses the extent of ARIEL capabilities: different datasets are built considering an increasing number of platforms for each dataset, taking care that the three types data distribution is balanced out. All the objects considered have periodic or aperiodic attitude regime.

Deep learning networks are a subset of Machine learning models. Different NN structures can also be employed such as CNN and RNN: CNNs are particularly indicated to retain the general features of the input, while, RNN, such as the Long-Short Term Memory (LSTM) cells, take into account the input’s time-dependence. After the NN setup, it needs to be trained and its performance assessed – mainly in terms of predictions’ Accuracy. Particular attention has to be given in the model structure and dataset provided to avoid over- or underfitting of the network.

Siamese networks have a slightly different architecture [8]: the overall dataset is divided in Anchor, the reference, Positive and Negative, the closest and the farthest prediction from the reference. Then, an embedding model extracts features from the inputs and the network evaluates

the distance Anchor-Positive and Anchor-Negative in order to bring the former closer and the latter farther. Thus a dedicated metrics, Similarity, is employed.

Architectures

Three different architectures are developed inside the ARIEL framework: ROGUE, LINDEN and SIERRA.

The Rocket bodies Light curves Identification (ROGUE) network aims at recognizing Rocket bodies among light curves of different types. The structure is a combination of CNN and LSTM cells. This test is conceived to verify the capability of the NN to identify a defined category of spacecraft.

The Light curve Identification and Correlation (LINDEN) NN compares two light curves and determines the correlation degree among the twos. Two models have to be therefore developed as shown in Figure 2:

- the Feature extraction part analyses the light curves and predicts the objects' type
- the Correlation evaluation block which, given the above-mentioned predictions, evaluates the distance between them.

The Feature extraction model is an improved version of the ROGUE model and the output gives a prediction vector over the class labels.

After having trained the Feature extraction part, it is inserted in the overall LINDEN Correlation block where the correlation between the prediction vectors is performed, thanks to a normalized dot product. As the Feature extraction model is frozen within the Correlation block, this allows to compute a correlation degree without being influenced by uncertainties in the model.

Siamese Network for Light curves Correlation (SIERRA) is a Siamese Network, which encompasses the above-mentioned Feature extraction block as embedding model.

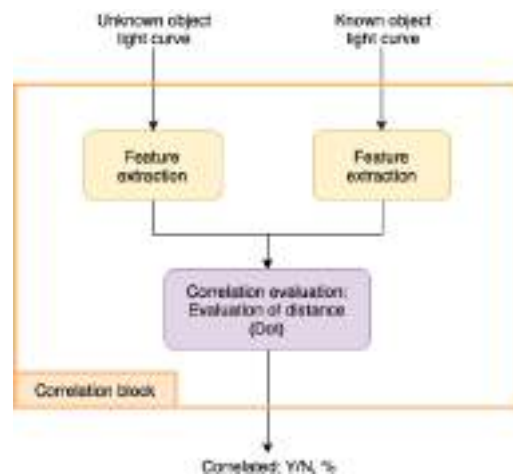


Figure 2 - LINDEN Structure

Results

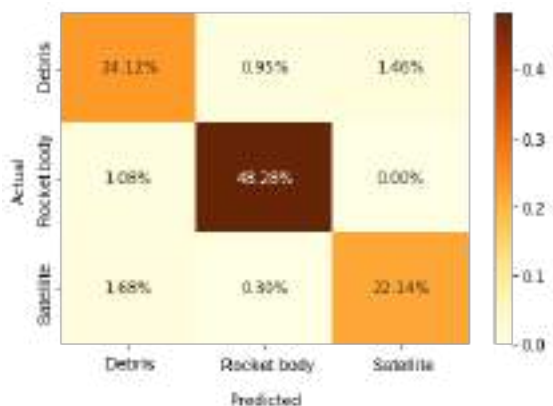


Figure 3 - Confusion matrix for LINDEN Feature extraction

Hereafter the results for ARIEL networks are summarized, obtained considering the above-mentioned datasets. The training has been performed using Google Colaboratory, where due to the limited GPU time availability, it has been divided in sessions from 100 to 200 epochs. The results are analyzed through confusion matrices, which compare predicted with actual labels. The more intense the color of the cell, the higher the prediction accuracy. An example can be shown in Figure 3 – where the results for LINDEN Feature Extraction for the second Nominal dataset are shown.

ROGUE: The results show around 97% accuracy for Nominal datasets while a drop can be observed for Variability sets – ranging from 95% to around 70%

accuracy for increasing number of platforms. All in all, ROGUE can best differentiate the Rocket body type among up to 20 different platforms. However Nominal datasets do not present overfitting as Variability sets do.

LINDEN: As previously mentioned, the Feature extraction block is trained separately and then inserted in the overall Correlation block.

Feature extraction block: The results display over 95% accuracy in differentiating the type of objects inputted, for Nominal sets. Variability datasets still reach over 90% accuracy for lower numbers of satellite platforms, while severe overfitting can be noticed with increasing variety, with accuracy dropping down to 50% in the best-performing model. Moreover, the Debris type is completely missing among output predictions, which enforces the idea that they are more difficult to categorize due to their nature.

Correlation block: The performances observed prove that, as the levels reached in the Feature extraction block leave room for uncertainty, the results obtained in the Correlation block are quite scarce, in particular for the Variability datasets. Overfitting is observed also in Nominal conditions becoming even more relevant for the Variability datasets. However, the confusion observed is still below the 10% bound.

All in all, LINDEN proves its capabilities by granting an accurate type recognition, which allows correlation between the two inputs to be established properly. However only up to 20 platforms can be considered at the same time in order to obtain accurate results.

SIERRA: As expected, the overfitting present in the Feature extraction block propagates to the NN. The Similarity obtained in the different datasets is roughly giving a 10 % gap, therefore the Positive and Negative outcomes are properly distinguished. While using the Variability dataset with the lowest number of platforms – around 20 –, a remarkable confusion was observed. This was maybe due to Anchor and Negative having common characteristics not considered during the Feature extraction block.

Conclusions

ARIEL provides a strategy to identify objects according to their type and to establish a degree of correlation between the unknown object and a catalogued one. This is done by the analysis of light curves through a deep learning model combining CNN and LSTM layers that grasp general and time-dependent features at the same time. Three architectures are thus proposed, each focusing on a different aspect of the problem at hand: ROGUE, LINDEN and SIERRA.

The light curves are obtained from the MMT-9 database and have been pre-processed, in particular filtered with the Savitzky-Golay smoothing filter.

After extensive training using different datasets, the performances have been assessed, showcasing a resulting accuracy of around 90% in most test cases. The significant gap observed for the similarity in SIERRA proves these networks predict the type of object with little confusion. However these NN are limited by datasets including diverse platforms, where accurate type recognition is hampered, thus preventing the correlation to be performed. Moreover, overfitting is omnipresent: in some cases it becomes substantial, therefore impacting the accuracy of the predictions done.

Some options can hence be proposed to improve ARIEL, e.g. consider a smaller number of different platforms or restrict the problem to the recognition of platforms among a same type, or a same attitude regime (i.e. periodic, aperiodic or non variable), or even focus on the problem of the Debris type recognition. In fact it is the most mistaken type, as some of these objects are unused satellites or intact rocket body parts. Therefore, a dedicated analysis among Debris may be needed if those objects are involved.

References

- [1] ESA Space Debris Office, “ESA annual space environment report,” Tech. Rep. 6, European Space Agency, Darmstadt, Germany, April 2022.
- [2] EU SST, “European space surveillance and tracking,” 2016. <https://www.eusst.eu>.

- [3] Montaruli, Marco Felice & Facchini, Luca & Di Lizia, Pierluigi & Massari, Mauro & Pupillo, Giuseppe & Bianchi, Germano & Naldi, Giovanni. (2022). Adaptive track estimation on a radar array system for space surveillance. *Acta Astronautica*. 198.
<https://doi.org/10.1016/j.actaastro.2022.05.051>
- [4] B. Bradley and P. Axelrad, "Lightcurve in- version for shape estimation of GEO objects from space-based sensors," ISSFD, 2014.
- [5] R. Linares and R. Furfaro, "Space object classification using deep convolutional neural networks," IEEE, 2016.
- [6] E. Kerr, G. Falco, N. Maric, D. Petit, P. Talon, E. Geistere Petersen, C. Dorn, S. Eves, N. Sánchez-Ortiz, R. Dominguez Gonzalez, and J. Nomen-Torres, "Light curves for GEO object characterisation," (Darmstadt, Germany), ESA, ESA Space Debris Office, 4 2021. Proc. 8th European Conference on Space Debris.
- [7] S. Karpov, E. Katkova, G. Beskin, A. Biryukov, S. Bondar, E. Davydov, E. Ivanov, A. Perkov, and V. Sasyuk, "Massive photometry of low altitude artificial satellites on Mini-Mega Tortora," 2015. Database: <http://mmt.favor2.info/satellites>
- [8] N. Gallagher, "Savitzky-Golay smoothing and differentiation filter," 2020.
<https://eigenvector.com/wp-content/uploads/2020/01/SavitzkyGolay.pdf>
- [9] H. Essam and S. Valdarrama, "Image similarity estimation using a Siamese Network with a Triplet loss," 2021. https://keras.io/examples/vision/siamese_network/

Development of a smart docking system for small satellites

Alex Caon^{1,a*}, Luca Lion^{1,b}, Lorenzo Olivieri^{1,c}, Francesco Branz^{2,d},
Alessandro Francesconi^{2,e}

¹C.I.S.A.S. - Centre of Studies and Activities for Space "G. Colombo", Via Venezia 15, Padova (Italy)

²Department of Industrial Engineering, University of Padova, via Venezia, 1, Padova (Italy)

^aalex.caon@unipd.it, ^bluca.lion.1@phd.unipd.it, ^clorenzo.olivieri@unipd.it,

^dfrancesco.branz@unipd.it, ^ealessandro.francesconi@unipd.it

Keywords: Docking system, Autonomous system, Space Rider, Space Rider Observer Cube

Abstract. DOCKS is a smart docking system for space vehicles developed by the Department of Industrial Engineering, University of Padova, within the framework of the Space Rider Observer Cube (SROC) mission. The design and development of SROC is being conducted by a consortium of Italian entities under contract with the European Space Agency (ESA). The SROC mission is designed to be a payload on the ESA Space Rider (SR) spaceship. The main objective of the mission is to demonstrate the critical capabilities and technologies required to execute a rendezvous and docking mission in a safety-sensitive context. The space system is composed by a nanosatellite (approximately 12U CubeSat) and a deployment/retrieval mechanism mounted inside the payload bay of SR. During the mission, SROC will be released by SR, will perform inspection manoeuvres on SR and, at the end of the mission, will dock back inside the bay of SR, before re-entering Earth with the mothership. The docking functionality is provided by DOCKS. DOCKS is suitable for use onboard micro- and nanosatellites and merges a classical probe drogue configuration with a gripper-like design, to manage the connection between the parts. The system is equipped with a suite of sensors to estimate the relative pose of the target and with a dedicated computer, making it a smart standalone system. A laboratory prototype has been assembled and functionally tested, aiming at the validation of the capability to passively manage misalignments during the docking manoeuvre.

Introduction

The docking system (DOCKS) has been developed in the framework of the Space Rider Observer Cube (SROC) mission. The purpose of the mission is to demonstrate the capabilities and technologies required for rendezvous and docking with a target vehicle [1]. A brief description of the operations performed by SROC is:

1. Launch and early operations. SROC is stored inside the bay of Space Rider (SR). Once in orbit, SROC is pushed away from SR in order to begin its operative phases.
2. Proximity Operations. SROC is in a relative orbit with respect to SR in order to perform its observations.
3. Docking and Retrieval Phase. SROC approaches SR and docks with it in order to be re-stored inside the bay and return to Earth safely.

DOCKS overview

The DOCKing System (DOCKS) has been developed to be a standalone docking mechanism with an integrated set of sensors and a computer. In the following, all the parts of DOCKS will be described.



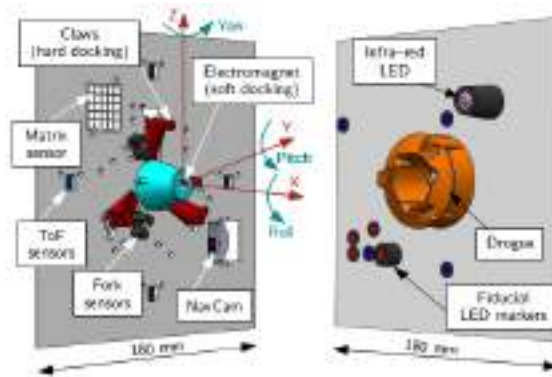


Figure 1: DOCKS-A and DOCKS-B. They are mounted on SROC and on SR respectively. In DOCKS-A it is also represented its frame of reference.

Docking mechanism

The mechanical connection between SROC and SR is provided by a docking mechanism that is composed by two main parts (Fig. 1). The first (DOCKS-A on SROC) is the active part with the mechanism, and the second (DOCKS-B on SR) is the counter part of the docking mechanism (the drogue) and the LEDs that allows the relative navigation.

The active part of docking mechanism is composed by two parts (shown in Fig. 2): a centring cone and three claws that provide the rigid mechanical connection.

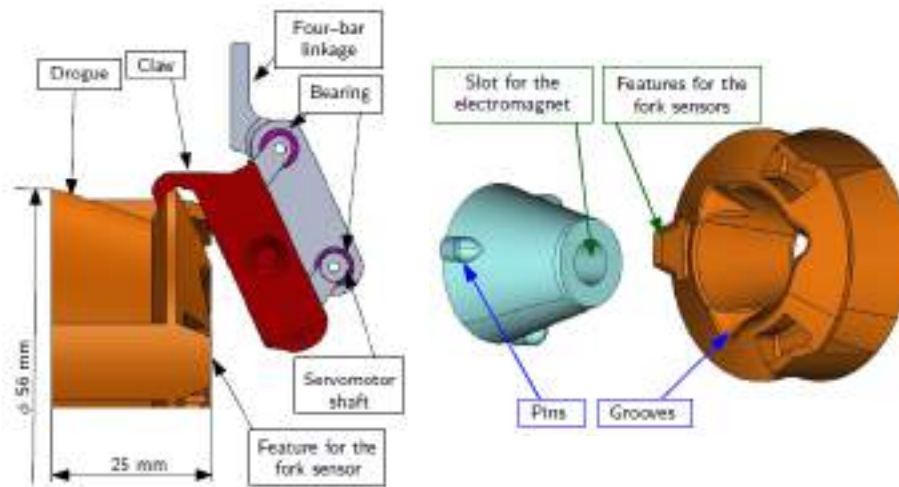


Figure 2: The centring cone and claws of DOCKS.

The centering cone has the purpose to force the alignment between SROC and SR when coupling with the drogue. In fact, the shape of the probe allows to tolerate 10 mm of lateral misalignment and 10 deg of pitch (and yaw) misalignment. In addition, the pins on the rim of the probe force the roll alignment, when they couple with the grooves on the drogue.

The hard docking is achieved with the three claws that ensure the rigid connection, by closing around the rim of the drogue. The claws are activated by a four-bar linkage in order to prevent linear actuations that could produce friction or jam the mechanism.

Sensor suite and estimation performances

As illustrated in Fig. 1, DOCKS-A is provided with three different sensors to measure the relative pose of DOCKS-B.

1. *A navigation camera.* Its purpose is to measure the entire relative pose of DOCKS-B. The NavCam with its computer, recognizes the pattern of LEDs on DOCKS-B and reconstruct its pose [2]. However, at distances lower than 50 mm, the camera is out of focus making the measurement unreliable.
2. *A set of four Time-of-Flight sensors.* They are employed to measure the distance and the relative pitch and yaw angles from 100 mm up to contact (as explained in Fig. 3) [3].
3. *A matrix sensor.* It is used to measure the relative position along the y and z axes (which is not measurable with the ToF sensors). The sensor employs a matrix of 5x5 phototransistors on DOCKS-A and an infrared LED on DOCKS-B. Depending on the relative position, the LED activates different pattern of phototransistors [4].

The ToF sensors are affected by a noise of approximately 4 mm at distances below 30 mm, causing an uncertainty on the measure of the relative angles of more than 5 deg. To improve the estimation, a Kalman filter has been applied to the measurements of the ToF sensors [5]. The tests performed on the sensor suite provided the estimation error reported in Tab.1.

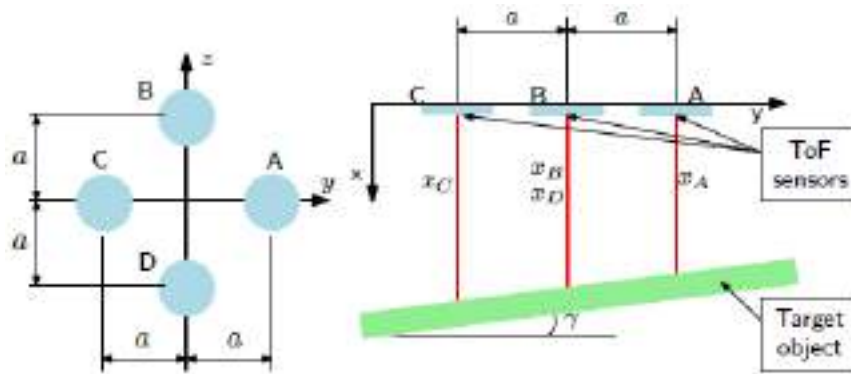


Figure 3: Measurement of the Time-of-Flight sensors.

Table 1: Estimation errors

	Error	X [mm]	Y [mm]	Z [mm]	Pitch [deg]	Yaw [yaw]
NavCam	Avg.	2.0	2.0	2.0	1.5	1.5
	Std. dev.	0.5	0.5	0.5	1.0	1.0
ToF + matrix	Avg.	0.14	1.16	1.41	0.52	0.11
	Std. dev.	0.43	0.13	2.13	0.64	0.68

Tests on DOCKS

DOCKS has undergone to a series of tests in order to verify its capabilities of DOCKS to tolerate relative misalignments and to self-align DOCKS-A to DOCKS-B. To this purpose, an ad-hoc experimental setup has been developed. DOCKS-A is mounted on the end-effector of a robotic arm, which has the purpose of moving DOCKS-A with an accuracy of 2 mm [6]. DOCKS-B is mounted on a frame DOCKS-B on a frame that blocks all the movements, except for the degree of freedom under tests for the self-alignment, as illustrated in Fig. 4.

At the beginning of the tests, the zero position has been defined as the perfect alignment between DOCKS-A and B. The tests have been conducted as follows: (1) a displacement has been imposed on DOCKS-B, (2) DOCKS-A has been moved along a linear trajectory to the zero position forcing the alignment between the parts. The test is considered successful if the claws close properly on the rim of the drogue without any residual displacement.

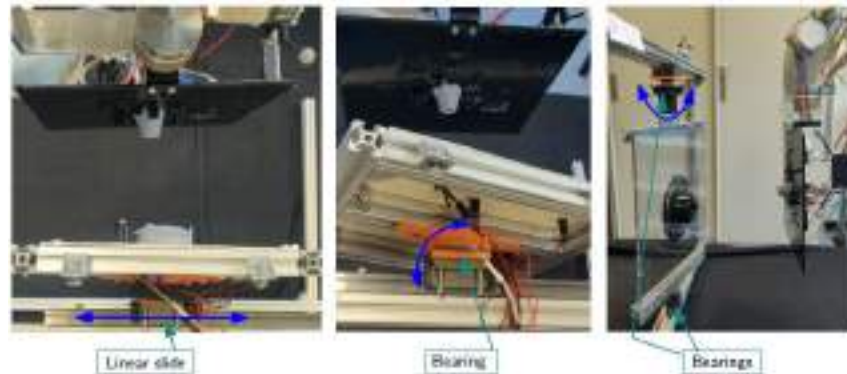


Figure 4: the experimental setups for the misalignment along the y axis, around the roll axis and around the yaw axis.

The results of the tests proved the capability of DOCKS to manage misalignment of 8.0 mm along the y and z axes, 9.0 deg around the yaw and pitch axes, and 10 deg around the roll axis.

Conclusions

This paper presents a brief description of an autonomous docking system, since it is equipped with (1) a set of sensors that, with a Kalman filter, are able to estimate the relative pose of the target; (2) three actuators and an electromagnet to execute the soft and the hard docking; and (3) an integrated computer that applies the required algorithms to manage the sensors and actuators.

In addition, DOCKS has been designed to manage misalignment between DOCKS-A and DOCKS-B. To this aim, its centring cone with three features matches its counterpart on the target and forces the alignment between the parts. The test executed on DOCKS, proved that it is able to tolerate misalignment that are five to eight times the estimation errors of the sensors.

References

- [1] S. Corpino, G. Ammirante, G. Daddi, F. Stesina, F. Corradino, A. Basler, A. Francesconi, F. Branz and J. Van den Eynde, "Space Rider Observer Cube - SROC: a CubeSat mission for proximity operations demonstration," in *73 International Astronautical Congress (IAC)*, Paris, France, 18-22 September 2022.
- [2] F. Sansone, F. Banz and A. Francesconi, "A relative sensor for CubeSat based on LED fiducial markers," *Acta Astronautica*, 2018. <https://doi.org/10.1016/j.actaastro.2018.02.028>
- [3] A. Caon, M. Peruffo, F. Branz and A. Francesconi, "Consensus sensor fusion to estimate the relative attitude during space capture operations," in *IEEE 9 International Workshop on Metrology for AeroSpace (MetroAeroSpace)*, 2022. <https://doi.org/10.1109/MetroAeroSpace54187.2022.9856096>
- [4] A. Caon, F. Branz and A. Francesconi, "Characterization of a new positioning sensor for space capture," in *IEEE 8 International Workshop on Metrology for AeroSpace (MetroAeroSpace)*, 2021. <https://doi.org/10.1109/MetroAeroSpace51421.2021.9511704>
- [5] A. Caon, F. Branz and A. Francesconi, "Smart capture tool for space robots," *Acta Astronautica*, 2023. <https://doi.org/10.1016/j.actaastro.2023.05.014>
- [6] A. Caon, F. Branz and A. Francesconi, "Development and test of a robotic arm for experiments on close proximity operations," *Acta Astronautica*, 195, pp. 287-294, 2022. <https://doi.org/10.1016/j.actaastro.2022.03.006>

AUTOMA project: technologies for autonomous in orbit assembly operations

Alex Caon^{1,a*}, Martina Imperatrice^{2,b}, Mattia Peruffo^{1,c}, Francesco Branz^{2,d},
Alessandro Francesconi^{2,e}

¹C.I.S.A.S. - Centre of Studies and Activities for Space "G. Colombo", Via Venezia 15, Padova (Italy)

²Department of Industrial Engineering, University of Padova, via Venezia, 1, Padova (Italy)

^aalex.caon@unipd.it, ^bmartina.imperatrice@studenti.unipd.it, ^cmattia.peruffo@unipd.it,

^dfrancesco.branz@unipd.it, ^ealessandro.francesconi@unipd.it

Keywords: In-Orbit Servicing, Space Robots, Capture Tool, Autonomous System

Abstract. The possibility of manipulating objects in space is at the basis of the In-Orbit Servicing missions with the purpose to extend or improve the life of existing satellites. This can be obtained by equipping a target satellite with additional modules capable of providing additional basic functions, like power, thrust or communication. One of the most promising technologies to accomplish to these purposes is presented by space robots (satellites with one or more robotic manipulators) equipped with dedicated tool. The manipulators have the dual purposes to capture the additional module and to manipulate and attach it to the target satellite. In order to advance in IOS technologies, the Department of Industrial Engineer has funded the AUTOMA (AUtonomous Technologies for Orbital servicing and Modular Assembly) project¹. The project aims to (1) upgrade an autonomous capture tool, (2) develop the additional module (EAU), and (3) execute tests in relevant laboratory scenarios. The autonomous tool is represented by SMACK (SMARt Capture Kit). SMACK is a capture system equipped with (1) different types of sensors to measure the relative pose during the entire approach for the capture and for the assembly; (2) a set of actuators to capture the module and keep a rigid connection during the manipulation; (3) a computer to execute locally the required software like guidance and navigation algorithms. The external module (Elementary Assembly Unit, EAU) is equipped with three features to be captured and manipulated by SMACK and a docking system to allow the assembly on the target structure. In order to test the assembly phase, SMACK has been mounted on the end-effector of a 6 degrees of freedom robotic arm in laboratory environment, while the target has been fixed on a frame. These tests proved the ability of SMACK to manage assembly tasks such as the control of a robotic arm with sufficient accuracy.

Introduction

In-Orbit Assembly missions have the purpose of assembling large structures in space such as telescopes or antennas [1]. Another fast-growing area is the possibility to install small building blocks onto existing satellites in order to provide additional functionalities such as communication, propulsion, power, etc. [2]. Both the objectives are achieved by the employment of small building blocks that are assembled by means of connecting ports. The assembly phase can be either performed by space robots that handle the blocks or executed autonomously by the blocks themselves.

The AUTOMA project has been funded in order to develop and test IOS technologies. In particular, the project focuses on the possibility to upgrade a capture tool, equipped with a set of

¹ This work was partially funded by Università degli Studi di Padova in the framework of the BIRD 2021 programme (BRAN_BIRD2121_01).



sensors, actuators and algorithms, able to autonomously perform different assembly tasks. To this aim, two main systems have been developed (see Fig. 1): the SMARt Capture Kit (SMACK) [3] and the Elementary Assembly Unit (EAU): the first has the purpose to catch and handle the second and assemble it on a target structure through a docking port.

The two systems have undergone a series of tests in order to evaluate their capabilities in terms of holding force of the gripper and the docking port, of the measurement error of each sensor, of the state estimation error and of the tolerated misalignment of both the gripper and of the docking port. A final functional system test consisted in letting SMACK to control the movements of the robot to perform the capture and the assembly of the EAU on the target structure. The use of the robotic arm ensures a positioning precision of 2 mm, which is lower than the errors of the sensors and algorithms of SMACK [4].

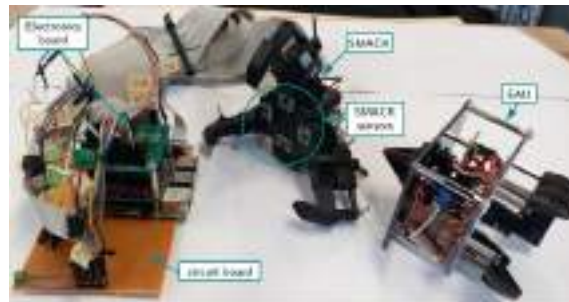


Figure 1: SMACK with its electronics and computer and the EAU.

SMARt Capture Kit (SMACK)

The SMARt Capture Kit (SMACK) has the purpose to identify, move and manage the assembly of the EAU on the target structure (or satellite). SMACK is equipped with a set of sensors, actuators and an integrated computer that renders it independent from the rest of the robotic arm on which it is mounted. The mechanical connection with the EAU is established by a gripper with three fingers. Each finger is individually actuated so that SMACK is able to capture the EAU even in case of relative misalignments by elongating differently each finger.

The sensors, coupled with the estimation algorithm, are employed to estimate the pose and the relative rates of the target. To this purpose, there are three types of sensors:

1. A NavCam that reconstructs the pose of a pattern of fiducial LED mounted on the target [5]. Measurement errors: 2.0 mm for the position and 1.5 deg for the attitude.
2. A set of four Time-of-Flight sensors that are employed to retrieve the distance and the relative yaw and pitch angles. In fact, if the target is tilted, the ToF sensors measure different distances, and allowing to indirectly measure the relative orientation, as illustrated in Fig. 2 [5]. They are coupled with a Kalman filter in order to improve their estimation capabilities. Estimation errors: 1.5 mm along the x axis and 1.5 deg for the yaw and pitch.
3. An in-plane matrix sensor that measures the position of the EAU along the x, y and z axes. The sensor is composed by a matrix of phototransistors activated by an infrared LED mounted on the EAU. The relative measure is computed based on the number of active phototransistors (second picture of Fig. 2) [6]. Measurement errors: 3.5 mm along the y and z axes.
4. A roll matrix to measure the relative roll angle. The sensors share the same working principle of the in-plane matrix (third picture of Fig. 2), but the active phototransistors are employed to measure the roll angle. Measurement error: 3.1 deg around the roll axis.

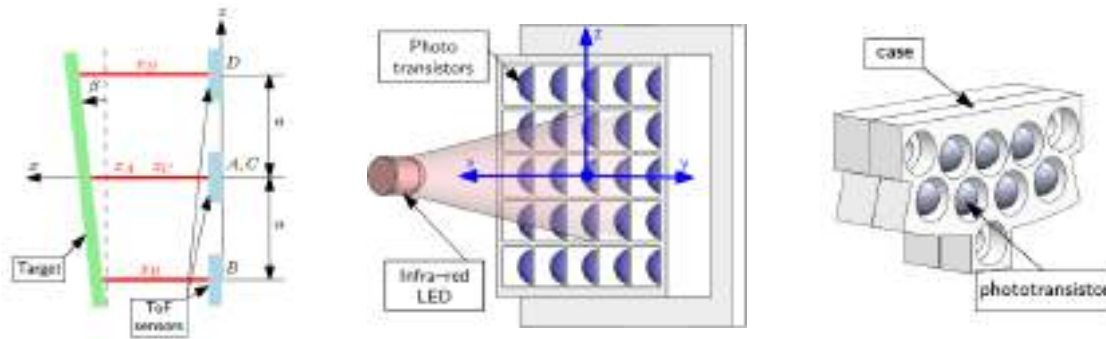


Figure 2: The measurement of a tilted object with the ToF sensors he in-plane matrix sensor, the roll matrix sensor and.

Elementary Assembly Unit (EAU)

The main purpose of the Elementary Assembly Unit (EAU) is to provide basic functionalities to the target interface, for example, additional power, communication, and thruster capabilities, etc. The EAU developed for this first stage is a box of size 100 mm by 100 mm by 50 mm, whose capabilities are limited to the mechanical connection by the means of a probe-drogue docking mechanism [8]. The tip of the probe can rotate in order to provide a rigid connection between the parts. The EAU is also equipped with three features to allow SMACK to catch it, a pattern of LEDs employed by the NavCam and two infrared LED beacons employed by the matrix sensors.

Assembly experiments

Both SMACK and the EAU have passed a series of tests to validate their capabilities in terms of (1) measurement and estimation capabilities; (2) holding force for both the gripper and the docking port; and (3) misalignment tolerance for the gripper and self-alignment management for the docking port. Then, a functional system test on the assembly procedure is required, to validate the involved mechanisms and the assembly procedure.

To execute the test, SMACK has been mounted on the end-effector of the robotic arm, the target frame has been mounted on a fixed frame, while the EAU has been placed in a known position. The procedure from the capture of the EAU to its assembly on the target frame has been divided into four main waypoints, which are transmitted to the robotic arm by SMACK, they are (referring to Fig. 3):

1. *Pre-capture*: in front of the EAU and aligned with it, but at a distance of 100 mm.
2. *Capture*: aligned with the EAU, in order to close the fingers and capture it.
3. *Post-capture*: after the capture, SMACK and the EAU are placed in front of the docking port at a distance of 100 mm.
4. *Docking*: the position where the docking mechanism can be activated.

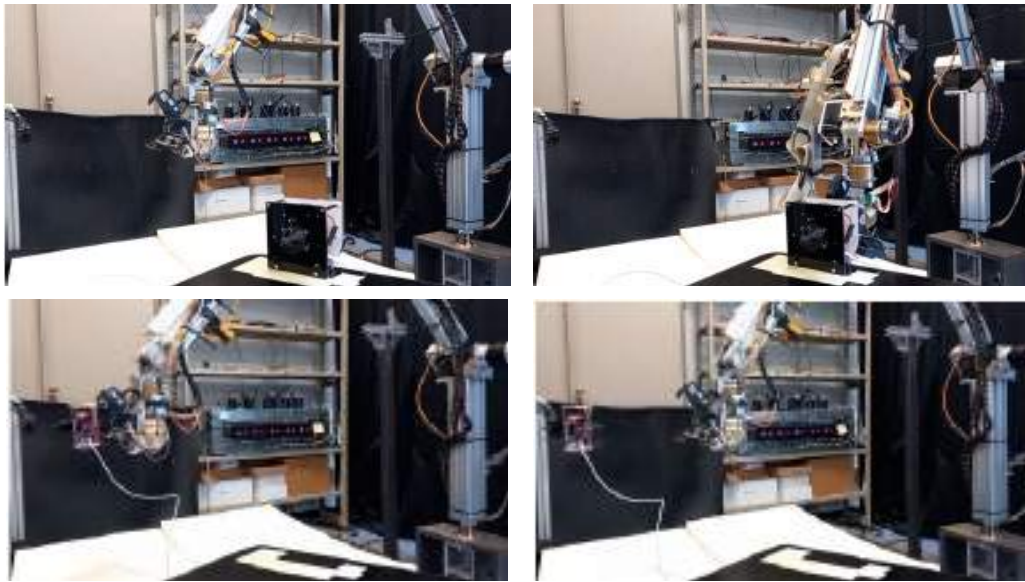


Figure 3: The waypoints of the phase.

Conclusions

This paper presents a brief overview of the AUTOMA project, that has the purpose to develop technologies in order to perform experiments on In-Orbit Assembly. Both the systems proved their capabilities through dedicated tests campaign. In particular, the relative state is estimated with an error lower than the tolerated misalignments, allowing SMACK to capture, handle and assemble the EAU to the target structure, as proved by the assembly experiment. The assembly phase and the involved mechanisms have been tested with a dedicated test which proved the abilities of the mechanisms to provide a rigid mechanical connection between the parts.

The next phase will focus on a closed-loop test in which SMACK has to perform an assembly with the use of its sensors and algorithms.

References

- [1] W. R. Oegerle, L. R. Purves, J. G. Budinoff, R. V. Moe, T. M. Carnahan, D. Evans and C. K. Kim, "Concept for a large scalable space telescope: in-space assembly," *SPIE*, 2006. <https://doi.org/10.1117/12.672244>
- [2] Northrop Grumman, "Space Logistics," 16 06 2023. [Online]. Available: <https://www.northropgrumman.com/space/space-logistics-services/>.
- [3] A. Caon, F. Branz and A. Francesconi, "Smart capture tool for space robots," *Acta Astronautica*, 2023. <https://doi.org/10.1016/j.actaastro.2023.05.014>
- [4] A. Caon, F. Branz and A. Francesconi, "Development and test of a robotic arm for experiments on close proximity operations," *Acta Astronautica*, 195, pp. 287-294, 2022. <https://doi.org/10.1016/j.actaastro.2022.03.006>
- [5] A. Caon, M. Peruffo, F. Branz and A. Francesconi, "Consensus sensor fusion to estimate the relative attitude during space capture operations," in *IEEE 9 International Workshop on Metrology for AeroSpace (MetroAeroSpace)*, 2022. <https://doi.org/10.1109/MetroAeroSpace54187.2022.9856096>
- [6] A. Caon, F. Branz and A. Francesconi, "Characterization of a new positioning sensor for space capture," in *IEEE 8 International Workshop on Metrology for AeroSpace (MetroAeroSpace)*, 2021. <https://doi.org/10.1109/MetroAeroSpace51421.2021.9511704>

- [7] F. Sansone, F. Banz and A. Francesconi, “A relative sensor for CubeSat based on LED fiducial markers,” *Acta Astronautica*, 2018. <https://doi.org/10.1016/j.actaastro.2018.02.028>
- [8] F. Banz, L. Olivieri, F. Sansone and A. Francesconi, “Miniature docking mechanism for CubeSats,” *Acta Astronautica*, pp. 510-519, 2020. <https://doi.org/10.1016/j.actaastro.2020.06.042>

Overview of spacecraft fragmentation testing

Stefano Lopresti^{1,a*}, Federico Basana^{1,b}, Lorenzo Olivieri^{1,c},
Cinzia Giacomuzzo^{1,d}, Alessandro Francesconi^{2,e}

¹ CISAS “G. Colombo”, University of Padova, Via Venezia 15, 35131 Padova, Pd, Italy

² CISAS “G. Colombo” - DII, University of Padova, Via Venezia 15, 35131 Padova, Pd, Italy

^astefano.lopresti@unipd.it, ^bfederico.basana@phd.unipd.it, ^clorenzo.olivieri@unipd.it,

^dcinzia.giacomuzzo@unipd.it, ^ealessandro.francesconi@unipd.it

Keywords: Space Debris, Fragmentation Testing, Cumulative Distribution, Satellites Break Up

Abstract. Spacecraft fragmentation due to collisions with space debris is a major concern for space agencies and commercial entities, since the production of collisional fragments is one of the major sources of space debris. It is in fact believed that, in certain circumstances, the increase of fragmentation events could trigger collisional cascade that makes the future debris environment not sustainable. Experimental studies have shown that the fragmentation process is highly complex and influenced by various factors, such as the material properties, the velocity and angle of the debris impact and the point of collision (e.g. central, glancing, on spacecraft appendages). In recent years, numerous impact tests have been performed, varying one or more of these parameters to better understand the physics behind these phenomena. In this context some tests have been also performed at the hypervelocity impact facility of the university of Padova. This paper provides an overview of the main experiments performed, the most critical issues observed and proposes some future directions for further research. Moreover, it summarizes the current state of research in spacecraft fragmentation, including the methods and techniques used to simulate debris impacts, the characterization of fragment properties and the analysis of the resulting debris cloud.

Introduction

The increasing presence of space debris poses a significant and escalating threat to the safety of space activities. Collisions with such debris are the primary sources of spacecraft fragmentation, leading to the generation of additional space debris and contributing to an increasingly congested orbital environment [1]. As a result, mitigating space debris has become a top priority for the international space community, necessitating the implementation of effective strategies to reduce the accumulation of space debris and ensure the safety of space operations [2]. Mathematical modelling of this phenomenon is very challenging due to the high velocities involved and the large energies generated during impact. It is therefore essential to perform impact tests that accurately represent the conditions that occur in orbit [3]. In addition, to properly calibrate the models, it is essential to perform parametric tests that allow the influence of the impact geometry (impact angle, velocity, point of impact, etc.) on debris generation to be isolated and studied individually.

To achieve these outcomes, it is crucial to have access to hyper-velocity facilities capable of executing impacts with excellent velocity control.

Hypervelocity impact facility

There are different types of Hypervelocity laboratories that perform impact tests, the most common are the powder-gas guns [4], it is possible to manufacture them in a two-stage light gas configuration that does not involve the use of explosive dust [5].

The conceptual process for both is similar: a piston is accelerated to compress a light gas (usually hydrogen) adiabatically inside a cylinder. The very quick compression leads to a sudden



increase in the gas temperature and pressure (about 5000K and 4000Bar peak). When the pressure reaches its peak a valve is opened (usually is a rupture disk that breaks due to high pressure) and the gas is discharged onto a projectile that is fired at high velocity into the target in a vacuum chamber.

The difference in functioning between the two guns is in the way the cylinder is accelerated in the first stage: the light gas gun uses high-pressure gas (e.g., Helium at 120bar) while the second uses gunpowder as a propellant. Both methods are very efficient and it is difficult to compare them, however, from tests, it seems that gunpowder accelerators are able to reach higher velocities while the process with the light-gas guns has higher repeatability, this is because the combustion process is more unstable than unloading a pressurized tank. Moreover, the light gas gun requires significantly less maintenance.

In recent years, research is being directed toward the possibility of manufacturing three-stage accelerators [6]. This achievement would be very interesting because it involves adding a powder stage upstream to existing light gas guns. This could improve the performance of the guns and achieve peak velocities of more than 10 km/s.



Figure 1: Two stage light gas gun in the hypervelocity facility of the university of Padova.

Fragmentation test

The use of a target with a realistic material distribution is essential to obtain representative results for the physical parameters of the debris. In recent years, there has been increased interest in satellite fragmentation tests to study the response of complex geometries to hypervelocity impacts. The first such impact study was the SOCIT (Satellite Orbital debris Characterization Impact Test) tests series, which was made up of four hypervelocity impacts on representative satellite in space. In particular, in the fourth test, Socit4, the target was a flight ready Navy Transit 1960 era satellite. [7]

An aluminium projectile with a diameter of 4.7cm (150 grammes) fired at a speed of 7km/s was used for the test. The shot was performed on a model of an old generation satellite, therefore the materials are different from those mounted on new-generation spacecraft, for this reason it was decided to carry out a further experimental campaign with more modern targets.

Two hypervelocity tests were conducted in the DebrisSat campaign. The first target was a representative upper stage model of a launch vehicle (DebrisLV) and the second a 56kg satellite (DebrisSat). For both tests, an aluminium cylinder measuring 8.6cm x 9cm was used as the projectile, which was fired at speeds of 6.8 and 6.9km/s, respectively.

DebrisLV was composed of 2 pressurised gas tanks of different material and size, the rest of the structure was composed of other materials used in space such as aluminium 6061 and stainless steel [8].

Debrisat is a representative model of a LEO satellite, with a diameter of 60 cm and a height of 50 cm. In addition to using more advanced materials, it was decided to make the satellite 45% more massive than the Socit test. In order to better study the fragmentation of the satellite, each sector of DebrisSat was built with different coloured material to better identify its origin [9].

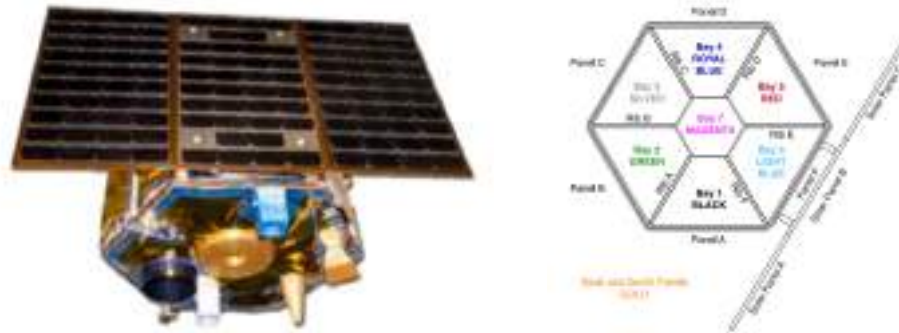


Figure 2: DebrisSat photo (left) and schematic representation of the colour subdivision (right).

A rigorous procedure was developed to collect the fragments; the foam panels placed inside the firing chamber were first scanned by X-ray. Once scanned, fragments larger than 2mm were identified, extracted, a characteristic length is measured (the average of the three largest orthogonal dimensions of the fragment) and a unique identification number is assigned. The fragments were then sorted by material, shape and colour and scanned in 2D or 3D [10]. The data were collected and cumulative graphs of mass, shape and size distribution were produced, as well as characteristic length plots with area to mass ratios. This data will be used to improve the modeling of the relationships of these physical characteristics to each other and to calculate more accurate distributions of such parameters.

A team of researchers from CARDC (China Aerodynamics Research and Development Center) carried out a fragmentation test on three cubic aluminium mock-ups of $40 \times 40 \times 40 \text{ cm}^3$ with increasing weights of 7.3, 8.2, and 13.1 kg respectively. Inside these mockups there were a cylindrical central body and representative electronic boxes also made of aluminium, some parts of a printed circuit board were also included. The impact occurred at a speed of approximately 3.5km/s. The fragments were collected and cumulative debris distributions were made in terms of area to mass ratio and cross-sectional area. [11].

A further study was carried out at THIOT Ingénierie and included the fragmentation of a nanosatellite measuring $15 \times 10 \times 10 \text{ cm}^3$. On the satellite were mounted components representative of those used in space such as a 4-cells battery pack, electronic boards, inertia wheels and a solar panel (although it should be noted that they were non-flight acceptable). The projectile used was a 9mm-diameter polycarbonate equilateral cylinder incorporating a second 4mm-diameter aluminium equilateral cylinder fired at approximately 6.7km/s. The size and weight of the fragments were then collected by a six-axis robotic arm that also performed a 3D scan of each analysed fragment [12].

In this context, CISAS also decided to start a test campaign on complex structures. Two tests were performed on a mockup of a Picosatellite of size $50 \times 50 \times 50 \text{ mm}^3$. The first shot was central, with the impact face perpendicular to the projectile (a), while the second test was a glancing impact, performed with the picosatellite inclined at 45° with respect to the projectile direction (b). For these tests, fragments were manually collected, divided by size, weighed and measured to obtain cumulative distributions, characteristic lengths and shape diagrams [13]. The results obtained from the tests were then compared with those predicted by models in the literature (c).

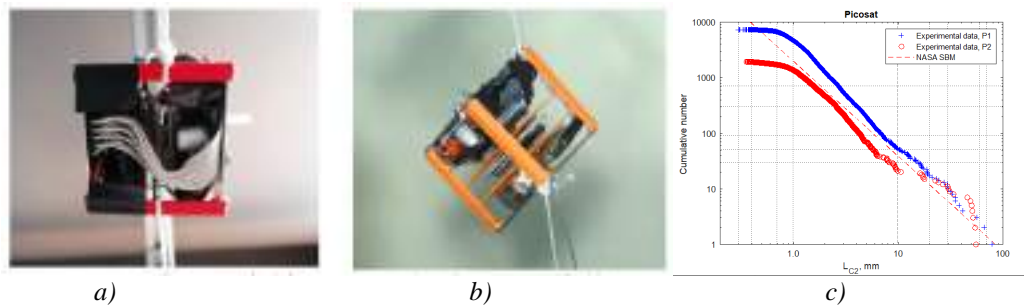


Figure 3: Experimental setups and characteristic length cumulative distribution.

The glancing impact produced less fragments compared to the other test and also compared to those predicted by the NASA SBM model. However, the inclination of the curves of the experimental and model data have a similar inclination.

Conclusion

Several tests have been performed in recent years to better understand the fragmentation dynamics of a hypervelocity impact. For the development of new models, it is of critical importance to have an increasingly rich and parameterized impact database available for the scientific community. Building new facilities or upgrading existing ones with the objective of reaching higher speeds and find fast and accurate fragment analysis procedures is a key target to achieve this goal.

References

- [1] A. Rossi et al, "Modelling the evolution of the space debris population," *Planet Space Sci*, 1988.
- [2] J.-R. Ribeiro et al, "Evolution of Policies and Technologies for Space Debris Mitigation Based on Bibliometric and Patent Analyses," *Space Policy*, pp. 40-56, 2018. <https://doi.org/10.1016/j.spacepol.2018.03.005>
- [3] D. McKnight, R. Maher and L. Nag, "Refined algorithms for structural breakup due to hypervelocity impact," *International Journal of Impact Engineering*, pp. 547-558, 1995. [https://doi.org/10.1016/0734-743X\(95\)99879-V](https://doi.org/10.1016/0734-743X(95)99879-V)
- [4] T. J. Ringrose, H. W. Doyle, P. S. Foster and al, "A hypervelocity impact facility optimised for the dynamic study of high pressure shock compression," *Procedia Engineering*, 2017. <https://doi.org/10.1016/j.proeng.2017.09.756>
- [5] A. Angrilli, D. Pavarin, M. De Cecco and A. Francesconi, "Impact facility based upon high frequency two-stage," *Acta Astronautica*, pp. 185 - 189, 2002. [https://doi.org/10.1016/S0094-5765\(02\)00207-2](https://doi.org/10.1016/S0094-5765(02)00207-2)
- [6] A. J. Piekutowski and K. L. Poormon, "Development of a three-stage, light-gas gun at the University of Dayton Research Institute," *International Journal of Impact Engineering*, 2006. <https://doi.org/10.1016/j.ijimpeng.2006.09.018>
- [7] J. Liou, J. Opiela, H. Cowardin, T. Huynh, M. Sorge, C. Griffice, P. Sheaffer, N. Fitz-Coy and M. Wilson, "Successful Hypervelocity Impacts of," *NASA Orbital Debris Quarterly News*, pp. 3-5, 2014.
- [8] H. Cowardin, J.-C. Liou, P. Anz-Meador, M. Sorge, J. Opiela, N. Fitz-Coy, T. Huynh and P. Krisko, "Characterization of orbital Debris via Hiper-velocity laboratory-based Tests," in *European Conference on Space Debris*, 2017.

- [9] M. Rivero, B. Shiotani, M. Carrasquilla, N. Fitz-Coy, J.-C. Liou, M. Sorge, T. Huynh, J. Opiela, P. Krisko and H. Cowardin, "DebrisSat fragment Characterization System and Processing Status," in *IAC*, Bremen, Germany, 2018.
- [10] M. Rivero, J. Kleespies and K. Patankar, "Characterization of Debris from the DebrisSat Hypervelocity Test," in *IAC*, 15.
- [11] S.-W. Lan, S. Liu, Y. Li, F.-W. Ke and j. Huang, "Debris area distribution of spacecraft under hypervelocity impact," *Acta Astronautica*, vol. 105, pp. 75-81, 2014. <https://doi.org/10.1016/j.actaastro.2014.08.011>
- [12] H. Abdulhamid, D. Bouat, A. Collè and Al, "On-ground HVI on a nanosatellite. Impact test, fragments recovery and characterization, impact simulations.," in *8th European Conference in Space Debris*, 2021.
- [13] L. Olivieri, P. A. Smocovich, C. Giacomuzzo and A. Francesconi, "Characterization of the fragments generated by a Picosatellite impact experiment," *International Journal of Impact Engineering*, vol. 168, 2022. <https://doi.org/10.1016/j.ijimpeng.2022.104313>

Feasibility analysis of a CubeSat mission for space rider observation and docking

Chilin Laura^{1*}, Bedendo Martina¹, Banzi Davide¹, Casara Riccardo¹,
Costa Giovanni¹, Dolejsi Elisabetta¹, Quitadamo Vincenzo¹, Trabacchin Nicolò¹,
Visconi Delia¹, Visentin Alessia¹, Basana Federico², Olivieri Lorenzo²,
Colombatti Giacomo³, Francesconi Alessandro³

¹University of Padova, Via 8 Febbraio 2, 35122 Padova

²CISAS G.Colombo, Via Venezia 15, 35131 Padova

³DII/CISAS, Via Venezia 1, 35131 Padova

*laura.chilin.1@studenti.unipd.it

Keywords: CubeSat, Manoeuvres, Inspection, Docking

Abstract. In the last few years the number of orbiting satellites has increased exponentially, in particular due to the development of the New Space Economy. Even if this phenomenon makes the space more accessible, bringing a great contribution to the scientific, economic and technological fields, on the other hand it contributes to the overpopulation of the space background. Therefore, it is necessary to develop new techniques to manage the space environment, such as in orbit servicing, which is a procedure that aims to refuel and repair satellites to extend their operational life. A first step to reach this goal is to inspect closely the object of interest to study its features. In this framework, the Space Rider Observer Cube (SROC) mission is being developed. SROC is a payload that will be deployed by Space Rider, an uncrewed and reusable robotic spacecraft designed by ESA. SROC is a 12U CubeSat, whose goal is to carry out inspection manoeuvres around the mothership, then re-enter on board using a safe docking system to come back to Earth. The feasibility of a mission similar to SROC has been simulated during a university class, starting from the definition of the system requirements with particular focus on the analysis of the payloads and subsystems, to ensure the achievement of the mission goals. In particular, the CubeSat is equipped with an optical instrument to capture high resolution images of Space Rider surface and a docking mechanism. Then the design of the orbit and the simulation of the effects of the space environment on the CubeSat have been studied using GMAT, SYSTEMA, MATLAB and other numerical tools. The results of the study are useful for future missions, aiming to inspect orbiting objects, such as operative satellites for in orbit servicing, space debris and dead satellites to study their geometries and plan their removal.

Introduction

As the number of orbiting objects around Earth is constantly rising, it is necessary to develop new strategies to manage the space environment. For this purpose, it's crucial to study the space objects in-situ with a close observation for future in orbit-servicing missions that will allow to extend the operative life of functional satellites. Examples of these missions are: Seeker, a 3U CubeSat used to complete autonomous mocking inspections [1] and AeroCube-10, a 1.5U CubeSat created to demonstrate precision satellite-to-satellite pointing [2]. However the number of space missions involving CubeSats meant to inspect other satellites remains low. The aim of this work is to contribute to this field studying a CubeSat inspired by SROC (Space Rider Observer Cube), a future mission designed by ESA in conjunction with Politecnico di Torino and Tyvak International, that aims to carry on inspections and docking manoeuvres with its mothership Space



Rider (SR), a reusable robotic spacecraft. In fact, SROC will reach its operative orbit inside Space Rider cargo bay and then will be deployed by it [3,4].

This project has been developed during a university class, and it started from the definition of the system requirements, followed by the selection of components and sizing of the subsystems, leading to the preliminary design of the system (Fig. 1).

Requirements and preliminary definition

Starting from the mission objectives of performing safe inspection and docking manoeuvres and transposing them into mission requirements, all the subsystems with their performance level have been defined. Afterwards, the design and operational requirements have been taken into account to reach a first iteration of requirements. Since the CubeSat is inspired by SROC, it has some similarities that have been included in the requirements such as its 12U structure, an imaging payload and a docking payload. It was established that Space Rider model orbit should be a 600 km dawn dusk 6 a.m. Sun Synchronous Orbit.

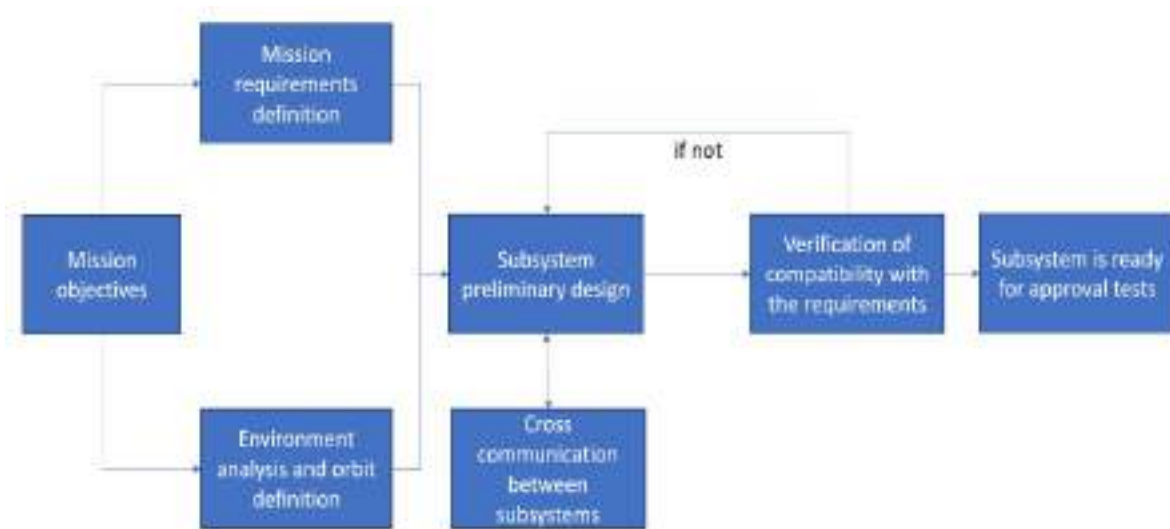


Fig. 1: Work procedure

Mission phases

The initial date of departure of the CubeSat from the mothership is set to be June 21, 2024, chosen to reduce the umbra periods and increase the electric power collected by the solar panels. Three reference frames have been designed for the simulations implemented in GMAT and MATLAB: the Earth inertial frame MJ2000Eq to define the mothership motion around the planet (Fig. 2a) [5]; radial in-track cross-track (RIC) centred in the mothership (Fig. 2a) and the CubeSat body frame to describe its relative orbit (Fig. 2b).

The motion of the CubeSat around the mothership is described by a Walking Safety Ellipse (WSE), chosen to be a safe orbit for both satellites. [6]

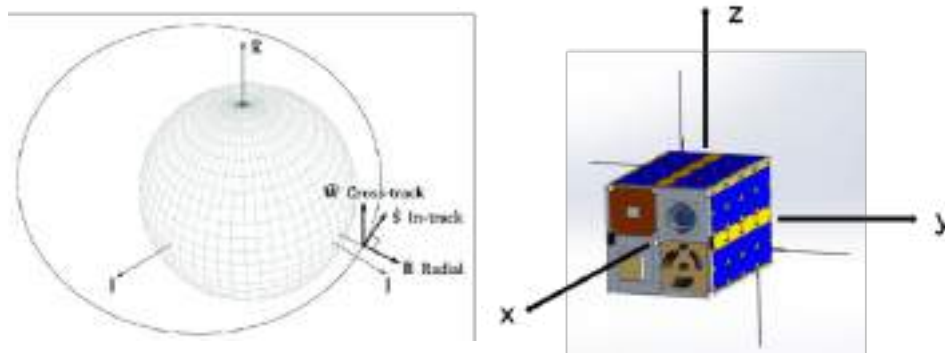


Fig. 2: a. MJ2000EQ and RIC frame system; b. Body system

The mission is designed to last 25 days, and its operative life can be divided in six phases:

1. Departure from Space Rider model (five hours): the CubeSat separates from the mothership and prepares for the first manoeuvre;
2. WSE entering phase (five hours): the CubeSat achieves the RIC coordinates to enter the WSE;
3. Inspection on a WSE orbital keeping: the CubeSat moves forward in the WSE for two days, then performs the orbital keeping manoeuvres to return to the initial conditions to repeat the inspection. This cycle is performed eleven times, to take pictures of the entire surface of the satellite in different conditions;
4. WSE departure: the CubeSat is brought to a stationary point, 100 m far from the mothership;
5. Hold Point approach (five hours): the CubeSat reaches a hold point at 50 m from SR model;
6. Rendezvous phase: the CubeSat reaches a 2 m distance from the mothership through a bang-bang technique.

CubeSat design

The CubeSat has the standard dimensions of a typical 12U CubeSat with a mass of 16kg. The skeleton of the external structure is made of Aluminium 6061, closed by graphene panels. Two other panels are added to the internal structure to create different zones inside the satellite and facilitate the storing of the components.

The satellite has two payloads: a camera (CMOS sensor and optical lens) that fits 1U and a partially external docking mechanism, whose dimensions are 1U. The camera is protected by a “Zerodur” layer. The images are taken and then transferred to the On-Board Computer (OBC) to be processed and then sent to Earth by the Telemetry and Tracking Control subsystem (TTC) antennas. The TTC communicates with ground stations using UHF band, through which the satellite also transmits telemetry data and receives commands.

The CubeSat is equipped with an Attitude Determination and Control Subsystem (ADCS) based on an Inertial Platform (Inertial Measurement Unit, IMU), navigation system GNSS, a magnetometer and multiple sun sensors to determine the configuration of the CubeSat around the Space Rider model. In addition, three reaction wheels are used for disturbances control and one for redundancy, together with three magnetorquers for their desaturation, while a momentum wheel is necessary to maintain the pointing towards SR during the inspection on the WSE.

The electric power, essential to all subsystems, is guaranteed by body mounted solar panels, positioned on the 6U faces and on the 4U face opposed to the camera lens, and a Li-Ion battery that comes into play when the energy provided by the panels is not sufficient. These components form the Electric Power Subsystem (EPS). The surface of the solar panels is covered with 125 μ m “Kapton”. The thickness has been chosen to resist erosion due to the atomic oxygen.

The environment analysis (external and internal) has been realised with MATLAB, SPENVIS and Systema, and it suggested that a passive Thermal Control Subsystem (TCS) is sufficient to guarantee the maintenance of the operative temperature for individual components: for that purpose, the ADCS components have been covered with a Multi-Layer Insulation (MLI) material. Furthermore, it is not necessary to equip the satellite with a device for dissipating the internal thermal energy, i.e. a radiator.

The propulsive system consists in three cold gas B1 thrusters, fuelled by N₂O propellant (nitrogen peroxide). This propellant is self-pressurising and has a good thermal control in space. This technology has been chosen because it presents a low power consumption, low mass and can perform every requested manoeuvre during the mission.

In the end, the CubeSat is provided with a drag sail that will be used in case of docking failure to guarantee the compliance with the Space Debris Mitigation Guidelines.

Discussion and conclusions

During this study, some issues related to the CubeSat design arose. The resolution of the camera has been one of the most challenging aspects, because it is not only related to the pictures quality level, but it is also fundamental for the choice of a technology that can fit in the CubeSat. Moreover, the communication frequency band has been discussed, starting from a S-band communication to send images and a UHF band for the telemetry and command data. Due to power consumption issues, the UHF band has been chosen. In fact, the body mounted configuration is not able to provide the electric power necessary to guarantee an S-band communication. This led to the definition of two configurations for the EPS: the first one consisting of Sun tracking deployable solar panels, the second using the same structure without the Sun tracking mechanism. Both alternatives proved to be unsuitable as one of the mission objectives is to provide a way to dock safely with the mothership.

This paper showed the feasibility of the mission, giving results that will be useful for future missions developed with the goal of making in orbit servicing a reality. Further details on this work will be provided in a future extended paper.

References

- [1] Brian Banker, Scott Askew “Seeker 1.0: Prototype Robotic Free Flying Inspector Mission Overview” NASA Johnson Space Center 2019
- [2] Gangestad, Joseph W., Catherine C. Venturini, David Hinkley and Garrett Kinum. “A Sat-to-Sat Inspection Demonstration with the AeroCube-10 1.5U CubeSats.” (2021).
- [3]<https://www.asi.it/en/technologies-and-engineering/micro-and-nanosatellites/esa-gstp-fly-program/sroc/> (accessed: June 2023)
- [4]https://www.esa.int/Enabling_Support/Space_Transportation/Space_Rider_overview (accessed: June 2023)
- [5] Kim, Eunhyouek & Han, Seungyeop & Sayegh, Amer. (2019). Sensitivity of the Gravity Model and Orbital Frame for On-board Real-Time Orbit Determination: Operational Results of GPS-12 GPS Receiver. Remote Sensing. 11. 1542. <https://doi.org/10.3390/rs11131542>
- [6] Gaylor, David & Barbee, Brent. (2007). Algorithms for safe spacecraft proximity operations. Advances in the Astronautical Sciences. 127. 133-152.



Fig. 3: CubeSat CAD without solar panels

Analysis of small spacecraft Mars aerocapture through a single-event drag modulation

Tobia Armando La Marca^{1,a,*}, Giorgio Isoletta^{2,b} and Michele Grassi^{2,c}

¹Scuola Superiore Meridionale, Largo San Marcellino 10, 80138 Naples, Italy

²Department of Industrial Engineering, University of Naples "Federico II", Piazzale Tecchio 80, 80125 Naples, Italy

^a tobiaarmando.lamarca-ssm@unina.it, ^b giorgio.isoletta@unina.it, ^c michele.grassi@unina.it

Keywords: Aerocapture, Drag Modulation, Mars Exploration, Small Spacecraft

Abstract. In the last years, the scientific interest in Mars exploration has become more and more relevant, driving the development of technologies aimed at improving the current capabilities to land scientific payloads or to insert probes into stable orbits around the planet. In this framework, the use of low-cost small satellites could represent an advantageous solution for both the mission scenarios. In planetary exploration, the aerocapture manoeuvre is considered a promising technique to overcome the limits imposed by specific volume and mass ratio constraints on the design of the propulsion system. Based on these premises, this work focuses on the 2D aerocapture manoeuvre of a small spacecraft equipped with a Deployable Heat Shield (DHS). Specifically, the analysis aims at assessing the aerocapture manoeuvre feasibility exploiting a single shield surface variation.

Introduction

The aerocapture is an aero-assisted manoeuvre to transfer a vehicle from a hyperbolic orbit to a closed one at lower energy, by exploiting the aerodynamic drag force through a single atmospheric passage with properly designed decelerators, such as DHS, drag skirt or inflatable drag devices. Once out of the atmosphere, the spacecraft performs a subsequent Pericenter Raise Manoeuvre (PRM) to avoid repeated atmospheric passages and stabilize the spacecraft on a scientific orbit or on a parking orbit, ready for suppletive Post-Aerocapture Manoeuvres (PAM). If compared to a purely propulsive orbit injection (OI), the aerocapture manoeuvre allows to drastically increase the delivered mass payload thanks to the propellant savings and the smaller weight of the aerodynamic decelerators compared to the propellant needed for propulsive OI. The reduction of the propellant mass decreases the costs per kg of payload, thus enabling or enhancing many potential planetary mission profiles [1]. Moreover, the aerocapture benefits of inherent reduction of the manoeuvring time with respect to the aerobraking manoeuvre, which instead exploits multiple atmospheric passages for depleting the right amount of energy to reach the final orbit. Although the consensus of recent studies about the possibility to use aerocapture for science mission at Titan, Mars and possibly Venus [2], it has never been implemented to date because of environmental and object related uncertainties, e.g., the limited knowledge of the local atmospheric density and/or the lack of real-time navigation data. However, both the growing scientific interest in Mars exploration and the technological readiness acquired in atmospheric flights during the last decades motivate further investigations on Mars aerocapture. This contribution specifically focuses on the aerocapture technique for a small satellite equipped with a DHS, exploiting a single-event drag modulation. The aerocapture has been studied from a purely dynamical point of view, and a multiparametric analysis has been carried out to identify suitable aerocapture corridors. The results of the single-event drag modulation strategy are compared with the outcomes of fixed shield aperture strategy to assess the benefits of this technique in terms of number and characteristics of possible solutions.



Finally, the conductive thermal heat at the pericenter has been estimated to evaluate the thermodynamical loads the spacecraft will encounter during the atmospheric crossing.

Methodology

The present work analyses the aerocapture manoeuvre of a spacecraft initially moving on a hyperbolic approaching trajectory, resulting from a patched conics approximation of the Earth-to-Mars interplanetary transfer. According to this construction, the spacecraft dynamics can be modelled as a two-body problem. The trajectory is then propagated up to the Mars Atmospheric Interface (AI), usually set to 150 km. Once the spacecraft crosses the atmosphere, the drag perturbs the motion as according to the following equation:

$$\ddot{\vec{r}} + \frac{\mu_{\text{Mars}}}{r^3} \vec{r} = \vec{a}_d \quad (1)$$

where \vec{r} is the spacecraft position vector in a 2D reference frame centred in Mars, μ_{Mars} is the planetary standard gravitational parameter, while \vec{a}_d the atmospheric drag perturbing acceleration modelled as:

$$\vec{a}_d = -\frac{2\rho}{3\beta} \vec{v} \quad (2)$$

In Eq. 2, ρ is the atmospheric density, \vec{v} is the spacecraft velocity vector relative to the atmosphere, v is its module and β is the ballistic coefficient defined as $\beta = \frac{m}{C_D S}$, being C_D the drag coefficient, S the shield cross-section and m the spacecraft mass. The velocity variation produced by the aerodynamic deceleration, Δv_{drag} , has been computed as the difference of the velocity at the pericentres of the arrival hyperbolic trajectory and the elliptical one obtained after the atmospheric crossing. Moreover, the impulsive burn Δv_{PRM} to circularize the elliptical exit orbit has been computed as a Hohmannian manoeuvre executed at the ellipse apoapsis as:

$$\Delta v_{\text{PRM}} = \sqrt{\frac{\mu_{\text{Mars}}}{r_a}} - \sqrt{\mu_{\text{Mars}} \left(\frac{2}{r_a} - \frac{1}{a_{\text{exit}}} \right)} \quad (3)$$

where r_a and a_{exit} are respectively the apocenter and the semi-major axis of the elliptical orbit. Finally, the Sutton and Graves [3] semi-empirical relation for stagnation-point convective heat rate has been employed to quantify the thermal conductive heat rate in W/m^2 :

$$\dot{q}_c = K_m \left(\frac{\rho}{R_N} \right)^{0.5} v^3 \quad (4)$$

in which K_m is the Mars atmospheric conductive constant ($1.898 \times 10^{-4} \text{ kg}^{0.5}/\text{m}$) and R_N is the shield nosecone radius. Results are then converted into W/cm^2 to compare them with literature ones.

Results

Results here provided refer to spacecraft characteristics in [4] (and references therein). The spacecraft of $m = 150 \text{ kg}$ is equipped with a DHS providing a maximum surface extension of $S_{\text{max}} = 7.065 \text{ m}^2$ and a R_N of 0.6 m. All the simulations have been conducted assuming the possibility of changing the shield surface after the spacecraft transit at the pericenter of the arrival trajectory. Several dynamics conditions have been evaluated, resulting from the combination of arrival velocities ($v_\infty = 2, 3, 5 \text{ km/s}$), Keplerian arrival pericenters ($h_p = 70, 75, 80, 85, 90 \text{ km}$) and trigger altitudes for the ballistic coefficient variation (h_{tr}), supposing two different possible values of β respectively equal to 2β and 3β , and analyzing all the trigger altitudes from the Keplerian pericenter up to the aerodynamic interface, with step of 5 km. Moreover, results here reported

refers to the density nominal condition for September 1st, 2031, of the Mars Global Reference Atmospheric Model (Mars-GRAM) [4], and to a $C_D = 1$. Figure 1 shows the apocentric altitude h_a and eccentricity e_{exit} of the orbit obtained after the atmospheric passage as function of h_{tr} and β for $v_\infty = 3\text{km/s}$, while Table 1 lists the values of \dot{q}_c at the pericenter, Δv_{drag} and Δv_{PRM} for some of the most relevant settings. In all the figures, dashed lines represent the solution achievable with the nominal (constant) ballistic coefficient.

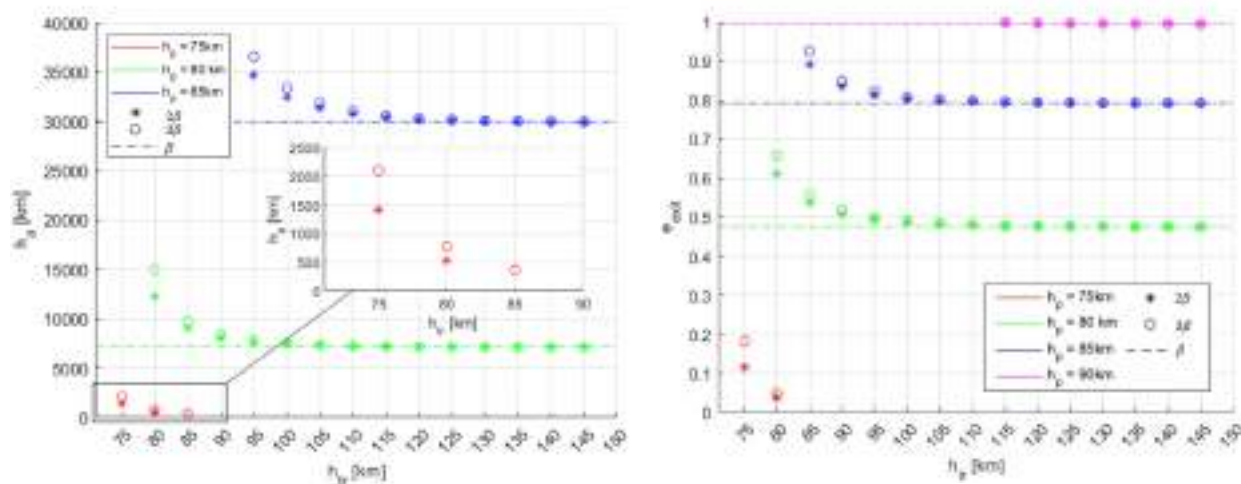


Figure 1 – exit orbit h_a and e_{exit} as function of h_{tr} for different h_p , β and $v_\infty = 3\text{ km/s}$

Table 1 - Most relevant results for $v_\infty = 3\text{ km/s}$

h_p [km]	h_{tr} [km]	$\Delta v_{drag,2\beta}$ [km/s]	$\Delta v_{drag,3\beta}$ [km/s]	$\Delta v_{PRM,2\beta}$ [km/s]	$\Delta v_{PRM,3\beta}$ [km/s]	\dot{q}_c [W/cm ²]
75	75	-1.607	-1.508	0.253	0.336	10.21
75	85	//	-1.780	//	0.0802	10.21
80	80	-0.906	-0.843	0.657	0.665	10.15
80	110	-1.086	-1.084	0.598	0.599	10.15
85	95	-0.645	-0.631	0.629	0.620	9.035
85	110	-0.669	-0.668	0.638	0.637	9.035

As expected, the largest variation of the exit orbit parameters is obtained when the ballistic coefficient modulation is triggered soon after the transit of the spacecraft at the pericenter. In particular, because of the larger density values encountered during the atmospheric crossing, the smaller is the h_p , the more circular is the exit orbit (i.e. the smaller are both e_{exit} and h_a). In turn, up to $h_p=80\text{km}$, Δv_{PRM} reduces with increasing h_{tr} , because of the larger amount of time spent with S_{max} at low altitudes. On the other hand, \dot{q}_c values at the pericenters are in line with those expected from the literature [3], showing a small variation with h_p . Finally, an important result is that, thanks to the variation of β , it is possible to have solutions also at pericenter altitude where we have no solutions with the nominal β (i.e. 75 km), that are of high interest due to the possibility to reduce the eccentricity of the exit orbits. However, no solutions have been obtained for h_p smaller than 75 km or larger than 85 km. To better understand the range of aerocapture solutions, in Fig. 2 the results for $v_\infty = 2$ and 5 km/s are depicted, while Tab.2 focuses on most relevant results obtained.

When the hyperbolic speed is of 5 km/s, it is possible to have solution only for $h_p = 75\text{ km}$. On the contrary, when the satellite arrival speed is smaller, solutions have been obtained only for h_p higher than 75km, since the atmospheric drag at those altitudes is considerably smaller. However, as previously described, the final h_a is again severely affected by the h_p and v_∞ values.

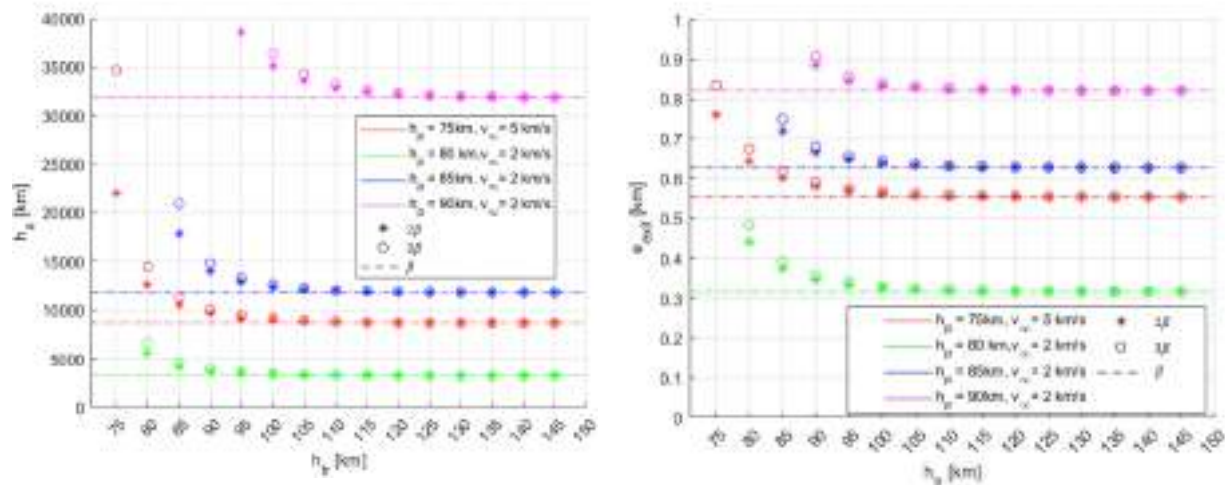


Figure 2 - exit orbit h_a and e_{exit} as function of h_{tr} for different h_p , β and $v_{\infty} = 2$ and 5 km/s

Table 2 - Most relevant results for $v_{\infty} = 2$ and 5 km/s

h_p [km]	h_{tr} [km]	$\Delta v_{drag,2\beta}$ [km/s]	$\Delta v_{drag,3\beta}$ [km/s]	$\Delta v_{PRM,2\beta}$ [km/s]	$\Delta v_{PRM,3\beta}$ [km/s]	\dot{q}_c [W/cm^2]
75	75	-1.43	-1.34	0.661	0.627	15.72
75	110	-1.71	-1.71	0.626	0.627	15.72
80	80	-0.94	-0.88	0.553	0.583	8.74
80	110	-1.12	-1.12	0.442	0.443	8.74
90	95	-0.40	-0.38	0.614	0.606	6.72
90	120	-0.42	-0.42	0.633	0.633	6.72

Conclusions

This work presents an analysis of a single-event aerocapture manoeuvre for a small spacecraft equipped with a DHS. Results confirm the increasing number of solutions achievable with a ballistic coefficient modulation, although a strong dependency on the arrival conditions emerges. Additionally, aerocapture enables some otherwise unattainable exit orbits. For relatively high arrival speed, the atmospheric aerocapture corridor shortens in such a way to suggest further investigation of possible control techniques for a finer modulation of the deployable shield aperture. Thus, future development will focus on 3D aerocapture analysis with the definition of a deployable shield modulation logic.

References

- [1] J. L. Hall, M. A. Noca, and R. W. Bailey, "Cost-Benefit Analysis of the Aerocapture Mission Set," *J Spacecr Rockets*, vol. 42, no. 2, pp. 309–320, Mar. 2005. <https://doi.org/10.2514/1.4118>
- [2] T. R. Spilker *et al.*, "Qualitative Assessment of Aerocapture and Applications to Future Missions," *J Spacecr Rockets*, vol. 56, no. 2, pp. 536–545, Nov. 2018. <https://doi.org/10.2514/1.A34056>
- [3] Z. R. Putnam and R. D. Braun, "Drag-Modulation Flight-Control System Options for Planetary Aerocapture," *J Spacecr Rockets*, vol. 51, no. 1, pp. 139–150, Aug. 2013. <https://doi.org/10.2514/1.A32589>
- [4] G. Isoletta, M. Grassi, E. Fantino, D. de la Torre Sangrà, and J. Peláez, "Feasibility Study of Aerocapture at Mars with an Innovative Deployable Heat Shield," *J Spacecr Rockets*, vol. 58, no. 6, pp. 1752–1761, Jun. 2021. <https://doi.org/10.2514/1.A35016>

Onboard autonomous conjunction analysis with optical sensor

Luca Capocchiano^{1,a}, Michele Maestrini^{1,b}, Mauro Massari^{1,c}, Pierluigi Di Lizia^{1,d}

¹Department of Aerospace Science and Technology, Politecnico di Milano, Via Giuseppe La Masa 54 20156, Milano

^aluca.capocchiano@mail.polimi.it, ^bmichele.maestrini@polimi.it, ^cmauro.massari@polimi.it, ^dpierluigi.dilizia@polimi.it

Keywords: Relative Orbit Determination, Optical Sensor, Batch Filter, Conjunction Analysis

Abstract. The increasingly high number of spacecrafts orbiting our planet requires continuous observation to predict hazardous conjunctions. Direct onboard analysis would allow to ease the burden on ground infrastructure and increase the catalogued debris. A spaceborne optical sensor is used to assess the performance in terms of different targets visibility. A fast relative orbit determination algorithm is then proposed to compute the probability of collision for a particular case study and compared to a more accurate ground analysis.

Introduction

The growing number of satellite launches increases the risk of in-orbit collision, with potential cascade effects, further worsening the situation. Given the high number of close encounters every day, estimation processes must be frequently updated to avoid the occurrence of catastrophic collisions such as the Iridium-33/Cosmos-2251 event. The possibility to autonomously analyze any conjunction directly onboard would allow to significantly reduce the burden on ground infrastructure, leading to a faster update rate and lower risk of unexpected collisions. Therefore, in this research, a satellite is equipped with an optical sensor to determine the visibility performance with respect to a catalogue of potentially hazardous objects, with different parameters considered relevant for a significant statistical analysis. The closest encounters are then identified and a novel approach is presented for an accurate and computational efficient onboard orbit determination algorithm, providing results directly at the Time of Closest Approach (TCA), where the conjunctions are analyzed onto the B-plane.

Simulation design

The simulation consists of an asset spacecraft, based on the real satellite COSMO-SkyMed 4, operating in a Sun-Synchronous Low Earth Orbit, and a catalogue of 425 possible threats. The sensitivity analysis is carried out in the first eight days of September 2022. The chosen optical sensor is characterized by a limiting magnitude of 15, 30° field of view and 30° minimum Sun separation, operating in tracking mode; the camera is inertially pointed at the expected target direction, at the beginning of each visibility window, without any attitude information. The chosen sensor allows to see objects as small as 10 cm up to 6000 km [1]. The simulation is carried out through *SOPAC* (Space Object PASS Calculator), a Python library developed by *Politecnico di Milano* to compute all the possible observation opportunities for a given sensor network [2]. First, a sensitivity analysis is carried out, with the sensor performance evaluated both in terms of total visibility and revisit times for all the computed windows and compared to the asset observation uniformity along its orbit. Of the six main keplerian elements, only right ascension of the ascending node (or RAAN) shows a remarkable trend; higher semi-major axis may grant higher visibility, yet the considered catalogue is too limited for a significant inference. The total visibility time is shown on the left of Fig. 1, expressed in hours for three different sensor limits: pure geometry,



only illumination and full limitations, as defined before. As expected, the presence of the Earth shadow strongly reduces the total time to values lower than 25 hours, while limiting magnitude and Sun separation have a relevant influence only for particularly small objects. The second relation highlights the total time as function of RAAN and uniformity index, computed dividing the asset orbit in 36 sections covering 10° in true anomaly and counting how many contains at least one potential observation. It is thus an important indication of the quality of measurements taken for the specific target.

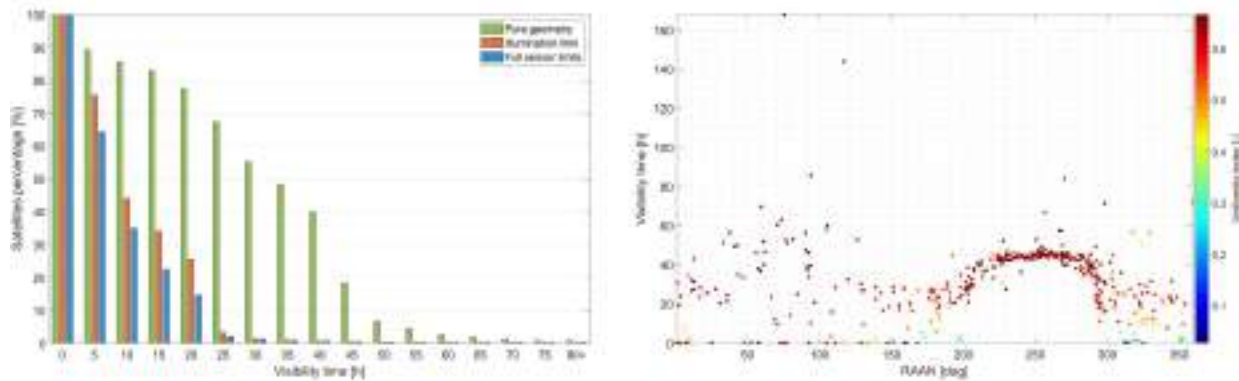


Figure 1 Total visibility time expressed in hours for three different sensor limits (left) and function of RAAN and uniformity index (right).

Objects with RAAN between 200 and 300 degrees are characterized by a higher time and higher uniformity index with no significant influence from initial target conditions. This is an expected result as COSMO-SkyMed 4 has a RAAN of about 70° , approximately 180° apart, resulting in encounters being mostly “head-on”. On the contrary, objects with RAAN similar to the asset may reach higher values, though they are strongly dependent on the initial relative position.

An important parameter when scheduling observations is the revisit time, the time between two consecutive passages, reported on the left of Fig. 2. The maximum and minimum revisits are highlighted as function of RAAN, with an upper limit of 3000 seconds. At around 250 degrees, the two values are almost coincident at approximately 2000 seconds.

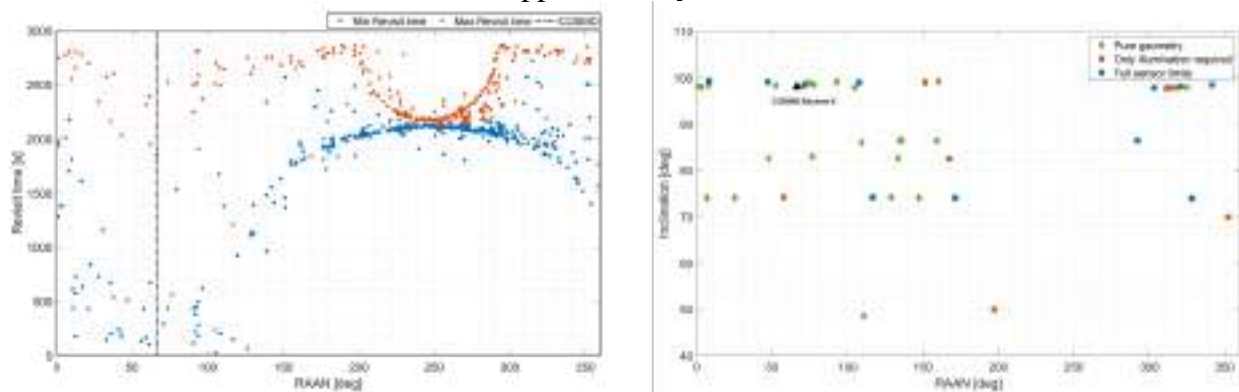


Figure 2 Maximum and minimum revisit (left), non-visible objects as function of inclination and RAAN (right)

Concerning non-visible objects, on the right of Fig. 2, out of the 425 objects, 25 are never visible due to geometric limitations, 7 due to lack of Sun illumination and 11 due to the specific sensor adopted. Once again, satellites with RAAN between 200° and 300° are always visible, regardless of the considered limit.

Methodology

The conjunction events are searched in the 8 days after the statistical analysis. The optical sensor accuracy is set at 0.01° for both right ascension and declination, to account for lower performance of an onboard system, as well as possible mounting errors. Since the proposed filtering method is based on the linear, minimum variance Least Squares, the propagation should be close to the real motion to ensure accurate results even with a single iteration. The best compromise is found by propagating directly from the TLEs using SGP4, allowing to keep a low computational time and high accuracy. On the contrary, the contribution of the State Transition Matrix (STM) is much less sensitive to inaccurate orbit modeling and a simple J2 effect can be implemented without excessively diminishing the estimation accuracy. The proposed method is based on the property of the STM to map each observation to the relative state directly at the TCA, without the need to further propagate the solution, which would result in a higher computational time and lower accuracy. If the primary spacecraft motion is assumed to be perfectly known, then the relative state deviation is equal to the target one, allowing to work in terms of absolute quantities, as reported in Algorithm 1. Although the asset spacecraft is tracked by ground stations providing accurate orbit determination, its trajectory is still affected by uncertainties, included in the filter post-processing through the Consider Covariance Analysis (CCA) [3]. Given the solution of the filtering process, relative position and covariance at the TCA are projected onto the B-plane, reducing the state dimension from six to only two positional coordinates, greatly simplifying the conjunction analysis and a potential CAM design [4]. The probability of collision is thus computed according to the Chan formulation, truncated to the third order [5]. The results provided by the onboard algorithm are compared to the ones obtained with a classic Unscented Kalman Filter (UKF), with observations coming from a set of three stations part of the EU SST sensor network (EU Space Surveillance and Tracking): S3TSR, MFDR and Cassini.

Algorithm 1: OnBoard conjunction analysis

- 1 Identify conjunction events and visibility windows
 - 2 Simulate real measurements, according to the defined camera frame
 - 3 Propagate reference trajectory from TLEs
 - 4 **For** each measurement
 - 5 Compute reference observations
 - 6 Compute measurements deviation
 - 7 Integrate STM to linearly map each observation to TCA
 - 8 **end**
 - 9 Compute target state and covariance at TCA
 - 10 Project onto the b-plane and compute probability of collision
-

Conjunction result

The results of the onboard relative orbit determination and conjunction analysis are here presented for the closest event, involving Falcon 1 rocket body, orbiting in a quasi-equatorial orbit of 9° inclination at approximately 650 km of altitude. Despite the low visibility time of only 16 hours, 284 measurements are processed. As highlighted in Fig. 3, the estimated error is 23 m, with a covariance of 76 m computed from the Least Squares, and 120 m added from the CCA. Considering the miss distance of 871 meters, the probability of collision is effectively equal to zero. The ground-based analysis is performed for all the involved objects, computing error and covariance of the orbit determination process alone, in order to directly compare the two methodologies. The square root of the covariance trace and the positional error highlight similar trends for both the asset and the target spacecrafts. The final values are 33 and 23 meters

respectively for COSMO, 110 m and 120 m for Falcon 1. The latter lies in correspondence of a spike, though the steady-state values are comparable to the asset. In general, the UKF results are slightly better, especially in terms of covariance, with the advantage of a real-time estimation process; however, the difference in computational time is considerable, with the Least Squares providing results in few seconds. Furthermore, the space-based platform is capable of seeing objects with very different orbits, still with a sufficiently high number of measurements, thus showing greater flexibility especially for low-inclination targets.

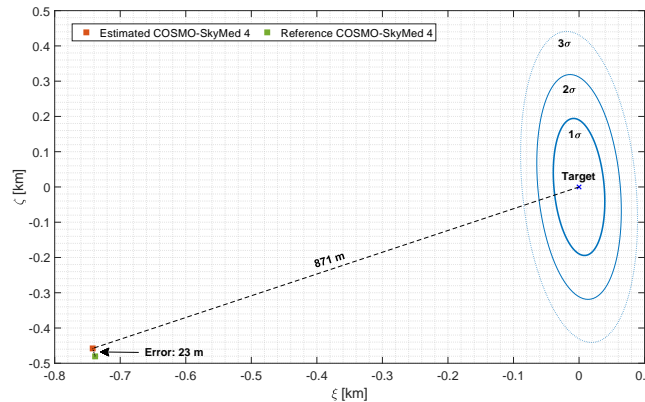


Figure 3 COSMO-SkyMed 4 and Falcon 1 projected onto the B-plane at the conjunction epoch. The combined covariance is centered at the target.

Conclusions

The proposed filtering method allows to estimate target position and covariance directly at the conjunction epoch in a fraction of the time required by typical ground-based algorithms. The sensitivity analysis performed for the onboard camera showed good performance in terms of target visibility for all the objects characterized by RAAN between 200 and 300 degrees. In future, the method could be expanded to include fully autonomous initial orbit determination and threat detection, allowing to reduce the burden on ground infrastructure and improve the sustainability of human activities in space.

References

- [1] A. Morselli. High order methods for space situational awareness. 2014.
- [2] N. Faraco, G. Purpura, P. Di Lizia, M. Massari, M. Peroni, A. Panico, A. Cecchini, F. Del Prete. SNOS: automatic optical observation scheduling for sensor networks. 9th European Conference for Aerospace Sciences (EUCASS 2022), pages 1–11, 2022.
- [3] B. Schutz, B. Tapley, and G. H. Born. Statistical orbit determination. Elsevier, 2004.
<https://doi.org/10.1016/B978-012683630-1/50020-5>
- [4] A. De Vittori, M. F. Palermo, P. Di Lizia, and R. Armellin. Low-thrust collision avoidance maneuver optimization. Journal of Guidance, Control, and Dynamics, 45(10):1815–1829, 2022.
<https://doi.org/10.2514/1.G006630>
- [5] F. K. Chan et al. Spacecraft collision probability. Aerospace Press El Segundo, CA, 2008.
<https://doi.org/10.2514/4.989186>

Mini-IRENE, a successful re-entry flight of a deployable heatshield capsule

Stefano Mungiguerra^{1,a*}, Raffaele Savino^{1,b}, Paolo Vernillo^{2,c}, Luca Ferracina^{7,d},
Francesco Punzo^{3,e}, Roberto Gardi^{2,f}, Maurizio Ruggiero^{4,g},
Renato Aurigemma^{4,h}, Pasquale Dell'Aversana^{6,i}, Luciano Gramiccia^{5,j},
Samantha Ianelli^{8,k}, Giovanni D'Aniello^{5,l}, Marta Albano^{8,m}

¹University of Naples Federico II, 80 Piazzale Tecchio, Naples, 80125, Italy

²CIRA "Italian Aerospace Research Centre", 81043 Capua, Italy

³ALI S.c.a r.l. Naples, Italy

⁴Euro.Soft, Naples, Italy

⁵SRS-ED, Naples, Italy

⁶Lead Tech, Naples, Italy

⁷ESA, European Space Agency, Noordwijk, The Netherlands

⁸ASI, Italian Space Agency, Rome, Italy

^astefano.mungiguerra@unina.it, ^brasavino@unina.it, ^cp.vernillo@cira.it,

^dLuca.Ferracina@esa.int, ^efrancesco.punzo@aliscarl.it, ^fR.Gardi@cira.it,

^gm.ruggiero@eurosoftsrl.eu, ^hr.aurigemma@eurosoftsrl.eu, ⁱpasquale.dellaversana@leadtech.it,

^jluciano.gramiccia@srsed.it, ^ksamantha.ianelli@asi.it, ^lgiovanni.daniello@srsed.it,

^mmarta.albano@asi.it

Keywords: Deployable Capsule, Sub-Orbital Flight, Flight Data, Aero-Thermo-Dynamic Loads

Abstract. This paper presents some of the results of the suborbital flight of the Mini-IRENE Flight Experiment (MIFE), flight demonstrator of the IRENE technology. A capsule equipped with a deployable heat shield was successfully launched with a VSB-30 suborbital rocket, achieving an apogee of 260 km, a peak deceleration of 12g and surviving the landing with successful retrieval. A huge set of telemetry data was acquired, including GPS, attitude, temperature, acceleration measurements. The capsule showed aerodynamic stability at all flight regimes. The derived drag coefficient was different from the predicted one, possibly due to flexible aero-brake deformation.

Introduction

The paper describes the main outcomes of the qualification flight of Mini-IRENE, a capsule launched with a Maser sounding rocket on 23rd November 2022 during the SSC S1X3-M15 campaign. The flight has represented the clou of the Mini-IRENE Flight Experiment (MIFE) project [1], funded by the Italian Space Agency (ASI) and managed by the European Space Agency (ESA) in the framework of a GSTP (General Support Technology Program). The project aimed at increasing the ripeness of an innovative technology for atmospheric (re-)entry up to TRL 6, developed by the companies of the ALI consortium, CIRA and University of Naples Federico II, as part of the wider IRENE program [2], and featured by an innovative deployable heat shield, resulting in a very low ballistic coefficient, allowing the exploitation of off-the-shelf materials for the thermal protection system, because of the acceptable heat fluxes, mechanical loads and final descent velocity [3]. The IRENE program aimed at developing a low-cost re-entry capsule, able to return payloads to Earth from the ISS and/or short-duration, scientific missions in Low Earth



Orbit (LEO). MIFE was the latest phase of the IRENE program, with the objectives to design and test a Ground Demonstrator (GD) for the thermal qualification in a Plasma Wind Tunnel, and realize a Flight Demonstrator (FD) to be qualified in a sub-orbital flight with a Sounding Rocket.

All the qualification tests have been performed successfully. The GD was qualified in the CIRA Scirocco Plasma Wind Tunnel for the thermal loads of a specific re-entry mission; the FD has successfully achieved the two main objectives of the sub-orbital flight mentioned above after ejection from the sounding rocket, namely the verification of the stability in every flight regime and the resistance of the heat shield under the thermal and mechanical loads due to the impact with the atmosphere.

This paper is focused on the analysis of the re-entry flight based both on recorded data and telemetry data. The recorded data have been retrieved from an Inertial Unit and a sensors suite while the telemetry data were transmitted to ground even in the supersonic regime.

The suborbital flight

A CAD model of the FD is shown in Fig. 1a, in the deployed configuration. For the launch, it was stowed inside an external shell composed of three panels, as shown in Fig. 1b.

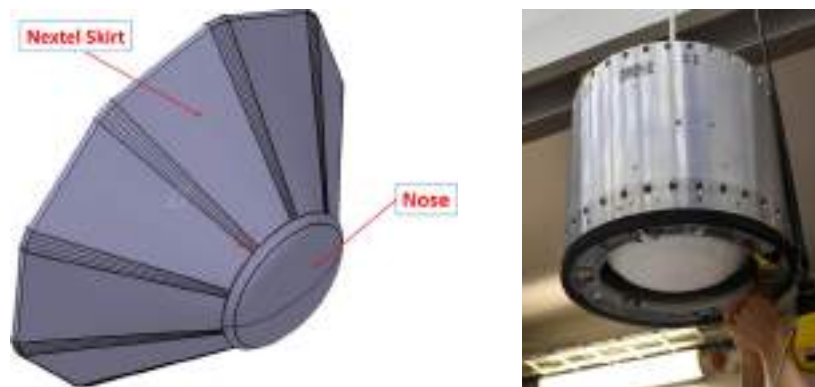


Fig. 1 (a) CAD of the deployed capsule, (b) picture of the stowed capsule before launch.

The capsule was launched from the Esrange base, in Sweden, on 23rd November 2022, onboard a VSB-30 rocket, in the Maser 15 mission (Fig. 2a). The capsule successfully completed its suborbital flight, with a correct aero-brake deployment, and was retrieved few minutes after landing thanks to GPS coordinates and telemetry data provided even after ground impact (Fig. 2b). The capsule trajectory was monitored by GPS and is compared with the nominal predicted trajectory in Fig. 3. A slightly lower apogee than expected was achieved (257 km instead of 261 km). The trajectory showed a sharp deviation in east direction, which was attributed to wind (thanks to balloon measurements) and not to any asymmetry in the capsule aerodynamics. Video recordings, together with magnetometers and accelerometers measurements, demonstrated that MIFE did not lose stability nor tumbled in any flight regime, even in the critical transonic phase. A significant spin rate was measured at the beginning of the continuum regime, possibly due to minor geometrical asymmetries in the TPS or center-of-mass unbalance.



Fig. 2 (a) A picture of the launch, (b) the capsule retrieved after landing

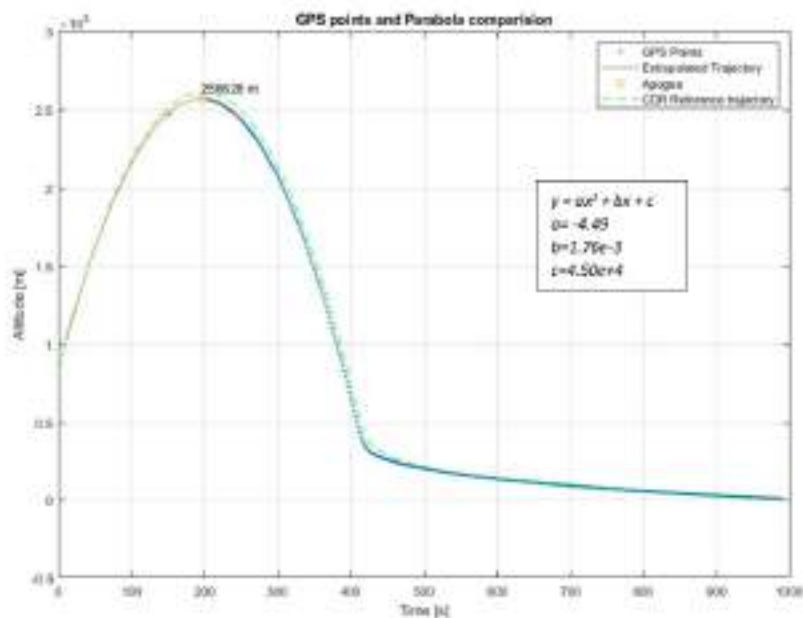


Fig. 3 Capsule parabolic trajectory, measured and predicted

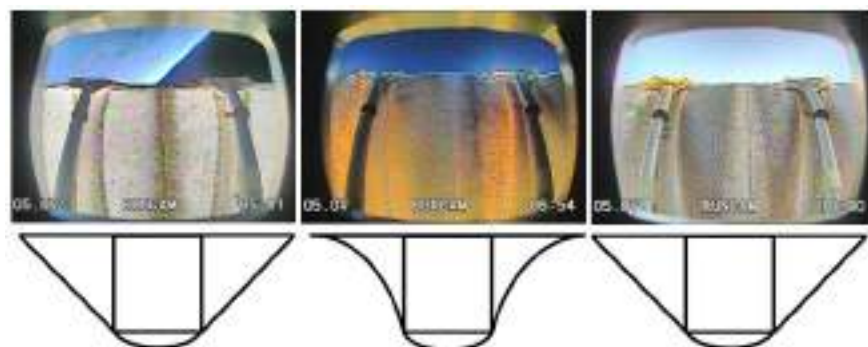


Fig. 4 Three images of the flexible TPS in free fall, during the peak of dynamic pressure, and during the final part of the flight; and a schematic representation

The capsule deceleration was higher than expected (12g versus 10.5g), and the peak of dynamic pressure occurred at a lower altitude. This allowed testing the system in a even harsher aerodynamic environment, which caused a deformation of the flexible TPS (Fig. 4), that had not been taken into account in the derivation of the aerodynamic database. This may be one of the

reasons for the differences between the expected and rebuilt drag coefficient, whose trend with Mach number from supersonic to subsonic regime is shown in Fig. 5. The “flight” drag coefficient, computed on the basis of velocity and acceleration measurements, is lower than nominal in supersonic and higher in subsonic, even when considering a $\pm 10\%$ error on the standard atmospheric density used for the calculation. Further analyses, including CFD simulations of the aerodynamics of the deformed TPS, will be carried out for a deeper understanding of this discrepancy.

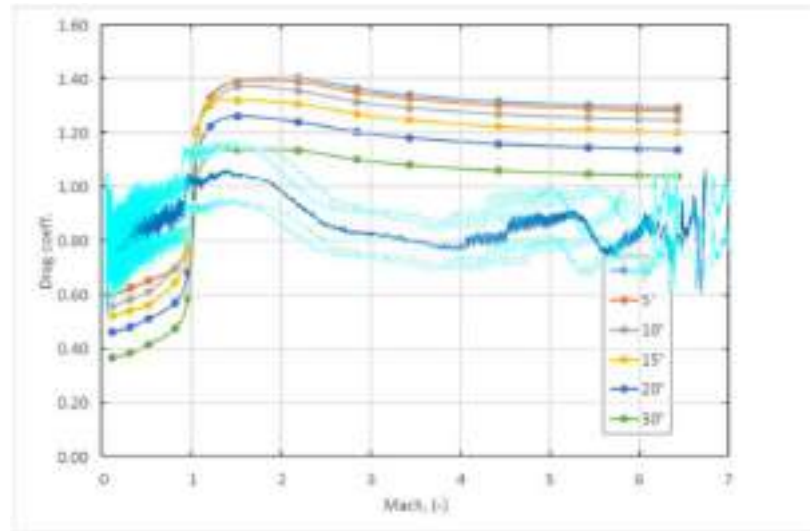


Fig. 5 Drag coefficient estimated based on flight data (blue line), with $\pm 10\%$ uncertainty (light blue lines), compared with numerical aerodynamic database, versus Mach number

Conclusions

The Mini-IRENE Flight Experiment (MIFE) project was successfully concluded with the suborbital launch of the flight demonstrator, which achieved all the mission objectives, including effective separation from the launcher, complete mechanism deployment, aerodynamic stability at all regimes, capsule survival to the aerothermodynamic loads, telemetry data acquisition and capsule retrieval after flight. Flight data analysis is still ongoing for a full comprehension of the capsule behavior and to learn important lessons for the future design of an orbital system based on the IRENE technology.

References

- [1] A. Fedele, S. Mungiguerra, Aerodynamics and flight mechanics activities for a suborbital flight test of a deployable heat shield capsule, *Acta Astronaut.* 151 (2018) 324-333, <https://doi.org/10.1016/j.actaastro.2018.05.044>
- [2] E. Bassano, et al., IRENE - Italian Re-Entry Nacelle for Microgravity Experiments, 62nd International Astronautical Congress Cape Town, South Africa, 2011
- [3] A. Alunni, et al., Pterodactyl: Trade Study for an Integrated Control System Design of a Mechanically Deployed Entry Vehicle, *AIAA SciTech 2020 Forum*, Orlando, FL, 2020. <https://doi.org/10.2514/6.2020-1014>

Electro-thermal dynamic simulations and results of a deorbiting tethered system

G. Anese^{1,*}, G. Colombatti¹, A. Brunello¹, A. Valmorbida¹, G. Polato¹,
S. Chiodini¹, E.C. Lorenzini¹

¹ University of Padova, Department of Industrial Engineering, Via Venezia 1, Padova

giovanni.anese@unipd.it

Keywords: Space Tethers, Electrodynamics, Numerical Simulations, Satellites Deorbiting

Abstract. Deorbiting techniques with small or better no propellant consumption are an important and critical field of space studies for the mitigation of orbital debris. Electrodynamic tethers (EDTs) are of particular interest because they make possible to deorbit space debris by exploiting the Lorentz force that is provided by the current flowing in the tether thanks to the interaction of the system with the Earth's magnetosphere and the ionosphere. This paper focuses on the differences between two software packages built at the University of Padova (FLEX and FLEXSIM) and their results in simulating various deorbiting scenarios. Both FLEXSIM and FLEX simulate the electro-thermal behaviour and the dynamics of an EDT. However, while the first one has the simplifying assumption that the tether is always aligned with the local vertical, the second one considers also the overall system attitude with respect to the radial direction and the tether flexibility. The computational times of these S/W are very different and it is important to understand the scenarios that are more appropriate for their use. Results aim to show the impact of different solar activity (simulations are done at different epochs) and lengths of conductive and non conductive segments of tether, in the range of a few hundreds of meters, on the total re-entry time. As expected, deorbiting is faster for high solar activity and conductive tether length but the performance must be balanced against the dynamics stability. The issue of stability over the deorbiting time is evaluated numerically for specific cases by using FLEX.

Introduction

The interest in the space exploration is increasing day by day because of a steady growth of orbital debris around the Earth. Thus, it's important to find ways to mitigate this growth and electrodynamic tethers (EDTs) represent a possible green and effective solution. Indeed, they don't use the traditional propulsive systems (chemical and electrical), because they can provide good drag forces (i.e., Lorentz forces) by operating in a passive way, that is, exploiting only environmental factors: the ionosphere and the Earth magnetic field.

This work presents briefly how these systems work and then focuses on some analysis of their performances in different deorbiting scenarios. Solar activity influences space environmental characteristics, like the atmospheric and plasma densities, and consequently also the deorbiting time. Consequently, specific simulations are performed to understand how the reentry time and the dynamics of a deorbiting kit based on an EDT change with respect to the solar activity.

Moreover, the effects of the tether length is also analyzed, because it impacts directly the current produced by the tether itself and consequently the Lorentz force generated by the system.

FLEX and FLEXSIM software packages (built by the University of Padova) are used to simulate the different mission scenarios, understand the differences between them and analyze the performance of EDT systems for deorbiting.



Electro-dynamic tether systems

Electrodynamic tether systems are one typology of space tethers [1]; they are based on a conductive tether (or tape) that links two satellites at its ends. If they operate in a passive way, they exploit the current that flows in the tether from the collection of ionospheric electrons on the bare tether anode, that are then re-emitted at the cathode at the opposite end of the tether. The current produces a Lorentz force through the interaction with the geomagnetic field, as follows:

$$\mathbf{F}_L = \int_0^L \mathbf{I} \times \mathbf{B} \, dx \approx I_{av} L (\mathbf{u}_t \times \mathbf{B}) \quad (1)$$

In the case of the passive mode, this force is opposite to the orbital velocity of the system, that is, a drag force that progressively decreases the altitude of the spacecraft.

However, electrodynamic tethers can be used in Low Earth Orbits (LEO) to have sizeable performances, because at higher altitude the electron density is too low to generate usable currents.

Software packages

FLEXSIM and FLEX are the chosen software packages to perform simulations. They were both built at the University of Padova for the E.T.PACK initiative [2] to study the electro-thermal dynamic of an EDT deorbiting system. They are different because in FLEXSIM a simplification is assumed: the tether is straight and always aligned with the local vertical and does neither oscillate nor flex, as in a real case. This assumption allows to use FLEXSIM as a first iteration step in the mission evaluation, especially for what concerns the deorbiting time and the computation of the average current in the tether. On the other hand, FLEX simulates the tether dynamics allowing the evaluation of dynamics stability, which is discussed later.

From the modelling point of view, while FLEXSIM considers the tether as a single element, FLEX divides the tether in different segments and computes the dynamics of each one. In FLEXSIM an average current of all the conductive length is considered and used in Eq. 1. In FLEX, instead, an average current and thus a Lorentz force is computed for each segment, leading to a more detailed dynamics of the tether, as stated above.

These two simplifications reduce drastically the computation time of FLEXSIM with respect to FLEX. The codes use a set of subroutines that allows to evaluate the environmental characteristics [3,4,5]. A critical element is the current subroutine, based on [6], that computes the current $I(x)$ as a function of the electron density, the motional-electric field and the voltage drop at the cathode.

Numerical Simulations

Several simulations were done to evaluate the performances of the deorbiting tethered system. As just mentioned, the environmental characteristics that determine the current on the tether are influenced by solar activity. Therefore, the same mission is simulated with both FLEX and FLEXSIM at three different epochs, with low, medium and high solar activity (based on the F10.7 index), in order to understand the solar activity impact on the reentry time.

All these simulations were conducted on an EDT with a tape of 500 m (450 m of Aluminum and 50 m of PEEK, the inert segment) and two tip masses of 12 kg. This is the baseline configuration of the In-Orbit Demonstration flight, presently planned for 2025 for E.T.PACK-F. The system is initially on a circular orbit at 600 km height inclined of 51.5°; the mission is considered completed when the system reaches an altitude of 250 km where the atmospheric density is strong enough to reenter the system in a few orbits. As mentioned earlier, the tether length is also investigated as a driving parameter. The investigated scenarios is the same of the previous simulations, but the tether length changes from 400 to 700 m, with a constant percentage of conductive (90%) and non-conductive (10%) tether for all cases. These simulations are done with FLEX, so that, not only the deorbiting time is evaluated, but also the system dynamics,

because the variable length leads to a different behavior, allowing for the study of dynamics stability.

Results

Simulations results are now presented, starting from the effects of solar activity. As shown in Table 1 for the case of E.T.PACK-F with 500-m tether, the deorbiting time decreases at higher solar activities, since the electron density increases [7], leading to an improvement of electron collection on the tether and consequently higher currents (Fig. 1) and Lorentz forces.

Table 1 Deorbiting time [days] for different solar activities with FLEXSIM and FLEX

	Low solar activity	Medium solar activity	High solar activity
FLEXSIM [days]	94.152	25.161	19.706
FLEX [days]	88.182	23.267	18.075

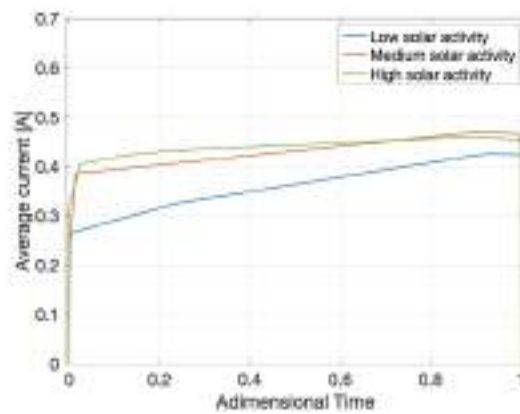


Figure 1 Envelope of current peaks vs time scaled (0 start of mission, 1 end of mission) for low, mean and high solar activity (FLEXSIM)

The differences between FLEXSIM and FLEX in deorbiting times is due to the tether dynamics, which helps the electromotive force (e.m.f.) thanks to the out-of-plane tether dynamics..

Varying the tether lengths at fixed environmental conditions (high solar activity), it is possible to see in Table 2 and Fig. 2, that increasing the length the time of reentry is lower. This is due to the increase in the e.m.f. that generates higher currents and the increased overall Lorentz force that acts on a longer tether length. However, with a 700 m tether (or longer) instability occurred, the system begins to tumble and could not be controlled. This is due to the increased Lorentz force, and indeed longer tethers require heavier tip masses to be stabilised.

Table 2 Deorbiting time as function of tether length (with high solar flux)

Tether length [m]	400 (360 Al-40 PEEK)	450 (395 Al-45 PEEK)	500 (450 Al-50 PEEK)	600 (540 Al-60 PEEK)	650 (585 Al-65 PEEK)	700 (630 Al-70 PEEK)
Deorbiting time [days]	25.226	21.369	18.075	15.815	13.374	instability

Fig. 3 shows the in and out of plane angles for the configurations with 400 m and 650 m of tether (both stable since the angles never reach the 90 deg). It's possible to see that the blue lines have more peaks than the orange ones, indicating oscillations of longer tether are more persistent, hence these systems are less stable.

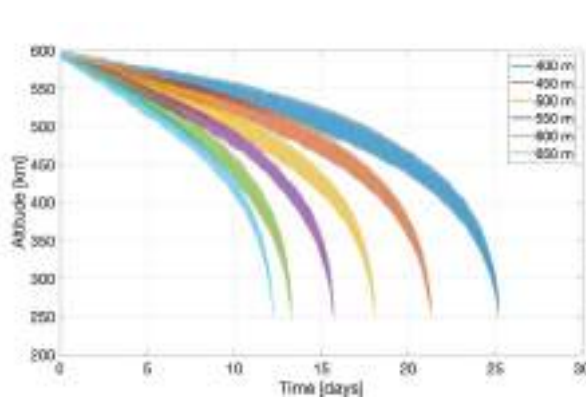


Figure 2 Center of mass altitude vs time as function of tether lengths (FLEX)

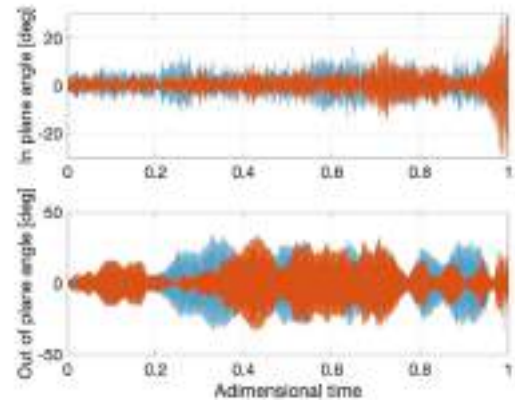


Figure 3 In and out of plane angles for tether length of 400 m (orange) and 650 m (blue)

Conclusions

The focus of this paper is the use of EDT systems for the deorbiting of space debris and the investigation of software packages (FLEX and FLEXSIM) that allow to study EDT performances and their dynamics. From the simulations done for this work, it is possible to confirm that EDTs have better performances at higher solar activities (where they can generate higher Lorentz forces) and with longer tethers. This increased performance must be balanced against the dynamics stability of the system that must be evaluated to assess the feasibility of the mission.

FLEX and FLEXSIM are valid software packages to investigate the performance of EDTs. They are also the starting point to evaluate other applications of tethered system, like EDT operating in active mode for generating thrust to allow a wider spectrum of orbital maneuvers.

Acknowledgments

This work was supported by Horizon Europe EIC Transition Programme under Grant Agreement No. 101058166 (E.T.PACK-F)

References

- [1] M.L. Cosmo, E.C. Lorenzini, *Tethers In Space Handbook*, Third ed., Smithsonian Astrophysical Observatory, Cambridge (Massachussets), 1997.
- [2] Information on <https://etpack.eu/e-t-pack-f/>.
- [3] J. Picone et al., NRLMSISE-00 empirical model of the atmosphere: Statistical comparisons and scientific issues, *J. Geophysical Research: Space Physics*, 107 (2002). <https://doi.org/10.1029/2002JA009430>
- [4] D. Bilitza, B.W. Reinisch, International reference ionosphere 2007: Improvements and new parameters, *Advances in space research*, 42 (2008). <https://doi.org/10.1016/j.asr.2007.07.048>
- [5] M. Mandea et al., International geomagnetic reference field—2000, *Physics of the Earth and planetary interiors*, 120 (2000). [https://doi.org/10.1016/S0031-9201\(00\)00153-9](https://doi.org/10.1016/S0031-9201(00)00153-9)
- [6] M. Sanjurjo-Rivo et al., Efficient Computation of Current Collection in Bare Electrodynamical Tethers in and beyond OML Regime, *J. Aerospace Engineering*, 28 (2015), [https://doi.org/10.1061/\(ASCE\)AS.1943-5525.0000479](https://doi.org/10.1061/(ASCE)AS.1943-5525.0000479)
- [7] Liu, L. et al., The dependence of plasma density in the topside ionosphere on the solar activity level, *Ann. Geophys.*, 25 (2007), 1337–1343. <https://doi.org/10.5194/angeo-25-1337-2007>

Mechanical and pneumatic design and testing of a floating module for zero-gravity motion simulation

Simone Galleani^{1,a*}, Thomas Berthod^{1,b}, Alex Caon^{2,c}, Luca Lion^{2,d},
Federico Basana^{2,e}, Lorenzo Olivieri^{2,f}, Francesco Branz^{3,g},
Alessandro Francesconi^{3,h}

¹University of Padova, Padova (Italy)

²C.I.S.A.S – Centre of Studies and Activities for Space “G. Colombo”, Via Venezia 15, Padova (Italy)

³Department of Industrial Engineering, University of Padova, Via Venezia 1, Padova (Italy)

^asimone.galleani@studenti.unipd.it, ^bthomas.berthod@studenti.unipd.it, ^calex.caon@unipd.it,
^dluca.lion.1@phd.unipd.it, ^efederico.basana@phd.unipd.it, ^florenzo.olivieri@unipd.it,
^gfrancesco.branz@unipd.it, ^halessandro.francesconi@unipd.it

Keywords: Floating Module, Low Friction Table, Pneumatic Tests

Abstract Close proximity operations demand an accurate control in a micro-gravity environment, hence they must be reproduced and simulated systematically. Consequently, laboratory tests are a crucial aspect to validate the performances of space systems. This paper presents the development of a floating pneumatic module, whose dimensions and mass are representative of a 12U CubeSat. The vehicle has been designed to perform planar low friction motion over a levelled table for docking experiments. The paper focuses on the pneumatic and mechanical designs and on the laboratory tests of the module. The pneumatic design regards the air-compressed pneumatic system. The major specifics have been determined by the requirement of performing a docking procedure by starting from a distance of 500 mm. The mechanical design has been guided by two main requirements. The first is the possibility to accommodate different docking systems (e.g.: docking port). The second is the possibility to control the position of the centre of mass of the module. Several tests have been performed to verify the capabilities of the vehicle, such as: (1) pneumatic tests to evaluate the thrust of the propulsion system through the execution of linear motions and (2) mechanical measurements with dedicated setups to improve the estimation of the position of the centre of mass from the CAD model of the system.

Introduction

A Close Proximity Operation (CPO) of an on-orbit spacecraft can be defined as a manoeuvre of one spacecraft (chaser) in a relative orbit with respect to another spacecraft (target) [1]. These operations are performed in micro-gravity conditions and include docking manoeuvres which require a systematic characterization of the forces and torques arising from the interaction of the chaser and the target. Therefore, laboratory tests and the realization of dedicated facilities are a critical aspect to validate the performances of docking mechanisms.

Among various microgravity simulation methods, such as parabolic flights, drop towers or robotic manipulators, an achievable solution for a laboratory environment is the use of planar Air-Bearings (ABs), which allows floating of tested devices [2] with the creation of a thin film of pressured gas between an internal porous structure and a surface. Thus, a planar 3 DoF motion can be achieved in a quasi-frictionless condition. Although a reduced number of DoF is obtained compared to the 6 DoF of an on-orbit motion, planar ABs are usually used as a support for dedicated vehicles which are equipped with thrusters and/or reaction wheels to simulate a satellite for CPOs and, specifically, docking manoeuvres experiments [2].



This paper presents the development of a floating pneumatic module, which has been designed to perform 3 DoF low-friction planar motion with three ABs over a levelled table. The module has a volume of $330 \times 224 \times 224 \text{ mm}^3$ with a mass of approximately 12 kg, so that it represents the mass properties of a 12U CubeSat.

With a dedicated propulsion system, the main goal of the vehicle is to simulate docking manoeuvres starting from a distance of 500 mm. The vehicle can operate both as a chaser, active mode, and as a target, passive mode, and it can accommodate different docking systems.

Pneumatic design

The pneumatic system has been designed to allow the vehicle to float with three round ABs and perform translational and rotational manoeuvres over a levelled table with a compressed air propulsion system.

Furthermore, the pneumatic system has been realized to satisfy the following requirements: (1) motion is provided by 8 thrusters (2 thrusts for each corner of the vehicle); (2) each thruster is activated by one Electro-Valve (EV); (3) the pneumatic circuit ensures a total floating time of 3 min and performs an acceleration of 50 mm/s^2 .

Requirements (2) and (3) have led to the following specifications: (a) the three ABs with a diameter of 40 mm are able to lift a total weight of approximately 68 kg at an input pressure of 3.9 bar; (b) each thrust is composed by two nozzles with a throat diameter of 1.3 mm to improve the produced force and reduce the working pressure; (c) the total air volume should be at least 2 L at 10 bar. Therefore, the pneumatic circuit has been realized with a 2.5 L tank and a single pressure regulator to control ABs and thrusters at the same pressure.

Mechanical design

The mechanical design has revolved around the positioning and sizing of components, so that they would fit inside the total volume of the module. The mechanical design has been guided by three main requirements: (1) the module accommodates different docking systems with a dedicated volume of $100 \times 224 \times 224 \text{ mm}^3$ in the front part; (2) the three ABs are positioned in an equilateral triangular configuration and the Centre of Mass (CoM) of the module is controlled to be coincident (with an error of 1 mm) with the centroid of the ABs to guarantee uniform floating of the vehicle; (3) the centroid of the thrusters is aligned with the CoM of the system to allow pure rotational motions. Additionally, the centroid of the ABs coincides with the Geometrical Centre (GC) of the $330 \times 224 \times 224 \text{ mm}^3$ volume of the system.

Figure 1 shows (a) the CAD model of the vehicle with the reference frame at the GC used to refer the position of the CoM and (b) the assembled module.

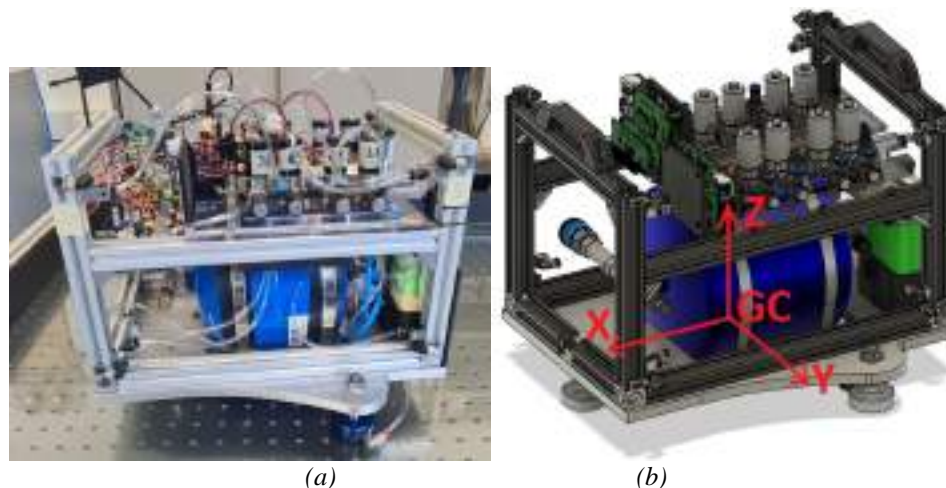


Figure 1: (a) CAD model of the vehicle (b) Assembled module

An estimation of the position of the CoM has been obtained from the complete CAD model. With a total estimated mass of 8.2 kg with no payload, the CoM has been placed at -27.4 mm along the X axis and -0.9 mm along the Y axis with respect to the GC (Figure 1a). Moreover, the fully assembled module of Figure 2b has a greater total mass of 8.4 kg, because it includes electrical components and wiring which have not been considered in the CAD model.

A possible solution to control the position of the CoM of a system is the realization of custom masses which can be moved either automatically with motors [3] or manually [4]. For this reason and to get closer to the goal of a total mass of 12 kg, a group of manually movable steel masses has been designed and their masses have been determined from the CAD estimation.

In particular, three sets of masses have been designed: (1) a set of fixed masses (total mass of 620 g) to be mounted on the front part of the system to bring the CoM closer to the GC; (2) a couple of movable masses of 687 g each to control the X coordinate of the CoM; (3) a movable mass of 240 g to control the Y coordinate of the CoM.

Furthermore, considering a mass of 1 kg to represent a generic payload, by acting on the moving masses, it is possible to shift the X and Y coordinates of the CoM in a ± 5 mm and ± 2 mm ranges which contain the centroid of the ABs.

Tests on the pneumatic system

The tests on the pneumatic system have involved the execution of linear motions over the levelled table to estimate the provided thrust. The position of the module has been measured by a motion capture system (OptiTrack Prime^x 13 with an accuracy of ± 0.2 mm). Figure 2 shows the setup for the tests on the pneumatic system.



Figure 2: Main setup for the tests on the pneumatic systems

By commanding an impulse of 1 s to the EVs, two linear trajectories along the X and Y axes have been performed. By analysing the data of the measured position, the resulting thrusts have been estimated to be 1.541 N along the X axis and 1.531 N along the Y axis. The expected thrust has been calculated to be 2.225 N; the discrepancy could be related to the localized pressure losses in the pneumatic system.

Measurement of the position of the centre of mass

Mechanical measurements have been performed to estimate and balance the position of the CoM of the module. The position of the CoM has been measured with a setup of three load cells (rated load of 10 kg with an output of 2 ± 0.2 mV/V) placed under the supports of the three ABs. Figure

3 presents (a) the CAD model of the setup of the load cells and (b) the assembled setup with the module placed on top.

A Matlab algorithm has taken the three outputs of the load cells as inputs and converted them into mass values to compute the position of the CoM. With no payload and no fixed or movable masses (total mass of 8.4 kg), ten measurements have been acquired to account for the noise of the load cells. With an uncertainty of ± 1 mm ($\sim 0.4\%$ of the dimensions of the module), the mean value of the ten positions has placed the CoM at -25.6 mm and -3.1 mm along the X and Y axes with respect to the GC. The discrepancy from the CAD estimation is approximately 0.7%.

By mounting and acting on the moving masses, the CoM can be aligned with the GC within a ± 1 mm range.

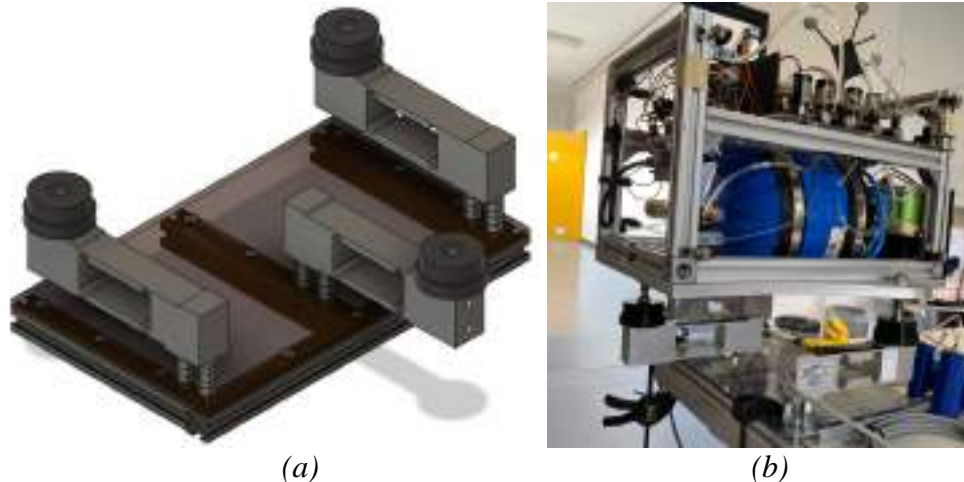


Figure 3: (a) CAD model of the load cells setup – (b) Assembled load cells setup with module

Conclusions

This paper presents an overview of the pneumatic and mechanical designs and the performed tests and measurements of a floating pneumatic module which has been designed to execute 3 DoF planar low friction motion.

The thrust provided by the propulsion system has been quantified and the capability of the module to perform simple linear trajectories proven.

The position of the CoM has been measured with an uncertainty of ± 1 mm, through a dedicated measuring setup.

The next steps of the development will involve the execution of rotational motions around the main axis over the levelled table to estimate the inertia of the module.

References

- [1] Markus Wilde et al., Historical survey of kinematic and dynamic spacecraft simulators for laboratory experimentation of on-orbit proximity manoeuvres, Progress in Aerospace Sciences, <https://doi.org/10.1016/j.paerosci.2019.100552>
- [2] Tomasz Rybus et al., Planar air-bearing microgravity simulators: Review of applications, existing solutions and design parameters, Acta Astronautica, <https://doi.org/10.1016/j.actaastro.2015.12.018>
- [3] Chesi et al (2014), Automatic Mass Balancing of a Spacecraft Three-Axis Simulator: Analysis and Experimentation. Journal of Guidance, Control, and Dynamics, <https://doi.org/10.2514/1.60380>
- [4] Marcello Romano et al., Acquisition, tracking and pointing control of the Bifocal Relay Mirror spacecraft, Acta Astronautica, [https://doi.org/10.1016/S0094-5765\(03\)80011-5](https://doi.org/10.1016/S0094-5765(03)80011-5)

Simulations for in-flight stellar calibration aimed at monitoring space instruments optical performance

Casini Chiara^{1,2,5,a*}, P. Chioetto^{1,4}, A. Comisso¹, A. Corso¹, F. Frassetto^{1,5},
P. Zuppella^{1,4}, V. Da Deppo^{1,3}

¹ CNR-IFN, Via Trasea 7, 35131 Padova, Italy

² Centre of Studies and Activities for Space “Giuseppe Colombo”, Via Venezia 15, 35131 Padova, Italy

³ INAF-OAPd, Vicolo dell'Osservatorio 5, 35122, Padova, Italy

⁴ INAF-OAA, Largo Enrico Fermi 5, 50125 Firenze, Italy

⁵ INAF-OATo, Via Osservatorio 20, 10025 Pino Torinese, Torino, Italy

^achiara.casini@pd.ifn.cnr.it

Keywords: In-Flight Calibration, Space Instruments, Metis, STC

Abstract. Stellar in-flight calibrations have a relevant impact on the ability of space optical instruments, such as telescopes or cameras, to provide reliable scientific products, i.e. accurate calibrated data. Indeed, by using the in-flight star images, the instrument optical performance can be checked and compared with the on-ground measurements. The results of the analysis of star images, throughout the whole instrument lifetime in space, will allow tracking the changes in instrument performance and sensitivity due to optical components degradation or misalignment. In this paper we present the concept, the necessary input and the available outputs of the simulations performed to predict the stars visible in the FoV of a specific space instrument. As an example of the method, its application to two specific cases, i.e. Metis coronagraph on-board Solar Orbiter and the stereo camera STC on-board BepiColombo, will be given. Indeed, due to their operation in proximity to the Sun, and also to Mercury for STC, both instruments operate in a hostile environment, are subjected to high temperatures and experience high temperature variations. Performance optical monitoring is thus extremely important.

Introduction

The proper calibration of a space instrument allows its optimal performance throughout the entire mission duration.

Space is a hostile environment: e.g. a mission going near the Sun experience hot temperatures, likely to induce component degradation, even if the mission is carefully planned and built.

The instrument response to a well-known source, e.g. star acquisition, is a valuable mean for monitoring the optical performance of space instrument and, if necessary, to update and correct the image calibration.

In this paper, a description of the possible in-flight stellar calibrations, and their related simulations, are given and then applied to two space instruments: on board of Solar Orbiter [1] on board of Solar Orbiter; and of SIMBIO-SYS have an original optical design [2] on board of BepiColombo. Both instrument have an original optical design and are working in very hostile environments, near the Sun, and at distances rarely reached so far by other space missions. Comparing on-ground calibration with simulations and in-flight calibration is a key element for assuring the correct performance of these space instruments.



In the next sections the emphasis will be put on: the importance of the calibration, a brief description of the instrumentation where the simulations are applied, how the simulations have been performed and the results obtained are then presented.

Calibrations

Calibration is a key and fundamental step in achieving accurate and reliable scientific measurements from space instruments. To this end, on-ground calibration is crucial. Both are important to validate instrument design, mitigate systematic errors, ensures data consistency. For the in-flight calibration, by comparing the instrument response to known stellar characteristics, any deviations or discrepancies in the optical performance can be detected and corrected. This process enhances the quality and reliability of the acquired scientific data, making calibration an essential component of space missions.

In-flight calibration basically consists in following a star moving across the detector during several minutes. Repeated stellar observations, at different times during the lifetime of the instrument, are important to track the changes in instrument sensitivity due to optical elements or detector degradation and other causes. Systematic observations of several stars will track sensitivity changes, and comparison between the in-flight and on-ground results can give important information on the status and performance of the instrument.

Following such stars requires achieving high accuracy acquisitions over high dynamic range, which is a fundamental challenge. Yet, it is necessary to determine an accurate absolute calibration for astronomical photometry. Direct comparisons of stellar outputs with calibrated flux sources can generally only be made for very bright stars.

Concretely, our goal is to find the stars on a Metis, and on a STC image. Our approach is based on defining an upper limit on a grayscale image in intensity (mean value $+3\sigma$): every pixel with a higher intensity corresponds to a star. Then around the maximum value we define a box, usually is 10 pixels x 10 pixels, and we plot a 2D gaussian, from which we extrapolate information like PSF. Knowing the PSF all over the detector gives us the information on some defocus, vignetting and so on.

Besides, every detector has a linearity curve. On ground we can measure this curve with a uniform light source like an integration sphere, it can give very useful information about the efficiency of each pixel. In flight our light source is the light from the stars. We can use them as calibration sources, acquiring the light of the same star for different Integration Times (IT), and analyzing the response of the detector pixels.

And finally, through the passage of stars all over the detector we can identify defects such as shadows and bad pixels. It is important to know if such defects are stable over time or are changing, which would have an impact on imaging (the Sun or Mercury in our context). To do so we have to analyze the stars in any parts of the detector to know if it responds differently.

Instrumentations: Metis and STC

The Metis coronagraph and STC have innovative optical design due to their respective missions. Metis makes linearly polarized measurements of the solar corona in the visible spectral range, and simultaneously acquires images in the ultraviolet Ly- α neutral hydrogen line 121.6 nm, with an annular field of view from 1.5° to 2.9° and with an unprecedented temporal resolution among other space coronagraphs (10s). Metis will observe the Sun as close as 0.28 AU, so it is important to reduce the extremely high thermal load, therefore an Inverted Externally Occulted configuration is used to block the light of the solar disk. Indeed, to reduce the thermal load, the light of the photosphere enters in Metis through the Inverted External Occulter (IEO) and is then rejected towards the entrance aperture by the mirror M_0 that is acting as an occulter as shown in **Figure 1** (a). Coronal light is reflected by mirror M_1 towards mirror M_2 , which also induces diffused light

from real images of the edges of the IEO and the M_0 mirror. Therefore, an internal occulter (IO) and a Lyot Stop (LS) are respectively introduced, the rest of the diffused light being blocked by a Field Stop (FS). Then, the coronal light is reflected by mirror M_2 in the direction of the dichroic beam-splitter, the Interferential Filter (IF). The IF is optimized for narrowband spectral transmission in the ultraviolet (UV, 121.6 nm, H I Lyman- α), and broadband spectral reflection in the visible (VL, 580–640 nm). The visible light reflected by IF enters in a polarimetric unit and arrives on the detector. Both channels have a CMOS sensor, a 1024 x 1024 pixel matrix for the ultraviolet, and a 2048 x 2048 pixel matrix for the visible [1].

STC is a double wide-angle camera which main scientific aim is the mapping of the entire surface of Mercury in 3D. As shown in *Figure 1* (b), the STC camera consists of two sub-channels named High (H) and Low (L) with respect to the mounting interface on the spacecraft. There are also two different fore optics for each sub-channel plus a common modified Schmidt telescope. The light scattered by Mercury passes through the external baffle, is reflected inside a rhomboid prism, passes through a correcting doublet, the aperture stop (AS), and arrives on the spherical mirror M_1 . It reflects on a telescope mirror, positioned off axis, which in turn reflects into a two-lens field corrector and arrives on the focal plane assembly (FPA). The STC detector can read a maximum of six specific windows. Nominally, these windows correspond to the areas of the 6 filter: two panchromatic (PAN) with FoV $5,3^\circ \times 2,4^\circ$ and four colored filter with FoV $5,3^\circ \times 0,4^\circ$ [2]. The tridimensional modeling of the instrument is available on [5].

Knowing the accurate location of the spacecraft and the optical path going through the instruments enables to perform simulations on what may be acquired by the instruments. This is of major importance to enhance *in fine* the performances of the in-flight calibrations.

Simulations

Simulations have emerged as powerful tools for addressing the challenges associated with in-flight stellar calibration. They enable scientists to create virtual environments that accurately mimic the behaviour of space instruments and their interaction with celestial objects. These virtual experiments allow for the optimization of calibration strategies, evaluation of instrument design choices, and testing of data analysis techniques. Simulations offer a cost-effective and efficient means of exploring a wide range of scenarios that may not be feasible in real-world settings.

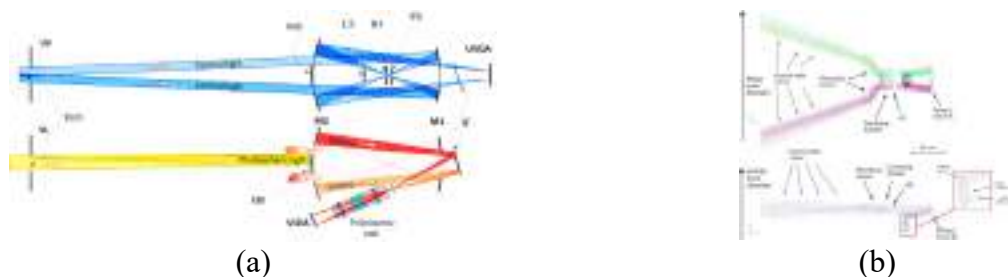


Figure 1 Optical path inside the Metis coronagraph (a), and STC (b) [4].

The keystone of these simulations, performed in Python, is the SPICE kernel (Spacecraft, Planet, Instrument, Camera pointing, and Events). For each space instrument, the SPICE kernel gives, among other things, the information of the location of the spacecraft in the past and in the future, the boresight of each specific channel and the Field of View (FoV).

This kernel is used alongside the SIMBAD catalogue, which exhaustive for our purposes because it provides extensive stellar data. The Metis team and Slemer et al. for STC [3] performed the analysis for determining the maximum apparent magnitude of a star detectable by the instruments. Combining the SPICE kernel with the SIMBAD catalogue allowed us to obtain the results described in the next paragraph.

Results

The simulations reported for both instruments have been performed on the same day: 10-03-2026 at the 8:58:05, in order to highlight the fact that they are looking at different places. For this reason, the results of the stars seen by each channel is different.

The stars seen by the Metis coronagraph are presented in the *Figure 2*, respectively for the Visible channel (VL, (a)) and for the Ultraviolet channel (UV, (b)). Inside the Field of View there are 18 stars. Metis acquires in two channels but is looking at the same objects. The results appear mirrored because of the reflection inside the elements of the coronagraph.

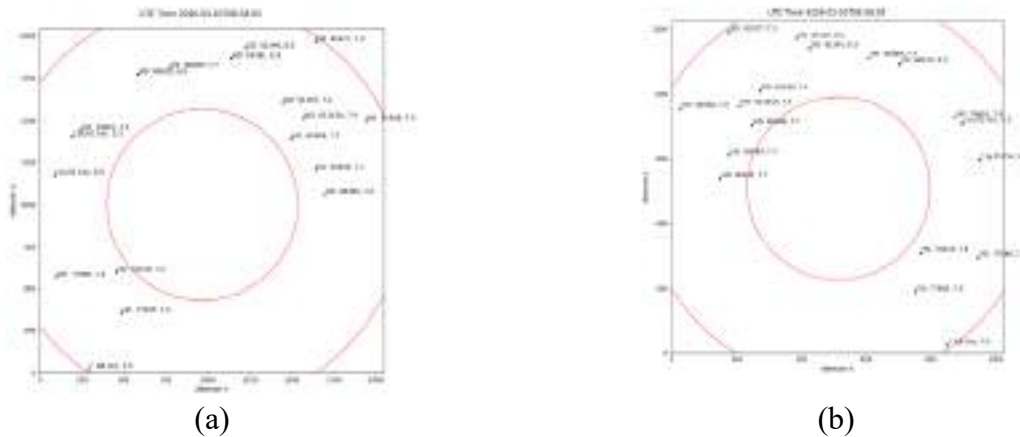


Figure 2 Simulations of the stars seen by the Metis the day 10-03-2026 at the 8:58:05 in the visible (a) and UV (b).

For STC, in the FoV of the two panchromatic on March 10th 2026 at 8:58:05 are shown in *Figure 3* (a) and (b). The stars seen by the Pan L and Pan H are respectively, 24 and 29 stars. Because they are looking at 20° of difference respect to the Nadir.

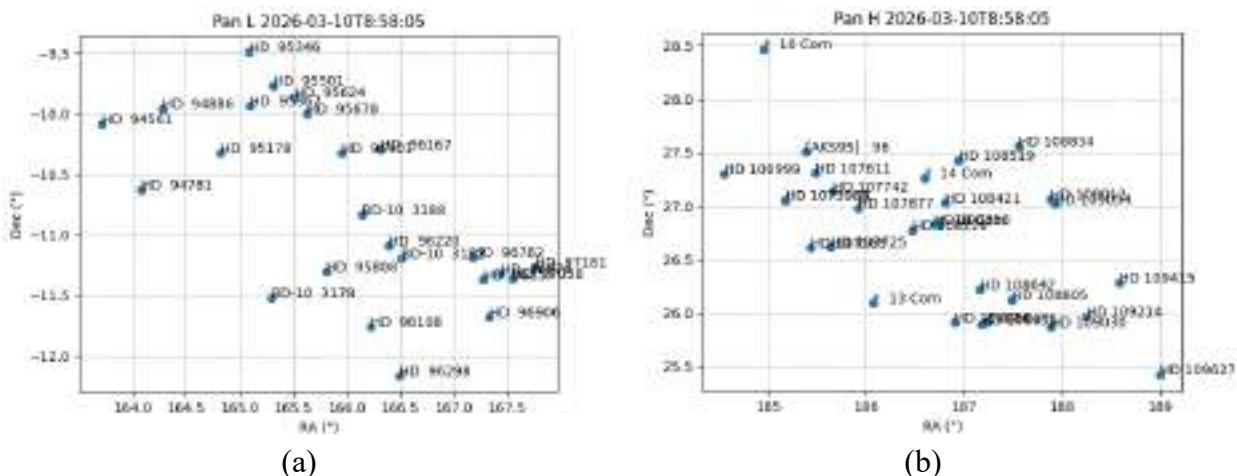


Figure 3 Simulations of the stars seen by the panchromatic L (a) and H (b) the day 10-03-2026 at the 8:58:05.

The difference between the imaged simulated for Metis and STC are the display of the results. Knowing the stars can be seen from the instruments give us the opportunity to select the best target for the in-flight calibration.

Conclusion

In this paper, the problematics of stellar in-flight calibration have been presented, in particular the importance of the calibrations (on-ground and in-flight), and the crucial role of the stars as in-flight

calibration light sources have been highlighted. We report the simulations to determine the stars observable by two instruments: the Metis coronagraph on board of Solar Orbiter, and STC on board of BepiColombo. This simulation activity is part of an on-going work, associated with on-ground and in-flight, acquired and simulated images.

Fundings

This activity has been carried on in the framework of the ASI-INAF Contracts Agreement N. 2018-30-HH.0 and 2017-47-H.0.

References

- [1] Fineschi, S. et al., Optical design of the multi-wavelength imaging coronagraph Metis for the solar orbiter mission. *Exp Astron*, 49, 239-263 (2020). <https://doi.org/10.1007/s10686-020-09662-z>
- [2] G. Cremonese, et al., SIMBIO-SYS: Scientific Cameras and Spectrometer for the BepiColombo Mission, *Space Sci Rev* 216, 75, 2020. <https://doi.org/10.1007/s11214-020-00704-8>
- [3] A.Slemer et al., Setting the parameters for the stellar calibration of the SIMBIO-SYS STC camera on-board the ESA BepiColombo Mission. *Proc. of SPIE Vol. 11443* 1144374-1. <https://doi.org/10.1117/12.2560648>
- [4] V. Da Deppo et al., Optical design of the single-detector planetary stereo camera for the BepiColombo European Space Agency mission to Mercury. *App. Opt.* xx. <https://doi.org/10.1364/AO.49.002910>
- [5] Information on <https://www.dei.unipd.it/~dadeppo/STC.html>

Reduced-order modelling of the deployment of a modified flasher origami for aerospace applications

A. Troise^{1,a*}, P. Celli^{2,b}, M. Cinefra^{1,c}, V. Netti^{1,d}, A. Buscicchio^{1,e}

¹ Department of Mathematics Mechanics and Management, Polytechnic University of Bari, Via Edoardo Orabona, 4, 70125 Bari, Italy

² Department of Civil Engineering, Stony Brook University, Stony Brook, NY 11794, USA

^aa.troise@phd.poliba.it, ^bpaolo.celli@stonybrook.edu, ^cmaria.cinefra@poliba.it,
^dvittorio.netti@poliba.it, ^ealessandro.buscicchio@poliba.it

Keywords: Origami Structures, Deployable Structures, Bar-and-Hinge, Mechanics

Abstract. In this paper, we simulate the nonlinear deployment mechanics of a modified flasher origami structure designed to be a deployable solar panel. We compare reduced-order bar-and-hinge simulations, where panels are modelled as bar assemblies connected by joints and torsional springs, with results obtained from commercial finite element software. Through this comparison, we demonstrate the ability of the bar-and-hinge approach to capture key features of the origami behaviour at a fraction of the time needed to perform regular finite-element simulations. We also provide details on how to properly tune the bar properties to simulate panels made bonding printed circuit boards to textile, and the joint properties to mimic folds that are made of fabric and flexible circuit interconnects.

Introduction

In the past few decades, origami structures have attracted significant attention in the field of science and engineering, due to their unique mechanical properties and reconfigurable and tuneable attributes. These properties make origami designs suitable for applications in fields such as robotics, medicine, and especially aerospace.

The task of modelling origami structures for space applications presents several challenges. First, modelling origami requires accounting for significant geometric nonlinearity due to the large rotations that the panels undergo during deployment and stowage. Additionally, real-life origami structures do not deploy following rigid body motions and are instead characterized by panel bending. Additional challenges appear when the origami systems to be modelled are made of multi-layer materials such as rigid-flex printed circuit boards (PCB). These materials are typically used in CubeSat applications, in which origami techniques are applied to deployable solar panels, communication devices and solar sails. Finally, origami simulations must yield information on the forces exerted by the deployment on the spacecraft.

Research investigations on the deployment of origami structures have been conducted utilizing a variety of finite element software and techniques, including ABAQUS 5, formulations based on Hamilton's equations to capture the dynamics of deployment with validation using ADAMS multibody dynamics [2], and quasi-static bar and hinge methods [3]. The fundamental principle of the bar-and-hinge approach, elucidated by Schenk and Guest [4] as well as Filipov et al. [5], centers on the simplification of the mechanics in origami, by replacing panels with assemblies of bars, hinges and torsional springs that limit out-of-plane rotations. This approach leverages the inherent limitations of permissible deformations within origami structures: in-plane stretching, out-of-plane folding along creases, and out-of-plane bending of panels. Bars are strategically positioned along straight fold lines and across panels to ensure in-plane stiffness. Rotational hinges are incorporated along the bars connecting panels to simulate crease folding, as well as along the bars traversing



panels to replicate panel bending. The method solves the equilibrium equations iteratively, using a displacement-controlled algorithm. Despite having a limited number of degrees of freedom, the reduced-order bar-and-hinge model accurately predicts the overall mechanical behaviour of origami structures [6].

Here, we use the bar-and-hinge method to simulate the deployment of a modified flasher origami for space applications and compare the results to shell FEM results from ANSYS Motion.

Model generation workflow

The selected folding pattern is a modified Flasher origami, which is renowned for its radial deployment mechanism and has been notably utilized in the design of the NASA Starshade prototype, for which the modification amounts to an octagonal variation of the folding technique. The geometry is initially designed in 2D and saved as .svg. A specific color convention is used to distinguish between mountain folds and valley folds, as illustrated in Figure 1 (left): mountain folds are red, valleys are blue and boundary edges are black.

To simulate the deployment process, we need a closed version of this origami structure. This closed configuration is obtained using the interactive origami software (*Origami simulator*) by Ghassaei et al. [7]. The structure before and at a stage of partial folding are shown in Figure 1 (center and right).

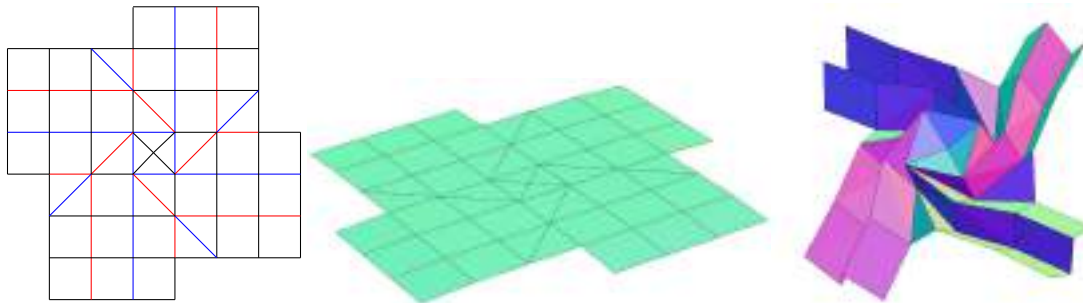


Figure 1 – Origami pattern in .svg file (left), 3D open configuration (center) and 3D partially closed (right). The image in the center and the one on the right have been rendered from the code in [7].

After obtaining the closed version of the origami structure, we export it as .obj file and import it in Merlin 2 (written in MATLAB) [2]. Prior to using it, the nodal coordinates from the .obj file are modified to better fit the desired geometry. The geometry of the origami structure is a 10x10x10 centimeters cube.

After importing the geometry, we set boundary conditions and loads. The only boundary condition imposed on the model is a complete translational block along the three axes to the central node of the horizontal panel. The loads are represented by four displacement constraints of 385 millimeters imposed on the top four vertices of the outermost panels.

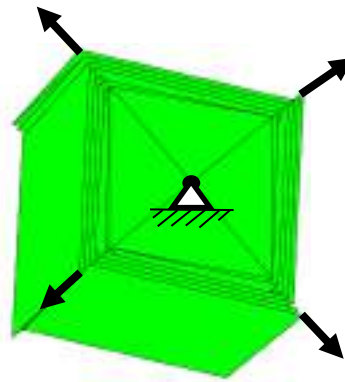


Figure 2 – Closed geometry of the flasher with graphical representation of boundary conditions and loads

In Merlin 2, the most important modelling parameters are the type of discretization of each panel, the material properties and the thickness of the geometry elements. The discretization alternatives for the analysis are called N4B5, which includes four nodes and five bars for every square panel and N5B8, including five nodes and eight bars for every square panel; here, we choose the latter.



Figure 3 – N5B8 (left) and N4B5 (right) discretization, images from [2]

The parameters imposed for the material properties come from experimental data on a specific textile-based electronics substrate [8], used for the realization of the physical prototype that will be subjected to experimental tests to validate the data coming from both models.

The code allows to obtain a load-displacement curve for any node from the simulation, together with information concerning the stored energy of the bending and folding hinges in the geometry. The result of our analysis is shown in Figure 4. At large displacements, the load increases asymptotically since the deployment is complete at 360 millimeters and any further loading engages the high axial stiffness of the panels. The detail of the load-displacement curve, shown on the right, shows a gradual increase of the force from zero to 350 millimeters.

It can also be noticed that the first part of the plot shows a zero load, due to an initial free rotation given by the imperfect alignment of the forces in the model.

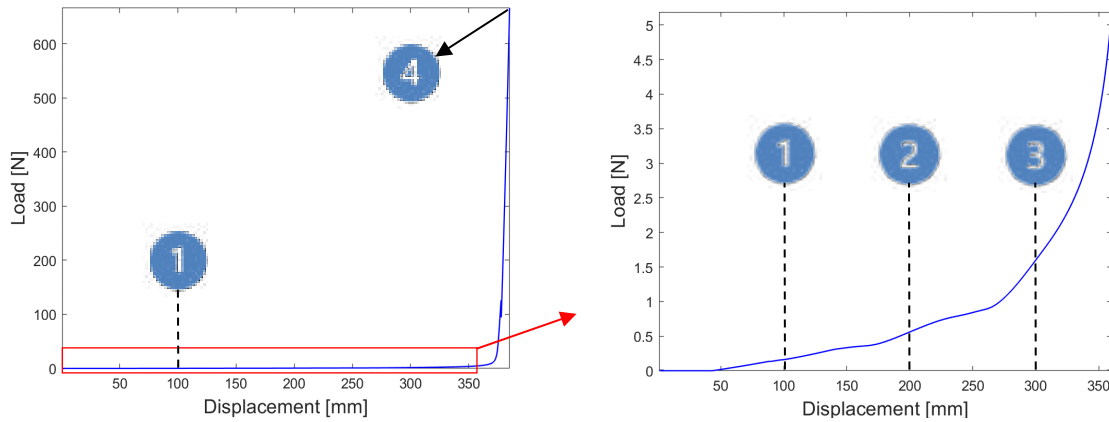


Figure 4 – Full load-displacement curve (left) and partial graph from 0 to 360 mm

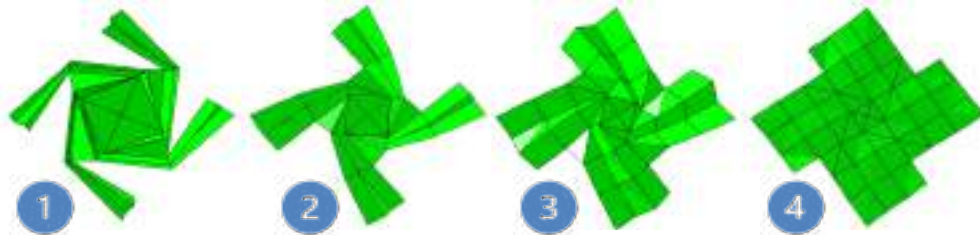


Figure 5 – Four configurations of flasher origami pattern during different phases of deployment, the numbers next to each configuration are related to the Load-Displacement curve in Figure 4

Anslys Motion

The same geometry is imported in the finite element software ANSYS Motion, with the objective of obtaining a comparison between the reduced order model and the finite-element one for validation purposes. To import a .obj geometry in ANSYS, we first import it in Solidworks, export it as a 2D geometry to the Ansys Workbench environment and successively modify it using SpaceClaim.

The material properties imposed to the ANSYS model are the same utilized for the reduced order model, with the approximation of elastic isotropic material, which is suitable for the expected large deformations and small strains. The contact constraint has been created for every panel to accurately model the interaction between the geometric elements.

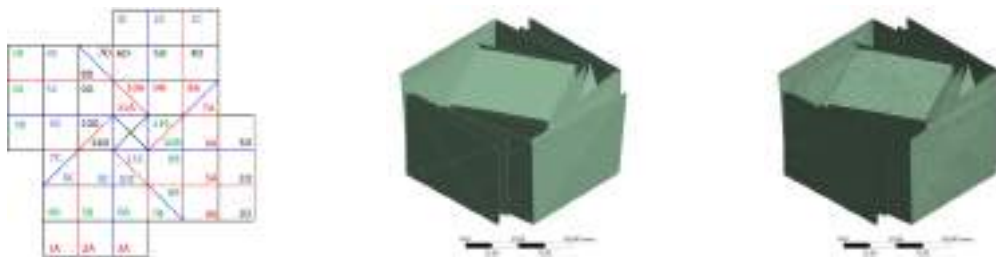


Figure 6 – From left to right: schematics used for constraints enumeration in ANSYS, geometry imported in ANSYS Workbench and geometry discretized using shell elements

The geometry in the closed configuration is renamed according to Figure 6 (left) to make the constraint-imposition process more efficient. The discretization is carried out using shell elements. All the boundary conditions and loads have been set up to create a simulation identical to the bar-and-hinge one. The main difference between the two models is the absence of folding springs in the ANSYS one, which causes zero resistance during deployment and therefore does not allow to

validate load-displacement curves. As we can see, both models capture the same kinematics of deployment.

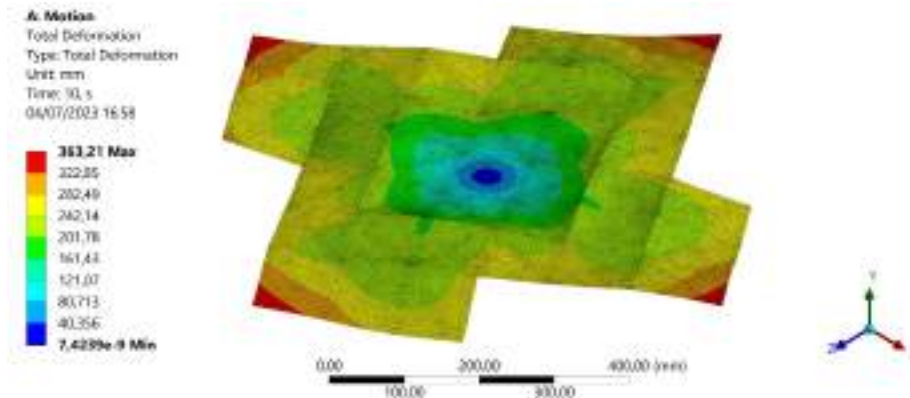


Figure 7 - Diagram of deformation in the final configuration

Conclusions and future developments

The finite element model and the bar and hinge one capture different aspects of the behaviour of the structure. FEM pursues this task through the utilization of higher-order elements, such as plates/shells or volumetric elements, with the same amount of information for the material properties under the approximation of linear isotropic behaviour. Bar-and-hinge models are an efficient tool for approximating the mechanical behaviour of origami structures. Despite their simplicity, these models can be used to capture out-of-plane bending and in-plane shearing, allowing to obtain a conspicuous amount of information with a reduced computational expense compared to the finite element models.

As a next step, we plan an in-depth analysis of the results of the two models (introducing torsional springs in the FEM as well), with a campaign of experimental tests on a physical prototype of the origami structure. This will allow a complete validation of the results, as well as the opportunity to refine the models and the material properties.

Up to now, deployment is simulated as outward radial applied displacements. To accurately capture the forces exerted on the spacecraft during deployment, we will implement a follower load in both models and change the boundary conditions by blocking rotations along the structure's axis; this should allow us to extract the moment produced on the structure during deployment – which will be useful to design the actuation device for deployment.

References

- [1] Cai, Jianguo, et al. "Deployment simulation of foldable origami membrane structures." *Aerospace Science and Technology* 67 (2017): 343-353. <https://doi.org/10.1016/j.ast.2017.04.002>
- [2] Jihui Li, Qingjun Li, Tongtong Sun, Zhiwei Zhu, Zichen Deng, A general formulation for simulating the dynamic deployment of thick origami, *International Journal of Solids and Structures*, Volume 274, 2023, 112279, ISSN 0020-7683. <https://doi.org/10.1016/j.ijsolstr.2023.112279>
- [3] E.T. Filipov, K. Liu, T. Tachi, M. Schenk, G.H. Paulino, Bar and hinge models for scalable analysis of origami, *International Journal of Solids and Structures*, Volume 124, 2017, 26-45, ISSN 0020-7683. <https://doi.org/10.1016/j.ijsolstr.2017.05.028>
- [4] Mark Schenk and Simon D Guest. "Origami folding: A structural engineering approach." In *Origami 5*, edited by Patsy Wang-Iverson, Robert J Lang, and Mark Yim, pp. 293–305. CRC Press, 2011.

- [5] E. T. Filipov, K. Liu, T. Tachi, M. Schenk, and G. H. Paulino. “Bar and hinge models for scalable analysis of origami.” *International Journal of Solids and Structures* 124 (2017), 26–45. <https://doi.org/10.1016/j.ijsolstr.2017.05.028>
- [6] K. Liu and G. H. Paulino, “Highly efficient nonlinear structural analysis of origami assemblages using the MERLIN2 software.” *Origami*, 2018, 7: 1167-1182.
- [7] Amanda Ghassaei, Erik Demaine, and Neil Gershenfeld, “Fast, Interactive Origami Simulation using GPU Computation.” (2018).
- [8] Alessandro Buscicchio, et al. "FRET (Flexible Reinforced Electronics with Textile): A Novel Technology Enabler for Deployable Origami-Inspired Lightweight Aerospace Structures." In *AIAA SCITECH 2023 Forum*, p. 2081. 2023. <https://doi.org/10.2514/6.2023-2081>.

Deployment profile analysis for tethered deorbiting technologies

G. Polato^{1,a*}, A. Valmorbida^{1,2}, A. Brunello², G. Anese¹, S. Chiodini^{1,2},
G. Colombatti^{1,2}, E.C. Lorenzini^{1,2}

¹University of Padova, Department of Industrial Engineering, Via Venezia 1, Padova, Italy

²University of Padova, Center for Studies and Activities for Space (CISAS) "Giuseppe Colombo",
Via Venezia 15, Padova, Italy

^agiulio.polato@unipd.it

Keywords: Tether Deployment, Optimization, Deorbiting, Clean Space

Abstract. Over the past few decades, the man-made space debris has become an increasingly concerning problem for future space missions. Fortunately, some innovative "green" deorbiting technologies have been emerged. Among these strategies, electrodynamic tethers have demonstrated to be a promising option, thanks to their passive and fuel-free characteristics. By leveraging the Earth's ionosphere and the geomagnetic field, an electrodynamic tether generates a Lorentz drag force, that can significantly reduce the altitude of a satellite and ultimately cause it to re-enter the atmosphere. The goal of this research is to investigate a critical part of satellite tethered technology, namely the deployment phase. To accomplish this, we utilized a software tool developed by the University of Padova to simulate the dynamics of the deployment phase and optimize its trajectory, in order to meet the desired boundary conditions. This paper gives a description of the software and shows the results of a sensitivity analysis on the trajectory profile that examines the impact of variations in the release angle of the tether and the speed profile actuated by the motor that controls the deployment speed.

Introduction

Tethered satellites technology has been studied for almost 60 years (first mission, Gemini 11 in 1966) [1]. These satellites can be used for many different purposes such as generating artificial gravity, electrical power generation or electrodynamic thrust [2]. One of the most critical part of a tethered satellite mission is the deployment phase. Depending on the purpose of the mission, the deployment profile followed by the tether, in order to meet the desired final conditions, must be carefully controlled. There are two possible ways to control the tether deployment: by imposing either a tension profile or a length/velocity profile on the reeled-out tether [3]. For the purpose of our study, we chose the second option, where a velocity profile is given as input to a motor that controls the angular velocity of a spool, where the tether is wound. The goal is to reach a final condition where the two satellite are aligned along the local vertical. The advantage of the second strategy is that the reel-out velocity can be more easily measured than the tension on a moving tether and also it can be accurately controlled by a motor with a feedback velocity control.

Mathematical model

The dynamic of tethered satellite is strongly non-linear and is influenced by several parameters. In order to reduce the complexity of the problem, we use a classical Dumbbell model for the system



dynamics that assumes a rigid, straight, length-variable and mass-less tether [4]. The reference system and the parameters used are shown in Fig. 1.

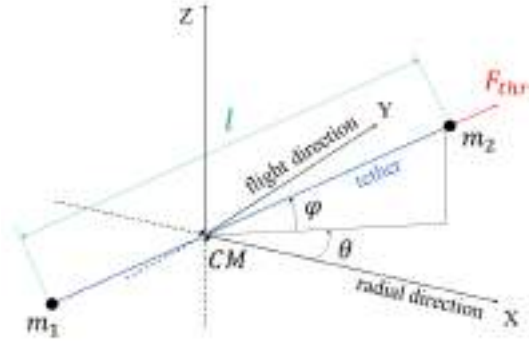


Fig. 1: Reference system frame for tethered satellite

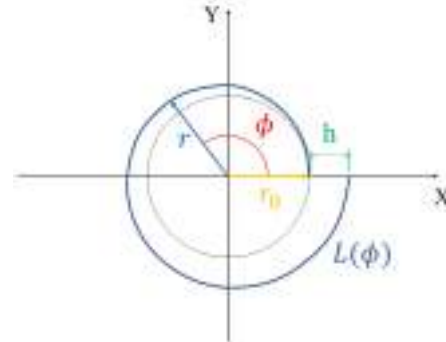


Fig. 2: Archimedean spiral parameters used to model the tape-shaped tether

The equations describing the deployment of a tethered system are the following:

$$\ddot{l} = l \cdot \left[(\dot{\theta} + \omega_o)^2 (\varphi) - \omega_o^2 + \varphi^2 + 3 \omega_o^2 (\theta) (\varphi) \right] + \frac{F_{thr}}{m_2} - \frac{T_p}{m_R} \quad (1)$$

$$\ddot{\theta} = -2 \left[\frac{l}{\dot{l}} + \dot{\varphi} \tan \tan (\varphi) \right] (\dot{\theta} + \omega_o) + 3 \omega_o^2 \cos \cos (\theta) \sin \sin (\theta) \quad (2)$$

$$\ddot{\varphi} = -2 m_R \frac{l}{\dot{l}} \dot{\varphi} - \left[(\dot{\theta} + \omega_o)^2 + 3 \omega_o^2 (\theta) \right] \cos \cos (\varphi) \sin \sin (\varphi) \quad (3)$$

where l is the tether length, θ the in-plane libration angle, φ the out-of-plane libration angle, F_{thr} the thrust applied on the second mass m_2 , $m_R = \frac{m_1 m_2}{(m_1 + m_2)}$ the reduced mass, T_p the tether tension, and ω_o the orbital angular velocity. For the reference deployment profile computation only the in-plane libration dynamics is considered ($\varphi, \dot{\varphi}, \ddot{\varphi} = 0$); the out of plane oscillation is used only for the sensibility analysis.

Finally, in order to derive the control profile of the motor that extracts the tether from the stationary spool, we use the Archimedean spiral to model the tape-shaped tether winded on the spool [5] (see Fig. 2):

$$r = r_0 + \frac{h}{2\pi} \phi \quad (4)$$

$$L = \frac{h}{4\pi} \left[\phi \sqrt{\phi^2 + 1} + \ln \ln \left(\phi + \sqrt{\phi^2 + 1} \right) \right] \quad (5)$$

where r_0 is the initial radius, h the tether width, ϕ the angular coordinate of the spiral, $r(\phi)$ the radial coordinate of the spiral, and L the tether length in the spool varying from r_0 to r .

Software implementation

The software utilized for implementing the dynamics of the deployment was developed by the E.T.PACK-F team of the University of Padova. It mainly consists of four phases: the first three phases are used to derive the reference profile trajectory [6], and the last one is used to derive the input motor profile.

First Phase. In order to simulate the separation phase at the beginning of the deployment, we impose an acceleration profile driven by an initial thrust provided by the thrusters on board the module with mass m_2 . As boundary conditions we imposed the maximum tether velocity that we

want to reach and a time of 50 s needed to reach it. These values are compatible with the performance of the thrusters and the deployment motor.

Second Phase. During this phase, starting from the final conditions of the first phase, the trajectory is optimized using the software BOCOP [7], that approximates the optimal control problem with a finite-dimension optimization problem (NLP) through a time discretization. The boundary conditions to solve this problem are: the initial and final state conditions, i.e., tether length, length rate, libration angle and libration rate, the total deployment time, and upper and lower bounds of the state variables during the optimization process.

Third Phase. The last step for the trajectory profile derivation is to smooth out the transition between the first and the second phase, and the final part of the trajectory. This phase is important because we want to avoid sudden change in the acceleration profile, hence a sudden change in the tension of the tether that can lead to its rupture. In order to obtain a continuity of the second derivative (the acceleration) and a final acceleration equal to zero, we use an 8th-order polynomial to approximate the length profile.

Fourth Phase: Finally, the velocity profile is converted to an angular velocity, using the Archimedean spiral model. The angular velocity is converted from deg/s to rpm which can be used as a reference profile for the motor that controls the spool mechanism.

Sensibility analysis

In order to study the stability of the reference trajectory we introduced errors in our simulations associated with the orientation misalignment of the modules at the beginning of the deployment ($\varepsilon_\theta = \pm 10 \text{ deg}$, $\varepsilon_\varphi = \pm 10 \text{ deg}$) on the in-plane and out-of-plane angles, respectively. In addition, we evaluated the influence of errors on the actual angular velocity of the deployment motor with respect to the reference profile ($\varepsilon_t = \pm 15 \text{ deg/turns}$), e.g., with an error of $\varepsilon_t = 9 \text{ deg/turn}$ the spool performs 1,025 turns instead of 1 turn, hence the motor is running faster than the reference velocity. The values considered for the ε_t error is exaggerated with respect to the actual performance of our motor, but we decided to use these values in order to have a better understanding of the general trend of the error.

The analysis was conducted by varying one driving variable at a time, in order to understand how each parameter affects the deployment dynamics and quantify its contribution to the error on the desired libration amplitude. For the demonstration flight of E.T.PACK-F, the requirement on the final libration amplitude is 10 deg [8].

Results

The following Fig. 3 show the results obtained while Table 1 summarizes the upper bounds of the limit cases. From the Fig. 3 it is possible to understand that the out-of-plane angle error has a smaller influence on the libration amplitude than the in-plane angle error.

Moreover from Fig. 4 it is shown the three trajectory obtained for the limit case of the three errors compared to the nominal trajectory. From this figure it is possible to visualize the effects of these three errors.

Table. 1 upper and lower bound error on the final libration angle

	ε_θ	ε_φ	ε_t
θ_{libr} lower bound error	0.9065 [deg]	$5.5247 \cdot 10^{-3}$ [deg]	-0.4385 [deg]
θ_{libr} upper bound error	-0.1651 [deg]	$0.1689 \cdot 10^{-3}$ [deg]	0.7656 [deg]

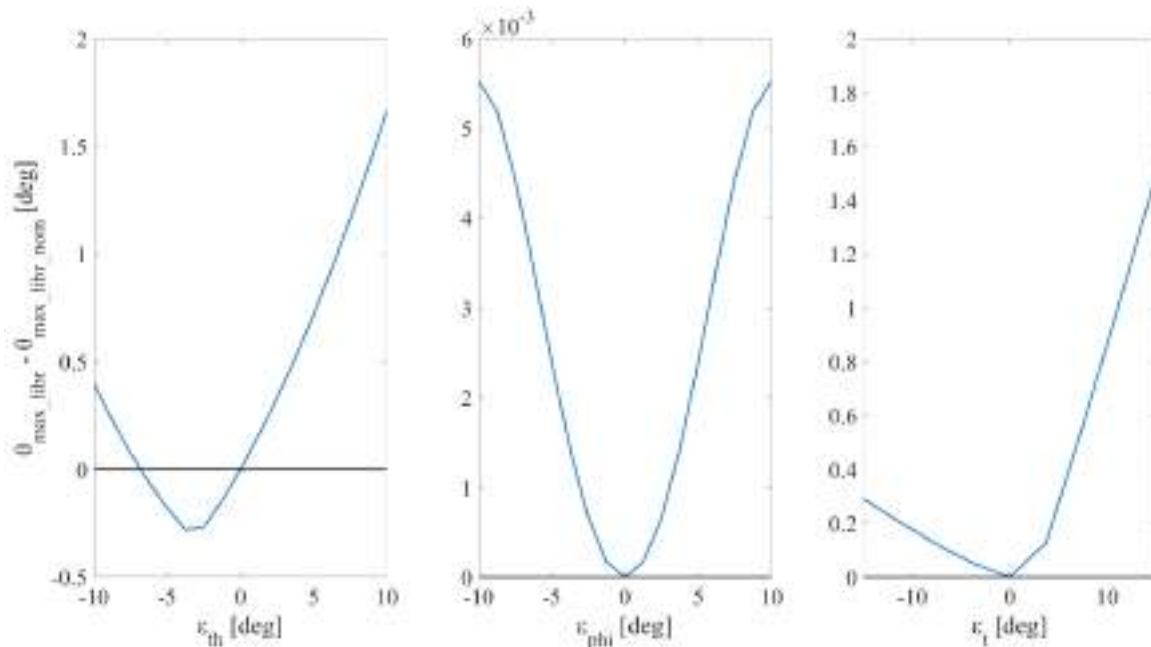


Fig. 3: Results of the sensibility analysis, where on the y-axis is indicated the difference between the free libration amplitude and the nominal libration amplitude

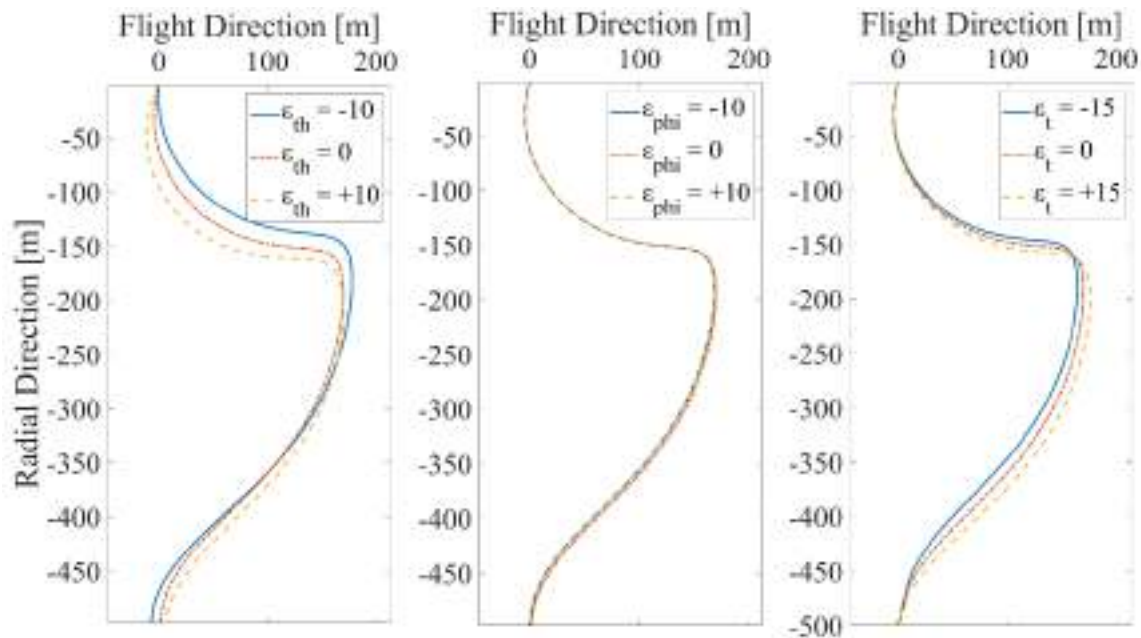


Fig. 4: Comparison of the trajectories for a the limit case of the three errors and the nominal trajectory

Finally, we can conclude also that having a higher velocity than the nominal brings to a higher error on the libration amplitude. Overall, the in-plane angle error has more influences on the libration amplitude, and it has the same order of error as the velocity error.

Conclusions

In this paper, we presented the software developed for the E.T.PACK-F project to compute the deployment reference trajectory and described the four phases of its operation. By considering initial and final conditions, we were able to determine an optimized trajectory that fulfills our deployment requirements. After that, we identified potential errors that could impact the post-

deployment libration amplitude. To assess their influence, we conducted a sensitivity analysis evaluating the effects of each error individually. Based on the simulations conducted, we can conclude that the post-deployment libration amplitude is less than 2 deg, which satisfies the 10 deg requirement. This confirms that the computed reference trajectory for deployment shows a good robustness to the errors considered in this study.

Acknowledgments

This work was supported by Horizon Europe EIC Transition Programme under Grant Agreement No. 101058166 (E.T.PACK-F)

References

- [1] Y. Chen, et al., History of the tether concept and tether missions: a review, *International Scholarly Research Notices* 2013 (2013). <http://dx.doi.org/10.1155/2013/502973>
- [2] M. Kruijff, *Tethers in Space: A propellantless propulsion in-orbit demonstration.*, Ph.D. Thesis, Technical Univ. of Delft, Delft, The Netherlands, (2011).
- [3] E. C. Lorenzini, et al., Control and flight performance of tethered satellite small expendable deployment system-II, *Journal of Guidance, Control, and Dynamics* 19.5 (1996): 1148-1156. <https://doi.org/10.2514/3.21757>
- [4] P. Mantri, *Deployment Dynamic of Space Tether Systems*, Ph.D. Thesis, Faculty of North Carolina State University (2007).
- [5] from: https://en.wikipedia.org/wiki/Archimedean_spiral
- [6] from: <https://research.dii.unipd.it/mts/>
- [7] Team Commands, I. Saclay, BOCOP: an open-source toolbox for optimal control. (2017), See: <http://bocop.org>
- [8] G. Sarego, et al., Deployment requirements for deorbiting electrodynamic tether technology, *CEAS Space Journal* 13.4 (2021): 567-581. <https://doi.org/10.1007/s12567-021-00349-5>

The Janus COM mechanism onboard the JUICE probe to the Jovian system

G. Colombatti^{*,1,2}, A. Aboudan¹, M. Bartolomei¹, S. Chiodini^{1,2}, A. Dattolo³,
G. Noci³, F. Sarti³, T. Bilotta³, A. Colosimo³

¹CISAS Giuseppe Colombo, University of Padova, via Venezia 15, Padova Italy

²Department of Industrial Engineering DII, University of Padova, via Venezia 1, Padova Italy

³Leonardo SpA, Firenze, Italy

*giacomo.colombatti@unipd.it

Keywords: Telescope, Jupiter, JUICE, Qualification

Abstract. After the successful launch of the JUICE (JUpter ICy moons Explorer) on the 14th of April 2023 all the on board subsystems and instrument are testing their functionalities. The JANUS (Jovis, Amorum ac Natorum Undique. Scrutator) telescope is the imaging system on board the spacecraft and is an optical camera devoted to the study of global, regional and local morphology and processes on the Jovian moons, and to perform mapping of the clouds on Jupiter. Following the heritage of the successful design of the OSIRIS WAC camera, on board the Rosetta mission, the group of researchers at CISAS “Giuseppe Colombo”- Università degli studi di Padova, led by prof. S. Debei, in collaboration with colleagues of the Leonardo spa Company developed the mechanism responsible for the protection of the telescope during cruise phase. The COVer Mechanism (COM) provides the external closure of the JANUS Optical Head Unit (OHU). It shields the optical parts from contamination, it is light and dust tight and works in the plane of the telescope entrance window avoiding the exposure of the inner surface of the cover itself and the core part of the telescope to the external dust and pollution. The lower part of the cover provides, also, a reference surface for the in-flight calibration of the telescopes. The main functional and environmental requirements of this mechanism can be identified and summarized as follows: the door provides optics and detector protection from sunlight and contamination; the subsystem, located at the main entrance of the JANUS OHU outer Baffle, provides the function of opening and closing of the cover. The opened Cover allows the JANUS OHU and detector to face the outer environment to perform planetary observations during science mission phases and to perform in-flight calibration observation of different targets (e.g., moons, stellar fields). This paper presents the design, the mechanical solutions adopted for a reliable system and the results of the test performed on ground in order to qualify the JANUS COM mechanism before flight.

Introduction

The astonishing JUICE mission, launched early this year, will perform a very detailed exploration of the ocean layers and analysis of subsurface water reservoirs; it will study the Ganymede's intrinsic magnetic field, its topographical, geological and compositional maps. The JUICE mission was designed to investigate the physical properties of the icy crusts and of the internal mass distribution of jovian moons [1]. It will arrive at Jupiter in January 2031 after 7.6-years using an Earth–Venus–Earth–Earth gravity assist sequence.

Among the JUICE payload, JANUS (Jovis Amorum ac Natorum Undique Scrutator) is the narrow-angle camera selected as the visible (from near UV to NIR) imager onboard JUICE. An overview of the scientific goals of JANUS, together with measurements needed to fulfil the specific goal, is given in the following. The detailed investigation of the Galilean icy satellites, which are believed to harbor subsurface water oceans, is central to elucidating the conditions for



habitability of icy worlds. Visible wavelength imaging is needed to determine the formation and characteristics of magmatic, tectonic, and impact features, relate them to surface forming processes, constrain global and regional surface ages, and investigate the processes of erosion and deposition [2]. The JANUS instrument is composed by the following functional (and physically independent) subsystems:

- Optical Head Unit (OHU), mounted on the S/C Optical Bench
- Proximity Electronics Unit (PEU), located close to OHU on S/C Optical Bench
- Main Electronics Unit (MEU), located in the S/C vault
- Interconnecting harness

The COVer Mechanism (COM) provides the external closure of the JANUS Optical Head Unit (OHU). It protects the optical parts from contamination; it is dust tight and works in the plane of the entrance window avoiding the exposure of the inner surface of the cover itself and the core part of the telescope to the external dust and pollution. The lower part of the cover provides, also, a reference surface for the in-flight calibration of the telescopes.

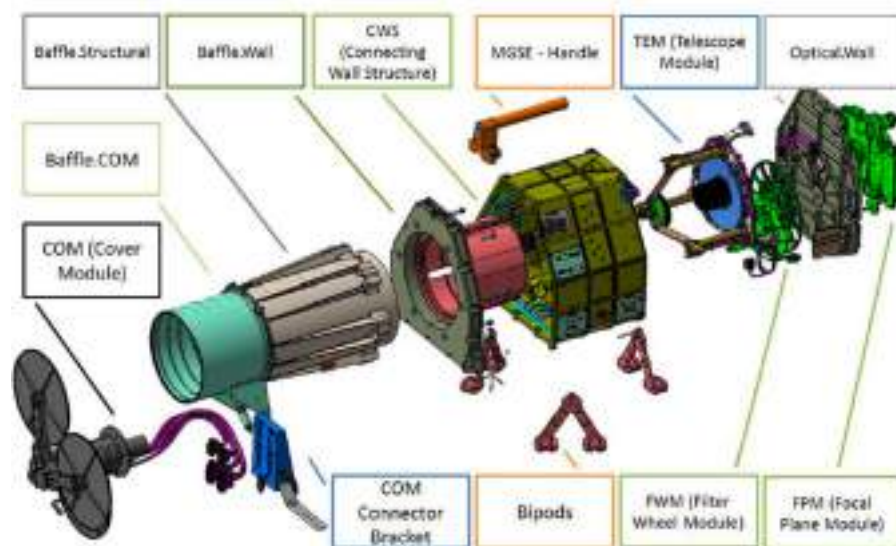


Fig. 1. OHU unit layout overview; on the left side of image the JANUS COM subsystem [1].

COM Subsystem Requirements and Baseline Design

The main functional and environmental requirements of this mechanism can be identified and summarized as follows:

- the cover provides optics and detector protection from sunlight and contamination;
- the subsystem, located at the main entrance of the JANUS OHU outer Baffle, provides the function of opening and closing the door;
- the subsystem mechanism implements the following needed functionalities in each flight condition:
 - Closed - Locked position: to protect of the optical elements and detector from contamination by the inner part of the door during launch (pre-loaded);
 - Closed - not Locked (Cruise) position: to protect the optical elements and detector from contamination during the cruise phase and to prevent long-term sticking of the COM door and the OHU Baffle I/F;

- Open - Locked position: to allow the JANUS OHU and detector to face the outer environment to perform planetary observations during science mission phases and to perform in-flight calibration observation of different targets (e.g., moons, stellar fields).
- single-point failure tolerance requires redundancy and the ability to open the door permanently in the case if an irreversible system failure occurs (fail-safe device);
- requirement to validate open and closed positions;
- dynamic load during launch;
- non-operational temperature range (-40 to $+35$ °C) implies a design for high differential thermal loads within the mechanisms.

COM Subsystem

The COM subsystem is mainly composed by the following parts, which can be seen in Figure 2:

- the stepper motor (MT) for controlling the position of the cover;
- the interface flange (FL) for fixing the mechanism to the baffle of the telescope;
- the main body (BD) where the mechanical parts for allowing the movements are present;
- the main shaft (MS) governing the vertical movement;
- the bracket (BR) holding the cover shield;



Figure 2: COM subsystem together with its components; left image: rendering; right image: flight model.

Mechanism Functional Test and Calibration

To demonstrate that mechanism functionality in the presence of environmental loads a life test has been executed during the thermal cycles. Due to waiting time between each activation, all the activations have been divided in 3 slots. The activations have been distributed along each cycle at different temperatures. The total activations are 5520 cycles divided as shown in Table 1.

The mechanism open and closed position has been calibrated with repeatability tests. Figure 3 shows repeatability test performed on EQM, data collected on 15 runs, both resistant torque and the switch status are reported, and highlights the repeatability of the mechanism performances.

Table 1 COM lifetime test activations

Phase	P [Pa]	T [°C]	Cycles
1	amb	amb	500
2	5e-3	Ambo	500
3	5e-3	-45...-20	2880
4	5e-3	-20...+10	720
5	5e-3	+10...+35	920

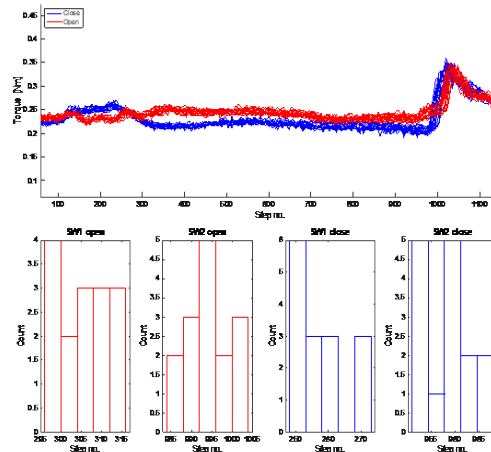


Figure 3: Repeatability test performed on EQM, data collected on 15 runs, both resistant torque and the switch status are reported, and highlights the repeatability of the mechanism performances.

Thermal Monitoring

COM temperature is measured by five Pt1000 thermistors, three are located on the external surface of the COM close to the heaters (see Figure 4), other two are mounted on the motor chassis.

COM temperature is controlled by means of two heaters (2 nominal and 2 redundant) located on the COM external surface. The survival thermal control subsystem is composed by the three Pt1000 plus two magnetically self-compensating heaters on the COM mantle.



Figure 4: Monitoring PT1000: located in COM main body near the thermal regulation heater.

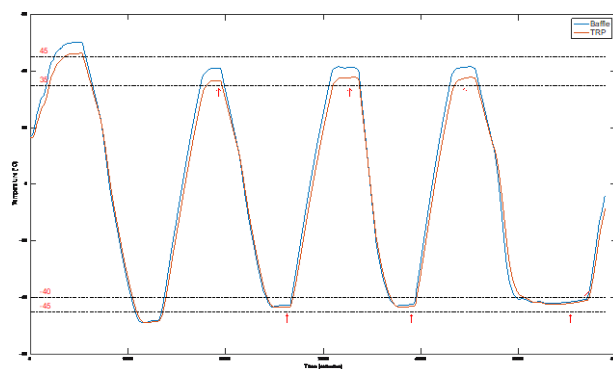


Figure 5: Thermal cycles (-45°C...+45°C); red arrows show the activation events; red cross shows the SMA activation event d highlights the repeatability of the mechanism performances.

Conclusion

The JANUS COM Team members are very grateful to prof. Stefano Debei for his inspiring scientific activity and for all the precious suggestions he gave us for the design, development and testing of the last space exploration equipment he lead at the CISAS “Giuseppe Colombo” space center of the University of Padova and for his valuable ideas collaborating with the members of Leonardo SPA- Florence company.

References

- [1] Grasset, Olivier, et al. "Jupiter ICy moons Explorer (JUICE): An ESA mission to orbit Ganymede and to characterise the Jupiter system." *Planetary and Space Science* 78 (2013): 1-21. <https://doi.org/10.1016/j.pss.2012.12.002>
- [2] Della Corte, Vincenzo, et al. "Scientific objectives of JANUS Instrument onboard JUICE mission and key technical solutions for its Optical Head." 2019 IEEE 5th International workshop on metrology for aerospace (MetroAeroSpace). IEEE, 2019. <https://doi.org/10.1109/MetroAeroSpace.2019.8869584>

Comparison of LARES 1 and LARES 2 missions - one year after the launch

Ignazio Ciufolini^{1,a}, Antonio Paolozzi^{2,b}, Emiliano Ortore^{2,c}, Claudio Paris^{2,d*},
Erricos C. Pavlis^{3,e}, John C. Ries^{4,f} and Richard Matzner^{5,g}

¹Group of Astrodynamics for the Use of Space Systems (Gauss), Via Sambuca Pistoiese 70,
00138 Rome, Italy

²Scuola di Ingegneria Aerospaziale, Sapienza University, Via Salaria 851 – 00138 Rome, Italy

³GESTAR II - University of Maryland, Baltimore County (UMBC) & NASA Goddard, 61A, TRC
#182, 1000 Hilltop Circle, Baltimore, Maryland, USA 21250

⁴Center for Space Research, University of Texas at Austin, Austin, USA

⁵Center for Gravitational Physics, Weinberg Center, University of Texas at Austin, Austin, USA

^aignazio.ciufolini@gmail.com, ^bantonio.paolozzi@uniroma1.it, ^cemiliano.ortore@uniroma1.it

^dclaudio.paris@uniroma1.it, ^eepavlis@umbc.edu, ^fries@csr.utexas.edu,

^grichard.matzner@sbcglobal.net

Keywords: LARES 2, Satellite Design, Laser Ranging, General Relativity, Frame-Dragging

Abstract. The LARES 1 and LARES 2 missions were designed to test an intriguing phenomenon predicted by the theory of general relativity: the *Lense-Thirring (frame-dragging)* effect. In particular, the LARES 2 mission was designed with the goal of reaching an accuracy 10 times better than that obtained with LARES 1, launched 10 years earlier. To reach this demanding goal a special orbit and a specific satellite design was required. Knowledge of the gravitational field of Earth of ever-increasing accuracy, thanks to the Follow-on GRACE space mission together with the spectacular orbital injection accuracy provided by the Avio-ASI-ESA launcher VEGA C, will make possible an even better accuracy after a few years of data analysis. In this paper the two missions are compared along with the results obtained from the LARES 1 mission and those expected from LARES 2.

Introduction

LARES 2, was successfully launched from the European spaceport in French Guyana on the inaugural flight of VEGA C (13 July, 2022). This launch occurred 10 years after the maiden flight of VEGA that carried as main payload the LARES 1 satellite. Both launch vehicles were developed, financed and managed by ASI, Avio and ESA. The two orbits are quite special. Particularly the LARES 2 orbit needed to be quite high compared to classical LEO orbits, and in comparison, to the case of LARES 1 there were very tight tolerances in the orbit parameters. The injection accuracy for LARES 1 was very high, but for LARES 2 the accuracy was spectacular; it matched the orbit to 10 times better accuracy than previously required, affording the prerequisites for even better results than originally designed [1]. This will allow an improvement in the accuracy of the frame-dragging (Lense-Thirring effect) measurement by one order of magnitude with respect to obtained using LARES 1 [2], allowing an accuracy of at least as good as a few parts per thousand. Frame-dragging is measured by observing how the node of a satellite orbit is shifted by the dragging of spacetime induced by the Earth rotation. In general relativity spacetime is deformed by mass-energy but also by currents of mass-energy, such as Earth's rotation. Laser ranging provides the most accurate ranging measurement achievable today in near-Earth space and



is capable of providing the necessary data for the LARES missions. The main problem in measurement of frame dragging arises from classical gravitational and non-gravitational perturbations whose effects on the node are huge compared to frame-dragging. A combination of the data of the two LARES satellites and the two LAGEOS satellites is required, together with very accurate knowledge of the gravitational field of Earth is necessary to extract the frame dragging values during the analysis. (The gravitational fields from GRACE and GRACE Follow On missions are used.)

Frame-dragging of general relativity

General relativity (GR) is the best theory of gravitation interaction available today [3,4]. However, there are still open issues such as its reconciliation with quantum mechanics and the problem of spacetime singularities inside black holes where all known physical theories break down, and whose existence is a robust prediction of general relativity [5]. The accelerating expansion of the universe [6] is another mystery that increases the interest in experimental verification of GR. In this framework LARES 1 and LARES 2 missions find their natural environment, to measure the effect of Earth rotation on spacetime: the Lense-Thirring effect, named after the two Austrian physicists that derived it in 1918. In principle the measurement is relatively easy because it would be sufficient to measure the node shift of one satellite orbit and compare it with the prediction of GR. Unfortunately, the shift due to GR is only about 118.5 mas/y for LARES 1 and about 30.7 mas/y for LARES 2, translating to only about 4 m/y and 2 m/y respectively, while classical perturbations produce shifts about 7 orders of magnitude larger, translating to node shifts of many thousands of km per year. The original idea to circumvent this problem was proposed and published in references [7-12]; the key is to use two satellites orbiting at the same altitude but with supplementary inclinations or in other words to use a so-called butterfly configuration (Fig. 1). Originally, in the 80's, the mission was named LAGEOS 3 and was supposed to put a copy of LAGEOS 1 and 2 in the supplementary orbit now occupied by LARES 2. In 2012 ESA and ASI offered a launch opportunity with the inaugural flight of the VEGA launcher developed by Avio. The launch envelope of the inaugural flight was limited to 1500 km and so a different approach to eliminate the effect on the node of the even-zonal harmonics was devised [2]. In this case the combination of the three satellites LAGEOS 1, LAGEOS 2 and LARES 1 was necessary to eliminate major disturbances due to the uncertainties of the first two even-zonal harmonics: J_2 and J_4 . Intermediate results were reported in the years that followed the launch (see for instance [13]), culminating 7 years after the launch in reaching the mission goal of 1-2% accuracy in the frame-dragging [2]. Frame-dragging around Earth is tiny and very difficult to measure, but observable with high accuracy with the LARES missions. In extreme astrophysical/cosmological phenomena such as the formation of accretion disks of rotating black holes and in explaining the fixed direction of jets in active galactic nuclei, frame dragging is very important, large, but difficult to determine to high accuracy. Also, black hole mergers which produce gravitational waves observed by the LIGO-Virgo-KAGRA laser interferometer detectors [14], are strongly influenced by frame-dragging.

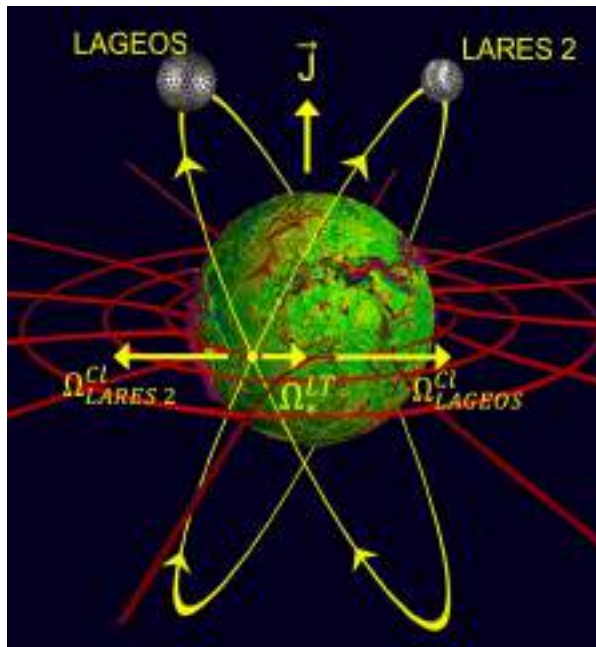


Fig. 1. The even zonal gravitational harmonics of the Earth produce the very large and well-known shift of the node Ω^{Cl} (the superscript Cl reminds us that the shift is due to classical perturbation) while $\Omega^{LT} = \Omega_{LAGEOS}^{LT} + \Omega_{LARES 2}^{LT}$ (LT stands for: Lense-Thirring effect) is the tiny shift due to the dragging of inertial frames predicted by the theory of general relativity and \mathbf{J} is the Earth angular momentum. The small variations of the gravitational field of Earth are represented in false colors and report actual experimental values obtained for instance by the GRACE and GRACE FO space missions. The red lines are a pictorial representation on how spacetime is dragged by the Earth rotation.

LARES 1 and LARES 2 missions

Both missions are based on the precise orbit determinations of the two satellites along with those of the two LAGEOS satellites. Laser ranging is used to measure the satellite orbits to a few millimeters' accuracy. Both LARES satellite bodies are made in one single piece, differently from all other geodetic passive satellites; LARES 2 has a novel CCR distribution which is not regular along the parallels. In Table 1 are compared other characteristics. In Fig. 2 is reported the last LT measurement obtained with LARES 1 mission that shows the mission goal was fulfilled.

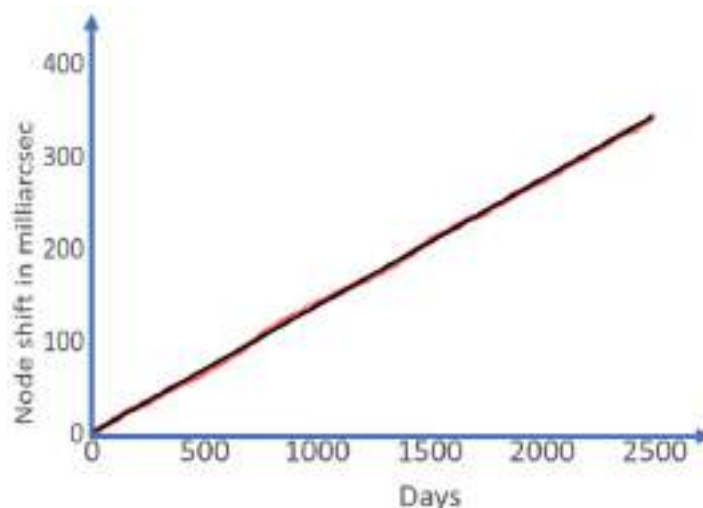


Fig. 2. Result of the LARES 1 mission [2]. The figure reports the LT effect measurement obtained by analyzing 7 years of orbital data of three satellites: the two LAGEOS and LARES 1. The horizontal axis reports the number of days. In red are the actual data and in black a linear fit. Taking 1 as the theoretical value of LT effect we have obtained 0.9910 ± 0.02 , i.e., with 0.02 systematic error and with 0.001 formal error.

The orbital analysis of LARES 2 combined with that of LAGEOS 1 is in progress. The current availability of approximately one year of data is not sufficient to reduce the effects on the satellite nodes of the large perturbations due to some tides and, so far, to improve the accuracy of the measurement of LT in Fig. 2. By applying proper averaging and fits of such orbital perturbations, using data of a longer period of time, an improved measurement will be obtained in a few years.

Table 1. Comparison of the LAGEOS with the two LARES satellites. S and M are the surface and the mass of the satellites respectively. S/M is calculated relative to the value of LAGEOS 1.

	ORBITAL PARAMETERS			Metal alloy	D [m]	M [kg]	CC R No.	CCR dia [in]	S/M relative
	i [°]	a [km]	e						
LARES 1	69.44	7827.598	0.0009	W	0.364	386.8	92	1.5"	0.39
LARES 2	70.158	12266.198	0.00027	Ni	0.424	294.8	303	1.0"	0.69
LAGEOS 1	109.844	12269.988	0.004	Al-Cu	0.6	407	426	1.5"	1

Acknowledgments. The authors acknowledge the Italian Space Agency (ASI) for supporting the LARES 1 and LARES 2 missions and the International Laser Ranging Service (ILRS) for tracking the satellites. E. C. Pavlis acknowledges the support of NASA Grant 80NSSC22M0001.

References

- [1] Ciufolini, I., Pavlis, E.C., Sindoni, G., ... Koenig, R., Paris, C. A new laser-ranged satellite for General Relativity and space geodesy: II. Monte Carlo simulations and covariance analyses of the LARES 2 experiment, *European Physical Journal Plus*, 2017, 132(8), 337. <https://doi.org/10.1140/epjp/i2017-11636-0>
- [2] Ciufolini, I., Paolozzi, A., Pavlis, E.C., ...Gurzadyan, V., Penrose, R., An improved test of the general relativistic effect of frame-dragging using the LARES and LAGEOS satellites, *European Physical Journal C*, 2019, 79(10), 872. <https://doi.org/10.1140/epjc/s10052-019-7386-z>
- [3] C.W. Misner, K.S. Thorne, J.A. Wheeler, *Gravitation* (Freeman, San Francisco, 1973).
- [4] I. Ciufolini, J.A. Wheeler, *Gravitation and Inertia* (Princeton University Press, Princeton, New Jersey, 1995). <https://doi.org/10.1515/9780691190198>
- [5] R. Penrose, *Gravitational Collapse and Space-Time Singularities*, *Phys. Rev. Lett.* 14, 57–59 (1965). <https://doi.org/10.1103/PhysRevLett.14.57>
- [6] A. Riess et al., *Astron. J.*, Observational evidence from supernovae for an accelerating universe and a cosmological constant, 116, 1009–1038 (1998). <https://doi.org/10.1086/300499>
- [7] I. Ciufolini, Measurement of the Lense-Thirring drag on high-altitude, laser-ranged artificial satellites, *Phys. Rev. Lett.* 56, 278 (27 Jan 1986). <https://doi.org/10.1103/PhysRevLett.56.278>
- [8] I. Ciufolini, A comprehensive introduction to the LAGEOS gravitomagnetic experiment: from the importance of the gravitomagnetic field in physics to preliminary error analysis and error budget, *International Journal of Modern Physics A*, 4, No. 13, pp. 3083-3145 (1989). <https://doi.org/10.1142/S0217751X89001266>
- [9] B. Tapley, J.C. Ries, R.J. Eanes, M.M. Watkins, NASA-ASI Study on LAGEOS III, CSR-UT publication n. CSR-89-3, Austin, Texas (1989).
- [10] I. Ciufolini et al., ASI-NASA Study on LAGEOS III (CNR, Rome, Italy, 1989).
- [11] I. Ciufolini, *Theory and experiments in general relativity and other metric theories*. Ph.D dissertation, advisors: John A. Wheeler, Richard Matzner and Steven Weinberg. Univ. of Texas, Austin (Ann Arbor, Michigan, 1984).
- [12] J.C. Ries, *Simulation of an experiment to measure the LenseThirring precession using a second LAGEOS satellite*. Ph.D Dissertation, Univ. of Texas, Austin, 1989.
- [13] Ciufolini, I., Paolozzi, A., Pavlis, E.C., Sindoni, G., Paris, C., Preliminary orbital analysis of the LARES space experiment, *European Physical Journal Plus*, 2015, 130(7), 133. <https://doi.org/10.1140/epjp/i2015-15133-2>
- [14] B.P. Abbott et al., Observation of Gravitational Waves from a Binary Black Hole Merger, *Phys. Rev. Lett.* 116, 061102 (2016). https://doi.org/10.1142/9789814699662_0011

Tracking particles ejected from active asteroid Bennu with event-based vision

Loïc James Azzalini^{1,a*}, Dario Izzo^{1,b}

¹ Advanced Concepts Team, European Space Agency, European Space Research and Technology Centre (ESTEC), Keplerlaan 1, 2201 AZ Noordwijk, The Netherlands

^ajazzalin@outlook.com, ^bdario.izzo@esa.int

Keywords: Neuromorphic Vision, Event-Based Sensing, Multi-Object Tracking

Abstract. Early detection and tracking of ejecta in the vicinity of small solar system bodies is crucial to guarantee spacecraft safety and support scientific observation. During the visit of active asteroid Bennu, the OSIRIS-REx spacecraft relied on the analysis of images captured by onboard navigation cameras to detect particle ejection events, which ultimately became one of the mission's scientific highlights. To increase the scientific return of similar time-constrained missions, this work proposes an event-based solution that is dedicated to the detection and tracking of centimetre-sized particles. Unlike a standard frame-based camera, the pixels of an event-based camera independently trigger events indicating whether the scene brightness has increased or decreased at that time and location in the sensor plane. As a result of the sparse and asynchronous spatiotemporal output, event cameras combine very high dynamic range and temporal resolution with low-power consumption, which could complement existing onboard imaging techniques. This paper motivates the use of a scientific event camera by reconstructing the particle ejection episodes reported by the OSIRIS-REx mission in a photorealistic scene generator and in turn, simulating event-based observations. The resulting streams of spatiotemporal data support future work on event-based multi-object tracking.

Introduction

An active asteroid shows evidence of mass loss caused by natural processes or as a result of human-planned activities, sharing characteristics more often associated with comets. Detecting and interpreting the dynamic properties of these small solar system bodies (SSSB) constitute important scientific objectives of sample-return and flyby missions as they may hold the key to understanding their past and future [1]. In the case of asteroid Bennu, such activity was only detected in situ as the navigation cameras of visiting spacecraft OSIRIS-REx captured centimetre-size rocks being ejected from the surface. Whether for situational awareness to guarantee spacecraft safety or scientific observation, missions to active asteroids or comets benefit from early detection and tracking of such events [2]. Currently, extensive offline image analysis is needed to balance the brightness of the body and the dimness of the particles (stray light reduction), to negate the static objects in the scene (image differencing) and to detect the relative motion of the particles (blinking) [1]. Given the time-constrained nature of these missions, techniques that automate the detection and tracking of particles, such as the frame-based multi-object tracking algorithm proposed in [3], could significantly contribute to the mission's scientific returns.

This work proposes a solution based on the principles of dynamic vision sensing and the event camera, a novel imaging sensor inspired by the neural pathways of the retina [4, 5]. Where a standard frame-based camera would capture redundant static information, an event camera would only report pixel-level brightness changes induced by the dynamics present in the scene. The sparse and asynchronous output of the sensor and its large dynamic range provide an effective low-power solution to detection and tracking problems in challenging lighting conditions [6]. Given particularly dynamic environments around SSSBs as a result of plumes, dust and/or particle



ejecta, we theorise that event-based technology could augment onboard navigation and scientific cameras, streamlining current approaches based on offline image analysis.

The apparent advantages of these dynamic vision sensors for space applications have recently been reviewed in [7]. While the principles of dynamic vision have yet to be applied to the detection and tracking of particles around an active asteroid, similar work on event-based star tracking [8] and (event-based) space situational awareness [9, 10] provide valuable insights into the challenges posed by the problem at hand. Unlike the streaks produced by resident space objects (RSOs) crossing the field of view of a ground-based or in-orbit telescope, the particles of interest in this study undergo more complex dynamics locally, given the proximity of the SSSB, limiting the utility of classical approaches such as the Hough transforms. Moreover, the problem of associating observations to tracks is exacerbated by significant measurement noise that is inherent to the event camera. Popular multi-object tracking solutions such as the (probabilistic) multiple hypothesis tracking filters have been adapted to event-based representations of RSOs [9, 11], suggesting that these algorithms also lend themselves to the analysis of particle dynamics in the vicinity of an SSSB.

To support the evaluation of event-based multi-particle tracking, we use the navigation and ancillary information of the OSIRIS-REx mission in simulation as well as reports of notable particle ejection episodes [12] to highlight how an event-based sensor can augment visual data capture and contribute to the mission's scientific objectives. The dynamic scene, composed of asteroid Bennu and several centimetre-size particles ejected from its surface, is first reconstructed with photorealistic computer graphics tools from the point of view of the visiting spacecraft [13]. Dynamic vision sensing is subsequently simulated by emulating the sensitivity and noise characteristics of a real event camera [14, 15]. In turn, we demonstrate that, in the absence of frames, asynchronous streams of events capture sufficient information about the scene to enable fast and continuous tracking of multiple particles. This constitutes an essential step to support future research on event-based determination of the size and orbit of RSOs.

The following section introduces the principle of operation underlying the high temporal resolution and high dynamic range of the event camera. Section Simulation and Results describes the simulation environment in which the dynamic scene is reproduced and the preliminary results on event-based tracking of particle ejecta. Given the sparse and asynchronous output of the event camera, future work will focus on the formulation of a multi-object tracking problem that is compatible with the event-based representation of the particle tracks.

Theoretical Background

Event-Based Vision. The pixels of a dynamic vision sensor independently report changes in scene brightness, which is generally taken to be the log intensity (i.e., $\log I$), resulting in a sparse and asynchronous stream of *events*. The pixel at location (x, y) in the sensor plane outputs a 1 (alternatively, 0) if the sensed brightness at time t increased (decreased) by the predefined magnitude Θ_{ON} (Θ_{OFF}) known as the contrast thresholds. Thus, an event can be represented by the 4-tuple (t, x, y, p) , where p denotes the polarity of the brightness change. After triggering an event, the pixel resets its baseline from which to monitor subsequent changes in brightness to the current log intensity, as depicted in Figure 1 (a). Figure 1 (b) shows a synthetic example of a stream of events output by an event camera capturing a black dot spinning on a white disk. As only the motion of the black dot contributes changes in brightness in the scene, the spatiotemporal output of the sensor takes the form of a spiral.

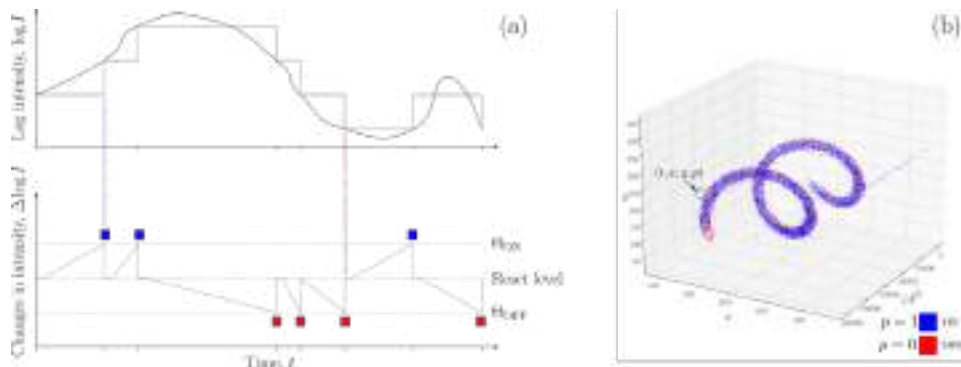


Figure 1 Dynamic vision sensing overview: (a) principle of operation of a DVS pixel (adapted from [4]) (b) example output from an event camera capturing a black dot spinning on a white disk (based on synthetic data from Prophesee's Metavision toolkit [16])

The sparsity of the output allows for high readout rates in the range of 2 – 1200 MHz, high temporal resolution (in the order of μ s), low-power consumption and, owing to the logarithmic scale used by each pixel, high dynamic range [5]. While these are appealing characteristics for an onboard sensor, the event camera is inherently noisy due to the complex transistor circuits underlying its differential mode of operation. Figure 1 (b) captures some of these noisy contributions in the form of sporadic streaks of ON events at several pixel locations in the sensor plane. These artefacts are the result of nonidealities such as hot pixels and leak currents which produce events irrespective of the scene dynamics. In order to faithfully simulate the output of these sensors, event camera emulators [14, 15] model these sources of noise and other hardware-related nonidealities (e.g., shot noise).

Simulation and Results

The first step of the simulation of dynamic vision sensing around active asteroid Bennu consists in extracting the relative position of the OSIRIS-REx spacecraft, the Sun and the ejected particles. The Orbital C mission phase is of particular interest given that it was dedicated to particle monitoring, resulting in a higher cadence of imaging. Specifically, a time window centred on the particle ejection episode of September 13th, 2019, is considered in this work given that out of the 30 particles detected, 22 tracks led to successful orbit determination [12]. Figure 2 depicts the reconstructed particle ejection episode based on the interpolation of the relevant SPICE kernels.

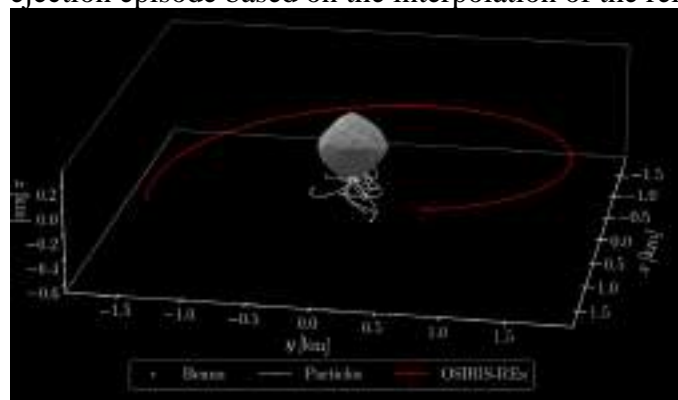


Figure 2 Bennu-fixed particle ejection visualization based on the interpolation of SPICE kernels from 2019-09-13T21:00:00 to 2019-09-14T00:00:00 [12]

Given the dynamic nature of the event camera, the ejection scene depicted in Figure 2 is then animated in Blender, using photorealistic models of the asteroid and the particles. Different textures and reflectance properties are used to reproduce the rubble pile appearance of Bennu [13] based on the position of the Sun during the Orbital C phase. The simulated ejecta consists of 14

particles with sizes ranging from 1 – 11 *cm* according to the average diameters reported in [1]. We emulate the large field of view and image sensor size of the onboard navigation camera (NavCam 1) by configuring the Blender perspective camera with $W = 2592$ px, $H = 1944$ px and a horizontal field of view of $\vartheta = 44^\circ$. Then, the positions of the particles and the emulated camera along the Orbital C trajectory are updated to capture frames of the ejection episode, as shown in Figure 3 (a) (cropped near the limb where the ejecta emanate).

Overall, 40 additional renders are generated and combined into a video at 30 *FPS* tracing the path of the particles from the surface of Bennu to the lower-left borders of the field of view. To study an event-based representation of the scene dynamics, the video is then passed to an event camera emulator [14, 15], which converts the video to spatiotemporal streams of events based on the operation principle described in Section Event-Based Vision. In the interest of qualitative comparison with the original renders, synthetic events are binned into event-frames over short time windows such that the original frame rate is recovered.

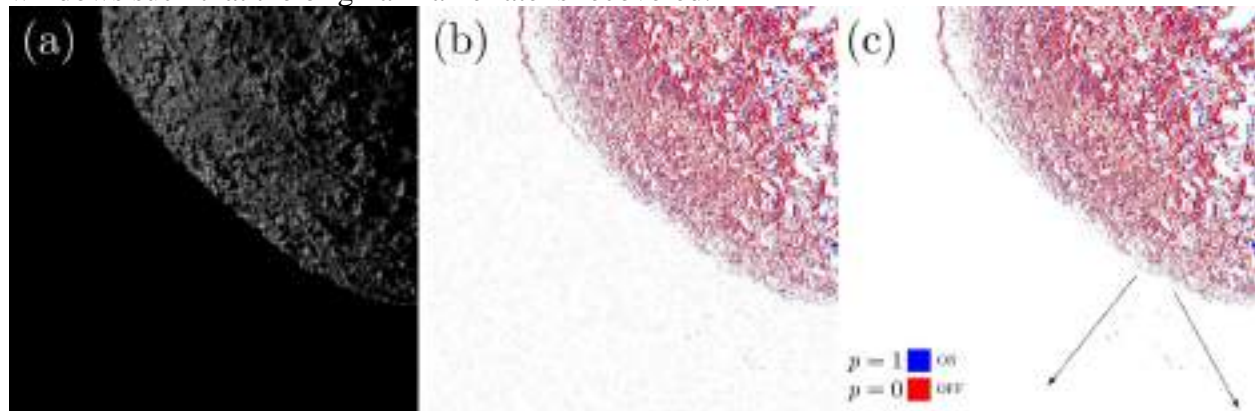


Figure 3 Reconstruction of a 14-particle ejection episode: (a) the particles are difficult to detect in the photorealistic render, (b) accumulation of synthetic events in a single frame with are more easily identifiable against a dynamic noisy background (b) and clearly visible in the absence of noise (c), where the arrows indicate the ejecta direction.

While the low-light conditions depicted in Figure 3 (a) significantly challenge the detection of any particles, the accumulation of synthetic events depicted in (b) allows the particles to be visually distinguished from the asteroid, despite significant noise contributions from the sensor emulation (to aid in locating the particles, frame (c) depicts a noiseless emulation of the same event camera).

Conclusion

This work showcases preliminary results on the scientific use of event cameras onboard a spacecraft in dynamic environments around small solar system bodies. After reconstructing the scene of a particle ejection episode from the SPICE kernels of the OSIRIS-REx mission, we emulate the viewpoint of an event camera to gain familiarity with event-based representations of particle tracks. In follow-up work, we will evaluate the formulation of a multi-object tracking problem, given event-based observations of an unknown (and potentially time-varying) number of particles. Multi-object tracking algorithms may be applied directly to the event-frames shown in Figure 3. However, this defeats the purpose of emulating an event camera in the first place, as by so doing, solutions do not take full advantage of the sparsity and temporal resolution of the data. Instead, we will consider approaches that process events in an online manner.

References

- [1] Lauretta, D. S. et al. (2019). Episodes of particle ejection from the surface of the active asteroid (101955) Bennu. *Science*, 366 (6470), <https://doi.org/10.1126/science.aay3544>

- [2] Chesley, S. R. et al. (2020). Trajectory estimation for particles observed in the vicinity of (101955) Bennu. *Journal of Geophysical Research: Planets*, 125, e2019JE006363. <https://doi.org/10.1029/2019JE006363>
- [3] Liounis, A. J. et al. (2020). Autonomous detection of particles and tracks in optical images. *Earth and Space Science*, 7, e2019EA000843. <https://doi.org/10.1029/2019EA000843>
- [4] Liu, S.-C., & Delbruck, T. (2010). Neuromorphic sensory systems. *Current Opinion in Neurobiology*, 20 (3), 288-295. <https://doi.org/10.1016/j.conb.2010.03.007>
- [5] Gallego, G. et al. (2022). Event-based vision: A survey. *IEEE Transactions on Pattern Analysis and Machine Intelligence*, 44 (1), 154-180. <https://doi.org/10.1109/TPAMI.2020.3008413>
- [6] Lagorce, X. et al. (2015). Asynchronous Event-Based Multikernel Algorithm for High-Speed Visual Features Tracking. *IEEE Transactions on Neural Networks and Learning Systems*, vol. 26, no. 8, pp. 1710-1720. <https://doi.org/10.1109/TNNLS.2014.2352401>
- [7] Izzo, D. et al. (2022). Neuromorphic computing and sensing in space. *arXiv preprint arXiv:2212.05236*. <https://doi.org/10.48550/arXiv.2212.05236>
- [8] Chin, T.-J., et al. (2019). Star tracking using an event camera. In *2019 IEEE/CVF Conference on Computer Vision and Pattern Recognition Workshops (CVPRW)* (p. 1646-1655). <https://doi.org/10.1109/CVPRW.2019.00208>
- [9] Cheung, B. et al. (2018). Probabilistic multi hypothesis tracker for an event based sensor. In *2018 21st International Conference on Information Fusion (fusion)* (p. 1-8). <https://doi.org/10.23919/ICIF.2018.8455718>
- [10] Afshar, S. et al. (2020). Event-Based Object Detection and Tracking for Space Situational Awareness. *IEEE Sensors Journal*, vol. 20, no. 24, pp. 15117-15132. <https://doi.org/10.1109/JSEN.2020.3009687>
- [11] Oliver, R. et al. (2022). Event-based sensor multiple hypothesis tracker for space domain awareness. In *AMOS Conference 2022*. <https://doi.org/10.5167/uzh-231276>
- [12] Hergenrother, C. W. et al. (2020). Photometry of particles ejected from active asteroid (101955) Bennu. *Journal of Geophysical Research: Planets*, 125, e2020JE006381. <https://doi.org/10.1029/2020JE006381>
- [13] Pajusalu M. et al. (2022) SISPO: Space Imaging Simulator for Proximity Operations. *PLOS ONE* 17(3): e0263882. <https://doi.org/10.1371/journal.pone.0263882>
- [14] Gehrig, D. et al. (2020). Video to events: Recycling video datasets for event cameras. In *2020 IEEE/CVF Conference on Computer Vision and Pattern Recognition (CVPR)* (p. 3583-3592). <https://doi.org/10.1109/CVPR42600.2020.00364>
- [15] Hu, Y. et al. (2021). v2e: From Video Frames to Realistic DVS Events. *2021 IEEE/CVF Conference on Computer Vision and Pattern Recognition Workshops (CVPRW)*, Nashville, TN, USA, 2021, pp. 1312-1321, <https://doi.org/10.1109/CVPRW53098.2021.00144>
- [16] Prophesee.ai. Metavision SDK Docs – Recordings and Datasets, <https://docs.prophesee.ai/>

Totimorphic structures for space application

Amy Thomas^{1,a*}, Jai Grover^{1,a}, Dario Izzo^{1,a} and Dominik Dold^{1,a}

¹European Space Agency, Advanced Concepts Team, European Space Research and Technology Centre, Keplerlaan 1, 2201 AZ Noordwijk, The Netherlands

^a{firstname.surname}@esa.int

Keywords: Morphing Structure, Deployable Structure, Multi-Functional Metamaterial, Totimorphic, Programmable Material

Abstract. We propose to use a recently introduced *Totimorphic* metamaterial for constructing morphable space structures. As a first step to investigate the feasibility of this concept, we present a method for morphing such structures autonomously between different shapes using physically plausible actuations. The presented method is part of a currently developed Python library bundling non-rigid morphing and finite element analysis code, which will be made publicly available in the future. With this work, we aim to lay a foundation for exploring a promising and novel class of multi-functional, reconfigurable space structures.

Introduction

The last decade has seen rapid expansion and interest in the field of advanced materials and structures, especially in the development of programmable, multi-functional, and morphable structures. Such structures are particularly suited for space environments, where payload mass and volume are tightly constrained, making light structures capable of performing multiple functions highly desirable. For instance, Origami principles have already been used in the development of deployable solar panels and antennae, and applications for other advanced structures, such as NASA's starshade [1], have been proposed [2,3]. However, most deployable space structures are currently limited between strict configurations (typically stowed and deployed), often prohibiting any reconfiguration thereafter.

Here, we explore a recently proposed metamaterial called a *Totimorphic structure* [4] whose characteristic properties might enable designs capable of redeployment and reconfiguration into many different shapes after initial deployment. This is especially intriguing for constructing adaptive structures, as many recent papers [5,6] have demonstrated the feasibility of changing a structure's mechanical properties through geometric alterations alone. Such systems might enable mission designs capable of complex and efficient post-launch reconfiguration, adjusting to changing mission goals or conditions in situ and providing space missions with greater flexibility, thus fundamentally changing the types of missions possible in the future.

In the following, we first explain the concept of totimorphic structures before introducing a computational method for obtaining the actuations needed to morph them into different shapes.

Methodology

Totimorphic structures are composed of neutrally-stable unit cells (also called Totimorphic Unit Cells, TUCs) [4] shown in Fig. 1a,b. A TUC consists of a beam with a ball joint in its middle (A-P-B in Fig. 1a), a lever connecting to the joint (P-C) and two springs connecting the ends of the beam with the end of the lever (A-C and B-C). The neutrally stable behaviour of TUCs arises from the lever-spring motive: if the two springs are zero-length springs with identical spring stiffness, any position of the lever results in zero moment acting on the lever. The result of this property is propagated across larger structures built from TUCs (e.g. Fig. 1c), such that in the absence of external forces (e.g. gravity), the totimorphic structure will retain its shape while remaining



completely compliant to any external force or displacement. By selective locking and unlocking of the structure's joints, we predict that the totimorphic property will allow the structure to be smoothly morphed between different shapes via beam/lever rotations alone – which we exploit in our method presented in the next section. Once the desired target shape is reached, the structure can be made rigid by locking all joints.

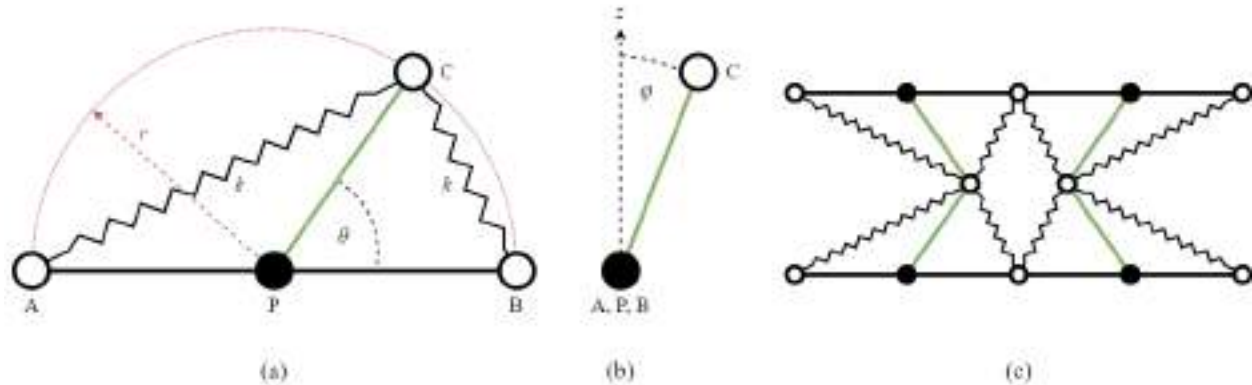


Figure 1: (a) Illustration of a TUC with lever rotation θ . (b) The TUCs beam rotation is given by ϕ , i.e., A-P-B is seen from the side here. (c) A simple auxetic structure built from four TUCs.

Before presenting our approach for morphing such structures, we first introduce the used mathematical description. Each TUC is geometrically fully defined by its position vector P , the beam vector AB , the lever length r , the angle between beam and lever θ , and the roll angle of the lever from the vertical ϕ (Fig. 1b). TUCs may be connected to each other at the A, B, C nodes, however for this paper's analysis, only A-B and C-C connections were considered. Additionally, r was set to be equal for all TUCs. If the coordinates of A, B or C are already known (i.e. the unit cell is attached to another unit cell), the unit cell can be described just by AB , θ , and ϕ – which is useful for implementing the morphing method.

Results

Our morphing method works as follows. We first define the initial and target geometries, set a maximally allowed change in AB , θ , and ϕ per iteration (same for all TUCs), and a subset of nodes are set as 'pinned' (i.e. their position is fixed, but they are allowed to rotate). We also 'activate' the pinned cells, (i.e. allow them to morph). Then we run the following iteration until the structure's geometry is within some tolerance of the desired target geometry: each activated TUC changes AB , θ and ϕ as much as possible to reach its target configuration while still maintaining structural cohesion (i.e. no beams breaking/prolonging/squeezing or TUCs separating). Then they become 'fixed' (cannot be activated anymore in this iteration, so the TUCs are frozen in place) and inform their neighbouring cells that they should move next (they activate their neighbours). This process is repeated until all cells are fixed. Consequently, all TUCs are unfixed and the next iteration begins. Intuitively, a wave of 'cell activation' moves through the structure, where activated cells are moved closer to their target and become immovable (fixed) afterwards.

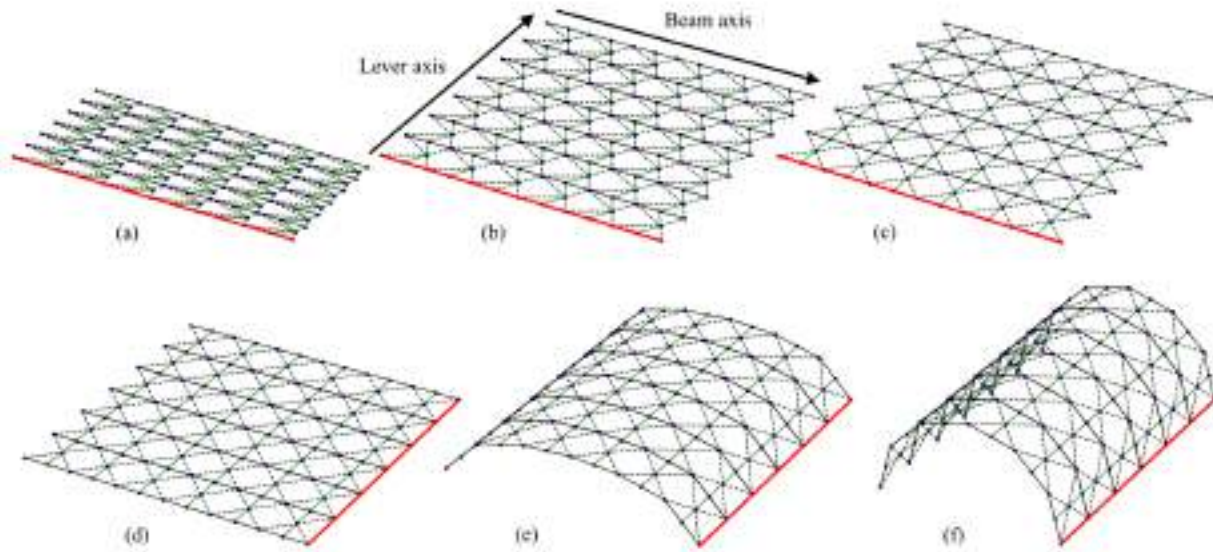


Figure 2: A totimorphic structure morphing continuously from a stowed plane to a square plane (a) $\theta=30$ (b) $\theta=60$ (c) $\theta=90$, and then into a semi-cylinder (d-f). Red lines indicate pinned nodes with fixed coordinates.

The morphing method is illustrated in Fig. 2 for continuously morphing a structure to different target shapes: (a-c) turning a stowed geometry into a large flat surface, and (d-f) turning the flat surface into a half-cylinder. Although we halt at the shape in Fig. 2f here, in principle the structure can be mapped to any developable surface of an equal or smaller surface area [4], so long as there is a valid target geometry for the method.

In comparison with an Origami structure, which must necessarily unfold and change its thickness during deployment, we can see in (a-c) that the stowed totimorphic structure can continuously increase its surface area without any increase in the stowing thickness, resulting in a large stowed-to-deployed surface area ratio. Further, the stowing of the totimorphic structure does not constrain its final structural geometry, since it is possible for the structure to morph into intermediary states that enable better deployment before morphing into the final configuration.

Discussion

For the presented method to work, one requires knowledge about the exact initial and target configuration of the totimorphic structure (including angles) instead of just the shapes. Moreover, the choice of pinned nodes is crucial to ensure convergence to the target shape. Thus, we plan to develop an improved non-rigid morphing methodology that is both more robust and general, based on a model that predicts the whole structure's response to small perturbations. Such a model might further allow us to use inverse design approaches from artificial intelligence [6] to autonomously find configurations that possess desired effective mechanical properties.

Although totimorphic structures are more flexible in their morphing capabilities than Origami-based structures, they come with the drawback of having a high number of degrees of freedom as well as many movable mechanical parts. We anticipate that this will lead to challenges in the production of a physical prototype, which have to be overcome first for totimorphic structures to compete with alternative approaches. For instance, the neutrally stable behaviour will most likely not be perfectly realised in a physical system due to effects such as bending of the beam in a TUC from radial forces applied through the lever – an effect that has to be considered during the design and testing stages of a real prototype.

We are confident that totimorphic structures are ideally suited for deployment in extremely-low gravity environments such as orbits and deep space, where no external loads due to gravity interfere with the morphing process and the neutrally stable behaviour can be utilised to its fullest. As noted in [7], the gravitational forces experienced on planetary bodies will impede the morphing of totimorphic structures, the extent of which has to be investigated in future work.

To lock and unlock the joints as well as induce beam/lever rotations, we envision a thin and foldable support layer glued to the totimorphic structure through which lock, unlock and rotation commands, e.g., from a microcontroller, can be relayed electronically. For instance, since only a small number of cells are unlocked at a time, electrical pulses could be used with a shared bus to realise an efficient and economic solution.

Conclusion

Totimorphic structures offer unique structural characteristics that make them ideal for space missions – providing a high degree of flexibility coupled with a low mass and volume. They are suitable for a multitude of potential space applications; such as deployable habitats and structures, tools (e.g. nets for grabbing something), or for building moving structures by creating locomotion from morphing. Hence, we believe that totimorphic structures are a promising candidate in the search for technologies that enable morphable, multi-functional space structures.

Acknowledgments

We would like to thank Derek Aranguren van Egmond and Michael Mallon for helpful discussions, and our colleagues at ESA's Advanced Concepts Team for their ongoing support. AT and DD acknowledge support through ESA's fellowship and young graduate trainee programs.

References

- [1] Information on <https://exoplanets.nasa.gov/exep/technology/starshade/>. Accessed: 05/07/23.
- [2] Ynchausti, C., Roubicek, C., Erickson, J., Sargent, B., Magleby, S. P., and Howell, L. Hexagonal Twist Origami Pattern for Deployable Space Arrays ASME Open J. Engineering ASME. January 2022 1 011041 doi: <https://doi.org/10.1115/1.4055357>
- [3] Biswas, A., Zekios, C.L., Ynchausti, C. et al. An ultra-wideband origami microwave absorber. Sci Rep 12, 13449 (2022). <https://doi.org/10.1038/s41598-022-17648-4>
- [4] Chaudhary, G., Ganga Prasath, S., Soucy, E. and Mahadevan, L., 2021. Totimorphic assemblies from neutrally stable units. Proceedings of the National Academy of Sciences, 118(42), p.e2107003118. <https://doi.org/10.1073/pnas.2107003118>
- [5] Yazdani, H., Aranguren van, D., Esmail, I., Genest, M., Paquet, C., Ashrafi, B., Bioinspired Stochastic Design: Tough and Stiff Ceramic Systems. Adv. Funct. Mater. 2022, 32, 2108492. <https://doi.org/10.1002/adfm.202108492>
- [6] Dominik Dold, Derek Aranguren van Egmond, Differentiable graph-structured models for inverse design of lattice materials, arXiv (2022), <https://doi.org/10.48550/arXiv.2304.05422>
- [7] Schenk, M. and Guest, S.D., 2014. On zero stiffness. Proceedings of the Institution of Mechanical Engineers, Part C: Journal of Mechanical Engineering Science, 228(10), pp.1701-1714. <https://doi.org/10.1177/0954406213511903>

Pushing the limits of re-entry technology: an overview of the Efesto-2 project and the advancements in inflatable heat shields

Giuseppe Guidotti¹, Giuseppe Governale^{2,*}, Nicole Viola², Ingrid Dietleinc,
Steffen Callsen³, Kevin Bergmann³, Junnai Zhai⁴, Roberto Gardi⁵,
Barbara Tiseo⁵, Ysolde Prevereaud⁶, Yann Dauvois⁶, Giovanni Gambacciani⁷,
Giada Dammacco⁷

¹DEIMOS Space S.L.U, Tres Cantos 28760, Spain

²Department of Mechanical and Aerospace Engineering, Politecnico di Torino, Turin – Italy

³Deutsches Zentrum für Luft- Und Raumfahrt e.V. (DLR), Bremen 28359, Germany

⁴Deutsches Zentrum für Luft- Und Raumfahrt e.V. (DLR), Köln, Germany

⁵Centro Italiano Ricerche Aerospaziali (CIRA), Capua – Caserta, Italy

⁶Office National d'Etudes et de Recherches Aerospatiales (ONERA), Toulouse, France

⁷Pangaia Grado Zero SRL (PGZ), Firenze 50056, Italy

*giuseppe.guidotti@deimos-space.com; giuseppe.governale@polito.it

Keywords: Re-Entry Technology, Inflatable Heat Shields, Thermal Protection System, Horizon Europe

Abstract. As space exploration technology advances, the need for reliable re-entry systems becomes increasingly critical. The European Flexible Heat Shields: Advanced TPS Design and Tests for Future In-Orbit Demonstration – 2 (EFESTO-2) project is a Horizon Europe-funded initiative aimed at improving the Technology Readiness Level of Inflatable Heat Shields (IHS), an innovative thermal protection system that can be deployed during re-entry. The project seeks to further advance the work achieved in the EFESTO project, with a focus on expanding investigations into critical aspects of IHS and increasing the confidence level and robustness of the tools and models used in the field. The EFESTO-2 project is built on four pillars, including consolidating the use-case applicability through a business case analysis for a meaningful space application, extending the investigation spectrum of the father project EFESTO to other critical aspects of the IHS field, increasing the confidence level and robustness of tools/models, and consolidating the roadmap to guarantee continuity in presiding the IHS field in Europe among the scientific and industrial community. This paper provides an overview of the EFESTO-2 project's objectives, achievements, ongoing activities, and planned activities up to completion. The project's advancements in the fields of thermal protection systems, inflatable heat shields, and technology readiness level are described in detail, highlighting the project's contributions to the European re-entry technology roadmap. Through this project, the European Space Program aims to push the limits of re-entry technology and reinforce its position as a leader in innovative technology for space exploration. This project has received funding from the European Union's Horizon Europe research and innovation program under grant agreement No 1010811041.



Introduction

The EFESTO-2 project builds upon the success of the previous H2020 EFESTO project and aims to advance European expertise in the field of Inflatable Heat Shields (IHS). With the increasing demand for reusable space transportation systems, the development of innovative thermal protection solutions is crucial for safe and cost-effective space missions. Inflatable Heat Shields have shown great potential in enabling controlled re-entry and recovery of spacecraft, making them a promising technology also for future space exploration missions.

Project Objectives

The EFESTO-2 project, funded by the European Union's Horizon Europe program, aims to achieve the following objectives. Firstly, it seeks to consolidate the use-case applicability of Inflatable Heat Shields (IHSs) through a comprehensive business case analysis for a meaningful space application. Secondly, it aims to expand the investigation spectrum by conducting extensive tests focused on aerodynamics and mechanical aspects, complementing the previous EFESTO project. Thirdly, the project aims to enhance the confidence level and robustness of the tools and models developed in EFESTO by incorporating test data. Lastly, it aims to consolidate the definition of a roadmap towards the near-future development of IHS technology up to Technology Readiness Level 7 (TRL7). The study-logic applicable within the EFESTO-2 initiative for implementing the planned effort is represented in Figure 1.



Figure 1 EFESTO-2 project study-logic

Business Case Analysis

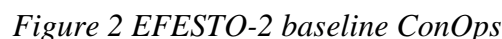
The Business Case Analysis (BCA) was conducted as the initial task in the EFESTO-2 project to identify the most promising use-case application for inflatable heat shields (IHSs) and guide the subsequent design study for a reference mission/system. The BCA focused on exploring potential applications of IHSs in the re-entry and recovery of space systems meant for reuse. Examples of potential applications included the recovery of launch system stages, ISS cargo systems, and de-orbiting and recovery of reusable satellites.

The BCA workflow involved several stages. An overview of target markets for IHS technology was conducted, followed by the identification of the most promising commercial applications using a trade-off analysis. Qualitative evaluations were performed using frameworks such as SWOT and PESTEL, considering market trends, substitutes, competitors, and potential customers. Additionally, a cost-oriented assessment of a reference use-case for re-entry and recovery was carried out.

The evaluation of IHSs application scenarios considered different planetary re-entry scenarios, including Earth, Mars, and others. The trade-off criteria included market size, market timeline, complexity, and technological score. The outcomes indicated that stage reusability, small payload recovery, and space mining cargo recovery were promising applications for IHS adoption.

Therefore, the recovery of an LV stage will serve as the reference use-case for the subsequent work presented in the conference paper.

A review of over 70 launch systems worldwide resulted in the identification of 20 potential candidates. Key parameters and indicators were considered to classify the launch systems into four clusters. Cluster II was selected as the most promising due to its compatibility with the IHS technology development and a significant technology development step already taken during the EFESTO project. The concept of operations (ConOps) for the Inflatable Heat Shield exploitation is based on the recovery of a launch vehicle upper stage. The ConOps includes two main phases: LEOP/ORBITAL and RECOVERY. The baseline strategy for the EFESTO-2 project is to execute the recovery via mid-air retrieval by helicopter. The engineering effort focused on the re-entry part of the recovery, and the descent and mid-air retrieval phases are out-of-scope.



A parametric analysis was conducted to determine the combination of boundary conditions that offer a good initial flight path angle range and compliance with system constraints. Reference and sizing trajectories were calculated, and a Monte Carlo analysis confirmed compliance with all constraints.

System Design

578

estimation. Further efforts were made to reduce system mass, resulting in a minor reduction in the diameter of the inflated IHS.

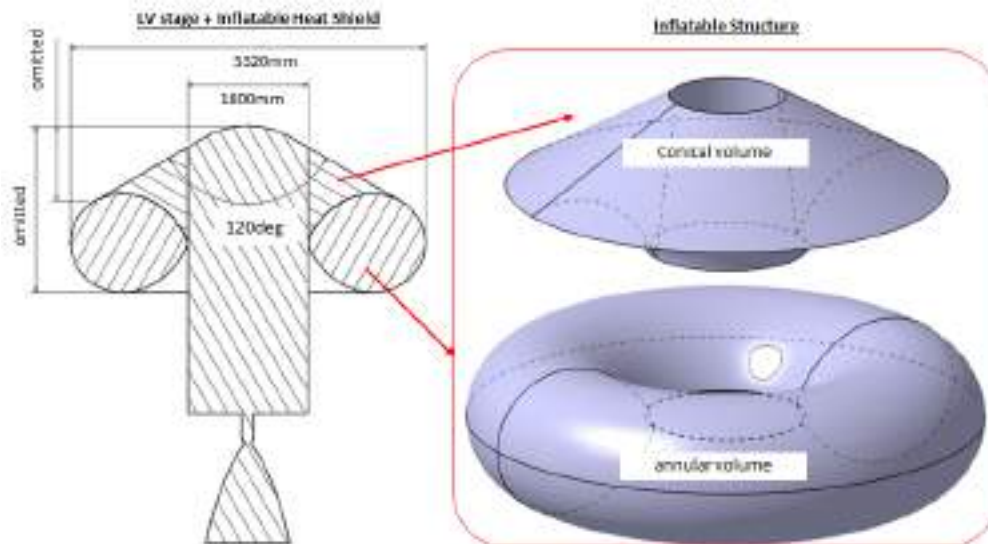


Figure 3 LV-stage and Inflatable Heat Shield integration (left), Inflatable Structure model (right)

Future Work

In the future, the project will focus on conducting ground tests for aerodynamics and flying qualities, as well as mechanical characterization of the Inflatable Structure. The aerodynamics testing will involve wind tunnel experiments with subscale models to study stability, while the mechanical characterization will use a ground demonstrator to evaluate structural behavior. The collected data will be used to improve numerical models and enhance the understanding of inflatable heat shield technology. The project aims to consolidate the technology up to TRL7 and has made progress in the initial stages, including a Business Case Analysis and reference system design. The project will conclude with test campaigns and the dissemination of findings through additional papers.

Acknowledgement

The EFESTO-2 project acknowledges the funding received from the European Union Horizon Europe research and innovation programme under grant agreement No 1010811041.

References

- [1] Hughes, S. J. et al. 2013. Hypersonic Inflatable Aerodynamic Decelerator (HIAD) Technology Development Overview. In: 13rd International Planetary Probe Workshop.
- [2] Marraffa, L., Boutamine, D. 2006. IRDT 2R Mission, First Results". In Proceedings of the 5th European Workshop of Thermal Protection Systems and Hot Structures. Edited by K. Fletcher. ESA SP-631.
- [3] LOFTID flight: <https://www.nasa.gov/feature/loftid-inflatable-heat-shield-test-a-success-early-results-show>
- [4] Dillman, R. A. et al. 2018. Planned Orbital Flight Test of a 6m HIAD. In: 15th International Planetary Probe Workshop.
- [5] Guidotti, G. et al. 2022. The EFESTO project: Advanced European re-entry system based on inflatable heat shield. In: 2nd International Conference on Flight Vehicles, Aerothermodynamics and Re-entry Missions & Engineering, Heilbronn, Germany, 2022.
- [6] Schleutker, T. et al. 2022. Flexible TPS design and testing for advanced European re-entry system based on inflatable heat shield for EFESTO project. In: 2nd International Conference on

Flight Vehicles, Aerothermodynamics and Re-entry Missions & Engineering, Heilbronn, Germany, 2022.

[7] Gardi, R. et al. 2022. Design development and testing of the Inflatable Structure and its Demonstrator for the EFESTO project. In: 2nd International Conference on Flight Vehicles, Aerothermodynamics and Re-entry Missions & Engineering, Heilbronn, Germany, 2022.

[8] DeRoy S.R., et al. 2016. Vulcan, Aces And Beyond: Providing Launch Services For Tomorrow's Spacecraft. AAS 16-052.

[9] Chandra, A., Thangavelautham, J. 2018. De-orbiting Small Satellites Using Inflatables. Space and Terrestrial Robotic Exploration Laboratory, Department of Aerospace and Mechanical Engineering, University of Arizona

[10] Andrews, J. et al. 2011. Nanosat Deorbit and Recovery System to Enable New Missions. In: 25th annual AIAA/USU Conference on Small Satellites. SSC11-X-3.

The ATEMO device: a compact solution for earth monitoring

Federico Toson^{1,a*}, Alessio Aboudan^{1,b}, Carlo Bettanini^{1,2,c},
Giacomo Colombatti^{1,2,d}, Irene Terlizzi^{3,e}, Sebastiano Chiodini^{1,2,f},
Lorenzo Olivieri^{1,g}

¹ CISAS G. Colombo, University of Padova, Italy

² DII, University of Padova, Italy

³ DAFNAE, University of Padova, Italy

^afederico.toson@phd.unipd.it, ^balessio.aboudan@unipd.it, ^ccarlo.bettanini@unipd.it,
^dgiacomo.colombatti@unipd.it, ^eirene.terlizzi@unipd.it, ^fsebastiano.chiodini@unipd.it,
^glorenzo.olivieri@unipd.it

Keywords: Earth Monitoring, Light Pollution, Air Pollution, Vegetation Indices

Abstract. In today's context, where climate change is increasingly topical and of global interest, the ATEMO (Atmospheric Technologies for Earth Monitoring and Observation) project proposes a multi-purpose solution, which can be integrated on board drones or stratospheric balloons, to provide a framework for environmental assessment in areas of interest. Specifically, ATEMO, equipped with a set of cameras and sensors, aims to enrich data on air pollution, light pollution and vegetation health with high spatial resolution and rapid deployment.

Introduction

In environmental protection, monitoring activities are crucial for determining preventive strategies or large-scale solutions; particular interest is arisen regarding Earth observation from space [1]. However, due to low spatial and, mainly, temporal resolution of such instrumentation, information about an area or site of interest is often not sufficient and may need to be validated by other measurement and analysis methods.

The ATEMO project therefore aims to increase knowledge on environmental issues with the development of a versatile device that can be used in various contexts and environments, from the analysis of atmospheric composition, through the detection of substances and pollutants such as VOCs (Volatile Organic Compounds), NO_x (Oxides of Nitrogen), SO_x (Oxides of Sulphur), CO₂ (Carbon Dioxide), O₃ (Ozone), to the determination of ground-based light sources and their characterisation. Furthermore, in order to understand how these factors may influence ecosystems, ATEMO also aims to determine ground vegetation indices (e.g. the NDVI - Normalized Difference Vegetation Index). The ultimate goals are comparing these data with the ones obtained from satellites [2] and to look for a correlation between the various investigated parameters. In fact, while the influence of air pollutants and night lighting on ecosystems, plants and humans is already known [3], recent studies suggested that the combined effect of light and air pollution leads to the formation of harmful and worsening reaction by-products [4] of the already critical situation.

In the remainder of this paper, the ATEMO device will be introduced, and the main design solutions will be described: the selected solution allows compactness and integrability on different vehicles (drones, tethered balloons and stratospheric balloons). Last, the tests campaign planned to validate the device functional requirements will be briefly introduced.

Design of ATEMO experiment

Due to the desired versatility of ATEMO, the device is strictly constrained in both mass and size. The device has a weight of 2.5 kg, a base of 17 cm x 17 cm and a height of 25 cm; as shown in Fig. 1, the instrument consists of an external aluminium frame to which are attached 3D-printed



components that guarantee both the safe integration of the various sensors and cameras and their easy attachment and removal in the event of a change of setup. In fact, one of ATEMO's main strengths is its modularity and scalability, which allows it to best adapt its physical and measurement characteristics to the application context.

Regarding the sensing part of the device, ATEMO is equipped with two cameras (one monochrome and one colour) Basler ace 2 both with Sony's IMX546, an 8MP square CMOS sensor with a wide relative response spectrum (from approximately 400 nm to 1000 nm). In addition, a FLIR typology Vue Pro R thermal imaging camera is mounted on board. There are also several sensors for temperature, pressure, humidity, detection of O₃, CO₂ and other substances, a GPS tracking system and an SQM-L (Sky Quality Meter - L type), a sensor that allows to measure the brightness of the night sky in magnitudes per square arc second.

The two cameras are used for two main purposes: the estimation of vegetation indices during the day and the analysis of light sources at night. For the two cases, the setup of the cameras obviously slightly changes in function of the required light filtering. In the case of the vegetation analysis, the colour camera is equipped with a triple-band filter (475, 550 and 850 nm) and the monochrome camera with a band-pass filter (735 nm), both of which are designed to reproduce indices already calculated by means of Planet satellites [5]. In the night-time application, however, the two cameras are used with a filtering solution similar to that of the MINLU experiment [6], another project conducted by our research group. In order to easily switch filters, a filter wheel driven by a stepper motor has been chosen; its attachment points can be seen in Fig.1, at the centre of the camera compartment in the view from below.

The cameras field of view (FOV) is another additional key point to consider. In fact, the choice of optics is made according to the host vehicle; in the case of integration on drones or balloons tethered at a height of 50-100 m, optics with large apertures are used, while in the case of stratospheric balloons, optics with much narrower apertures are favoured.



Figure 1: On the left: the complete assembled experiment. On the right the main components: the SQM with its 3D-printed baffled and the cameras at the bottom.

The system is controlled by a Raspberry Pi 3, programmed with Python, which, thanks to a 20000 mAh lithium battery, acquires data from on-board instrumentation and manages electrical and electronic systems for more than 6 hours. ATEMO's power consumption is in the range between 6 W and 14 W, depending on the sampling frequency and the subsystems in use.

For a correct interpretation of the data provided by ATEMO, a calibration using a commercial spectrometer (Black Comet C-SR-14) was necessary; the on-board cameras were characterised in the various filtering configurations since the input information is affected by the transmission of

the optics, the filter, and the response of the CMOS sensor. Using a selection of known sources and the spectrometer, the response function of the system was thus defined, making the collected results consistent and comparable with those of other measurement systems (e.g., satellites).

It shall be underlined that the current design choices may be affected by the experimental activities planned in the next years and briefly introduced in the following section; thanks to its modularity, it is expected to easily adapt ATEMO with only minor modifications to the bus.

Test programme

Several test campaigns have been planned over the next three years to verify the functioning of ATEMO. These campaigns retrace previous experiments already conducted by the research group, but with a more compact configuration that encompasses them all.

This summer (2023), some experiments have already begun in collaboration with the Department of Agronomy, Food, Natural Resources, Animals, and the Environment (DAFNAE) of the University of Padova. The aim is to evaluate the effects of differential irrigation of soybean fields in order to understand whether it is possible to obtain abundant harvests with a considerable saving of water. In this situation, the experiment is integrated aboard a tethered balloon and stationed for a day at the same location at a height of 50 metres (Fig. 2).

Of course, this is only one of the possible configurations in which ATEMO will be involved in measurement campaigns. In the coming months, in fact, other collaborations will be launched, e.g. with the Chilean PUCV (Pontificia Universidad Católica de Valparaíso) University for the determination of light pollution.



Figure 2: In the first two photos, on the left, the release phase, on the right, the tethered balloon at an altitude of 50 metres.

Conclusions

In this paper, the ATEMO device for Earth monitoring has been presented. To date, the device is in the early stages of testing; the different application cases will be investigated in the next months. Functional and operational tests will be consequently performed by the research team, which has an excellent knowledge of drone flights [7], stratospheric balloons [8] and the assessment of air [9] and light pollution [10].

In conclusion, ATEMO is promising for its potential to provide a global environmental image of an area of interest, thus proving useful in a variety of fields, from atmospheric monitoring in populated areas to precision agriculture and in the verification of satellite data.

Acknowledgments

Design, manufacturing, testing and validation of ATEMOS acquisitions are possible thanks to the collaborations between CISAS G. Colombo with the Department of Industrial Engineering (DII) and the Department of Agronomy, Food, Natural Resources, Animals, and the Environment (DAFNAE) of the University of Padova. Soybean analyses are performed in the framework of the Prin (Project of Significant National Interest) 'Rewatering'; the light pollution activities are in collaboration with the Chilean PUCV University.

References

- [1] "Europe's eyes on Earth," U.E., 2022. [Online]. Available: <https://www.copernicus.eu/en>.
- [2] "Sentinel Online," ESA, [Online]. Available: <https://sentinels.copernicus.eu>.
- [3] J. Schwartz, "The Distributed Lag between Air Pollution and Daily Deaths," *Epidemiology*, vol. 11, no. 3, pp. 320-326, May 2000. <https://doi.org/10.1097/00001648-200005000-00016>
- [4] F. E. Blacet, "Photochemistry in the lower Atmosphere," in *XIIth International Congress of Pure and Applied Chemistry*, New York, 1951.
- [5] Planet, "Daily Earth Data to See Change and Make Better Decisions," Planet, 2023. [Online]. Available: <https://www.planet.com>.
- [6] C. Bettanini, M. Bartolomei, A. Aboudan, G. Colombatti and P. Fiorentin, "Evaluation of light pollution sources over Tuscany with an autonomous payload for sounding balloons," in *Aerospace Europe Conference*, Warsaw, 2021.
- [7] G. M. Bolla, M. Casagrande, A. Comazzetto, R. Dal Moro, M. Destro, E. Fantin, G. Colombatti, A. Aboudan and E. C. Lorenzini, "ARIA: Air Pollutants Monitoring Using UAVs," in *5th IEEE International Workshop on Metrology for AeroSpace (MetroAeroSpace)*, Rome, 2018. <https://doi.org/10.1109/MetroAeroSpace.2018.8453584>
- [8] M. Fulchignoni, A. Aboudan, F. Angrilli, M. Antonello, S. Bastianello, C. Bettanini, G. Bianchini, G. Colombatti, F. Ferri and e. al, "A stratospheric balloon experiment to test the Huygens atmospheric structure instrument (HASI)," *Planetary and Space Science*, vol. 52, pp. 867-880, 18 May 2004. <https://doi.org/10.1016/j.pss.2004.02.009>
- [9] F. Toson, M. Pulice, M. Furiato, M. Pavan, S. Sandon, D. Sandu and R. Giovanni, "Launch of an Innovative Air Pollutant Sampler up to 27,000 Metres Using a Stratospheric Balloon," *Aerotecnica Missili & Spazio*, vol. 102, no. 2, pp. 127-138, June 2023. <https://doi.org/10.1007/s42496-023-00151-y>
- [10] C. Bettanini, M. Bartolomei, P. Fiorentin, A. Aboudan and S. Cavazzani, "Evaluation of Sources of Artificial Light at Night With an Autonomous Payload in a Sounding Balloon Flight," *IEEE Journal of selected topics in applied Earth observations and remote sensing*, vol. 16, pp. 2318-2326, 2023. <https://doi.org/10.1109/JSTARS.2023.3245190>

The Hera Milani mission

M. Cardi^{1,a,*}, M. Pavoni^{1,b}, D. Calvi^{1,c}, F. Perez², P. Martino², I. Carnelli²
and Milani consortium members

¹Tyvak International srl, Via Orvieto 19, 10149 Torino (TO), Italy

²European Space Research & Technology Centre (ESTEC), ESA, Postbus 299, 2200 AG, Noordwijk, The Netherlands

^amargherita@tyvak.eu, ^bmarco.pavoni@tyvak.eu, ^cdaniele.calvi@tyvak.eu

Keywords: Asteroid, Nanosatellite, Hera, Milani, Impact, Didymos

Abstract. Hera is the European part of the Asteroid Impact & Deflection Assessment (AIDA) international collaboration with NASA who is responsible for the DART (Double Asteroid Redirection Test) kinetic impactor spacecraft. Hera will be launched in October 2024 and will arrive at Didymos in January 2027. The Hera mothercraft will accommodate two 6U Nanosatellite, Milani and Juventas. The Milani Nanosatellite is developed by Tyvak International leading a consortium of European Universities, Research Centers and Firms from Italy, Czech Republic, Finland. During the cruise to the Asteroid (+2 years), Milani Nanosatellite will be hosted inside the Hera mothercraft, periodically checked for health and charged. At arrival it will be deployed and commissioned while HERA is performing the Didymos detailed characterization phase, at about 10 to 20 km distance from the asteroid. The Milani mission objectives are defined as to add scientific value to the overall Hera mission: i) Map the global composition of the Didymos asteroids, ii) Characterize the surface of the Didymos asteroids, iii) Evaluate DART impacts effects on Didymos asteroids and support gravity field determination, iv) Characterize dust clouds around the Didymos asteroid, enhancing the scientific return of the whole HERA mission. The scientific payloads supporting the achievement of these objectives are the main Payload “ASPECT” (developed by VTT, Finland), a SWIR, NIR and VIS imaging spectrometer and the secondary Payload “VISTA” (developed by INAF, Italy), a thermogravimeter aiming at collecting and characterizing volatiles and dust particles below 10µm. The Milani mission and the project team is facing challenges such as, among others, the use of COTS components in deep space environment, optical navigation implementation, interfaces management with the HERA mothercraft since the very beginning of the design up to the mission. Tyvak International work focuses on the development and integration of the Milani vehicle, including mission specifics development enabling the mission and vehicle models enabling early interface testing with Hera mothercraft.

Introduction

In 2027, the Hera spacecraft will rendezvous with the binary asteroid 65803 Didymos as the European contribution to the AIDA (Asteroid Impact and Deflection Assessment) international collaboration. NASA is responsible for the Double Asteroid Redirection Test (DART) kinetic impactor spacecraft. Hera and DART have been conceived to be mutually independent, however, their value is increased when combined. Indeed, Hera is a planetary defense mission aimed to investigate the effect of DART impact, with clear scientific objectives as a bonus. In proximity to the target, Hera will release two 6U Nanosatellites called Milani and Juventas. The two nanosatellites will be the first Nanosatellites to orbit in the close proximity of a small body and the first to perform scientific and technological operations around a binary asteroid.



Tyvak International is responsible for the Milani system development and is leading (as Prime Contractor) a large consortium made by 10+ entities from Italy, Czech Republic and Finland. Milani will contribute to the scientific value of the Hera planetary defense mission, mainly through the visual inspection of the asteroid (main payload: ASPECT) and dust detection (secondary payload: VISTA).

Didymos properties

Didymos is a binary Near-Earth Asteroid (NEA) of S-type discovered in 1996 formed by Didymos, or D1 (the primary) and Dimorphos, or D2 (the secondary). Up-to-date data about Didymos and Dimorphos are reported in the following tables:

Table 1. Binary system parameters (semi-major axis, eccentricity, inclination, revolution period)

System parameters			
a	e	i	T
1.66446 AU	0.3839	3.4083 deg	770 days

Table 2. Didymos and Dimorphos mass and spin periods properties

System parameters			
M1	M2	T1	T2
5.226×10^{11} kg	4.860×10^9 kg	2.26h	11.92h

The orbital properties are retrieved from the up-to-date kernels of the Hera mission. In the up-to-date reference model, Dimorphos and Didymos are assumed to share the same equatorial plane on which their relative motion occurs and Dimorphos is assumed to be in a tidally locked configuration with Didymos. In this work, two reference frames are used. “DidymosEclipJ2000” is a quasi-inertial reference frame, centered in the system barycenter with the axis directed as the inertial EclipJ2000 reference frame. This frame can be considered inertial for intervals of time negligible with respect to Didymos heliocentric motion. “DidymosEquatorialSunSouth” is a non-inertial reference frame in which the trajectories are shown. It is centered in the system barycenter and has the X-Y plane on the asteroid equatorial plane. The X axis is aligned with the projection of the Sun vector on the equatorial plane and the Z-axis is aligned to the south pole of Didymos.

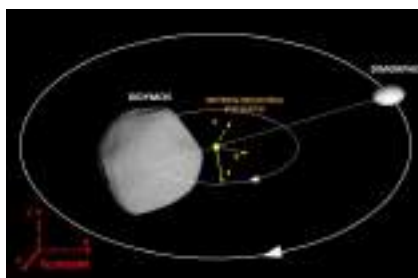


Figure 1. Didymos geometry. The reference frames are highlighted. The red frame is the inertial Eclip2000 which corresponds to the quasi-inertial DidymosEclipJ2000 when centred in the system barycentre. The yellow frame is the Didymos Equatorial Sun South (Courtesy: Politecnico di Milano)

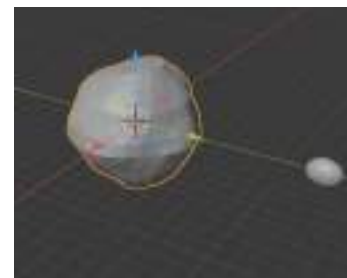


Figure 2. Didymos system geometry: polyhedral radar shape model of D1 and triaxial ellipsoidal model of D2 in D1_Body reference frame. (Courtesy: Politecnico di Milano)

Scientific goals and operational constraints

Milani scientific phases design has been mostly driven by its main payload, ASPECT. ASPECT is a passive payload, equipped with a four-channel visible to near-infrared hyperspectral imager and will be used on Milani to perform global mapping of the asteroids with detailed observation of the DART crater on Dimorphos. ASPECT main scientific goals can be summarized in three actions:

1. Imaging both the asteroids with a spatial resolution better than 2 m/pixel
2. Imaging the secondary asteroid with a spatial resolution better than 1 m/pixel
3. Imaging the DART crater with a spatial resolution better than 0.5 m/pixel at phase angle (Sun-Asteroid-Milani angle) in the range [0-10] deg and [30-60] deg.

In terms of trajectory design, spatial resolution requirements drive the maximum range at which scientific observations can be performed. From an operational point of view, Milani's communication with ground will be performed via Inter-Satellite Link (ISL) using Hera as data relay. For this reason, data downlink and uplink must be performed within the same communication windows used by Hera. Operations will be scheduled considering:

- Hera mission operations requirements
- Milani Nanosatellite mission operations requirements
- Mission Data downlink (Milani-to-Hera)
- Communication window (Hera-to-Earth)

In order to avoid open-loop manoeuvres, Milani needs to select the manoeuvring frequency to be as close as possible to Hera's pattern (4-3 days). This is not mandatory, however, it ensures the compatibility of the strategy with the requirement on the Turn-Around time (TAT)¹ of 48 h.

Scientific goals and operational constraints are the results of an initial phase of requirements definition and consolidations, led by Politecnico di Torino team and have been the main driver for the detailed design of the main phases of Milani's mission: Far Range Phase (FRP) and Close Range Phase (CRP). The scientific goals that mostly drove the mission design of Milani have been derived from its main payload, ASPECT, presented in the following sections.

Milani Mission profile and Concept of Operations (ConOps)

The Milani Mission is designed by Politecnico di Milano (PoliMI). Milani trajectory design has been mainly driven by the main scientific goals of the mission, but it has also been influenced by both technical and operational constraints. Due to the low gravity environment around the asteroids, selecting Keplerian orbits as nominal trajectories would require a demanding station keeping strategy to counteract the SRP effect. For this reason, a patched-arc manoeuvring strategy that leverages the SRP acceleration to target pre-selected waypoints has been implemented. This strategy has flight heritage in small-body environment. It is the one currently envisaged by the Hera spacecraft during its operational phases and previously performed by the Rosetta spacecraft during its initial scientific phase, after rendezvous with comet 67-P/Churyumov-Gerasimenko. The waypoints selection has been mostly influenced by the passive nature of Milani's payload as well by the on-board navigation strategy, which forces the Nanosatellite to avoid the night-side. The resulting trajectories are loop orbits with manoeuvres points placed as far away from each other as possible to maximize the time spent in proximity to the system. Main Milani mission phases are hereafter presented:



Figure 3. Milani mission phases

- **Low Earth Orbit Commissioning Phase (LEOP)**, will be done on Hera spacecraft upon launch; a specific list of checkout tests will be executed also on Milani Nanosatellite to verify the basic functionalities that can be verified in stowed and integrated Configurations
- **Mission Transfer Phase (MTP)**, or interplanetary cruise, will be characterized by regular checkout tests to be executed on Milani Nanosatellite to verify the basic functionalities
- **Ejection and separation phase (ESP)**, will start upon arrival to the asteroids and will be characterized by checkout test in stowed configuration, ejection of Milani Nanosatellite outside Hera, pre-deployment checkout in exposed configuration, Milani Nanosatellite separation from Hera
- **Commissioning Phase (COP)**, checkout, stabilization, and calibrations
- **Far Range Operations Phase (FRP)**, transfer to the operative orbits, first global mapping, and technologies demonstration
- **Close Range Operations Phase (CRP)**, transfer to the operative orbits closer to the asteroids, Close-up observation of Didymos bodies, additional technology demonstration, observation of the DART impact crater
- **Experimental Phase (EXP)**, foreseeing the landing on the asteroids or transfer on a heliocentric graveyard orbit, currently under evaluation
- **Disposal Phase (DIP)**, Passivation

System Overview

The Nanosatellite leverages on Tyvak Trestles platform architecture, avionics technology Mark II. This is a standard platform, however, some customizations were made specifically for Milani mission. In the following figure, the vehicle configuration is shown.

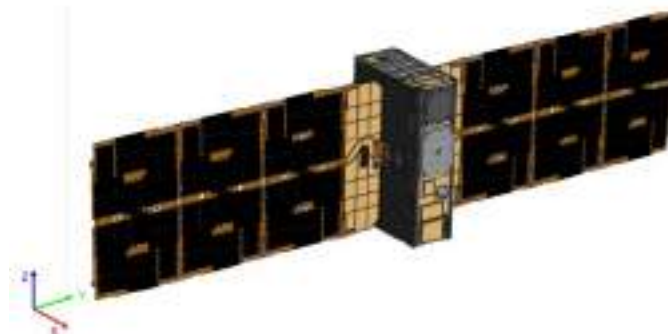


Figure 4. Milani nanosatellite – Deployed configuration

The system is composed of the following elements:

- Avionics (Tyvak Mark II technology), including Flight Computer, Electrical Power System, ADCS
- Primary Payload (ASPECT)
- Secondary Payload (VISTA)

- Cold-gas propulsion system, enabling technology
- External Inter-satellite link (ISL) radio + antennas
- Navigation Camera
- COTS components
- Mission Specific Interfaces (such as Payload Interface Board, PIB)
- Interfaces with the Hera mothercraft:
 - o Milani is integrated into the Deep Space Deployer (DSD) developed by ISIS, providing also a specific CubeSat Interface Board to interface the Milani CubeSat with the DSD
 - o The main interface with the assembly constituted by the DSD and Milani Nanosat with the Hera mothercraft is the Life Support Interface Board (LSIB), developed by KUVA Space and allowing the exchange of power and data between the two spacecraft and so the execution of the checkout tests during the stowed and exposed configuration.

A radiation-related analysis was executed to mitigate risks associated to the execution of the mission in deep space environment. The radiation analysis effort was led by Politecnico di Torino team and included both fault injection approaches and dedicated radiation testing on a subset of components identified as critical for the mission.

Conclusions

To date, the Milani project is in Assembly Integration and Test phase. Upon successful vehicle qualification, a System Validation Testing (SVT) Phase will be foreseen aiming at testing the end-to-end communication with the Hera mothercraft at ESTEC. A risk mitigation approach was implemented during the project through the reduced EM and Structural and Thermal Interface Model (STIM) development and delivery.

Acknowledgement

This work has been performed within the scope of ESA Contract No. 1222343567/62/NL/GLC. The authors would like to acknowledge the support received by the whole Milani Consortium and European Space Agency team following and supporting the Milani mission development.

References

- [1] <https://www.sciencedirect.com/science/article/pii/S0273117720309078>
- [2] <https://meetingorganizer.copernicus.org/EPSC2021/EPSC2021-732.html>
- [3] Analysis of Asteroid 65803 Didymos for the European Space Agency Asteroid Impact Mission” by P. Michel et al. (2016)
- [4] The Double Asteroid Redirection Test (DART): Deflection and Impact Monitoring (DIM) Mission” by Carnelli et al. (2020)

Small celestial body exploration with CubeSat Swarms

Emmanuel Blazquez^{1,a *}, Dario Izzo^{1,b}, Francesco Biscani², Roger Walker³ and Franco Perez-Lissi³

¹European Space and Research Technology Centre, Advanced Concepts and Studies Office, European Space Agency, Keplerlan 1, 2201AZ Noordwijk (The Netherlands)

² European Space Operations Centre, , European Space Agency, Robert-Bosch-Straße 5, 64293 Darmstadt (Germany)

³ European Space and Research Technology Centre, Cubesat Systems Unit, European Space Agency, Keplerlan 1, 2201AZ Noordwijk (The Netherlands)

^aemmanuel.blazquez@esa.int, ^bdario.izzo@esa.int

Keywords: CubeSat Swarms, Small Celestial Bodies, Mission Analysis

Abstract. This work presents a large-scale simulation study investigating the deployment and operation of distributed swarms of CubeSats for interplanetary missions to small celestial bodies. Utilizing Taylor numerical integration and advanced collision detection techniques, we explore the potential of large CubeSat swarms in capturing gravity signals and reconstructing the internal mass distribution of a small celestial body while minimizing risks and Delta V budget. Our results offer insight into the applicability of this approach for future deep space exploration missions.

Introduction

In the last decade CubeSats have emerged as an innovative and cost-effective platform for testing new satellite technologies, with applications ranging from Earth observation to deep space missions. For instance, the HERA interplanetary mission that will explore the Didymos binary system in 2025 will embark two CubeSats to perform a detailed exploration of the system. [1] In this context, distributed swarms of CubeSats are a promising strategy for future exploration missions to small celestial bodies, enabling increased scientific return while minimizing risks associated with operating in an unknown environment. [2]

In this work, we present a large-scale simulation study of the deployment and operation of many CubeSats around small celestial bodies, with the aim of assessing the applicability of large CubeSats swarms for distributed operations during interplanetary missions to asteroids and comets. Our approach leverages the *cascade* and *heyoka* C++/Python libraries to propagate the evolution of the swarm, reliably detecting close encounters and collisions using high-order Taylor numerical integration and collision detection. [3] We assume that the swarm is deployed sequentially by a “mother” spacecraft operating in proximity of the celestial body of interest, and that each CubeSat has the capability of performing 6-DoF orbital manoeuvres with limited ΔV budget. We use mascon mass models to have a representation of the mass distribution of the bodies around which the swarm is orbiting and consider CubeSat deployment uncertainty in position and velocity as well as a fully automated trajectory control strategy aimed at keeping the overall Delta V budget under control while maximizing scientific return and controlling the risk of conjunctions. Our simulations offer insights into the trade-offs involved in deploying and maintaining large CubeSat swarms for distributed operations in deep space.

Background and Models

In this study, we consider a prospective advanced mission concept inspired by the European Space Agency’s HERA mission. [1] We assume that a mothership satellite is inserted into orbit around a small celestial body of irregular shape and will consequently deploy a swarm of CubeSats from a



common orbit. The swarm's objective is to capture gravity signal around the body to assess its mass distribution at a later stage following the procedure described in the *geodesyNETs* project. [4] The swarm CubeSats will have to orbit around the body without colliding with each other, staying within a spherical region defined by a minimum safety radius to the body's center of mass and a maximum radius of operations. These operations will have to be performed with minimum ΔV budget requirements.

Small celestial bodies of interest for this study will have their internal mass distribution represented by a heterogeneous mascon model. In other words, they will be modelled as a set of point masses located in specific positions and with some given mass. The mascon models used for this study were developed in the *geodesyNETs* project. [4] The dynamics of the swarm around the spacecraft are simulated via cascade simulations making use of the *heyoka* high-performance Taylor integrator. The equations of motion are represented by a gravitational N -body problem where N is the number of mascons, plus the solar radiation pressure integrated in an inertial reference frame and consider a rotating celestial body. Terminal events are added to the equations of motion to enforce a maneuver when a spacecraft enters the safety sphere around the body or exits the operations sphere.

We assume that each CubeSat of the swarm has the capability of performing maneuvers with full degrees of freedom whenever it gets close to another element of the swarm, to the central body or flies too far away. A 2-phase collision detection algorithm is used to detect when two elements of the swarm get too close to each-other. It exploits the availability, at each step, of Taylor polynomial expansions of the system dynamics that are the product of the integration scheme offered by *heyoka* and therefore come at no additional cost. *Cascade* makes use of these expansions to compute Axis Aligned Bounding Boxes (AABB) encapsulating the positions of each orbiting object within a chosen collisional timestep. The algorithm operates in two phases: a broad phase with a Bounding Volume Hierarchy (BVH) over the 4-dimensional AABB defined in cartesian coordinates, followed by a narrow phase more computationally demanding making use of a polynomial root finding algorithm. This approach is well-suited to parallelization and particularly performant in non-collision rich environments such as the ones considered in this study.

Simulations and Results

We apply our framework to simulate swarm missions to Itokawa, Bennu and Ryugu. [5,6,7] For each body four swarm configurations are considered, with 5, 10, 25 and 50 spacecraft respectively. Itokawa is modelled using 24800 mascons, Bennu with 17400 mascons and Ryugu with 26800 mascons. The mothership is initially located on a circular orbit around the body of interest with a semi-major axis of 1.5km, an inclination of 90° and a mean anomaly of 90° . The solar radiation pressure acting on the swarm spacecraft is computed considering a wet area of 1 m^2 , with the sun direction being selected arbitrarily in the ecliptic plane. The spacecraft must remain in an ellipsoidal region around the asteroid, with a no-entry safety ellipsoid whose dimensions are those of the celestial body with a factor 1.3 and a no-exit sphere of radius 3 km for Itokawa and 2 km for Bennu and Ryugu. The relative release velocities of the swarm spacecrafts with respect to the mothership are randomly selected in $[1.5, 3.5] \text{ cm/s}$. 100 collisional timesteps are processed in parallel to account for CubeSat collisions, where one timestep is defined as $1/60^{\text{th}}$ of the orbital period of the mothership spacecraft and is also representative of the release frequency of the CubeSats in the swarm. The collisional radius, the minimum relative distance required between two CubeSats to avoid collisions, is set to 5 m. The dynamics and operations of the swarm are simulated in each case for a total duration of 4 days.

Table 1: Simulation results for swarms orbiting around Itokawa/Bennu/Ryugu,

	Itokawa				Bennu				Ryugu			
Swarm size	5	10	25	50	5	10	25	50	5	20	25	50
ΔV_{\min} [m/s]	0.1	0.1	0.1	0.1	0	0	0	0.03	0	0	0	0
ΔV_{\max} [m/s]	1.4	2.6	3	3.7	0,66	2.9	2.6	4.5	0.26	0.26	1.04	1.63
ΔV_{mean} [m/s]	0.82	0.85	0.97	1.4	0.39	0.68	0.7	0.92	0.08	0.05	0.12	0.34
Collision events	2	2	5	12	2	9	51	89	4	4	21	77
Safety events	7	9	39	191	34	15	40	78	4	4	12	36
Re-entry events	39	82	192	393	46	114	259	481	4	9	26	142

Table 1 showcases the Results obtained from the simulations. The number of events requiring maneuvers is in general dominated by re-entry requirements when the satellites are in danger of exiting their operational region around the asteroid. As expected, the size of the swarm has a direct impact on the ΔV budget for the mission. The increase observed in the maximum ΔV required for swarms with a higher number of spacecrafts is partially due to the increased number of collisional events recorded, especially for Bennu and Ryugu. However, re-entry events account for most of the budget and increase proportionally with the number of satellites in the swarm. This is because, on average, every CubeSat of the swarm will need to be actuated several times to stay within the operational region for the mission. Safety events are more predominant for Itokawa due to the elongated shape of the body that makes trajectory correction maneuvers more likely to cause future safety events.

Of particular interest is the fact that the trade-off for the number of satellites in the swarm, therefore gravity signal recovery, versus the ΔV budget of the mission is dependent on the shape and mass distribution of the body. Itokawa sees an 18% increase in mean ΔV going from 5 to 25 satellites in the swarm, for a drastic increase in recovered gravity signal and therefore internal shape reconstruction. But the increase from 25 to 50 satellites leads to a 44% increase in mean ΔV : the number of collision events increases enough to create a cascade of safety events that increase the overall budget significantly. The tradeoff for Bennu and Ryugu appears at different sizes for the swarm but exhibits a similar behavior: an increased number of collisional events leads to an increased number of safety and re-entry events and therefore hinders the mission budget. This could signify that the number of collision events dominates the trade-off analysis and could be a suitable preliminary indicator to size the swarm when gravity signal reconstruction is sufficient. Regularity in the shape of the body seems to be correlated with a higher number of collisional events but overall lower maintenance budgets, as the cascade phenomenon is not as pronounced. This analysis will be refined in future work with a more robust optimization setup, the purpose of this work being principally to propose and make available a framework for the efficient parallel simulation of CubeSat swarm operations around small celestial bodies.

Fig. 2 presents a top-view of a 50-spacecraft swarm simulation orbiting Itokawa as well as the asteroid shape reconstruction from the gravity signal gathered from the swarm after 4 days of operations and using the procedure described in the *geodesyNETs* project, along with the ΔV budget distribution for the swarm. [4]

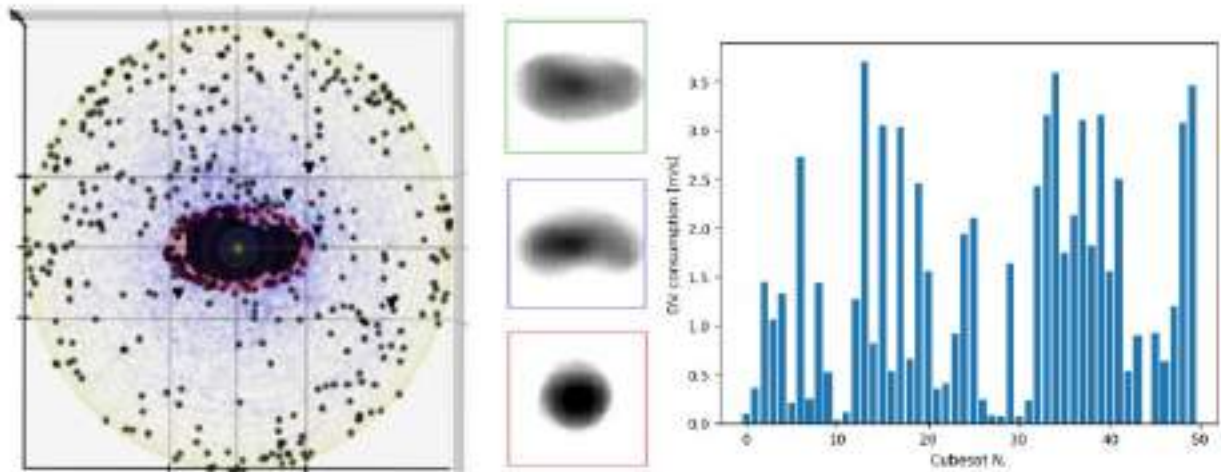


Figure 2: Itokawa study case, (left) simulation of a collision-free swarm of 50 elements. The position of the swarm elements during the gravity field measurements are shown in blue.

Impulsive maneuvers to keep the swarm in safe proximity are shown in black (collision avoidance, triangles). (middle) reconstruction of the asteroid shape after 4 days of operation. (right) ΔV budget distribution across the CubeSats in the swarm.

Conclusion

In this work we have applied our framework to simulate CubeSat swarm missions to Itokawa, Bennu and Ryugu. We show how swarms of different sizes, ranging from a few CubeSats to several dozen, can efficiently capture gravity signal and reconstruct spherical harmonic expansions while minimizing the risk of conjunction and counteracting the effects of environmental disturbances. Our results showcase the potential of large CubeSat swarms for future exploration missions to small celestial bodies and propose an Open-source framework for preliminary mission analysis studies in such scenario. The code used for this study will be made publicly available at <https://gitlab.com/EuropeanSpaceAgency/collision-free-swarm>, and the *cascade* library used for this work is an open source python module available at <https://github.com/esa/cascade>.

References

- [1] Michel, P., Kueppers, M., Sierks, H., Carnelli, I. et al. (2018). European component of the AIDA mission to a binary asteroid: Characterization and interpretation of the impact of the DART mission. In *Advances in Space Research* (Vol. 62, Issue 8, pp. 2261–2272). Elsevier BV. <https://doi.org/10.1016/j.asr.2017.12.020>
- [2] Stacey, N., Dennison, K., and D'Amico, S. (2022). Autonomous Asteroid Characterization through Nanosatellite Swarming. In *2022 IEEE Aerospace Conference (AERO)*. 2022 IEEE Aerospace Conference (AERO). IEEE. <https://doi.org/10.1109/aero53065.2022.9843328>
- [3] Biscani, F., and Izzo, D. (2021). Revisiting high-order Taylor methods for astrodynamics and celestial mechanics. In *Monthly Notices of the Royal Astronomical Society* (Vol. 504, Issue 2, pp. 2614–2628). Oxford University Press (OUP). <https://doi.org/10.1093/mnras/stab1032>
- [4] Izzo, D., and Gómez, P. (2022). Geodesy of irregular small bodies via neural density fields. In *Communications Engineering* (Vol. 1, Issue 1). Springer Science and Business Media LLC. <https://doi.org/10.1038/s44172-022-00050-3>
- [5] Fujiwara, A., Kawaguchi, J., Yeomans, D. K. et al. (2006). The Rubble-Pile Asteroid Itokawa as Observed by Hayabusa. In *Science* (Vol. 312, Issue 5778, pp. 1330–1334). American Association for the Advancement of Science (AAAS). <https://doi.org/10.1126/science.1125841>

- [6] Saiki, T., Takei, Y., Takahashi, T. et al. (2021). Overview of Hayabusa2 Asteroid Proximity Operation Planning and Preliminary Results. In Transaction of the Japan Society for Aeronautical and Space Sciences, Aerospace Technology Japan (Vol. 19, Issue 1, pp. 52–60). Japan Society for Aeronautical and Space Sciences. <https://doi.org/10.2322/tastj.19.52>
- [7] Lauretta, D. S., DellaGiustina, D. N., Bennett, C. A. et al. (2019). The unexpected surface of asteroid (101955) Bennu. In Nature (Vol. 568, Issue 7750, pp. 55–60). Springer Science and Business Media LLC. <https://doi.org/10.1038/s41586-019-1033-6>

Space Flight Mechanics

Low-energy earth-moon mission analysis using low-thrust optimal and feedback control

A. Almonte^{1,a}, I. Ziccardi^{1,b}, A. Adriani^{1,c}, A. Marchetti^{1,d}, M. Pontani^{2,e}

¹Thales Alenia Space Italia (TAS-I), Via Saccomuro 24, 00131 Rome, Italy

²Department of Astronautical, Electrical, and Energy Engineering, Sapienza University of Rome, via Salaria 851, 00138 Rome, Italy

^aalessio.almonte@gmail.com, ^birene.ziccardi@thalesalieniaspace.com₁

^candrea.adriani@thalesalieniaspace.com, ^dandrea.marchetti@thalesalieniaspace.com₁

^emauro.pontani@uniroma1.it

Keywords: Earth-Moon Transfers, Low Energy Transfers, Low-Thrust Spacecraft, Optimal Control, Feedback Guidance and Control, Particle Swarm Optimization

Abstract. This work is focused on designing a low-energy orbit transfer in the Earth-Moon system, aimed at reaching stable capture in a highly elliptical lunar orbit, with the use of low-thrust propulsion. The mission at hand includes three different phases: low-energy ballistic transfer starting from Earth, low-thrust minimum-fuel arc, and low-thrust lunar orbit insertion using variable-thrust nonlinear orbit control. First, a reference trajectory is generated in the framework of the Patched Planar Circular Restricted Three-Body Problem (PPCR3BP), leveraging invariant manifold dynamics. Trajectory propagation is performed using the Bicircular Restricted Four-Body Problem (BR4BP) model. Particle swarm optimization is applied for trajectory refinement and to detect the subsequent minimum-fuel low-thrust arc. Finally, the lunar orbit is entered thanks to the use of variable-thrust nonlinear orbit control.

Introduction

Low-energy Earth-Moon transfers have been studied extensively in the last decades. Some missions have already exploited the results from these studies, leading to considerable propellant savings and other advantages, such as flexibility in target orbit selection, extended launch windows, and more relaxed operational schedules. At the end of the 60s Conley [1] used elements of dynamical systems theory to identify temporary lunar capture conditions. Three decades ago, Belbruno and Miller [2] developed the Weak Stability Boundary (WSB) technique and applied it to lunar transfers, discovering a low-energy transfer through the equilibrium regions of the Sun-Earth-Moon system. Koon *et al* [3] obtained similar results by following the Conley methodology, taking advantage of invariant manifolds of planar Lyapunov orbits around the Earth-Moon L2 libration point. More recently Mingotti *et al* [4] designed low-energy low-thrust transfers, using PPCR3BP for the low-energy trajectory arc and optimal control with a direct method for the low-thrust lunar capture arc. An alternative approach to reach a stable capture orbit is represented by variable-thrust nonlinear orbit control, as described by Gurfil in [5] and Pontani *et al.* in [6]. In fact, using a feedback control law allows applying real-time control and compensate perturbations, with no need of a reference trajectory.

This work is focused on designing a low-energy Earth-Moon transfer starting from a GTO parking orbit and aimed at reaching a stable lunar capture orbit, with the use of low-thrust propulsion. Several design approaches are being employed: (a) use of the invariant manifold dynamics, to obtain a low-energy planar reference trajectory from Earth to Moon, (b) optimal control with the use of the particle swarm algorithm (PSO) to detect the subsequent minimum-fuel low-thrust arc, and (c) variable-thrust nonlinear orbit control to enter the desired lunar orbit. This



work intends to show that the mission design techniques proposed in this study represent a convenient approach to preliminary Earth-Moon mission analysis.

MISSION Analysis and results

The mission is composed of two phases, analyzed using different reference frames, to simplify the design. Phase 1 covers the low-energy low-thrust Earth-Moon transfer. A planar low-energy exterior transfer is found using invariant manifold dynamics in the PPCR3BP framework. First, two convenient Jacobi constants $C_{SE} = 3.0075$ and $C_{EM} = 3.15$ are selected for the Sun-Earth and Earth-Moon three body system. Then, Sun-Earth L2 and Earth-Moon L2 planar Lyapunov orbits associated with those constants are found by exploiting their symmetry properties with the use of PSO. Invariant manifolds are propagated from Lyapunov orbits. Invariant manifolds in PCR3BP are a subset of the phase space, and separate bouncing trajectories from transit orbits. Taking advantage of this property, invariant manifolds are cut with Poincaré sections, reducing the phase space dimension to 2. Manifold cuts and Poincaré sections are shown in Figure 1, where section S_A cuts stable manifold $W_S^+(\gamma_2)$ and section S_B cuts unstable manifold $W_U^-(\gamma_2)$ of Sun-Earth L2 Lyapunov orbit γ_2 ; instead, section S_C cuts stable manifold $W_S^+(\delta_2)$ of Earth-Moon L2 Lyapunov orbit δ_2 .

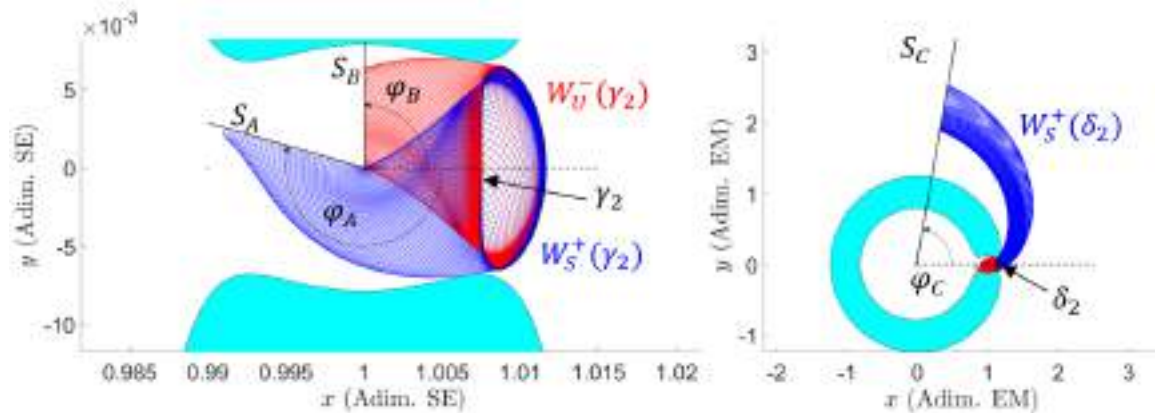


Figure 1: Manifolds cut and Poincaré sections

Intersections are evaluated in the $r_2 - \dot{r}_2$ plane, shown in Figure 2, where r_2 is the distance and \dot{r}_2 the radial velocity with respect to Earth, secondary body in the Sun-Earth three-body system.

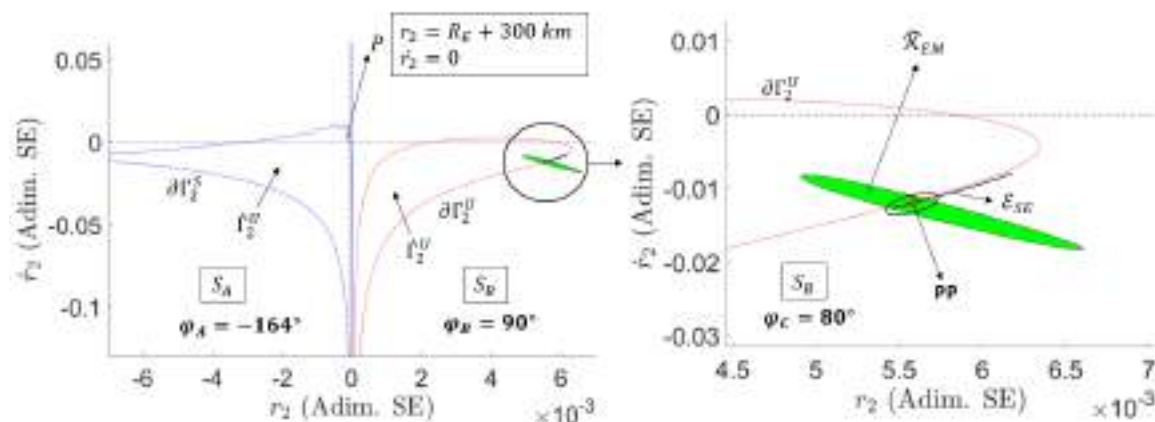


Figure 2: Manifolds intersection in $r_2 - \dot{r}_2$ plane

From figure 2 it is possible to see that the angle φ_A is tuned to move the $W_S^+(\gamma_2)$ stable manifold cut $\partial\Gamma_2^S$ close to the starting point P corresponding to GTO pericenter conditions. Trajectories starting from P in S_A end in the \mathcal{E}_{SE} set on section S_B , at external points close to the $W_U^-(\gamma_2)$ unstable manifold cut $\partial\Gamma_2^U$. Tuning angle φ_C allows moving the set $\widetilde{\mathcal{K}}_{EM}$, until intersection with \mathcal{E}_{SE} occurs. The set $\mathcal{E}_{SE} \cap \widetilde{\mathcal{K}}_{EM}$ represents temporary ballistic capture trajectories and here the Patch Point (PP) between Sun-Earth and Earth-Moon trajectory arcs is chosen. The PP conditions are then integrated backward using the Bicircular Restricted Four-Body Problem (BR4BP), to reach (through backward integration) the GTO orbit, with parameters $a = 24363.57$ km, $e = 0.7036$, $i = 23.45^\circ$, $\Omega = 0^\circ$, $\omega = 163.72^\circ$, $\theta_* = 0^\circ$. The velocity change to perform Translunar Injection (TLI) is $\Delta v^{(TLI)} = 671.8$ m/s and the time of flight is $\Delta t_1 = 142.47$ days. The small maneuver necessary at patch point to link the trajectories is substituted with a low-thrust arc obtained with minimum-fuel optimal control. The low thrust propulsion system is identified by $u_T^{(max)} = \frac{T_{max}}{m_0} = 2 \cdot 10^{-4}$ m/s and $c = g_0 I_{sp} = 18.142$ km/s. The state vector is defined as $\mathbf{X} = [x, y, v_x, v_y, \frac{m}{m_0}]^T = [x_1, x_2, x_3, x_4, x_5]^T$ and the control vector is $\mathbf{u} = [u_T, \alpha]$, where $u_T = T/m_0$ with $0 \leq u_T \leq u_T^{(max)}$ and α is the angle between the thrust direction and the line from the Sun and the Earth-Moon barycenter. The objective of minimum-fuel optimal control is to find the control \mathbf{u}_T and the constant parameters vector \mathbf{p} such that the cost function $J = -m_f$ is minimized, while satisfying the state equations $\dot{\mathbf{X}} = \mathbf{f}(\mathbf{X}, \mathbf{u}, t, \mathbf{p})$ and the boundary conditions $\Psi(\mathbf{X}_0, \mathbf{X}_f, t_0, t_f, \mathbf{p}) = \mathbf{0}$. Additional constraints are added to the Lunar Orbit Insertion (LOI) condition, limited to orbits with $e \in (0.6, 0.7)$, to arrive at a capture orbit, and $r_p = R_M + 100$ km to avoid Moon impact. These constraints are written in terms of equality constraints using the parameter vector \mathbf{p} . Exploiting the necessary optimality conditions and the Pontryagin minimum principle it is possible to obtain the control law, depending on co-state vector $\boldsymbol{\lambda} = [\lambda_1, \lambda_2, \lambda_3, \lambda_4, \lambda_5]^T$. The minimum set of unknown parameters is $\boldsymbol{\chi} = \{\boldsymbol{\lambda}_0, t_f, \mathbf{p}\}$ and is found using PSO. The minimum time of flight is $t_f = 13.30$ days, with $\frac{m_f}{m_0} = 0.994$. The time histories of the thrust angle are shown in Figure 3.

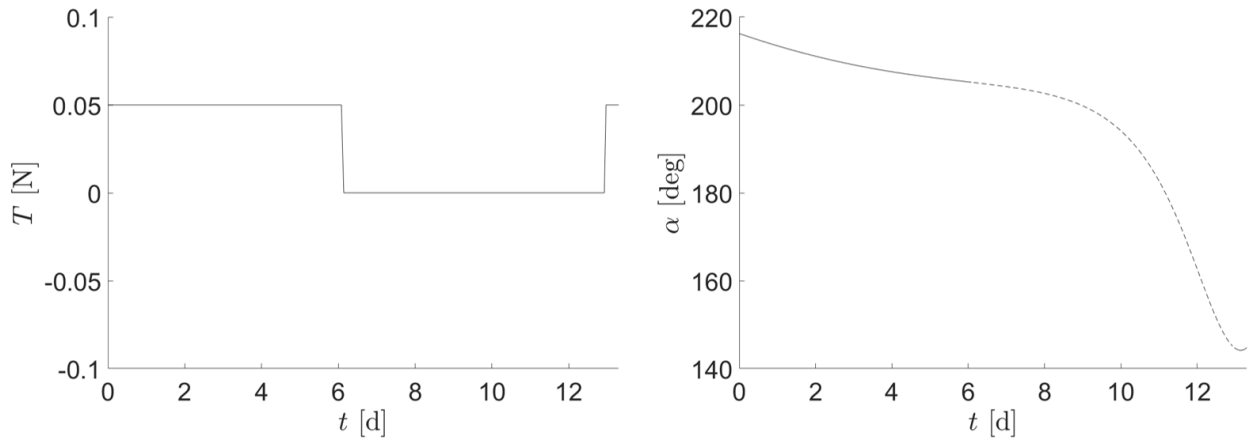


Figure 3: Time histories of thrust T and thrust direction α

In Phase 2 of the mission nonlinear control was employed to enter a stable lunar orbit. This control enjoys quasi-global stability properties and allows compensating perturbations [6]. The main objective of this phase is convergence to the target orbit, while compensating perturbations due to Earth and Sun. In this framework the state vector is given by the Modified Equinoctial

Elements (MEE) and the mass ratio, i.e. $\mathbf{X} = \left[p, l, m, n, s, q, \frac{m}{m_0} \right]^T = [x_1, x_2, x_3, x_4, x_5, x_6, x_7]^T = [z, x_6, x_7]^T$, whereas the control vector is $\mathbf{u}_T = \mathbf{T}/m_0$ with $0 \leq u_T \leq u_T^{(\max)}$. The target set is defined in terms of MEE as

$$\Psi = \left[x_1 - a_d(1 - e_d^2), x_2 - e_d \cos(\Omega_d + \omega_d), x_3 - e_d \sin(\Omega_d + \omega_d), x_4 - \tan\left(\frac{i_d}{2}\right) \cos(\Omega_d), x_5 - \tan\left(\frac{i_d}{2}\right) \sin(\Omega_d) \right]^T.$$

The dynamics is governed by the Lagrange Equations with MEE [6]. The control law is derived in [6] and yields \mathbf{a}_T , i.e. the thrust acceleration as a function of the state, the boundary condition violation, and the perturbing acceleration. The latter includes the effect of Earth and Sun as third bodies. Matrix \mathbf{K} is a positive definite diagonal matrix of gains, selected after trial-and-attempt tuning. The target orbit is reached in a time of flight $t_f = 77.52$ days, with $\frac{m_f}{m_0} = 0.920$. After 100 days from Lunar Orbit Injection (LOI) the mass ratio reduces to $\frac{m_f}{m_0} = 0.909$, because propellant is used to compensate the perturbations. The orbit elements of the planar capture orbit reached at the end of Phase 1, together with target parameters and parameters after 100 days of propagation, are shown in Table 1. The trajectory in Phase 2 and the full trajectory are shown in Figure 4.

	a [km]	e	i [deg]	Ω [deg]	ω [deg]
LOI	108058	0.7000	0	-23.78	48.14
Target orbit	9751	0.6870	55.70	120.00	90.00
Final	9772	0.6871	55.71	120.01	89.99

Table 1: orbit elements at LOI and along the target orbit

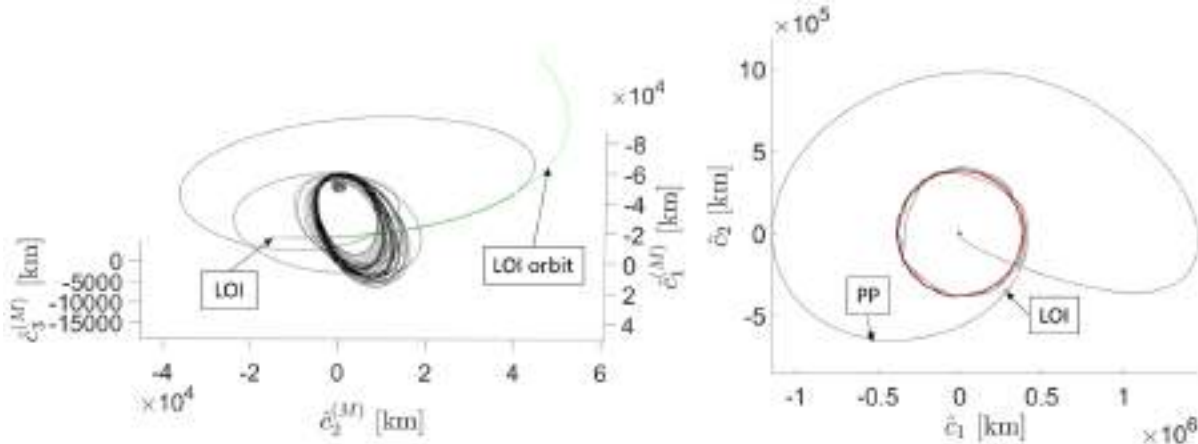


Figure 4: a) Trajectory in Phase 2, in MCI reference frame b) Full transfer in ECI reference frame

Concluding Remarks

This paper proposes a preliminary mission analysis for a low-energy low-thrust Earth-Moon transfer, starting from a GTO orbit and aimed at reaching a lunar highly elliptical orbit. In Phase 1 of the mission, regarding the Earth-Moon transfer, invariant manifold dynamics is used to obtain a low-energy planar reference trajectory, thus reducing the trajectory design to the research of a point in the phase space. The PSO algorithm allows further refinement of the trajectory in the framework of the BR4BP. Then, the same algorithm is employed to find the subsequent minimum-fuel low-thrust arc. In Phase 2 the final highly elliptic lunar orbit is reached using variable thrust nonlinear orbit control, with perturbations compensation and no need of a reference trajectory.

Assuming that the departure from GTO is demanded to the launch vehicle, as a part of its operations, the overall propellant consumption for the spacecraft equals 8% of its initial mass. In the end, the combination of the techniques described in this study allows defining an Earth-Moon mission profile with modest propellant consumption. In principle, the methodology at hand is also applicable to a variety of departure and target orbits in the Earth-Moon system.

References

- [1] Conley, C., On the Ultimate Behavior of Orbits with Respect to an Unstable Critical Point I. Oscillating, Asymptotic, and Capture Orbits, *Journal of Differential Equations*, No. 5, 1969, pp 136–158. [https://doi.org/10.1016/0022-0396\(69\)90108-9](https://doi.org/10.1016/0022-0396(69)90108-9)
- [2] Belbruno, E. A., Miller, J. K., Sun-Perturbed Earth-to-Moon Transfers with Ballistic Capture, *Journal of Guidance, Control and Dynamics*, Vol. 16, No.4, 1993, pp 770-775. <https://doi.org/10.2514/3.21079>
- [3] Koon, W. S., Lo, M. W., Marsden, J. E., Ross, S. D., Low Energy Transfer to the Moon, *Celestial Mechanics and Dynamical Astronomy*, Vol. 81, 2001, pp 63-73. https://doi.org/10.1007/978-94-017-1327-6_8
- [4] Mingotti, G., Topputo, F., Bernelli-Zazzera, F., Efficient Invariant-Manifold, Low-Thrust Planar Trajectories to the Moon, *Communications in Nonlinear Science and Numerical Simulation*, Vol. 17, Issue 2, 2012, pp 817-831. <https://doi.org/10.1016/j.cnsns.2011.06.033>
- [5] Gurfil, P., Nonlinear feedback control of low-thrust orbital transfer in a central gravitational field, *Acta Astronautica*, Vol. 60, 2007, pp 631-648. <https://doi.org/10.1016/j.actaastro.2006.10.001>
- [6] Pontani, M., Pustorino, M., Nonlinear Earth orbit control using low-thrust propulsion, *Acta Astronautica*, Vol. 179, 2021, pp 296–310. <https://doi.org/10.1016/j.actaastro.2020.10.037>

The application of modal effective mass for PCB friction lock compliance against spacecraft launch random vibration spectrum

Mark Wylie^{1*}, Leonardo Barilaro²

¹South East Technological University (SETU), Aerospace, Mechanical and Electronic Engineering Department, Carlow campus, Kilkenny Rd, Moanacurragh, Co. Carlow, Ireland

²The Malta College of Arts, Science & Technology, Aviation Department, Triq Kordin, Paola PLA 9032, Malta

* mark.wylie@setu.ie

Keywords: Modal Finite Element Analysis, Electronics, Spacecraft Structures, Friction-Locking Devices, Random Vibration Analysis

Abstract. Modern spacecraft design requires high density, low mass, modular electronic system architectures. This format often utilises a common backplane with Printed Circuit Boards (PCBs) interconnects. Adaptable electronic systems, such as modular Data Acquisition (DAQ) systems, allow for configuration via insertion and removal of modules to meet the mission requirements. Common methods to mechanically fix the PCB to the chassis are by using stand-offs, with the primary function to minimise displacement through structural rigidity and to provide strain relief to the electronic connectors. Other methods, such as PCB friction lock allow for strain relief, improved thermal grounding of the PCB to the chassis but also allows for easy insertion and removal of the PCBs. One disadvantage of this system is that the retention force of the PCB is carried by a friction lock device and under acceleration loads, typically experienced in the launch environment, may cause failure. This paper presents a method to establish compliance of PCB friction lock devices using modal Finite Element Analysis (FEA) to predict the resonant frequencies and their Mass Participation Factor (MPF). Using this data, it is proposed that the use of an adaptation of the Miles Equation along with an equivalent g-RMS estimation can be used to determine the Random Vibration Load Factors (RVLF). A comparison of the RVLF with the retention force of the friction lock device can then give insight to the friction joint compliance.

Introduction

Quasi-Static Load (QSL), Shock Response Spectrum (SRS), sine and random vibration Acceleration Spectral Density (ASD) are typical acceleration loads required for qualification of space bound hardware. They represent loads during maneuvers (e.g., roll/tilt and orbital), pyrotechnic events (separation and fairing jettison) and motor induced vibrations. Payload flight equipment is designed against a defined set of these acceleration loads but are often equated to Load Factors (LF) which are equivalent accelerations (expressed in g's) and applied through the Centre of Gravity (CoG) of the structure [1]. This paper considers Random Vibration Load Factor (RVLF) and its equivalent g (force) for verification of PCBs friction lock mechanisms (see Fig 1). This efficient design allows for high density electronic architectures and modularization via insertion/extraction into a chassis by accessing front side only. This verification technique is an effort saving technique for the purposes of Proto Flight development.



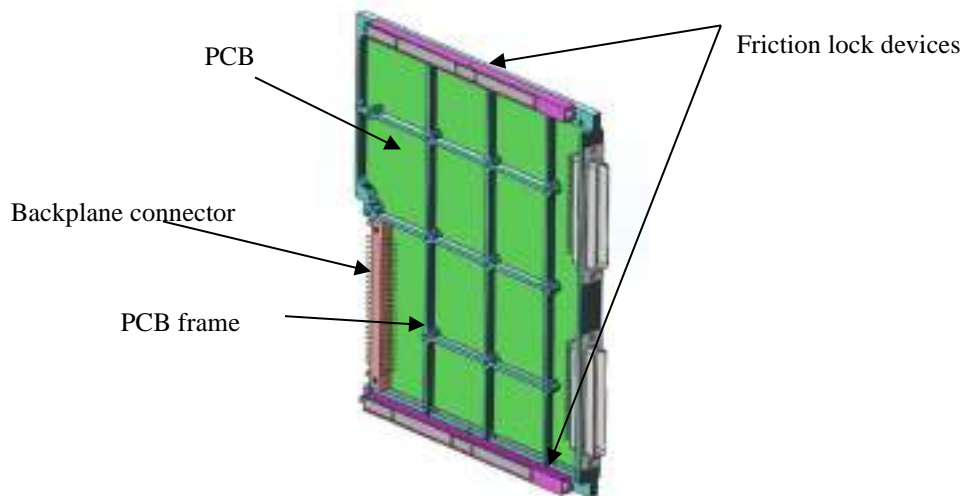


Fig 1: PCB on AA6082-T6 PCB frame with QTY 2 friction locking devices (NVENT).

In theory, structures may contain millions of Degrees of Freedom (D.O.F), each having a resonant frequency. Of these modes, high resonant frequencies (>2000 Hz or $> 10,000$ Hz) may be deemed to have low structural impact, one; because it is beyond the typical random vibration spectrum upper frequency limit (2000 Hz) and SRS (10,000 Hz) and two; because displacement is inversely proportional to modal frequency and often do not constitute a ductile failure mode (notwithstanding that these modes should still be considered for load spectra for the purposes of fatigue compliance and failure modes for brittle ceramic components). The amount of mass moving in any direction is a function of the mode participation factor and the effective mass at that mode. This is sometimes called Mass Participation Factor (MPF) and it is common, using modal FEA, to evaluate MPF such that the summation accounts for > 90 % of the total structural mass in all orthogonal directions [2]. Significant modes of interest are extracted from this data (typically with $MPF > 5$ %). The resonant frequency of the structure in each orthogonal axis can also be identified as the first significant mode (i.e., lowest mode frequency typically with > 5 % MPF) in each orthogonal direction. On consideration for structural analysis of the PCB friction lock compliance, the following data is of importance; the mode frequency (Hz), the MPF and the orthogonal direction in which it acts. Mode frequency because it is inversely proportional to displacement and using Steinberg studies can determine electronic component survivability [3], MPF because of the inertia involved with this mode frequency and finally direction (mode shape), because in some cases, the direction in which it acts may coincide with friction locking mechanism or its deformation may cause collision with adjacent structures (i.e., adjacent PCBs components). This analysis considers the modes that are parallel to direction of the friction lock and the MPF at these modes. From this, the force response In-Plane (IP) with the PCB friction lock can be compared to the friction force holding the PCB in-situ. In summary, this method aims to determine if the PCB friction lock will be compromised by random vibration ASD load. Displacement and translation can cause a critical failure, especially for electronic systems that rely on a common backplane for interconnects. In the next section a proposed pass/fail criteria to determine if the friction lock joint will survive the random vibration acceleration load case is presented.

Method

The random vibration spectrum is non-deterministic but when analysed statistically over a period of time the g-RMS is constant and the likelihood of peaks (g) outside of the RMS are given by a Gaussian distribution (3σ). The random vibration spectrum is a base excitation to the hardware and typically ranges from 20-2000 Hz but allows for numerous frequencies to be excited at the same time. A conservative assumption for the analysis of PCBs within an electronic chassis is to

assume no attenuation of the base excitation to the PCBs. However, it has been shown for shock inputs that structural discontinuities can significantly attenuate the shock pulse, this is known as the 3-joint rule [4]. For frequencies above 2000 Hz or for systems where the resonant frequencies are unknown, the RVLF can be approximated by multiplying the overall g-RMS by 3 (i.e. 3σ). Standard methods used to formulate the RVLF are based on the Miles Equation [1][5] where the base input amplitude is taken at the resonant frequency and the amplitude (g^2/Hz) is taken as a maximum value from the ASD plateau and considered constant across the entire frequency domain. This is over conservative unless the ASD is flat or within one octave either side of the resonant frequency [7] because typically the ASD plot has a ramp up (+3 dB) to the knee point and decline (-5 dB) after the plateau knee point (e.g. MIL-STL-1540C [6]) where levels are lower in these regions. A more accurate method would be to predict the resonant frequencies and MPF using modal FEA and, using Q (often estimated as $Q = 20$ or approximated using $Q = \sqrt{Fn_{PCB}}$) [3] calculate the g-RMS (\ddot{X}_{g-RMS}) using the following equation Eq 1.

$$\ddot{X}_{g-RMS} = 3\sigma \cdot \sqrt{\sum_{i=1}^N \frac{[1 + (2\xi(\frac{F_i}{F_n})^2)]}{[1 - (\frac{F_i}{F_n})^2]^2 + [2\xi(\frac{F_i}{F_n})]^2}} \quad (1)$$

The derivation of this method, taken by others [5][7] and adapted for PCB friction lock compliance, is based on the system's response to a typical random vibration ASD. This method allows for the inclusion of the ASD amplitude to vary across the frequency range of interest, i.e. representing the ramp and declines typically found in random vibration ASDs. Once the g-RMS been calculated the total RVLF can be calculated using Eq 2:

$$RVLF = m \cdot (MPF \cdot \ddot{X}_{g-RMS, mode i} + ((1 - MPF) \cdot \ddot{X}_{g-RMS, ASD})) \quad (2)$$

Where; m = mass of PCB and PCB frame, MPF = MPF at resonant frequency of the system in direction of the friction lock, $\ddot{X}_{g-RMS, mode i}$ = g-RMS at resonant frequency using $Q = 20$, $\xi = 1/2Q$, 3σ and $\ddot{X}_{RMS, spectrum}$ = g-RMS of overall spectrum multiplied by 3σ . The RVLF is an estimation of the forces acting on the PCB friction lock device in the direction of slippage due to the random vibration load case. The retention force (F_{max}) from a friction lock device (typical values NVENT CardLock systems $F_{lock} = 400\text{-}3000$ N) opposing this is F_{max} and is calculated using Eq 3:

$$F_{max} = \mu \cdot F_{lock} \cdot \text{number of friction lock devices} \quad (3)$$

Friction coefficient (μ) is taken as 0.3 for static aluminum-aluminum interfaces [8]. Failure of the locking device is established when the RVLF exceeds the F_{max} . A sample calculation is provided for the PCB and PCB frame in Fig. 1 against the random vibration ASD in Tab. 1. with g-RMS of 14.7 g. A modal FEA study of the assembly predicts an IP resonant frequency of 1318 Hz with an MPF of 0.2 %. This was the only significant mode within an order of magnitude below 2000 Hz.

Tab 1: Random vibration ASD used in study.

Frequency	g^2/Hz
20	0.08
100	0.4
300	0.4
2000	0.017

Results

This paper presents a methodology for the analysis of PCB and PCB frame assemblies that are fixed using friction lock devices against random vibration acceleration load case that are experienced during spacecraft launch. A sample calculation based on the assembly in Fig.1 is presented:

$$RVLF = 0.415 \times [(0.002 \times 120.8) + (0.998 \times 44.1)] = 18.35 \text{ N} \quad (4)$$

Where:

$$M_{\text{Frame+PCB}} = 0.415 \text{ kg}$$

$$MPF_1 = 0.002 \text{ @ } 1317.8 \text{ Hz}$$

$$X_{\text{RMS, mode i}} = 120.8 \text{ g (3 } \sigma \text{ and Q = 20), see Fig. 2 and Eq. 1, implemented using MS Excel}$$

$$X_{\text{RMS, spectrum}} = 14.7 \text{ g-rms} \times 3 \sigma = 44.1 \text{ g}$$

As per Eq. 3, assuming the use of NVENT Schroff Series 48-5 (1418 N retention force each)

$$F_{\text{max}} = 0.3 \times 1481 \times 2 = 888.6 \text{ N} \quad (5)$$

$$\text{Therefore: } M.o.S = \frac{888.6}{18.35} - 1 = 47.4 \quad (6)$$

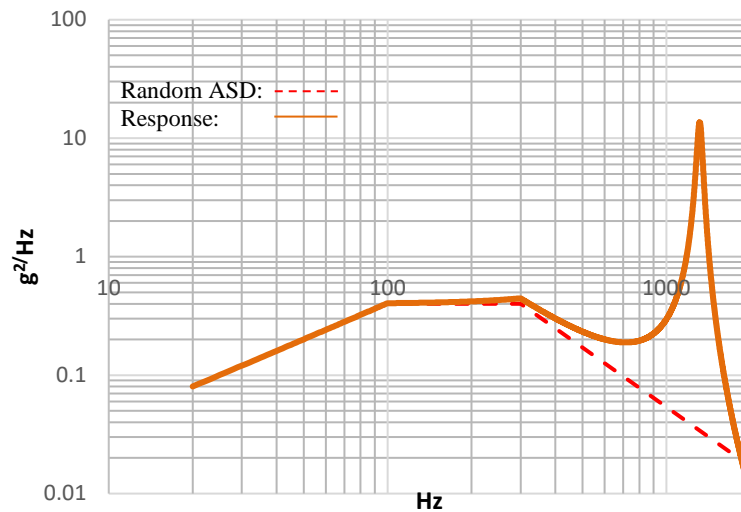


Fig 2: Random vibration ASD response based on Eq. 1 and resonant frequency of PCB assembly.

Conclusion

This research is based on flight hardware destined to be launched on the Ariane 6-2 in 2026 and is currently under development. The hardware has passed system qualification testing for acceleration load cases. The sample calculation shows very low force response acting on the PCB assembly IP (18.35 g) which is primarily due to the low MPF (0.2 %) within the ASD limit range (2000 Hz). It is also due to the vehicle IP random vibration requirements of 14.7 g-rms. The Out-of-Plane (OOP) is greater at 22.7 g-rms. Nevertheless, given the retention force of the NVENT product and excluding any Factors of Safety (FoS), Local Design Factors (LDF), Qualification Loads (QL), Design Loads (DL) etc., the MoS for slip is high at 47.4 and presents a low risk for movement or failure. This study would benefit from a more detailed validation of the PCB assembly modes by locally instrumenting low-mass triaxial accelerometers on PCB locations and

spectra analysis of multiple accelerometers across the PCB which can allow for validation of the MPF and mode shapes. It is a laborious technique and one such example of this is presented by Sandia National Laboratories [9]. Furthermore, an experimental apparatus capable of measuring forces on such friction lock devices could be used to establish the random vibration ASD thresholds for slip and failure.

References

- [1] L. Trittoni & M. Martini, Force-limited Acceleration Spectra Derivation by Random Vibration Analysis, Alenia Spazio, www.vibrationdata.com, (2004).
- [2] Xie J., Sun D., Xu C. and Wu J. The Influence of Finite Element Meshing Accuracy on a Welding Machine for Offshore Platform's Modal Analysis. Polish Maritime Research, Vol.25 (I3), pp. 147-153. (2018). <https://doi.org/10.2478/pomr-2018-0124>
- [3] T. Irvine, Extending Steinberg's Fatigue Analysis of Electronics Equipment Methodology to a Full Relative Displacement vs. Cycles Curve. Rev C, www.vibrationdata.com, (2013).
- [4] V. Babuska, S P. Gomez, S A. Smith, C Hammetter and D Murphy. "Spacecraft Pyroshock Attenuation in Three Parts," AIAA 2017-0633. 58th AIAA Structures, Structural Dynamics, & Materials Conference, (2017). <https://doi.org/10.2514/6.2017-0633>
- [5] J.W. Miles, "On Structural Fatigue under Random Loading", Acoustical Society of America Journal, vol. 29, no. 1, p. 176, doi:10.1121/1.1918447, (1957). <https://doi.org/10.1121/1.1918447>
- [6] MIL-STD-1540C, Test Requirements for Launch, Upper-Stage and Space Vehicles, (1994).
- [7] T. Irvine, An Introduction to the Random Vibration Spectrum, Section 17. http://www.vibrationdata.com/tutorials2/Tom_book_12_1_19.pdf, (2019).
- [8] D. Fuller. Excerpt from "Theory and Practice of Lubrication for Engineers". Coefficients of Friction. <https://web.mit.edu/8.13/8.13c/references-fall/aip/aip-handbook-section2d.pdf>, (1970).
- [9] R. Mayes et al, Efficient Method of Measuring Effective Mass of a System, Experimental Mechanics, NDE and Model Validation Department, Sandia National Laboratories, (2014).

Near-optimal feedback guidance for low-thrust earth orbit transfers

D. Atmaca^{1,a} and M. Pontani^{2,b}

¹M.S. in Space and Astronautical Engineering, Sapienza University of Rome, via Eudossiana 18, 00184 Rome, Italy

²Department of Astronautical, Electrical, and Energy Engineering, Sapienza University of Rome, via Salaria 851, 00138 Rome, Italy

^amauro.pontani@uniroma1.it, ^bdirencatmaca@gmail.com

Abstract. This research proposes a near-optimal feedback guidance based on nonlinear control for low-thrust Earth orbit transfers. For the numerical simulations, two flight conditions are defined: (i) nominal conditions and (ii) nonnominal conditions that account for the orbit injection errors and the stochastic failures of the propulsion system. Condition (ii) is studied through an extensive Monte Carlo Analysis, to demonstrate the nonlinear feedback guidance's numerical stability and convergence properties. To illustrate the performance under both conditions, an orbit transfer from low Earth orbit to geostationary orbit is considered. Near-optimality of the feedback guidance comes from carefully selecting the nonlinear control gains. Comparison of the transfer with an existing study that uses optimal control reveals that orbit transfers based on feedback orbit control are very close to the optimal solution.

Keywords: Earth Orbit Transfers, Low-Thrust Spacecraft, Feedback Guidance and Control

Introduction

Orbit control is a critical part of spacecraft control design and was extensively studied over the last century. Most studies focus on impulsive transfers. However, near-optimal and nonlinear strategies for low-thrust transfers are becoming popular since they allow compensation of orbital perturbations.

The study of nonlinear and near-optimal feedback guidance for low-thrust spacecraft is a reasonably new topic, with significant publications taking place over the last three decades. An important contribution is due to Gurfil [1], who utilizes nonlinear control with modified equinoctial orbit elements for low-thrust orbit transfers. The study guarantees asymptotic convergence from an initial elliptical orbit to any final elliptical orbit using Gauss's variational equations. Pontani and Pustorino [2] have recently applied nonlinear control strategies to orbit injection and maintenance problems where the control scheme takes advantage of Lyapunov stability combined with LaSalle's invariance principle. Gao [3] presents a linear feedback guidance approach that exhibits near-optimality for low-thrust Earth orbit transfers using orbital averaging. Kluever [4] proposed a simple closed-loop feedback-driven scheme for low-thrust orbit transfers that allows calculating sub-optimal trajectories. Petropoulos [5] developed a simple strategy based on candidate Lyapunov functions for low-thrust orbit transfers while coining the term proximity quotient or Q-Law. There are several other studies based on Q-Law [6, 7], and they focus on mitigating the sub-optimality of this strategy.

This research proposes a near-optimal feedback guidance based on nonlinear control for low-thrust Earth orbit transfers. Both eclipse condition and orbit perturbations (i.e., several Earth gravitational harmonics, solar radiation pressure, aerodynamic drag, and gravitational attraction due to Sun and Moon) are modeled. Two flight conditions are defined: (i) nominal conditions and (ii) nonnominal conditions that account for orbit injection errors and stochastic failures of the propulsion system. An orbit transfer from low Earth orbit to geostationary orbit is considered. The



initial and final orbit elements are taken from an existing study on optimal orbit control [8] for the purpose of comparing and demonstrating the near-optimality of the nonlinear feedback guidance.

Nonlinear orbit control using modified equinoctial elements

Orbit elements lead to singularities in the Gauss planetary equations for circular and equatorial orbits. To avoid similar issues, this study utilizes Modified Equinoctial Orbit Elements (MEE), defined as

$$p = a(1 - e^2) \quad l = e \cos(\Omega + \omega) \quad m = e \sin(\Omega + \omega) \quad n = \tan \frac{i}{2} \cos \Omega \quad s = \tan \frac{i}{2} \sin \Omega \quad q = \Omega + \omega + \theta_* \quad (1)$$

where $a, e, \Omega, \omega, i, \theta_*$ are semimajor axis, eccentricity, right ascension of the ascending node (RAAN), argument of periapsis, inclination, and true anomaly, respectively. Five of them are collected in \mathbf{z} , defined as $\mathbf{z} = [x_1 \ x_2 \ x_3 \ x_4 \ x_5]^T = [p \ l \ m \ n \ s]^T$, and subject to the governing equation

$$\dot{\mathbf{z}} = \mathbf{G}(\mathbf{z}, x_6) \mathbf{a} \quad (2)$$

The last element is $x_6 = q$. The \mathbf{a} term in (2) includes the projections of both perturbing and thrust acceleration onto the LVLH-frame. The explicit expression of \mathbf{G} and the governing equation for x_6 are reported in [2]. Two (constant) parameters identify the characteristics of the low-thrust propulsion system: $u_T^{(max)} = T_{max}/m_0$ and c , where T_{max} , m_0 , and c denote respectively maximum thrust magnitude, initial mass, and effective exhaust velocity. As a result, letting $x_7 = m/m_0$ (where m is the instantaneous mass), one obtains $\dot{x}_7 = -u_T/c$, with $u_T = T/m_0$. Thus, $\mathbf{a}_T = \mathbf{u}_T/x_7$ defines the instantaneous thrust acceleration. The term \mathbf{a} includes two contributions, $\mathbf{a} = \mathbf{a}_T + \mathbf{a}_p$, where the \mathbf{a}_p term refers to the perturbing acceleration. For this study, four types of orbital perturbations are considered: (a) the Earth gravitational harmonics (with $|J_{l,m}| > 10^{-6}$), (b) solar radiation pressure, (c) third-body attraction due to the Sun and the Moon, and (d) aerodynamic drag. The drag is modeled by assuming a reference surface area of 23.569 m^2 and ballistic coefficient equal to $0.0576 \text{ m}^2/\text{kg}$. In addition, the solar radiation pressure is modeled using a fully reflective surface area where the reflective coefficient is equal to 2. In the end, $\mathbf{x} = [\mathbf{z}^T \ x_6 \ x_7]^T = [x_1 \ x_2 \ x_3 \ x_4 \ x_5 \ x_6 \ x_7]^T$ identifies the complete state vector in compact form, whereas \mathbf{u}_T is the control vector.

Nonlinear orbit control allows identifying a feedback law that can drive the spacecraft toward the desired orbit while ensuring global asymptotic stability. For the problem at hand, the target set, associated with the final orbit, is $\boldsymbol{\psi} = [x_1 - p_d \ x_2^2 + x_3^2 - e_d^2 \ x_4^2 + x_5^2 - \tan^2(i_d/2)]^T$, where subscript d denotes the desired value of the respective variable. The feedback law

$$\mathbf{u}_T = -u_T^{(max)} \frac{x_7(\mathbf{b} + \mathbf{a}_p)}{\max\{u_T^{(max)}, |x_7(\mathbf{b} + \mathbf{a}_p)|\}}, \text{ with } \mathbf{b} = \mathbf{G}^T \left(\frac{\partial \boldsymbol{\psi}}{\partial \mathbf{z}} \right)^T \mathbf{K} \boldsymbol{\psi} \text{ and } \mathbf{K} = \text{diag}\{k_1, k_2, k_3\} \quad (3)$$

is proven to enjoy quasi global stability [2], using the Lyapunov direct method, in conjunction with the LaSalle's principle. However, the choice of the three gains (k_1, k_2, k_3) plays a crucial role for the purpose of speeding up convergence to the target set. This study proposes and applies a gain selection method composed of two sequential steps:

Step 1. Exhaustive table search that includes different gain combinations; each gain is changed with increment by $10^{0.1}$, in the interval $1 \leq k_i \leq 10^6$.

Step 2. Using the values found at step 1, the native “fminsearch” MATLAB routine, which employs a Nelder-Mead simplex algorithm, is used.

The preceding two steps are completed for different initial orbits, associated with identical values of semimajor axis, eccentricity, RAAN, and argument of perigee, and different initial inclinations. The propulsion parameters for the gain optimization process are assumed to be $c = 30$ km/s and $u_T^{(\max)} = 10^{-4} g_0$ with $g_0 = 9.8065$ m/s².

Numerical results

The near-optimal feedback guidance proposed in this study is tested under nominal and nonnominal conditions. For both cases, initial and final orbit elements and the propulsion parameters are taken from an existing study focusing on optimal orbit control [8]. The final orbit is geostationary, whereas the initial orbit is circular, with $a_0 = 6927$ km and $i_0 = 28.5^\circ$. The propulsion parameters are $c = 32.361$ km/s and $u_T^{(\max)} = 3.348 \cdot 10^{-4}$ m/s², and they characterize a low-thrust propulsion system. The gain values are selected from the preceding systematic study and are $k_1 = 0.9722$, $k_2 = 1056$, and $k_3 = 967$. For the transfer time and final mass ratios reported in this section, the following criteria are used to indicate the end of the transfer:

$$|p - p_d| \leq 10 \text{ km} \quad e \leq 0.005 \quad i \leq 0.5^\circ \quad (4)$$

Nominal Conditions

This subsection reports the numerical results under nominal conditions and compares the proposed nonlinear feedback guidance with the existing optimal solution. Figure 1 shows the near-optimal transfer path, with eclipse arcs (where propulsion is unavailable) highlighted in blue.

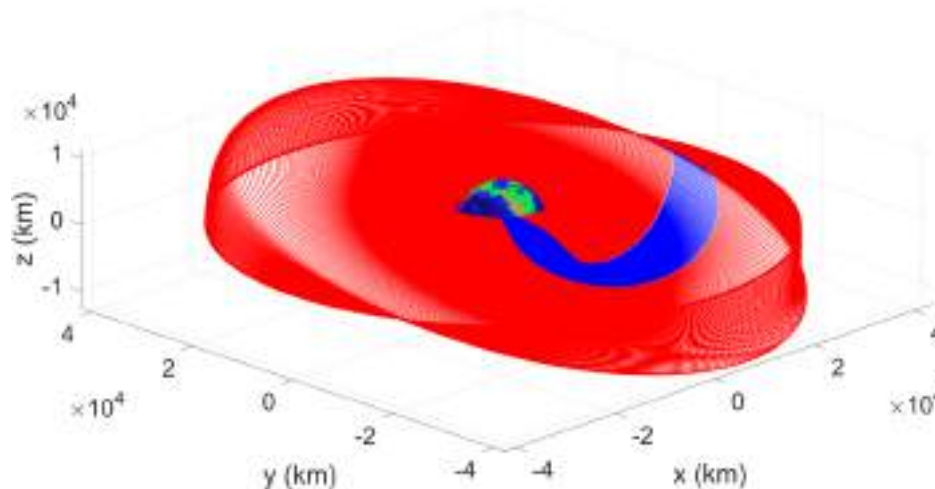


Figure 1: Cartesian motion of the spacecraft in the ECI frame (blue lines indicate eclipse)

At the beginning of the transfer, the perturbing acceleration is higher than the thrust acceleration. However, the perturbing term quickly decays to low values as the osculating radius increases. Using the criteria defined by (4), the transfer time is $t_f = 228.2$ days with a final mass ratio, $x_{\gamma_f} = 0.8245$. This result is compared to the optimal solution found in [8], which considers shadowing (but neglects orbit perturbations). The optimal path is completed in 215.9 days, with final mass ratio $x_{\gamma_f} = 0.8394$. Therefore, with the proposed nonlinear feedback approach, the transfer time is only 5.71% higher, and the final mass ratio is 1.78% lower than the optimal solution. Hence, this demonstrates that nonlinear feedback control can generate a transfer path very close to the optimal, minimum-time solution.

Monte Carlo Analysis

This subsection concentrates on nonnominal flight conditions, which account for the orbit injection errors and the stochastic failures of the propulsion system. The propulsion parameters, initial and final orbits, and gain values are the same as in the nominal case. Orbit injection errors are modeled by randomizing the initial orbit elements, using a uniform distribution. More specifically, the perigee and apogee radii (r_p and r_a) and inclination i have uniform distribution in the following ranges: $r_p = [350, 549] \text{ km} + R_E$ and $r_a = [549, 750] \text{ km} + R_E$ (where R_E is the Earth radius), and $i = [22.5, 34.5] \text{ deg}$. Moreover, RAAN, argument of perigee, and true anomaly have uniform distribution in the entire range of definition. The stochastic failure of the propulsion system is modeled by specifying the starting point of failure and its duration. These two stochastic variables, denoted respectively with t_{fail} and t_{dur} have uniform distribution as well, i.e. $t_{fail} = [1, 100] \text{ days}$ and $t_{dur} = [5, 20] \text{ days}$.

In spite of initial errors at orbit injection and stochastic propulsion failures, feedback control successfully drives the spacecraft to the desired orbit. Table 1 reports the Monte Carlo Analysis's statistical results, based on 1000 simulations, and compares the proposed feedback guidance and existing optimal solutions. These results testify to the excellent stability properties of feedback control as well as to the effectiveness of the gain selection method.

Table 1: Statistical results of the Monte Carlo Analysis and comparison with the optimal solution

	Mean	Std. Dev.	Optimal Solution
t_f (days)	236.41	10.51	215.94
x_7	0.8234	0.0063	0.8394

Concluding Remarks

This paper proposes and applies a near-optimal feedback guidance strategy based on nonlinear orbit control to low-thrust Earth orbit transfers. Feedback guidance utilizes some fundamental principles of Lyapunov stability theory and LaSalle's invariance principle. A novel gain selection strategy that involves an exhaustive table search and a numerical optimization algorithm provides near-optimality of the optimal paths traveled through feedback guidance. Two different flight conditions are considered: (i) *nominal conditions* and (ii) *nonnominal conditions that account for the orbit injection errors and the stochastic failures of the propulsion system*. The numerical results testify to the excellent stability properties of feedback control, as well as to the effectiveness of the gain selection method, even in nonnominal flight conditions.

References

- [1] P. Gurfil, "Nonlinear Feedback Control of Low-Thrust Orbital Transfer in a Central Gravitational Field," *Acta Astronautica*, vol. 60, no. 8 & 9, pp. 631-648, 2007.
<https://doi.org/10.1016/j.actaastro.2006.10.001>
- [2] M. Pontani and M. Pustorino, "Nonlinear Earth Orbit Control Using Low-Thrust Propulsion," *Acta Astronautica*, vol. 179, pp. 296-310, 2021.
<https://doi.org/10.1016/j.actaastro.2020.10.037>
- [3] Y. Gao, "Linear Feedback Guidance for Low-Thrust Many-Revolution Earth-Orbit Transfers," *Journal of Spacecraft and Rockets*, vol. 46, no. 6, pp. 1320-1325, 2009.
<https://doi.org/10.2514/1.43395>

- [4] C. A. Kluever, "Simple Guidance Scheme for Low-Thrust Orbit Transfers," *Journal of Guidance, Control, and Dynamics*, vol. 21, no. 6, pp. 1015-1017, 1998. <https://doi.org/10.2514/2.4344>
- [5] A. E. Petropoulos, "Low-Thrust Orbit Transfers Using Candidate Lyapunov Functions with a Mechanism for Coasting," in *AIAA/AAS Astrodynamics Specialist Conference and Exhibit*, Rhode Island, 2004. <https://doi.org/10.2514/6.2004-5089>
- [6] B. B. Jagannatha, J.-B. H. Bouvier and K. Ho, "Preliminary Design of Low-Energy, Low-Thrust Transfers to Halo Orbits Using Feedback Control," *Journal of Guidance, Control, and Dynamics*, vol. 42, no. 2, pp. 1-12, 2018. <https://doi.org/10.2514/1.G003759>
- [7] H. Holt, R. Armellin, A. Scorsoglio and R. Furfaro, "Low-thrust Trajectory Design using Closed-loop Feedback-driven Control Laws and State-dependent Parameters," in *AIAA Scitech 2020 Forum*, Orlando, 2020. <https://doi.org/10.2514/6.2020-1694>
- [8] M. Pontani and F. Corallo, "Optimal Low-Thrust Orbit Transfers with Shadowing Effect Using a Multiple-Arc Formulation," in *72nd International Astronautical Congress*, Dubai, 2021. <https://doi.org/10.1016/j.actaastro.2022.06.034>

Reduced-attitude stabilization for spacecraft boresight pointing using magnetorquers

Fabio Celani

School of Aerospace Engineering, Sapienza University of Rome, Via Salaria 851 00138 Roma
Italy

fabio.celani@uniroma1.it mail

Keywords: Boresight Pointing, Magnetorquers, Reduced Attitude, Stability

Abstract. This paper presents a method for achieving a desired boresight pointing of an instrument on a spacecraft using only magnetorquers as torque actuators. The desired pointing direction is inertially fixed. The proposed method is of proportional-derivate type and stabilizes the boresight pointing. Numerical simulations illustrate the effectiveness of the method and show that convergence to the desired pointing direction occurs faster than employing a three-axis stabilization approach.

Introduction

Pointing of the boresight of an instrument is a common task of many spacecraft during their operational life. For example, it might be required to point a telescope at a star, to point a transmitting or receiving antenna at a ground station, or to point the Sun with solar panels. A common approach for boresight control is performing three-axis attitude control which requires knowledge of the full attitude of the spacecraft. However, in boresight pointing applications, only the pointing direction is relevant and the rotation about the boresight is not considered. In this sense, full attitude knowledge is not required for boresight control, and it suffices to measure the reduced-attitude vector defined on the two-dimensional sphere. Motivated by this practical consideration this research presents a method for reduced-attitude stabilization for a spacecraft that uses only magnetorquers as torque actuators.

Magnetorquers are planar current-driven coils rigidly placed on the spacecraft typically along three orthogonal axes. The interaction between the magnetic dipole moment generated by those coils and the Earth magnetic field creates a torque that attempts to align the magnetic dipole moment in the direction of the field. Magnetorquers present the following benefits: (i) they are simple, reliable, and low cost; (ii) they need only renewable electrical power to be operated; (iii) they save weight with respect to any other class of torque actuators. On the other hand, magnetorquers have the following important limitations: (i) the control torque generated by magnetorquers is constrained to belong to the plane orthogonal to the Earth magnetic field; (ii) the maximum torque they can generate is substantially smaller than for other types of torque actuators. Due to these limitations, using only magnetorquers for attitude stabilization leads to smaller pointing accuracy and slower convergence compared to other torque actuators. Thus, it is considered a feasible option especially for low-cost micro and nano satellites, and for satellites with a failure in the main torque actuators.

This work proposes a boresight stabilization law for an inertially pointing spacecraft equipped only with magnetorquers as torque actuators. Numerical simulations for a case study show the effectiveness of the proposed law.

Spacecraft Boresight Pointing

Consider the problem of aligning a body-fixed boresight axis of an instrument on a spacecraft with an inertially-fixed reference axis. In addition, once the alignment condition is achieved the



spacecraft must not rotate about the reference axis to avoid blurred measurements from the instrument. The body-fixed boresight axis is expressed by the constant column matrix of its body coordinates $\mathbf{a} \in \mathbb{S}^2 = \{\mathbf{v} \in \mathbb{R}^3: \mathbf{v}^T \mathbf{v} = \mathbf{1}\}$. The inertially-fixed reference axis is expressed by the constant column matrix $\mathbf{a}_r^i \in \mathbb{S}^2$ of its coordinates along the standard Earth-Centered Inertial (ECI) frame [1]. Let \mathbf{R} be the rotation matrix that transforms a column matrix of body coordinates into the corresponding column matrix of ECI coordinates. Thus, the reference axis expressed in body-coordinates is given by $\mathbf{a}_r^b = \mathbf{R}^T \mathbf{a}_r^i$. Column matrix \mathbf{a}_r^b describes a reduced attitude and obeys the following kinematics [2]

$$\dot{\mathbf{a}}_r^b = \mathbf{a}_r^b \times \boldsymbol{\omega} \quad (1)$$

where $\boldsymbol{\omega}$ is the column matrix of body coordinates of the angular velocity of the body frame with respect to the ECI frame. The spacecraft is modeled as a rigid body and its attitude dynamics are given by [2]

$$\mathbf{J} \dot{\boldsymbol{\omega}} + \boldsymbol{\omega} \times (\mathbf{J} \boldsymbol{\omega}) = \mathbf{T}_c + \mathbf{T}_d \quad (2)$$

where \mathbf{J} is the spacecraft inertia matrix, \mathbf{T}_c is the column matrix of body coordinates of the control torque, and \mathbf{T}_d is column matrix of body coordinates of the sum of all disturbance torques acting on the spacecraft. The control torque is generated by three magnetorquers aligned with the body axes. Thus, it can be expressed as follows

$$\mathbf{T}_c = \mathbf{m}_c \times \mathbf{b}^b \quad (3)$$

where \mathbf{m}_c is the column matrix of the control magnetic dipole moments generated by the three magnetorquers, and \mathbf{b}^b is the column matrix of body coordinates of the geomagnetic induction.

The proposed boresight stabilization law is given by

$$\mathbf{m}_c = \mathbf{b}^b \times [k_p (\mathbf{a} \times \mathbf{a}_r^b) - k_d \boldsymbol{\omega}] \quad (4)$$

where k_p and k_d are positive scalar gains. The stabilization law is obtained by modifying the proportional-derivative like law for fully actuated spacecraft presented in [2]. Specifically, the cross product with \mathbf{b}^b is introduced to enforce that \mathbf{m}_c is perpendicular to \mathbf{b}^b . The latter property allows to save energy since Eq. 3 shows that a term in \mathbf{m}_c parallel to \mathbf{b}^b does not give any contribution to the control torque \mathbf{T}_c .

Stability Analysis

In this section a stability result of the proposed boresight stabilization law is presented. The stability analysis is carried out by adopting the inclined dipole model for the geomagnetic field [1]. Consider a circular orbit for the spacecraft and let $\mathbf{b}^i(t)$ denote the column matrix of ECI coordinates of the geomagnetic induction along the orbit. The adoption of the inclined dipole model leads to an almost periodic time behavior for $\mathbf{b}^i(t)$. Consider matrix

$$\boldsymbol{\Gamma}^i(t) = \mathbf{b}^i(t)^T \mathbf{b}^i(t) \mathbf{I}_{3 \times 3} - \mathbf{b}^i(t) \mathbf{b}^i(t)^T \quad (5)$$

where $\mathbf{I}_{3 \times 3}$ is the identity matrix. Note that $\boldsymbol{\Gamma}^i(t)$ is also almost periodic, and consider the following average value

$$\mathbf{\Gamma}_{av}^i = \lim_{T \rightarrow \infty} \frac{1}{T} \int_0^T \mathbf{\Gamma}^i(\tau) d\tau \quad (6)$$

It can be shown that the following stability result holds true.

Proposition. If $\det(\mathbf{\Gamma}_{av}^i) \neq \mathbf{0}$ then it is possible to determine positive values for k_p and k_d so that the equilibrium $(\mathbf{a}_r^b, \boldsymbol{\omega}) = (\mathbf{a}, \mathbf{0})$ of the closed-loop in Eqs. 1-4 with $\mathbf{T}_d = \mathbf{0}$ is asymptotically stable.

It can be obtained that condition $\det(\mathbf{\Gamma}_{av}^i) \neq \mathbf{0}$ is fulfilled if the orbit inclination is not too low.

Numerical Simulations

The goal of this section is to validate by numerical simulations the boresight stabilization law in Eq. (4). Consider a spacecraft with inertia matrix equal to $\mathbf{J} = \text{diag}[27 \ 25 \ 17] \text{ kg m}^2$ which follows a circular orbit with 450 km altitude, 87 deg inclination, and zero RAAN. The orbital period is about 5600 sec. The maximum value for each element of \mathbf{m}_c is set to 10 A m². The body-fixed boresight axis and the inertially-fixed reference axes are set equal to $\mathbf{a} = \mathbf{a}_r^i = [0 \ 0 \ 1]^T$. Disturbance torques included in the simulations are gravity-gradient torque, residual magnetization torque, and aerodynamic drag torque modeled as in [3]. The gains of the stabilization law are set to $k_p = 4.9 \cdot 10^4$ $k_d = 1.2 \cdot 10^9$. Since $\mathbf{a} = \mathbf{a}_r^i$ the required boresight pointing can also be achieved through a three-axis attitude stabilization action that aligns the body frame with the ECI frame. Thus, the performances of the proposed boresight stabilization law are compared with those of the following proportional-derivative-like three-axis attitude stabilization law [2]

$$\mathbf{m}_c = \mathbf{b}^b \times [-k_p \sum_{i=1}^3 (\mathbf{e}_i \times \mathbf{R} \mathbf{e}_i) - k_d \boldsymbol{\omega}] \quad (7)$$

in which \mathbf{e}_i is the i -th column of the identity matrix $\mathbf{I}_{3 \times 3}$. The numerical values of k_p and k_d are the same as for the boresight stabilization law.

A Monte Carlo campaign of 40 simulations is run by considering random initial attitude and random initial angular velocity with maximum amplitude of 3 deg/sec. The time behaviors of the pointing error and of the control magnetic dipole moment are reported in Fig. 1. In each simulation the pointing accuracy is evaluated through the magnitude $\Theta_{max \ ss}$ which denotes the maximum pointing error in steady-state. Table 1 reports the mean values $\overline{\Theta_{max \ ss}}$ and the standard deviations $\sigma(\Theta_{max \ ss})$ obtained with the two types of stabilization.

Table 1. Statistics of the Monte Carlo campaign

type of stabilization	$\overline{\Theta_{max \ ss}}$ [deg]	$\sigma(\Theta_{max \ ss})$ [deg]
boresight	17.68	3.22
three-axis	18.25	0.60

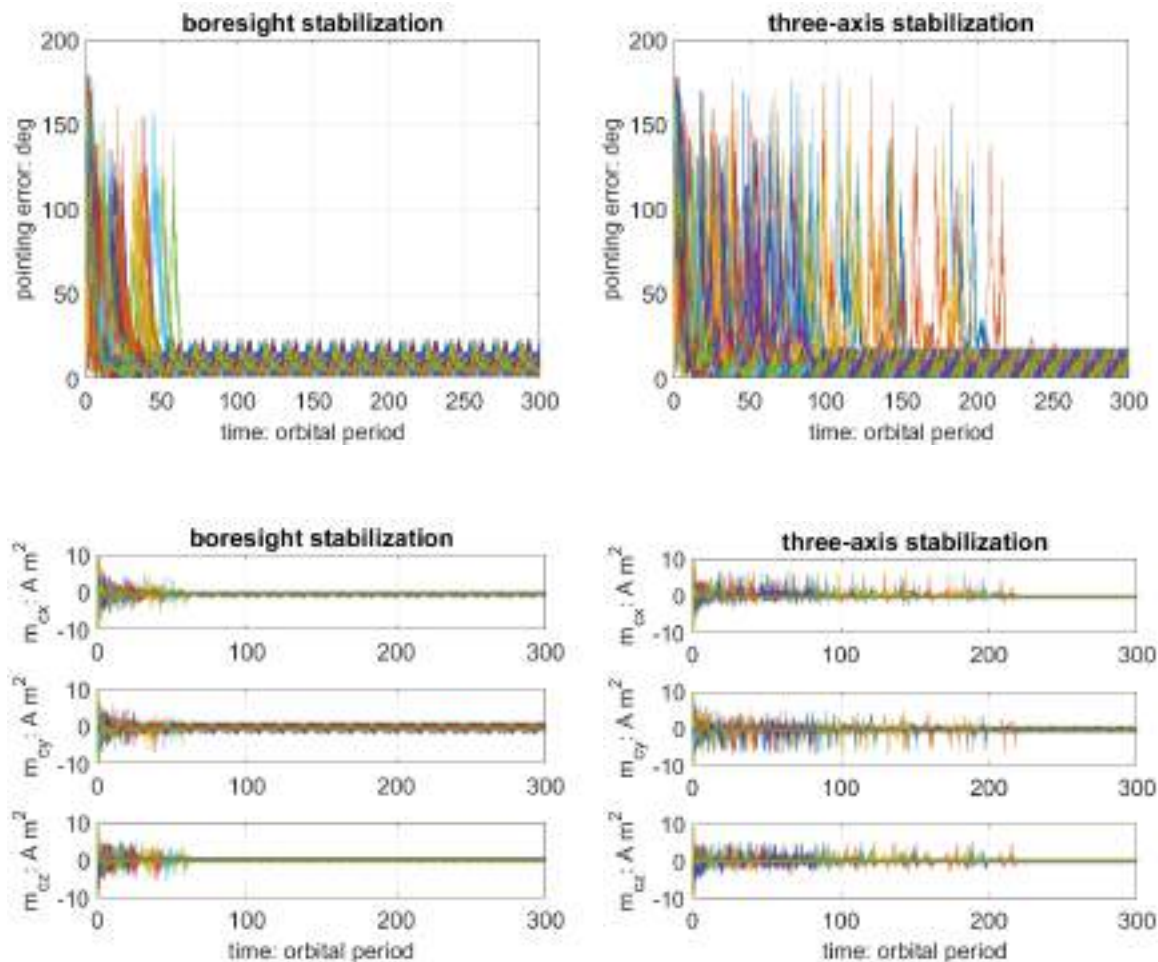


Figure 1. Time histories of the pointing error and of the control magnetic dipole moment.

The statistics show that the pointing accuracies of the two types of stabilization are similar. However, through visual inspection of the time behaviors of the pointing error obtain that boresight stabilization achieves a faster convergence to the steady-state behavior. Specifically, by employing boresight stabilization converge is obtained after approximately 60 orbital periods in the worst simulation run whereas with three-axis stabilization it is obtained only after about 250 orbital periods in the worst case. Faster convergence is probably due to the fact that the objective of boresight stabilization is achieving the desired alignment only for the boresight axis rather than for of all three body axis.

References

- [1] J.R. Wertz (Ed.), *Spacecraft Attitude Determination and Control*, Kluwer Academic, Dordrecht, 1978.
- [2] N.A. Chaturvedi, A.K. Sanyal, N.H. McClamroch, Rigid-body attitude control, *IEEE Control Systems Magazine* 31 (2011), 30-51. <https://doi.org/10.1109/MCS.2011.940459>
- [3] F. Celani, Spacecraft attitude stabilization using magnetorquers with separation between measurement and actuation, *Journal of Guidance, Control, and Dynamics* 39 (2016), 2184-2191. <https://doi.org/10.2514/1.G001804>

Trajectory optimization and multiple-sliding-surface terminal guidance in the lifting atmospheric reentry

Edoardo Maria Leonardi^{1,a*} and Mauro Pontani^{2,c}

¹Department of Astronautical, Electrical, and Energy Engineering, Sapienza University of Rome, via Salaria 851, 00138 Rome, Italy

^aedoardomaria.leonardi@uniroma1.it, ^bmauro.pontani@uniroma1.it

Keywords: Lifting Reentry, Optimal Guidance, Sliding-Mode

Abstract. In this paper the problem of guiding a vehicle from the entry interface to the ground is addressed. The Space Shuttle Orbiter is assumed as the reference vehicle and its aerodynamics data are interpolated in order to properly simulate its dynamics. The transatmospheric guidance is based on an open-loop optimal strategy which minimizes the total heat input absorbed by the vehicle while satisfying all the constraints. Instead, the terminal phase guidance is achieved through a multiple-sliding-surface technique, able to drive the vehicle toward a specified landing point, with desired heading angle and vertical velocity at touchdown, even in the presence of nonnominal initial conditions. The time derivatives of lift coefficient and bank angle are used as control inputs, while the sliding surfaces are defined so that these two inputs are involved simultaneously in the lateral and vertical guidance. The terminal guidance strategy is successfully tested through a Monte Carlo campaign, in the presence of stochastic winds and wide dispersions on the initial conditions at the Terminal Area Energy Management, in more critical scenarios with respect to the orbiter safety criteria.

Introduction

The development of an effective guidance architecture for atmospheric reentry and precise landing represents a crucial issue for the design of reusable vehicles capable of performing safe planetary reentry. Unsurprisingly, the interest in guidance and control technologies for atmospheric reentry and landing of winged vehicles has increased [1-2], as the flexibility and controllability of the reentry trajectory can be increased through the employment of lifting bodies. However, this implies a greater sensitivity to the environmental conditions. Thus, the usefulness of a real-time guidance algorithm, able to generate online trajectories, is evident, for the purpose of guaranteeing safe descent and landing even in the presence of nonnominal conditions and dispersions caused by the preceding transatmospheric phase.

The guidance and control strategy of the Space Shuttle relied on the modulation of the bank angle to follow a pre-computed reference drag profile, and could only account for small deviations from the nominal conditions [3]. Mease and Kremer and Mease et al. [4] revisited the Shuttle reentry guidance, using nonlinear geometric methods. Later on, Benito and Mease [5] developed and applied a new controller based on model prediction, where the bank angle is modulated to minimize an effective cost function which accounts for the error in drag acceleration and downrange. Nonlinear predictive control was employed by Minwen and Dayi to generate skip entry trajectories for low lift-to-drag vehicles [6]. Most recently, Lu [7] considered a unified guidance methodology based on a predictor-corrector algorithm, for vehicles with different aerodynamic efficiency, while satisfying the boundaries on the thermic flux and load factor. Instead, a more limited number of papers addressed the terminal descent and landing, which is traveled after the Terminal Area Energy Management (TAEM) interface. Kluever [8] developed a guidance scheme for an unpowered vehicle with limited normal acceleration capabilities. Bollino



et al. [9] employed a pseudospectral-based algorithm for optimal feedback guidance of reentry spacecraft, in the presence of large uncertainties and disturbances. Fahroo and Doman [10] used again a pseudospectral method in a mission scenario with actuation failures. Finally, reinforcement learning was used for autonomous guidance algorithms for precise landing [11]. Recently, sliding mode control was proposed as an effective nonlinear approach to yield real-time feedback control laws able to drive an unpowered space vehicle toward a specified landing site [3,12]. Depending on the instantaneous state and the desired final conditions, sliding mode control was already shown to be effective for generating feasible atmospheric paths leading to safe landing in finite time, even when several nonnominal flight conditions may occur that can significantly deviate the vehicle from the desired trajectory, e.g. winds or atmospheric density fluctuations [13].

In this work, an open-loop optimal guidance is developed for the transatmospheric arc, capable of minimizing the total heat input while driving the vehicle toward the TAEM. The Space Shuttle Orbiter is taken as the reference vehicle and an analytical method is employed to keep the maximum thermic flux below the safety limit, while accounting for the saturation on the control variables. Finally, the multiple-sliding-surface guidance is employed in order to drive the vehicle from the TAEM to the landing point, with accurate aerodynamic modelling, while including stochastic winds and large dispersions on the initial values of the state and control variables.

Reentry dynamics

The reentry vehicle is modelled as a 3-DOF lifting body and the position of the centre of mass is identified by a set of three spherical coordinates (r, λ_g, φ) , representing respectively the instantaneous radius, the geographical longitude and the latitude. The additional variables are given by the relative velocity with respect to the Earth surface \mathbf{v}_r , the heading angle ζ_r and the flight path angle γ_r . The trajectory equations describe the motion of the center of mass due to the effect of the forces acting on it [14].

The Space Shuttle Orbiter is taken as the reference vehicle for numerical simulations. It is assumed that the lift and drag coefficients (C_L and C_D) depend only on the angle of attack α and Mach number M , while the sideslip coefficient C_Q depends only of the sideslip angle β and Mach number M . The aerodynamics coefficients are obtained from wind tunnel tests [15] and are interpolated in order to derive their expressions as continuous functions of the aerodynamic angles and Mach number ($C_L = C_L(\alpha, M)$, $C_D = C_D(\alpha, M)$, $C_Q = C_Q(\beta, M)$).

Transatmospheric phase

The transatmospheric guidance drives the vehicle from the entry interface towards the TAEM, while keeping the thermic flux per unit area at the stagnation point q_s below the maximum value and minimizing the cost function

$$J = k_r \Delta_r + k_y \Delta_y + k_z \Delta_z + k_v \Delta_v + k_\zeta \Delta_\zeta + k_\gamma \Delta_\gamma + k_q \int_0^{t_f} q_s dt \quad (1)$$

where the coefficients k are chosen to balance the different contributions, while the terms Δ represent the deviations on the state variables at the final time, located at the TAEM. The reentry trajectory is sampled at equally-spaced time instants t_k from the entry interface to the TAEM and the guidance law is determined through parametric optimization of the following parameters:

- sampled values of the bank angle;
- sampled values of the angle of attack from $M = 6$ to the TAEM;
- the total time of flight t_f from the reentry interface to the TAEM;

- the Mach number M^* at the end of the constant-angle-of-attack flight profile;
- the argument of latitude u_0 at the initial time;

The boundary conditions reflect the typical descent profile of the Space Shuttle [16] ($r_0 = 122000$ m, $v_{r0} = 7300$ m/s, $\gamma_{r0} = -1.4^\circ$, $r_f = 25000$ m, $v_{rf} = 762$ m/s, $\varphi_f = 29.41^\circ$, $\lambda_g = -81.46^\circ$, $\zeta_f = -60.24^\circ$) and the algorithm must keep the thermic flux below the maximum allowable value, equal to 681.39 kW/m², even lower than the typical value reported in the scientific literature, i.e. 794.43 kW/m² [17]. The dynamic pressure must be less than 16.375 kPa.

Thermic flux saturation. The thermic flux at the leading edge can be computed as $q_s = q_a q_r$, where $q_r = a\sqrt{\rho}(bv_r)^n$ and $q_a = c_0 + c_1\alpha + c_2\alpha^2 + c_3\alpha^3$, with $a = 17700$, $b = 0.0001$ and $n = 3.07$ [17]. The derivative of the thermic flux can be easily computed as $\dot{q}_s = Fq_r + q_a G\dot{\alpha}$, where F and G are auxiliary functions that do not depend on the input variable ($\dot{\alpha}$). Therefore, the time derivative of the lift coefficient can be computed as

$$\dot{C}_l = \frac{dC_l}{d\alpha}\dot{\alpha} - \frac{dC_l}{d\alpha} \frac{F}{G} \frac{q_a}{q_r} \quad (2)$$

Guidance strategy. The descent of the vehicle through the atmosphere is controlled through modulation of the angle of attack and bank angle. In particular, the variation of the angle of attack follows the succession of four distinct flight profiles:

- constant-angle-of-attack flight from the entry interface to $M = M^*$;
- variable-angle-of-attack flight as described by Eq. 10;
- variable-angle-of attack flight following a sinusoidal profile from $M = M^*$ to $\tilde{M} = 6$;
- variable-angle-of-attack flight optimized by the guidance algorithm.

Numerical results. Table 1 reports the results of the optimization. The guidance algorithm is able to drive the vehicle through the atmosphere, with limited dispersions on the final state at the TAEM (cf. Table 1), along a descent path close to the actual trajectory of the Orbiter [16].

Table 1: displacements of the state variables from the boundary values at TAEM

Q [MJ/m ²]	Δr [m]	Δy [m]	Δz [m]	Δv_r [m/s]	$\Delta \zeta_r$ [°]	$\Delta \gamma_r$ [°]
325.87	2.05	0.32	53.95	9.50	$6.35 \cdot 10^{-4}$	$1.26 \cdot 10^{-5}$

Fig. 1 and 2 highlight the time history of the angle of attack, which keeps the thermic flux below the maximum value. Saturation of the thermal flux occurs after about 200 s, as shown

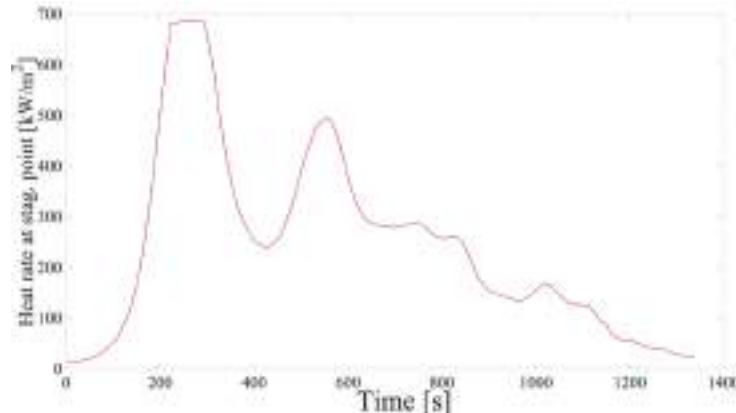


Fig. 1: time histories of the thermal flux along the transatmospheric arc

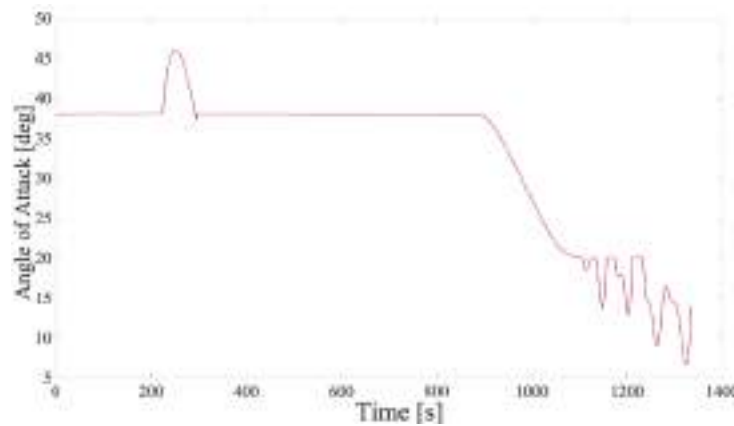


Fig. 2: time histories of the angle of attack along the transatmospheric arc

Terminal guidance

Along the transatmospheric arc, different factors may modify the reentry trajectory from the reference profile. Therefore, the terminal guidance must be able to drive the vehicle despite a wide range of initial conditions. In a previous work, sliding-mode control was already employed as a nonlinear approach to yield real-time feedback guidance laws in an accurate dynamic framework, including winds and large deviations from the initial trajectory variables [13]. In this study, significant improvements are developed with respect to the previous research:

- sliding-mode guidance is tested for a longer time period (i.e. from the TAEM to ground) and the aerodynamic modeling is based on real data rather than approximate analytical expressions;
- the saturation of the control variables is accounted inside the expression of the control input, so that only feasible trajectories are generated;
- the guidance gains are updated through an adaptive strategy, allowing further extension of the capability of the algorithm.

Numerical results. A total number of 500 simulations are run and the initial conditions are randomly generated with upper/lower bounds set to $\pm 2\sigma_s$ (where σ_s denotes the standard deviation of the variable of interest). Stochastic wind is also accounted for, whose intensity and direction is stronger than the safety limits prescribed for the Space Shuttle Orbiter landing [18]. Table 2 collects the initial conditions and associated standard deviations, which reflect the actual reference flight profile of the Space Shuttle [16]. Instead, Table 3 collects the results of the Monte Carlo campaign.

Table 2: initial conditions and standard deviations

Variable	$x(0)$ [m]	$y(0)$ [m]	$z(0)$ [m]	$v_r(0)$ [m/s]	$\zeta_r(0)$ [deg]	$\gamma_r(0)$ [deg]	$C_L(0)$ [-]	$\sigma(0)$ [deg]
Initial Conditions	24050	-54850	95932	762	ζ_f	-8	0.3969	0
Std. Dev.	0	2500	2500	15	5	1	0.01	5

Table 3: results of the Montecarlo campaign

Variable	r_{down} [m]	r_{cross} [m]	\dot{x} [m/s]	v_r [m/s]	ζ_r [deg]	γ_r [deg]	α [deg]	σ [deg]
Mean	761.61	4.41	-1.02	138.69	-60.23	-0.43	6.26	-0.07
Std. Dev.	$-5.66 \cdot 10^{-3}$	$5.04 \cdot 10^{-3}$	0.10	16.63	0.02	0.09	1.74	1.17

From inspection of Table 3, it is evident that the algorithm is able to drive the vehicle to the prescribed landing point, which is located 762 m beyond the runway threshold, with limited crossrange component and vertical velocity at touchdown, and the proper alignment with the runway [16]. Figure 3 shows the stream of trajectories from the TAEM to the landing runway.

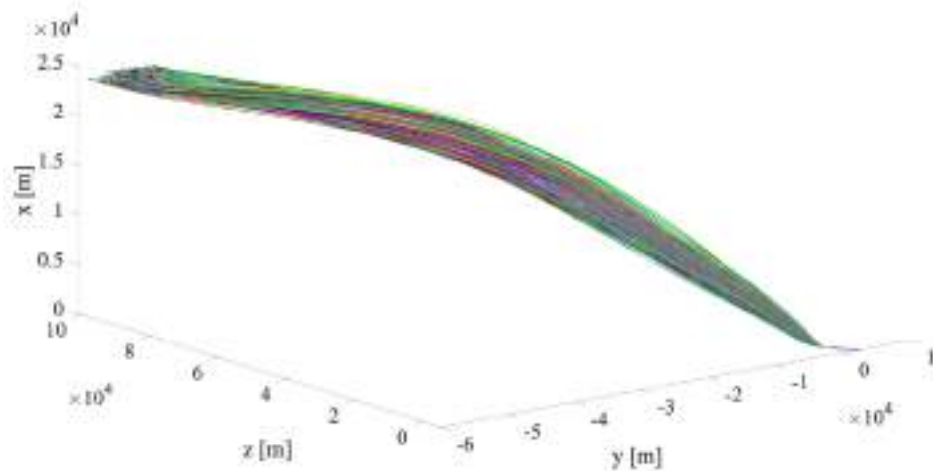


Fig. 3: stream of trajectories

Concluding remarks

This paper addresses the problem of driving a winged vehicle (i.e. the Space Shuttle Orbiter) from the entry interface to landing, while satisfying all the constraints. The transatmospheric guidance is based on an open-loop algorithm that minimizes the total heat input and saturates the maximum thermal flux. The terminal guidance is based on a multiple-sliding-surface strategy, which allows online generation of trajectories. The simulation setup includes a complete dynamic framework with an accurate aerodynamics modeling based on wind tunnel tests. *The numerical results* show the ability of the proposed guidance to modulate the angle of attack to avoid exceeding the maximum thermal flux, while compensating for winds and dispersions of position and velocity from the nominal trajectory during the terminal phase. The vehicle reaches the landing point with the proper alignment with the runway and a safe vertical velocity.

References

- [1] R. Haya, L. T. Castellani and A. Ayuso, "Reentry GNC concept for a reusable orbital platform (space rider)", *69th International Astronautical Congress*, Bremen, Germany, *IAC-18 D*, Vol. 2, 2018, p. 5.
- [2] Z. Krevor, R. Howard, T. Mosher and K. Scott, "Dream Chaser Commercial Crewed Spacecraft Overview", *17th AIAA International Space Planes and Hypersonic Systems and Technologies Conference*, AIAA Paper 2011-2245, 2011. <https://doi.org/10.2514/6.2011-2245>
- [3] N. Harl and S. Balakrishnan, "Reentry terminal guidance through sliding mode control", *Journal of Guidance, Control and Dynamics*, Vol. 33, No. 1, pp. 186-199, 2010. <https://doi.org/10.2514/1.42654>
- [4] K. D. Mease and J.-P. Kremer, "Shuttle Entry Guidance Revisited Using Nonlinear Geometric Methods", *Journal of Guidance, Control and Dynamics*, Vol. 17, No. 6, 1994, pp. 1350-1356. <https://doi.org/10.2514/3.21355>
- [5] J. Benito and K. D. Mease, "Nonlinear Predictive Controller for Drag Tracking in Entry Guidance", *AIAA/AAS Astrodynamics Specialist Conference and Exhibit*, AIAA Paper 2008-7350, 2008. <https://doi.org/10.2514/6.2008-7350>
- [6] G. Minwen and W. Dayi, "Guidance Law for Low-Lift Skip Reentry Subject to Control Saturation Based on Nonlinear Predictive Control", *Aerospace Science and Technology*, Vol. 37, No. 6, 2014, pp. 48-54. <https://doi.org/10.1016/j.ast.2014.05.004>
- [7] P. Lu, "Entry Guidance: A Unified Method", *Journal of Guidance, Control and Dynamics*, Vol. 37, No. 3, 2014, pp. 713-728. <https://doi.org/10.2514/1.62605>
- [8] C. A. Kluever, "Unpowered Approach and Landing Guidance Using Trajectory Planning", *Journal of Guidance, Control and Dynamics*, Vol. 27, No. 6, 2004, pp. 967-974. <https://doi.org/10.2514/1.7877>
- [9] M. R. K. Bollino and D. Doman, "Optimal Nonlinear Feedback Guidance for Reentry Vehicles", *AIAA Guidance, Navigation and Control Conference and Exhibit*, AIAA Paper 2006-6074, 2006. <https://doi.org/10.2514/6.2006-6074>
- [10] F. Fahroo and D. Doman, "A Direct Method for Approach and Landing Trajectory Reshaping with Failure Effect Estimation", *AIAA Guidance, Navigation and Control Conference and Exhibit*, AIAA Paper 2004-4772, 2004. <https://doi.org/10.2514/6.2004-4772>
- [11] B. Gaude, R. Linares and R. Furfaro, "Deep reinforcement learning for six degree-of-freedom planetary landing", *Advances in Space Research*, Vol. 65, No. 7, pp. 1723-1741, 2020. <https://doi.org/10.1016/j.asr.2019.12.030>
- [12] X. Liu, F. Li, Y. Zhao, "Approach and Landing Guidance Design for Reusable Launch Vehicle Using Multiple Sliding Surfaces Techniques", *Chinese Journal of Aeronautics*, Vol. 30, No. 4, 2017, pp. 1582-1591. <https://doi.org/10.1016/j.cja.2017.06.008>
- [13] A. Vitiello, E. M. Leonardi and M. Pontani, "Multiple-Sliding-Surface Guidance and Control for Terminal Atmospheric Reentry and Precise Landing", *Journal of Spacecraft and Rockets*, Vol. 60, No. 3, pp. 912-923, 2023. <https://doi.org/10.2514/1.A35438>
- [14] M. Pontani, *Advanced Spacecraft Dynamics*, 1st ed., Edizioni Efesto, Rome, 2023, pp. 253-259.
- [15] C. Weiland, *Aerodynamic Data of Space Vehicles*, 1st ed., Springer Berlin, Heidelberg, 2014, pp. 174-197. https://doi.org/10.1007/978-3-642-54168-1_1
- [16] D. R. Jenkins, *Space Shuttle: The History of the National Space Transportation System: The First 100 Missions*, D. R. Jenkins, Cape Canaveral, 2008, pp. 260-261.
- [17] J. T. Betts, *Practical methods for optimal control and estimation using nonlinear programming*, 2nd ed., SIAM, Philadelphia, 2010, pp. 247-256. <https://doi.org/10.1137/1.9780898718577>
- [19] S. Siceloff, "Nasa-Space Shuttle Weather Launch Commit Criteria and KSC End of Mission Weather Landing Criteria", 2003.

Analytic formulation for J2 perturbed orbits

Silvano Sgubini^{1,a*}, Giovanni B. Palmerini^{1,b}

¹ Scuola di ingegneria Aerospaziale, Sapienza Università di Roma via Salaria 851 – 00138
Roma, Italy

^a silvano.sgubini@gmail.com, ^b giovanni.palmerini@uniroma1.it

Keywords: Orbit Propagation, Orbit Perturbations, J2 Effects, Formation Flying

Abstract. The paper deals with a technique developed along the years at the Scuola di Ingegneria Aerospaziale to provide an exact solution for J2 perturbed orbits, here applied to spacecraft formations. Analytic solutions are useful in the design phase and can help in operations to identify and to efficiently maintain a suitable configuration. The approach is based on the elaboration, conveniently performed by means of a symbolic software tool, of a set of equations analogous to the Lagrange planetary relations. Resulting parameters are expressed through Fourier series depending only on the initial conditions. Comparison with standard, longer to obtain and less accurate numerical propagation clarify the advantage of the technique, which is limited only by the number of terms taken into account in the expansion.

Introduction

Numerical propagation of orbits gained widespread acceptance due to the availability of large computation resources and to the possibility to include the effects of all perturbations. However, analytic formulations – when available – offer an exact and really fast solution and helps in the understanding of the problem, with obvious advantages in design. It is well known that Keplerian trajectories can be expressed as an expansion of terms, providing an analytical solution, even if practically limited by the number of terms taken into account. Taylor expansions in powers of the time or of the eccentricity and Fourier expansion in terms of the anomaly are possible, with a bound on eccentricity values in order to ensure convergence [1, 2]. It is interesting to similarly act for real orbits, where perturbations have to be considered. There is a large interval of orbital altitudes, between 600 and 900 km, where – for standard spacecraft, i.e. the ones missing extremely large appendages – the dominant perturbation is the one due to the aspherical gravitational potential of the Earth. Furthermore, the second harmonic of the Earth potential, the one representing the oblate or polar-flattened Earth and shortly indicated as J2, is definitely the most relevant term, so that the analysis can be conveniently limited to it. Interestingly, this interval of altitudes is highly important for Earth observation missions. In such a frame, an analytic solution – with obvious advantages with respect to numerical propagation in terms of time and accuracy – can be of significant interest. The present study is inspired to the original approach by Broglio [3], and has been step-by-step improved and applied to tracking and orbit determination and in previous works by present authors [4,5,6]. In this paper the focus is mostly on the computation of the distances among satellites, i.e. in the field of formation flying. The ultimate goal would be to obtain results similar to the ones provided by extensive numerical simulations aimed to identify J2 invariant formations [7] and to help in the relevant analysis [8], with the target to limit the effort required to control the configuration [9].



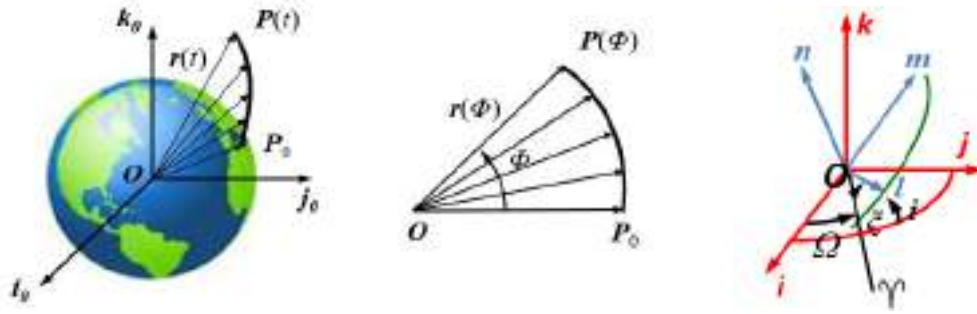


Fig. 1 – Sketch of a J2-perturbed orbit (not anymore laying on a plane) with the parameters adopted to describe the position of the satellite (adapted from [4]).

Approach

The position of the satellite along the orbit can be defined, according to the frame reported in Fig. 1, by the radius and the three angles Ω , i and ξ . The dynamics (Laplace planetary equations) can be written as

$$\begin{aligned} i' &= a_n \frac{r^3}{K^2} \cos \xi & \Omega' &= a_n \frac{r^3}{K^2} \frac{\sin \xi}{\sin i} & \xi' &= 1 - a_n \frac{r^3}{K^2} \frac{\sin \xi}{\tan i} \\ \frac{K'}{K} &= a_m \frac{r^3}{K^2} & t' &= \frac{r^2}{K} & \left(\frac{1}{r} \right)' + \frac{1}{r} &= -\frac{r^2}{K^2} \left[a_l + r \left(\frac{1}{r} \right)' a_m \right] \end{aligned} \quad (1)$$

where K is the angular momentum, t the time and derivatives, represented by the apex ($'$), refer to the angular variable and the a coefficients, if we limit to the case of the J2 effect, are simply given as

$$\begin{aligned} a_l &= \frac{\mu}{r^2} - \frac{3}{2} \mu J_2 R_\oplus^2 \frac{1}{r^4} (1 - 3 \sin^2 i \sin^2 \xi) \\ a_m &= -\frac{3}{2} \mu J_2 R_\oplus^2 \frac{1}{r^4} \sin^2 i \sin 2\xi & a_n &= -\frac{3}{2} \mu J_2 R_\oplus^2 \frac{1}{r^4} \sin 2i \sin \xi \end{aligned} \quad (2)$$

After a significant mathematical elaboration (see [5]), the set of Eq.(1) leads to an expression for r and for the three angles Ω , i and ξ as in following Eq. 3. Coefficients depend on the initial conditions only, and can be evaluated until the desired order. Notice that nowadays such an elaboration has been helped by symbolic software (e.g. MATLAB [10] in the present case).

$$\begin{aligned} r &= R'_0 + \sum_h \left[R'_h \cos \left(h \frac{2\pi}{T} (t - t_{iniz}) \right) + R''_h \sin \left(h \frac{2\pi}{T} (t - t_{iniz}) \right) \right] \\ \Omega &= \Omega'_0 - \frac{3}{2} J_2 \cos i_{iniz} \left(\frac{R_\oplus \mu_\oplus}{K_{iniz}^2} \right)^2 \frac{2\pi(t-t_{iniz})}{T} + \sum_h \left[\Omega'_h \cos \left(h \frac{2\pi}{T} (t - t_{iniz}) \right) + \Omega''_h \sin \left(h \frac{2\pi}{T} (t - t_{iniz}) \right) \right] \\ i &= I'_0 + \sum_h \left[I'_h \cos \left(h \frac{2\pi}{T} (t - t_{iniz}) \right) + I''_h \sin \left(h \frac{2\pi}{T} (t - t_{iniz}) \right) \right] \\ \xi &= \xi'_0 + \frac{2\pi}{T} (t - t_{iniz}) - \frac{3}{2} J_2 \cos i_{iniz} \left(\frac{R_\oplus \mu_\oplus}{K_{iniz}^2} \right)^2 \frac{2\pi(t-t_{iniz})}{T} + \sum_h \left[\xi'_h \cos \left(h \frac{2\pi}{T} (t - t_{iniz}) \right) + \xi''_h \sin \left(h \frac{2\pi}{T} (t - t_{iniz}) \right) \right] \end{aligned} \quad (3)$$

The correctness of the solution can be easily estimated by the comparison with a standard numerical propagation (see Fig. 2 for examples relevant to two parameters of interest).

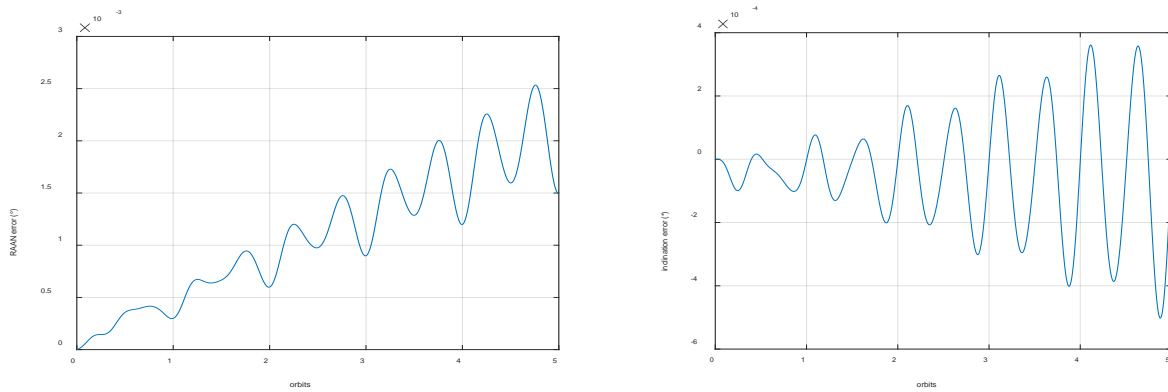


Fig. 2 – Differences between analytical approach and numerical integration.

Formations

The very same approach can be iterated for different spacecraft. However, it is extremely important to remark the relevance of the initial conditions to be imposed to the satellites belonging to the formation. A simple computation of the distance between generic, yet close initial conditions gives the results presented in Fig. 3 for two spacecraft. Notice that the distance is given by the difference between the two vectors representing the radii, with three backward rotations in the angles Ω_1 , i_1 , ζ_1 for the first spacecraft and Ω_2 , i_2 and ζ_2 for the second one to obtain the components along the inertial frame's axes.

Within the concept of formation flying, it is desired that a configuration with limited inter-satellite distances should last in time. So, additional constraints can be applied among the parameters referred to the two - or more – spacecraft belonging to the formation. A first preliminary indication can be given by imposing the same energy to the two satellites (Fig. 4).

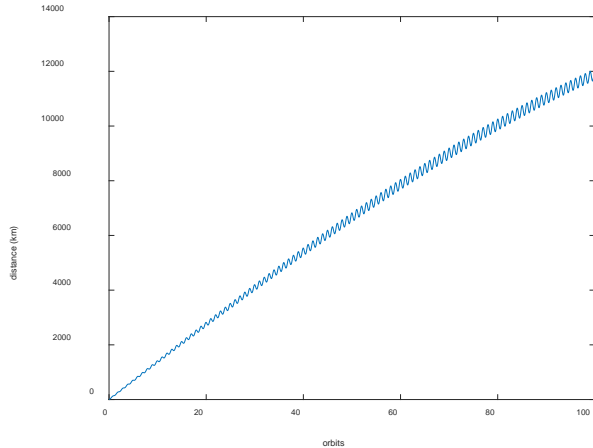


Fig. 3 – Distance between two close satellites.

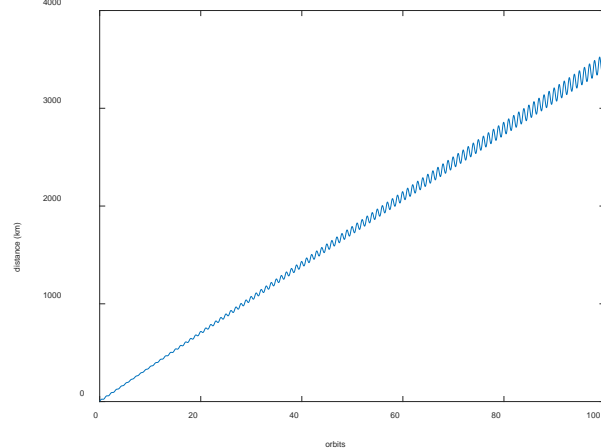


Fig. 4 – Distance imposing equal energy.

A first constraint is given by equal period, that is a requirement to avoid divergence. A second constraint is related to the inclination, that has to be assumed as quite close for the satellites to stay in formation: in fact, even 1 degree if difference would create a distance in the order of 120 km for orbits of 600 km altitude. Furthermore, larger differences end up in a different environment in terms of other perturbations, so an almost equal inclination can be reasonably assessed. A third constraint is given by the equal precession of the ascending nodes. Note that the analytical solution gives a secular term: this term vanishes for some critical inclinations. Once all of these constraints are imposed, the results plotted in Fig. 5-6 can be obtained.

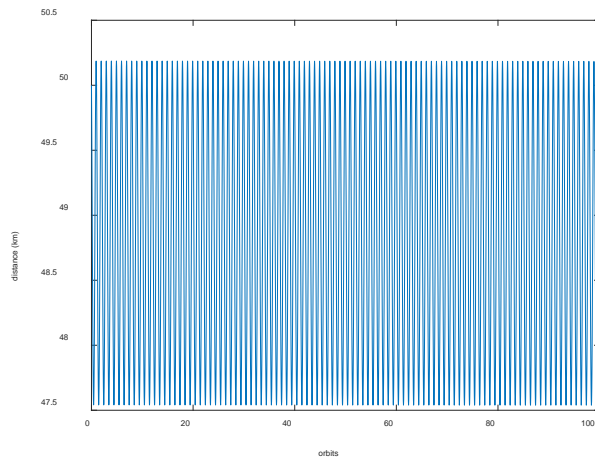


Fig. 5 – Distance imposing the condition of an equal location after a short time interval (8s).

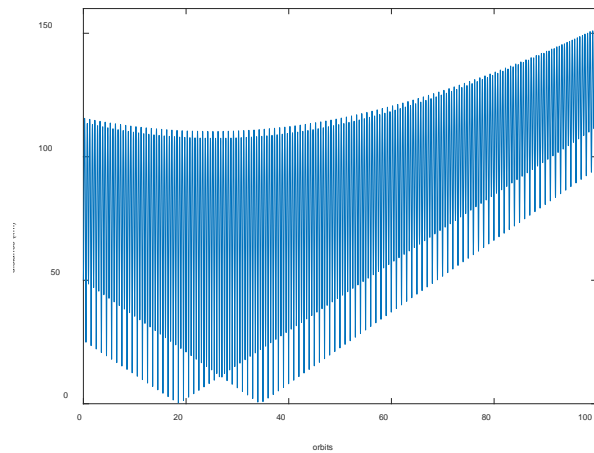


Fig. 6 Initial conditions as per Fig.4 adding constraints of equal period and secular drift.

Final Remarks

Design and operations phases of formation flying missions can be helped by the availability of analytic solutions taking into account the oblateness effects. The work, following the path pursued along the years by the authors, proposes analytic formulas for the distances between satellites considering the dominant effect of the J2 term, and prove their correctness and their appeal even if only a limited number of terms in the expansion should be used.

References

- [1] R.F. Moulton. Introduction to Celestial Mechanics. McMillian, New York, 1914.
- [2] S.A. Klioner. Lecture Notes on Basic Celestial Mechanics, Technische Universitaet Dresden, 2016. <https://doi.org/10.48550/arXiv.1609.00915>
- [3] L. Broglio. Lezioni di Meccanica del Volo Spaziale (a cura di S. Sgubini), Scuola di Ingegneria Aerospaziale, Università di Roma “La Sapienza”, 1973.
- [4] S. Sgubini, G.B. Palmerini. A fast approach for relative orbital determination in spacecraft formations, in “IEEE Aerospace Conference Proceedings”, Big Sky (MT, USA), 2012.
- [5] S. Sgubini, G.B. Palmerini. Efficient Techniques for Relative Motion Analysis between Eccentric Orbits under J2 Effect, in “IEEE Aerospace Conference Proceedings”, Big Sky (MT, USA), 2013.
- [6] S. Sgubini, G.B. Palmerini. Fast Analytical Evaluation of Near-Keplerian Orbit Evolution in Multiple Launch Release. Congresso Nazionale AIDAA, Roma, 2019.
- [7] M. Sabatini, D. Izzo, G.B. Palmerini. Analysis and control of convenient orbital configuration for formation flying missions. Adv. Astronaut. Sci. 124, (2006) 313–330.
- [8] S.R. Vadali, P. Sengupta, H. Yan, K.T. Alfriend. On the fundamental frequencies of relative motion and the control of satellite formations. Adv. Astronaut. Sci. 129 (2008) 2747–2766.
- [9] M. Sabatini, D. Izzo, G.B. Palmerini. Minimum control for spacecraft formations in a J2 perturbed environment, Celest. Mech. Dyn. Astron. 105 (2009) 141-157. <https://doi.org/10.1007/s10569-009-9214-5>
- [10] Symbolic Math Toolbox™ User's Guide, The MathWorks Inc., 2023.

Low-thrust maneuver anomaly detection of a cooperative asset using publicly available orbital data

Riccardo Cipollone^{1,a *}, Pierluigi di Lizia^{1,b}

¹Department of Aerospace Science and Technology, Politecnico Di Milano, Via Giuseppe La Masa 54 20156, Milano, Italy

^ariccardo.cipollone@polimi.it, ^bpierluigi.dilizia@polimi.it

Keywords: Low-Thrust Maneuver Estimation, Semi-analytic Method, Anomaly Detection

Abstract. This work presents a novel method to estimate perturbations with respect to nominal maneuver planning by exploiting Two-Line-Element (TLE) data as initial step, then moving on to Global Positioning System (GPS) processed data. The case study is a low-thrust engine validation mission in Low Earth Orbit. The first algorithm exploits a couple of TLEs as boundary conditions to set up a least-squares problem and find the tangential thrust magnitude and firing duration to best fit the bounding orbital states, making use of Taylor differential algebra and Picard iterations. The second one makes use of a sequence of GPS states to apply multistep finite differences and a root-finding algorithm to retrieve information about both thrust profile and firing bounding times.

Introduction

Over the past few decades, there has been a steady growth in the quantity of scientific and commercial Earth-bound space missions. This upward trend has led to a significant expansion of activities and programs focused on Space Situational Awareness. Up-to-date orbital data obtained by updating ephemeris data with new observations play a vital role in effectively tracking cooperative target assets, offering valuable information to ensure a mission's success [1]. The main product provided by the processing pipelines used to exploit measurements' information are regularly maintained Resident Space Object catalogs [2].

The kind of anomaly detection performed in this framework is usually linked with the orbital motion of the satellite and to its routine maneuvers. The high-level workflow starts by exploiting available intel about known objects to build predictions of a target's nominal behavior and compare it to the actual incoming acquisitions. If any properly defined distance from the nominal path trespasses some user defined threshold, the anomalous event is recorded, and further analysis can be carried out. This specific case of anomaly identification widely overlaps with maneuver detection and characterization of a tracked object. The reason for this is that according to how much it is known about the nominal trajectory and control policy of an object, any anomalous event involving the dynamics of the target can be modeled as a maneuver, steering it away from the nominal path, and characterized as such, in terms of an equivalent acceleration or expense. Examples in literature are diverse, most of them stemming from the theory of maneuver target tracking, dealing with observations that partially describe the state at observation epoch. These techniques are usually based on adaptive Kalman filtering modeling an input term as a stochastic process or a deterministic input to be estimated when the measurement innovation term fails a Gaussian test, meaning that the modeled uncertainty is no longer enough to explain deviations from the prediction [3]. As for a more SST-tailored application, the work in [4], shows how State Transition Matrix theory can be remodeled to linearly map small variations of control, modeled as an impulsive ΔV , to variations in the final orbital state. Following the usual optimal control assumption, the residual between the predicted final state and the actual one is minimized, linking the pre- and post-maneuver orbit with an impulsive magnitude and a firing epoch. This last method represents the basis for the one proposed in this work, allowing to connect two TLEs, by leveraging



some assumptions based on the knowledge of the target features, by a high-order Taylor expansion of both thrust and firing epochs. As for the module exploiting GPS states, due to lack of rich literature, for the low-thrust case, a finite different method has been envisaged as first approach to test if an acceleration profile and accurate onset and termination times can be directly extracted from the states sequence.

Fundamentals and method

The theoretical tools used for the TLE-based maneuver anomaly detection are mainly Taylor Differential Algebra (DA) and Picard iterations, allowing for the condensation of iterative function evaluations in a single polynomial map, function of both thrust magnitude and time variations with respect to the reference onset and termination epochs.

DA provides a solution to analytical problems through an algebraic approach by means of the Taylor polynomial algebra. A Taylor expansion up to an arbitrary order k can be used to represent any deterministic function f of v variables that is C^{k+1} in the domain of interest $[-1, 1]^v$ (scaled according to the needs), with limited computational effort:

$$f(x) = \sum_{k=0}^N \frac{f^{(k)}(x_0)}{k!} (x - x_0)^k \quad (1)$$

Thus, variables are represented as truncated power series around an expansion point x_0 , instead of standard types [5]. The DA framework is implemented in a C++ computational environment through the DACE library. The key feature of DA leveraged for this technique is the flow expansion of an Ordinary Differential Equation (ODE): this feature relieves the processing burden due to iterative integrators embedding the whole integration scheme in a single function evaluation.

As for Picard iterations, they are implemented exploiting the same C++ computational environment following the scheme to obtain a k -order time expansion [6]:

$$\phi_0(t) = y_0 \quad (2)$$

$$\phi_{k+1}(t) = y_0 + \int_{t_0}^t f(s, \phi_k(\tau)) dk \quad (3)$$

Where $\phi_{k+1}(t)$ is the order k expansion, y_0 is the function value at the center of the expansion and f is ϕ function's time derivative expression, used to iteratively integrate around the reference time t_0 .

As regards the GPS data-based technique, multi-step, high-order finite differences are used to provide an estimate of the acceleration and jerk directly from the velocity provided with the GPS states. The general formulation used to compose the coefficients involved in the differentiation scheme are derived from the Fronberg method reported in [7] to compute a 1-D derivative of arbitrarily high order on a uniformly spaced grid for a given number of points. To detect the onset and termination epochs of each firing instead, a thresholding method is employed, based on the variance computed on the cumulative sequence of data to detect abrupt changes in it, such as peaks or steps [8]. A final refinement step is performed to resolve the above-mentioned epochs below the sampling frequency of the given GPS states by exploiting a non-linear system root-finding algorithm (MATLAB fsolve) to put to zero the residuals corresponding to the first sampled GPS state downstream the discontinuities as a function of their corresponding epoch.

Concerning the method itself, the TLE-based module is based on several assumptions to limit the complexity of the problem: constant and tangential thrust during the firing, constant burning rate and known onset time. The process starts by propagating the state coming from the first TLE file by augmenting the state with thrust and mass and by using the nominally controlled trajectory as reference for the expansion. The number of firing arcs to be included between the TLE couple

can vary, increasing the number of variables of the problem and, therefore, the number of possible solutions. The DA variables are initialized to order 4. They model the constant thrust norm perturbations of each firing arc together with its termination time, computed by 4 Picard iterations around the expected termination time. The process is repeated for every firing arc, composing TPSs mapping perturbations for each of them to the one on the orbital state. The process outputs a propagated final state used to build a residual with respect to the one derived from the second TLE file. This residual function is then fed to MATLAB fsolve so to find perturbations putting it to zero with limited computational effort. The firings' modeling process is summed up in Fig. 1.

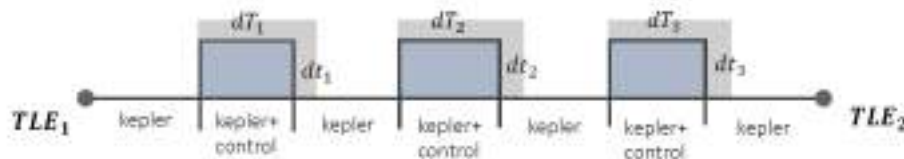


Figure 1. DA variables configuration for a 3-firing case, dT_n being thrust magnitude perturbations, dt_n termination time perturbations.

As for the GPS-based technique, the assumptions are two: the thrust is constant and tangential throughout the firing and so is the burning rate. It starts by simply computing the second time derivative of the velocity extracted from the sampled states. The norm of this quantity (jerk) is then employed to build residuals with respect to the second derivative norm of the expected trajectory velocity, computed by differencing only once, starting from the expression of the nominal dynamics. This sequence of residuals is scanned for abrupt changes by analyzing the variance computed on a progressively higher number of elements and checking whether it overcomes a predefined threshold.



Figure 2. Segments of data used to accurately differentiate the GPS velocity time series.

The discontinuity points identified are used to perform a composite finite difference method, splitting the time series of velocities into 7 segments for every arc, divided by the onset and termination times (as shown in Fig. 2). The method is composed of a backward finite differencing scheme of order 6 for the samples immediately before the discontinuities, a forward scheme of order 6 for the values just after it and a centered scheme of order 8 for the rest. In this way, a first estimate of the thrust profile can be obtained to give reliable boundary conditions to the boundary time estimates refinement. This last step is performed with a propagation across each discontinuity that is only a function of the related epoch. Residuals on the downstream state are defined and put to zero by MATLAB fsolve. Once the actual onset and termination times are obtained, the composite finite differencing scheme is performed once again with updated epochs and mass profile, and the final thrust estimate is retrieved.

Uncertainty propagation is embedded in both modules by means of linear projection of available covariances to the estimated quantities space (via the Jacobian of the transform).

Results

The scenario used to test the TLE-based module is simulated starting from a LEO object with the following Keplerian elements:

$$\mathbf{e} = [7.5805e + 03 \text{ km}, 0.0760, 0.7151 \text{ rad}, 5.9935 \text{ rad}, 2.1723 \text{ rad}] \quad (4)$$

performing from 1 to 3 nominal firing arcs of 1100 s duration with a constant tangential thrust of 10 mN. The nominal trajectory is then perturbed with a 10 mN thrust parasitic magnitude and a 7 s firing termination time delay for the single firing case to generate the post-maneuver TLE. The same is done for the 2-firing (10 mN, 7 s for the first one, -7 mN, -3 s for the second one) and 3-firing cases (10 mN, 7 s, -7 mN, -3 s, -3 mN, 5 s). The tests show errors in below $1e-4$ mN in thrust perturbation magnitude and $1e-5$ s in termination time perturbation both in the 1 and the 2-firing cases, while the 3-firing one results in convergence to wrong local minima, due to solution multiplicity of the non-linear system.

As for the GPS-based module test scenario, the same target is involved and the thrust magnitude, onset and termination times perturbations are (4 mN thrust magnitude perturbation, -17 s onset perturbation, 35 s termination perturbation), used to sample the GPS states with a 5 s time step. In this case results show fair performance with $1e-1$ mN as average error order of magnitude on thrust profile and errors of $1e-4$ s for both onset and termination time perturbations.

Conclusions

This work presents a method to effectively exploit publicly available orbital data to perform maneuver anomaly detection on a cooperative asset. A crucial detail to understand the current performance of the technique resides in the fact that, due to the kind of preliminary study conducted on them to be then further elaborated, these first tests have been conducted without adding any noise to the states used as measurements. The first further step to take is in facts to study how sensitive these techniques are to measurement noise and whether to integrate the pipeline with filtering techniques to take this aspect into account and even it out.

References

- [1] Montaruli, Marco Felice, Purpura, Giovanni, Cipollone, Riccardo, De Vittori, Andrea, Di Lizia, Pierluigi, Massari, Mauro, Peroni, Moreno, Panico, Alessandro, Cecchini, Andrea, and Rigamonti Marco, 'A Software Suite for Orbit Determination in Space Surveillance and Tracking Applications', EUCASS-3AF 2022. <https://doi.org/10.13009/EUCASS2022-7338>
- [2] ESA Space Debris Office, 'Esa's Annual Space Environment Report', tech. rep., European Space Agency, April 2022
- [3] Rong Li X. , Jilkov Vesselin P. , A Survey of Maneuvering Target Tracking—Part IV: Decision-Based Methods, Proceedings of SPIE Conference on Signal and Data Processing of Small Targets, Orlando, FL, USA, April 2002
- [4] Pastor, G. Escribano, and D. Escobar, "Satellite maneuver detection with optical survey observations," Advanced Maui Optical and Space Surveillance Technologies Conference, 2020.
- [5] Wittig A., Di Lizia P., Armellin R., Makino K., Bernelli-Zazzera F., and Berz M., Propagation of large uncertainty sets in orbital dynamics by automatic domain splitting. *Celestial Mechanics and Dynamical Astronomy*, 122(3):239–261, 2015. <https://doi.org/10.1007/s10569-015-9618-3>
- [6] Vitolo M., Maestrini M., Di Lizia P., Sampling-Based Strategy for On-Orbit Satellite Inspection, 25th Conference of the Italian Association of Aeronautics and Astronautics (AIDAA 2019)

- [7] Fornberg, Bengt. 'Generation of Finite Difference Formulas on Arbitrarily Spaced Grids'. *Mathematics of Computation* 51, no. 184 (1988): 699–706. <https://doi.org/10.1090/S0025-5718-1988-0935077-0>
- [8] Killick R., P. Fearnhead, and I.A. Eckley. "Optimal detection of changepoints with a linear computational cost." *Journal of the American Statistical Association*. Vol. 107, Number 500, 2012, pp.1590-1598. <https://doi.org/10.1080/01621459.2012.737745>

Efficient models for low thrust collision avoidance in space

Juan Luis Gonzalo^{1,a*}, Camilla Colombo¹, Pierluigi Di Lizia¹, Andrea De Vittori¹,
Michele Maestrini¹, Pau Gago Padreny², Marc Torras Ribell²,
Diego Escobar Antón²

¹Politecnico di Milano, Department of Aerospace Science and Technology, Via la Masa 34,
20158 Milan (Italy)

²GMV, Calle de Isaac Newton 11, 28760 Tres Cantos, Madrid (Spain)

^ajuanluis.gonzalo@polimi.it

Keywords: Space Collision Avoidance, Low Thrust Propulsion, Spaceflight Mechanics, Analytical Models, Space Traffic Management

Abstract. A family of analytical and semi-analytical models for the characterization and design of low thrust collision avoidance manoeuvres (CAMs) in space is presented. The orbit modification due to the CAM is quantified through the change in Keplerian elements, and their evolution in time is described by analytical expressions separating secular and oscillatory components. Furthermore, quasi-optimal, piecewise-constant control profiles are derived from impulsive CAM models. The development of these models is part of an ESA-funded project to advance existing tools for collision avoidance activities.

Introduction

The number of objects in orbit around the Earth is growing at an accelerating pace, due to both the increasing number of public entities and private companies leveraging space assets for diverse applications and the accumulation of space debris. Regarding active satellites, their numbers are soaring owing to the deployment of large constellations like Starlink, and the democratization of access to space enabled by lower launch costs and smaller, cost-effective platforms like CubeSats. The increasing congestion in space presents multiple challenges for Space Traffic Management and Space Situational Awareness, and demands the implementation of space debris mitigation actions like end-of-life deorbiting and collision avoidance (COLA) to curb the increase of space debris. However, an increasing portion of satellites are equipping low thrust propulsion systems, which, although more efficient, present a smaller control authority and complicate the design of disposal and collision avoidance manoeuvres (CAMs), particularly for last-time scenarios. As a result, new models and tools are needed to support low thrust COLA activities in congested orbital regions like low Earth orbit (LEO) and geostationary orbit (GEO).

In this context, GMV, UC3M and Politecnico di Milano are developing the ELECTROCAM project, funded by the European Space Agency to advance their models and tools for the analysis of low thrust COLA activities. The project covers several aspects of COLA activities, including the assessment of current capabilities of low thrust satellites [1], propagation of uncertainties [2,3], efficient analytical and semi-analytical models for CAMs [4], and update of ESA's operational software tool ARES.

This work deals with some of the analytical and semi-analytical CAM models developed within the ELECTROCAM project. The models are focused on computational efficiency, to serve as initial guesses for more accurate, higher-cost numerical algorithms, and to perform sensitivity analyses over large sets of data. To this end, a single-averaging of the thrust-perturbed equations of motion is performed to express the evolution of the Keplerian elements as the combination of linear and oscillatory contributions, both expressed through exact or approximated analytical



expressions. A simplified control law is also proposed, leveraging analogous models for the impulse propulsion case. The performance of the models has been assessed through sensitivity analyses in relevant COLA scenarios, and some selected results are presented here.

Single-averaged low-thrust CAM model

Let us consider a predicted close approach (CA) at a given time of closest approach (TCA) between a low-thrust-capable spacecraft and a debris (in general, a non-collaborative object). The CAM is modelled following the scheme proposed in [5], composed of three steps. First, the orbit modification due to the CAM is quantified through the change $\delta\alpha$ of its vector of Keplerian elements $\alpha=[a,e,i,\Omega,\omega,M]$, whose components are, respectively, semimajor axis, eccentricity, inclination, right ascension of the ascending node, argument of pericentre, and mean anomaly. Second, the change in orbital elements is mapped to changes in position and velocity at the TCA using a linearized relative motion model with the nominal trajectory as reference orbit. Because the displacements associated to CAMs in practical scenarios are typically small, the loss of accuracy due to the use of a linearized model is limited. Finally, the outcome from the CAM is projected and characterized in the nominal encounter plane at TCA, and the change in collision probability quantified.

The most complex step is the derivation of (semi-)analytical expressions for $\delta\alpha$ under a continuous thrust acceleration \mathbf{a}_t . The models considered here are based on the single-averaging of Gauss's planetary equations over one revolution, under the assumption of small thrust acceleration. This assumption allows to linearize the equations of motion in thrust acceleration and study the tangential and normal components separately (denoted by superscripts t and n):

$$\dot{\alpha} = \mathbf{G}(\alpha, t; \mathbf{a}_t) \approx \mathbf{G}^t(\alpha_0 + \delta\alpha^t, t; a_t^t) + \mathbf{G}^n(\alpha_0 + \delta\alpha^n, t; a_t^n) + \dot{\alpha}_0 = \delta\dot{\alpha}^t + \delta\dot{\alpha}^n + \dot{\alpha}_0. \quad (1)$$

Where \mathbf{G} represents Gauss's planetary equations, and $\dot{\alpha}_0$ is the evolution of mean anomaly for the unperturbed orbit. The solutions for $\delta\alpha^t$ and $\delta\alpha^n$ from Eq. 1 fall into three categories. First, some Keplerian elements are unaffected by the corresponding thrust component (Ω and i for tangential, a , i and Ω for normal). Then, some elements have only oscillatory behaviours, and their expressions can be integrated directly (ω for tangential, e for normal). Finally, the rest of elements combine secular behaviours with time scale proportional to the thrust magnitude, and oscillatory components with period linked to the orbital one. This is the case for a and e under tangential thrust, and ω under normal thrust. The secular expressions are obtained changing the independent variable in the equations of motion from time to eccentric anomaly E , and averaging the ODEs over 1 revolution. The resulting secular terms are linear, with slopes function of complete elliptic integrals of the first and second kind of the reference eccentricity e_{ref} . The oscillatory terms are obtained as a series expansion in e_{ref} and involve harmonics of the orbital period in E . The detailed derivation of the single-averaged analytical models and resulting expressions can be found in [5,6,7,4].

The proposed expressions for $\delta\alpha$ have E as independent variable. A time law for $E(t)$ can be obtained from the differential equation for E , introducing the analytical approximation obtained for $\alpha(E)=\alpha_0+\delta\alpha(E)$. The resulting time law is explicit to compute time as function of anomaly, $t(E)$, but implicit to compute $E(t)$. This situation is analogous to that of the Kepler's equation, to which it reduces for $\mathbf{a}_t=0$, and prevents the solution from being fully analytical

Quasi-optimal control law

The previous models allow to evaluate the outcome of a CAM without a numerical integration, but to optimize the CAM they should be used within an iterative numerical optimizer. A more computationally efficient approach is proposed based on analogous models developed for impulsive CAMs [8]. The optimization problem for impulsive CAMs can be reduced to an

eigenproblem, where the eigenvector associated to the largest eigenvalue determines the optimal direction of thrust. Then, a piecewise-constant low-thrust CAM can be defined by dividing the thrust arc in segments and assigning to each of them the orientation of the impulsive CAM at its middle point. Furthermore, given that optimal fuel manoeuvres follow bang-bang structures, the magnitude of thrust at each segment will be either maximum or 0. To define in which segments is more convenient to thrust, it can be proven that the eigenvalue of the impulsive CAM at each segment serves as proxy for the local efficiency of the CAM compared to the other segments.

Test case

Multiple scenarios for low-thrust CAMs have been studied within the ELECTROCAM project. For brevity, a single case is presented here. The Keplerian elements at TCA of the spacecraft are $\alpha_{sc} = [7552.1 \text{ km}, 0.0012, 87.93 \text{ deg}, 1.95 \text{ deg}, 127.53 \text{ deg}, 5.10 \text{ deg}]$, while for the debris $\alpha_{deb} = [7575.5 \text{ km}, 0.0100, 89.39 \text{ deg}, 179.03 \text{ deg}, 112.64 \text{ deg}, 295.72 \text{ deg}]$. The elements of the combined covariance matrix in the B-plane (defined as in [5]) are $\sigma_\xi = 0.0179 \text{ km}$, $\sigma_\zeta = 0.0214 \text{ km}$, $\rho_{\xi\zeta} = -0.0524$. Fig. 1 shows the results in terms of probability of collision PoC and displacement inside the B-plane δb , for a single-thrust-arc CAM with fixed thrust magnitude (10^{-8} km/s or 10^{-9} km/s) and different values of the thrust arc duration, Δt_{CAM} , and the coast arc between thrust end and TCA, Δt_{coast} . Times are expressed as fractions of the nominal orbital period T .

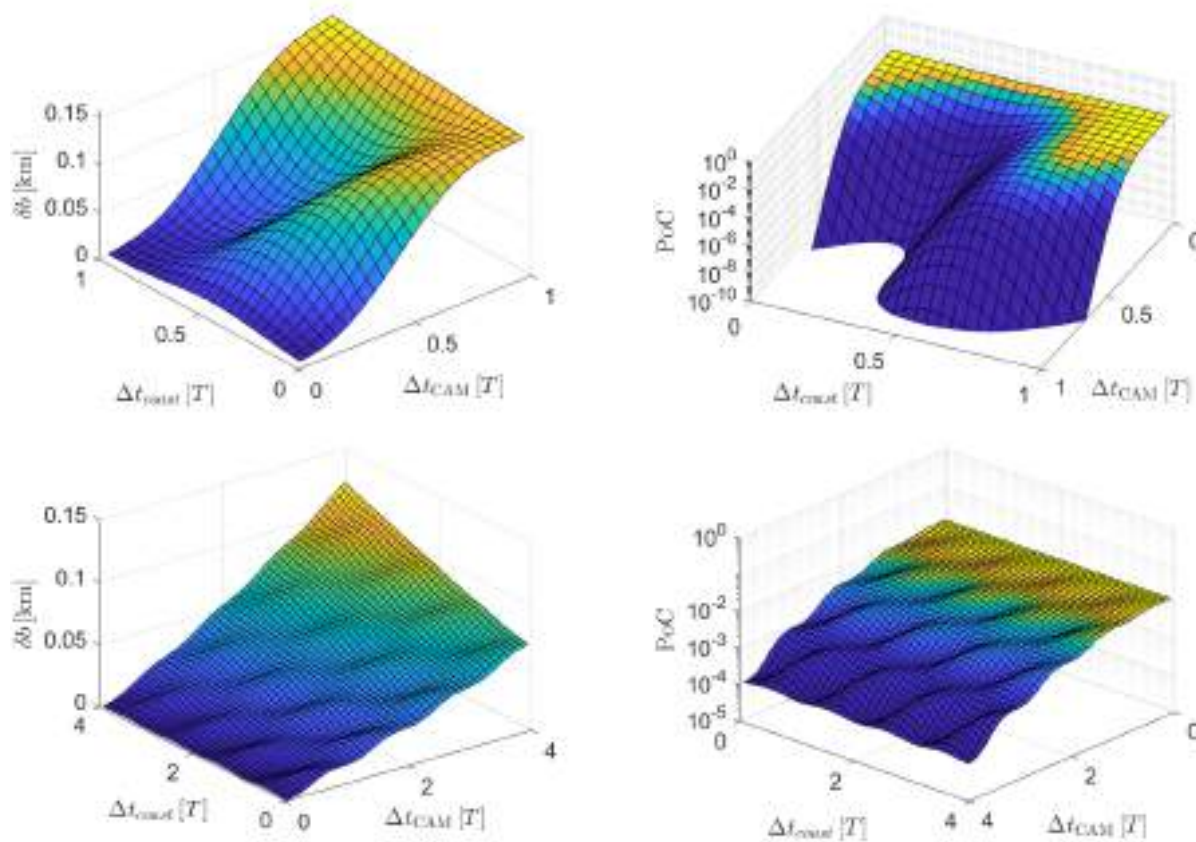


Figure 1. Displacement and PoC for test case in LEO, with $a_t = 10^{-8} \text{ km/s}$ (top) and $a_t = 10^{-9} \text{ km/s}$ (bottom)

Conclusions

The latest developments in a novel family of analytical and semi-analytical models for low-thrust CAM computation and design have been presented. These models rely on the single-averaging of the equations of motion in Keplerian elements to derive approximate analytical solutions separating the secular and oscillatory components for the orbit evolution induced by the CAM. For

CAM design, instead, quasi-optimal piecewise-constant thrust profiles are derived from the impulsive counterpart of the models. Part of these developments have been performed within the ESA-funded ELECTROCAM project.

Acknowledgements

This work has received funding from the European Space Agency through the project "ELECTROCAM: Assessment of collision avoidance manoeuvre planning for low-thrust missions" (call AO/1-10666/21/D/SR).

Juan Luis Gonzalo also thanks the funding of his research position by the Italian Ministero dell'Università e della Ricerca, Programma Operativo Nazionale (PON) "Ricerca e Innovazione" 2014-2020, contract RTDA – DM 1062 (REACT-EU).

References

- [1] C. Colombo, A. De Vittori, M. Omodei, J.L. Gonzalo, M. Maestrini, P. Di Lizia, P. Gago Padreny, M. Torras Ribell, A. Gallego Torrego, D. Escobar Antón, Roberto Armellin, Sensitivity analysis of collision avoidance manoeuvre with low thrust propulsion, Aerospace Europe Conference 2023 (10th EUCASS - 9th CEAS), Lausanne, Switzerland, 9-13 July 2023
- [2] M. Maestrini, A. De Vittori, P. Di Lizia, C. Colombo, Dynamics-Based Uncertainty Propagation with Low-Thrust, 2022 AAS/AIAA Astrodynamics Specialist Conference, Charlotte, NC, USA, 7-11 Aug. 2022
- [3] M. Maestrini, A. De Vittori, J.L. Gonzalo, C. Colombo, P. Di Lizia, J. Míguez Arenas, M. Sanjurjo Rivo, A. Diez Martín, P. Gago Padreny, D. Escobar Antón, ELECTROCAM: Assessing the Effect of Low-Thrust Uncertainties on Orbit Propagation, 2nd ESA NEO and debris detection conference, Darmstadt, Germany, 24-26 Jan. 2023
- [4] J.L. Gonzalo, C. Colombo, P. Di Lizia, Single-averaged models for low-thrust collision avoidance under uncertainties, 73rd IAC, Paris, France, 18-22 Sept. 2022
- [5] J.L. Gonzalo, C. Colombo, P. Di Lizia, Introducing MISS, a new tool for collision avoidance analysis and design, Journal of Space Safety Engineering, 7:3 (2020), 282-289.
<https://doi.org/10.1016/j.jsse.2020.07.010>
- [6] J.L. Gonzalo, C. Colombo, P. Di Lizia, A semianalytical approach to low-thrust collision avoidance manoeuvre design, 70th IAC, Washington, D.C., USA, 21-25 Oct. 2019. Paper no. IAC-19.A6.2.3
- [7] J.L. Gonzalo, C. Colombo, P. Di Lizia, Computationally efficient approaches for low-thrust collision avoidance activities, 72nd IAC, Dubai, UAE, 25-29 Oct. 2021. Paper no. IAC-21-A6.10-B6.5.5
- [8] J.L. Gonzalo, C. Colombo, P. Di Lizia, Analytical framework for space debris collision avoidance maneuver design, J. Guid. Control Dyn., 44:3 (2021), 469-487.
<https://doi.org/10.2514/1.G005398>

An overview of the ArgoMoon and LICIACube flight dynamics operations

Marco Lombardo^{1,a*}, Luis Gomez Casajus², Marco Zannoni^{1,2,b}, Igor Gai²,
Edoardo Gramigna¹, Paolo Tortora^{1,2}, Elisabetta Dotto³, Marilena Amoroso⁴,
Simone Pirrotta⁴, Valerio Di Tana⁵, Biagio Cotugno⁵, Silvio Patruno⁵,
Francesco Cavallo⁵, and the *LICIACube* Team^{1,2,3,4,5}

¹Dipartimento di Ingegneria Industriale (DIN), Alma Mater Studiorum – Università di Bologna,
Via Fontanelle 40, 47121, Forlì, Italy

²Centro Interdipartimentale di Ricerca Industriale Aerospaziale (CIRI AERO), Alma Mater
Studiorum— Università di Bologna, Via Baldassarre Carnaccini 12, 47121 Forlì, Italy

³INAF Osservatorio Astronomico di Roma, Monte Porzio Catone, Italy

⁴Agenzia Spaziale Italiana, Via del Politecnico, 00133 Roma, Italy

⁵Argotec S.r.l., Via Cervino 52, 10155 Torino, Italy

^amarco.lombardo14@unibo.it, ^bm.zannoni@unibo.it

Keywords: ArgoMoon, LICIACube, Deep Space, Cis-Lunar, Navigation, Orbit Determination, Flight Path Control, IRIS, Moon, Dimorphos, Didymos, Artemis-1, DART

Abstract CubeSats are becoming a reliable alternative for low-cost space applications in deep space, as mission companions or as standalone missions. The use of CubeSats in deep space requires to address many operational challenges, particularly those related to navigation. LICIACube and ArgoMoon are the first two 6U CubeSat missions to the outer space funded and managed by the Italian Space Agency, whose spacecrafts have been developed and operated by Argotec. The flight dynamics operations of both missions were performed by the flight dynamics team of the University of Bologna using NASA/JPL's navigation software MONTE. This paper gives a brief presentation of the flight dynamics operations of ArgoMoon and LICIACube and presents the obtained results highlighting the challenges of cis-lunar and deep space CubeSat navigation as well as the achieved successes.

Introduction

The CubeSat standard identifies a category of small satellites whose design is based on an elementary form factor of 1 U, that corresponds to a cube of 10 cm of latus [1]. The use of compact and lightweight spacecraft (S/C) enables a reduction of costs (design, assembly, integration, and launch) without sacrificing research objectives. Many CubeSats have been launched in Low Earth Orbit (LEO) [2], demonstrating that this small satellite technology is also trustworthy for complex missions other than educational or technological demonstrations. These characteristics made CubeSats appealing for deep space and cis-lunar exploration [3], either as stand-alone missions or as companions to conventional, larger spacecrafts. Two recent and relevant cis-lunar and deep space CubeSat missions, that successfully proved the capabilities of the platform and ground teams to operate in the outer space, are LICIACube and ArgoMoon.

Light Italian CubeSat for Imaging of Asteroids (LICIACube)

LICIACube is a 6U CubeSat mission of the Italian Space Agency (ASI) [4] that participated to the Double Asteroid Redirection Test (DART) mission of NASA [5]. The DART mission aimed to perform a technology demonstration to examine asteroid redirection by performing a controlled high velocity impact [6]. The objective of LICIACube was to take thorough and relevant photos



of the effects of DART impact on Dimorphos. LICIACube was equipped with an active attitude determination and control system, a cold-gas orbital Propulsion System (PS), and a star tracker, while the core of the scientific payload was composed of two optical cameras [7]. LICIACube was placed into DART as a secondary payload and, after a cruise of 10 months, it was released into space on September 11, 2022, 15 days before the planned impact [8].

LICIACube ground-based navigation has been performed by the Radio Science and Planetary Exploration Laboratory (RSLab) of the University of Bologna (UNIBO), and independently also by the NASA's Jet Propulsion Laboratory (JPL), both using the NASA/JPL's orbit determination software MONTE [9]. The navigation strategy was based on two-way radiometric observables, Doppler and range, acquired by the Deep Space Network (DSN) [10]. The navigation aimed to fly LICIACube through a specific region of the Dimorphos B-plane defined from the mission high-level scientific requirements. The primary navigation requirements were to maintain the nominal trajectory and fly-by conditions to prevent collisions with the impact ejecta debris, maintain the impact scene within the cameras field of view, and prevent the saturation of the reaction wheels during the high-rate rotation phase to point at Dimorphos near the closest approach. The mission timeline included a calibration maneuver (CAL1) to check the thrusters, a targeting maneuver (Orbital Maneuver 1 - OM1) to address the aimpoint, and two clean-up maneuvers (OM2, OM3) to clear potential trajectory deviations during the operations.

On the first hours after the LICIACube deployment from DART, the acquired Doppler data showed a signature compatible with a tumbling motion caused by the S/C, which entered in safe mode because of the release event. However, the tumbling motion was then successfully damped by the CubeSat before the end of the first tracking pass. To properly fit the data of the first two tracking passes, a Doppler bias of ~ 1.86 Hz had to be estimated. Then, a commanded re-configuration of the LICIACube transponder during the second pass removed the latter bias, leaving only a small residual bias of ~ 0.025 Hz to be estimated. The Doppler biases were caused by a quantization error on the on-board digital IRIS [11] transponder. Stochastic accelerations were implemented and estimated to fit the data to the noise level. A detailed inspection of the stochastic accelerations shown signatures currently attributed to larger than expected non-gravitation accelerations. Despite the challenges, the team managed to design all the necessary maneuvers to reach the target point and to reconstruct the trajectory of LICIACube, satisfying all the navigation requirements. Figure 1 reports the Orbit Determination (OD) solutions of OM1, OM2, and OM3 deliveries, on the Dimorphos B-plane. As can be seen from the presented results, after OM2, the predicted trajectory and its $3\text{-}\sigma$ state uncertainty were widely contained in the requirement region and, as consequence, OM3 was scrubbed.

On September 26, 2022, LICIACube flew by Dimorphos at a distance of ~ 58 km and at a relative velocity of ~ 6.1 km/s [8], successfully acquiring the images before and after the DART impact on the asteroid including the ejection plume.

ArgoMoon

NASA selected 10 CubeSats as secondary payloads of the Space Launch System (SLS) for the Artemis-1 mission. Among them, ASI's ArgoMoon was chosen as an essential technological demonstrator [12]. The ArgoMoon S/C is based on the same 6U CubeSat platform of LICIACube, and the main goals of the mission were to autonomously fly around the Interim Cryogenic Propulsion Stage (ICPS), to capture images of the stage, and to confirm that the other CubeSats

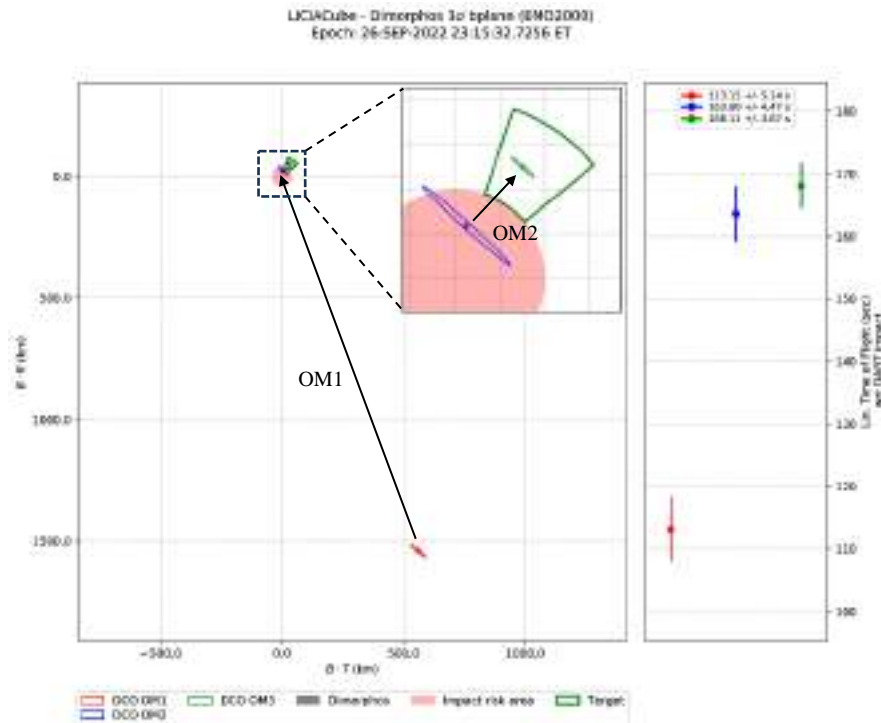


Figure 1: LICIACube predicted trajectory and 3- σ uncertainties mapped to the Dimorphos B-plane for the OD solutions of OM1, OM2 and OM3 deliveries.

were deployed during the first six hours of the mission. After the deployment, the mission foresaw a highly elliptical geocentric orbit for 180 days, with multiple encounters with the Moon. As for LICIACube, the cis-lunar radiometric navigation of ArgoMoon was performed by the RSLab of UNIBO [13] using MONTE and exploited two-way radiometric data, Doppler and range, acquired by the DSN and the European Space Tracking (ESTRACK). The flight path control aimed to follow the reference trajectory through a dedicated optimal control strategy [13]. The ArgoMoon navigation requirements were designed to guarantee the correct pointing of the S/C from the DSN stations, prevent impacts with Earth and Moon, and allow the S/C disposal in a heliocentric orbit at the end of the mission.

ArgoMoon was successfully launched on November 16, 2022, at 06:47:44 UTC by the SLS. The S/C was released from ICPS after 3 hours and 49 minutes and the first signal acquisition successfully occurred at 10:37 UTC. During its mission, ArgoMoon performed 4 orbital maneuvers (Orbit Trim Maneuver 1B - OTM1B, Statistical Trim Maneuver 0 - STM0, STM1, STM2). However, no maneuver reached the commanded ΔV , showing a significantly underperforming thruster. Moreover, after STM0, a signature on the stochastic accelerations raised the doubt that the S/C thruster could have been leaking, but this assumption is still under investigation. A successful fly-by of the Moon was accomplished on November 21 at 16:07 UTC, about 48 minutes earlier than scheduled. Due to the differences between the commanded ΔV and that actually produced by thruster, the error on the B-plane with respect to the reference trajectory was of 5000 km, as can be seen from UBO007-10 of Figure 2. After the Moon's fly-by, ArgoMoon flew by the Earth at ~166000 km on November 24, 2022, at 18:38 UTC. The S/C was unable to follow a geocentric orbit due to the altered geometry of the Moon's fly-by, effectively entering into a heliocentric orbit.

During the operations, the navigation team delivered a total of 10 OD solutions (UBO001 to UBO010) and 5 orbital maneuvers (where 4 of them have been commanded and executed, and one used as backup) [14]. The quality of the ArgoMoon radiometric data were mostly affected by the

S/C's rotational dynamics, the IRIS radio design and configuration, and the on-board activates (for example safe mode, reboot, desaturation maneuvers).

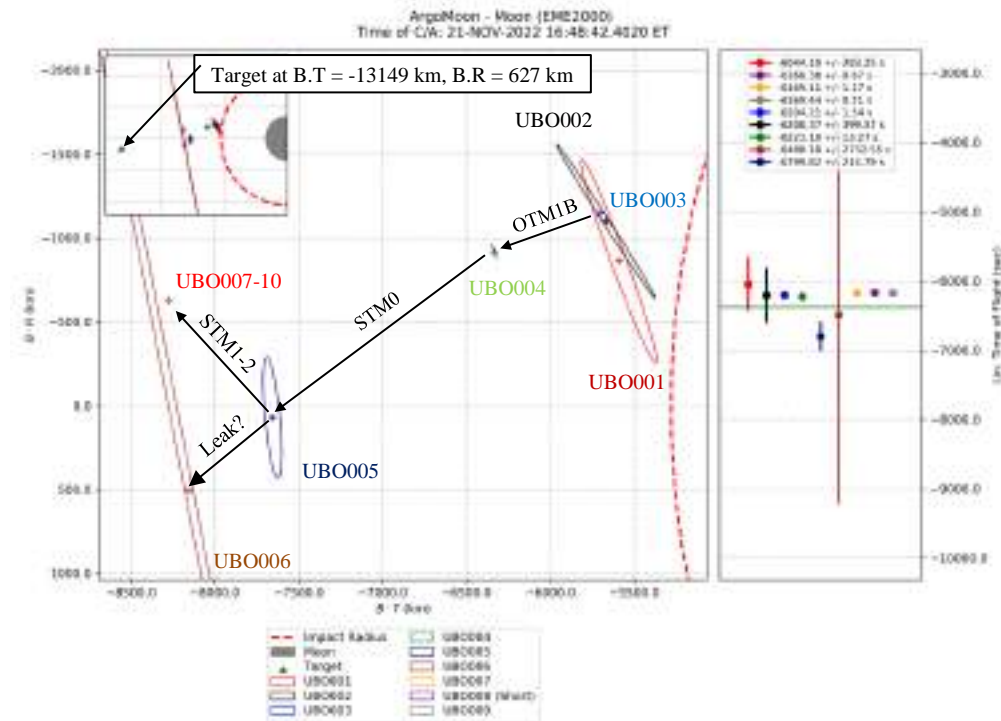


Figure 2: Summary of the delivered ArgoMoon OD solutions mapped on the Moon B-plane.

Conclusions

Using CubeSats in deep space requires addressing many operational challenges, particularly those related to the navigation, given the platform limitations related to the off-the-shelf components that are employed in the CubeSat philosophy and the strong requirements, similar to classical large deep space missions.

The navigation of LICIAcube and ArgoMoon has proven the capability of CubeSats platforms to operate in deep space and achieve complex objectives. The navigation results show a performance on the residuals as good as any typical deep space mission. The Doppler and range residuals of LICIAcube show a Root Mean Square (RMS) of 0.05 mm/s and 80 cm, respectively, while ArgoMoon had a RMS of 0.1 mm/s on Doppler and 30 cm on range. For both missions, the UNIBO navigation team was able to fulfill the navigation requirements, even with a very stringent contingency timeline, proving the reliability of the designed navigation procedures. Thanks to the obtained success, the pioneering flights carried on by LICIAcube and ArgoMoon will surely provide a relevant heritage for the upcoming deep space and cis-lunar CubeSats missions.

References

- [1] Johnstone, Alicia. CubeSat design specification Rev. 14.1 the CubeSat program. Cal Poly SLO (2022).
- [2] Kulu, Erik. Nanosatellite Launch Forecasts-Track Record and Latest Prediction. (2022).
- [3] Walker, Roger, et al. Deep-space CubeSats: thinking inside the box. Astronomy & Geophysics 59.5 (2018). <https://doi.org/10.1093/astrogeo/aty232>
- [4] Dotto, Elisabetta, et al. LICIAcube - The Light Italian Cubesat for Imaging of Asteroids In support of the NASA DART mission towards asteroid (65803) Didymos. Planet. Space Sci. 199, 105185 (2021). <https://doi.org/10.1016/j.pss.2021.105185>

- [5] Rivkin, Andrew S., et al. The Double Asteroid Redirection Test (DART): Planetary Defense Investigations and Requirements, *The Planetary Science Journal*, 3(7), 153 (2022).
- [6] Cheng, Andrew F. et al. Momentum transfer from the DART mission kinetic impact on asteroid Dimorphos, *Nature* (2023).
- [7] Tortora, Paolo and Valerio, Di Tana. LICIACube, the Italian Witness of DART Impact on Didymos, 2019 IEEE 5th International Workshop on Metrology for AeroSpace (MetroAeroSpace), Turin, Italy, pp. 314-317 (2019). <https://doi.org/10.1109/MetroAeroSpace.2019.8869672>
- [8] Dotto, Elisabetta and Zinzi, Angelo. Impact observations of asteroid Dimorphos via Light Italian CubeSat for imaging of asteroids (LICIACube). *Nat Commun* 14, 3055 (2023). <https://doi.org/10.1038/s41467-023-38705-0>
- [9] Evans, Scott, et al. MONTE: The next generation of mission design and navigation software, *CEAS Space Journal* 10.1, pp. 79-86 (2018). <https://doi.org/10.1007/s12567-017-0171-7>
- [10] Gai, Igor, et al. Orbit Determination of LICIACube: Expected Performance and Attainable Accuracy. *Geophysical Research Abstracts*. Vol. 21 (2019).
- [11] Duncan, Courtney, and Amy Smith. IRIS Deep Space CubeSat Transponder. *Proceedings of the 11th CubeSat Workshop*, San Luis Obispo, CA (2014).
- [12] Pirrotta, Simone, et al. ArgoMoon: the Italian cubesat for Artemis1 mission. *European Planetary Science Congress* (2021). <https://doi.org/10.5194/epsc2021-879>
- [13] Lombardo, Marco, et al. Design and Analysis of the Cis-Lunar Navigation for the Argo-Moon CubeSat Mission, *Aerospace*, MDPI (2022). <https://doi.org/10.3390/aerospace9110659>
- [14] Lombardo, Marco (2023). Navigation design and flight dynamics operations of the ArgoMoon Cis-Lunar CubeSat (Doctoral Thesis). Available on AMSDottorato, Alma Mater Studiorum - University of Bologna, Bologna, Italy.

Re-entry predictions of space objects and impact on air traffic

Franco Bernelli-Zazzera^{1,a*}, Camilla Colombo^{1,b}, Mattia Recchia^{1,c}

¹ Department of Aerospace Science and Technology, Politecnico di Milano, Via La Masa 34,
20156 Milano, Italy

^a franco.bernelli@polimi.it, ^b camilla.colombo@polimi.it, ^c mattia.recchia@mail.polimi.it

Keywords: Spacecraft Re-Entry, Breakup, Air Traffic

Abstract. This work focuses on predicting the re-entry of an uncontrolled re-entry vehicle (RV) and how this affects air traffic. It includes the propagation of the nominal trajectory and that of the fragments resulting from the breakup of the object. The breakup does not occur at a fixed altitude but is a consequence of the thermal and dynamic loads acting on the RV as it re-enters the atmosphere. The purpose of the analysis is to identify a dangerous area at specific heights (flight levels) to be evacuated in time for air traffic. The hazard area is defined as that which includes all the impact points of the fragments at this altitude taking into account the additional safety margins. The study also considers the presence of uncertainties affecting the initial state of the vehicle. Accordingly, a Monte Carlo analysis is performed to predict the worst-case scenario and to better estimate the hazard area. Once the area has been defined, an evacuation algorithm calculates, for each aircraft, the trajectory changes necessary to clear or avoid the zone over time.

Introduction

When a spacecraft, usually at the end of its life, leaves its nominal operating orbit, either due to some planned maneuver or natural decay caused by disturbances, and begins to approach increasingly dense atmospheric layers, it is said to be re-entering the Earth. Some reentry vehicles are designed to survive in Earth's atmosphere and be recovered, so they may have additional capabilities, such as the ability to develop lift forces to perform a soft landing [1]. Other vehicles, on the other hand, are not designed to withstand aerodynamic and thermal loads during the final phase of the trajectory and can suffer partial or total fragmentation. This case is called destructive reentry [2].

In this research, starting from the state of the vehicle at an altitude of 120 km, in which the reentry is supposed to start, the trajectory is propagated until the breakup conditions are met, thus defining the breakup point. At this altitude, the reentry vehicle (RV) is assumed to experience complete fragmentation caused by the high dynamic and thermal loads to which it is subjected. Therefore, a debris cloud is generated at the breakup point, composed of fragments each characterized by different parameters. Once the cloud of debris is generated, all fragments fall until they reach the level of interest (Flight Level) at which their dispersion is evaluated.

Since reentries are subject to many uncertainties, a Monte Carlo (MC) analysis is performed to account for some errors that may be present in the initial state of the vehicle and to evaluate how they affect the expected impact location. All fragment trajectories resulting from the MC analysis are then used to define the Hazard Area (HA) which includes all predicted debris locations and represents the area posing a risk to local air traffic. Once the danger zone has been defined, the affected aircraft must be redirected to evacuate or avoid the zone.

The procedures explained are applied to a simulated re-entry event in which real-traffic data are used to simulate a realistic scenario.



Methodology

The analysis starts by assigning the RV initial conditions, typically referring to the beginning of the reentry, arbitrary set at an altitude of 120 km [2]. The nominal trajectory, corresponding to the initial re-entry vehicle state, is propagated in time. At each propagation step, it is verified if the breakup conditions are satisfied. When the conditions are met, the RV breakups and the debris cloud is formed. For the cloud generation, it is assumed that the object experiences a complete fragmentation at a single altitude and all the fragments are generated at the same time. Once the debris are generated, for each one of them the new initial conditions are computed taking into account both the pre-breakup state and the velocity increment with the proper direction. At this point, all the fragments are considered as single independent entities and their trajectory is evaluated until they reach the altitude of interest, that could be ground level or an altitude corresponding to a particular Flight Level. Finally, the fragments dispersion is evaluated, in terms of longitude and latitude, at the altitude of interest. This debris distribution will be useful for the following study analyzing the effects on the air traffic.

Breakup Models. Two fragmentation methods are implemented in this work, both providing very similar results.

The first implemented model is based on the NASA Standard Breakup Model [3] and for this reason is called the NASA-Based Breakup Model (NBBM). The NASA Standard Breakup Model derives from the analyses of the fragmentation, due to both explosions and collisions, of spacecraft and rocket bodies in Low Earth Orbit (LEO) and it aims at defining each fragment with three different parameters: the characteristic length (L_c), the Area-to-Mass ratio (AM) and the velocity variation imparted (ΔV). All these features are described in terms of probability distributions. The models used in this research assume that the RV breakup occurs as a consequence of a fictitious collision with air. For this reason, the implemented power law distribution that provides the number of fragments of a given size and larger (N_{Lc}) is the one used in the NASA Breakup Model for collision events.

The second model proposed in this work is called Independent-Based Breakup Model (IBBM). This method tries to merge some features of the NASA Standard Breakup Model [3] with others implemented in the Independent discrete fragmentation model [4], which is applied mainly for asteroid entry analyses. Specifically, the IBBM implements the same distributions of the NASA Breakup Model for the computation of the fragment's characteristic length and Area-to-Mass ratio. The main difference between the IBBM and the NBBM is in the computation of the velocity variation.

In this work, both the dynamic and thermal loads are supposed to be able to cause the RV's breakup. In particular, the complete fragmentation is triggered whether the dynamic pressure acting on the vehicle exceed its ultimate tensile strength or if the temperature reaches the melting point of the material composing the RV. For this purpose, the RV is assumed to be made entirely of aluminum and a relation linking the aluminum ultimate tensile strength to the material temperature is implemented.

Dynamics. The nominal trajectory and the post-breakup fragments trajectories are evaluated adopting the following assumptions. The RV is a non-lifting object, not capable of generating any lift force ($L = 0$). The motion is over a spherical, non-rotating Earth ($\omega_E = 0$). A ballistic entry is assumed, with no thrust force ($T = 0$) and no propellant mass flow ($\dot{m} = 0$). The mass ablation of both the RV and the related fragments is neglected.

With the assumptions just mentioned, the equations of motion become the following set of six first order ordinary differential equations (ODEs) [1]:

$$\left\{ \begin{array}{l} \dot{h} = v \sin \gamma \\ \dot{\lambda} = \frac{v \cos \gamma \sin \psi}{r \cos \varphi} \\ \dot{\varphi} = \frac{v}{r} \cos \gamma \cos \psi \\ \dot{v} = -\frac{D}{m} - g \sin \gamma \\ \dot{\gamma} = -\left(g - \frac{v^2}{r}\right) \frac{\cos \gamma}{v} \\ \dot{\psi} = \frac{v}{r} \cos \gamma \sin \psi \tan \varphi \end{array} \right. \quad (1)$$

where D is the drag force and the state $x = \{h; \lambda; \varphi; v; \gamma; \psi\}$, is composed, respectively, by the altitude, longitude, latitude, velocity, climb angle and heading angle.

Monte Carlo Analysis. Earth re-entries are affected by lots of uncertainties that could have non negligible effects on the prediction of the hazard area that poses risk to the air traffic. To statistically predict that area, a Monte Carlo (MC) analysis is performed. Each sample generated for the MC analysis represents a set of new initial conditions at the nominal altitude of 120 km. The re-entry simulation is therefore repeated for each sample and the resulting debris dispersion at Flight Level 400 (FL400) are recorded. Once the MC simulation is completed, an area enclosing all the fragments footprints at FL400 can be defined. The final Hazard Area is then retrieved by adding some additional safety margin. Figure 1 shows both the pre and post-breakup trajectories, while Figure 2 reports both the fragments dispersion at the altitude of interest and the computed Hazard Area.

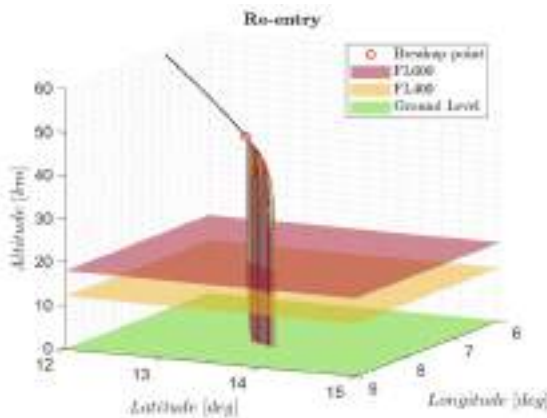


Figure 1: Re-entry trajectories.

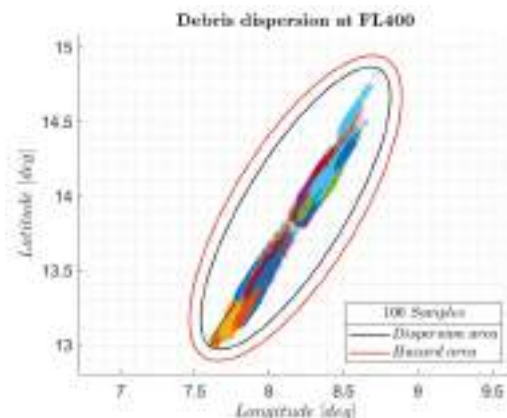


Figure 2: Hazard area and debris dispersion.

Air Traffic management. Two different actions, inferred from [5], are proposed for the management of the air traffic in presence of an hazard area.

The first algorithm is used to evacuate aircraft that are within the hazard area at the time it is computed. The algorithm's logic is to find the required changes in the aircraft heading which allow the shortest evacuation time. The following assumptions are made: 1) the aircraft are assumed to move with constant velocity during all the operations; 2) after completing the required turns, the aircraft move on a straight trajectory; 3) it is assumed that aircraft can only perform horizontal maneuvers.

The second algorithm is applied to an aircraft which is outside the hazard area at the moment it is computed but it is expected to enter it. The following assumptions are made: 1) the aircraft are assumed to move with constant velocity throughout the path; 2) the nominal path is assumed to be aligned in the same direction of the initial velocity vector; 3) turn maneuvers are not considered in

the computation of the alternative path and aircraft are supposed to be able to turn instantaneously;
4) only horizontal maneuvers are taken into account. The algorithm then computes an alternative flight path that allows the aircraft to avoid the hazard area.

Figures 3 and 4 show examples of the evacuation and avoidance procedures.

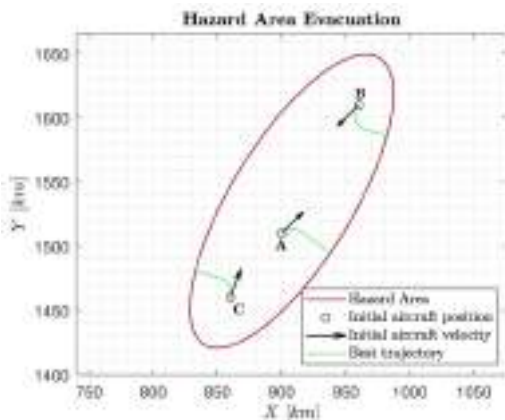


Figure 3: evacuation procedures.

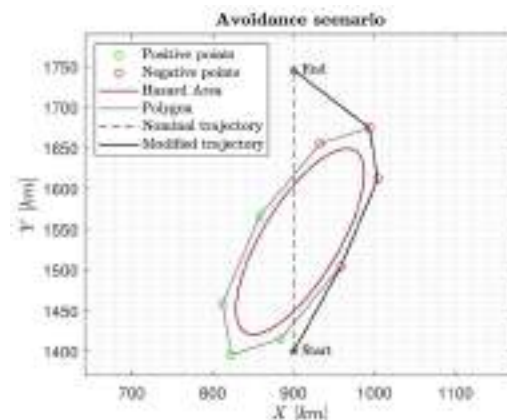


Figure 4: hazard area avoidance procedure.

Real Scenario

A generic reentry event is analyzed, leading to the definition of a Hazard Area. Then, to assess the re-entry impact on the local air traffic, real traffic data are retrieved from Flightradar24 [6] filtering only the flights at the altitude corresponding to the FL400 (40000 ft) and at a particular time instant. Finally, the algorithms discussed are used to manage the air traffic according to the aircraft positions. The simulated path are shown in Figure 5 in which stars represent the aircraft initial positions while dots the final ones.

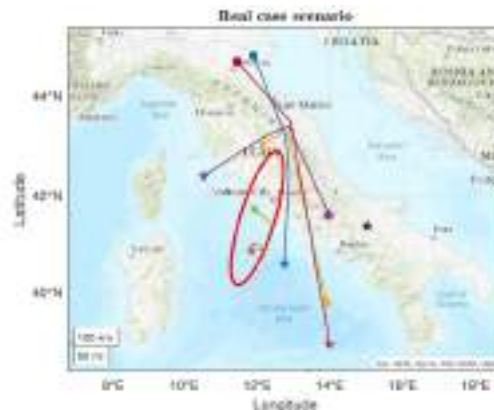


Figure 5: Evacuation and avoidance simulated paths.

Conclusions

This work has shown a preliminary assessment of the impacts Earth's re-entries have on the air traffic. Some future developments can be easily integrated while keeping the overall structure intact. Particularly, improvements in the breakup models with the introduction of new distribution functions that better describe the atmosphere's fragmentation can be integrated. Also the air traffic management algorithms could be upgraded with new procedures that ensure minimization of the impact on the routes while still avoiding collisions.

References

- [1] F. J. Regan and S. M. Anandkrishnan. Dynamics of Atmospheric Re-Entry. AIAA Education Series. American Institute of Aeronautics and Astronautics, 1993. ISBN 9781600860461. <https://doi.org/10.2514/4.861741>

- [2] F. Sanson. On-ground risk estimation of reentering human-made space objects. PhD thesis, 09 2019.
- [3] N.L. Johnson, P. Krisko, J.-C Liou, and P. Anz-Meador. Nasa's new breakup model of evolve 4.0. *Advances in Space Research*, 28:1377–1384, 12 2001..
[https://doi.org/10.1016/S0273-1177\(01\)00423-9](https://doi.org/10.1016/S0273-1177(01)00423-9)
- [4] P. Mehta, E. Minisci, and M. Vasile. Breakup modelling and trajectory simulation under uncertainty for asteroids. 04 2015.
- [5] Ganghuai W., Zheng T., T. Masek, and J. Schwartz. A monte carlo simulation tool for evaluating space launch and re-entry operations. In *2016 Integrated Communications Navigation and Surveillance (ICNS)*, pages 9A3–1–9A3–15, 2016.
[dhhttps://doi.org/10.1109/ICNSURV.2016.7486392](https://doi.org/10.1109/ICNSURV.2016.7486392)
- [6] Flightradar24. flightradar24:live air traffic, Accessed on 25 May 2023.

Space Propulsion

Update on green chemical propulsion activities and achievements by the University of Padua and its spin-off T4i

F. Barato^{1*}, A. Ruffin², M. Santi², M. Fagherazzi², N. Bellomo² and D. Pavarin^{1,2}

¹Department of Industrial Engineering, University of Padua, Via Venezia 1, 35131, Padua, Italy

²Technology for Propulsion and Innovation S.p.a, Via Emilia 15, 35043, Monselice, Italy

* francesco.barato@unipd.it

Keywords: Hydrogen Peroxide, Green Chemical Propulsion, Hybrid Rockets, Liquid Thrusters, Sounding Rocket, Throttling, Regenerative Cooling, Additive Manufacturing

Abstract. In recent years, there has been a great research interest on green propulsion, both for environmental, cost and ease-of-use considerations, further accelerated by the needs of the NewSpace Economy. Hydrogen peroxide is a green and versatile propellant that is suitable for a lot of different uses in space applications. Following a previous AIDAA publication of 2019, this paper updates the research performed on hydrogen peroxide-based propulsion by the University of Padua and its spin-off T4i with the latest achievements. Starting from the simplest propulsion systems, several monopropellant thrusters have been successfully designed and tested, ranging from a propulsion module of 1 N, to a 10 N and 200 N flight-weight items. The thrusters can operate in blowdown or pressure-regulated mode, and they have been tested for hundreds of seconds of continuous operation and for thousands of pulses. A 450 N liquid bipropellant motor that burns the monopropellant exhausts with diesel fuel has also been developed and tested. The motor uses an unconventional internal vortex flow field to achieve stability, efficiency, and self-cooling of the chamber. The nozzle throat region temperature is kept under control by regenerative cooling channels fed by the peroxide. All thrusters make extensive use of additive manufacturing. The hydrogen peroxide technology has also been applied on hybrid propulsion, which was the initial main expertise of the Padua University propulsion group. Hundreds of tests have been performed at lab-scale, mainly with paraffin wax and polyethylene as fuels, with burning time up to 80 seconds. The motors are able to start, stop and restart multiple times. A cavitating pintle valve has been developed in house in order to control the oxidizer mass flow. With this valve, the hybrid motors are able to throttle the thrust in a range of 1:12.6. A similar valve has been also employed in the integrated monopropellant propulsion system of a lunar drone, composed by a 400 N throttleable engine together with 4 small 14 N on-off attitude control thrusters. Moreover, several dozens of hybrid tests have been performed at 5-10 kN scale up to 50 seconds. Finally, a composite sounding rocket powered by a pressure-regulated 5 kN hybrid rocket has been fully designed and successfully flight tested.

Introduction

The chemical propulsion group at University of Padua was established around 2006, working on hybrid propulsion with green oxidizer (N_2O , GOX) and plastic fuels, mainly HDPE and paraffin wax. For the story before the shift to hydrogen peroxide, the reader is referred to a previous AIDAA paper [1]. Since 2014, the propulsion team and its spin-off Technology for Propulsion and Innovation (T4i) have been focused their effort on the development of hydrogen peroxide-based propulsion systems.

The choice of hydrogen peroxide is due to the fact that is a very versatile green propellant because it can be decomposed relatively easily in liquid phase and can be used in restartable and throttleable liquid monopropellants, bipropellants, hybrids and gas generators. Moreover, it can be



stored at room temperatures at any pressure and can feed the engines with very repeatable performance.

The primary feature of this research effort is the use of stabilized hydrogen peroxide concentrated in-situ from commercial feedstock. A distillation plant capable of concentrating 1 kg/hour of hydrogen peroxide from 60% to 92% has been operated for years with little maintenance. The plant runs autonomously 24/7 and has concentrated several tons of propellant up to now. In little less than a decade the group has performed nearly a thousand monopropellant, bipropellant and hybrid rocket tests with hydrogen peroxide. In the following paragraphs the different types of motors will be described.

Monopropellant propulsion

Several monopropellant systems, ranging from 1N to 200 N, have been developed in order to operate as main engines and/or attitude control thrusters for space vehicles [2-3].

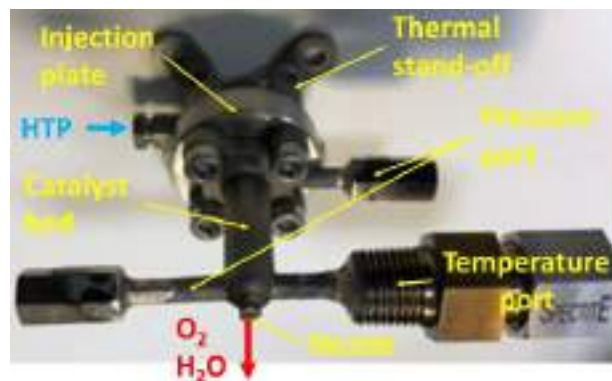


Fig 1. 1 N monopropellant thruster engineering model

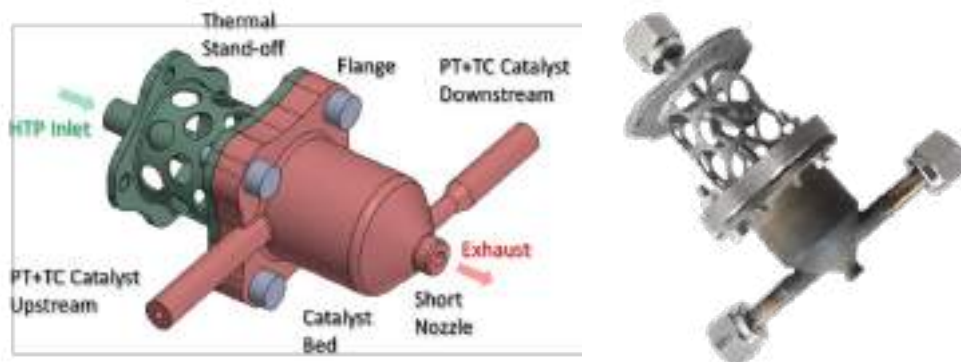


Fig 2. 10 N monopropellant thruster engineering model

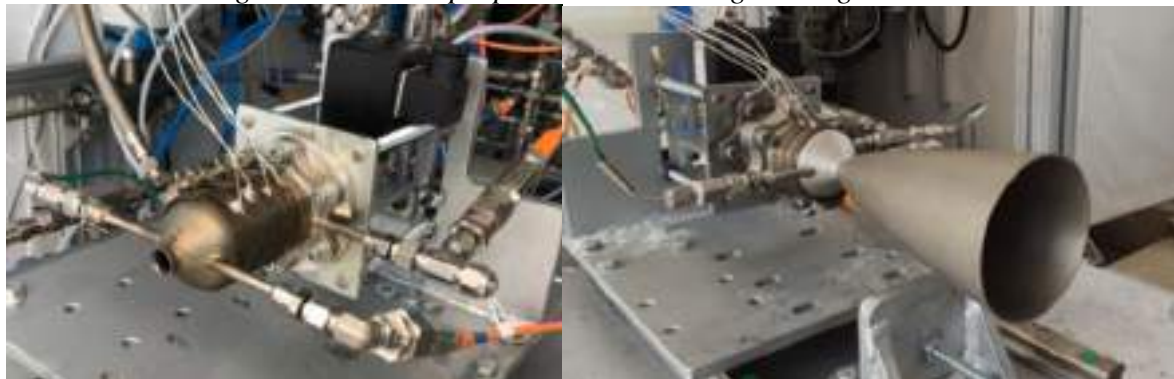


Fig 3. 200 N monopropellant thruster engineering models

The thrusters can be used both in blowdown and pressure-regulated mode from 5 bar to more than 40 bar. The thrusters are actuated with on-off solenoid valve and operated in continuous and bang-bang mode. Efficiencies above 95% have been achieved with continuous firing times up to above 1000 s. More than 4000 pulses have also been demonstrated. Depending on thruster size, valve timing can go from 30 to 100 ms. The catalyst is able of cold starting without pre-heating. The thrusters are manufactured with 3D printing Selective Laser Melting (SLM) technology. The engineering models have flanges to disassemble the thrusters and pressure/temperature sensor ports while the flight weight units have a minimum number of interfaces/components.

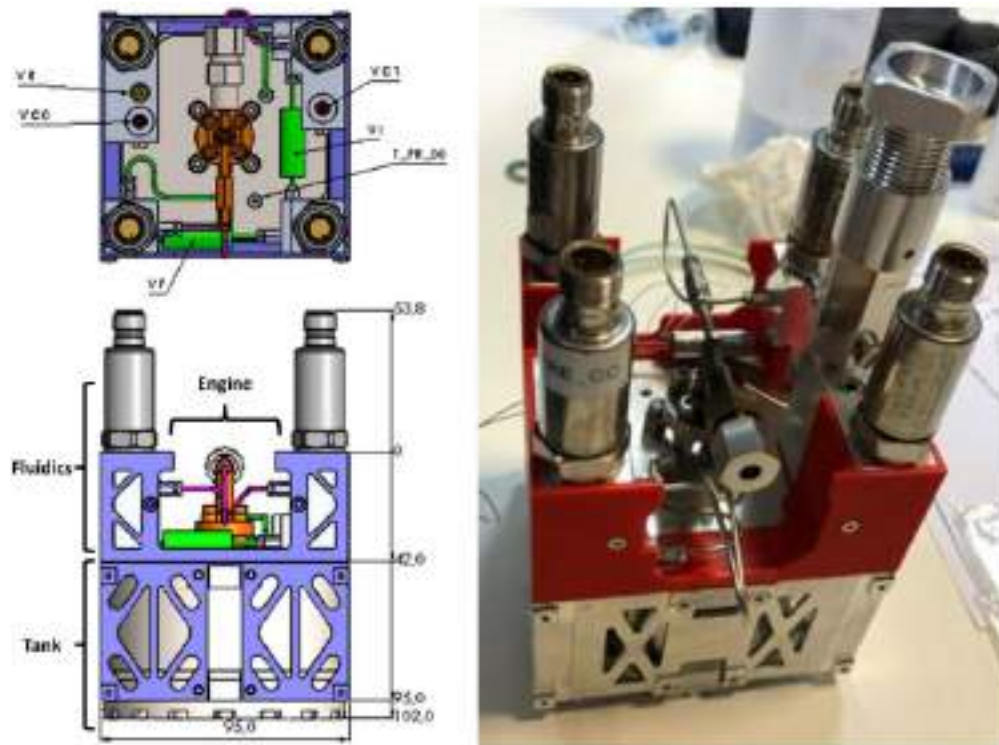


Fig 4. 1U monopropellant propulsion module engineering model

An entire monopropellant propulsion module has been developed in the frame of the PM³ project, a modular multi-mission platform founded by the Italian Ministry of Education, Universities and Research [4]. The fundamental objective of the project was the study of a 50 kg class satellite platform characterized by the ability to accommodate multiple interoperable payloads. The propulsion system architecture is based on a simple unregulated blowdown discharge starting from a MEOP of 50 bars. The engine initial thrust in vacuum is 1N and then slowly decreases to 0.5 N at EOL as the tank pressure decreases. The fluidic line is composed by a custom piston-separated tank and few COTS components: an isolation valve, the fill and drain valves, and the firing valve. The tank is designed to be easily extended to increase propellant volume and meet the additional total impulse that may be required for other missions. Despite the tested system being an engineering model, the overall design has been flight-oriented, including the required amount of propellant in the 1U envelope. Only pressure sensors used only for test monitoring have been accommodated outside this envelope.



Fig 5. Moon Drone propulsion system (laid upside down): 400 N throttleable main engine (top) and four bang-bang 14 N attitude thrusters (bottom)



Fig 6. Moon Drone 400 N Main Engine Flow Control Valve

Another program involving monopropellant hydrogen peroxide is Moon drone, a small platform scouting the surrounding environment that has been proposed in support of a rover mission on the Moon [5]. The design of the Moon Drone has been performed through an ESA TRP study lead by Thales Alenia Space with partners GMV, Brno University of Technology and T4i. An Earth-related flight prototype will be tested within the program and T4i is in charge of all the thrusters' development with the support of the University of Padova. After a trade-off between several possibilities performed by TAS with T4i/UNIPD support, the propulsion design proceeded with a configuration composed by a single throttleable main engine used for the main displacements aided by 4 small thrusters operated in bang-bang for attitude control. All the thrusters were fed by the same tank, which is pressurized by nitrogen. The main engine has 400 N maximum thrust; it has a continuous regulating cavitating pintle flow control valve driven by a stepper motor in feedback, a development from a previous one already developed in-house for a hybrid rocket. The rearranged flow control valve differs from the older version for the valve body that has been optimized and

reduced consistently in weight. The attitude control thrusters have a maximum thrust of 14 N, they are operated with a commercial on-off solenoid valve controlled at 10 Hz. Both types of thrusters have been designed, manufactured and thoroughly tested, demonstrating the proper fulfillment of the defined specifications and they are ready for the flight campaign of the Moon Drone prototype.

Bipropellant propulsion

A 450 N hydrogen peroxide-based bipropellant liquid engine has been designed and tested. The motor is a staged combustion engine that features a vortex-cooled combustion chamber based on a swirled oxidizer injection and uses standard automotive diesel as fuel, which is injected on the catalytic decomposed peroxide stream [6]. The cooling solution for the thrust chamber is characterized by a double co-spinning counter-flowing vortex flow. It is well known that a swirled flow improves mixing and residence time thus enhancing the combustion efficiency. Moreover, this particular flowfield allows the flame to be trapped in the inner vortex while the outer one composed only by the oxidizer act as a shield that extracts heat from the chamber walls. The motor has been successfully tested, achieving smooth ignition and shut down, stable steady combustion and efficiencies above 96%.

Afterwards a regenerative cooling for the nozzle throat region with H_2O_2 has been designed through a numerical steady 1-D code [7-8]. The nozzle with its internal channels has been produced by additive manufacturing in Inconel® 718. The cooling has been tested successfully, demonstrating the capability to keep the metal parts at reasonable temperatures in steady state and showing only moderate heating of the liquid H_2O_2 .

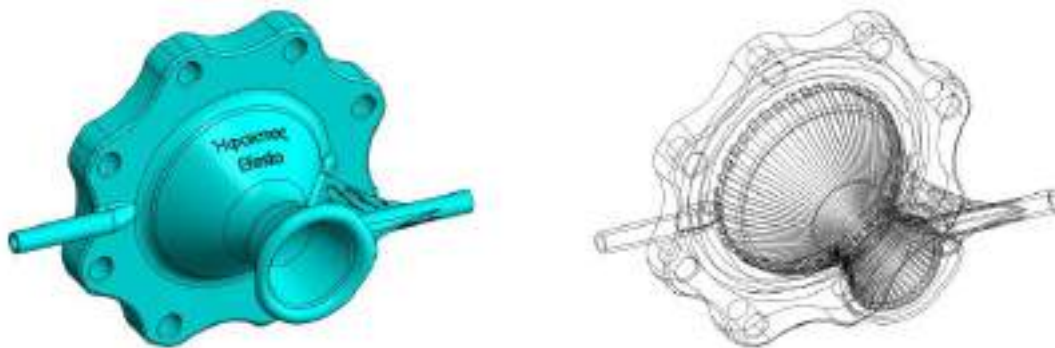


Fig 7. 450 N liquid thruster regenerative nozzle: external view (left), lattice view (right)



Fig 8. 450 N liquid bipropellant fire test with regenerative cooling

Hybrid propulsion

Starting in 2014, hundreds of hybrid rocket tests with hydrogen peroxide have been performed at lab-scale (100-1000 N). Hybrid firing times up to 80 s have been achieved [9]. More than 50 scale up tests with thrust above 5 kN (sea level) have also been performed up to date.

Thanks to the catalyst decomposition of the hydrogen peroxide, the hybrid motors have the capability to cold start, to run stable and efficiently, to stop and restart multiple times and to be throttled. The motors can be adapted to different missions in terms of thrust and burning times, tailoring the regression rate level of the fuel by varying the intensity of the swirled injection [10].



Fig 9. H_2O_2 hybrid rocket firing (5 kN at sea level)

A cavitating venturi variable pintle flow control valve has been developed in house [11]. The valve is able to choke the oxidizer mass flow and decouple the feed system from the combustion chamber dynamic. Afterwards a stepper electric motor has been connected to the movable flow control valve [12]. With this set-up an outstanding real time throttling ratio of 12.6:1 has been achieved showing the possibility to perform different thrust profiles on demand [13]. A remotely controlled human manual throttling test has been also performed.

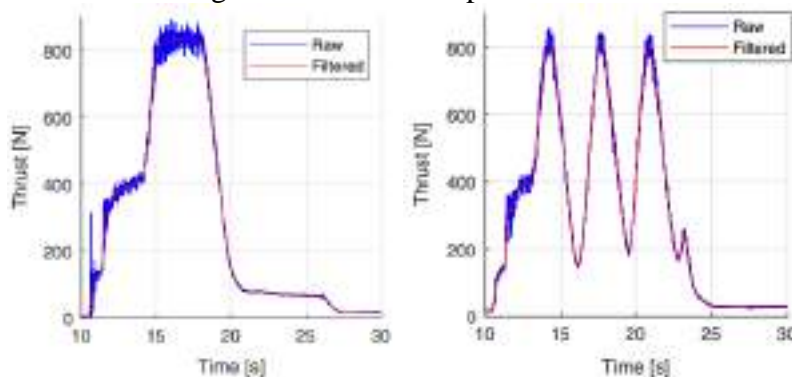


Fig 10. Throttling of a H_2O_2 hybrid rocket: step command (left), sinusoidal command (right)

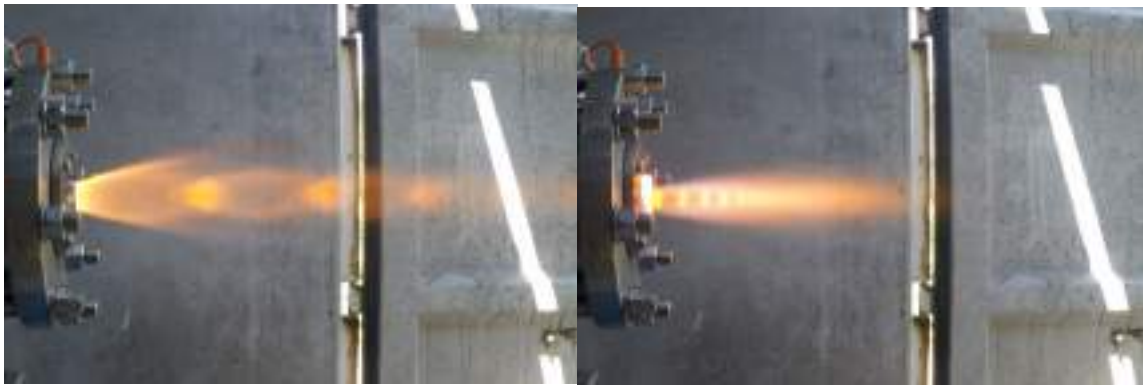


Fig 11. Throttling of a H_2O_2 hybrid rocket: max thrust (left), min thrust (right)

Afterwards, the team started to develop a 200 mm diameter, 6 m long sounding rocket propelled by a 5 kN thrust hydrogen peroxide-paraffin hybrid rocket [14]. The aim of the passive, aerodynamically stabilized, sounding rocket was to serve as a flight test bed for new technologies in the structures and propulsion system. The sounding rocket was finally launched successfully on February 24, 2022, from the Poligono Interforze of Salto di Quirra (PISQ) in Sardinia, within the project Aviolancio (Air-launch), coordinated by the Italian Research Center (Consiglio Nazionale delle Ricerche, CNR) and the Italian Air Force (Aeronautica Militare Italiana, AMI).



Fig 12. 5 kN H_2O_2 sounding rocket: on the ramp (left), at launch (right)

Conclusions

The University of Padua and its spin-off company T4i have been conducting research on green propulsion using hydrogen peroxide as a propellant since 2014. Hydrogen peroxide is a very versatile chemical that can be used in multiple propulsive applications.

The team has successfully designed and tested various monopropellant thrusters, ranging from 1 N to 200 N. These thrusters can operate in blowdown or pressure-regulated mode and have been tested for continuous and pulsed operations. Efficiencies above 95% have been achieved with continuous firing times up to above 1000 s. More than 4000 pulses have also been demonstrated. Depending on thruster size, valve timing can go from 30 to 100 ms. An entire 1U-1N unregulated blowdown pressure-fed propulsion unit has also been developed and tested.

The integrated propulsion system for a lunar drone, which includes a 400 N throttleable monoprop main engine and four 14 N bang-bang attitude control thrusters have been also developed and successfully tested. The main engine is actuated by a cavitating venturi pintle flow control valve developed in-house.

The team has also developed and tested a 450 N liquid bipropellant motor that burns the monopropellant exhausts with diesel fuel. This motor utilizes an unconventional internal vortex flow field for stability, efficiency, and self-cooling of the combustion chamber. The nozzle throat region is regeneratively cooled with the H_2O_2 . The motor has been successfully tested, achieving smooth ignition and shut down, efficiencies above 96%, stable steady combustion and proper thermomechanical behavior.

Both the monopropellant thrusters and the liquid motor extensively employ additive manufacturing techniques to reduce the number of parts and allow complex design features.

Finally, the hydrogen peroxide technology has also been applied to hybrid propulsion, initially the main expertise of the Padua University propulsion group. Numerous lab-scale tests have been carried out, mainly with paraffin wax and polyethylene as fuels, achieving burning times of up to 80 seconds. The hybrid motors can start, stop, and restart multiple times, again utilizing a cavitating pintle valve to control oxidizer mass flow and enable deep thrust throttling. Additionally, several dozen hybrid tests have been performed at 5-10 kN scale for up to 50 seconds. Lastly, a composite sounding rocket powered by a pressure-regulated 5 kN hybrid rocket has been designed and successfully flight tested.

References

- [1] F. Barato, N. Bellomo, A. Ruffin, E. Paccagnella, M. Santi, M. Franco and D. Pavarin, Status and Achievements of the Hydrogen Peroxide Chemical Propulsion Research at Padua University, Italian Association of Aeronautics and Astronautics (AIDAA) XXV International Congress, 9-12 September 2019, Rome, Italy.
- [2] M. Santi, I. Dorgnach, F. Barato, D. Pavarin. Design and Testing of a 3D Printed 10 N Hydrogen Peroxide Monopropellant Thruster, AIAA Propulsion and Energy Forum, Indianapolis, IN, USA (2019). <https://doi.org/10.2514/6.2019-4277>
- [3] D. Nissan, M. Santi, F. Barato, D. Pavarin, Testing of a Small HTP Monopropellant Thruster for Space Applications, International Astronautical Congress, Paris, France, 18-22 September 2022.
- [4] M. Santi, L. Gerolin, D. Antelo, B. Montanari, M. Fagherazzi, F. Barato, D. Pavarin, Development and testing of an engineering model of a hydrogen peroxide based 1N propulsion unit, International Astronautical Congress, Paris, France, 18-22 September 2022.
- [5] A. Ruffin, M. Fagherazzi, N. Bellomo, F. Barato, D. Pavarin, M. Pessana, Development of the Propulsion System for a Moon Drone Vehicle Demonstrator, AIAA 2021-3564, AIAA Propulsion and Energy 2021 Forum, 9-11 August, Virtual Event. <https://arc.aiaa.org/doi/abs/10.2514/6.2021-3564>
- [6] M. Santi, M. Fagherazzi, F. Barato, D. Pavarin, Design and Testing of a Hydrogen Peroxide Bipropellant Thruster, AIAA 2020-3827, AIAA Propulsion and Energy 2020 Forum, 24-28 August, Virtual Event. <https://doi.org/10.2514/6.2020-3827>.
- [7] M. Fagherazzi, M. Santi, F. Barato, D. Pavarin, Design and Testing of a 3D Printed Regenerative Cooled Nozzle for a Hydrogen Peroxide based Bi-Propellant Thruster, AIAA 2021-3235, AIAA Propulsion and Energy 2021 Forum, 9-11 August, Virtual Event. <https://arc.aiaa.org/doi/10.2514/6.2021-3235.c1>
- [8] M. Fagherazzi, M. Santi, F. Barato, M. Pizzarelli, Simplified Thermal Analysis Model for Regeneratively Cooled Rocket Engine Thrust Chambers and Its Calibration with Experimental Data, Aerospace 2023, 10(5), 403; <https://doi.org/10.3390/aerospace10050403>

- [9] E. Paccagnella, M. Santi, A. Ruffin, F. Barato, D. Pavarin, G. Misté, G. Venturelli, N. Bellomo. Testing of a Long-Burning-Time Paraffin-based Hybrid Rocket Motor. *Journal of Propulsion and Power*, Vol. 35, No. 2, pp. 432-442 (2019). <https://doi.org/10.2514/1.B37144>
- [10] M. Franco, F. Barato, E. Paccagnella, M. Santi, A. Battiston, A. Comazzetto and D. Pavarin, Regression Rate Design Tailoring Through Vortex Injection in Hybrid Rocket Motors, *Journal of Spacecraft and Rockets*, 7 November 2019. <https://doi.org/10.2514/1.A34539>
- [11] A. Ruffin, F. Barato, M. Santi, E. Paccagnella, N. Bellomo, G. Misté, G. Venturelli, D. Pavarin. Development of a Cavitating Pintle for a Throttleable Hybrid Rocket Motor, 7th European Conference for Aeronautics and Space Sciences (EUCASS), Milan, Italy (2017).
- [12] A. Ruffin, M. Santi, E. Paccagnella, F. Barato, N. Bellomo, G. Misté, G. Venturelli, D. Pavarin. Development of a Flow Control Valve for a Throttleable Hybrid Rocket Motor and Throttling Fire Tests, 54th AIAA/SAE/ASEE Joint Propulsion Conference, Cincinnati, OH, USA (2018). <https://doi.org/10.2514/6.2018-4664>
- [13] A. Ruffin, E. Paccagnella, M. Santi, F. Barato, D. Pavarin. Real Time Deep Throttling Tests of a Hydrogen Peroxide Hybrid Rocket Motor, *Journal of Propulsion and Power*, Published Online: 4 April 2022. <https://doi.org/10.2514/1.B38504>
- [14] F. Barato, D. Pavarin, Advanced Low-Cost Hypersonic Flight Test Platforms, HiSST: 2nd International Conference on High-Speed Vehicle Science Technology, 11–15 September 2022, Bruges, Belgium.

1D numerical simulations aimed to reproduce the operative conditions of a LOx/LCH₄ engine demonstrator

Angelo Romano^{1,a*}, Daniele Ricci^{1,b}, Francesco Battista^{1,c}

¹CIRA – Italian Aerospace Research Center, Italy

^aa.romano@cira.it, ^bd.ricci@cira.it, ^cf.battista@cira.it

Keywords: Liquid Rocket Engine, LOx/LCH₄, EcosimPro Simulations, Regenerative Cooling

Abstract. The present paper describes the results of the numerical simulations performed by means of the “*EcosimPro*” software, aimed at reproducing the operative conditions of the regenerative thrust chamber “DEMO-0A” designed by the Italian Aerospace Research Center. The operative conditions simulated are both cold flow and firing conditions. A validation of the numerical cold flow results has been performed by comparing them with the experimental data gathered during a cold flow campaign. Once validated the cold flow numerical model, various hot test conditions of the demonstrator have been simulated by considering different heat wall exchange coefficient correlations, in order to obtain information about the thermal power released during the combustion process and to assess the simulation capabilities of the “*EcosimPro*” software in predicting the behaviour of the demonstrator in firing conditions by modelling it with a 1-D approach.

Introduction

The utilization of liquid oxygen/liquid methane couple (LOx/LCH₄) as a potential candidate to substitute hypergolic propellants in the next future propulsion systems has arisen an increasing interest due to the advantages offered in terms of high specific impulse, cooling capabilities, re-usability and low environmental impact [1]. In this perspective, the Italian Aerospace Research Center manages the “HYPROB” research program, which includes also the realization of a LOx/LCH₄ demonstrator engine named “DEMO-0A”.

The thermal exchange in a liquid rocket engine regeneratively cooled represents a coupled heat transfer problem between the hot gases, the chamber wall and the coolant in the channels. Various approaches have been used to solve this problem: the possibility to use a 3-D modelling for the heat conduction through the wall and a 2-D approach, based on semiempirical correlations for the coolant and the hot gas flows, has been evaluated in [2], [3]. To overcome the complexity and the computational cost introduced by 3-D approaches, simplified quasi-2-D models have been extensively used to solve the heat transfer problem ([4], [5], [6]).

The aim of the present paper is to model the “DEMO-0A” engine designed and realized by the Italian Aerospace Research Center (CIRA) by means of 1-D components offered by the *EcosimPro* software. In particular, a series of numerical simulations have been performed to simulate cold flow and firing conditions, in which the coupled heat transfer problem between the hot gases, the chamber liner and the coolant has been solved by a 1-D approach. The scopes of these simulations, performed with a 1-D approach, consisted in: 1) validating the numerical results of the cooling system by a comparison with the experimental cold flow results; 2) investigating the effects on the thermal power released by the combustion chamber by considering different wall heat exchange semiempirical correlations; 3) assessing the capabilities of the 1-D model implemented in *EcosimPro* to predict the behaviour of the demonstrator in firing conditions.



The “DEMO-0A” Thrust chamber assembly

The “DEMO-0A” is a 30 kN thrust class demonstrator, fed with LOx/LCH₄, technologically representative of a thrust chamber assembly of an expander engine, regeneratively cooled by a counter-flow cooling jacket made up of 96 axial channels. The cooling channels of the “DEMO-0A” are obtained by joining an inner liner made of a copper alloy (CuCrZr) with two outer layers (the first one made of copper and the second one of nickel). The outer layers are deposited on the inner one by means of the electrodeposition technology. In a former version of the demonstrator the cooling channels were obtained by brazing the inner layer with an Inconel outer layer. Both liquid methane and water can be used to cool the engine ([7], [8]).

Figure 1 shows a model of the demonstrator that includes the igniter, the injector head with 18 coaxial recessed injectors and the thrust chamber with inlet/outlet manifolds for LCH₄ (or water).

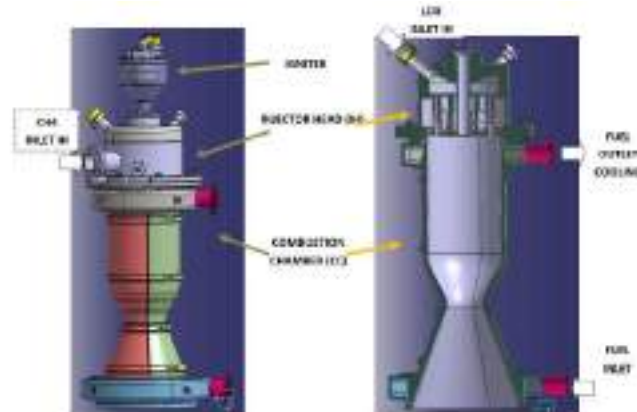


Figure 1: 3-D model of the «DEMO-0A» architecture

The main geometrical and performance parameters are reported in Table 1.

Table 1

“DEMO-0A” performance and geometrical parameters			
Performance		Geometry	
T [kN] @ sea level	23.7	L [mm]	440
I _{sp} [s]	286	D _{chamber} [mm]	119.6
m LCH ₄ [kg/s]	1.92	D _{throat} [mm]	59.8

Methodology

The numerical simulations have been performed by means of the *EcosimPro* software, a simulation tool that allows to model continuous and discrete systems.

The equations solved in the cold flow condition simulation are the mass conservation and the momentum conservation equations written under steady state conditions hypothesis ([9], [10]).

On the contrary, the system of governing equations of the combustor and cooling jacket coupling consists in the continuity equation written for the vaporized propellants, the momentum equation and the energy equation, all written under the hypothesis of steady state conditions [9]. The vapours are assumed to be fully released at the first node of the grid discretizing the combustor component assuming a characteristic vaporization time τ_{vap} set to 0.1 ms. The energy equation contains the term modelling the heat exchange between the hot gases, the chamber liner and the cooling jacket. Both convection and radiation are considered and *EcosimPro* offers three empirical correlations to calculate the wall heat exchange coefficient h_c : the Bartz, the modified Bartz and the Pavli correlations. The heat conduction in the cooling jacket liner is modelled by the Fourier equation. Regarding the combustion modelling a delayed equilibrium model has been chosen, in so doing a non-equilibrium combustor is simulated by introducing a time delay between the equilibrium condition and the actual burnt gases composition.

The discretization scheme considered is the AUSM with a 2nd order accuracy and the integration method is the «CVMODE_BDF_SPARSE» [9] with transient and steady tolerances set to $1 * 10^{-6}$ as recommended in [9] in order to reduce the simulation time. The final time of the simulation has been set to 20 s.

Results

The cold flow experimental campaign was carried out at the AVIO/ASI FAST2 facility in Colleferro (Rome) and was devoted to perform tests in order to measure the pressure drops along the cooling channels of the regenerative cooling system and to define a characteristic law to predict the pressure drops of the “DEMO-0A” cooling system.

A mesh sensitivity analysis has been performed in order to individuate the discretizing mesh that allows to obtain a good quality solution with the minimum number of nodes and in the end the mesh independence turned out to be a discretizing grid of 35 nodes.

The results of three out of the six cold flow tests simulations performed in *EcosimPro* in terms of coolant pressure drop are reported in Table 2. The numerical results slightly underestimate the experimental ones and it is possible to see that the estimation error is between 2% and 3%.

The water pressure profile along the cooling jacket is reported in Figure 2(a) (red line) and allows to appreciate that the larger pressure gradients are concentrated in the throat region, as expected.

Table 2

Cold flow tests results				
		EcosimPro	Experimental	$\varepsilon = \frac{\Delta X_{Eco} - \Delta X_{Exp}}{\Delta X_{Exp}}$
Test01	$\Delta_P_cool.$ [bar]	60.73	62.37	-2.63%
	Water MFR [kg/s]	5.12	5.12	0%
Test02	$\Delta_P_cool.$ [bar]	46.96	48.03	-2.23%
	Water MFR [kg/s]	4.47	4.49	-0.4%
Test03	$\Delta_P_cool.$ [bar]	35.83	36.68	-2.32%
	Water MFR [kg/s]	3.91	3.91	0%

By relating the pressure drops obtained during the six experimental tests with the squared water mass flow rates it is possible to note that their relation can be modelled as linear (Figure 2(b)).

The firing test campaign has been carried out at the AVIO/ASI FAST2 facility in Colleferro (Rome) and consisted in three tests. The mesh independence analysis, considered for the coupling of the cooling jacket with the combustor, differs from the one used in the cold flow simulations and is a discretizing grid made of 25 nodes.

In order to predict the temperature rise of the water inside the cooling channels, the three empirical correlations offered by *EcosimPro* to compute the wall heat exchange coefficient have been considered and the results in terms of water temperature rise and heat flux have been compared. These comparisons are here presented and they refer to the first firing test, labelled as «FT01».

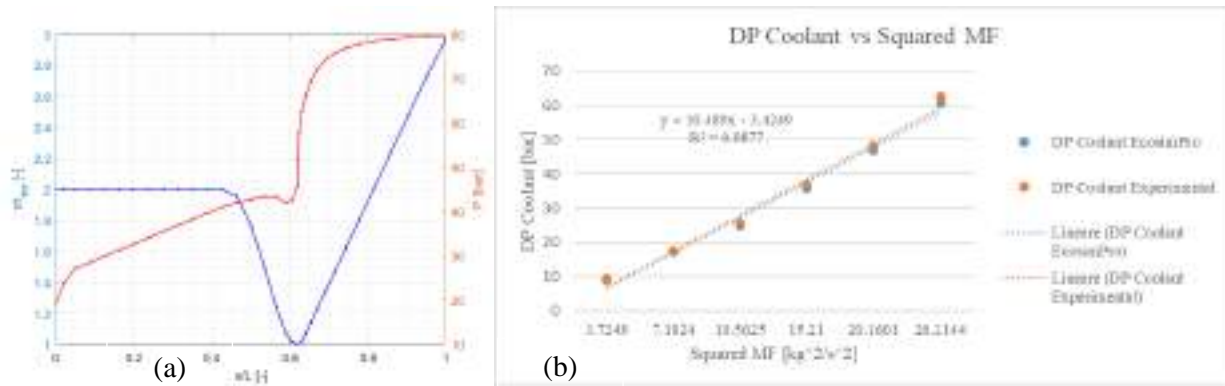


Figure 2: (a) Pressure variation along the cooling jacket. (Test01 results). (b) Pressure drop vs squared water MFR linear relation.

Figure 3(a) compares the water temperature profiles obtained with the Bartz, modified Bartz and Pavli correlations. The Bartz correlation underestimates the temperature increase while the modified Bartz and the Pavli correlations overestimate it.

The heat fluxes coming from the combustor are compared in Figure 3(b) and show how a peak is reached in the throat section, phenomenon due to the fact that in this region the exchange area (i.e. the lateral surface through which the thermal power coming from the combustor is exchanged) is the minimum. The heat flux obtained with the Pavli wall heat exchange correlation is characterized by the highest peak, on the contrary the Bartz correlation provides the lowest peak. Since the modified Bartz correlation provides the lowest error in estimating the water temperature rise, it has been considered as the correlation to use to predict the firing condition behaviour.

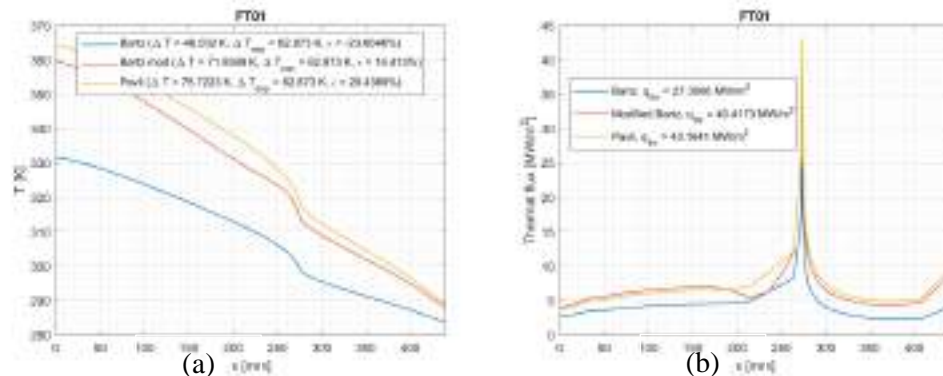


Figure 3: (a) Water temperature profiles comparison (FT01). (b) Heat fluxes comparison (FT01).

Table 3 reports a summary of the numerical and experimental results of the three firing tests. The numerical results well predict the pressure chamber, the coolant pressure drop and the thrust, on the contrary the coolant temperature rises are overpredicted. As expected, the higher thrusts occur during the tests where the chamber pressure is higher. Furthermore, the combustion efficiencies for the three tests are 93%, 89% and 93 %, respectively.

Table 3: Firing tests results

	FT01		FT02		FT03	
	Experimental	EcosimPro	Experimental	EcosimPro	Experimental	EcosimPro
P _{CC} [bar]	37.99	38	36.61	35.98	45.66	45.76
Water MFR [kg/s]	5.55	5.55	5.46	5.43	5.52	5.52
Water ΔP [bar]	67.86	69.19	65.72	66.99	66.85	68.46
Water ΔT [K]	62.87	71.93	61	73.16	71.92	83.23

Conclusions

The simulations performed by means of the *EcosimPro* software on the «DEMO-0A» to reproduce the cold flow operative conditions turned out to be very accurate for the prediction of the pressure drops experienced by the water in the cooling jacket that are slightly underestimated with respect to the experimental ones. This underestimation can be ascribed to the fact that the schematic used does not include the inlet and outlet manifolds that add further pressure drops. The simulations reproducing the firing conditions of the demonstrator had the aim to investigate the effects of the different wall heat exchange coefficient correlations on the thermal behaviour of the engine and the outcome of this study shows that the results obtained by considering the Bartz correlation underestimates the coolant temperature rise and thermal flux, on the contrary the modified Bartz and Pavli correlations overestimate them and the empirical correlation that provides results comparable to the experimental ones is the modified Bartz correlation. The results in terms of chamber pressure and temperature, pressure drop of the cooling jacket and thrust delivered are better predicted. In the end, the outcomes of the numerical simulations aimed at reproducing the firing conditions suggest that the *EcosimPro* software can be used to perform preliminary simulations able to provide accurate results in terms of chamber pressure, temperature and thrust, but with thermal results characterized by a lower accuracy due to the fact that the model developed is 1-D and does not take into account some phenomena that can occur in an engine and that are typically 2-D or 3-D, such as the thermal stratification of the coolant inside the cooling channels that changes the coolant thermophysical properties and consequently the thermal exchange occurring between the combustion chamber and the cooling jacket.

References

- [1] C. D. Brown, "Conceptual Investigations for a Methane-Fueled Expander Rocket Engine.," *40th AIAA/ASME/SAE/ASEE Joint Propuls. Conf. & Exhib.*, 2004. <https://doi.org/10.2514/6.2004-4210>
- [2] J. Jokhakar and M. Naraghi, "A CFD-RTE model for thermal analysis of regeneratively cooled rocket engines.," *44th AIAA/ASME/SAE/ASEE Joint Propulsion Conference & Exhibit. 2008.*, p. 4557, 2008. <https://doi.org/10.2514/6.2008-4557>
- [3] H. Kawashima, H. Negishi, T. Tomita, K. Obase and T. Kaneko, "Verification of Prediction methods for Methane Heat Transfer Characteristics.," *48th AIAA/ASME/SAE/ASEE Joint Propulsion Conference & Exhibit.*, p. 4120, 2012. <https://doi.org/10.2514/6.2012-4120>
- [4] M. Pizzarelli, S. Carapellese and F. Nasuti, "A quasi-2-D model for the prediction of the wall temperature of rocket engine cooling channels.," *Numerical Heat Transfer, Part A: Applications*, pp. 1-24, 2011. <https://doi.org/10.1080/10407782.2011.578011>
- [5] M. Leonardi, F. Di Matteo, J. Steelant, B. Betti, M. Pizzarelli, F. Nasuti and M. Onofri, "A zooming approach to investigate heat transfer in liquid rocket engines with ESPSS propulsion simulation tool.," *8th Aerothermodynamics Symposium*, 2015.

- [6] C. H. Marchi, F. Laroca, A. F. C. D. Silva and J. N. Hinckel, "Numerical solutions of flows in rocket engines with regenerative cooling.," *Numerical Heat Transfer, Part A: Applications*, pp. 699-717, 2004. <https://doi.org/10.1080/10407780490424307>
- [7] F. Battista, D. Ricci, P. Natale and et al., "The HYPROB demonstrator line: status of the LOX/LCH4 propulsion activities.," *8th European Conference for Aeronautics and Space Sciences, EUCASS2019-FP0621*, 2019.
- [8] Empresarios Agrupados, "EcosimPro ESPSS User Manual," 2020.
- [9] S. Omori, W. G. Klaus and A. Krebsbach, "Wall temperature distribution calculation for a rocket nozzle contour.," *NASA-TN-D-6825*, 1972.
- [10] B. Betti, M. Pizzarelli and F. Nasuti, "Coupled Heat Transfer Analysis in Regeneratively Cooled Thrust Chambers.," *Journal of Propulsion and Power*, pp. 360-367, 2014. <https://doi.org/10.2514/1.B34855>
- [11] D. Ricci, F. Battista, M. Ferraiuolo and et al., "Development of a Liquid Rocket Ground Demonstrator through thermal analyses," *Heat Transf. Eng.*, pp. 1100-1116, 2020. <https://doi.org/10.1080/01457632.2019.1600879>

Fast reconfiguration maneuvers of a micro-satellite constellation based on a hybrid rocket engine

Antonio Sannino^{1,a*}, Stefano Mungiguerra^{1,b}, Sergio Cassese^{1,c},
Raffaele Savino^{1,d}, Alberto Fedele^{2,e}, Silvia Natalucci^{2,f}

¹Departement of Industrial Engineering, University of Naples Federico II, 80 Piazzale Tecchio,
Naples, 80125, Italy

²Italian Space Agency, Via Del Politecnico, Rome, 00133, Italy

^aantonio.sannino2@unina.it*, ^bstefano.mungiguerra@unina.it, ^csergio.cassese@unina.it,
^draffaele.savino@unina.it, ^ealberto.fedele@asi.it, ^fsilvia.natalucci@asi.it

Keywords: Hybrid Rocket Engine, Hydrogen Peroxide, Cubesat Formation Flying, Orbital Maneuvers

Abstract. In this work, the formation flight of the CubeSat cluster RODiO (Radar for Earth Observation by synthetic aperture DIstributed on a cluster of cubesats equipped with high-technology micro-propellers for new Operative services [1]) with respect to a small satellite in LEO (Low Earth Orbit) has been analyzed. RODiO is an innovative mission concept funded by the Italian Space Agency (ASI) in the context of the Alcor program [2]. The small satellite is equipped with an antenna that allows it to function as a transmitter, whereas RODiO functions as a receiver. The extension of the virtual *SAR (Synthetic Aperture Radar) antenna* can be achieved by establishing an along-track baseline performing an orbital coplanar maneuver (a phasing maneuver). Another interesting scenario is the possibility to create a cross-track baseline performing an inclination change maneuver, useful for stereoradargrammetric applications. Such formation reconfiguration maneuvers can be achieved in relatively short times only by use of a high-thrust propulsion system, i.e. based on conventional chemical technologies. From the study of maneuvers, it is possible to identify the required ΔV , which represents an input parameter for the design of propulsion system. Among the different kinds of propulsion systems, a *Hybrid Rocket Engine* was chosen for its safety, compactness and re-ignition and throttle capabilities.

Introduction

In recent years, the use of CubeSats has become increasingly popular due to their simplicity of construction, cost and reduced production time compared to conventional satellites. These miniaturized satellites are well suited to formation flight for telecommunication and imaging purposes. In this study, the formation flight of a 16U CubeSat constellation (RODiO, consisting of four micro-satellites) was analyzed with respect to a LEO-satellite. The objective is to perform maneuvers to extend the virtual *SAR antenna*. The LEO-satellite is moving on a quasi-circular Sun-Synchronous Orbit (eccentricity $\approx 10^{-3}$, inclination $\approx 97^\circ$) at a mean altitude of ≈ 400 km (World Geodetic System-84), and RODiO cluster follows it on this orbit.

In the following sections the *orbital maneuvers* considered were described. Using *GMAT (General Mission Analysis Tool)* an estimation of the maneuvers ΔV budget was obtained. Identified the maneuvers costs, a preliminary design of the *Hybrid Rocket Engine* for the CubeSat was carried out, complying with the requirements for propulsion unit volume (<1.5 U) and mass (<2 kg).

Phasing maneuver

In this maneuver, the objective is to bring one of the satellites of the RODiO cluster, which follows the LEO-satellite in its orbit, from a distance in the range $[-90$ km, -50 km], to a distance in the

range [+50 km, +90 km]. In this way a *multistatic SAR data collection* with a triplet of acquisitions over the same area at three different observation angles is possible.

To this aim, a ΔV in the opposite direction of the motion must be applied. In this way the satellite RODiO reaches an elliptical orbit with an orbital period smaller than the period of the initial orbit and, after one orbit, the RODiO satellite reduces the along-track distance. After few orbits, the RODiO satellite reaches a new position beyond LEO-satellite and, at this point, a ΔV in the motion direction must be applied to establish a constant *along-track baseline*. The challenging point of this mission is the need to apply two ΔV but in opposite direction and evaluating the re-ignition capability of the propulsion system.

To study the relative motion between two satellites, the Hill reference frame defined in [3] was used, assuming that the LEO-satellite is the chief, while RODiO is the deputy. Combining the equations for the Hohmann transfer reported in [4] (under the assumptions of Keplerian mechanics), it is possible to write Eq. 1, which provides an initial estimate of the along-track baseline variation per orbit (ΔY_{orbit}):

$$\Delta Y_{orbit} = (\tau_{ci} - \tau_e) V_{ci} \quad (1)$$

where “ τ_{ci} ” is the orbital period of initial circular orbit, “ τ_e ” is the period of elliptical orbit, and “ V_{ci} ” is the velocity on the initial circular orbit. In Table 1 different cases are presented, and a simulation of relative motion using *GMAT* considering the presence of the atmosphere (*Jacchia-Roberts* model), the non-sphericity of the earth (*Earth Geopotential Model 96*), and solar radiation pressure, has been performed (results in Fig.1).

Table 1: Possible phasing maneuvers in the along-track distance ranges considered for different ΔV . (Y_i is the initial distance between a RODiO satellite and the LEO-satellite, Y_f is the final distance).

ΔV of single burn [m/s]	Y_i [km]	ΔY_{orbit} [km]	Number of orbits	Y_f [km]
2.5	-62.25	41.5	3	+62.25
3	-75	50	3	+75

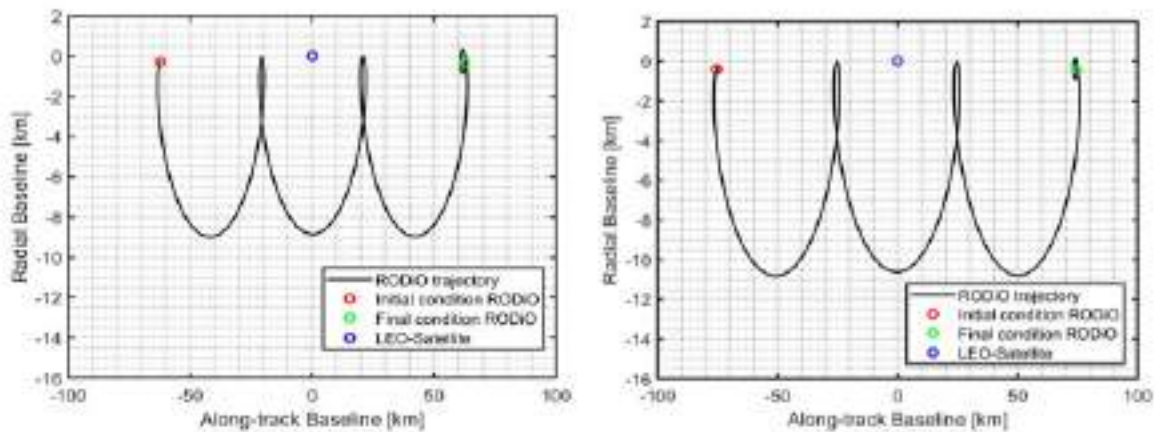


Fig. 1: RODiO trajectory in Hill reference frame with respect to LEO-Satellite (on the left, first case indicated in Table 1, on the right, second case indicated in Table 1).

Inclination change maneuver

The purpose of this maneuver is to change the inclination of the orbit of a satellite of the RODiO constellation by applying a normal ΔV to the orbital plane when the satellite arrives in the ascending node. In this way a relative drift of the nodes starts, and, after a certain time, a *cross-*

track baseline is established. Applying an impulsive burn in the same direction but where the satellite reaches the descending node, the *cross-track baseline* remains constant. An advantage of this maneuver is that the direction of ΔV does not change.

In *GMAT* the study of relative motion between two satellites of RODiO cluster has been analyzed (RODiO-1 is the chief, RODiO-2 is the deputy). Under the assumptions of a quasi-circular orbit, considering J2 effect, it is possible to simplify the equations of relative motion reported in [3] and calculate the *cross-track baseline* from Eq. 2:

$$z \approx a\delta\Omega \sin i \quad (2)$$

where “z” is the *cross-track baseline*, “a” is the semi-major axis, “ $\delta\Omega$ ” is the relative drift of ascending node consequent to the inclination change, and “i” is the inclination. In the Fig.2 the results obtained by *GMAT* for a $\Delta V = 3$ m/s (that yields a Δi of 0.02 deg [4]) for each burn and a waiting time of 15 days are shown.

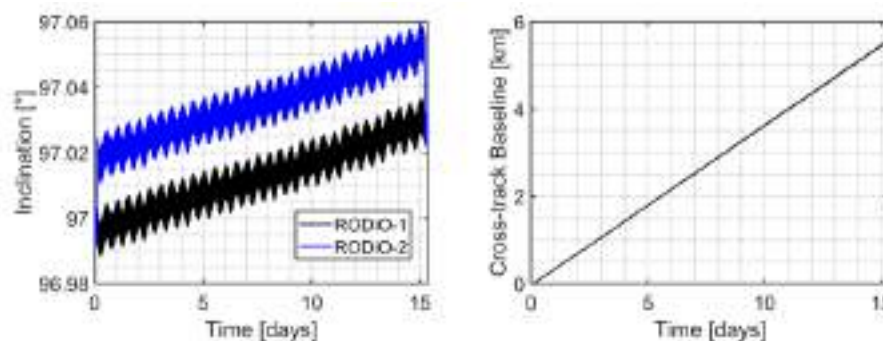


Fig. 2: Trend of inclination (on the left) and trend of cross-track baseline (on the right) with respect to mission time for $\Delta V = 3$ m/s.

Hybrid Rocket Engine preliminary design

A mixture with *Hydrogen Peroxide* as oxidant (91wt%) and *ABS (Acrylonitrile Butadiene Styrene)* as fuel grain is selected to evaluate the performance of the *Hybrid Rocket Engine*. In first approximation, the regression rate for a hybrid rocket motor is related to oxidizer mass flux (Eq.3):

$$\dot{r} = a (G_{ox})^n \quad (3)$$

where “a” and “n” are experimental coefficients which change for each couple of propellants. Using the procedure described in [5] and considering experimental value of “a” and “n” obtained from test conducted on this engine scale, an estimate of the performance of the thrust chamber was performed. Considering an oxidant flow rate of 3.5 g/s, a circular port fuel grain with an initial port diameter of 10 mm, a nozzle throat diameter of 2 mm and an Area Ratio of 15, the performance of the propulsion system in terms of thrust and specific impulse can be evaluated. The mass of the CubeSat is 22 kg, but for an initial estimation of the performance and sizing of the rocket, a 10 kg margin on the mass budget (total mass of 32 kg) and a 100% margin on the ΔV (total ΔV required for maneuvers 12 m/s instead of 6 m/s) are considered. Table 2 shows the performance of the *Hybrid Rocket Engine*. The *Hydrogen Peroxide* total mass required is 106.75 g. From the performance analysis, it is possible to preliminarily size the propulsion system, in particular the thrust chamber, which will include a case containing the fuel grain and nozzle. Fig. 3 shows a sectional view of the thrust chamber with all dimensions of interest indicated from which it is possible to observe a pre-combustion chamber (upstream to fuel grain) of 10 mm length, a post-

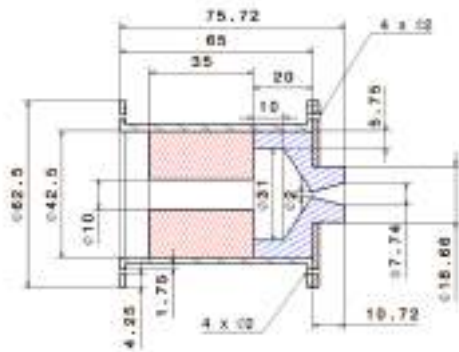


Fig. 3: CAD model section of thrust chamber (dimensions in mm). In blue the conical nozzle, in red the fuel grain, in black the external case, in brown a closing flange (wall thickness flange and case: 2 mm).

combustion chamber (downstream of the fuel grain) consisting of a cylindrical section (10 mm long) and the converging nozzle section (10 mm long). The pre- and post-chamber lengths shall be better defined by a more accurate study of the rocket's internal thermo-fluid dynamics. Considering graphite as material, the conical nozzle has a mass of 55 g. To reduce the length of the diverging section, a bell-shaped nozzle can be considered. In first approximation, the external case made up of steel, and its mass is 179 g. The mass of ABS fuel grain is 46 g. Since the dimensions of the thrust chamber are considerably smaller than the imposed limits (1.5 U, 10 cm x 10 cm x 15), it is reasonable to assume that there is sufficient space for the feed line, tanks, and catalytic chamber. With an appropriate choice of materials, the total mass requirement (<2kg) is also satisfied.

Table 2: Summary of mixture performance H_2O_2 (%wt 91) - ABS. Average values of regression rate, OF, vacuum thrust, specific vacuum impulse, fuel flow rate, chamber pressure, chamber temperature, and final grain diameter were reported (combustion efficiency and nozzle efficiency about 95%. Overall efficiency 90.25%).

t_b [s]	\dot{r} [mm/s]	OF	T_{vac} [N]	$I_{sp,vac}$ [s]	\dot{m}_f [g/s]	P_c [bar]	T_c [K]	D_{final} [mm]
30.5	0.53	2.31	12.6	255	1.53	22.6	1930	42.5

Concluding remarks

From numerical *GMAT* simulations it is possible to conclude that the *along-track baseline* variations are possible to move one RODiO satellite from the original position to a final position in few orbits, whereas a *cross-track baseline* variations up to few kilometers are possible with maneuvers duration of the orders of few days. Future developments could include a detailed design of the other main subsystems, numerical analysis of fluid dynamic, thermal and structural aspects, and the possibility of developing breadboards for ground testing of the propulsion unit.

References

- [1] A. Renga, et al., Design considerations and performance analysis for RODiO distributed SAR mission, *Acta Astronautica*, Volume 210, September 2023, Pages 474-482. <https://doi.org/10.1016/j.actaastro.2023.04.001>
- [2] G. Leccese, et al., Overview and Roadmap of Italian Space Agency Activities in the Micro- and Nano-Satellite Domain, 73rd IAC, Paris, France, 2022, 18 – 22 September.
- [3] M. D'Errico (ed.), *Distributed Space Missions for Earth System Monitoring*, Space Technology Library, Springer Science Business Media, New York 2013, pp. 125-162. https://doi.org/10.1007/978-1-4614-4541-8_3
- [4] D.A. Vallado, *Fundamentals of Astrodynamics and Applications*, Space Technology Library, Springer Dordrecht, edition 2, pp. 317-422.
- [5] S. Mungiguerra, et al., Characterization of novel ceramic composites for rocket nozzles in high-temperature harsh environments, *International Journal of Heat and Mass Transfer*, 163 (2020) 120492. <https://doi.org/10.1016/j.ijheatmasstransfer.2020.120492>

Tests and simulations on 200N paraffin-oxygen hybrid rocket engines with different fuel grain lengths

Stefano Mungiguerra^{1,a *}, Daniele Cardillo^{2,b}, Giuseppe Gallo^{3,c},
Raffaele Savino^{1,d}, Francesco Battista^{2,e}

¹Department of Industrial Engineering, University of Naples Federico II, 80 Piazzale Tecchio,
Naples, 80125, Italy

²CIRA "Italian Aerospace Research Centre", 81043 Capua, Italy

³Department of Mechanical and Space Engineering, Hokkaido University, Hokkaido 060-0808,
Japan

^astefano.mungiguerra@unina.it, ^bd.cardillo@cira.it, ^cgallo@eng.hokudai.ac.jp,

^drasavino@unina.it, ^ef.battista@cira.it

Keywords: Hybrid Rockets, Paraffin-Based Fuels, Characteristic Velocity, Nozzle Heat Transfer

Abstract. An experimental campaign, in the framework of the HYPROB-NEW hybrid rocket studies, was carried out on a 200N-thrust class hybrid rocket engine, using gaseous oxygen as the oxidizer and paraffin wax-based fuel, to investigate the effect of fuel grain length on motor performance and internal ballistics. Numerical analysis have been also performed to support the experimental findings. It was observed that, for given oxidizer flow rate, fuel grain length directly affects the characteristic velocity, because of its influence on residence time and mixing efficiency, so that the shortest grain configuration displayed the lowest performance. Moreover, CFD simulations provided an estimation of the regression rate profile along the grain length, providing a possible interpretation for the measured space-time-averaged fuel regression rate. Finally, a method for the rebuilding of the convective heat-transfer coefficient in the nozzle was used, based on a combination of numerical simulations and experimental acquisitions.

Introduction

The application field of hybrid rockets is currently still limited much probably for the low fuel regression rate compared to solid rockets, especially when the use of conventional polymeric fuels is foreseen, because of the diffusion-limited phenomena affecting grain regression [1]. One of the most investigated solutions to overcome limitation in fuel regression rate and thus rocket thrust is the use of liquefying fuels, characterized by a relevant liquid droplet entrainment component, which can substantially enhance fuel mass flow rate [2].

Within this framework, the HYPROB-NEW project, funded by Italian Ministry of Research and managed by the Italian Aerospace Research Centre (CIRA), envisaged a collaboration between CIRA and University of Naples Federico II, and was focused on the study of paraffin as a potential high-performance fuel for hybrid rockets. Among the various activities, firing test campaigns were carried out on a 200 N thrust-class hybrid rocket engine, using axially injected gaseous oxygen as oxidizer and a paraffin wax-based fuel. Different cylindrical fuel grain lengths were adopted to extend fuel characterization under different operating conditions, and to evaluate rocket performances and internal ballistics in the different configurations. In addition to data collected with 220 mm propellant grain length [³] (labeled as L), two further test campaigns were carried out considering 130 mm (labeled as M) and 70 mm (labeled as S) grain lengths. Full details on the experimental setup and results are reported in [4]. In this work, based on measurements of pressures, temperatures, thrust and mass flow rate, and with the support of Computational Fluid



Dynamic (CFD) simulations, some considerations on performance, regression rate and graphite nozzle heat transfer.

Characteristic velocity analysis

In this subsection, the motor performances of the three configurations are discussed. Fig. 1a represents the characteristic velocity obtained in the firing tests and compared with the ideal one computed by CEA software [5]. It can be seen that the motor length affects the mixing of the oxygen with the fuel. The motor shows a combustion efficiency close to 1 in the L configuration. This value decreases from 1 to about 0.9 and 0.75 in the M and S configurations, respectively.

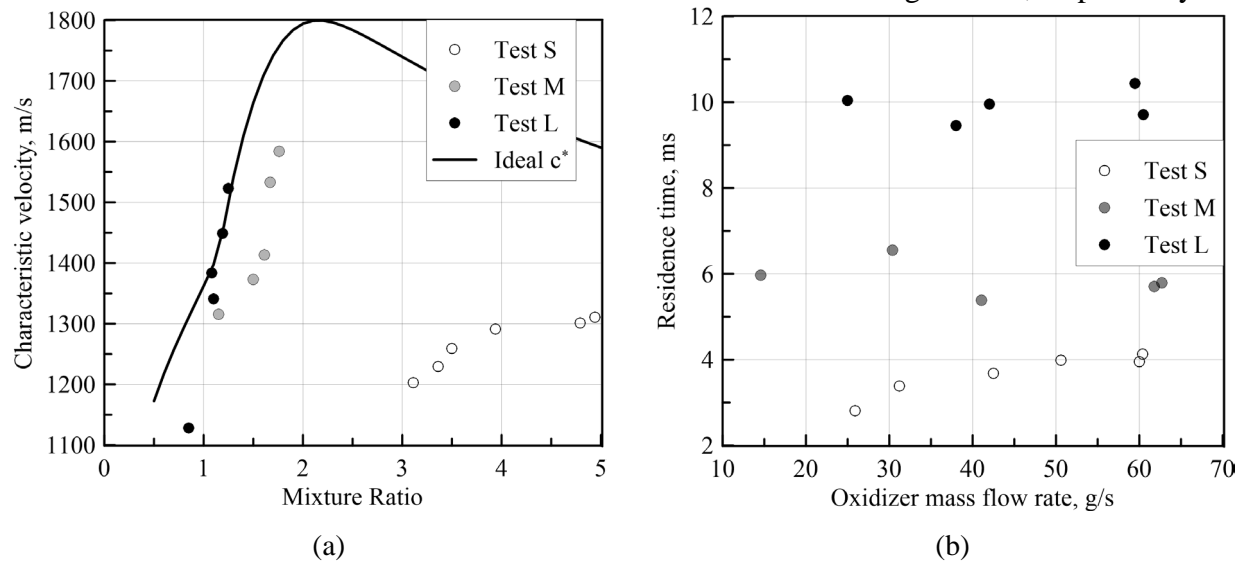


Fig. 1 (a) Ideal and experimental characteristic velocity of Test S, M and L versus O/F, (b) estimated gas residence time versus oxidizer mass flow rate in the different configurations.

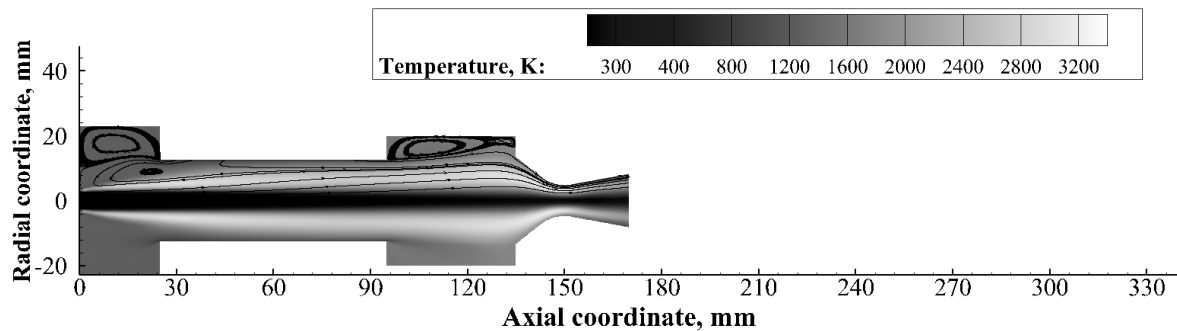


Fig. 2 Temperature contour plot with overlapped streamlines (top half) and mixture fraction iso-lines (bottom half) of test S at $\dot{m}_{ox} \approx 40$ g/s and at the average grain port diameter.

Therefore, it can be inferred that the grain length increases the motor combustion efficiency, because it increases the residence time of the gas mixture, which can be computed (Fig. 1b) as the ratio between the total motor length and the mean flow velocity in the chamber (weighted average among the flow velocities in pre-combustion chamber, grain port and post-combustion chamber, calculated by mass conservation using CEA software). The highest residence time (which is quite insensitive to mass flow rate) is shown by configuration L, which shows the highest combustion efficiency.

When the residence time is extremely low as in the case of Test S, the experimental characteristic velocity is also little affected by the change in the overall mixture ratio. This is likely due to the fact that, when the residence time is too low, the fuel released from the grain does not have enough time to reach the axis and therefore mixing efficiency is lower, as highlighted by Fig.

2, showing the results of CFD simulations carried out, by means of the model presented in [6], for test S at $\dot{m}_{ox} \approx 40 \text{ g/s}$ with the corresponding average grain port diameter.

Fuel regression rate analysis

Another major experimental finding was that the space-time-averaged fuel regression rate appeared to be affected by fuel grain length. First, regression rate in tests L was roughly 10-15% higher than for tests S. Moreover, axial recession was observed for tests M. To provide a possible explanation for these experimental observations, a CFD simulation was performed by the same model used above for the configuration L at $\dot{m}_{ox} \approx 40 \text{ g/s}$, computing the wall heat flux along the fuel grain wall, whose normalized trend is shown in Fig. 3. The wall heat flux behavior can be outlined as the product of the heat transfer coefficient, h_c , and ΔT . Indeed, \dot{q} increases with the temperature, reaching a maximum at the axial coordinate between 125 mm and 150 mm, where the stoichiometric conditions are achieved; then, it decreases because a fuel-rich mixture is obtained. Three stations are highlighted in the picture, which correspond to the lengths of the configuration S, M and L. It can be seen that the space-averaging process leads to an apparent underestimation of the fuel regression rate for the shortest configuration. Moreover, as shown, the peak of wall heat flux is approximately achieved at the end of configuration M, which explains the reason why this configuration was affected by the axial recession.

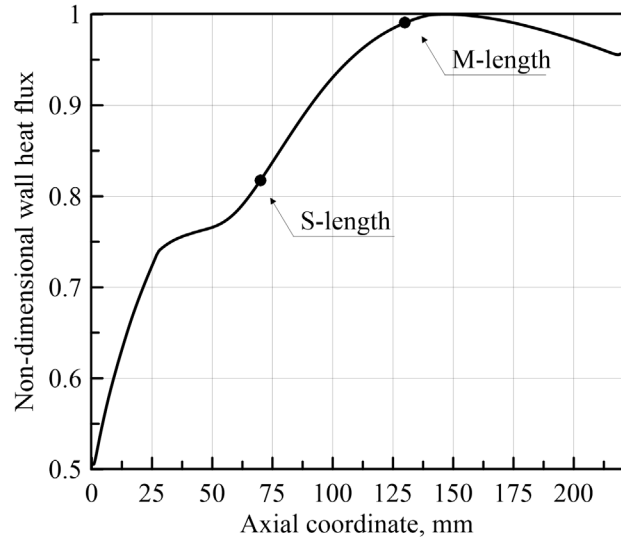


Fig. 3 Non-dimensional wall heat flux along the motor axis

Nozzle heat transfer rebuilding

Finally, measurement of temperature inside the graphite nozzle allowed for a rebuilding of wall heat flux in the S configuration (the most oxidizing) [4]. An iterative procedure was used to determine a profile of the convective heat transfer coefficient h_c matching the experimental temperature measurement, by solving the unsteady energy equation inside the nozzle with CFD simulations. The obtained coefficient was compared to that provided by empirical correlations. Fig. 4 shows this comparison for a test at $\dot{m}_{ox} \approx 40 \text{ g/s}$ and O/F ≈ 3.5 , and a test at $\dot{m}_{ox} \approx 60 \text{ g/s}$ and O/F ≈ 4.79 . It can be observed that, in the less oxidizing condition, the experimental trend of h_c deviates more from the empirical correlations, likely because in that condition the wall temperature remains almost always below the gasification temperature of the fuel, therefore creating a liquid paraffin layer at wall acting as insulator and heat sink.

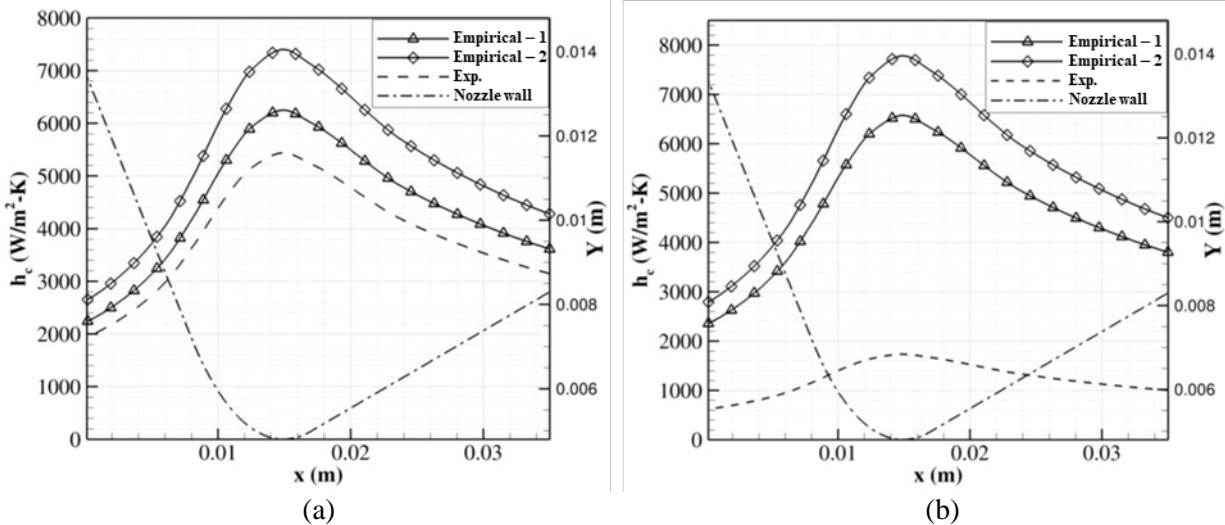


Fig. 4 Comparison of h_c predictions with different methods: tests at $\dot{m}_{ox} \approx 60$ g/s (a) and $\dot{m}_{ox} \approx 40$ g/s (b)

Conclusions

The following main conclusions can be drawn:

- The characteristic velocity is affected by the grain length, with increasing efficiency for increasing length, because of the corresponding increase of gas mixture residence time, enhancing propellant mixing.
- The space-averaging process in the regression rate calculation is affected by the axially increasing grain consumption. Longer grains exhibit a higher space-time-averaged regression rate for a given G_{ox} , but the regression rate trend in time is similar for all the configurations in the upstream region
- At low O/F, a significant part of the convective heat transfer to nozzle wall is absorbed by fuel gasification, leading to an overestimation of wall heat transfer by empirical correlation laws, while above a certain O/F threshold, the nozzle wall temperature is higher than fuel gasification temperature and the empirical correlations work properly.

References

- [1] D. Altman, et al., Hybrid Rocket Propulsion Systems, in: R.W. Humble, et al. (Eds.), Space Propulsion Analysis and Design, 1st ed., McGraw-Hill, New York, 1995, 365–370.
- [2] A. Mazzetti, et al., Paraffin-based hybrid rocket engines applications: a review and a market perspective, Acta Astronaut. 126 (2016) 286–297
- [3] G. D. Di Martino, et al., Two-Hundred-Newton Laboratory-Scale Hybrid Rocket Testing for Paraffin Fuel-Performance Characterization, J. Propuls. Power 35 (2019) 224-235, <https://doi.org/10.2514/1.B37017>
- [4] D. Cardillo, et al., Experimental Firing Test Campaign and Nozzle Heat Transfer Reconstruction in a 200 N Hybrid Rocket Engine with Different Paraffin-Based Fuel Grain Lengths. Aerosp. **2023**, 10, 546. <https://doi.org/10.3390/aerospace10060546>
- [5] S. Gordon, et al., Computer program of complex chemical equilibrium compositions and applications, NASA Ref. Publ. 1311 (1994).
- [6] G. Gallo, et al., New Entrainment Model for Modelling the Regression Rate in Hybrid Rocket Engines, J. Propuls. Power 37 (2021) 893-909, <https://doi.org/10.2514/1.B38333>

Thermite-for-demise (T4D): thermite characteristics heuristic optimization on object- and spacecraft-oriented re-entry models

Alessandro Finazzi^{1,a *}, Filippo Maggi^{1,b} and Tobias Lips^{2,c}

¹Dipartimento di Scienze e Tecnologie Aerospaziali, Politecnico di Milano, Via La Masa 34, 20156 Milano – Italy

²HTG - Hyperschall Technologie Göttingen GmbH, Am Handweisergraben 13, 37120 Bovenden – Germany

^aalessandro.finazzi@polimi.it, ^bfilippo.maggi@polimi.it, ^ct.lips@htg-gmbh.com

Keywords: Atmospheric Re-Entry, Genetic Algorithm, Thermite, Spacecraft Demise

Abstract. The major hazard associated with uncontrolled atmospheric re-entry is the casualty risk on ground. An innovative concept to support spacecraft demise that is now under investigation is the use of exothermic reactions. Thermites are good candidates for this role, being capable of releasing a noticeable amount of heat upon ignition. An appropriate selection of the metal-metal oxide couple can grant a formulation that is compliant with the main space operation needs, e.g., that is relatively insensitive to external stimuli and non-toxic. To support the selection of the energetic material for the experimental tests in the ESA-founded project SPADEXO and to preliminarily size the charge to be placed on board, the object-oriented code TRANSIT has been developed. This software has been compared to ESA's spacecraft-oriented code SCARAB (developed by HTG), that is capable to predict spacecraft re-entry with the highest possible level of detail. Both the models were subjected to a genetic algorithm optimization process to identify the best thermite properties and the foreseen energetic material mass for simple geometries applications. In this paper, the SCARAB results obtained for one geometry will be presented and compared with the ones retrieved by TRANSIT.

Introduction

The threat posed by space debris to the access and use of space is becoming more and more urgent every year. Recently, both the European Space Agency (ESA) and the Inter-Agency Space Debris Coordination Committee (IADC) have published their reports on the status of the space environment [1,2]. Considering the protected Low Earth Orbits (LEO) region as defined by IADC [3], the space traffic is now 10 times the level observed in 2000. However, both the cited documents demonstrate that the adoption of the space debris mitigation measures is insufficient. The ESA report [1] reveals that the 93% of small satellites (<10 kg) are naturally compliant with the 25-year rule, but for larger payloads the compliant share is significantly lower. Only between the 40% and 70% of the total payload mass is estimated to reach its end-of-life (EOL) in an orbit compliant with the current mitigation rules. If naturally compliant objects are discarded, until 2017 only between 10% and 40% of spacecrafts respected the mitigation guidelines [2]. Even if the trend in the last years has been generally positive, it is evident that the compliance rate is significantly lower than the internationally declared objective (90% [1,3,4]). Therefore, post-mission disposal (PMD) is still a problematic topic and the adoption of the current, if not even more stringent, mitigation rules is of paramount importance to reach a sustainable exploitation of space.

However, the necessity of de-orbiting spacecrafts from LEO involves an implicit casualty risk on ground. The current international guidelines [3] impose a maximum threshold for this risk of 10^{-4} . A first strategy to meet this requirement is to perform a high-thrust manoeuvre to force the



impact on an uninhabited area, with the subsequent impacts on costs (e.g., additional fuel) and design. A second option is to perform an uncontrolled re-entry, possibly after a low-thrust manoeuvre or the deployment of passive devices to limit the residence time in orbit coherently with the 25-years limit. In this case, the associated costs and impacts on the post-mission disposal reliability would be lower. The main limitation for the use of this second strategy is the casualty risk limit. Its value must be computed using re-entry software like ESA's Debris Risk Assessment and Mitigation Analysis (DRAMA) [5] or Spacecraft Atmospheric Re-entry and Aerothermal Breakup (SCARAB) [6]. The uncontrolled re-entry is allowed only if the casualty risk threshold is respected. As its value is strictly connected to the spacecraft mass and to the robustness of its components, a rather new field of research is now becoming more and more important. This approach, named Design-for-Demise (D4D), consists in the intentional design of the spacecraft to promote its demise during the atmospheric re-entry, to limit the number and the mass of the fragments reaching the ground. One of the D4D strategies involves the maximization of the available heat to aid the demise of the most robust equipment. The main proposed solutions to act in this sense are the modification of the ballistic coefficient of the spacecraft, the exploitation of particular shapes to increase the local heat fluxes, or the use of exothermic reactions to provide additional enthalpy. The latter approach is the focus of this paper.

The hereby named Thermite-for-Demise (T4D) technology consists in placing a pyrotechnic charge into the structural voids of some spacecraft components. The energetic material, once ignited, provides the additional enthalpy necessary to induce the demise of the equipment. Thermites are particularly interesting for this application, thanks to their high energetic density, high adiabatic flame temperature, tunability and intrinsic safety [7]. An appropriate selection of the starting metal-metal oxide couple allows to meet both performance and operational requirements [8]. Recent patents proposed the use of thermites to promote spacecraft demise [9,10], and wind tunnel tests proved the concept in relevant environment [11,12]. A systematic study on the topic is currently ongoing in the framework of ESA-TRP SPADEXO project [13].

One of the main aspects of this technique that needs to be defined are the minimum thermite mass to be used and the best ignition time. Even if these parameters are strictly connected to the particular application (e.g., re-entry path, equipment material and shape) a heuristic optimization is hereby proposed for a selected simple geometry. A genetic algorithm is used on both an object- and a spacecraft-oriented re-entry software to minimize the thermite mass. The impacts of the different level of detail of the numerical models will be assessed, as well as the ratio between the component and the thermite masses for the selected conditions.

Methodology

TRANSIT. The object-oriented re-entry software used for this analysis is the TRANsatmospheric SIMulation Tool (TRANSIT), developed to support the research on the T4D technology. The objective of this Python novel numerical model is to provide simple and fast simulations for a preliminary assessment on the efficacy of a T4D strategy for a given application. The selected atmospheric model is the NRL-MSISE00 [14] and the non-spherical shape of the Earth is described through a fourth-degree zonal harmonic description. The dynamic model that represents the ballistic re-entry is lumped and considers three degrees of freedom [15]. The aerodynamic model can handle three different geometries (sphere, cylinder, and box). The correlations for the computation of the coefficients of drag are taken from [16]. Shape factors are used to relate the heat load on the three randomly tumbling geometries with the stagnation heat flux on a flat plate [17] (for free molecular regime) or on a sphere [18] (for continuum regime). The hot air after the shock is considered as a non-calorically perfect gas in chemical equilibrium [19]. The thermal model is lumped, and the surface is assumed to regress uniformly.

SCARAB. The spacecraft-oriented software used for this study is SCARAB. It was developed since 1995 under the lead of HTG in the frame of ESA/ESOC contracts. It has been used to model

the re-entry of numerous European satellites and launcher stages, as well as for rebuilding test campaigns in hypersonic wind tunnels. It has been compared to other re-entry prediction tools and validated with in-flight measurements. The main characteristic that differentiates SCARAB with respect to the more common object-oriented codes is the panel-based description of the spacecraft. This discretization allows the use of the complete 6 degree-of-freedom equations for the trajectory computation and the more detailed description of the temperature field in the spacecraft and of its break-up process. This representation consents to abandon the common random tumbling assumption and to include conductive heat transfer in the space object. An arbitrarily complex geometry can be reconstructed and then studied.

Thermite model. The additional enthalpy provided by the thermite is modelled as an internal heat source, that is activated once the spacecraft reaches the ignition temperature. The effective heat transfer Q_{eff} from the thermite to its vessel is quantified as per Eq. 1, where η is the heat transfer efficiency (hereby considered equal to 0.6 [13]), m_{th} is the thermite mass on board, and Q_{react} is the theoretical reaction heat release (3958.20 kJ/kg).

$$Q_{eff} = \eta \cdot m_{th} Q_{react} \quad (1)$$

The additional enthalpy is released according to five different profiles (constant, gaussian, early triangular, late triangular, and centred triangular). The user can select the duration of the reaction. In SCARAB, the heat source is applied only on the internal panels of the geometry. The reaction is started once the mean temperature of the spacecraft (in TRANSIT) or the local temperature (in SCARAB) reaches the ignition threshold. The thermal inertia of the thermite charge is considered modifying the specific heat and the mass of the vessel.

Optimization approach. When it comes to determining the impact of a thermite charge on a re-entering spacecraft, the inherent complexity of the re-entry process must be considered. Trade-off effects can be difficult to estimate. For example, a higher thermite filling for a hollow object implies both a higher additional enthalpy release upon ignition and a higher thermal inertia for the system. A lower temperature of ignition could imply an early decrease in mass, with a change in the ballistic coefficient that can be beneficial or not. Moreover, an early ignition could anticipate so much the maximum temperature reached during the descent that could provoke a temperature increase not sufficient to reach the melting point of the spacecraft material. To consider the complexity of the process, the heuristic optimization adopted in this study involves the use of a genetic algorithm, based on the open-source Python package PyGAD [20]. An aluminium sphere, with radius of 0.5 m and thickness of 0.03 m, was selected for the optimization. The initial conditions and the boundaries of the optimization variables are respectively presented in Table 1 and Table 2. Table 3 shows the main genetic algorithm parameters for the optimization in TRANSIT and in SCARAB. Notice that the lower level of detail of the object-oriented code consented to perform an extensive number of simulations in a reasonable time, while the generation and population numbers for the SCARAB optimizations are more limited due to time constraints. The material properties used in both re-entry software were taken from ESA's ESTIMATE database [21]. No demise is predicted for the random tumbling cases without the additional enthalpy released by the thermite. In the SCARAB case in which the dynamic module was activated, the demise of around the 20% of the stating mass is registered for the case without thermite. The fitness function used for the optimization is shown in Eq. 2, where f is the fitness, m_f and m_{sp} are respectively the final and the initial mass of the spacecraft, and m_{th} is the thermite charge mass.

$$f = \frac{1}{m_f + \frac{m_{th}}{m_{sp}} + 0.0000001} \quad (2)$$

Table 1: Initial conditions of the test cases.

Variable	Value
Longitude [°]	0
Latitude [°]	0
Altitude [km]	120
Velocity [m/s]	7273
Flight path angle [°]	-2.612
Heading angle [°]	42.35
Temperature [K]	300

Table 2: Optimization variables and boundaries for the genetic algorithm. Notice that the melting temperature T_{melt} of the material of the test case is used as the upper boundary for the ignition temperature.

Optimization variables	Interval
Profile [-]	[1,5]
Burning time [s]	[1,100]
Thermite density [kg/m ³]	[781,1095]
Filling factor [-]	[0.1,1]
Ignition temperature [K]	[573, T_{melt}]

Table 3: Main genetic algorithm parameters used for the optimization processes in TRANSIT and in SCARAB.

Genetic algorithm parameters	Value, TRANSIT	Value, SCARAB
Number of generations	100	20
Population per generation	50	12
Number of parents mating	15	4

Results

Table 4 shows the results obtained for the genetic algorithm optimization in TRANSIT and SCARAB. Complete demise was reached in all cases, therefore the fitness function value is the

ratio between the starting spacecraft mass and the thermite charge one. It can be seen how its value is rather similar between all the simulations, around the 20-25% of the initial sphere mass. The optimization performed in TRANSIT appears as the worst case, implying the highest pyrotechnic charge mass. In the object-oriented code the best case is represented by a brief Gaussian heat release, while in the spacecraft-oriented one the best result is given by a centred triangle profile, for both the analysed conditions. In the one performed with SCARAB considering the dynamics of the sphere as computed by the dynamic module a rather long duration is preferred. This could be due to the lower impact of the burning time in SCARAB numerical model. Notice that these profiles inherently imply a delay between the ignition time and the maximum thermite heat release equal to the half of the burning time. Moreover, it must be considered that both the cases in random tumbling condition foresee a maximum temperature in case of failed ignition around 700 K. On the contrary, the third case already experiences partial demise without the thermite action. This behaviour explicates why a significant difference in the best ignition temperature can be observed between the random tumbling cases and the one in which the dynamic module of SCARAB is activated. Summarizing, all the optimized results show a release of additional enthalpy that is concentrated on the last phase of the re-entry, when the aerodynamic heat is more pronounced. This behaviour suggests that a late ignition is beneficial.

Table 4: Results of the genetic algorithm optimization for TRANSIT and SCARAB.

Variable	Variable value, TRANSIT (random tumbling)	Variable value, SCARAB (random tumbling)	Variable value, SCARAB (dynamic module)
Profile [-]	Gaussian	Centred Triangle	Centred Triangle
Burning time [s]	10.16	20.34	83.18
Thermite density [kg/m ³]	861.10	784.70	781.25
Filling factor [-]	0.16	0.14	0.16
Ignition temperature [K]	639.44	650.11	767.66
Fitness [-]	4.11	5.17	4.51

Conclusions

A genetic algorithm was applied on an object- and on a spacecraft-oriented code for a simple geometry, aiming at quantifying the best thermite properties for a T4D application, in terms of burning time, temperature of ignition and heat release profile. For the selected application, full demise was obtained in all cases. The methodology hereby presented could be applied to an arbitrary re-entry application. The TRANSIT result was more conservative than the ones achieved with SCARAB. It is suggested that this behaviour is due to the variation of shape that is considered in SCARAB once the geometry has started the demise process. This could imply that an object-oriented code could be a proper tool for a first sizing of the pyrotechnic charge, later to be verified and further optimized using a more detailed software. An extension of the presented study to other geometries and materials could strengthen this insight.

References

- [1] AA. VV., ESA's Annual Space Environment Report. Issue 6. European Space Agency Space Debris Office. Darmstadt, Germany. (2023).
- [2] AA. VV., IADC Report on the Status of the Space Debris Environment. Issue 1, Revision 0. Inter-Agency Space Debris Coordination Committee. (2023).
- [3] AA. VV., IADC Space Debris Mitigation Guidelines. Revision 2. Inter-Agency Space Debris Coordination Committee. (2020).
- [4] AA. VV., Tri-Agency Reliability Engineering Guidance: Post Mission Disposal and Extension Assessment. ESA-TECQQD-TN-025375 / CAA-2021025 / NASA/SP-20210024973. ESA, JAXA, and NASA. (2022).
- [5] AA.VV., Final Report - Upgrade of DRAMA's Spacecraft Entry Survival Analysis Codes. Contract No. 4000115057/15/D/SR. Issue 3, Revision 1.0.2. Hyperschall Technologie Göttingen GmbH. (2019).
- [6] Koppenwallner, G., B. Fritsche, T. Lips and H. Klinkrad, SCARAB - A multi-disciplinary code for destruction analysis of space-craft during re-entry. In: 5th European Symposium on Aerothermodynamics for Space Vehicles. Cologne, Germany. (2005).
- [7] Fischer, S.H. and N.C. Grubelich, Theoretical Energy Release of Thermites, Intermetallics, and Combustible Metals. 24th International Pyrotechnics Seminar. Monterey, CA. (1998). <https://doi.org/10.2172/658208>
- [8] Finazzi, A., F. Maggi, L. Galfetti, C. Paravan, S. Dossi, A. Murgia, T. Lips, G. Smet, Thermite-for-Demise (T4D): Material selection for exothermic reaction-aided spacecraft demise during re-entry. In : 2nd International Conference on Flight Vehicles, Aerothermodynamics and Re-entry Missions & Engineering (FAR). Heilbronn, Germany. (2022).
- [9] Dihlan, D., and P. Omaly, Élement de véhicule spatial a capacité d'autodestruction améliorée et procédure de fabrication d'un tel élément. Patent FR 2975080B1. (2011).
- [10] Seiler, R., and G. Smet, Exothermic reaction aided spacecraft demise during re-entry. Patent EP 3604143A1. (2018).
- [11] Monogarov, K.A., A.N. Pivkina, L.I. Grishin, Yu.V. Frolov and D. Dilhan, Uncontrolled re-entry of satellite parts after finishing their mission in LEO: Titanium alloy degradation by thermite reaction energy. *Acta Astronautica*. 135:69-75. (2017). <https://doi.org/10.1016/j.actaastro.2016.10.031>
- [12] Schleutker, T., A. Gülhan., B. Esser, and T. Lips., ERASD – Exothermic Reaction Aided Spacecraft Demise – Proof of Concept Testing. Test Report. DLR, Supersonic and Hypersonic Technologies Department. (2019).
- [13] Maggi, F., A. Finazzi, P. Finocchi, C. Paravan, L. Galfetti, S. Dossi, A. Murgia, T. Lips, G. Smet, K. Bodjona, Thermite-for-Demise: Preliminary on-Ground Heat Transfer Experimental Testing. In: AIAA SCITECH 2023 Forum. National Harbor, MD & Online. (2023). <https://doi.org/10.2514/6.2023-1778>
- [14] J.M. Picone, A.E. Hedin, D.P. Drob and A.C. Aikin, NRL-MSISE-00 Empirical Model of the Atmosphere: Statistical Comparisons and Scientific Issues, *J. Geophys. Res.*, Vol. 107, Issue A12, SIA 15-1:15-16. (2003). <https://doi.org/10.1029/2002JA009430>
- [15] A. Tewari, *Atmospheric and Space Flight Dynamics - Modeling and Simulation with MATLAB and Simulink*, Birkhäuser, Boston. (2007).

- [16] M. Trisolini, Space System Design for Demise and Survival, PhD Thesis, University of Southampton, Faculty of Engineering and the Environment, Department of Astronautics. (2018).
- [17] R.D. Klett, Drag coefficients and heating ratios for right circular cylinders in free-molecular and continuum flow from Mach 10 to 30, Report SC-RR-64-2141, Sandia Laboratory, Albuquerque. (1964). <https://doi.org/10.2172/4630398>
- [18] J.A. Fay and F.R. Riddell, Theory of stagnation point heat transfer in dissociated air, Journal of the Aerospace Sciences, Vol. 25, No.2, 73:85. (1958). <https://doi.org/10.2514/8.7517>
- [19] J.D. Anderson Jr, Hypersonic and high temperature gas dynamics, American Institute of Aeronautic and Astronautics, 2nd edition, Reston, Virginia, USA. (2006). <https://doi.org/10.2514/4.861956>
- [20] A.F. Gad, PyGAD: An Intuitive Genetic Algorithm Python Library, arXiv 2106.06158. (2021).
- [21] Anon., European Space maTerIal deMisability dATabase [Online], European Space Agency. <https://estimate.sdo.esoc.esa.int/> . Last access: 10/06/2023.

Numerical and experimental assessment of a linear aerospike

Emanuele Resta^{1,a,*}, Gaetano Maria Di Cicca^{1,b}, Michele Ferlauto^{1,c} and
Roberto Marsilio^{1,d}

¹DIMEAS, Politecnico di Torino, Corso Duca degli Abruzzi 24, Turin, Italy

^aemanuele.resta@polito.it, ^bgaetano.dicicca@polito.it, ^cmichele.ferlauto@polito.it,

^droberto.marsilio@polito.it

Keywords: Aerospike, Nozzle, Experimental, Numerical

Abstract. In the present work a linear aerospike nozzle model has been studied with cold flow experiments in various working conditions. A series of numerical 3D RANS simulations have been performed in order to directly compare numerical and experimental results. Mean pressure distributions have been measured on the nozzle model symmetry plane, in order to characterize the flow evolution along the walls of the plug. The presented results show a good agreement between numerical and experimental results.

Introduction

Key requirements of future space transportation systems are a drastic reduction of launch costs and an increased reliability. Single-Stage-to-Orbit (SSTO) and Two-Stage-to-Orbit (TSTO) configurations are being studied as possible architectures of future launchers. However, the performance of the rocket engines heavily influences the possibility of realization of these vehicles. The performances of existing rocket engines are always lower than the theoretical values because of the presence of several loss mechanisms. Some examples are: the imperfect mixing of oxidizer and fuel in the combustion chamber, losses due to the process of combustion, losses for divergence and non-uniformity of the exiting flow and a non-ideal expansion of the propellants [1]. The latter source of losses is the most important. In fact, as was for the Space Shuttle Main Engine (SSME), the non-adaptation of the exhaust gases can cause up to 15% decrease in performance during certain phases of the mission [2].

A possible solution for the design of the engine of SSTO vehicles may be found in aerospike nozzles (also called plug nozzles), which represent a valid alternative to conventional bell nozzles. In fact, aerospike nozzles provide, at least theoretically, continuous altitude adaptation up to their geometrical area ratio. For high area ratio nozzles with relatively short length, plug nozzles perform better than conventional bell nozzles [2,3]. For these reasons, experimental, analytical and numerical research on plug nozzles have been performed since the 50s worldwide. One notable example of an aerospike engine project and prototype is the linear aerospike engine XRS-2200, which was selected as candidate propulsion system for the Venture Star/X33 SSTO spaceplane in the 1990s. Moreover, the use of linear aerospike nozzles has also started to spark interest regarding the propulsion of high-speed aircraft [4]. Nozzle flow control, including thrust vectoring and external flow interactions, has become increasingly relevant for the controllability of aircrafts. Fluidic thrust vectoring techniques in particular, are gaining significant interest for their advantages over traditional methods, both for use with conventional and unconventional nozzles [5,6]. One example is, for instance, differential throttling, a simple control strategy which can be applied in clustered aerospike engines with multiple independent combustion chambers. Since the mass flow rate and the pressure can be controlled independently, it is possible to generate an asymmetry in thrust, creating a lateral force component [7]. Another possible solution could be the Shock Vector Control approach, which consists in injecting a secondary flow from the plug wall. This causes the flow to separate, generating a recirculation zone on the wall and a shock wave that



deflects the incoming flow. As a result, the pressure distribution on the nozzle walls becomes asymmetric, generating a lateral thrust component [8].

The aim of the study is to compare the pressure measurements obtained with an experimental setup, which was previously designed at Politecnico di Torino [9,10], with numerical simulation results. This experimental system will be able to be fitted with different types of nozzle geometries. The mean pressure is measured along the nozzle walls on the symmetry plane, and is compared with 3D numerical results for analogous working conditions.

Test Rig Set-Up and Instrumentation

The test-rig is composed of two subsystems: the air-supply control system and the nozzle model. The first subsystem provides the prescribed inlet flow conditions and is able to manage interchangeable nozzle models, both axisymmetric and linear, for example bell/dual-bell nozzles, and aerospikes. An interfacing duct may be required to generate the correct inlet flow conditions in the axisymmetric or 2D/3D case. The test rig is positioned on a frame, as shown in Figure 1. A corrugated metal hose with an inner diameter of 25 mm is used to provide compressed air to the system. It is connected to a diffuser, followed by a flow straightener.

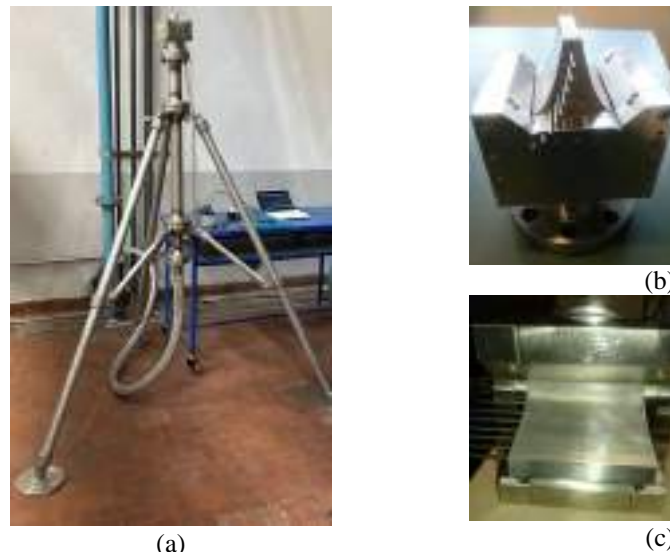


Fig. 1: Assembled Test-Rig (a). Two close-up views of the plug nozzle model (b-c)

For this work, a linear plug nozzle model was used, with a width to height throat ratio b/h_t equal to 30.41. The model is connected to the flange at the exit of the downstream duct. The exit Mach number M_e is equal to 1 and the design Nozzle Pressure Ratio NPR_d is equal to 200. Additional details on the dimensions of the nozzle plug are available in a previous paper [9].

The splines describing the plug surfaces of the nozzle have been designed using the method proposed by Angelino [11], with a tilt angle ϑ equal to 68.1° at the throat. The aerospoke plug geometry is truncated at 40% of the ideal length.

Mean pressure distributions are measured along the nozzle plug using a Scanivalve® DSA5000 pressure scanner. This device is capable of taking up to 16 individual pressure measurements at different locations along the plug, with the use of 16 temperature compensated piezo-resistive pressure transducers. Moreover, individual 24-bit A/D converters are included for each pressure sensor. This feature allows fully synchronous data collection and data stream up to 5000Hz (samples/channel/second). One resistance temperature detector (RTD) per pressure sensor is integrated in the unit and each RTD utilizes its own 24-bit A/D converter. The system accuracy is $\pm 0.04\%$ FS for a pressure range from 0 up to 250 psi (from 0 up to 17.2 bar).

The static wall pressures are measured thanks to the orifices (with a diameter equal to 0.6 mm) drilled perpendicularly into the nozzle plug wall (see Figure 1-a). The distance between two adjacent pressure ports is equal to 7 mm. These ports are connected through small steel tubes and Teflon tubes to the Scanivalve® pressure scanner.

Numerical and Experimental Results

Numerical simulations have been performed for the same values of Nozzle Pressure Ratio (NPR) used in the experiments. The commercial solver Star-CCM+ has been utilized to perform the steady RANS simulations. The numerical scheme is second order accurate in space and first order accurate in pseudo-time. A grid of about 1.2 million cells has been utilized for these simulations.

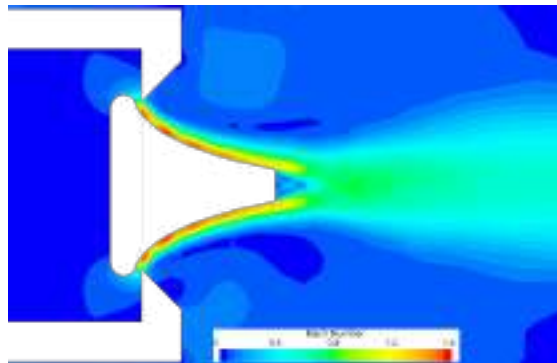


Fig. 2: Mach contour result of the flowfield in the symmetry plane of the nozzle

The Mach contour results from the numerical simulations are shown for the symmetry plane in Figure 2. The structure of the expanding flow is consistent with results from the literature regarding overexpanded flows in aerospike nozzles [2]. The presence of regions of compression and expansion can be clearly seen in this figure. A zone of recirculation on the base of the plug is also visible. In this region pressure is higher than on the walls or in the plume and that gives a positive contribution to thrust. Figure 3 shows a comparison in terms of wall static pressure between the measurements in the present experiment runs and the numerical results from the simulations. The measurements were performed for different NPRs, with the nozzle working in over-expanded conditions. The waviness of the pressure distributions highlights the presence of compression and expansion waves in the region close to the plug surface. The pressure distribution for NPR equal to 3 and 3.7 perfectly match the experimental data. What's more, there are some small differences between the numerical and experimental data for the remaining values of NPR. This could be due to numerical error of the simulation or imperfections in the manufacturing of the physical nozzle model. However, the results still match remarkably.

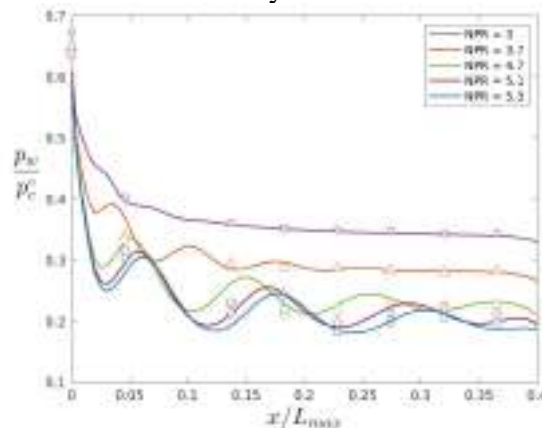


Fig. 3: Comparison between experimental and numerical wall mean pressure distributions.

Conclusions

An aerospike nozzle model has been tested experimentally to characterize the flow evolution along the walls of the plug. The experiments have been carried out in cold flow conditions at different values of NPR. The experimental results have been compared with 3D numerical simulation results, and are presented in terms of wall mean pressure distributions, and a very good agreement has been found.

References

- [1] D. Manski, G. Hagemann, "Influence of rocket design parameters on engine nozzle efficiencies", AIAA 30th Joint Prop. Conference, 1994. <https://doi.org/10.2514/6.1994-2756>
- [2] G. Hagemann, H. Immich, T. V. Nguyen, and G. E. Dumnov, "Advanced rocket nozzles," *Journal of Propulsion and Power*, vol. 14, no. 5, pp. 620–634, 1998. <https://doi.org/10.2514/2.5354>
- [3] R. C. Parsley, K. J. van Stelle, "Altitude Compensating Nozzle Evaluation", AIAA Paper 92-3456, Jul. 1992. <https://doi.org/10.2514/6.1992-3456>
- [4] T. Tomita, H. Tamura, and M. Takahashi, "An experimental evaluation of plug nozzle flow field," in 32nd AIAA Joint Prop. Conference, 1996. <https://doi.org/10.2514/6.1996-2632>
- [5] M. Ferlauto, R. Marsilio "Influence of the External Flow Conditions to the Jet-Vectoring Performances of a SVC Nozzle", AIAA Joint Prop. Conference, Indianapolis, IN, 2019. <https://doi.org/10.2514/6.2019-4343>
- [6] S. Eilers, M. Wilson, S. Whitmore, and Z. Peterson, "Side-force amplification on aerodynamically thrust-vectorred aerospike nozzle," *Journal of Propulsion and Power*, 2012. <https://doi.org/10.2514/6.2011-5531>
- [7] M. Ferlauto, A. Ferrero, M. Marsicovetere, and R. Marsilio, "A comparison of different technologies for thrust vectoring in a linear aerospike", ECCOMAS WCCM 2020, Paris, 2021. <https://doi.org/10.23967/wccm-eccomas.2020.006>
- [8] E Resta, R Marsilio, M Ferlauto "Thrust Vectoring of a Fixed Axisymmetric Supersonic Nozzle Using the Shock-Vector Control Method", *Fluids*. 6(12):441, 2021. <https://doi.org/10.3390/fluids6120441>
- [9] V. Bonnet, F. Ortone, G. M. Di Cicca, R. Marsilio, and M. Ferlauto, "Cold gas measurement system for linear aerospike nozzles," *IEEE Metrology for Aerospace* 2022, Pisa, Italy, 2022. <https://doi.org/10.1109/MetroAeroSpace54187.2022.9855979>
- [10] G. M. Di Cicca, J. Hassan, E. Resta, R. Marsilio, M. Ferlauto, "Experimental Characterization of a Linear Aerospike Nozzle Flow", *IEEE Metrology for Aerospace* 2023, Milan, Italy, 2023. <https://doi.org/10.1109/MetroAeroSpace57412.2023.10189981>
- [11] G. Angelino, "Approximate method for plug nozzle design", *AIAA Journal*, vol. 2, no. 10, pp. 1834–1835, 1964. <https://doi.org/10.2514/3.2682>

Numerical suite for the design, simulation and optimization of cathode-less plasma thrusters

Nabil Souhair^{1,2,a*}, Mirko Magarotto^{3,b}, Raoul Andriulli^{1,c}, Fabrizio Ponti^{1,d},

¹ Alma Propulsion Laboratory, Department of Industrial Engineering, University of Bologna, Forlì, 47122, Italy

² LERMA Laboratory, Aerospace and Automotive Engineering School, International University of Rabat, Sala al Jadida, Rabat, 11100, Morocco

³ Department of Electric Engineering, University of Padova, Padova, 35131, Italy

^anabil.souhair2@unibo.it, ^bmirko.magarotto@unipd.it, ^craoul.andriulli@unibo.it, ^dfabrizio.ponti@unibo.it

Keywords: Space Propulsion, Electric Propulsion, Cathode-Less Plasma Thrusters, Plasma Thrusters, Numerical Simulations, Global Plasma Models, Multi Fluid Approach, Particle-In-Cell

Abstract. A numerical suite developed for the analysis and design of cathodeless plasma thrusters is presented. The suite includes a Global Model that estimates the thruster's propulsive performance by means of a balance of electron energy and population density, and a 3D numerical strategy to assess plasma behavior. The suite incorporates a FLUID and EM modules to solve plasma transport and electromagnetic wave propagation within the discharge chamber. The PLUME module, managed by the Starfish code, handles plasma dynamics in the magnetic nozzle using the electrostatic particle-in-cell approach. The suite has been validated against thrust measurements from a Helicon Plasma Thruster demonstrating the suite's potential for optimizing the design and operation of cathodeless plasma thrusters for space propulsion applications.

1 Introduction

In the last decade, an active research has been conducted on the electric propulsion field [1,2]. Particular effort has been put in the development of cathodeless systems such as Helicon Plasma Thrusters (HPT) [3,4] and Electron Cyclotron Resonance Thrusters (ECRT) [5]. In these devices, plasma is produced within a dielectric tube where the neutral gas propellant is injected. An antenna, operated in the Radio Frequency (RF) or in the microwave frequency range, sustains the discharge coupling Electromagnetic (EM) power to the plasma [6]. Magnets produce a magnetostatic field that has three main functions: (i) increasing the efficiency of the source by enhancing the plasma confinement [7], (ii) driving the power coupling between the antenna and the plasma [8], (iii) improving the propulsive performance via the magnetic nozzle effect downstream the thruster outlet [9-12].

The key physical phenomena that govern the plasma dynamics in the production stage, with reference to Figure 1, are the EM wave propagation [13], the plasma transport [14], and their mutual coupling [15]. Instead, the acceleration and detachment phenomena [16] take place

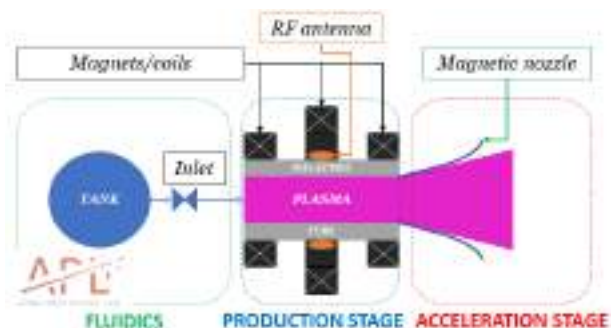


Figure 1. Schematic of a cathodeless plasma thruster. Magnetic field lines highlighted within the plasma source.

downstream the plasma source in the region identified as acceleration stage (see Figure 1). The latter is characterized by the formation of a plume where the plasma is more rarefied (density in the range $10^{16} - 10^{18} \text{ m}^{-3}$) than in the production stage [17]. Particle collisions and the geometry of the applied magnetostatic field govern the plasma behaviour in the region closer to the thruster [18]. Further downstream, the plasma expansion is driven by the thermal pressure, and the ambipolar diffusion [18]. Several analytical [19-21] and numerical approaches have been pursued in the literature for modelling both the production stage and the acceleration stage. The most relevant are: fluid [22], kinetic [23], Particle In Cell with Monte Carlo collisions (PIC-MCCs) [24], and hybrid [25].

In this work, a numerical suite for cathodeless plasma thrusters is presented and its exploitation in a low power case is discussed. A Global Model is devoted to the preliminary estimation of the propulsive performance [26]. More advanced tools have been developed to predict the plasma dynamics throughout the thruster. The 3D-VIRTUS code solves, with a fluid approach, the plasma transport within the production stage. The PIC tools Starfish [27] and have been customized to simulate the plasma dynamics within the magnetic nozzle. Starfish, which handles 2D axisymmetric domains, has been coupled to 3D-VIRTUS in order to estimate the propulsive performance.

II Methodology

II.A Global Model

The main assumptions associated to the Global Model [26] are: (i) cylindrical geometry of the plasma source, (ii) axisymmetric magnetostatic field, (iii) the presence of cusps in the source can be simulated, (iv) the paraxial approximation holds in the acceleration stage [19], (v) in the acceleration stage plasma is frozen to the field lines up to the detachment. The dynamics of the source is solved relying on the conservation of mass (Eq.1) and electron energy (Eq.2) equations

$$\frac{dn_I}{dt} = R_{chem}^I - R_{wall}^I - R_{ex}^I + R_{in}^I \quad (1)$$

$$\frac{d}{dt} \left(\frac{3}{2} n_e T_e \right) = P_w - P_{chem} - P_{wall} - P_{ex} \quad (2)$$

n_I is the number density of the I-th species, being this study focused on a xenon plasma $I=e, i, *, g$ for electrons, ions (Xe^+), excited (Xe^*), and ground state (Xe) particles respectively. T_e is the electron temperature in eV. $R_{chem}^I, R_{wall}^I, R_{ex}^I, R_{in}^I$, are the I-th particle source/sink terms associated to plasma reactions, wall losses, particles outflow and inflow respectively. $P_w, P_{chem}, P_{wall}, P_{ex}$ are the power coupled to the plasma, along with the source/sink terms associated to plasma reactions, wall losses, and particles outflow respectively. The plasma reactions considered are elastic scattering, ionization and excitation (see Table 1), therefore the R_{chem}^I and P_{chem} terms read [29]

$$R_{chem}^I = \sum_J K_{JI} n_J n_e - \sum_J K_{IJ} n_I n_e \quad (3)$$

$$P_{chem} = \sum_I \sum_J K_{IJ} n_I n_e \Delta U_{IJ} + \sum_I K_{II} n_I n_e \frac{3m_e}{m_I} T_e \quad (4)$$

Where K_{IJ} is the rate constant for the inelastic transitions from species I to species J, K_{II} is the rate constant for elastic collisions between species I and electrons, ΔU_{IJ} is the energy difference (in eV) between species I and species J, along with m_e and m_I are the electron mass and I species

mass respectively [30]. Assuming the Bohm sheath criterion at the source walls [26] and a sonic thruster outlet, similar expressions hold for R_{wall}^I and R_{ex}^I

$$R_{wall}^I = \frac{S_{wall}^I}{V} \Gamma_{wall}^I \quad (5a)$$

$$R_{ex}^I = \frac{S_{ex}^I}{V} \Gamma_{ex}^I \quad (5b)$$

Where V is the volume of the source, S^I is the equivalent surface of the source, and Γ^I is the particles flux. For ions and electrons $S^e = S^i$ and its expression, which accounts for the non-uniformity of the plasma within the source, can be found in [30]. Similarly $\Gamma^e = \Gamma^i = n_e u_B$ where u_B is the Bohm speed [31]. For neutrals $R_{wall}^g = -R_{wall}^e$ assuming total recombination at the walls [26]. Instead S_{ex}^g is equal to the physical thruster outlet surface and, assuming the neutrals are in the molecular regime, $\Gamma^g = 1/4 n_g u_{th}$ [26]; u_{th} is the neutrals thermal speed [31]. From the Bohm sheath criterion, the energy terms read [26]

$$P_{wall} = R_{wall}^e \left(2 + \log \sqrt{\frac{m_i}{2\pi m_e}} \right) T_e \quad (6a)$$

$$P_{ex} = R_{ex}^e \left(2 + \log \sqrt{\frac{m_i}{2\pi m_e}} \right) T_e \quad (6b)$$

Regarding the gas inflow, only neutral species are assumed to be injected into the source

$$R_{in}^g = \frac{\dot{m}_0}{V m_g} \quad (7)$$

where \dot{m}_0 is the mass flow rate.

Table 1: plasma reactions considered.

Reaction	Formula	Reference
Elastic scattering	$e + Xe \rightarrow e + Xe$	[29]
Ionization	$e + Xe \rightarrow 2e + Xe^+$	[29]
Excitation	$e + Xe \rightarrow e + Xe^* \rightarrow e + Xe + h\nu$	[29]

The thrust is computed according to the model presented in [19]. The contribution from the plasma is

$$F_p = \frac{M_{det}^2 + 1}{M_{det}} q n_e T_e S_{ex}^e \quad (8)$$

where q is the elementary charge, and M_{det} is the magnetic Mach number (v/u_B) at the detachment point. M_{det} is computed according to the detachment criterion prescribed in [19]. The contribution to the thrust due to neutral gas expansion is

$$F_g = p_g S^g_{ex} \quad (9)$$

where p_g is the neutral pressure. Total thrust and specific impulse, being g_0 the standard gravity, read

$$F = F_p + F_g \quad (10a)$$

$$I_{sp} = \frac{F}{g_0 \dot{m}_0} \quad (10b)$$

II.B Source Solver

The plasma source is handled with the 3D-VIRTUS code [15]. Plasma transport and EM wave propagation are solved self-consistently by means of two distinct modules, namely the Fluid module and the EM module, run iteratively. In the former, the plasma transport is solved in a 2D domain while the latter relies on a 3D domain [13]. The governing equations of the fluid module are continuity, energy and Poisson

$$\frac{\partial n_I}{\partial t} + \nabla \cdot \mathbf{\Gamma}_I = R^I_{chem} \quad (11a)$$

$$\frac{\partial n_\varepsilon}{\partial t} + \nabla \cdot \mathbf{\Gamma}_\varepsilon - \nabla \varphi \cdot \mathbf{\Gamma}_e = P_W - P_{chem} \quad (11b)$$

$$\nabla^2 \varphi = -q \left(\frac{n_i - n_e}{\varepsilon_0} \right) \quad (11c)$$

The species considered are electrons, ions (Xe^+) and neutrals (Xe). Where $n_\varepsilon = 3/2 n_e T_e$ is the energy density, φ is the plasma potential and ε_0 is the permittivity of vacuum. Formally, the terms R^I_{chem} and P_{chem} are reported in Eq.3 and Eq.4, but in 3D-VIRTUS they are scalar fields which depend on the position. Reactions considered are listed in Table 1. $\mathbf{\Gamma}_I$ is the particle flux of the species I that, according to the drift diffusion approximation, reads

$$\mathbf{\Gamma}_I = \pm \bar{\mu}_I n_I \nabla \varphi - \bar{D}_I \nabla n_I + \mathbf{u}_0 n_I \quad (12)$$

Where μ_I and D_I are the mobility and the diffusion coefficients of the species I whose values are prescribed in [32]. \mathbf{u}_0 is the convection speed assumed aligned with the thruster axis and equal, in modulus, to $1/4 v_{th}$ [7]. $\mathbf{\Gamma}_\varepsilon$ is the energy flux that reads

$$\mathbf{\Gamma}_\varepsilon = \bar{\mu}_\varepsilon n_\varepsilon \nabla \varphi - \bar{D}_\varepsilon \nabla n_\varepsilon + \mathbf{u}_0 n_\varepsilon \quad (13)$$

Where μ_ε and D_ε are derived according to the Einstein relations [15]. The power deposition profile is computed via the EM module and it reads [15]

$$P_W = \frac{1}{2q} \text{Re}(\mathbf{J}_{RF}^* \cdot \mathbf{E}_{RF}) \quad (14)$$

Where \mathbf{J}_{RF} and \mathbf{E}_{RF} are the complex values of the current density and electric field induced by the RF antenna onto the plasma.

A Robin type boundary condition is imposed to the electrons continuity and energy to enforce the Bohm sheath criterion [15]. A zero gradient Neumann type condition is imposed to the continuity of ions. At the walls, a Neumann condition is imposed to the continuity of the neutrals

in order to enforce the recombination of the charged species [15]. At the thruster outlet, the neutral density gradient is assumed null [7]. Finally, a Neumann type boundary condition is imposed to Poisson's equation to enforce the equality between ions and electrons fluxes at the walls [26]. The thruster outlet is grounded [15].

II.C Plume Solver

The plasma in the plume has been simulated with a fully kinetic Particle In Cell (PIC) solver, namely Starfish [27-28]. This handles axisymmetric domains even though the particles' speed is solved in 3D. Starfish has been coupled to 3D-VIRTUS in order to solve the plasma dynamics in the overall thruster and, in turn, to estimate the propulsive performance. The plasma in the acceleration stage is assumed collisionless [33], nonetheless the dynamics of both neutral (Xe) and charged species, namely electrons and ions (Xe⁺), are tracked. Particles' speed is solved from the discrete equation of motion

$$\frac{\mathbf{v}^{t+\frac{1}{2}} - \mathbf{v}^{t-\frac{1}{2}}}{\Delta t} = \frac{q_I}{m_I} \left(\mathbf{E}^t + \frac{\mathbf{v}^{t+\frac{1}{2}} + \mathbf{v}^{t-\frac{1}{2}}}{2} \times \mathbf{B}^t \right) \quad (15a)$$

$$\frac{\mathbf{r}^{t+1} - \mathbf{r}^t}{\Delta t} = \mathbf{v}^{t+\frac{1}{2}} \quad (15b)$$

Where \mathbf{r}^t is the particle position at time step t , \mathbf{v} is the particle speed, Δt is the time step, \mathbf{E} is the electric field and \mathbf{B} the magnetic field. A Boris scheme is used to advance particles [34]. Since the RF power deposition in the acceleration stage is assumed negligible [35] the EM fields in the plasma are calculated via the Poisson's equation. Therefore, \mathbf{B} consists in the background magnetostatic field and $\mathbf{E} = -\nabla\phi$ where

$$\varepsilon_0 \nabla^2 \phi = -\rho \quad (16)$$

and ρ is the charge density computed from particles position via a linear deposition scheme [33].

Regarding boundary conditions, Eq.17 holds for the Poisson's equation

$$\phi = 0 \quad \text{Thruster outlet} \quad (17a)$$

$$\phi = \phi_\infty \quad \text{Thruster case} \quad (17b)$$

$$\frac{d\phi}{dk} + \frac{1}{r}(\phi - \phi_\infty) = 0 \quad \text{External boundary} \quad (17c)$$

Where k is the direction normal to the external boundary, r is the distance between the centre of the thruster and the boundary, along with ϕ_∞ is the potential at infinity. Eq.17c derives from the assumption that $\phi \approx 1/r$ for $r \rightarrow \infty$ [36]. Regarding particles dynamics, ions and electrons that reach the thruster outlet and the thruster case are removed from the simulation domain [35]. The same condition holds for the ions at the external boundary [35] where an energy-based condition is defined to account for the electrons "trapped" by the potential drop across the plume [37]. The total energy of each electron that reaches the external boundary is computed according to Eq.18

$$E_{tot} = \frac{1}{2} m_I v^2 - q_I \phi \quad (18)$$

If $|E_{tot}| > |q\varphi_\infty|$ the electron is absorbed since its energy is high enough to escape at the infinity. If $|E_{tot}| \leq |q\varphi_\infty|$ the particle is considered “trapped” and it is subject to a specular reflection. A control loop has been implemented in order to enforce the current free and the quasi-neutrality conditions at the thruster outlet. The value of the potential at infinity is updated according to Eq.19.

$$\varphi_\infty^{t+1} = \varphi_\infty^t + \frac{1}{C} (I_{iB}^t + I_{eB}^t) \Delta t \quad (19)$$

Where C is an equivalent capacitance used to tune φ_∞ so that the current free condition holds. The ion flux at the thruster outlet is assumed constant (Eq.20a) [35] instead the electron flux is varied according to Eq.20b to ensure quasi-neutrality

$$I_{i0} = \frac{q_i \dot{m}_0}{M} \quad (20a)$$

$$I_{e*}^{t+1} = K \frac{n_{i0}^t}{n_{e0}^t} I_{e*}^t \quad (20b)$$

K is a positive constant and I_{e*} is the emitted electron flux. It is worth noting that the total electron flux (I_{e0}) depends also on the number of electrons absorbed at the thruster outlet which is mainly driven by the value of φ_∞ [35]. As a consequence the control strategy implemented relates φ_∞ to the flux of particles injected into the domain and allows to compute self-consistently the total potential drop across the plume (namely $-\varphi_\infty$). Finally, the thrust is computed according the Eq.21 [25]

$$F = \int \sum_I (m_I n_I v_{Iz} \mathbf{v}_z \cdot \hat{\mathbf{k}} + p_I \hat{\mathbf{z}} \cdot \hat{\mathbf{k}}) dS_B \quad (21)$$

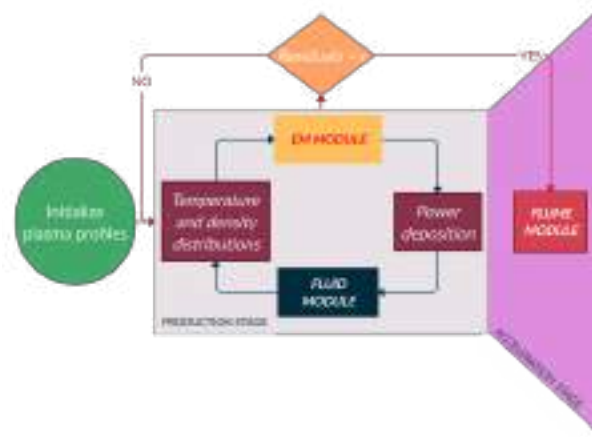


Figure 2. Schematic of the 2D thruster simulation tool. The Source solver (3D-VIRTUS) and the Plume solver (Starfish) run sequentially.

The coupling strategy between the production stage (i.e., 3D-VIRTUS) and the acceleration stage (i.e., Starfish) is schematically depicted in Figure 2. First, the source solver provides plasma profiles at the thruster outlet assuming a sonic condition for this boundary. Second the plume solver takes these profiles as an input and propagates the solution of the plasma expansion.

III Results

The thruster analysed in this work is a low power (50 W range) HPT. The plasma source is a cylinder whose dimensions are length $L=0.060$ m and diameter $D=0.014$ m. Magnetic field is generated by two rings of permanent magnets. At thruster outlet, the intensity of the magnetic field on the axis is $B_0=600$ G. The antenna is a five turns coil whose dimensions are length $L_A=0.020$ m, diameter $D_A=0.020$ m, wire width $w_A=0.002$ m. A mass flow rate of $\dot{m}_0=0.15$ mg/s has been assumed. The power provided to the antenna (P_W) varies in the range from 10 W up to 70 W. An antenna efficiency of $\eta_A=0.8$ has been assumed, so the power actually coupled to the plasma is $P_{Wp}=\eta_A P_W$.

A 2D simulation of the overall plasma thruster has been accomplished for an input power $P_W=55$ W. In Figure 3, the input power deposition profile adopted is shown, and is consistent with an inductive coupling mode [39,40].

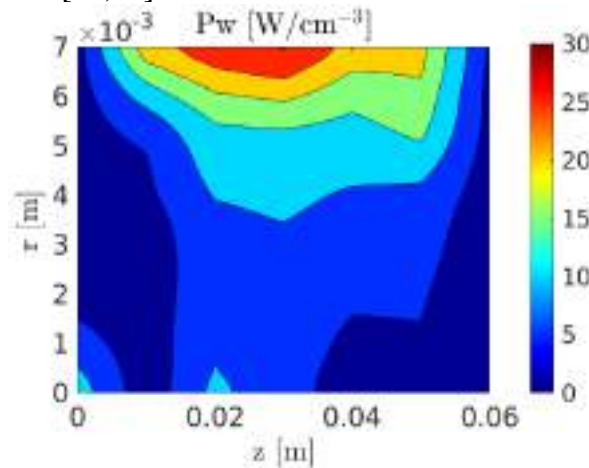


Figure 3. Deposited power map (P_w) function of the radial and axial positions (r - z) in the source.

The estimation of the propulsive performance obtained with both the GM and the 2D simulation of the HPT has been reported in Figure 4.

For what concerns the GM, due to the several assumptions considered, an uncertainty band of $\pm 20\%$ has been attributed to numerical results. The latter is mainly associated to the assumptions on plasma profiles (Eq.5) [26], interactions between the plasma and the walls of the source (Eq.6) [26], cross sections of the plasma reactions (Table 1) [26], and detachment criterion (Eq.8) [7]. The propulsive performance increases with the power coupled to the plasma. Trends predicted numerically and evaluated experimentally are in agreement. Moreover, numerical and experimental uncertainty bands overlap. This result can be considered sufficiently accurate for the scope of the GM which is meant for the preliminary characterization.

Regarding the 2D simulation, thrust has been computed coupling the solution of the production stage with both the semi-analytical formulation implemented in the Global Model (i.e., Eqs.8-10) and the results provided by Starfish (i.e., Eq.21). In both cases, the estimation of the propulsive performance matches better the experimental benchmark with respect to the Global Model. The most accurate result is provided coupling 3D-VIRTUS and Starfish being the difference between numerical and experimental results less than 20%.

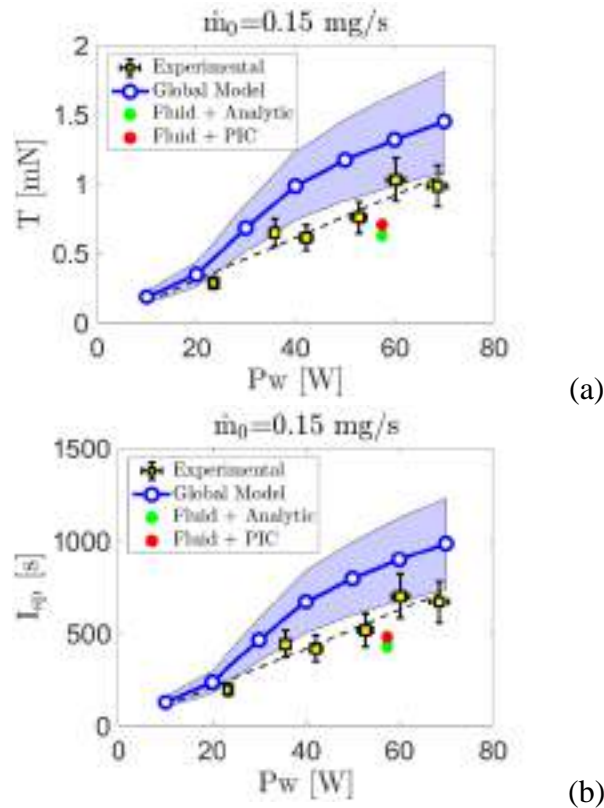


Figure 4. Performance predicted numerically compared against measures. (a) Thrust (T), and (b) specific impulse (I_{sp}) in function of the coupled power (P_w).

VI Conclusions

A numerical suite capable of simulating the propulsive performance and the plasma dynamics in a cathodeless plasma thruster is shown. It consists on a Global Model [26] for the preliminary simulation of the propulsive performance, the 3D-VIRTUS code [15] for the estimation of the plasma profile in the production stage, along with Starfish [27] for the solution of the acceleration stage. The results of the Global Model and of the coupling 3D-VIRTUS / Starfish have been benchmarked against measurements of the propulsive performance (i.e., thrust and specific impulse). The agreement between experiments and the Global Model is always better than 50%, whereas differences reduce to 20% with a multi-dimensional approach.

In future works the interfacing strategy between 3D-VIRTUS and Starfish will be improved adopting an iterative approach.

Finally, it is worth noting that the numerical suite presented in this work can simulate the plasma dynamics also in applications different from the electric propulsion as plasma antennas [43-47] and water treatment reactors [48].

References

- [1] S. Mazouffre (2016). Electric propulsion for satellites and spacecraft: established technologies and novel approaches. *Plasma Sources Science and Technology*, 25(3), 033002. <https://doi.org/10.1088/0963-0252/25/3/033002>
- [2] D. M. Goebel, I. Katz (2008). *Fundamentals of electric propulsion: ion and Hall thrusters* (Vol. 1). John Wiley & Sons. <https://doi.org/10.1002/9780470436448>
- [3] K. Takahashi (2019). Helicon-type radiofrequency plasma thrusters and magnetic plasma nozzles. *Reviews of Modern Plasma Physics*, 3(1), 1-61. <https://doi.org/10.1007/s41614-019-0024-2>

- [4] M. Manente, et al. (2019). REGULUS: A propulsion platform to boost small satellite missions. *Acta Astronautica*, 157, 241-249. <https://doi.org/10.1016/j.actaastro.2018.12.022>
- [5] F. Cannat, T. Lafleur, J. Jarrige, P. Chabert, P. Q. Elias, D. Packan (2015). Optimization of a coaxial electron cyclotron resonance plasma thruster with an analytical model. *Physics of Plasmas*, 22(5), 053503. <https://doi.org/10.1063/1.4920966>
- [6] D. Arnush, F. F. Chen (1998). Generalized theory of helicon waves. II. Excitation and absorption. *Physics of Plasmas*, 5(5), 1239-1254. <https://doi.org/10.1063/1.872782>
- [7] M. Magarotto, M. Manente, F. Trezzolani, D. Pavarin (2020). Numerical model of a helicon plasma thruster. *IEEE Transactions on Plasma Science*, 48(4), 835-844. <https://doi.org/10.1109/TPS.2020.2982541>
- [8] M. Magarotto, D. Melazzi, D. Pavarin (2019). Study on the influence of the magnetic field geometry on the power deposition in a helicon plasma source. *Journal of Plasma Physics*, 85(4). <https://doi.org/10.1017/S0022377819000473>
- [9] E. Ahedo, M. Merino (2010). Two-dimensional supersonic plasma acceleration in a magnetic nozzle. *Physics of Plasmas*, 17(7), 073501. <https://doi.org/10.1063/1.3442736>
- [10] N. Bellomo, et al. (2021). Design and In-orbit Demonstration of REGULUS, an Iodine electric propulsion system. *CEAS Space Journal*. <https://doi.org/10.1007/s12567-021-00374-4>
- [11] A. V. Arefiev, B. N. Breizman (2004). Theoretical components of the VASIMR plasma propulsion concept. *Physics of Plasmas*, 11(5), 2942-2949. <https://doi.org/10.1063/1.1666328>
- [12] K. Takahashi (2021). Magnetic nozzle radiofrequency plasma thruster approaching twenty percent thruster efficiency. *Scientific reports*, 11(1). <https://doi.org/10.1038/s41598-021-82471-2>
- [13] D. Melazzi, V. Lancellotti (2014). ADAMANT: A surface and volume integral-equation solver for the analysis and design of helicon plasma sources. *Computer Physics Communications*, 185(7), 1914-1925. <https://doi.org/10.1016/j.cpc.2014.03.019>
- [14] J. Zhou, D. Pérez-Grande, P. Fajardo, E. Ahedo (2019). Numerical treatment of a magnetized electron fluid model within an electromagnetic plasma thruster simulation code. *Plasma Sources Science and Technology*, 28(11), 115004. <https://doi.org/10.1088/1361-6595/ab4bd3>
- [15] M. Magarotto, D. Melazzi, D. Pavarin (2020). 3D-VIRTUS: Equilibrium condition solver of radio-frequency magnetized plasma discharges for space applications. *Computer Physics Communications*, 247, 106953. <https://doi.org/10.1016/j.cpc.2019.106953>
- [16] A. V. Arefiev, B. N. Breizman (2005). Magnetohydrodynamic scenario of plasma detachment in a magnetic nozzle. *Physics of Plasmas*, 12(4), 043504. <https://doi.org/10.1063/1.1875632>
- [17] G. Sánchez-Arriaga, J. Zhou, E. Ahedo, M. Martínez-Sánchez, J. J. Ramos (2018). Kinetic features and non-stationary electron trapping in paraxial magnetic nozzles. *Plasma Sources Science and Technology*, 27(3), 035002. <https://doi.org/10.1088/1361-6595/aaad7f>
- [18] F. Cichocki, A. Domínguez-Vázquez, M. Merino, E. Ahedo (2017). Hybrid 3D model for the interaction of plasma thruster plumes with nearby objects. *Plasma Sources Science and Technology*, 26(12), 125008. <https://doi.org/10.1088/1361-6595/aa986e>
- [19] T. Lafleur (2014). Helicon plasma thruster discharge model. *Physics of Plasmas*, 21(4), 043507. <https://doi.org/10.1063/1.4871727>

- [20] E. Ahedo, & J. Navarro-Cavallé (2013). Helicon thruster plasma modeling: Two-dimensional fluid-dynamics and propulsive performances. *Physics of Plasmas*, 20(4), 043512. <https://doi.org/10.1063/1.4798409>
- [21] A. Fruchtman, K. Takahashi, C. Charles, R. W. Boswell (2012). A magnetic nozzle calculation of the force on a plasma. *Physics of Plasmas*, 19(3), 033507. <https://doi.org/10.1063/1.3691650>
- [22] M. Magarotto, D. Pavarin (2020). Parametric study of a cathode-less radio frequency thruster. *IEEE Transactions on Plasma Science*, 48(8), 2723-2735. <https://doi.org/10.1109/TPS.2020.3006257>
- [23] E. Ahedo, S. Correyero, J. Navarro-Cavallé, M. Merino (2020). Macroscopic and parametric study of a kinetic plasma expansion in a paraxial magnetic nozzle. *Plasma Sources Science and Technology*, 29(4), 045017. <https://doi.org/10.1088/1361-6595/ab7855>
- [24] M. Li, M. Merino, E. Ahedo, H. Tang (2019). On electron boundary conditions in PIC plasma thruster plume simulations. *Plasma Sources Science and Technology*, 28(3), 034004. <https://doi.org/10.1088/1361-6595/ab0949>
- [25] Á. Sánchez-Villar, J. Zhou, E. Ahedo, M. Merino (2021). Coupled plasma transport and electromagnetic wave simulation of an ECR thruster. *Plasma Sources Science and Technology*, 30(4), 045005. <https://doi.org/10.1088/1361-6595/abde20>
- [26] N. Souhair, M. Magarotto, E. Majorana, F. Ponti, D. Pavarin (2021). Development of a lumping methodology for the analysis of the excited states in plasma discharges operated with argon, neon, krypton and xenon. *Physics of Plasmas*, 28(9). <https://doi.org/10.1063/5.0057494>
- [27] L. Brieda, M. Keidar (2012). Development of the Starfish Plasma Simulation Code and Update on Multiscale Modeling of Hall Thrusters. 48th AIAA Joint Propulsion Conference, Atlanta, GA, AIAA-2012-4015. <https://doi.org/10.2514/6.2012-4015>
- [28] J. F. Roussel, et al. (2008). SPIS open-source code: Methods, capabilities, achievements, and prospects. *IEEE transactions on plasma science*, 36(5), 2360-2368. <https://doi.org/10.1109/TPS.2008.2002327>
- [29] P. Chabert, J. Arancibia Monreal, J. Bredin, L. Popelier, A. Aanesland (2012). Global model of a gridded-ion thruster powered by a radiofrequency inductive coil. *Physics of Plasmas*, 19(7), 073512. <https://doi.org/10.1063/1.4737114>
- [30] M. A. Lieberman, A. J. Lichtenberg (2005). *Principles of plasma discharges and materials processing*. John Wiley & Sons. <https://doi.org/10.1002/0471724254>
- [31] F. F. Chen (2012). *Introduction to plasma physics*. Springer Science & Business Media.
- [32] N. Souhair, M. Magarotto, M. Manante, D. Pavarin, F. Ponti (2021). Improvement of a numerical tool for the simulation of a Helicon plasma thruster. *Space propulsion 2020+1*, On line conference, SP2020-00070.
- [33] G. Gallina, M. Magarotto, M. Manente, D. Pavarin (2019). Enhanced biDimensional pIc: an electrostatic/magnetostatic particle-in-cell code for plasma based systems. *Journal of Plasma Physics*, 85(2), 905850205. <https://doi.org/10.1017/S0022377819000205>
- [34] H. Qin, S. Zhang, J. Xiao, J. Liu, Y. Sun, W. M. Tang (2013). Why is Boris algorithm so good?. *Physics of Plasmas*, 20(8), 084503. <https://doi.org/10.1063/1.4818428>

- [35] S. Di Fede, M. Magarotto, S. Andrews, D. Pavarin (2021). Simulation of the plume of a Magnetically Enhanced Plasma Thruster with SPIS. *Journal of Plasma Physics*.
<https://doi.org/10.1017/S0022377821001057>
- [36] D. J. Griffiths (2005). Introduction to electrodynamics. <https://doi.org/10.1016/B978-1-85573-953-6.50026-X>
- [37] M. Martinez-Sanchez, J. Navarro-Cavallé, E. Ahedo (2015). Electron cooling and finite potential drop in a magnetized plasma expansion. *Physics of Plasmas*, 22(5), 053501.
<https://doi.org/10.1063/1.4919627>
- [38] F. Trezzolani, M. Magarotto, M. Manente, D. Pavarin (2018). Development of a counterbalanced pendulum thrust stand for electric propulsion. *Measurement*, 122, 494-501.
<https://doi.org/10.1016/j.measurement.2018.02.011>
- [39] F. Romano, et al. (2020). RF helicon-based inductive plasma thruster (IPT) design for an atmosphere-breathing electric propulsion system (ABEP). *Acta Astronautica*, 176, 476-483.
<https://doi.org/10.1016/j.actaastro.2020.07.008>
- [40] A. R. Ellingboe, R. W. Boswell (1996). Capacitive, inductive and helicon-wave modes of operation of a helicon plasma source. *Physics of Plasmas*, 3(7), 2797-2804.
<https://doi.org/10.1063/1.871713>
- [41] A. E. Vinci, S. Mazouffre (2021). Direct experimental comparison of krypton and xenon discharge properties in the magnetic nozzle of a helicon plasma source. *Physics of Plasmas*, 28(3), 033504. <https://doi.org/10.1063/5.0037117>
- [42] P. Molmud (1960). Expansion of a rarefied gas cloud into a vacuum. *The Physics of fluids*, 3(3), 362-366. <https://doi.org/10.1063/1.1706042>
- [43] G. Mansutti, et al. (2020). Modeling and design of a plasma-based transmit-array with beam scanning capabilities. *Results in Physics*, 16, 102923. <https://doi.org/10.1016/j.rinp.2019.102923>
- [44] A. Daykin-Iliopoulos, et al. (2020). Characterisation of a thermionic plasma source apparatus for high-density gaseous plasma antenna applications. *Plasma Sources Science and Technology*, 29(11), 115002. <https://doi.org/10.1088/1361-6595/abb21a>
- [45] M. Magarotto, P. De Carlo, G. Mansutti, F. J. Bosi, N. E. Buris, A. D. Capobianco, D. Pavarin (2020). Numerical suite for gaseous plasma antennas Simulation. *IEEE Transactions on Plasma Science*, 49(1), 285-297. <https://doi.org/10.1109/TPS.2020.3040008>
- [46] P. De Carlo, M. Magarotto, G. Mansutti, A. Selmo, A. D. Capobianco, D. Pavarin (2021). Feasibility study of a novel class of plasma antennas for SatCom navigation systems. *Acta Astronautica*, 178, 846-853. <https://doi.org/10.1016/j.actaastro.2020.10.015>
- [47] P. De Carlo, M. Magarotto, G. Mansutti, S. Boscolo, A. D. Capobianco, D. Pavarin (2021). Experimental Characterization of a Plasma Dipole in the UHF band. *IEEE Antennas and Wireless Propagation Letters*. <https://doi.org/10.1109/LAWP.2021.3091739>
- [48] M. Saleem (2020). Comparative performance assessment of plasma reactors for the treatment of PFOA; reactor design, kinetics, mineralization and energy yield. *Chemical Engineering Journal*, 382, 123031. <https://doi.org/10.1016/j.cej.2019.123031>

Particle migration modeling in solid propellants

Raoul Andriulli^{1,a*}, Nabil Souhair^{2,b}, Luca Fadigati^{1,c}, Mattia Magnani^{1,d} and
Fabrizio Ponti^{1,e}

¹ Alma Propulsion Lab, Alma Mater Studiorum-Università di Bologna, Via Fontanelle 40, 40121
Forlì, FC, Italy

² LERMA Laboratory Aerospace and Automotive Engineering School, International University of
Rabat Sala al Jadida, Rabat, 11100, Morocco

^araoul.andriulli@unibo.it, ^bnabil.souhair2@unibo.it, ^cluca.fadigati2@unibo.it,
^dmattia.magnani8@studio.unibo.it, ^efabrizio.ponti@unibo.it

Keywords: Solid Rocket Motors, Casting Process, Particle Migration, Numerical Simulation, OpenFOAM

Abstract. This work presents the development of an OpenFOAM solver to predict the migration of solid particles in concentrated suspensions under non-uniform shear flow. The solver modifies the *pimpleFoam* solver by implementing the conservation equation for particle volume fraction. It adapts the equation of motion for non-Newtonian flows and establishes a model for the viscous field using Krieger's correlation. The code is successfully validated by the experimental results from literature.

Introduction

Solid Rocket Motors (SRM) are commonly used in space propulsion. They provide additional thrust in the first phase of flight, either in conjunction with liquid engines (Ariane 5 and 6) or as the main thrust system (Vega C). While numerical modelling has considerably advanced [1, 2], there are still complex phenomena and uncertainties that make comprehensive performance descriptions challenging [3, 4]. Consequently, expensive testing is necessary to design and certify each SRM. The burning rate of the propellant plays a crucial role in predicting flight performance [2, 6, 7], affected by factors such as grain shape, particle orientation, air bubbles, and more [5, 8-14]. Manufacturing processes also impact ballistic performance [15-17], with macroscopic and microscopic phenomena potentially altering thrust profiles [18, 19]. One notable phenomenon is particle migration and segregation caused by the casting process, which gives rise to grain heterogeneity. All these aspects produce the so-called Hump effect, and its empirical evaluation is typically incorporated into internal ballistic simulations. However, a complete understanding and reliable prediction method for the Hump effect have not yet been achieved.

This study focuses on designing a CFD code using OpenFOAM [20] to simulate and describe particle migration. A bidimensional channel flow case is examined, and the simulation results are compared and validated against literature data. The validated approach can then be applied to simulate segregation phenomena in a motor. The paper is divided into two sections, one describing the developed model and the other presenting the results and validation using experimental data [21].

Theoretical model for particle migration

During the past few decades, it has become common knowledge that initially uniformly distributed particles will assume extremely nonuniform concentration distribution when subjected to a nonuniform shear flow. This non-homogeneous distribution is the result of a migration process which occurs at small values of particle Reynolds number ($\sim 10^{-4}$), so that the importance of inertial



effects can be precluded. In general, solid particles will move from regions characterized by a higher shear rate to the neighbouring areas where lower values are measured.

The diffusive-flux model for the prediction of particle distribution (ϕ) resulting from shear-induced migration, has been developed by Phillips et al. [22]. In particular, two separate contributions to the segregation process are present, the first being related to the frequency of impacts between solid particles while the other depending mainly on the non-uniform viscosity field.

The conservation equation for solid particles in the Eulerian frame may be written as:

$$\frac{D\phi}{Dt} = \alpha^2 K_c (\phi^2 \nabla \dot{\gamma} + \phi \dot{\gamma} \nabla \phi) + \alpha^2 K_\eta \nabla \cdot (\dot{\gamma} \phi^2 \nabla \ln \eta(\phi)) \quad (1)$$

where $\dot{\gamma} = (2\mathbf{D}:\mathbf{D})^{1/2}$ (\mathbf{D} being the deformation rate tensor) is the local value of the shear rate, K_c and K_η are two empirical constants, α is the solid particle diameter, and η is the viscosity.

The mathematical model for the viscosity is set following the work performed by Krieger in [23] through empirical observations.

$$\eta(\phi) = \eta_0 \left(1 - \frac{\phi}{\phi_m}\right)^{-c} \quad (2)$$

where c is obtained by fitting the experimental data. The original fitting was performed for volume fractions in the range $0.01 < \phi < 0.5$, however, for the sake of simplicity, many papers assume the model to be verified on a wider range, that is $0.01 < \phi < 0.68$. The asymptote in correspondence of the volume fraction ϕ_m is due to the fact that, beyond such limit, usually referred to as maximum packing fraction, the dispersed particles will create a rigid structure, and the fluid will cease to flow. The maximum packing fraction is evaluated as a function of the geometry of the solid particles and the microstructure that they form within the fluid, the value for a monomodal packing of rigid spheres is usually set to **0.63**, while for poly-dispersed packing, values are usually higher (up to **0.75 ÷ 0.80**). In this paper the chosen value for ϕ_m is **0.68** (in accordance with [24]).

Solver validation

The simulation of the bidimensional channel flow has been carried out for the duration of 12 seconds (time estimated for the reaching of steady conditions). The simulated channel is 35 mm and 1.7 mm wide. The time assumption shall be directly verified by considering the value of the variation of the volume fraction ($\Delta\phi$).

Considering the section of the channel at the position $L = 0.238$ m, i.e., where the data for the validation are going to be gathered, and the time $t = 12$ s, the maximum recorded value amounts to:

$$\max\{|\Delta\phi|_L\} \cong \max\left\{\left|\frac{\partial\phi}{\partial t}\right|\right\}_L \Delta t \cong 5.2 \cdot 10^{-7} \quad (3)$$

It is evident how the variation has not achieved a zero value yet, however, since the order of magnitude is considerably narrow, and the profile peak is already close to the maximum value of packing, it is realistic to assume that the steady condition has been reached. It is hence possible to compare the results produced by OpenFOAM with the two references.

This comparison is performed in Fig. 1; with respect to the set of experimental data measured by Lyon & Leal [21] and the 1D and 2D models introduced by Ilyoung Kwon et al. in [24].

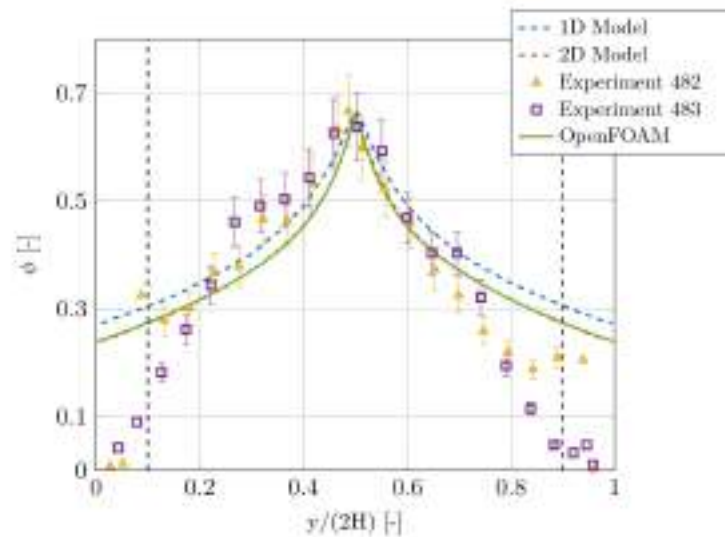


Figure 1: Comparison between OpenFOAM results and literature data of the particle distribution across the section of the channel ($L = 0.238$ m, $t = 12$ s). The 1D and 2D have been developed in [24], while the experimental data are measured in [21].

As it can be noticed, the OpenFOAM results emulate in a quite precise manner the behaviour of the 2D model. The global trend of the experimental data is respected, as the peak of the volume fraction is reached at the midpoint of the channel according to the theory and the observations. Furthermore, the right part of the curve, in the proximity of the centreline, appears to be quite close to the values of the two experiments. Adversely, on the left side, the situation is different, nonetheless, the reason may be also related to the precision of the measurements. Approaching the walls, the observed volume fraction diverges from the one predicted via CFD, the motivation might be due to the inaccuracy of the method adopted (i.e., LDV), which had the tendency to underestimate the particle concentration due to the drop of the signal-to-noise ratio caused by the solid boundaries.

Conclusion

The aim of this work was the development of an OpenFOAM solver aimed at correctly predicting the migration phenomenon that is experienced by the solid particles in concentrated suspensions when subjected to non-uniform shear flows. In order to simulate such behaviour, the conservation equation expressing the time variation of the particle volume fraction has been implemented in OpenFOAM. The chosen preexisting solver that has been modified is *pimpleFoam*, which discretizes the Navier-Stokes system of equation through the PIMPLE algorithm. As a first step, the formulation of the equation of motion has been adapted to correctly solve non-Newtonian flows. Successively, the model for the viscous field was established. The code implements the Krieger's correlation to include the viscosity variation over the domain due to the heterogeneity of the particle spatial distribution. Subsequently, the iterative cycle for the solution of the migration equation has been included within the time loop.

The above-mentioned code has been successfully validated by taking into account the measured data provided by the experiment of Lyon & Leal [21] and the results of the CFD code developed by Ilyoung Kwon et al. [24]. The flow that has been simulated in order to verify the capacity of the solver to approach the migration problem is a 2D channel flow. From the comparison between the results produced via OpenFOAM, with the finite volume discretization, and the data from

literature it has been verified that the particles volume fraction ϕ is predicted in a quite satisfactory way. The various operations that compose the solver *migrationPimpleFoam* are suitable for a 3D flow; therefore, more complex scenarios might be simulated.

References

- [1] REN P, WANG H, ZHOU G, et al (2021) Solid rocket motor propellant grain burnback simulation based on fast minimum distance function calculation and improved marching tetrahedron method. Chinese Journal of Aeronautics 34:208–224.
<https://doi.org/10.1016/j.cja.2020.08.052>
- [2] Wang X, Jackson TL, Massa L (2004) Numerical simulation of heterogeneous propellant combustion by a level set method. Combustion Theory and Modelling 8:227–254.
<https://doi.org/10.1088/1364-7830/8/2/003>
- [3] Sutton GP, Biblarz O (2016) Rocket Propulsion Elements, 9th ed. John Wiley & Sons
- [4] Breton P Le, Ribereau D (2002) Casting Process Impact on Small-Scale Solid Rocket Motor Ballistic Performance. J Propuls Power 18:1211–1217. <https://doi.org/10.2514/2.6055>
- [5] Ghose B, Kankane DK (2008) Estimation of location of defects in propellant grain by X-ray radiography. NDT & E International 41:125–128.
<https://doi.org/10.1016/j.ndteint.2007.08.005>
- [6] Wang X, Jackson TL, Buckmaster J (2007) Numerical simulation of the 3-dimensional combustion of aluminized heterogeneous propellants. Proceedings of the Combustion Institute
- [7] Jackson TL (2012) Modeling of Heterogeneous Propellant Combustion: A Survey. AIAA Journal 50:993–1006. <https://doi.org/10.2514/1.J051585>
- [8] Kochevets S, Buckmaster J, Jackson TL, Hegab A (2001) Random Packs and Their Use in Modeling Heterogeneous Solid Propellant Combustion. J Propuls Power 17:883–891.
<https://doi.org/10.2514/2.5820>
- [9] Plaud M, Gallier S, Morel M (2015) Simulations of heterogeneous propellant combustion: Effect of particle orientation and shape. Proceedings of the Combustion Institute 35:2447–2454. <https://doi.org/10.1016/j.proci.2014.05.020>
- [10] Ponti F, Mini S, Annovazzi A (2020) Numerical Evaluation of the Effects of Inclusions on Solid Rocket Motor Performance. AIAA Journal 58:4028–4036.
<https://doi.org/10.2514/1.J058735>
- [11] Ponti F, Mini S, Fadigati L, et al (2021) Effects of inclusions on the performance of a solid rocket motor. Acta Astronaut 189:283–297.
<https://doi.org/10.1016/j.actaastro.2021.08.030>
- [12] Ponti F, Mini S, Fadigati L, et al (2021) INFLUENCE OF NOZZLE RADIATION ON SOLID ROCKET MOTORS TAIL-OFF THRUST. International Journal of Energetic Materials and Chemical Propulsion 20:45–64.
<https://doi.org/10.1615/IntJEnergeticMaterialsChemProp.2021038491>
- [13] Mini S, Ponti F, Brusa A, et al (2023) Prediction of Tail-Off Pressure Peak Anomaly on Small-Scale Rocket Motors. Aerospace 10:169. <https://doi.org/10.3390/aerospace10020169>
- [14] Mini S, Ponti F, Annovazzi A, Gizzi E (2020) Impact of Thermal Protections Insulation Layer on Solid Rocket Motor Performance. In: AIAA Propulsion and Energy 2020 Forum. American Institute of Aeronautics and Astronautics, Reston, Virginia

- [15] Le Breton P, Ribereau D, Marraud C, Lamarque P (2002) Experimental and Numerical Study of Casting Process Effects on Small Scale Solid Rocket Motor Ballistic Behavior. *International Journal of Energetic Materials and Chemical Propulsion* 5:132–145. <https://doi.org/10.1615/IntJEnergeticMaterialsChemProp.v5.i1-6.160>
- [16] Mini S, Ponti F, Annovazzi A, et al (2022) A novel procedure to determine the effects of debonding on case exposure of solid rocket motors. *Acta Astronaut* 190:30–47. <https://doi.org/10.1016/j.actaastro.2021.09.016>
- [17] Ponti F, Mini S, Fadigati L, et al (2022) Theoretical Study on The Influence of Debondings on Solid Rocket Motor Performance. *International Journal of Energetic Materials and Chemical Propulsion* 21:21–45. <https://doi.org/10.1615/IntJEnergeticMaterialsChemProp.2021039436>
- [18] Ao W, Liu X, Rezaiguia H, et al (2017) Aluminum agglomeration involving the second merge of agglomerates on the solid propellants burning surface: Experiments and modeling. *Acta Astronaut* 136:219–229. <https://doi.org/10.1016/j.actaastro.2017.03.013>
- [19] Emelyanov VN, Teterina IV, Volkov KN (2020) Dynamics and combustion of single aluminium agglomerate in solid propellant environment. *Acta Astronaut* 176:682–694. <https://doi.org/10.1016/j.actaastro.2020.03.046>
- [20] (2023) OpenFOAM foam-extend toolbox. <https://sourceforge.net/projects/foam-extend/>. Accessed 26 Apr 2023
- [21] LYON MK, LEAL LG (1998) An experimental study of the motion of concentrated suspensions in two-dimensional channel flow. Part 1. Monodisperse systems. *J Fluid Mech* 363:25–56. <https://doi.org/10.1017/S0022112098008817>
- [22] Phillips RJ, Armstrong RC, Brown RA, et al (1992) A constitutive equation for concentrated suspensions that accounts for shear-induced particle migration. *Physics of Fluids A: Fluid Dynamics* 4:30–40. <https://doi.org/10.1063/1.858498>
- [23] Krieger IM (1972) Rheology of monodisperse latices. *Adv Colloid Interface Sci* 3:111–136. [https://doi.org/10.1016/0001-8686\(72\)80001-0](https://doi.org/10.1016/0001-8686(72)80001-0)
- [24] Kwon I, Jung HW, Hyun JC, et al (2018) Particle migration in planar Couette–Poiseuille flows of concentrated suspensions. *J Rheol (N Y N Y)* 62:419–435. <https://doi.org/10.1122/1.4989416>

Validation of a numerical strategy to simulate the expansion around a plug nozzle

Marco Daniel Gagliardi^{1,a}, Luca Fadigati^{1,b}, Nabil Souhair^{1,c} and Fabrizio Ponti^{1,d,*}

¹Alma Propulsion Lab, Alma Mater Studiorum-Università di Bologna, Via Fontanelle 40, 40121 Forlì, FC, Italy

^amarco.gagliardi2@studio.unibo.it, ^bluca.fadigati2@unibo.it, ^cnabil.souhair@unibo.it, ^dfabrizio.ponti@unibo.it

Keywords: Aerospike Engine, Plug Nozzle, HLLC Scheme, Numerical Simulation, OpenFOAM

Abstract. Rocket engines currently use traditional bell-shaped nozzles that have a fixed area ratio and can only operate at maximum efficiency at a given altitude. Plug nozzles have been proposed as an alternative solution to achieve higher performance over a larger altitude range. Unlike bell nozzles, the flow is free to expand along the plug, as it is no longer surrounded by solid boundaries. Therefore, plug nozzles can adapt to different altitudes by expanding the flow to ambient pressure, resulting in continuous altitude adaptation. Due to the high surface area that needs to be cooled, one of the main challenges of plug nozzle design is thermal management. However, the introduction of aerospike geometry, which is essentially a truncated plug nozzle, has helped mitigate this issue. Simulating an aerospike engine is challenging due to the interaction between the plume and the external flow, which is necessary to accurately predict thrust. In this work, a numerical strategy for predicting the performance of an aerospike engine, during a static fire, was developed and validated.

Introduction

Rocket engines commonly employ traditional bell-shaped nozzles with fixed area ratios, limiting their maximum efficiency to a specific altitude corresponding to the design Nozzle Pressure Ratio (NPR). Therefore, bell shaped nozzles operate sub-optimally for a significant portion of a launcher's flight. Various solutions have been proposed to address these limitations, but none have proven suitable for practical flight operations. In the 1950s, plug nozzles and aerospikes were introduced to achieve higher performance across a broader altitude range. Unlike other nozzle concepts, they offer continuous altitude adaptation. The advent of additive manufacturing techniques has sparked new developments in aerospike technology worldwide, as economically viable processes can address the geometrical complexity of the engine. Several research groups are actively exploring aerospike technology. The Beijing University of Aeronautics and Astronautics has developed an optimization method to design aerospike contours that maximize total impulse from sea level to the design altitude [1]. Technische Universität Dresden has studied thrust vectoring control systems and ceramic additive manufacturing techniques [2, 3]. Accurate thrust prediction in aerospike engines requires considering the interaction between the plume and external flow, posing a significant simulation challenge. This paper focuses on the development and validation of a numerical strategy aimed at predicting the performance of an aerospike engine. By utilizing advanced numerical simulations, the aim is to obtain crucial information impractical to measure during physical tests, such as pressure distribution along the plug and in the plume. The paper is divided into two main sections: the first one describes the developed model, the second one the results obtained and the validation using experimental data coming from literature.



Model structure

The CFD software employed to carry out the simulation is OpenFOAM, the chosen solver is *dbnsTurbFoam* that is contained in foam-extend. It has been chosen because it is considered particularly suitable for simulating supersonic turbulent flows and results the only compressible solver exploiting the Harten-Lax-van Leer-Contact (HLLC) approximate Riemann solver, crucial to correctly capture shock waves without smearing them [4]. In [5] the fidelity of *dbnsTurbFoam* is assessed: taking as references the Sod's shock tube (analytical solution, [6]) and the Onera S8 Transonic Channel (experimental data, [7]) scenarios, it is shown how *dbnsTurbFoam* is suitable to study high speed compressible flows. Turbulence is taken into account by means of the $k-\omega$ SST model developed by Menter [8]. A key feature of the SST model is the implementation of the stress limiter parameter, a_1 , in the definition of the eddy viscosity ν_t [9].

$$\nu_t = \frac{a_1 k}{\max(a_1 \omega; \Omega F_2)} \quad (1)$$

Such formulation of the eddy viscosity has been considered in the model in order to better account for the transport of the turbulent shear stress inside the boundary layer of compressible flows, largely improving the performance in case of adverse pressure gradients. Ω is the absolute value of vorticity, and F_2 is a blending function, equal to one for boundary layer flows and to zero for free shear layers, that, in this latter case, allows to return to the original definition $\nu_t = k/\omega$ [8]. The default value employed by Menter for a_1 is 0.31.

Results

The experimental work of S. B. Verma and M. Viji [10] consists in testing a linear plug nozzle. The nozzle is fed with air stored in a tank at ambient temperature and pressure, but both values are not explicitly provided in the reference paper; in this work, they have been assumed of 1 bar, as done also in [11], and 300 K, respectively. Fig. 1 shows the experimental setup and the nozzle geometry as given in [10]; the design Nozzle Pressure Ratio for the internal nozzle is 14, and the overall nozzle design NPR is 36, corresponding to a Mach 3 ± 0.1 exit flow; all tests have been performed in over-expansion conditions. The nozzle is provided with nine pressure ports distributed along the plug axis, as shown in Fig. 1, that allow measurements for the reconstruction of the time-averaged pressure distribution along the spike wall.

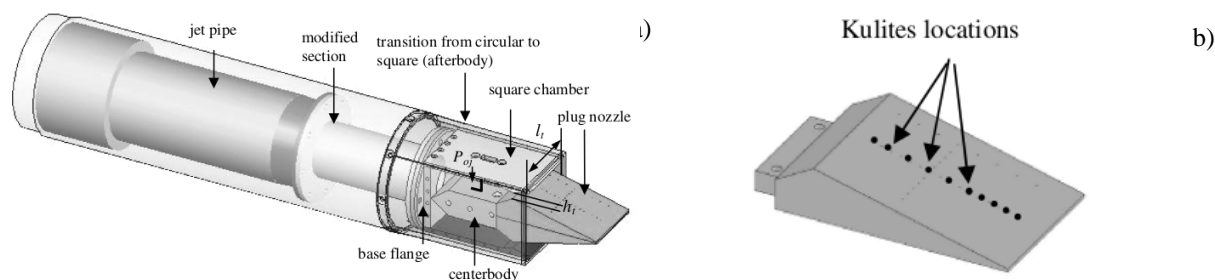


Fig. 1: Experimental setup for the analyses conducted in [10]: a) shows a section of the experimental setup, b) shows the position of the pressure measurements on the plug surface.
Images from [10]

The simulations have been run until the jet achieved stationary conditions, and the obtained results have been compared with the data available in the two reference papers ([10] and [11]) in terms of flow topology and time-averaged pressure distribution along the spike wall. In Fig. 2, for example, the numerical results at NPR = 3.1, from [11] are compared with those obtained in this

work. Fig. 3 shows the comparison between the experimental result and the ones from the simulations. On the horizontal axis, there is the coordinate along the spike normalized by $L = 0.1\text{m}$, that is the length of the spike itself from the throat section to the tip. The results are very close to the experimental.

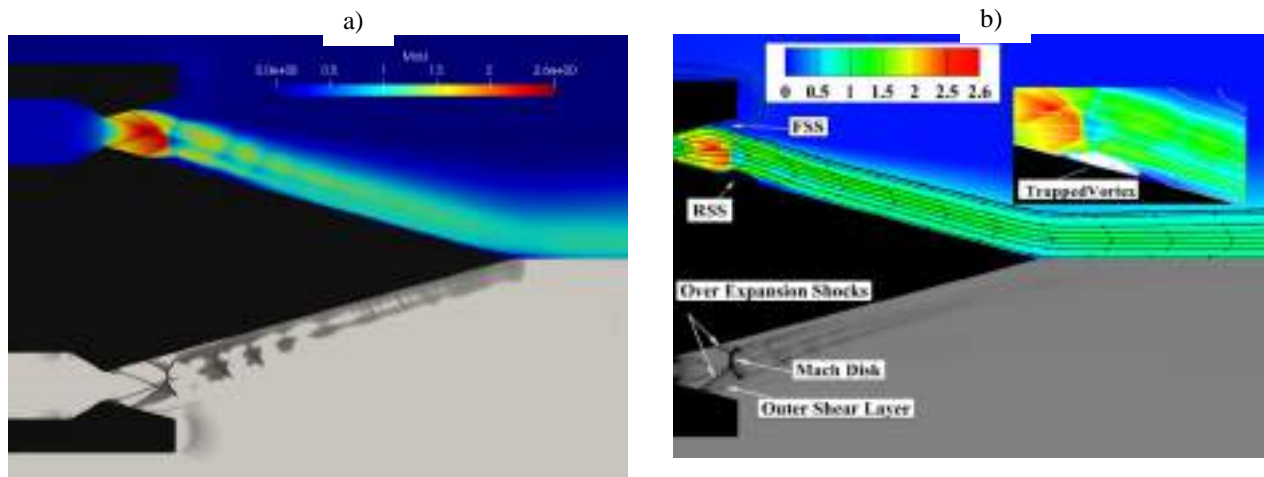


Fig. 1: A comparison between the numerical results provided by OpenFOAM (a) and ANSYS Fluent (b) at $\text{NPR} = 3.1$ [11].

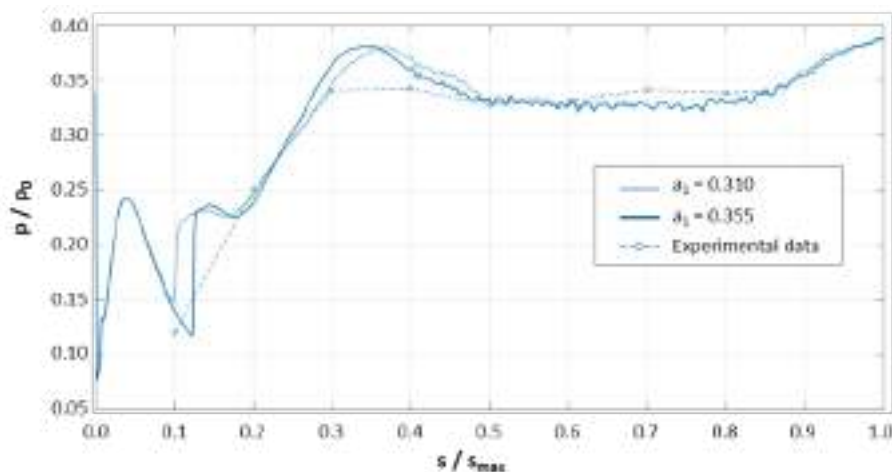


Fig. 3: Experimental spike wall pressure distribution (dots and linear interpolation) versus its numerical counterpart computed in OpenFOAM using two different values of the stress limiter in the turbulence model ($\text{NPR} = 3.1$).

Conclusion

The paper presents the definition of a model capable to simulate the supersonic flow at the exit of a plug nozzle. The simulation environment has been developed in OpenFOAM and based on the solver *dbnsTurbFoam*. The $k - \omega$ SST model has been used to simulate flow turbulence and different parametrizations of the model have been discussed and simulated. The model has been validated using experimental data found in literature, collected on a linear plug nozzle, both in terms of pressure measurements on the plug wall, and in terms of Schlieren pictures of the flow. From the results that have been obtained, despite all the uncertainties associated to the reference experimental setup, the performance of the solver can be definitely considered appropriate.

References

- [1] Wang C-H, Liu Y, Qin L-Z (2009) Aerospike nozzle contour design and its performance validation. *Acta Astronaut* 64:1264–1275. <https://doi.org/10.1016/j.actaastro.2008.01.045>

- [2] Sieder-Katzmann J, Propst M, Tajmar M, Bach C (2021) INVESTIGATION OF AERODYNAMIC THRUST-VECTOR CONTROL FOR AERO- SPIKE NOZZLES IN COLD-GAS EXPERIMENTS
- [3] Schwarzer-Fischer E, Abel J, Sieder-Katzmann J, et al (2022) Study on CerAMfacturing of Novel Alumina Aerospike Nozzles by Lithography-Based Ceramic Vat Photopolymerization (CerAM VPP). *Materials* 15:3279. <https://doi.org/10.3390/ma15093279>
- [4] Toro EF (2019) The HLLC Riemann solver. *Shock Waves* 29:1065–1082. <https://doi.org/10.1007/s00193-019-00912-4>
- [5] Chandramouli S, Gojon R, Fridh J, Mihaescu M (2017) Numerical Characterization of Entropy Noise With a Density Based Solver
- [6] Sod GA (1978) A survey of several finite difference methods for systems of nonlinear hyperbolic conservation laws. *J Comput Phys* 27:1–31. [https://doi.org/10.1016/0021-9991\(78\)90023-2](https://doi.org/10.1016/0021-9991(78)90023-2)
- [7] Delery J (1978) Analyse du décollement résultant d’une interaction choc-chouche limite turbulent en transsonique. *La Recherche Aérospatiale* 6:305–320
- [8] Menter FR (1994) Two-equation eddy-viscosity turbulence models for engineering applications. *AIAA Journal* 32:1598–1605. <https://doi.org/10.2514/3.12149>
- [9] Huang PG, Bradshaw P, Coakley TJ (1992) Assessment of closure coefficients for compressible-flow turbulence models. Ames Research Center, Moffett Field, California 94035-1000
- [10] Chutkey K, Viji M, Verma SB (2017) Effect of clustering on linear plug nozzle flow field for overexpanded internal jet. *Shock Waves* 27:623–633. <https://doi.org/10.1007/s00193-017-0707-y>
- [11] Soman S, Suryan A, Nair PP, Dong Kim H (2021) Numerical Analysis of Flowfield in Linear Plug Nozzle with Base Bleed. *J Spacecr Rockets* 58:1786–1798. <https://doi.org/10.2514/1.A34992>

Special Session in Memory of Professor Debei

Solar simulator facility for the verification of space hardware performance

C. Bettanini^{1,2} *, M. Bartolomei², S. Chiodini^{1,2}, L. Tasinato², P. Ramous²,
F. Dona² and S. Debei^{1,2}

¹ Department of Industrial Engineering, University of Padova, via Venezia 1, Padova (Italy)

² CISAS - Center for Studies and Activities for Space "Giuseppe Colombo", University of Padova, via Venezia 15, Padova (Italy)

* carlo.bettanini@unipd.it

Keywords: High Flux Solar Simulator, Flux Homogeneity, Test of Satellite Hardware

Abstract. The paper presents the main characteristics of the high flux solar simulator facility designed and developed at University of Padova as key enabling technology to evaluate the effectiveness of satellite hardware for missions to the inner planets of the Solar System. The designed solar simulator can reproduce the intensity and spectral distribution of the Sun's radiation up to 8 Solar constants (around 10000 Watt/m²) and the emitted flux can be directed to the viewport of a Thermal Vacuum Chamber in order to test the performance of space equipment under representative pressure and temperature conditions. Angles of incidence between 30° and 90° can be achieved using a motorised setup within the thermal chamber while different intensities of sunlight can be obtained by properly choosing the emitting lamp and regulating the electric power. After the verification of optical path alignment, a series of tests has been conducted to evaluate the flux homogeneity installing a commercial pyranometer on cartesian reference and moving the slide within the target area. A final Class A classification for the spatial non-uniformity of irradiance as for ASTM E927-19 has been achieved for the central target area. The facility has afterwards operated for validation campaign of satellite radiators in simulated orbital condition, verifying the repeatability of reproduced flux during continuous long-term operation.

Introduction

Solar simulators are used to mimic the light and heat conditions for materials, equipment and instruments subject to direct sunlight during operation; outdoor experiments can in fact be carried out but are strongly affected by variability of an uncontrollable environment. The Solar simulator design can be linked to two main categories of application: non-concentrating solar applications, employed for testing photovoltaic and solar water collectors and concentrating solar applications, for testing components and materials for high-temperature thermal and thermochemical applications.

The achieved flux density of simulators can so range from less than one tenth of the solar constant to tens of thousands of solar constants as in the so called High-Flux Solar Simulators (HFSS); examples are the SynLight built by DLR [1] or the solar simulator developed by ETH-Zurich [2] and [3] used for testing advanced high-temperature materials.

Several light sources can be considered for application in solar simulators to produce a radiation that approximates the natural light spectrum under controlled and repeatable conditions. A comparison of lamp wavelength spectrum, lamp intensity, cost, stability, durability, and hazards associated with use is provided in [4].

In particular, for space applications the European Space Agency has developed several solar simulators able to provide illumination beams of different diameter and intensity under vacuum to allow qualification of satellites for Earth and planetary missions. The most powerful solar



simulator (the Large Space Simulator) consists of an array of 19 xenon lamp modules, each with 25 kW power, capable of simulating 10 solar constants into an a target area of 2.7 m and has been used to simulate the BepiColombo satellite operational condition at Mercury.

Solar simulator design

The designed solar simulator can reproduce the intensity and spectral distribution of the Sun's radiation up to 8 Solar constants and has been installed near a Thermal Vacuum Chamber provided with a viewport in order to be able to test the performance of any space equipment under a range of pressure and temperature conditions, including different intensities of sunlight and different angles of incidence. A picture of the realised Solar simulator near the Thermal vacuum chamber is shown in figure 1.

The optical design of the simulator is aimed at guaranteeing repeatable values of flux and high levels of flux homogeneity across the target area; the light source is a Xenon arc lamp mounted vertically in the focus of a truncated ellipsoid reflector. The light path is afterward guided by multiple different reflecting surfaces mounted on a common optical bench; after the folding mirror, a primary mirror (spherical with 150 mm diameter), a fly-eye integrator mirror and finally a secondary mirror (spherical 500 with mm diameter) direct the flux onto the target area (Viewport with 200mm diameter). An overview of the optical path is provided in figure 2.

The fly-eye mirror has been realised to homogenize the uneven brightness of the light source by arranging multiple single lenses preserving the brightness of the beam and achieving a nearly-collimated beam with low divergence.



Figure 1 Solar simulator installed near the Optical aperture of Thermal Vacuum Chamber

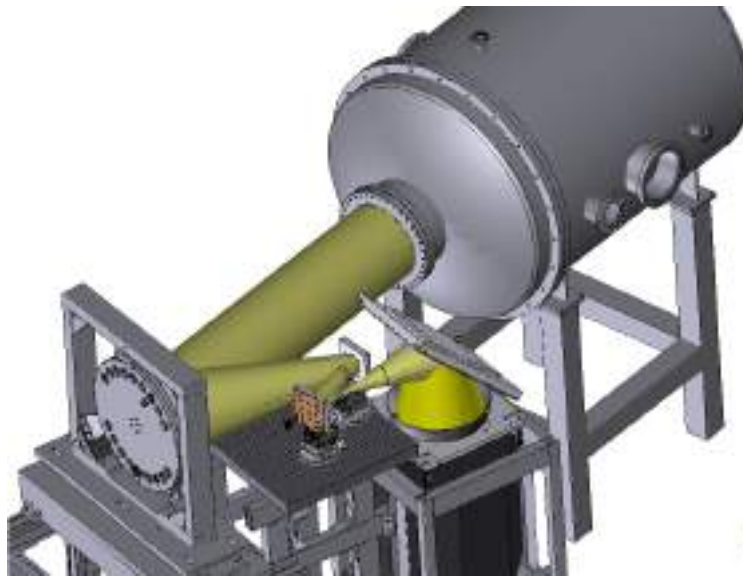


Figure 2 3D reconstruction of the Solar Simulator optical path

The presence of high energy concentrated onto the small mirror areas can lead to overheating and potential damage so dedicated cooling systems have been implemented in the setup. The emitting Xenon lamp is cooled by three fans, while thermal control of the folding mirror and the fly-eye integrator is achieved by heat exchangers cooled by a mixture of ethylene glycol-water pumped within a cooled loop circuit. The heat dissipation in the secondary spherical mirror and the folding mirror is achieved by directing a high-velocity stream of air across the rear area (creating a "knife-like" airflow) using a compressed air circuit.

Evaluation of achieved Solar flux uniformity

Flux homogeneity is a critical characteristic of a solar simulator that refers to the uniformity of the irradiance across the target area. This uniformity is essential because it ensures that the devices being tested receive a consistent and repeatable level of illumination. Inaccuracies in the irradiance level can cause significant variations in the performance of the device under test, making it challenging to compare results and draw meaningful conclusions about its performance.

To evaluate flux homogeneity, the distribution of radiative flux across the target area of the simulator has been measured using direct mapping flux measurement system: a LP PYRA 02 AC4 pyranometer by Delta Ohm S.r.l. positioned on an equidistant grid of 4 cm. A Xenon arc emitting lamp with nominal flux of 1 Solar constant has been used for the test.

Figure 3 provides an illustration of the reconstructed distribution, depicting the mapping of radiative flux at the viewport of the thermal vacuum chamber with the lamp in operation. The flux distribution approaches an ellipsoidal Gaussian distribution, with the peak flux reaching about 1355 W/m².

To assess the homogeneity of the flux, the measured flux's deviation from the interpolation of the measures with an ellipsoidal Gaussian distribution was evaluated; this analysis provides valuable insights into the uniformity of the irradiance across the target area of the solar simulator.

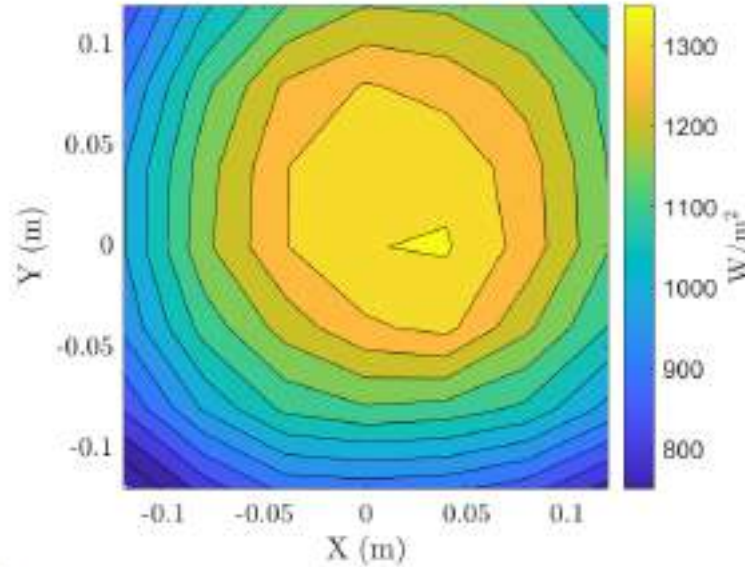


Figure 3 Mapping of radiative flux at the viewport of the thermal vacuum chamber as measured by the pyranometer.

Figure 4 depicts the differences between the measured and interpolated Solar fluxes. Panel (b) shows a histogram of the frequency of deviations from the interpolated flux, while panel (a) maps the inhomogeneities between the measured and interpolated fluxes.

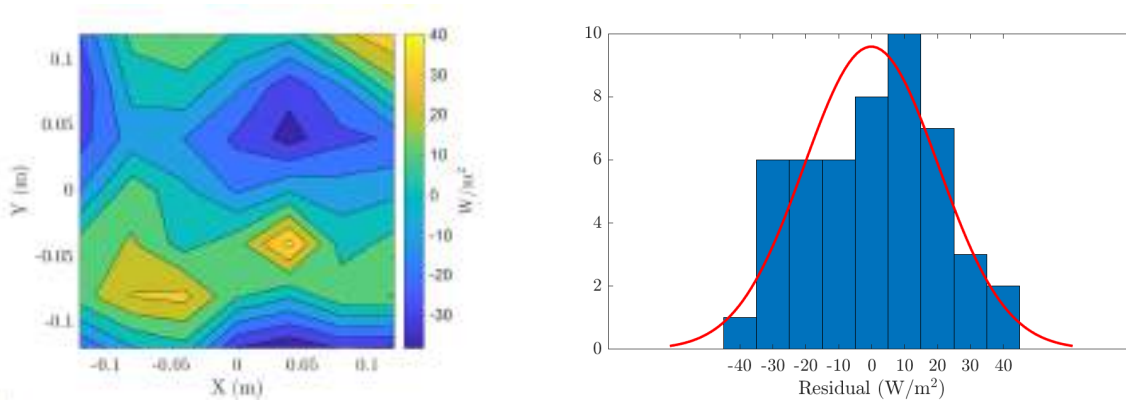


Figure 4 (a) Map of inhomogeneities between measured Solar flux and flux interpolated via Gaussian ellipsoid. (b) Distribution of inhomogeneities for measured points. The histogram shows the frequency of deviations from the flux interpolated via Gaussian ellipsoid."

The spatial non-uniformity of irradiance S_{NE} was evaluated according to ASTM E927-19 [5][5] from the interpolated solar flux W given by Table 1 parameters for different TV chamber viewport diameter. The S_{NE} is given by Equation (3).

$$S_{NE} = 100 \frac{\max W - \min W}{\max W + \min W} \quad (3)$$

Table 1 shows the class corresponding to the S_{NE} calculated for the various diameters. Considering an entrance window with a diameter of 9 cm, the solar simulator is of Class A for the spatial non-uniformity of irradiance. The Class passes to B if we consider the standard deviation of the interpolation residuals.

Table 1 Spatial non-uniformity of irradiance calculated according to ASTM E927-19 without and considering the measurement uncertainty for different TV chamber viewport diameter.

TV chamber viewport diameter	S_{NE} (Classification as from ASTM E927-19)	S_{NE} with 95% confidence uncertainties (Classification as from ASTM E927-19))
20 cm	8.5 % (Class C)	11.8 % (Class U)
15 cm	4.8 % (Class B)	8.0 % (Class C)
9 cm	1.7 % (Class A)	4.9 % (Class B)

Conclusions

The Solar Simulator Facility designed and developed at University of Padova has been tested to evaluate the flux homogeneity and repeatability using a 1 Solar Constant rated Xenon arc lamp.

The results show achieved spatial non-uniformity of the light beam on the target area allows to reach Class A on a 9 cm diameter target according to ASTM E927-19.

The facility can so be successfully used to test space hardware in representative pressure, temperature and direct sun illumination conditions with the capability to reproduce intensity and spectral distribution of the Sun's radiation up to 8 Solar constants.

References

- [1] K. Wiegardt, D. Laaber, V. Dohmen, P. Hilger, D. Korber, K.-H. Funken, B. Hoffschmidt, Synlight-A new facility for large-scale testing in CSP and solar chemistry, in: AIP Conference Proceedings, vol. 2033, AIP Publishing LLC, 2018, pp. 040042. <https://doi.org/10.1063/1.5067078>
- [2] D. Hirsch, P. Zedtwitz and et al. 2003 A new 75 kW high-flux solar simulator for high-temperature thermal and thermochemical research J. Sol. Energy Eng. 125(1) 117-120. <https://doi.org/10.1115/1.1528922>
- [3] J. Petrasch, P. Coray, A. Meier, M. Brack, P. Häberling, D. Wüillemin, A. Steinfeld A Novel 50kW 11,000 suns High-Flux Solar Simulator Based on an Array of Xenon Arc Lamps J. Sol. Energy Eng., 129 (2006), pp. 405-411D. Codd and A. e. a. Carlson 2010 A low cost high flux solar simulator Sol. Energy 84 (12) 2202-2212. <https://doi.org/10.1115/1.2769701>
- [4] M. Tawfik, X.Tonnellier,C. Sansom , “Light source selection for a solar simulator for thermal applications: A review”, Renewable and Sustainable Energy Reviews , Volume 90, July 2018, Pages 802-813. <https://doi.org/10.1016/j.rser.2018.03.059>
- [5] ASTM E927-19 Standard Classification for Solar Simulators for Electrical Performance Testing of Photovoltaic Devices.

Trajectory reconstruction by means of an event-camera-based visual odometry method and machine learned features

S. Chiodini^{1,a,*}, G. Trevisanuto^{2,b}, C. Bettanini^{1,c}, G. Colombatti^{1,d} and M. Pertile^{3,e}

¹Department of Industrial Engineering, University of Padova, via Venezia 1, Padova (Italy)

²CISAS - Center for Studies and Activities for Space "Giuseppe Colombo", University of Padova, via Venezia 15, Padova (Italy)

³School of Engineering, University of Padova, Via Gradenigo 6/a, Padova, Italy

^asebastiano.chiodini@unipd.it, ^bgiovanni.trevisanuto@studenti.unipd.it, ^ccarlo.bettanini@unipd.it, ^dgiacomo.colombatti@unipd.it, ^emarco.pertile@unipd.it

Keywords: Visual Odometry, Computer Vision, Machine Learning

Abstract. This paper presents a machine learned feature detector targeted to event-camera based visual odometry methods for unmanned aerial vehicles trajectory reconstruction. The proposed method uses machine-learned features to enhance the accuracy of the trajectory reconstruction. Traditional visual odometry methods suffer from poor performance in low light conditions and high-speed motion. The event-camera-based approach overcomes these limitations by detecting and processing only the changes in the visual scene. The machine-learned features are crafted to capture the unique characteristics of the event-camera data, enhancing the accuracy of the trajectory reconstruction. The inference pipeline is composed of a module repeated twice in sequence, formed by a Squeeze-and-Excite block and a ConvLSTM block with residual connection; it is followed by a final convolutional layer that provides the trajectories of the corners as a sequence of heatmaps. In the experimental part, a sequence of images was collected using an event-camera in outdoor environments for training and test.

Introduction

Bio-inspired systems are becoming increasingly widespread in the field of robotics. The advantages are related to the reduced use of resources, both in terms of power consumption and computational load. In terms of perception, Event-based vision sensors, such as Dynamic Vision Sensor (DVS) devices represent one of the intriguing advancements in image sensor technology. These devices incorporate in-pixel circuitry that can detect temporal changes in intensity and communicate these changes as binary "events" to the external world. Essentially, only the pixels that detect changes in light intensity transmit data, enabling data compression at the sensor level and facilitating low-latency operations. This is made possible because individual pixel changes can be transmitted without the need to read out full frame image frames [1]. Event-based cameras offer significant advantages over traditional cameras. Latency, which is the time delay in processing sensor data, is a critical factor, event-based cameras drastically reduce latency by transmitting data through events, which have microsecond-level latencies. Furthermore, event-based cameras possess a remarkably high dynamic range of 130 dB compared to the 60 dB range of standard cameras. This makes them well-suited for scenes with substantial illumination changes.

Certainly, one of the most promising applications for this type of camera is in the navigation of highly agile robots such as drones [2], as well as for the aspects of entry, descent, and landing of planetary probes [3]. To utilize these sensors for such purposes, it is necessary to adapt or invent new algorithms for Visual Odometry (VO). This ensures that the cameras can effectively support the navigation and mapping tasks required in these dynamic scenarios.



For VO, it is crucial to have keypoints that are repeatable and accurate across consecutive frames. Currently, there are handcrafted methods inspired by classical computer vision theory that allow the extraction of a series of features, such as the eHarris-based approach [3]. Inspired by the work of [4], we have chosen to utilize machine-learned features that exhibit a certain level of temporal stability. In this work, we present the method for training these machine-learned features, demonstrate how to integrate them into a visual odometry system, and showcase some preliminary results.

Method

The adopted event keypoint detection method is adapted from work of [4] and is based on receiving an event tensor (also called event cube) $E(x, y, t)$ of dimension $H \times W \times B$ as input and predicts a set of heatmaps as keypoint location. Regarding the event tensor input, H and W represent the height and width of the image sensor, respectively, and B indicates the number of temporal bins, which is 12 in our case. Generation of the event tensor involves several steps: as first the change in light $L_{xy,i}$ at pixel (x_i, y_i) crosses a threshold, a spike is generated; then the event camera outputs a spike stream with coordinates (x_i, y_i) and timestamp t_i , finally event stream is converted into an event tensor by considering an integration period Δt .

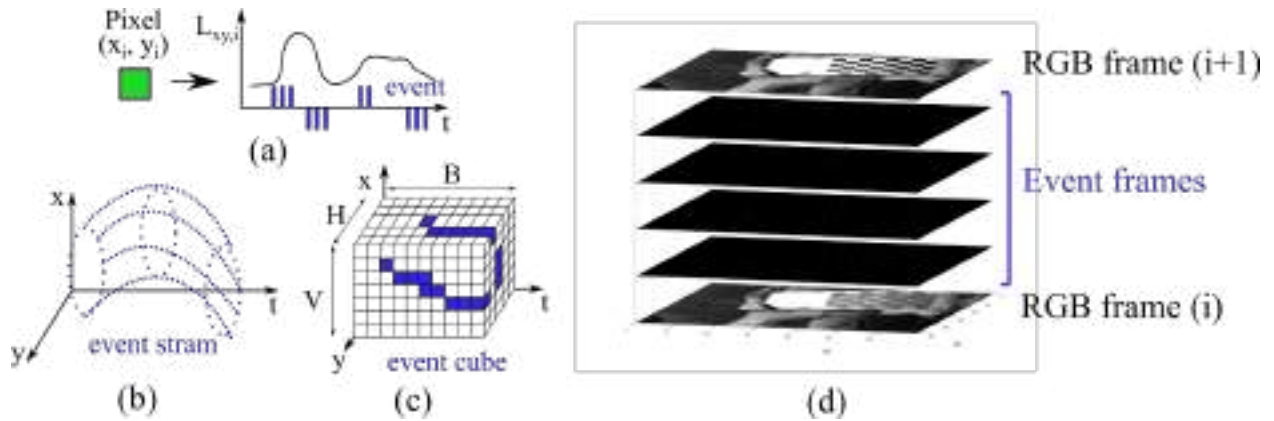


Figure 1 Event tensor generation: (a) when the change in light $L_{xy,i}$ pixel (x_i, y_i) crosses a threshold a spike is generated, (b) the event camera outputs a spike stream in time t_i and space (x_i, y_i) , (c) the event stream is converted in an event tensor considering and integration period Δt . (d) Event tensor $E(x, y, t)$ used for detector training, the training points are detected using Harris on grayscale frame and interpolating their position on the event frames.

The event tensor $E(x, y, t)$ is utilized for detector training, where training points are detected using Harris on grayscale frames and then their positions are interpolated between two consecutive event frames and filtered based on epipolar constraint. The whole event tensor generation and training point selection is depicted in Figure 1.

The loss function is based on the Binary Cross Entropy (BCE) between the predicted heatmaps $\mathcal{H}_h(x, y)$ and the interpolated keypoints positions $\hat{\mathcal{H}}_h(x, y)$:

$$\mathcal{L} = \sum_{h \in [1, n_h]} \sum_{(x, y)} \text{BCE}(\mathcal{H}_h(x, y), \hat{\mathcal{H}}_h(x, y)) \quad (1)$$

The first sum is over the n_h predicted heatmaps. The second sum is over the image locations (x, y) . The neural network architecture used in this work is based on [5] and consists of a fully

convolutional network with five layers, each utilizing 3x3 kernels. Each layer has 12 channels and incorporates residual connections. ConvLSTMs are employed in the second and fourth layers. The final layer, responsible for heatmap prediction, is a conventional convolutional layer. The remaining feed-forward layers utilize Squeeze-Excite (SE) connections. The training parameters are given in Table 1.

Table 1 Training parameters.

Num epochs	Learning rate	Num ev cubes	Num ev	Num keypoints	Num keypoint/ev frame (avg)
40	0.0001	6750	13.5×10^6	5442164	67.187

Results

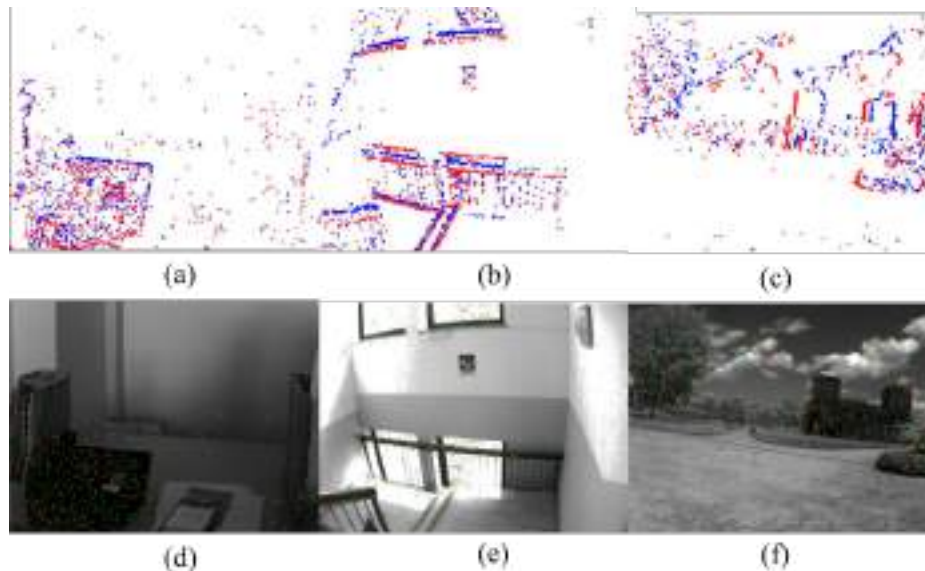


Figure 2 (a-c) Events frames obtained from the integration of 2000 events. (d,e) Corresponding RGB images of keypoints extracted from the respective event frames using the machine-learned detector (red) and a handcrafted feature detector such as eHarris (green).

To gather the frames and events required for training, sequences of images were collected in both outdoor and indoor environments. The DAVIS 346 camera from Inivation was employed for the acquisitions. The DAVIS 346 camera is a DVS event camera with a resolution of 346 x 260 pixels and includes an active pixel frame sensor. Figure 2 shows the event frames obtained from the integration of 2000 events and the corresponding RGB images with the detected keypoints. During the testing phase, the event cubes were provided as input to the machine-learned detector to extract the corresponding peak heatmaps. To verify the stability of the keypoints, a Nearest Neighbor (NN) algorithm was employed to track the keypoints in subsequent event frames. Figure 3 shows the graphs depicting the number of keypoints extracted, matched (between two consecutive frames using NN and filtered with RANSAC), and tracked (i.e., keypoints that, after being merged into tracks, belong to a track spanning at least 20 event frames).

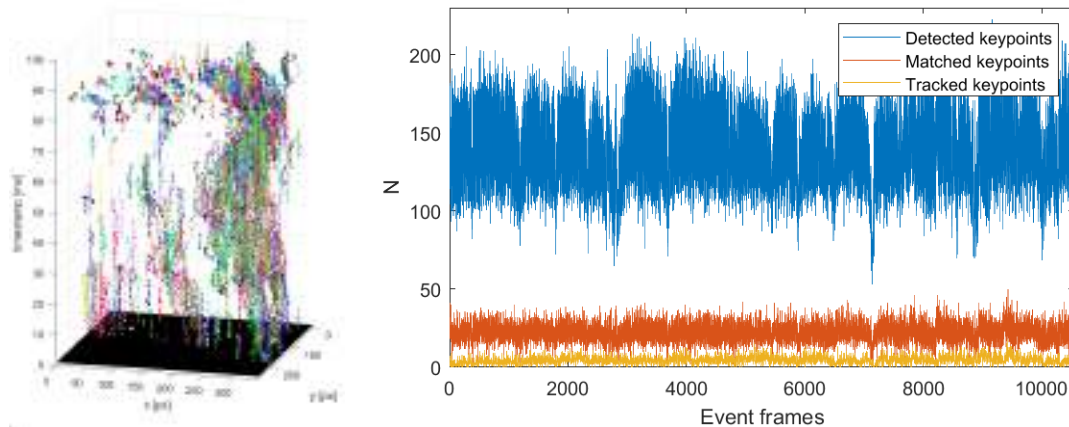


Figure 3 Detected, matched and tracked keypoints for the event stream collected outdoor.

Conclusions

In this work, the initial steps have been taken towards utilizing an event camera for the autonomous navigation of highly agile robots such as drones and entry descent and landing probes. The training of a stable keypoints detector across consecutive frames has been conducted. In future work, we will integrate this keypoint detector into a Visual Odometry pipeline and test the system on a tethered balloon.

Acknowledgements

The DVS/DAVIS technology was developed by the Sensors group of the Institute of Neuroinformatics (University of Zurich and ETH Zurich), which was funded by the EU FP7 SeeBetter project (grant 270324).

References

- [1] Lichtsteiner, P., Posch, C., & Delbruck, T. (2008). A 128 \times 128 120 dB 15 μ s latency asynchronous temporal contrast vision sensor. *IEEE journal of solid-state circuits*, 43(2), 566-576. <https://doi.org/10.1109/JSSC.2007.914337>
- [2] Mueggler, E., Rebecq, H., Gallego, G., Delbruck, T., & Scaramuzza, D. (2017). The event-camera dataset and simulator: Event-based data for pose estimation, visual odometry, and SLAM. *The International Journal of Robotics Research*, 36(2), 142-149. <https://doi.org/10.1177/0278364917691115>
- [3] Sikorski, O., Izzo, D., & Meoni, G. (2021). Event-based spacecraft landing using time-to-contact. In *Proceedings of the IEEE/CVF Conference on Computer Vision and Pattern Recognition* (pp. 1941-1950). <https://doi.org/10.1109/CVPRW53098.2021.00222>
- [4] Vasco, V., Glover, A., Bartolozzi, C.: Fast Event-Based Harris Corner Detection Exploiting the Advantages of Event-Driven Cameras. In: *IEEE/RSJ International Conference on Intelligent Robots and Systems (IROS)*. pp. 4144–4149 (2016). <https://doi.org/10.1109/IROS.2016.7759610>
- [5] Chiberre, P., Perot, E., Sironi, A., & Lepetit, V. (2022). Long-Lived Accurate Keypoint in Event Streams. *arXiv preprint arXiv:2209.10385*.

The wide angle camera of rosetta

Giampiero Naletto

Department of Physics and Astronomy, University of Padova, Via Marzolo 8, Padova, Italy

giampiero.naletto@unipd.it

Keywords: Space Instrument, Wide Angle Camera, Rosetta

Abstract. Rosetta was the ESA cornerstone missions which investigated the comet 67P/Churyumov-Gerasimenko. One of the on board instruments was the OSIRIS imaging system, which included the Wide Angle Camera. This camera was designed, realized, integrated, aligned and tested at the Padova University. Several challenges had to be faced and solved, due to stringent requirements and the very peculiar mission profile which foresaw a long interplanetary travel with very different thermal environments. Rosetta has been a very successful mission which returned plenty of fundamental information about comets and more in general about the solar system origin. In this paper we summarize the main characteristics of the WAC and describe one of the many scientific results that it had returned.

Introduction

Rosetta was one of the ESA cornerstone missions, and it was dedicated to the investigation of the comet 67P/Churyumov-Gerasimenko. Launched on 2 March 2004, after a 10-year journey it arrived at the comet on 6 August 2014 and orbited around it until the controlled landing on the comet nucleus on 30 September 2016. One of the on-board instruments was the OSIRIS [1] imaging system, which consisted of two cameras, the Narrow Angle Camera and the Wide Angle Camera (WAC). The latter was realized under Italian responsibility, with contributions from other European partners. In particular, this instrument has been designed, realized, integrated, aligned and tested at the Padova University, with a coordinate effort of several departments.

The realization and testing of the WAC lasted several years during which also many young researchers have been involved, at their first work experience on a space instrument. The project started with the optical design and tolerance analysis, then the thermomechanical design followed. Different breadboard models were realized to check the subsystem's performance; then the camera qualification model was integrated and fully checked, and finally the flight model was prepared for launch after calibration. Several challenges had to be faced and solved during the instrument realization, due to the very peculiar mission profile which foresaw a long interplanetary travel with very different thermal environments. Rosetta has been a very successful mission which returned plenty of fundamental information about comets and more in general about the solar system origin.

The OSIRIS Wide Angle Camera

The two cameras of OSIRIS had complementary objectives. On one side, the Narrow Angle Camera had to be a system with high spatial resolution, to study the comet nucleus comet and in particular its structure and geological features. On the other, the WAC had a lower spatial resolution but a wider field of view and higher sensitivity, for observing the gas and dust flow around the nucleus [2]. The WAC optical configuration was an all-reflective two-mirror design, realized with an off-axis convex oblate ellipsoidal mirror followed by an almost on-axis concave oblate ellipsoidal mirror. The field of view was about $12^\circ \times 12^\circ$, collected by a 2048×2048 CCD providing an average image scale of 21 arcsec/pixel. The optical performance was diffraction limited. The covered spectral range, 240-750 nm was selectable by 14 different filters, defined on the basis of the scientific requirements.



The WAC structure was based on a closed box made of aluminum alloy (see Fig. 1); it was lightweighted by electro-erosion machining. The structure was designed to prevent noise induced through vibration and to minimize vibration amplification at interfaces with mechanisms. Very challenging was the thermo-mechanical design [3], that had to satisfy the optical alignment tolerances. In fact, it was verified by ray-tracing simulation that the system could tolerate a relative shift of $\pm 10 \mu\text{m}$ between the two mirrors, that is over a distance of 30 cm, during all mission lifetime: by thermal modelling, it was verified that to maintain this tolerance, the operational temperature of the WAC optical bench had to be maintained within the $12 \pm 5^\circ\text{C}$ range. For an instrument that had to operate from 4 au to 1 au, that is with a great thermal excursion, having a square entrance aperture of about 15 cm side through which heat is exchanged with the space environment, this was a very critical requirement to be satisfied.

To guarantee the optimal optical performance notwithstanding the great thermal excursion over the mission, great care was dedicated to the thermo-structural design. In particular, the WAC interfaced with the payload spacecraft panel by three kinematic mounting feet, which minimized the heat exchange. A truss structure was designed to improve the thermal decoupling between the large external baffle (this was the most critical element for the thermal design, and at the end a glass reinforced epoxy structure with absorber coating, thermally insulated from the camera, was shown to be the best solution) and the optical bench and to minimize the temperature gradient. Finally, the telescope was covered by a thermal blanket. In addition, the optic supports were made of the same material as the optical bench to minimize distortion. Even if this allowed to limit the heat exchange of the WAC with the environment, it was necessary to introduce an active control system in the camera by suitable radiators (visible on the bottom of the optical bench in Fig. 1 left).

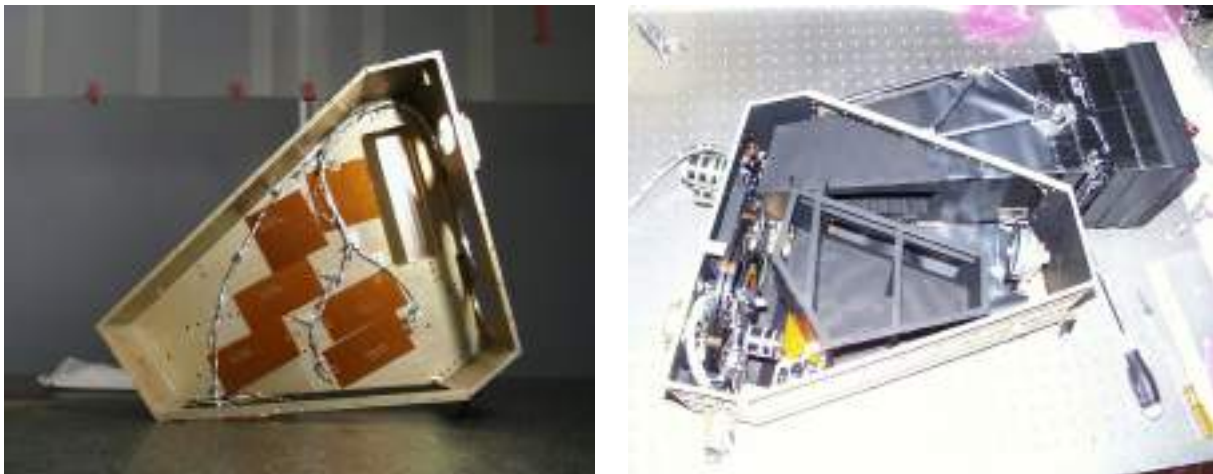


Fig. 1. On the left there is the WAC structure, obtained by excavating a single Al piece. On the right the WAC structure populated with all the optical elements.

As an example of the various mechanisms installed on the WAC, we describe here some of the characteristics of its shutter [4] (see Fig. 2), which has been the most operated one over the whole mission (more than 70k cycles). The shutter could expose a $28 \times 28 \text{ mm}^2$ area (the sensor sensitive area was about $26 \times 26 \text{ mm}^2$) with a uniformity better than 1/500. The shutter was realized by two blades travelling in front of the CCD, driven by a four-bar mechanism actioned by brushless dc motors. A customized encoder for each blade was mounted to the motor shaft and a position sensor at the final position verified that the first blade completed its travel, when reaching the lock device which kept it in open position. Then, when the exposure was completed, the second blade was released and unlocked the first, to back-travel together to the rest position by means of springs.



Fig. 2. WAC shutter mechanism; the blades are at the bottom, each joined to two moving bars.

WAC scientific results highlights

Rosetta, and in particular its imaging system OSIRIS, had a very large scientific return (e.g. [5],[6],[7]). Here we limit to recall one of the investigations realized with the WAC, and that took advantage of its extremely high contrast performance. In fact, this camera had as a target the observation of dust and gas in the comet coma and, because of the extremely low irradiance of these comet components, it was designed with an unobstructed optical configuration to minimize diffraction tails in the point spread function and nominally reach a contrast of more than 1000 at the comet nucleus-coma edge, and larger beyond. This optical design, coupled to the 16 bit detector dynamic range, allowed to detect extremely faint features close to the comet nucleus.

One of the key investigations of OSIRIS was monitoring the cometary jet activity and to look at the characteristics of the nucleus surface at the origin of these jets. In [8] the study of jets emitted in the period between Dec. 2014 and Oct. 2015, so including the perihelion, allowed to map the locations of jet sources on comet surface as a function of time. This confirmed the difference between the two comet “hemispheres”, with different behaviors between North and South, following a seasonal trend. Thanks to the great quality images provided by the WAC, several extremely faint jets have been studied and their source located using a reverse propagation analysis (see, as an example, Fig. 3).

Acknowledgements

One of the main contributors to the WAC realization was Stefano Debei, who had been involved in the definition of the mechanical and thermal characteristics of the instrument since the beginning of his career. This paper is dedicated to his memory.

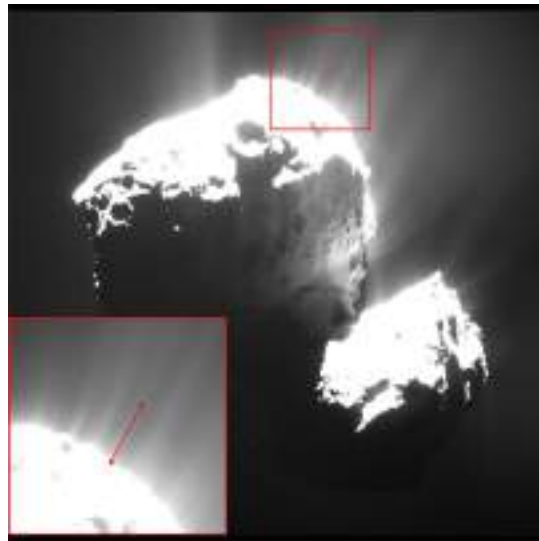


Fig. 3. WAC image (2014 Dec. 30): the image brightness has been adjusted to highlight the jets otherwise not visible. In the insert it is shown an example of jet identification. Image from [8].

References

- [1] H.U. Keller, et al., “OSIRIS - The Scientific Camera System Onboard Rosetta”, Space Science Reviews 128, Issue 1-4, pp. 433-506 (2007). <http://doi.org/10.1007/s11214-006-9128-4>
- [2] G. Naletto, et al., “Optical design of the Wide Angle Camera for the Rosetta mission”, Appl. Opt. 41(7), pp. 1446-1453 (2002). <http://doi.org/10.1364/AO.41.001446>.
- [3] B. Saggin, et al., Thermal design of the Wide Angle Camera for Rosetta, presented at the International Astronautical Federation (IAF) Congress Bremen, Germany. Published Online (2012). <http://doi.org/10.2514/6.IAC-03-Q.5.04>
- [4] De Cecco, M., et al., “High performance shutter for space applications”, SPIE Proc. 4771, pp. 186-197 (2002). [HTTP://DOI.ORG/10.1117/12.482160](http://doi.org/10.1117/12.482160)
- [5] H. Sierks, et al. “On the nucleus structure and activity of comet 67P/Churyumov-Gerasimenko”, Science 347 Issue 6220, id. aaa0444, p. 6 (2015). <http://doi.org/10.1126/science.aaa1044>.
- [6] A. Rotundi, et al. “Dust Measurements in the Coma of Comet 67P/Churyumov-Gerasimenko Inbound to the Sun Between 3.7 and 3.4 AU”, Science 347 Issue 6220, id. aaa03905, p. 7 (2015). <http://doi.org/10.1126/science.aaa3905>
- [7] N. Thomas, et al. “The Morphological Diversity of Comet 67P/Churyumov-Gerasimenko”, Science 347 Issue 6220, id. aaa0440, p. 7 (2015). [HTTP://DOI.ORG/10.1126/science.aaa0440](http://doi.org/10.1126/science.aaa0440).
- [8] M.I. Schmitt, et al., “Long-term monitoring of comet 67P/Churyumov-Gerasimenko’s jets with OSIRIS onboard Rosetta”, MNRAS 469 (Suppl. 2), pp. S380–S385 (2017). <http://doi.org/10.1093/mnras/stx1780>

Development of a modular central electronic unit (CEU) for data handling and management in Martian atmosphere investigations

L. Marrocchi^{1 *}, M. Marchetti², F. Costa¹ and S. Debei^{3,4}

¹ TEMIS Srl, via Donizetti 20, Corbetta (MI) (Italy)

² ART Spa, via Via Voc. Pischello 20, Passignano sul Trasimeno (PG) (Italy)

³ Department of Industrial Engineering, University of Padova, via Venezia 1, Padova (Italy)

⁴ CISAS - Center for Studies and Activities for Space "Giuseppe Colombo", University of Padova, via Venezia 15, Padova (Italy)

* luca.marrocchi@temissrl.com

Keywords: Telemetry, Space Avionics, Sensor Acquisition, Data Merging

Abstract. This article describes the development of a highly modular Central Electronic Unit (CEU) for data handling and management in Martian atmosphere investigations as part of the DREAMS experiment in ExoMARS 2016 Mission. The CEU was developed by TEMIS and Centro Interdipartimentale di Studi e Attività Spaziali G. Colombo (CISAS) to handle, acquire and transmit medium and low-rate data from sensors dedicated to investigating the Martian atmosphere. The CEU subsystem was designed to communicate with an external host to receive commands and transfer telemetry, transform power from different sources, perform sensors' switch on and off, acquire scientific sensors and their housekeeping monitors, and provide CEU health status. The high modularity of the CEU architecture makes it easy to customize and interface with different types of equipment and instrumentation for various missions. The CEU subsystem is housed on Entry and Descent Module (EDM) and serves as the data handling platform of the DREAMS payload for the EXOMARS 2016 Mission. The CEU has proven to be an effective and flexible solution for data handling and management in Martian atmosphere investigations.

Introduction

The Dust characterization, Risk assessment, and Environment Analyser on the Martian Surface (DREAMS) [1] mission was part of the ExoMARS 2016 mission, which aimed to explore the Martian environment and gather data on meteorological conditions, hazards, and atmospheric electric phenomena. The Central Electronic Unit (CEU) subsystem was developed by TEMIS and CISAS to serve as the data handling platform [2] for the DREAMS payload and was installed inside the warm compartment of Entry and Descent Module (EDM) [3].

The CEU subsystem consisted of primary boards and expansion boards, which distributed functionalities among various modules. The primary boards included the CEU Backplane and the On-Board Data Handling (OBDH) Board, while the expansion boards included the Analog-to-Digital Converter (ADC) Board and the Central Processing Unit (CPU) Board.

The DREAMS payload included additional subsystems such as MarsTem (thermometer), DREAMS-P (pressure sensor), DREAMS-H (humidity sensor), MetWind (wind sensor),



Fig. 1 - CEU subsystem

MicroARES (electric probe), SIS (Solar Irradiance Sensor), and a primary battery. These subsystems worked in conjunction with the CEU to fulfil the mission objectives.

CEU Architecture

The CEU subsystem [4] was designed to fulfil its objectives through the implementation of two sets of boards: primary boards and expansion boards. The primary boards are responsible for supplying power, managing the entire subsystem (including sensor configuration), and processing and transmitting data from the sensors to the external host. On the other hand, the expansion boards are specifically designed to interface with various types of sensors (analog and/or digital) by adapting the electronics accordingly. To ensure modularity and efficient distribution of functionalities, the CEU was developed with a plug-in design and a common backplane, allowing for the integration of different boards and modules.

Primary boards

1) CEU Backplane:

The CEU was a modular equipment designed to grant power connections to supply all the boards and enable communication interfaces between the peripheral boards and the CEU Core (OBDH Board). The backplane of CEU (Fig. 2) was a fully passive PCB populated with one connector for each board. The passive backplane strategy was useful during integration as it allowed inspection of the assembled PCB to ensure compliance with requirements without specific electrical tests. This streamlined the AIT phase and enabled adding one board at a time using the backplane as a consolidated part.



Fig. 2 - CEU Backplane

2) OBDH Board

The OBDH Board (Fig. 3) comprised several main blocks, namely a host interface for communication with an external unit, a microprocessor based on LEON2 (Atmel AT697F) along with its associated support memories, an FPGA (RT PROASIC3L) for expanding the microprocessor interfaces and handling low-level control of peripherals, and a non-volatile mass memory (1 Gbyte NAND FLASH). The interfaces used for communication with the expansion boards were implemented on the FPGA, offering customization options based on user requirements within the limitations of the RT PROASIC3L technology. The microprocessor had the capability to operate with a core clock of up to 100 MHz, providing a performance of 86 MIPS (Dhrystone 2.1). The communication interface between the microprocessor and the FPGA could be selected from the following choices: a PCI interface up to 33 MHz, an asynchronous 32-bit memory-mapped interface up to 20 Mbyte/s, or up to 2 UART interfaces up to 250 Kbit.

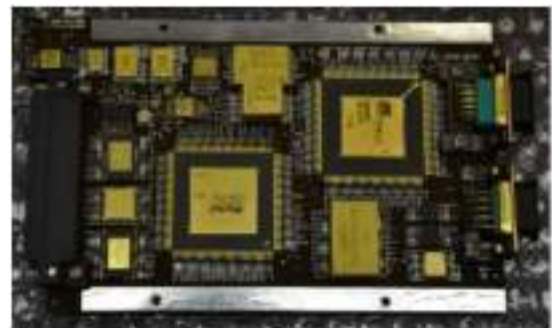


Fig. 3 - OBDH Board

3) DCDC Board

The DC/DC Board (Fig. 4) was responsible for managing the primary power supply source and distributing power to all the CEU boards. It generated the necessary secondary power rails, including $\pm 12V$, 5V, 3.3V, and 1.8V.

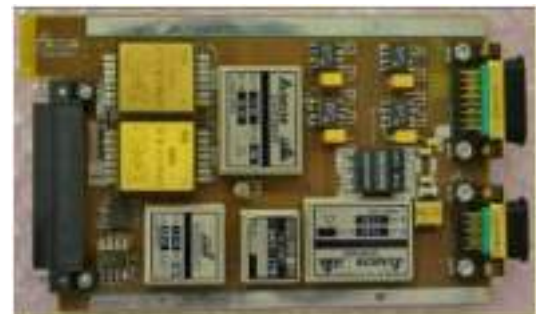


Fig. 4 - DCDC Board

Extension boards

1) ADC board:

The ADC board (Fig. 5) was specifically designed to facilitate the interface between the CEU and sensors that required analog-to-digital conversion and dedicated conditioning electronics. Its main components consisted of an ADC section utilizing the Aeroflex 14-bit Analog-to-Digital Converter (RHD5950) with 16 input channels, and an Acquisition Handler FPGA (RT PROASIC3L device) responsible for managing acquisitions and establishing communication with the OBDH board.

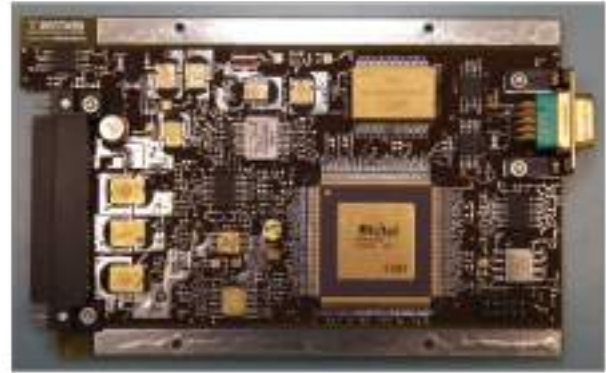


Fig. 5 - ADC Board

2) CPU board:

The CPU board (Fig. 6) was developed to establish connections with digital sensors. It included an Interfaces section that could be customized to meet the specific requirements of the sensors, an Acquisition Handler FPGA (RT PROASIC3L device) for managing acquisitions and interfacing with the OBDH board, and a 256 Mbyte SDRAM memory connected to the FPGA to support onboard data manipulation.

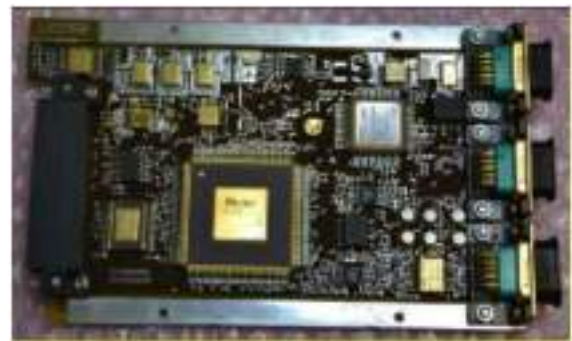


Fig. 6 - CPU Board

Both boards were equipped with onboard FPGAs, allowing for the manipulation of scientific data acquired from the sensors before transmitting them to the CEU's mass memory. Additionally, the FPGAs handled low-level control of peripherals and established communication with the OBDH board.

Power Consumption

The overall efficiency of the CEU was around 70%. To save power, the CEU was designed to have a "low power" mode where only the FPGA on the OBDH board was powered on while all other parts of the OBDH and other CEU boards were powered off. This configuration allowed the CEU system to consume less than 1 W of power.

The interfaces used to communicate with the expansion boards were implemented on FPGA and could be customized based on user requirements. The microprocessor worked with a core clock up to 100 MHz, resulting in a performance of 86 MIPS (Dhrystone 2.1). The communication interface between the microprocessor and the FPGA could be chosen from options such as PCI interface up to 33 MHz, Asynchronous 32-bit memory-mapped interface up to 20 Mbyte/s, or Up to 2 UART interfaces up to 250 Kbit.

Failures management

To automatically detect and correct failures, a detailed monitoring system was implemented to track critical parameters of the CEU boards and DREAMS sensors. This information was used by the CEU's Application Software (ASW) to make decisions to ensure safety and guarantee mission continuity even with reduced functionalities or performance degradations.

Conclusions

The CEU subsystem played a vital role in handling data, managing power, and controlling interfaces for the DREAMS payload during the EXOMARS 2016 mission. The modular design

and flexibility of the CEU allowed customization and integration of different boards and sensors, making it suitable for various scientific missions. The successful deployment and operation of the CEU subsystem contributed to the scientific success of the EXOMARS 2016 mission by providing valuable data about the Martian environment during the dust storm season.

During the descent of EDM of the Exomars 2016 mission and its subsequent impact on the Martian surface, both the CEU subsystem and the DREAMS payload performed their designated tasks flawlessly. The CEU subsystem remained fully functional throughout the descent process, demonstrating its reliability in the challenging Martian environment. Likewise, the DREAMS payload successfully carried out its scientific measurements and data acquisition during the descent and impact phase. This successful performance of the CEU and DREAMS subsystems further solidified their capabilities and effectiveness in capturing vital scientific data in extreme conditions on Mars.

In addition to their successful performance during the descent and impact of the ExoMARS 2016 EDM, the CEU subsystem and the DREAMS payload also demonstrated their reliability and optimal health during the intermediate checkout phase while the spacecraft was en route to Mars. During this period, the CEU and DREAMS experiment effectively conducted the necessary checkouts and provided crucial health information about the experiments. Their flawless operation and optimal health state reassured the mission team about the robustness and functionality of the CEU and DREAMS systems, further enhancing confidence in their capabilities to carry out scientific investigations on Mars.

References

- [1] F. Esposito, et al., "DREAMS for the ExoMars 2016 mission: a suite of sensors for the characterization of Martian environment" (PDF). European Planetary Science Congress 2013, EPSC Abstracts Vol. 8, EPSC2013-815 (2013)
- [2] L. Marrocchi et al., "High performance, high configurability modular telemetry system for launch vehicles," 2014 IEEE Metrology for Aerospace (MetroAeroSpace), Benevento, Italy, 2014, pp. 594-598. <https://doi.org/10.1109/MetroAeroSpace.2014.6865994>
- [3] Ball, Andrew & Blancquaert, Thierry & Bayle, Olivier & Lorenzoni, Leila & Haldemann, A.. (2022). The ExoMars Schiaparelli Entry, Descent and Landing Demonstrator Module (EDM) System Design. Space Science Reviews. 218. <https://doi.org/10.1007/s11214-022-00898-z>
- [4] M. Marchetti et al., "Data handling equipment for payload sub-systems," 2014 IEEE Metrology for Aerospace (MetroAeroSpace), Benevento, Italy, 2014, pp. 456-461. <https://doi.org/10.1109/MetroAeroSpace.2014.6865968>

SIMBIO-SYS, the remote sensing instruments on board the BepiColombo mission

G. Cremonese^{1a*}, C. Re^{1b}, and the SIMBIO-SYS team

¹Osservatorio Astronomico di Padova, INAF, vicolo Osservatorio 5, Padova, Italy

^agabriele.cremonese@inaf.it, ^bcristina.re@inaf.it

Keywords: Remote Sensing Instruments, Space Missions, Planets: Mercury

Abstract. The SIMBIO-SYS (Spectrometer and Imaging for MPO BepiColombo Integrated Observatory SYStem) is a complex instrument suite part of the scientific payload of the Mercury Planetary Orbiter for the BepiColombo mission, the last of the cornerstone missions of the European Space Agency (ESA) Horizon + science program. It will explore Mercury, the closest planet to the Sun. The SIMBIO-SYS instrument will provide all the science imaging capability of the BepiColombo MPO spacecraft. It consists of three channels: the STereo imaging Channel (STC), with broad spectral band in the 410-930 nm range and medium spatial resolution (up to 60 m/px), that will provide Digital Terrain Model of the entire surface of the planet with an accuracy better than 80 m; the High Resolution Imaging Channel (HRIC), with broad spectral bands in the 530-900 nm range and high spatial resolution (up to 6 m/px), that will provide high resolution images of about 10% of the surface, and the Visible and near-Infrared Hyperspectral Imaging channel (VIHI), with high spectral resolution (up to 6 nm) in the 400-2000 nm range and spatial resolution up to 120 m/px, it will provide the global coverage at 480 m/px with the spectral information, assuming the first orbit around Mercury with periherm at 480 km from the surface. It has been funded by the two space agencies, ASI (Italian Space Agency) and CNES (French Space Agency) and it is the result of the collaboration between more than 100 scientists and engineers of 12 different countries all over the world, with the Italian prime contractor Leonardo spa. It is the first time that a planetary mission has three remote sensing instruments integrated in a system, sharing the Main Electronics, and under the responsibility of one team.

Introduction

The Spectrometer and Imagers for MPO Bepicolombo Integrated Observatory SYStem (SIMBIO-SYS) is a suite of three independent optical heads that will provide images and spectroscopic observations of Mercury's surface. The SIMBIO-SYS instrument on board the Mercury Planetary Orbiter (MPO), one of the two modules of the BepiColombo mission, is composed of HRIC (High Resolution Imaging Camera), STC (STereo Channel), and VIHI (Visible and Infrared Hyperspectral Imager). The scientific objectives at mission level are to obtain a global mapping of the surface with STC and VIHI in the first 6 months of the 1 year nominal mission. Both channels will provide data on the surface composition, the surface geology as well as Digital Terrain Models (DTMs) of the entire planet.

The observing strategy of SIMBIO-SYS is based on the global mapping requirement and includes high-resolution images of 10% of the surface (HRIC). In the second 6 months, STC and VIHI will fill in gaps possibly left in the global mapping. In this phase, VIHI will observe selected regions at a spatial resolution of a factor of four better than during the previous phase. STC will acquire 4 color images of selected regions.

The BepiColombo mission will arrive at Mercury in December 2025, the instrument commissioning will be in March 2026 with the starting nominal mission in April 2026.

It is the first time that a planetary mission has three remote sensing instruments integrated in a system sharing some hardware components. The Main Electronics (ME) and the onboard software



are the same, allowing for synergistic management of operations, data handling, and compression of all the acquired data. A single factory provided all the detectors that are similar for the three cameras. From an engineering point of view, the systemic approach to the design has had several advantages:

- the technical management structure allowed the management of the developing and testing phases with the main target of optimizing the overall performance and capabilities of SIMBIO-SYS;
- the integration of the common parts allowed a better control and the optimization of the resources as mass and power;
- mechanical, thermal, and electrical interfaces towards the spacecraft have been handled at a unified level.

From a scientific point of view, the systemic approach with the same management will provide many advantages:

- cross-calibration and co-alignment of the three channels is included in the commissioning and operations;
- co-registration and data fusion are easier and included in the scientific activities;
- common science planning is applied.

Scientific objectives

The SIMBIO-SYS integrated package [1](Figure 1) aims to provide answers to almost all the main scientific questions of the BepiColombo mission concerning the Mercury surface and composition, and to provide important contributions to the understanding of its interior and exosphere. The main scientific questions can be summarized in the following topics:

- shape and morphology;
- crustal mineralogy;
- geological mapping and stratigraphy;
- volatiles;
- interior;
- Hermean extreme environment;
- exosphere;
- surface changes;
- opportunity science

Technical description

To fulfil the scientific goals of the mission, in compliance with the limited resources available on the MPO and the harsh operative environment, several solutions and technologies have been implemented, namely:

- A very compact design for HRIC
- A wide spectral coverage with a single channel instrument for VIHI
- A single detector dual channel design for STC
- A special coating (ITO) and baffle (Stavroudis design) for heat load rejection
- Diamond turned mirrors in RSA905 Aluminum alloy
- Spectral and radiometric in-flight calibration unit with no moving parts
- Large use of composite materials for structural parts
- Capabilities of stereo imaging

In addition, an instrument architecture with three dedicated Proximity Electronics (PE) and a common Main Electronics (ME) was designed, aimed at the best use of the available electrical resources thanks to the sharing of functions among the three channels.

Each channel of the SIMBIO-SYS Flight Model (FM) has been successfully tested and characterized at Leonardo SpA premises by means of two dedicated Optical Ground Support Equipment (OGSE) which have been developed and manufactured for this purpose.

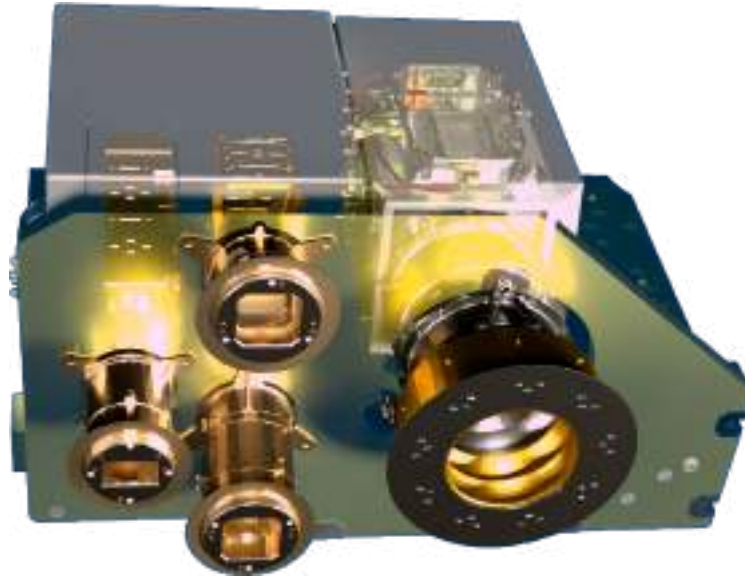


Figure 1: The three channels together representing SIMBIO-SYS, including the Proximity Electronics (PE), on the left VIHI, in the middle STC and on the right HRIC

High Resolution Camera

HRIC is a camera operating in the 530 nm to 900 nm spectral range with 6 m resolution on ground from the orbital altitude of 480 km.

The camera is equipped with a main panchromatic channel and three broadband spectral channels centred at 550 nm, 750 nm and 880 nm with 40 nm bandwidth.

The HRIC optical system [2] is composed of a telescope with a Ritchey-Chretien configuration modified with three-lenses corrector aimed to guarantee the optical quality over the whole squared 1.47° FoV. The instrument has a focal length of 800 mm and is equipped with a dioptric image corrector adapting the FoV to a 2048 x 2048 pixels detector with a pixel size of 10 μm . The focal ratio is F#8.9, to be diffraction limited at 400 nm and to optimize radiometric flux and overall mechanical dimensions. Due to the large amount of heat flux coming from Mercury, the camera aperture is protected from the planet radiation by means of a baffle, in Stavroudis configuration, and a filter, named Thermal Infrared Rejection Device (TIRD), which can be considered as part of the HRIC thermo-optical system.

The selected Stavroudis configuration for the baffle is composed of six elliptical and five hyperbolic internally high-reflecting surfaces interconnected together. All the surfaces have two common foci and this provides the baffle with the geometrical property to reject externally, after a given number of multiple reflections, all the rays impacting on the conical surfaces from an angular direction within the two foci.

Stereo Camera

STC represents one of the first push-frame stereo cameras on board a planetary mission. Based on a new concept, STC integrates the compactness of a single-detector telescope with the photogrammetric capabilities of bidirectional cameras [3]. Two separate incoming optical path oriented at $\pm 20^\circ$ with respect to nadir allow the instrument to acquire images of the same surface region with a different viewing angle at two very close moments, taking advantage of the along-track movement of the S/C. The optical system is an advanced compact catadioptric layout concept, which consists of a front-end optical separation group of mirrors inclined in order to realize $\pm 20^\circ$ stereo channels and a common telescope, based on an off-axis modified 'Schmidt corrector' design.

Visible Infrared Hyperspectral Imager

The VIHI channel has been designed to perform hyperspectral imaging observations of the whole Hermean surface in the VIS-NearIR range [1]. The channel concept is based on a collecting telescope and a diffraction-grating spectrometer ideally joined on the telescope focal plane, where the spectrometer entrance slit is located. The image of the slit is dispersed by the diffraction grating on a bi-dimensional detector. The instantaneous acquisition on the bi-dimensional detector consists of the slit image diffracted by the grating over the spectral range. The image itself is built in time by subsequent slit acquisitions, matching the S/C track speed with the slit size projected on ground (push broom mode). The final result is an hyperspectral cube, which associates a VIS-NearIR spectrum to each pixel on ground. VIHI has been designed to achieve an IFoV of $250 \mu\text{rad}$ (corresponding to 120m @ 480km altitude) and to cover a spectral range of $400\text{-}2000\text{nm}$ with a spectral sampling of 6.25nm .

References

- [1] G.Cremonese, et al., SIMBIO-SYS: scientific cameras and spectrometer for the BepiColombo mission. 2020, Space Scie.Rev., 216, 75.
- [2] M.Zusi, R.Paolinetti, V.Della Corte, G.Marra, M.Baroni, P.Palumbo, G.Cremonese, Optical design of the High Resolution Imaging Channel of SIMBIO-SYS. 2019, Applied Optics, 58, 4059. <https://doi.org/10.1364/AO.58.004059>
- [3] V.Da Deppo, G.Naletto, G.Cremonese, L.Calamai, Optical design of the single-detector planetary stereo-camera for the BepiColombo ESA mission to Mercury, 2010, Applied Optics, 49, 2910. <https://doi.org/10.1364/AO.49.002910>

The ESA PANGAEA programme: training astronauts in field science

Matteo Massironi ^{1,2*}, Francesco Sauro ^{3,4}, Samuel J. Payler ³,
Riccardo Pozzobon ^{1,2}, Harald Hiesinger ⁵, Nicolas Mangold ⁶,
Charles S. Cockell ⁷, Jesus Martínez Frias ⁸, Kåre Kullerud ⁹,
Leonardo Turchi ^{3,10}, Igor Drozdovskiy ³, Loredana Bessone ³

¹ Dipartimento di Geoscienze, University of Padua, Italy

² CISAS University of Padova, Italy

³ Directorate of Human and Robotics Exploration, European Space Agency, France

⁴ Miles Beyond Srl, Italy

⁵ Institut für Planetologie, Westfälische Wilhelms-Universität Münster, Germany

⁶ Laboratoire Planetologie et Geosciences, CNRS, Nantes, France

⁷ School of Physics and Astronomy, University of Edinburgh, UK

⁸ Instituto de Geociencias, IGEO (CSIC-UCM), Spain

⁹ Norwegian Mining Museum, Kongsberg, Norway

¹⁰ Spaceclick Srl, Italy

*matteo.massironi@unipd.it

Keywords: Planetary Geology, Human Space Exploration, Astronauts Training

Abstract. PANGAEA (Planetary ANalogue Geological and Astrobiological Exercise for Astronauts) is a field training course designed by the European Space Agency (ESA) that, since 2016, has imparted to ESA and NASA astronauts, and Roscosmos cosmonauts the basic theoretical and practical knowledge of geology and astrobiology and trained them in the field. Hence developing independent field skills, including working with a remotely located science team, is a key part of the training. For this reason, classroom and field lessons are tightly interwoven so that the concepts introduced in the classroom are shown in the field soon afterwards. The primary field sites selected for the course are the Permo-Triassic sedimentary sequences in the Italian Dolomites, analogue to the Martian alluvial plains ones, the impact geological environment of the Ries Crater, Germany, a comprehensive suite of volcanic emplacements and deposits in Lanzarote, Spain, and the anorthosite outcrops, analogue to lunar highlands rocks, in Lofoten, Norway. Each site is used as a base to deliver the main learning sessions, respectively: 1) Earth geology, rock recognition and sedimentology on Earth and Mars, 2) Lunar geology and impact cratering, 3) volcanism on Earth, Moon, and Mars, and astrobiology 4) intrusive rocks and lunar primordial crustal evolution. The four sessions are designed to increase the trainees' autonomy in the field up to autonomously executed geological traverses including sampling activities. Whilst PANGAEA's primary focus is astronaut training, where appropriate, technologies being developed for future missions are used to evaluate their performances in analogue field environments and to train the astronauts in using technologies that might support future missions.

Introduction

In 2016 some of the authors proposed to ESA the first field course for astronauts in geological and astrobiological planetary exploration named PANGAEA (Planetary ANalogue Geological and Astrobiological Exercise for Astronauts). This was possible thanks to the far-sightedness of prof.



Debei which immediately understood the potential of a course like PANGAEA for future human exploration of the Moon and Mars and made available all the needed facilities of the University of Padua to carry out the first edition which was attended by the ESA astronauts Luca Parmitano, Pedro Duque and Matthias Maurer. Other 4 editions of the training have been implemented since 2016, with a sixth one foreseen in 2023. In total, 10 astronauts from ESA, NASA and Roscosmos and additional 5 non-astronaut trainees including space engineers, EVA and operation specialists have attended the course. In this work we will summarise the course strategy, structure and lessons learned, but for a more detailed description the reader is referred to Sauro et al. [1] .

Goals and structure

The course forms part of the basic and pre-assignment training for European astronauts, and is open to trainees from other agencies. Significant focus is given to skills relevant to future field exploration, such as practical geological and geobiological field training, execution of self directed traverses in the field, ability to provide clear scientific descriptions of geological landscapes and features, and efficient documentation of sampling sites. For this reason, although minor portions of the course are taught in classrooms, most of the activities are in analogue geological environments, as done in the seventies during the preparation for the Apollo missions [1, 2]. PANGAEA course integrates both geology and astrobiology (including planetary protection) enabling overlapping concepts and ideas to be explored thoroughly. Trainees also have the opportunity to practice conducting field science under the additional constraints imposed by realistic spaceflight operational conditions.

Teaching in analogue sites

The primary field sites selected for the course are Permo-Triassic terrigenous sequences in the Italian Dolomites, impact lithologies in the Ries Crater, Germany, a comprehensive suite of volcanic deposits in Lanzarote, Spain and the Flakstadøy intrusive complex in the Lofoten archipelago, Norway. Each is used as a base to deliver the main learning sessions, respectively; 1) Earth geology, rock recognition and sedimentology on Earth and Mars, 2) Lunar geology and impact cratering, and 3) volcanism on Earth, Moon and Mars, execution of geological traverses, and sampling techniques and 4) Anorthosite and Mg-Suite intrusive complexes and lunar highlands. Classroom lessons are conducted at these field sites using local facilities often provided by Geoparks (e.g. Bletterbach Geopark in Italy, Ries Geopark in Germany and Lanzarote Geopark in Canary Islands). For the field work component, trainees are initially shown the basics of field geology and astrobiology during the first two sessions. In the third session they begin a process of becoming independent field scientists conducting geological traverses with realistic scientific goals, such as determine the contact relationship between geological units and the relative timing of events, recognise stratigraphic and tectonic structures, and sample rocks representative of the location or affected by different alteration processes (e.g. hydrothermal alteration). Trainees are

initially accompanied by their instructors, but the coaching is progressively reduced until the field crew is supported by a remote science team, simulating a science back room in mission control.



Fig. 1. a) Self directed traverse in Lanzarote by ESA astronaut Alexander Gerst and NASA astronaut Stephanie Wilson. b) ESA astronaut Samantha Cristoforetti acquiring a microbiological sample in a lava tube in Lanzarote. c) ESA astronaut Matthias Maurer sampling an anorthositic block in Lofoten.; d) NASA astronaut Kathleen Rubins observing at a sample in Ries.

Lessons learned

Astronauts tend to be practically minded, and long theoretical lessons do not provide them with the best opportunity to learn. For this reason each theoretical lesson must be always coupled with field activities and firmly connected to examples on how the specific knowledge can be applied in the future missions. Dissociating lessons from these goals can lead trainees to lose interest and eventually question the point of the learning. For this reason the classroom has been conducted in facilities close to the field sites so that classroom lessons and field trips often occur on the same day.

Typically, field trips used for academic teaching involve visiting locations to learn more about a particular environment in context. For training astronauts, these types of field trips are still important, however bringing in some elements of planetary surface exploration and in field scientific research realism is pivotal to sustain trainees motivation and knowledge retention. PANGAEA achieves these objectives performing increasingly autonomous traverses through geological landscapes with predefined science goals and remotely located science teams. This contextualises the knowledge trainees gained through the regular field trips in a planetary exploration setting and promote the trainee's independence forcing a flexible execution in the field. Adding to the traverses real scientific objectives, defined with the local experts, with potential for

further science advancements and publications, is also a very important motivational factor fostering the engagement of the trainees.

The course is also very enriching for the scientists involved who had to learn about operational constraints and simplify the communication to be the most effective as possible.

When available, traverses should include technological capabilities relevant to planetary exploration. Although the exact set of capabilities for EVAs on the lunar or Martian surface are yet to be designed and built, the core concepts of scientific data collection, documentation, and communication can still be effectively demonstrated by using Commercial off-the-shelf (COTS) hardware, prototypes and low TRL (technology readiness level) instruments to emulate the capabilities that should be available to astronauts conducting geological exploration on the Moon or Mars. This includes ways to collect images, notes, spectra, and other scientific data [e.g. 3]. Incorporating such systems into the training was found to be a highly effective way to allow astronauts to understand the types of information required for performing effective science during planetary surface exploration with remotely located science teams. Overall, it allowed them to appreciate the importance of quality data collection for enabling scientific interpretation.

Conclusion

The time constraints and areal extent of lunar surface exploration will be extended significantly during future Artemis missions thanks to the technological advancements made since the Apollo era. It is therefore particularly important to train astronauts to self-directed field work and efficient communication with ground based science teams. Astronauts that will be not specifically launched to the Moon or Mars, will be in any case likely involved in the planning, preparation and implementation of such missions. Training key personnel in geology and astrobiology in terrestrial field analogues as in the ESA-PANGAEA course will be essential to the success of such expensive and high-risk endeavours

References

- [1] Sauro F. , Payler S. J., Massironi M., Pozzobon R., Hiesinger H., Mangold N., Cockell C. S. , Martínez Frias J., Kullerud K., Turchi L., Drozdovskiy I., Bessone L., (2023). Training astronauts for scientific exploration on planetary surfaces: the ESA PANGAEA programme. *Acta Astronautica* 204, 222-238. <https://doi.org/10.1016/j.actaastro.2022.12.034>
- [2] Schmitt H. H, Snoke, A., Helper, M., Hurtado, J., Hodges, K. and Rice, J., (2011) Motives, methods, and essential preparation for planetary field geology on the Moon and Mars. *Geological Society of America Special Papers*, 483, 1-1. [https://doi.org/10.1130/2011.2483\(01\)](https://doi.org/10.1130/2011.2483(01))
- [3] Turchi Payler, S.J., Sauro, F., Pozzobon, R., Massironi, M. and Bessone, L. (2021) The Electronic FieldBook: A system for supporting distributed field science operations during astronaut training and human planetary exploration. *Planetary and Space Science*, 197, 105-164. <https://doi.org/10.1016/j.pss.2021.105164>

Front cover for space optical telescopes. a legacy from ROSETTA to JUICE

G. Parzianello^{1,a,*}, M. Bartolomei^{2,b}, S. Chiodini^{2,c}, M. Zaccariotto^{2,d},
G. Colombatti^{2,e}, A. Aboudan^{2,f}, C. Bettanini^{2,g}, S. Debei^{2,h}

¹ European Space Research and Technology Centre – European Space Agency - ESA-
ESTEC, Kepleerlaan 1 - Noordwijk (NL)

² CISAS - Center for Studies and Activities for Space "Giuseppe Colombo", University of
Padova, via Venezia 15, Padova (Italy)

^agiorgio.parzianello@esa.int, ^bmirco.bartolomei@unipd.it, ^csebastiano.chiodini@unipd.it,
^dmirco.zaccariotto@unipd.it, ^egiacomo.colombatti@unipd.it, ^falessio.aboudan@unipd.it,
^gcarlo.bettanini@unipd.it

Keywords: Front Door, Cover, Telescope, Space Mechanism, Rosetta, JUICE

Abstract. The reliability of a telescope's front cover for a space mission constitutes its primary demand, not to compromise the functionality of the entire instrument. Avoidance to expose possible reference surfaces to the external environment and contamination often drives the selection of the motion of the cover. The Front Door Mechanism (FDM) for the OSIRIS experiment of the ROSETTA mission has been developed and optimised to provide protection of the telescope, reliable functioning and being single point failure tolerant. Its combined translational and rotational motion allowed also the preservation of internal calibration surface for the entire duration of the mission. The ROSETTA mission was launched in 2004 and reached the comet in 2014 after several gravity assists, and deep space hibernation. It has been orbiting around the comet for roughly two years collecting enormous amount of data of the peculiar celestial body and ended in September 2016. As legacy of the successful design of the front cover for the ROSETTA mission, another cover mechanics (Cover Mechanism – COM) for the JANUS Optical Head Unit of the JUICE mission has been prepared with minor modifications to the initial design. All qualification has been performed and the JUICE mission has been launched successfully on 14 April 2023 and is now travelling towards Jupiter and its moons.

Introduction

Observation and collection of scientific data by means of telescopes is a very widely used approach for instrumentation for space missions. Such instruments allow coverage of very wide spectral ranges, with applications ranging from infrared to X-ray bands and with various techniques from imaging to spectroscopy.

To provide the quality needed to achieve the increasingly demanding scientific objectives, the instruments have to be protected from external contamination that would dramatically degrade the performance. Protection must take place both before and during the mission lifetime, especially with the increase of duration of planned space missions. Cleanliness measures are put in place during the entire assembly phases at different levels, from unit, to instrument, to satellite and also, after integration into the launcher, including purging, where needed.

After the fairing separation, still at low altitudes, the possible contamination comes from residual air density and from auto contamination from satellite outgassing. Finally, for missions with celestial bodies or planetary observation, the presence of an atmosphere or of emissions from the surface can constitute an important source of contamination.



Contamination protection of observation instruments such as telescopes can be increased by the usage of cover systems that close the telescope's baffle opening, thus avoiding direct exposure of the inner parts of the instrument.

By their own nature, covers constitute also one of the highest risks for the instrument itself. A failure of actuation of the cover would in fact result in the entire loss of the instrument.

Reliability of such systems plays therefore the main focus in their design and development, and redundant solutions to make them failure tolerant is one of the prime objectives of a proper cover design approach.

Several papers have been published describing the design and test results of the Front Door Mechanism (FDM) of the OSIRIS instrument [2, 3]. This paper deals mainly with the main concepts and the relevant aspects that enhanced the proven robustness and flexibility of the FDM and the heritage of its design for the JANUS instrument of the JUICE mission. The two missions are significantly different, but with similar telescope's protection needs.

FDM design

OSIRIS (Optical, Spectroscopic and Infrared Remote Imaging System) is one of the instruments of the ROSETTA mission, an ESA cornerstone science spacecraft launched in 2004 to study in close proximity a comet.

The OSIRIS instrument is composed by two telescopes, the Wide Angle Camera (WAC) and the Narrow Angle Camera (NAC) providing wide and detailed optical imaging of the comet. Some subsystems of both telescopes are identical, such as the Front Door Mechanism (FDM), the Shutter Mechanisms (SHM), the Shutter Electronics (SHE), the Filter Wheel Mechanism (FWM) [1]. Among the peculiarities of the ROSETTA mission, for the instruments protection concept, the long journey in hibernation to reach the comet and the long observation period around the comet during its rising activity while approaching the Sun are the two main drivers of the conceptual selection for the protection cover system for both telescopes. Rather than a significantly simpler one-off opening system, a fully reversible mechanism approach has been chosen to allow the repeated closure and protection of the telescope in case of adverse conditions.



Figure 1: Front Door Mechanism Flight Model in open position during characterisation (left) and mounted on the Flight Model WAC telescope (right)

The possibility to select a variable lift of the cover from the baffle, appeared quickly as a significant advantage allowing the selection of tightness of the closure and avoiding any possible adhesion risk during the long hibernation phase. The inner surface of the cover is used as reference for the instrument internal calibration, and as such, avoiding its direct exposure to the external space, to avoid its contamination, became also a concept driver. A 3D motion achieved by the combination of a double cam system, linked by an internal pin has been finally selected for the actuation mechanism.

The Front Door Mechanism (FDM) during the opening motion performs four different phases:

- 1) Unlocking

- 2) Initial translational lift
- 3) Rototranslation to achieve final lift and rotation of 90 degrees
- 4) Locking

The cover motion is determined by the joint interaction of the internal pin, the fixed external cam and the moving internal cam, driven by a stepper motor. Fig. 2 explains the coupling concept. By the definition of the shape of the internal and external cam the desired motion can be achieved. This allows great flexibility in the motion to be performed by the cover.

One peculiarity of the cam design is its self-locking feature, both in closed and in open position. This allows the maintenance of the position without any power and is obtained by the kinematic design of the cams. A rotation of the inner cam of more than 45 degrees is needed to unlock the system from any of the two locked positions. No motion of the cover (except for compliance in the cams and couplings) is possible before the resting position, fully closed or fully open, is unlocked.

Various measures are also implemented to minimise any risk of jamming of the relative motion between the cams, pin and cover shaft, including main guiding bearings, various bushes and additional kinematical bearings. Moreover, on top of the standard redundancies included in the mechanism design, another additional fail-safe system, completely independent from the nominal motion and capable of opening irreversibly the field of view has been implemented inside the cover arm.

Light and dust tight closure is achieved by preloading the cover against the baffle using the stiffness of the arm, and also variable preload is possible.

On top of verification of the qualification requirements tests, including lifetime tests (> 10000 activations) on the QM model, an accurate characterisation of the performance and the repeatability of the parameters, especially those available in the telemetry, has been performed for each model.

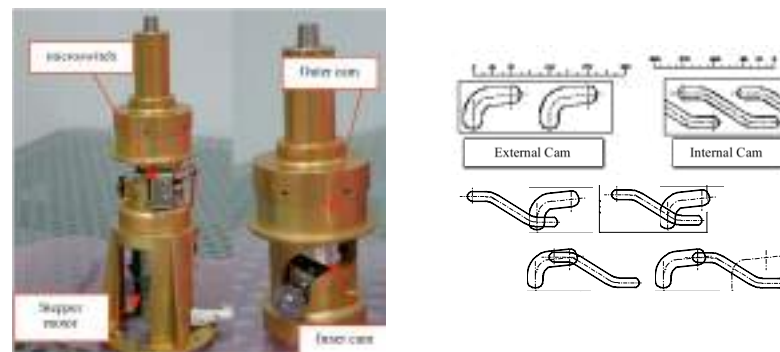


Figure 2: Front Door mechanism description (left) and cam design and conceptual interaction during the four phases(right)

In orbit

ROSETTA was launched on 2nd March 2004 for a long journey toward the encounter with the comet 67P/Churyumov-Gerasimenko that eventually happened in August 2014, after a series of gravity assist manoeuvres, Mars and asteroids fly-bys and after more than three years of hibernation and six months of orbits correction and approach to manage orbiting around the comet with a newly discovered and quite irregular shape [4].

During all the phases of the mission the Front Door Mechanism both of WAC and of NAC cameras operated flawlessly from the commissioning phase to the end of mission. They allowed

the tight closure of the telescopes baffles openings during the initial phases, provided the telescopes' internal calibration reference surface and protected from contamination the optical elements during the spacecraft journey and when the instrument was not in use.

Its design proved its robustness, versatility and reliability allowing the extraordinary achievements of the OSIRIS experiment of the pioneering ROSETTA mission [5, 6, 7].

Legacy: JANUS instrument for the JUICE mission

On 14th April 2023, almost 20 years after the launch of ROSETTA, the JUICE satellite was launched, carrying onboard as one of the instruments JANUS, a narrow angle camera imager in the visible range. The JUICE mission aims to explore the Jovian moons (Ganymede, Europa and Callisto), including ocean layers and subsurface water reservoirs, magnetic field and geological features. It will reach Jupiter in January 2031 after a 7.6-year travel with various Earth–Venus–Earth–Earth gravity assist manoeuvres. JANUS instrument will enable visible wavelength imaging, crucial for understanding the formation and characteristics of various geological features, surface processes and erosion/deposition processes on icy satellites.

JANUS consists of independent subsystems, including the Optical Head Unit (OHU), Proximity Electronics Unit (PEU), Main Electronics Unit (MEU), and Interconnecting harness. The COVer Mechanism (COM), used to protect JANUS and its delicate optical elements, is a direct derivation of the innovative design used for the FDM for the OSIRIS telescopes. It ensures protection of the OHU from contamination and provides a reference surface for telescope calibration during the mission [8].

Considering the very successful design of the Front Door Mechanism (FDM) for the OSIRIS experiment on ROSETTA, along with similar requirements and the nominal operation of the mechanism throughout an Interplanetary mission, it was decided to adapt the FDM to craft the COVer Mechanism (COM) for JANUS.

The main functional and environmental requirements for JANUS' cover mechanism are in fact similar: protection of optics and detectors from sunlight and contamination, offer different positions for various flight conditions (closed-locked for launch, closed-not locked for cruise, open-locked for observation and calibration. Reliability and single-point failure tolerance is also obviously required, as it is the case for all instrument covers, as already discussed.

The main differences in the design of JANUS' COVer Mechanism (COM) compared to ROSETTA's FDM are as follows.

Some geometric parameters needed adjustment such as the arm size and the body height and a partial redesign of the fail safe system. The geometry of the internal cams was also optimised for minimal resistant torque. Moreover, the material for the sealing under the door has been modified, while maintaining the same goals of dust and light tightness and vibration damping.

Fig. 3 shows the JANUS COM subsystem final design and flight model.



Figure 3 : COM subsystem and its components in rendering (left), flight model (centre), during vibration tests (right).

The JANUS COM successfully underwent the full qualification campaign maintaining its functional performance unaltered. It has been successfully integrated in JANUS instrument and onboard JUICE satellite and successfully launched in April 2023.

Conclusions

The innovative design of the cover system developed for the protection of the telescopes of the OSIRIS experiment of the ROSETTA mission, allowed a variety of options in its utilisation, from full dust and light tightness, to just partial detachment from the baffle surface and also provided the reference surface for internal calibration of the instrument.

Its reliability and robustness in wide range of operative conditions has been the main focus due to the extreme criticality of its potential failure, and it has been demonstrated during the entire mission

Acknowledgements:

This paper has been intended as a short overview and reflection on how a robust and adaptable design of a space unit could serve the needs of very different missions, decades away in time. Gratitude goes to all the many ones who contributed in several ways to realisation of the units from the very first prototype to the recently flown ones. A special mention and memory is deserved for our colleague and friend **Stefano**. He made, among many other things, also this legacy possible. We all owe him a lot!

References

- [1] H. U. Keller, C. Barbieri, P. Lamy et al., "OSIRIS – The scientific camera system onboard Rosetta", *Space Science Reviews* 128(1): 433-506 – February 2007
- [2] S. Debei, M. De Cecco, G. Parzianello, A. Francesconi, F. Angrilli, "Design, Qualification and Acceptance of the Front Door Mechanism for the OSIRIS experiment of ROSETTA mission", *International Symposium on Optical Science and Technology – 9th September 2002– Seattle, WA (USA) – Proceedings Volume 4771*. <https://doi.org/10.1117/12.482161>
- [3] G. Parzianello, S. Debei, F. Angrilli, "Reliability oriented design and testing of a telescope's front cover for long life space missions", *54th Congress of the International Astronautical Federation (IAF) – 29 September – 03 October 2003 – Bremen, Germany*. <https://doi.org/10.2514/6.IAC-03-IP.10>
- [4] F. Preusker, F. Scholten et al, "The global meter-level shape model of comet 67P/Churyumov-Gerasimenko", *Astronomy & Astrophysics*, Vol 607, L1 (2017).
- [5] H. Sierks et al., "E-type asteroid (2867) steins as imaged by OSIRIS on board Rosetta", *Science*, vol. 327, no. 5962, pp. 190-193, 2010. <https://doi.org/10.1126/science.1179559>
- [6] H. Sierks et al., "On the nucleus structure and activity of comet 67P/Churyumov-Gerasimenko", *Science*, vol. 347, no. 6220, January 2015.
- [7] A. Accomazzo, P. Ferri, S. Lodiot, J.L. Pellon-Bailon, A. Hubault, J. Urbanek, et al., "The final year of the Rosetta mission", *Acta Astronautica*, vol. 136, pp. 354-359, July 2017. <https://doi.org/10.1016/j.actaastro.2017.03.027>
- [8] Della Corte, Vincenzo, et al. "Scientific objectives of JANUS Instrument onboard JUICE mission and key technical solutions for its Optical Head." *2019 IEEE 5th International workshop on metrology for aerospace (MetroAeroSpace)*. IEEE, 2019. <https://doi.org/10.1109/MetroAeroSpace.2019.8869584>

Vibroacoustics

In-vacuo structured fabrics for vibration control

Paolo Gardonio^{1,a*}, Sofia Baldini^{1,b}, Emiliano Rustighi^{2,c},
Ciro Malacarne^{3,d}, Matteo Perini^{4,e}

¹DPIA, Università degli Studi di Udine, Via Delle Scienze 206, 33100, Udine, Italy

²DIEA, Università degli Studi di Trento, Via Sommarive 9, 38123 Trento, Italy

³ProM Facility – Trentino Sviluppo S.p.A., Via Fortunato Zeni 8, 38068 Rovereto (TN), Italy

^apaolo.gardonio@uniud.it, ^bbaldini.sofia@spes.uniud.it, ^cemiliano.rustighi@unitn.it,

^dciro.malacarne@trentinosviluppo.it, ^ematteo.perini@trentinosviluppo.it

Keywords: Tunable Structured Fabric, In Vacuo Material, Adaptive Material, Tuneable Vibration Absorber

Abstract. This paper presents a study on a new tuneable material for vibration control purposes. The material is formed by a structured fabric wrapped in a deflated bag. The fabric is made of an interwoven mesh of rigid truss-like particles. The vacuum inside the casing produces a jamming effect. Hence, the elasticity and damping of the packaged fabric can be tuned by changing the level of vacuum in the bag. This material can be conveniently employed to develop new vibration control treatments and devices. In this respect, the paper first presents the tests carried out with a six-point bending machine to characterise the static and dynamic stiffness of the material as well as its damping properties. Then it demonstrates an application, where the material is used as a tuneable vibration absorber.

Introduction

The material considered in this paper presents is formed by a structured fabric wrapped in a vacuum casing [1]. The fabric is made by an interwoven mesh of rigid truss-like particles, which forms a loose flexible construction, such as for example a chain mail armour. The fabric is packaged into a deflated plastic bag, whose level of vacuum is controlled online with a micro-compressor. The vacuum generated inside the casing produces a jamming effect, which results from both interlocking and friction between neighbouring particles [2]. In this way, the elasticity and damping of the packaged fabric can be conveniently tuned by changing the level of vacuum in the case. The result is thus a tuneable lightweight material, which can be effectively employed to develop new treatments, e.g., tuneable liners, and devices, e.g., Tuneable Vibration Absorbers (TVA), for passive and semi-active vibration and noise control [3,4].

Material layouts and test facilities

This paper presents two types of experiments on prototype beam-like in-vacuo structured fabrics, which, as shown in Fig. 1 and summarised in Table 1, encompass either single- or double-mails made with cubic, octahedral, spheric truss-like particles. As shown in Fig. 2a, In the first experiment, the beam-like in-vacuo fabrics are pinned at the two ends and excited in the middle by a shaker via a pinning jaw such that they work as pinned beams excited in bending. As shown in Fig. 2b, in the second experiment, the beam-like in-vacuo fabrics are mounted on a shaker such that they work as “flapping vibration absorbers”. Table 1 summarises the principal properties of the structured fabrics analysed in this study.



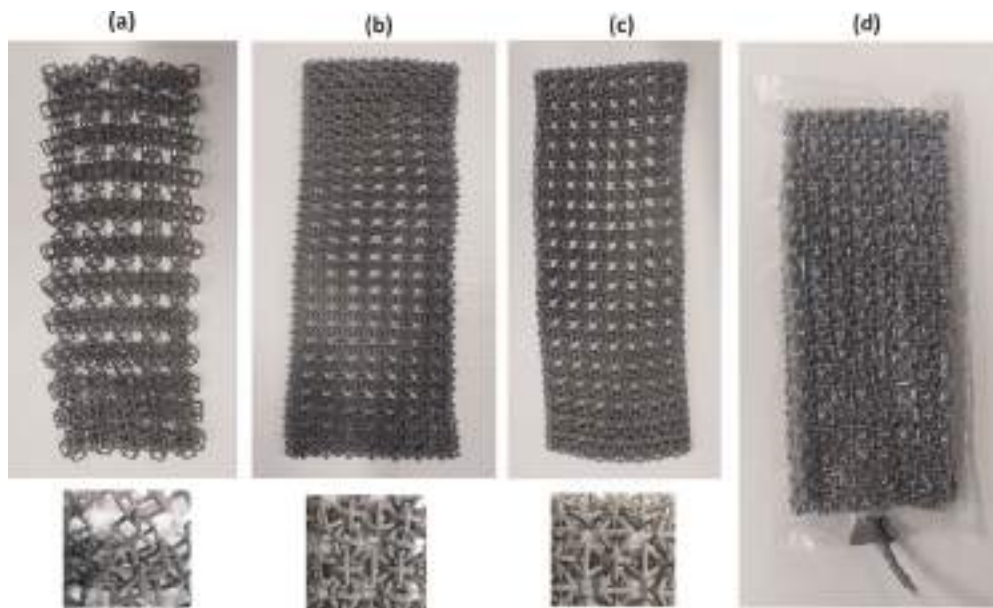





Fig. 1 structured fabrics made with (a) cubic, (b) spherical octahedral, (c) octahedral chain mails. (d) Beam specimen made by the fabric in a deflated bag.

Table 1: Prototyped structured fabrics studied in this paper with dimensions and weight

Name	Geometry	Width (mm)	Length (mm)	Thickness (mm)	Mass (g)
Spheres		100	210	10	49
Octahedra		110	240	15	62
Cubes		110	190	15	39

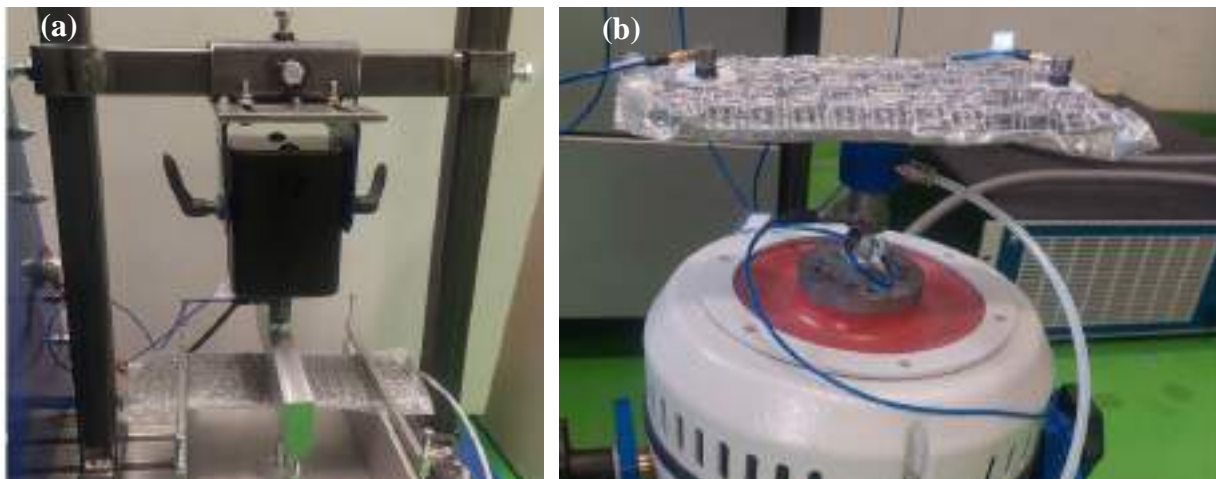


Fig. 2 (a) Six points bending machine with the tested beam specimen. (b) tuneable structured fabric vibration absorber mounted on a shaker vibration source.

Mechanical properties

Figure 3a shows the modulus and phase of the dynamic stiffness measured with the six-point bending machine with respect to the vacuum pressure in the deflated bag with the cubic structured

fabric. The plot shows the typical spectrum of the middle point dynamic stiffness of a simply supported beam, which is characterised by a stiffness-like asymptotic response at low frequencies and a mass-like asymptotic response at high frequencies. At mid frequencies there is a sharp resonance through due indeed to the resonant response of the fundamental bending mode of the beam specimen. The graph shows that the vacuum shifts to higher frequencies the static bending stiffness of the material but has no effect on its apparent mass. As a result, it shifts to higher frequency the fundamental resonance too. Indeed, the graph in Figure 3b shows that, when pressure is increased from 5 kPa to 80 kPa, the resonance frequency of the specimens grows by about 20% to 25%. Also, the specimens with double layer fabrics have about 50 % to 100 % higher resonance frequency than their single layer counterparts. In general, the specimens encompassing the fabrics made with cubic grains show the highest bending stiffness and thus the highest, and widest, resonance frequency ranges. The graph in Figure 3c indicates that the loss factor of the specimens, derived with the half power bandwidth method at the first resonance frequency, are characterised by quite similar values for the three types of fabrics, which are confined between 5 % and 7 % for the single layer configuration and between 5.5 % and 9 % for the double-layer configuration.

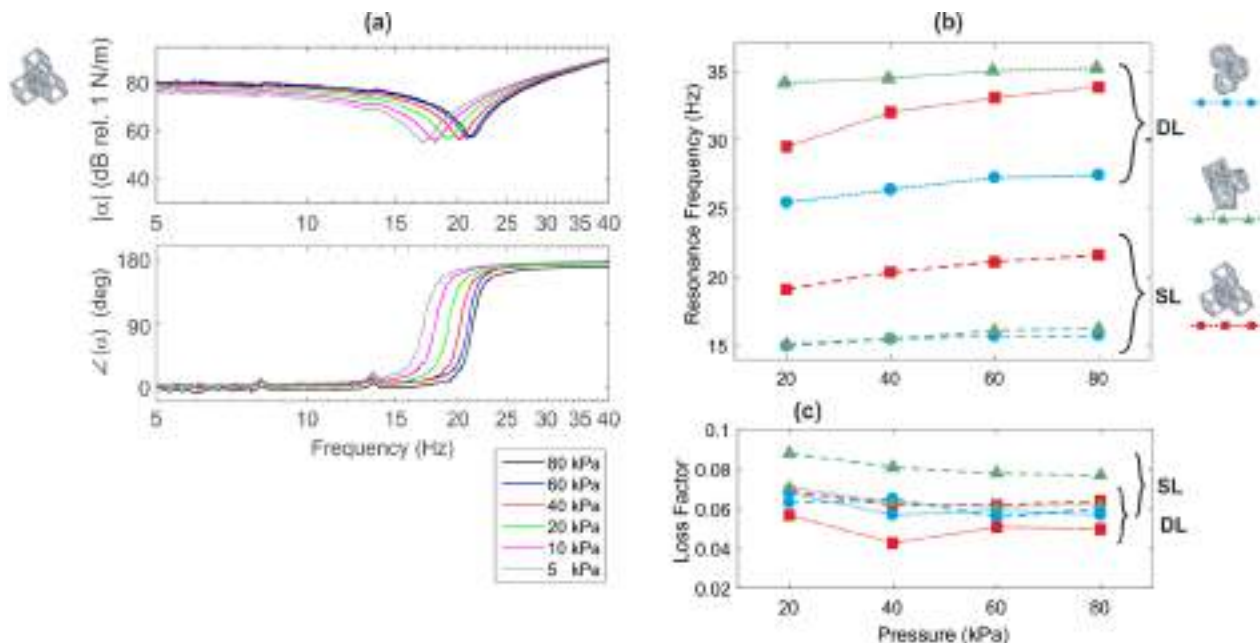


Fig. 3 Dynamic stiffness frequency response function (a) and resonance (b), loss factor (c) parameters with respect to the vacuum pressure.

Tunable Vibration Absorber

The beam specimen can be suitably used to construct a TVA. For instance, Fig. 2b shows a prototype device, which is mounted on the vibration table of a big shaker. In this case, the structured fabrics are insert in a fully sealed plastic bag, which is equipped in the middle span with a sealed inlet port built in plastic using 3D printing technology. In this way the in vacuo structured fabric acted as a two-arms beam clamped in the middle span to the inlet port, which acts as a post too. Indeed, the inlet port was designed in such a way as it served both as a connector for the vacuum tube and as a mechanical joint to fix the two-arms in-vacuo structured fabric beam to the hosting mechanical system. The vacuum was generated with an off the shelf pump and a simple circuit encompassing two valves and a vacuum gauge.

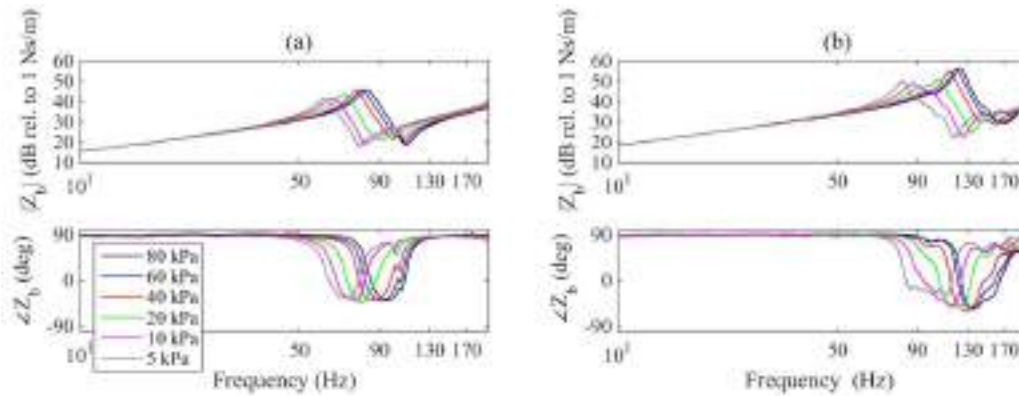


Figure 4: Impedance response for cubes assembled with one (a) or two (b) overlapped layers.

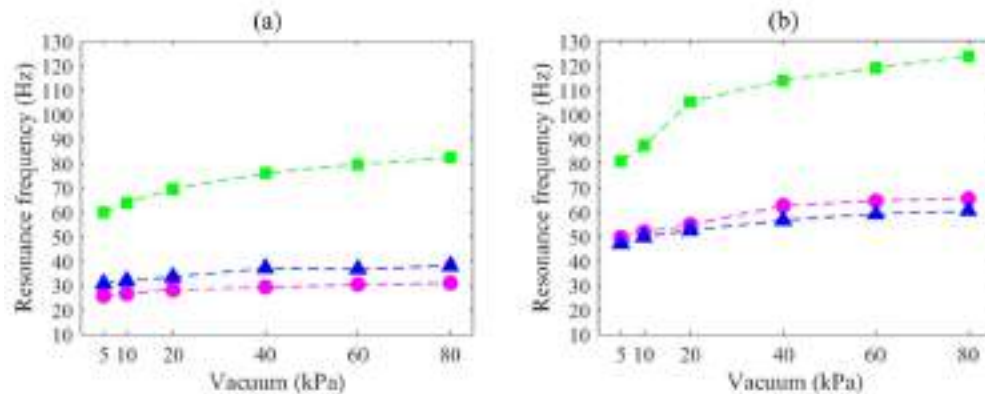


Figure 5: Measured resonance frequency of the tuneable structured fabrics assembled with one (a) or two (b) overlapped layers. Magenta for spheres, blue for octahedra and green for cubes.

Figure 4 shows the modulus and phase of the base impedance measured on the specimens encompassing either a single (left hand side plots) or a double (right hand side plots) cubic fabric vibration absorber with reference to vacuum pressure that grows from 5 kPa to 80 kPa. The spectra show the typical base impedance of a seismic mass connected to a base mass via a spring damper lumped element. Indeed, at low frequencies the spectrum is characterised by a modulus that rises proportionally to the circular frequency and a constant phase value of about $+90^\circ$. There is then a resonance peak followed by an antiresonance through, with the phase that initially falls down to -90° and then recovers to $+90^\circ$. At higher frequencies the spectrum shows again a modulus that rises proportionally to the circular frequency and a phase that maintains the $+90^\circ$ value. All this indicates that at low and high frequencies the device presents a mass effect. More precisely, measurements taken with the accelerometers have shown that at low frequencies the in-vacuo structured fabric beam behaves as a solid body together with the junction component, with negligible flapping effects. Therefore, the base impedance is given by the whole mass of the beam and base component. Alternatively, at higher frequencies, despite the base vibrations, the two ends of the in-vacuo structured fabric are characterised by little vibrations such that the base impedance is controlled by the mass of the base component. At resonance frequency the two ends of the in-vacuo structured fabric display large counter oscillations to the base oscillations, which generate the desired vibration absorption effect. The extent of these oscillations is controlled by the damping of the in-vacuo structured beam. Normally, to counteract harmonic vibrations, the vibration absorber is tuned in such a way as it resonates at the tonal disturbance and its damping is kept to the minimum possible value such that the hosting structure faces a large impedance load.

Alternatively, for broadband vibrations the vibration absorber is tuned in such a way it resonates at the resonance frequency of the hosting system, but in this case the damping is brought up such that the double resonant response of the combined hosting structure-TVA modes is optimally dampened.

Overall, the graphs shown in Fig. 5 indicates that the resonance frequency of the TVAs can be suitably shifted to higher/lower values by increasing/lowering the level of vacuum in the bags. For the 5 to 80 kPa pressure range, the single layer TVAs are characterised by resonance frequencies comprised between 60-85 Hz (cube grains), 25-30 Hz (sphere grains), 30-40 Hz (octahedra grains). Alternatively, the double layer TVAs are characterised by resonance frequencies comprised between 80-125 Hz (cube grains), 50-65 Hz (sphere grains), 45-60 Hz (octahedra grains). This confirms that the resonance frequency of the TVAs can be suitably tuned over significant ranges by varying the vacuum pressure. Moreover, these ranges can be further enlarged by adopting multiple layers with combinations of different grains.

Summary

The experiments presented in this paper have shown that the bending stiffness of the in vacuo structured fabric beams can be suitably varied by changing the vacuum pressure in the bag. This effect depends on the type of elementary truss grains of the fabric and on the number of layers wrapped in the bag. For instance, the cubic and octahedral fabrics offers the highest bending stiffness respectively for the single- and double-layer configurations. When the vacuum pressure is raised from 5 to 80 kPa, the stiffness of two-layers cubic fabric beam is doubled. Also, the double layer octahedral structured fabric shows 5 times higher stiffness than the single layer one. These properties can be suitably employed to shift the resonance frequency of the fundamental flapping flexural mode when the in vacuo structured fabric is operated as a vibration absorber. For instance, the study has shown that, for 5 to 80 kPa pressure range, the resonance frequency of either the single- or double-layer vibration absorbers can be increased by 30% to 40%. Also, the resonance frequency of the double layer vibration absorbers is about 50% higher than that of the single layer absorber.

References

- [1] Y. Wang, L. Li, D. Hofmann, J. E. Andrade, and C. Daraio, Structured fabrics with tunable mechanical properties, *Nature*, 596 no. 7871, (2021) 238–243. <https://doi.org/10.1038/s41586-021-03698-7>
- [2] R. P. Behringer and B. Chakraborty, The physics of jamming for granular materials: a review,” *Reports on Progress in Physics*, 82 no. 1, (2018). <https://doi.org/10.1088/1361-6633/aadc3c>
- [3] E. Rustighi, P. Gardonio, N. Cignolini, S. Baldini, C. Malacarne, M. Perini, Vibration response of tuneable structured fabrics, In proceedings of the International Conference on Noise and Vibration Engineering (ISMA 2022), Katholieke Universiteit Leuven, Belgium, 12–14 September 2022.
- [4] S. Baldini, E. Rustighi, P. Gardonio, C. Malacarne, M. Perini, Invacuo structured fabric tuneable vibration absorber, In Proceedings of the X ECCOMAS Thematic Conference on Smart Structures and Materials (SMART 2023), Patras, Greece, 3 - 6 July 2023. <https://doi.org/10.7712/150123.9779.444503>

Experimental application of pseudo-equivalent deterministic excitation method for the reproduction of a structural response to a turbulent boundary layer excitation

Giulia Mazzeo^{1,a *}, Mohamed Ichchou^{1,b}, Giuseppe Petrone^{2,c}, Olivier Bareille^{1,d},
Francesco Franco^{2,e}, Sergio De Rosa^{2,f}

¹LTDS— Laboratoire de Tribologie et Dynamique des Systèmes, Ecole Centrale de Lyon Ecully
69130, France

²PASTA LAB — Laboratory for Promoting Experiences in Aeronautical Structures and
Acoustics, University “Federico II” of Naples, Naples 80125, Italy

^agiulia.mazzeo@ec-lyon.fr, ^bmohamed.ichchou@ec-lyon.fr, ^cgiuseppe.petrone@unina.it,
^dolivier.bareille@ec-lyon.fr, ^efrancesco.franco@unina.it, ^fsergio.derosa@unina.it

Keywords: Turbulent Boundary Layer (TBL), Wall-Pressure Fluctuations (WPFs), Structural Vibrational Response, Deterministic Forces

Abstract. The use of wind tunnels for studying the vibrational response of structures subjected to turbulent flows presents various challenges, such as background noise and complex setup requirements. This work introduces an alternative experimental method called X-PEDEm (eXperimental Pseudo-Equivalent Deterministic Excitation) that aims to reproduce an equivalent structural response to a Turbulent Boundary Layer (TBL) excitation without the need for a wind tunnel. X-PEDEm involves coupling the experimental acquisition of the structure's vibrational response with deterministic forces, such as an impulse force from a hammer, followed by post-processing. The method has been validated for different boundary conditions and flow speeds, offering versatility in recreating various types of TBL. While not an exact reproduction of turbulent flow-induced responses, X-PEDEm provides an optimal approximation with low time and resource requirements, making it easy to implement experimentally.

Introduction

In the field of transportation vehicle design and production, such as aircraft, ships, trains, and automobiles, there is ongoing research on the sound emissions caused by the interaction between fluids and structures. A key area of focus is predicting how structures respond to Wall-Pressure Fluctuations (WPFs) generated by a Turbulent Boundary Layer (TBL).

Currently, researchers rely on semi-empirical models, often represented as 2-points Cross-Spectral Density (CSD) functions like the Corcos model [1]. However, these models can be computationally intensive when applied in Finite Element Analysis (FEA) and have limitations in representing responses across a broad frequency range [2]. Consequently, there is a growing interest in alternative experimental methods for predicting the structural response to TBL excitation. Many researchers have used loudspeakers as a means to reproduce a TBL-like pressure field, but this approach can also present challenges [3, 4].

In this study, the authors aim to experimentally validate an alternative method based on the Pseudo-Equivalent Deterministic Excitation method (PEDEm) [5]. The potential of PEDEm and its numerical validation for experimental purposes have been previously presented [6]. Here, the focus is on experimentally validating the application of PEDEm, referred to as X-PEDEm, considering different sample panels under different boundary conditions and subjected to TBL excitation at various flow velocities.



Background theory and methodology

Leaving the reader free to explore how PEDEm was created and developed [5, 6], here the main formulations are presented in Eq. 1-3 and discussed.

$$[S_{FF}(\omega)] = \sum_{i=1}^{NG} d_i(\omega) \{\Theta^{(i)}\} \{\Theta^{(i)}\}^T \quad (1)$$

$$\{w(\omega, i)\} = [\Phi][H(\omega)][\Phi]^T \{\Theta^{(i)}\} \sqrt{d_i(\omega)} \quad (2)$$

$$[S_{WW}(\omega)] = \sum_{i=1}^{NG} \{w(\omega, i)\} \{w(\omega, i)\}^T \quad (3)$$

PEDEm is based on the reformulation of the CSD displacement matrix $[S_{WW}(\omega)]$ as shown in Eq. 2 and Eq. 3 by considering the modal decomposition of the CSD load matrix $[S_{FF}(\omega)]$ in eigenvectors $\{\Theta^{(i)}\}$ and eigenvalues $d_i(\omega)$ as expressed in Eq. 1. In particular, PEDEm considers two asymptotic behaviors of these eigensolutions:

- in a low frequency (LF) domain, the eigensolutions represent a spatial distribution totally correlated, for which the eigenvector matrix $[\Theta]$ is an all-1 matrix and only the first eigenvalue is non-null;
- in a high frequency (HF) domain, the eigensolutions represent a spatial distribution totally uncorrelated, for which the eigenvector matrix is an identity matrix, and all eigenvalues are equal and non-null.

X-PEDEm uses the same equations and the same asymptotic behaviors of PEDEm for the post-processing phase of experimental data that can be obtained with an easy experimental campaign as a hammer test. Indeed, X-PEDEm requires just the acquisition of the experimental Frequency Response Functions (FRFs) between acquisition points and excitation points. The acquisition points can be chosen randomly, and they should not be less than five, while the excitation points must respect the position configuration shown in Fig. 1a and they should not be less than ten.

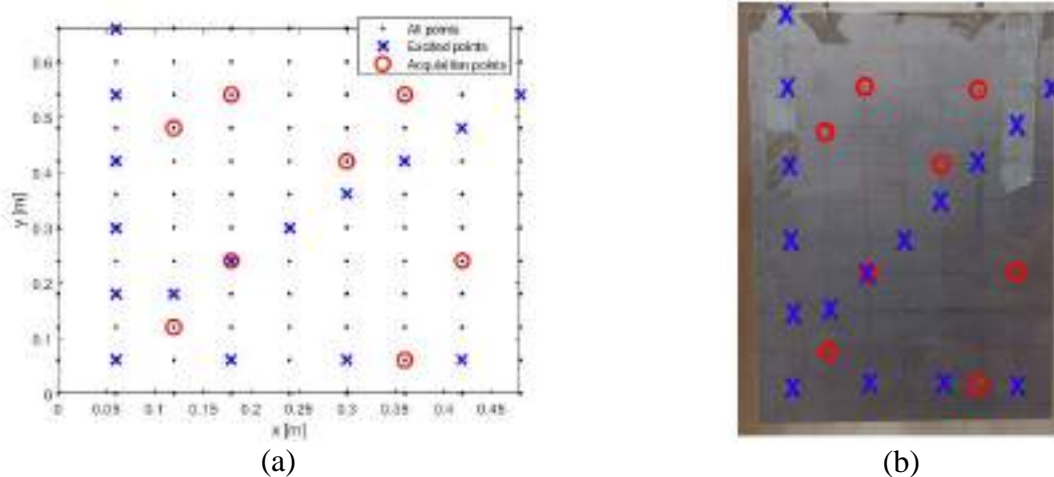


Fig. 1 – Selection of acquisition points (red circles) and excitation points (blue crosses) over the structural mesh of sample panel “PAN_A”. (a) Numerical mesh; (b) experimental mesh.

Experimental method validation

X-PEDEm has been experimentally validated with a hammer test campaign performed over three different sample panels, for three different boundary conditions and for different flow velocities. For a matter of space, only the results for panel “PAN_A” (Fig. 1b), with totally free edges as boundary conditions, are here shown in Fig. 2. The numerical FSR is here considered as reference

solution and it is calculated by using the Corcos model [1] with the following empirical coefficients values: $\alpha_x = 0.116$, $\alpha_y = 0.700$ and $U_c = 0.8U_0$. X-PEDEm, on the other hand, has been evaluated by using the experimental FRFs collected during the hammer test campaign by considering the acquisition and excitation points shown in Fig. 1b. The numerical formulation of X-PEDEm, developed with a MATLAB® code, is shown too for further validation. It is possible to appreciate how X-PEDEm (numerical and experimental) is able to follow the numerical FSR solution for three different flow velocities U_0 . With the increase of U_0 , the convective coincidence frequency f_c increases too. f_c is used as approximated indicator to establish which asymptotic behavior one should refer to: below the f_c , the asymptotic behaviour for LF domain is considered, while above f_c , it is chosen the asymptotic behavior for HF domain.

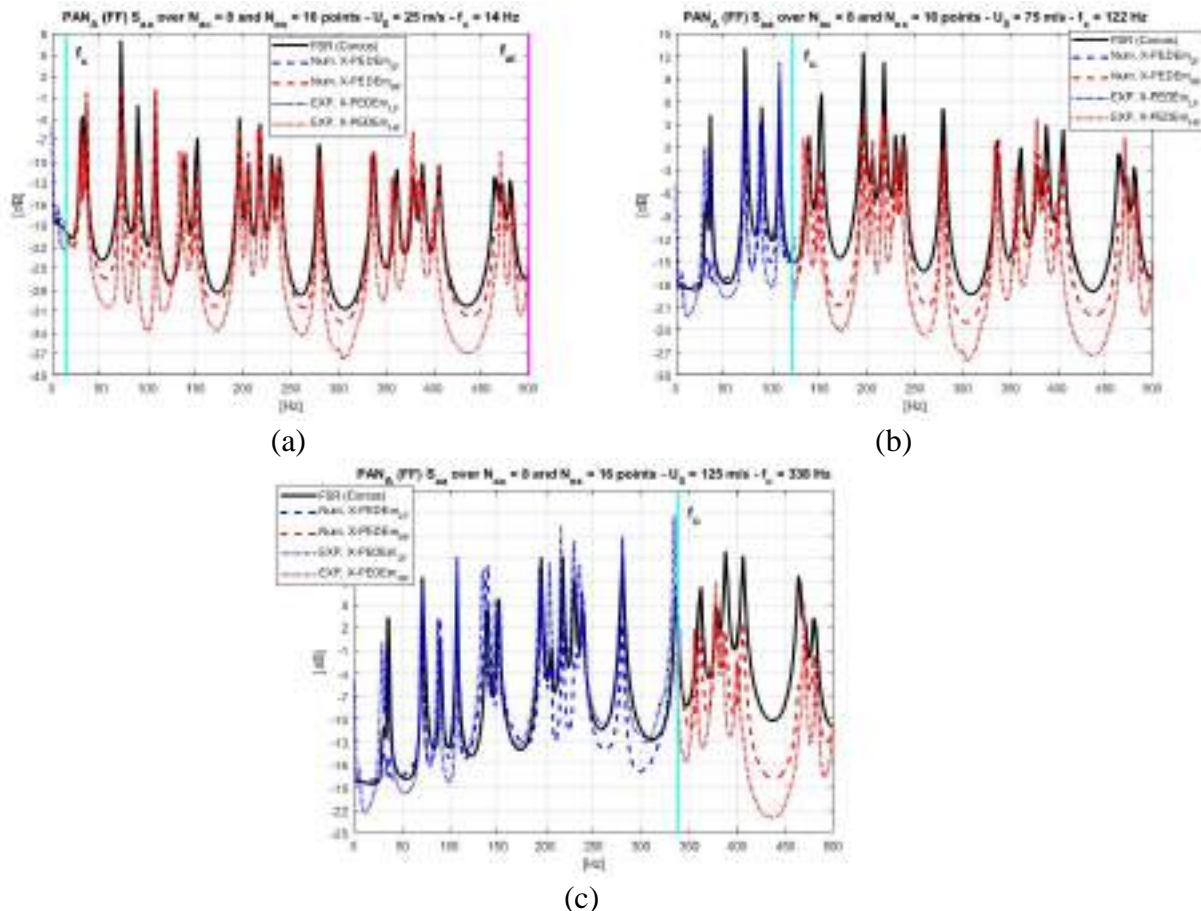


Fig. 2 – Comparison between the FSR calculated with Corcos model (solid black line), numerical X-PEDEm solution (dashed line) and experimental X-PEDEm obtained with a hammer test (dotted line); blue color for X-PEDEm in the LF domain, red color for X-PEDEm in the HF domain. (a) Solution for $U_0 = 25$ m/s; (b) solution for $U_0 = 75$ m/s; (c) solution for $U_0 = 125$ m/s.

Conclusions

X-PEDEm proves to be valid as alternative experimental method for the reproduction of the structural response to a TBL excitation. It can be performed with an easy experimental set-up and with fast post-processing of the experimental data. It ensures versatility for what concerning type of panels, boundary conditions and asymptotic flow velocities. It may be pointed out that a hammer test is not able to maintain reliable FRFs in a broadband frequency region, but X-PEDEm can be performed with different experimental tools, as for example a shaker.

Nevertheless, there are still some open issues:

- It is important to find an accurate indicator that establish the frequency limits for the two asymptotic behaviors.
- A direct comparison between the experimental results obtained in a wind tunnel and the ones obtained with X-PEDEm is required for a final validation of the method.

References

- [1] G. M. Corcos, Resolution of Pressure in Turbulence, *J. Acoust. Soc. Am.* 35, 192–199 (1963). <https://doi.org/10.1121/1.1918431>
- [2] S. De Rosa, F. Franco, Exact and numerical responses of a plate under a turbulent boundary layer excitation, *J. Fluids Struct.* 24, 212-230 (2008). <https://doi.org/10.1016/j.jfluidstructs.2007.07.007>
- [3] M. Aucejo, L. Maxit, J.-L. Guyader, Experimental simulation of turbulent boundary layer induced vibrations by using a synthetic array, *J. Sound Vib.* 331, 3824-3843 (2012). <https://doi.org/10.1016/j.jsv.2012.04.010>
- [4] O. Robin, A. Berry, S. Moreau, Experimental Synthesis of Spatially-Correlated Pressure Fields for the Vibroacoustic Testing of Panels. In: E. Ciappi, S. De Rosa, F. Franco, J.-L. Guyader, S. Hambric (Eds), *Flinovia - Flow Induced Noise and Vibration Issues and Aspects*, Springer, Cham. 2015. https://doi.org/10.1007/978-3-319-09713-8_8
- [5] S. De Rosa, F. Franco, E. Ciappi, A simplified method for the analysis of the stochastic response in discrete coordinates, *J. Sound Vib.* 339, 359-375 (2015). <https://doi.org/10.1016/j.jsv.2014.11.010>
- [6] G. Mazzeo, M. Ichchou, G. Petrone, O. Bareille, S. De Rosa, F. Franco, Pseudo-equivalent deterministic excitation method application for experimental reproduction of a structural response to a turbulent boundary layer excitation, *J. Acoust. Soc. Am.* 152, 1498–1514 (2022). <https://doi.org/10.1121/10.0013424>

Labyrinth quarter-wavelength tubes array for the reduction of machinery noise

G. Catapane^{1,a,*}, G. Petrone^{1,b}, O. Robin^{2,c}, J.-C. Gauthier-Marquis^{3,d}, S. De Rosa^{1,e}

¹ PASTA-Lab (Laboratory for Promoting experiences in Aeronautical Structures and Acoustics), Università degli Studi di Napoli "Federico II", Via Claudio 21, Napoli, 80125, Italy

² Centre de Recherche Acoustique-Signal-Humain, Université de Sherbrooke, 2500 boulevard de l'Université, Sherbrooke, J1K 2R1, Quebec, Canada

³ Innovation Maritime, 53, rue Saint-Germain Ouest, Rimouski, 5L 4B4, Quebec, Canada

^agiuseppe.catapane@unina.it, ^bgiuseppe.petrone@unina.it, ^colivier.robin@USherbrooke.ca, ^djcgmarquis@imar.ca, ^esergio.derosa@unina.it

Keywords: Underwater Noise, Acoustic Resonators, Noise Control

Abstract. Anthropogenic noise from navigation is a major contributor to the disturbance of the acoustic soundscape in underwater environments. The noise generated by ship's machinery exhibits energetic tonal harmonic peaks at multiples of the rotating and firing frequency, that occur in the 20-200 Hz frequency range and difficult to control with classical soundproofing materials. Quarter wavelength tubes (QWT) can be a concrete solution since their absorption peaks are harmonic odd integers of the first resonance frequency. The main issue of QWT is their tuning length, which equals 1.43 m for a 60 Hz resonator. The problem is solved by coiling the tube into a labyrinth. Three labyrinth quarter wavelength tubes are tuned respectively at 60, 90 and 120 Hz. Samples are printed with filament 3D additive manufacturing techniques using PLA and tested with a square impedance tube designed for low-frequency measurements. Measurement results are in good agreement with analytical and numerical predictions. An array including four 60 Hz, four 90 Hz and four 120 Hz labyrinths QWTs is finally tested.

Introduction

The most important source of noise of an internal combustion engine powered vehicle or equipment is usually the engine itself. The sound disturbance produced by a ship is dominated by machinery noise at low speed, and by cavitation and propeller noise at higher speeds.

The low frequency spectrum of the noise produced by an internal combustion engine is dominated by the engine rotating and firing frequencies and the associated harmonics [1]. Most of the internal combustion engines are four-stroke engines and those will be under consideration in this work. The explosion frequency f_{ex} of a four-stroke engine with N cylinders at a given speed rpm can be calculated following:

$$f_{ex} = \frac{N}{2} \frac{rpm}{60}, \quad (1)$$

Let's take as an example a diesel engine that is a 6 cylinder - 4 stroke engine. With symmetric firings, 6 explosions occur on a complete cycle (two crankshaft rotations, and thus three ignition events occur per crankshaft revolution). Vibration measurements were conducted on a CAT C9 diesel engine at *Innovation Maritime*. With an average rotation speed of 1800 rpm, the engine exhibits an explosion frequency $f_{ex} = 90$ Hz. This frequency and its harmonics (multiples of f_{ex}) are generally the most energetic peaks in the noise and spectrum spectra. The two other important

noise generation mechanisms are those associated with the rotation frequency of the crankshaft (in this case, $\frac{rpm}{60} = 30$ Hz) and those generated by the ignition imperfections or unbalance on a complete cycle (typically half of the rotation frequency, $\frac{1}{2} \cdot \frac{rpm}{60} = 15$ Hz). In Figure 1, significant peaks are identified each 15 Hz with a dominance at f_{ex} and its harmonics. This frequency spectrum is common to diesel engines used in the marine industry. Quarter wavelength tubes could be an efficient solution to limit this disturbance. Indeed, a quarter wavelength tube (QWT) is an open-closed tube (Figure 2a) that has resonant frequencies f_{qwt} when the tube length L is an odd-integer multiple of the quarter of the acoustic wavelength $\lambda = c_0/f$:

$$f_{qwt} = \frac{(2m - 1)c_0}{4L}, \quad m = 1, 2, 3 \dots \quad (2)$$

At their successive harmonic resonances, large sound absorption can be achieved, above all for the first harmonics. This behavior is well adapted to the defined problem of reducing the harmonic noise generated by reciprocating engines. One issue is related to the required length for a QWT. To cope with this, the QWT is stretched into a labyrinth (Figure 2b) or following a spiral path, depending on the application, which guarantees similar sound absorption properties compared with a straight tube.

Theory and numerical implementation for labyrinth resonators

The acoustic impedance of a labyrinth resonator (LR) is studied according to the analytical approach proposed by Magnani et al. [2], where the labyrinth resonator is evaluated as a perforated plate followed by a QWT. The QWT of length L has an impedance equal to $Z_{QWT} = -jZ_{eff} \cot(k_{eff}L_{eff})$, based on Low Reduced Frequency theory (LRF) [3], which studies the sound wave propagation with a lossy Helmholtz equation which takes into account viscous and thermal dissipation by modelling the effective density ρ_{eff} and speed of sound c_{eff} , and consequently the effective impedance $Z_{eff} = \rho_{eff}c_{eff}$ and the effective wavenumber $k_{eff} = \omega/c_{eff}$. $L_{eff} = L - (4 - \pi)\frac{d}{2}(n - 1)$ is the effective length to tune a labyrinth resonator, with n number of branches and d width of the channel [4].

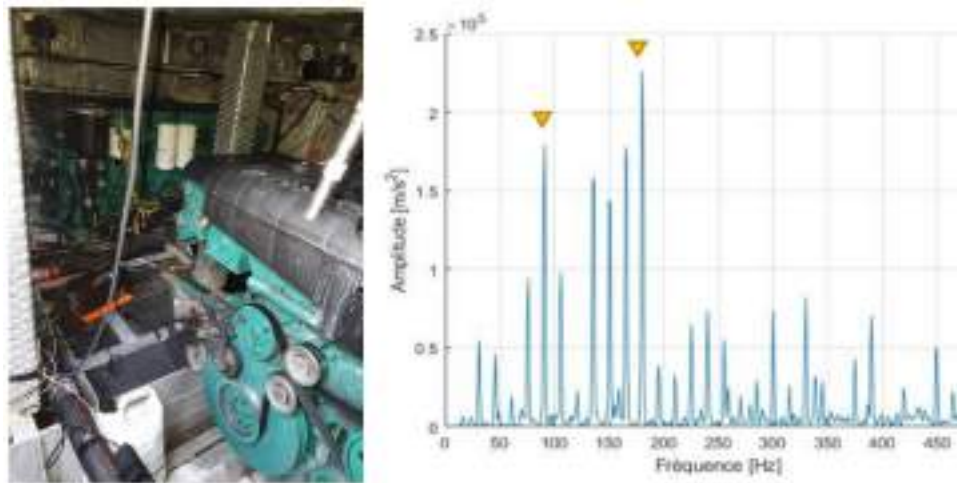


Figure 1: Result of a vibration measurement conducted on the crankshaft axis of a C9 diesel engine. The yellow triangles indicate the firing frequency of the pistons (90 Hz), as well as its first harmonic (180 Hz).

The plate of thickness t_d with the square inlet hole of side-length d is defined through Johnson-Champoux-Allard (JCA) approach [5]. The impedance of the labyrinth resonator Z_{LR} is:

$$Z_{LR} = \frac{1}{\phi_{inlet}} \left[Z_{d,JCA} \frac{-jZ_{QWT} \cot(k_{d,JCA} t_d) + Z_{d,JCA}}{Z_{QWT} - jZ_{d,JCA} \cot(k_{d,JCA} t_d)} \right], \quad (3)$$

where $Z_{d,JCA} = \rho_{JCA} c_{JCA}$ and $k_{d,JCA} = \omega/c_{JCA}$ are respectively the impedance and the complex wavenumber of the perforated plate, with $c_{JCA} = \sqrt{K_{JCA}/\rho_{JCA}}$, ρ_{JCA} and K_{JCA} effective speed of sound, density and bulk modulus. $\phi_{inlet} = A_{hole}/A_{plate}$ is the perforatio ratio between the hole area and the plate area. Labyrinth resonators are positioned inside a box to have several peaks at the desired frequencies. According to the electro-acoustic analogy, this implies that the impedance of the global system Z_{tot} and the sound absorption coefficient α_{theory} are respectively:

$$Z_{tot} = \left[\sum_{i=1}^N \frac{1}{Z_{LR,i}} \right]^{-1} \quad \alpha_{theory} = \frac{4Re(Z_{tot}/Z_0)}{|Z_{tot}/Z_0|^2 + 2Re(Z_{tot}/Z_0) + 1} \quad (4)$$

The sound absorption of the box is experimentally evaluated with a 1 ft x 1 ft impedance tube: a speaker placed at one end of the tube excites it with a normal plane wave radiation, and the sample is placed at the opposite end, backed by a rigid wall. Two microphones separated by a distance s evaluate sound pressure in the tube, with P_2 at a distance x_2 respect to the sample, and P_1 at a distance $x_1 = x_2 + s$. The sound absorption coefficient under normal incidence is estimated according to the ISO 10534-2 1998 standard. Numerical simulations mimic this experimental measurement. Analyses are made with COMSOL Multiphysics, *Pressure Acoustics Module*, with the impedance tube and labyrinth walls considered as rigid.



Figure 2: a) Quarter wavelength tube excited by a plane wave radiation (PWR); b) labyrinth resonator excited by a PWR.

Results

Three labyrinth resonators are modelled with their fundamental resonance peak at 60, 90, 120 Hz, and 3D printed to form a box with multiple resonators to have high sound absorption at 60, 90, 120 and 180 Hz. The latter is the second harmonic of the 60 Hz labyrinth. Their height (thickness of the sample) is fixed at 100 mm, to place them in a limited space. The 60 Hz labyrinth has lateral dimension of 97 mm times 97 mm, the 90 Hz has lateral dimension of 145 mm times 49 mm, and the 120 Hz has lateral dimension of 73 mm times 73 mm. A wooden box is designed to include all the resonators is a single unit of 1 foot by 1 foot area, that can be directly installed inside the impedance tube (of 1 foot by 1 foot square section), with four 60 Hz, four 90 Hz and four 120 Hz LR (Figure 3a). In Figure 3b), the experimental sound absorption coefficient of the box with multiple resonators is plotted, comparing it with theory and simulation. Resonances are clearly distinguished even for experiments, with the sound absorption at each peak always bigger than 0.7

up to 500 Hz. Each tone is at its precise tuned frequency. In addition, their combination gives non-zero absorption in the entire frequency range studied.

Conclusion

The multi-resonator box shows convincing sound absorption properties and opens interesting perspectives. Experimental results are compared with analytical and numerical methods: the experimental peaks appear at the predicted frequencies, with an amplitude difference that can be attributed to the rigid wall hypothesis. Future developments will be pursued with an experimental campaign, in a water basin or ideally in the engine cabin of a ship.

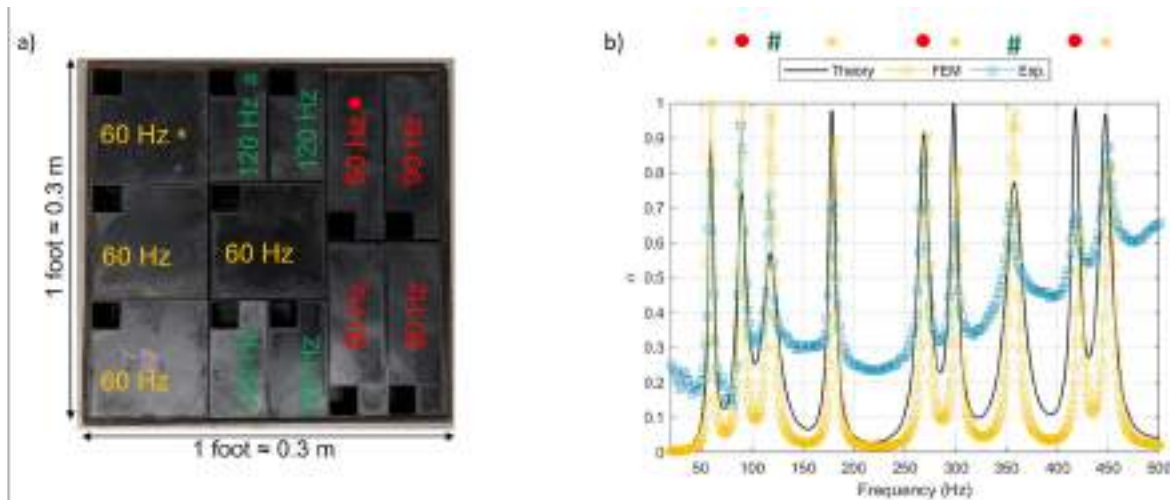


Figure 3: a) Picture of the multi-resonators box; b) Sound absorption of the labyrinth resonator box excited by a normally incident plane wave – comparison of analytical, numerical, and experimental results.

Acknowledgments

This research was supported by the Réseau Québec Maritime through the PLAINE research program (grant number PLAINE-2022PS04).

References

- [1] B. M. Spessert, E.-A.-H. Jena, M. Fischer, and B. Kühn, “Combustion Engine Noise-a Historical Review, Internoise 2019, Madrid, Spain.
- [2] A. Magnani, C. Marescotti, and F. Pompoli, “Acoustic absorption modeling of single and multiple coiled-up resonators,” *Applied Acoustics*, vol. 186 (2022).
<https://doi.org/10.1016/j.apacoust.2021.108504>
- [3] C. Zwikker and C. W. Kosten, “Sound Absorbing Materials,” *Elsevier Publishing company*, 1949.
- [4] G. Catapane, D. Magliacano, G. Petrone, A. Casaburo, F. Franco, and S. De Rosa, “Labyrinth Resonator Design for Low-Frequency Acoustic Meta-Structures,” in *Recent Trends in Wave Mechanics and Vibrations*, 2022, pp. 681–694.
<https://doi.org/10.1016/j.apacoust.2021.108504>
- [5] N. Atalla and F. Sgard, “Modeling of perforated plates and screens using rigid frame porous models,” *J Sound Vib*, vol. 303 (1–2), 195–208 (2007).
<https://doi.org/10.1016/j.jsv.2007.01.012>

Comparative study of shock response synthesis techniques for aerospace applications

Ada Ranieri^{1,a,*}, Simone De Carolis^{1,b}, Giuseppe Carbone^{1,c}, Michele Dassisti^{1,d},
Andrea De Cesaris^{2,e}, Leonardo Soria^{1,f}

¹ Polytechnic University of Bari, Bari, Italy

² Sitael, Mola di Bari (BA), Italy

^aada.ranieri@poliba.it, ^bsimone.decarolis@poliba.it, ^cgiuseppe.carbone@poliba.it,
^dmichele.dassisti@poliba.it, ^eandrea.decesaris@sitael.com, ^fleonardo.soria@poliba.it

Keywords: Shock Response Spectrum, Synthesis, Wavelets, Damped Sinusoids, Enveloped Sinusoids

Abstract. The Shock Response Spectrum (SRS) is a widely used tool for analyzing and characterizing the response of mechanical systems to shock and transient events. In the aerospace industry, the SRS is used to compute the severity of the shock event on the electrical and optical equipment of a spacecraft. However, the SRS only provides magnitude information and does not retain temporal or phase information. Moving to the time domain is not a straightforward process because a time history has a unique SRS, but the converse is not true. Therefore, it is challenging to find the right time history that reproduces an SRS when simulating a given input profile using pyrotechnic devices or when computing the response to a shock input profile in the time-domain. For a given SRS an infinite combination of time pulses is possible. Synthesizing an SRS involves recovering a time-domain pulse that can accurately replicate the given SRS. There are many methods which are already widely utilized in the aerospace industry, including the use of damped sinusoids, enveloped sinusoids and wavelets. In this paper we compare different techniques, with the objective of identifying the most suitable method based on the considered frequency range and type of impulse. The case study under consideration is an SRS input profile corresponding to a real industrial case. Three artificial SRS accelerations have been generated to replicate the input, and the percentage errors of each method in comparison to the reference signal have been assessed. Further development will involve the use of optimization algorithms to generate the SRS profile with the smallest possible error.

Introduction

One of the most significant challenges in the space industry is the design and testing of aerospace structures and systems for reliable and safe operation in harsh environments, including the sudden and impulsive loads occurring during the launch phase. The most intense events are commonly caused by pyrotechnic devices actuating at the base of the spacecraft. The firing of these devices results in impulsive loads characterized by high peak acceleration, high-frequency content, and short duration. This poses a significant threat to the reliability and safety of electrical and optical components of the spacecraft, which are sensitive to high frequency loads. To demonstrate its compliance to shock requirements, the structure has to be tested by applying the shock load on the base interface. The accepted standard for implicit description of the pyroshock environment is the Shock Response Spectrum (SRS), which is a useful tool for estimating the damage potential of the shock pulse and for test level specification. The SRS finds its first applications in the 50's by the seismic and aerospace community. An SRS is generated by plotting in the frequency domain the peak response of a series of Single Degree of Freedom (SDoF) oscillating systems subjected to the same transient base acceleration input. The damping is usually assumed to be 5% ($Q=10$), while

the natural frequency of each SDOF system is chosen to be different. The primary limitation of the SRS is its inability to provide temporal or phase information, as it only gives magnitude information. As a result, when subjecting a structure to electro-dynamic shaker testing for shock qualification, the SRS cannot be directly utilized [1]. Instead, it becomes necessary to synthesize an SRS-compatible acceleration time history. A similar challenge arises when analyzing nonlinear structures, where a modal approach is not feasible, and a modal transient analysis must be conducted to account for the phase among the peak responses of individual modes.

The aforementioned waveform can be obtained using a series of sinusoids [1,2] or wavelets [3], tailored to resemble an actual pyrotechnic shock pulse.

Shock Response Spectrum Synthesis

While a unique impulse in the time domain corresponds to a specific SRS, the opposite is not true. In fact, an SRS corresponds to an infinite number of possible pulses. As a result, there are several techniques available to obtain SRS-compatible acceleration time history. In this work we will investigate the accuracy of SRS synthesis throughout the summation of damped sines, enveloped sines and wavelets.

Wavelets. A wavelet is a discrete waveform of limited duration that is suited for approximating data with sharp discontinuities [4]. The original signal can be reconstructed as a summation of a set of wavelets with specified parameters. The equation of a single wavelet $W_m(t)$ is:

$$W_m(t) = \begin{cases} 0, & \text{for } t < t_{dm} \\ A_m \sin\left[\frac{2\pi f_m}{N_m}(t - t_{dm})\right] \sin[2\pi f_m(t - t_{dm})], & \text{for } t_{dm} \leq t \leq \left[t_{dm} + \frac{N_m}{2f_m}\right] \\ 0, & \text{for } t > \left[t_{dm} + \frac{N_m}{2f_m}\right] \end{cases} \quad (1)$$

A discrete wavelet has a sinusoidal motion with a finite and odd number of half sine oscillations N_m with unique parameters for frequency f_m , amplitude A_m and time delay t_{dm} .

Damped sinusoids. The sinusoid approach shows a difference in the way the rise, peak and decay of the waveform is controlled, compared to the previously presented method. In this case the parameters to control are slightly different:

$$W_m(t) = \begin{cases} 0, & \text{for } t < t_{dm} \\ A_m e^{-\xi_m 2\pi f_m(t-t_{dm})} \sin\left[\frac{2\pi f_m}{N_m}(t - t_{dm})\right] \sin[2\pi f_m(t - t_{dm})], & \text{for } t \geq t_{dm} \end{cases} \quad (2)$$

It can be noted an extra term ξ_m , that is the damped sinusoid damping ratio.

Enveloped sinusoids. The enveloped sinusoids with random phase angles approach is similar to the one of damped sinusoids. The equation for enveloped sinusoids is given by:

$$W_m(t) = E(t)A_m \sin(2\pi f_m t + \varphi_m). \quad (3)$$

Where φ_m are random phase angles for each frequency n . The rise, plateau and decay of $W_m(t)$ is controlled by an envelope function $E(t)$ rather than damping.

For all the three methods, iterations for the parameters of a set of m waveforms a time t yield a synthesized acceleration that is expressed as:

$$\ddot{x}(t) = \sum_{m=1}^{N_m} W_m(t). \quad (4)$$

An example of a synthesized time history from the SRS input in Table 1 with a duration of $T=0.06$ s can be seen in Fig.1.

Table 1. Shock load input

Frequency [Hz]	Amplitude [g]
100	56
1000	2820
10000	2820

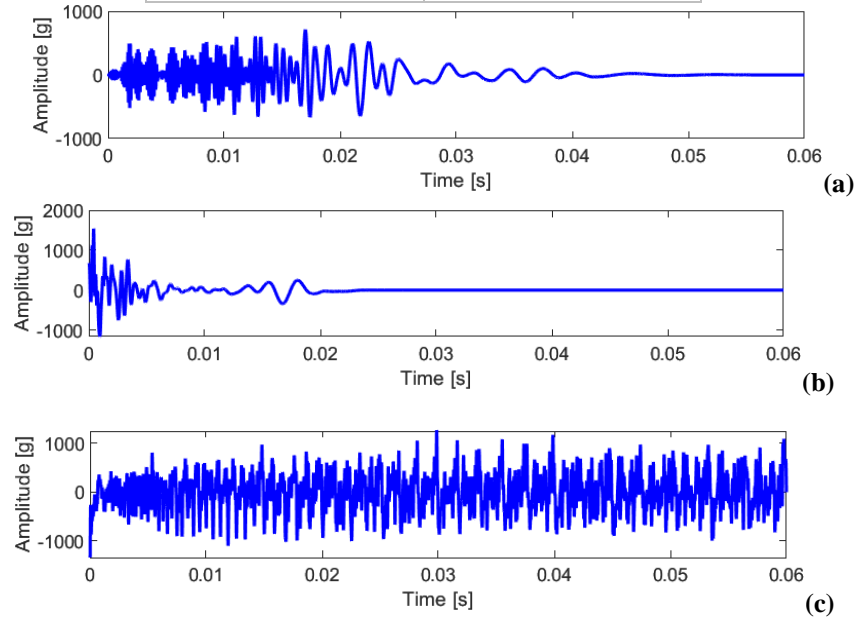
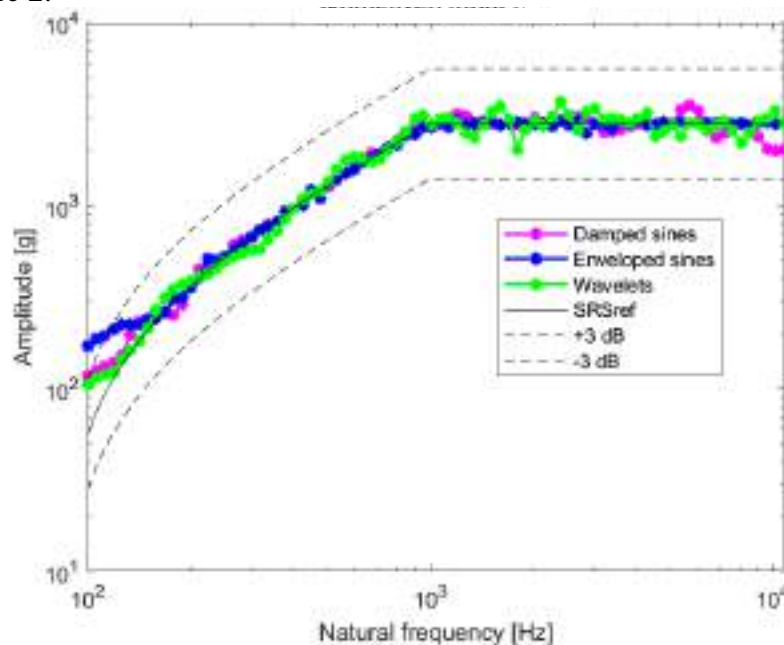


Figure 1. Reconstructed time history of a shock input with (a) wavelets, (b) damped sines, (c) enveloped sines

The synthesized accelerations have been converted to SRS and compared to the reference input as shown in Figure 2.



2. Synthesized SRS comparison

Table 2. Synthesis correlation coefficient

	Damped sines	Enveloped sines	Wavelets
100-200 Hz	0.98186	0.99566	0.99773
200-1000 Hz	0.97651	0.98699	0.9659
1000-10K Hz	0.98934	0.99421	0.98707

Furthermore, the Synthesis Correlation Coefficient (*COR*) [5] in Table 2 has been computed in low, middle and high frequency range to compare the efficiency.

$$COR = \frac{|\sum_{f_1}^{f_2} SRS_r(f_n) SRS_s(f_n)|^2}{\sum_{f_1}^{f_2} SRS_r(f_n)^2 \sum_{f_1}^{f_2} SRS_s(f_n)^2} \quad (5)$$

Where SRS_r and SRS_s are respectively the reference and synthesized SRS. Globally, a good level of accuracy (near the unity) has been achieved. In particular, the enveloped sines method seems to be the most effective. It can be observed that the methods are less accurate in the middle frequency range (200-1000 Hz).

Conclusions and future developments

In conclusion, the investigated techniques, namely the summation of damped sines, enveloped sines, and wavelets, have shown good levels of accuracy in reproducing the desired SRS input. Further studies should be conducted by exploring different parameter settings and types of input profiles to enhance the understanding of these techniques. Additionally, the development of an optimization algorithm, such as the least square fitting method or genetic algorithm, should be pursued to combine the methods and synthesize a single SRS that minimizes the error and achieves a higher level of accuracy.

References

- [1] T. Irvine, Shock Response Spectrum Synthesis Via Damped Sinusoids, Vibrationdata, 2012
- [3] J. E. Alexander, A New Method to Synthesize an SRS Compatible Base Acceleration with Energy and Temporal Moments to Improve MDOF System Response, IMAC 36 Orlando, 7 Sound & Vibration, 2018.
- [2] T. Irvine, Shock Response Spectrum Synthesis Via Wavelets, Vibrationdata, 2000.
- [4] A. Grasps, An Introduction to Wavelets, IEEE Computational Science and Engineering vol. 2, num. 2, published by the IEEE Computer Society, Los Alamitos, 1995.
<https://doi.org/10.1109/99.388960>
- [5] R.G. Allemang, Vibrations: Experimental Modal Analysis, 1999. UC-SDRL-CN-20-263-662

Vibro-acoustic analysis of additively manufactured acoustic metamaterial via CUF adaptive finite elements

M. Rossi^{1a}, M.C. Moruzzi^{1b*}, S. Bagassi^{1c}, M. Corsi^{1d}, M. Cinefra^{2e}

¹Department of Industrial Engineering, University of Bologna, Italy

²Department of Mechanical, Mathematics and Management, Polytechnic of Bari, Italy

^amattia.rossi17@studio.unibo.it, ^bmartinocarlo.moruzz2@unibo.it, ^csara.bagassi@unibo.it,

^dmarzia.corsi2@unibo.it, ^emaria.cinefra@poliba.it

Keywords: Aircraft Noise, Vibro-acoustics, Acoustic Metamaterials, Carrera's Unified Formulation

Abstract. In the field of noise and vibrations control inside the cabin, passive noise solutions coupled with the development of new unconventional materials, called Acoustic Metamaterials (AMMs) can be very promising to stop incoming noise and guarantee the passenger's comfort without an increase in aircraft weight. Within the framework of Carrera's Unified Formulation (CUF), we study the acoustic properties of double pierced AMM plate printed with Fused deposition modelling technique (FDM). The influence of several geometrical parameters is investigated, such as the size and location of the holes and the perforation ratio. The properties of this AMM are derived from vibro-acoustic analyses of the finite element software, Mul2, developed by *Politecnico di Torino*, that exploits the CUF. In order to study the AMM complex structure in the CUF framework, the Adaptive finite elements are exploited. This new class of 2D elements, recently developed, allows us to model with shell elements the AMM structure, which presents several discontinuities in the mid-surface due to the presence of corners and internal cavities.

Introduction

The problem of noise in commercial aircraft is usually related to the emission of sound waves outwards, resulting in noise pollution problems in areas near airports or landing and take-off paths [1]. However, noise is also an internal problem of the aircraft, where sound waves follow paths internal to the aircraft structures or are generated by sources that are already internal (e.g., the air conditioning system) [2]. Internal noise negatively affects the comfort of passengers and crew during flight, weakening the competitiveness of the aircraft compared to other methods of travel.

In order to decrease the amount of noise in the passenger cabin, there are several proposed solutions. The simplest solution in terms of both implementation and logic leads to shielding the passenger cabin by means of insulating panels in the cavity between the fuselage and the cabin panel [3]. In this work, we focus on the low and medium frequencies that are traditionally difficult to shield with conventional materials. For this reason, it was decided to use materials with special acoustic properties, acoustic metamaterials (AMMs). With AMMs, high absorption coefficients in a certain frequency range can be achieved with lightweight structures by using appropriate elementary cell geometries repeated periodically in the absorber panel. However, these new materials present problems related to the field of numerical analysis compared to the results of the current structure. The use of numerical models, the Finite Element Method (FEM) for the low and medium frequencies, is essential both in the preliminary stages to have extensive design flexibility, but even more in the later stages to study the AMM in the aircraft environment, where the analysis is scaled from the characterization of a simple plate to that of several panels in the aircraft fuselage.



The major problem is in the process of numerical homogenization of the AMM, which brings with it the hypothesis of a perfect repetition of the elementary cell. Small manufacturing errors can lead to significant differences between experimental and numerical results. To avoid this problem, the following work has chosen to use an AMM produced with additive printing based on literature [4], that can guarantee high precision in the production of the AMM and the study of a geometry difficult to obtain with conventional production methods.

A second problem is the numerical method used in the finite element field to solve the vibro-acoustic problem. Indeed, as will be further described, the proposed AMM has internal cavities pierced with the presence of double fluid-structure interfaces that would require the use of solid elements with conventional FEM methods. In order to avoid an excessive number of Degrees of Freedom (DoF) without losing accuracy, Carrera's Unified Formulation (CUF) has been chosen [5], which allows us to exploit different theories for plates, both Equivalent Single Layer (ESL) and Layer Wise (LW). The geometry of the material also required integration into the formulation of a new class of elements, the Adaptive finite elements [6, 7], to handle corners and intersections between the various elements.

Vibro-acoustic problem in the CUF-FEM framework

The vibro-acoustic problem that describes the AMM of this work is that it includes an elastic structure coupled to internal cavities. The following system must then be resolved before information on dynamic behaviour and Transmission Loss (TL) can be obtained:

$$\begin{bmatrix} -\omega^2 \mathbf{M} + \mathbf{K} & \mathbf{S} \\ -\rho_f \omega^2 \mathbf{S} & -\omega^2 \mathbf{Q} + \mathbf{H} \end{bmatrix} \cdot \begin{Bmatrix} U \\ P \end{Bmatrix} = \begin{Bmatrix} \mathbf{F} \\ 0 \end{Bmatrix}$$

where we have the mass matrix \mathbf{M} , \mathbf{Q} and stiffness \mathbf{K} , \mathbf{H} of structure and fluid respectively, the coupling matrix \mathbf{S} and the vector of the external loads on the structure \mathbf{F} . The previous matrices and vectors are defined according to the fundamental nuclei formulation [8]. The vectors of the unknown are U and P , the three displacements and the pressure respectively. The properties of the fluid are defined by the density ρ_f and speed of the sound c_f , while those of the structure are defined by the elasticity matrix \mathbf{C} . The problem is solved in the frequency domain, represented by the angular frequency ω . In the FEM approximation, the unknowns are the nodal values, the transition to the continuous field is guaranteed by the shape functions N .

According to the CUF, the three-dimensional field of a shell can be split into a two-dimensional field on the shell plane and an expansion on the thickness F_τ , called thickness function [5]. The choice of thickness functions leads to the use of different plate models. In this work, the Lagrange polynomials are used to have a Layer Wise approach. In addition, the integration of the Adaptive finite element leads to the use of a new three-dimensional shape function L , which combines the shape and thickness functions, in the calculation of the integral and the Jacobian. Then the displacement field is defined by the following equation:

$$u_\tau^k(x, y, z) = (N_i F_\tau^{ki}) \mathbf{u}_{\tau i}^k = L_{\tau i}^k(x, y, z) \mathbf{u}_{\tau i}^k$$

For the pressure field, being defined by three-dimensional elements, the conventional FEM formulation is applied.

Acoustic solution

The design of sandwich panels has been the subject of various studies during the past decades [9]. Since the panels' faces are not designed to absorb sound, the choice of the core turned out to be particularly crucial for the reduction of noise [10]. Instead, by using plates with small holes and an air cavity in the centre, the so-called micro-perforated panels (MPPs), the sandwich plate can have a positive impact on noise reduction, improving sound absorption. The research by Meng et al. [4] is chosen as a reference since it focuses on the influences of holes' diameter of an additively produced AMM.

It comes to light that the porosity, location, and diameter of the holes all affected the sound transmission loss. Following this direction, various AMM models have been developed to comprehend how the noise operates at low- to middle-frequency levels in various design parameter combinations. The dimension of the holes, the position of the holes, and the perforation ratio are the three main parameters of interest for the model definition in this study. The porosity or perforation ratio $PR_{\%}$, which is typically given in percentages, describes how much of a plate is made up of holes:

$$A_h = PR_{\%} \cdot A_e$$

where A_h is the circular area of the holes and A_e is the elementary cell area.

Then, a series of models are created, shown in Tab. 1 and the third one is reported in Fig. 1(a). The production method chosen is the fused deposition modelling technique (FDM) with a Fortus 250 mc and ABS Plus p430, as a material, on which preliminary studies have already been carried out [11-13]. Although it may not be one of the most precise printing techniques, it allows a sufficiently robust structure to be obtained and to direct the filament deposition path to increase the accuracy of the AMM's holes, especially on the oblique plates. All models were printed correctly except the fourth due to the excessively small size of the holes (i.e., 0.5 mm). Fig. 1(b) shows one of the printed models.

Table 1: AMM models' properties, the first model is not pierced.

Models	AMM density [kg/m ³]	$PR_{\%}$	Holes diameter [mm]	Holes location
1	1040	-	-	No holes
2	1039	0.349	1	Upper plate
3	1037	0.349	1	Upper plate & core
4	1037	0.349	0.5	Upper plate & core
5	1037	0.698	2	Upper plate & core
6	1035	0.175	1	Upper plate & core
7	1039	0.175	1	Upper plate & core

The numerical study of the models allows us to derive a priori the TL. In order to avoid errors, the model has been pre-validated by comparing its natural frequencies with those obtained from commercial software. Then, a direct frequency analysis is performed on a simply supported AMM plate, loaded with constant amplitude load (1 N). The results in terms of TL show that the presence of the holes, their size and position is decisive in defining the acoustic behaviour of the AMM. Among the various results reported in a complete way in Rossi's work [14], it is interesting to note that the third and fifth models (which have the same homogenized density) have significant TLs between 1000 and 1900 Hz in Fig. 2, although for the fifth with several peaks and discontinuities. While the fundamental frequency of the seventh model is the highest among the six models. The fourth model was not produced; therefore, it was not studied.

Conclusions

This work is intended to provide a preliminary basis for further study of AMMs produced with additive techniques for noise reduction in aircraft. The results demonstrate the excellent acoustic properties of these structures and the possibility to study them with innovative numerical methods.

In the future, it is necessary to validate the numerical results through experimental tests in the anechoic chamber or with an impedance tube and then scale the problem to study the AMM in the working environment. Finally, FDM is only one of the available additive techniques. The advantages or disadvantages of other technologies for AMM production need to be evaluated with appropriate research.

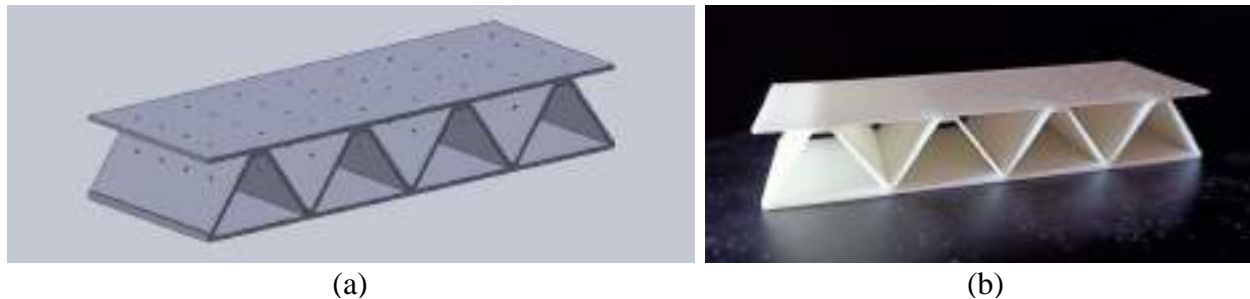


Figure 2: The AMM designed in this work and based on the work by Meng et al [4]. (a) The third model isometric representation. (b) The first model after the production process.

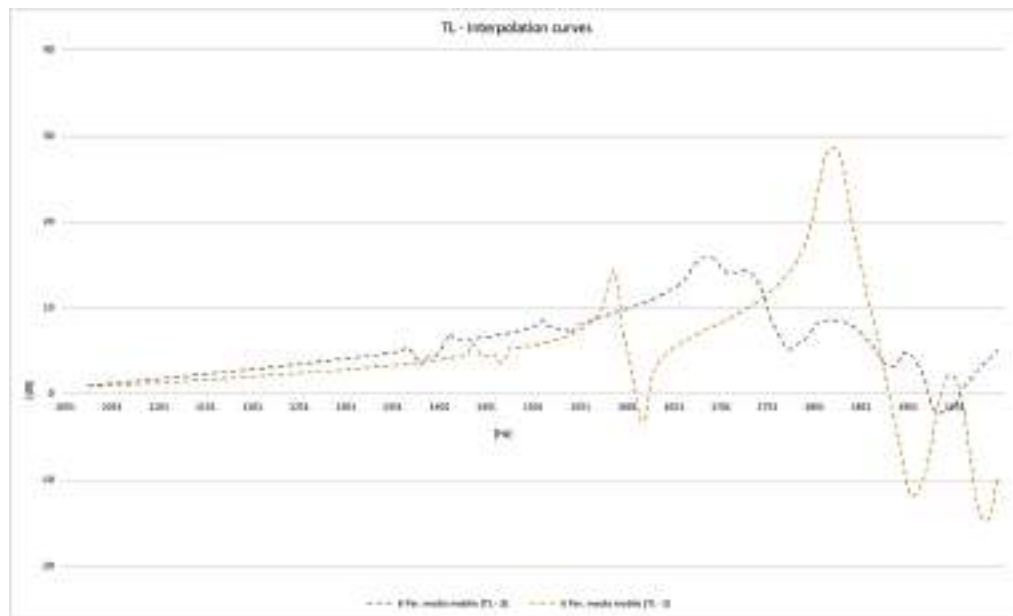


Figure 2: The average TL [dB] from 1000 Hz to 2000 Hz for the third model (grey line) and the fifth one (yellow line).

References

- [1] LL. Beranek. The noisy dawn of the jet age. *Sound and Vibration*, 41:94–99, 2007.
- [2] N. Hu, H. Buchholz, M. Herr, C. Spehr, and S. Haxter. Contributions of different aeroacoustic sources to aircraft cabin noise. In *19th AIAA/CEAS Aeroacoustics Conference*, 2013. <https://doi.org/10.2514/6.2013-2030>
- [3] MC. Moruzzi, M. Cinefra, and S. Bagassi. Vibroacoustic analysis of an innovative windowless cabin with metamaterial trim panels in regional turboprops. *Mechanics of Advanced Materials and Structures*, 28:1–13, 2019. <https://doi.org/10.1080/15376494.2019.1682729>
- [4] H. Meng, MA. Galland, M. Ichchou, O. Bareille, FX. Xin, TJ. Lu. Small perforations in corrugated sandwich panel significantly enhance low frequency sound absorption and

transmission loss, *Composite Structures*, Volume 182: 1-11, 2017.

<https://doi.org/10.1016/j.compstruct.2017.08.103>

[5] E. Carrera, M. Cinefra, M. Petrolo, and E. Zappino. Finite element analysis of structures through unified formulation. Wiley, 2014. <https://doi.org/10.1002/9781118536643>

[6] M. Cinefra. Non-conventional 1d and 2d finite elements based on cuf for the analysis of non-orthogonal geometries. *European Journal of Mechanics/A Solids*, 88:104273, 2021.

<https://doi.org/10.1016/j.euromechsol.2021.104273>

[7] MC. Moruzzi, M. Cinefra, S. Bagassi, E. Zappino. Vibro-acoustic analysis of multi-layer cylindrical shell-cavity systems via CUF finite elements, 33rd Congress of the international council of the aeronautical sciences, 2022. <https://doi.org/10.1016/j.compstruct.2020.113428>

[8] M. Cinefra, MC. Moruzzi, S. Bagassi, E. Zappino, E. Carrera. Vibro-acoustic analysis of composite plate-cavity systems via CUF finite elements, *Composite Structures*, Vol. 259, 2021. <https://doi.org/10.1016/j.compstruct.2020.113428>

[9] V. Birman and GA. Kardomateas. Review of current trends in research and applications of sandwich structures. In: *Composites Part B: Engineering* 142:221–240, 2018. <https://doi.org/10.1016/j.compositesb.2018.01.027>

[10] MP. Arunkumar, J. Pitchaimani, KV. Gangadharan, MC. Lenin Babu. Influence of nature of core on vibro acoustic behavior of sandwich aerospace structures, *Aerospace Science and Technology*, Volume 56: 155-167, 2016. <https://doi.org/10.1016/j.ast.2016.07.009>

[11] M. Corsi, S. Bagassi, MC. Moruzzi, and L. Seccia. Correlation between production parameters and mechanical properties of ABS Plus p430 fused deposition material. *Proceedings of the Institution of Mechanical Engineers, Part C: Journal of Mechanical Engineering Science*, 236(5):2478–2487, Mar 2022. <https://doi.org/10.1177/09544062211027205>

[12] MC. Moruzzi, S. Bagassi, M. Cinefra, M. Corsi, M. Rossi. Design of additively manufactured metamaterial for cabin noise and vibrations reduction, XXVI AIDAA International Congress, 2021.

[13] H. Rezayat, W. Zhou, A. Siriruk, D. Penumadu, and SS. Babu. Structure–mechanical property relationship in fused deposition modelling. *Materials Science and Technology*, 31(8):895–903, 2015. <https://doi.org/10.1179/1743284715Y.0000000010>

[14] M. Rossi. Vibro-acoustic analysis of additively manufactured acoustic metamaterials. Ms Thesis. University of Bologna, 2022.

XR and Human Factors for Future Air Mobility

A brief review of pilots' workload assessment using flight simulators: subjective and objective metrics

Giuseppe Iacolino^{1, a *}, Antonio Esposito^{1, b}, Calogero Orlando^{1, c} and
Andrea Alaimo^{1, d}

¹Faculty of Engineering and Architecture, Kore University of Enna, 94100 Enna, EN, Italy

^agiuseppe.iacolino@unikorestudent.it, ^bantonio.esposito@unikore.it,

^ccalogero.orlando@unikore.it, ^dandrea.alaimo@unikore.it

Keywords: Human Factor, Subjective Methods, Objective Methods, Full Flight Simulator

Abstract. This study explores subjective and objective metrics to assess pilots WL, with a particular focus on the use of full flight simulators (FFS). The results show that FFS-based research demonstrates no significant differences compared to real flight experiences, highlighting the validity of FFS as a tool for studying pilots' performance. However, further research is needed to understand the impact of other parameters on pilots' performance, and to address human factor-related risks for enhanced aviation safety.

Introduction

Nowadays, workload (WL) can be considered one of the biggest challenges in the aeronautical field. The continuous growth of air traffic has led pilots to work under pressure and for extended periods of time. As reported in [1], 75% of aircraft accidents are linked to human errors and most of them are related to high levels of mental WL and fatigue. This is important in critical situations such as take-off, landing or emergency procedures. WL is associated with the onset of stress, a phenomenon with multiple facets ranging from neuroendocrine to psychological [2]. Pilots require training to effectively respond to both internal and external stimuli. Hence, using a flight simulator represents the most reliable, safe, time and cost savings way to study pilot's performances today [3]. Consequentially, it is necessary to employ some metrics that can better capture the pilots' stress level while performing the task. To do this, subjective and objective methods are widely exploited, and this work aims to describe such measures, with particular attention paid to the studies conducted using a full flight simulator (FFS).

Subjective and Objective Metrics

The concept of mental WL is described in [4] as a collection of mental, and composite brain states that influence human performance in various perceptual, cognitive, and sensorimotor abilities. Thus, it is crucial to choose the right metrics to evaluate it. Subjective and objective measures represent an important contribution on pilots' WL level evaluation. In detail, subjective WL measures comprise some tests which are administered while, before or after the performance. Being such subjective, they can be highly influenced by the pilot's psychological condition. That's why it is good practice to link them with the objective ones which represent the physical condition of the subject. The objective measures are mainly obtained via sensors which can detect some physiological parameters. In this work, subjective methods will be described first and objective ones after. The most reliable subjective methods are here mentioned.

The *NASA Task Load Index (TLX)* was first developed by Hart and Staveland in 1988. The TLX is widely recognized and extensively employed globally. The test has three stages to evaluate the pilot's WL. The first one obtains a global index across six dimensions: mental, physical, time demands, performance, effort, and frustration. Each dimension is divided into twenty intervals. In the second stage, pairs of dimensions are assessed, determining the ones with the greatest impact



on WL. The third stage assigns scores to selected dimensions, with 0 for insignificant dimensions and 5 for the most important one [5]. On the other hand, the *Subjective Workload Assessment Technique (SWAT)* involves obtaining subjective ratings from participants regarding three dimensions of WL: time load, mental effort load, and psychological stress load. During the activity, participants are encouraged to assess their workload across three dimensions and rate it on a scale of low, medium, or high. A mental workload range scale is then calculated by combining the scores from all three dimensions. This assessment method relies on the self-report of participants [6]. Other subjective techniques are not mentioned for the sake of conciseness.

Regarding the objective metrics, some of them are reported here as well. As evidence, in [7] the eye movement provides indications on the pilot's visual perception, or [8] aimed to investigate the potential utility of α – Amy levels as a biomarker for stress in pilots operating within a high-stress environment. However, the heart rate variability (HRV) is one of the most employed parameters today. HRV is the spontaneous fluctuation in time between consecutive heartbeats, as measured by the distance between two successive R peaks on an electrocardiogram. This parameter can be studied in both frequency and time domain. In particular, the time domain measures also include the NN interval series standard deviation (SDNN). Based on the existing literature, a reduction in this parameter indicates an elevation in both mental WL and physical demands [9]. As previously mentioned, the study of HRV extends to the frequency domain. In this context, the fast Fourier transform is employed to estimate the Power Spectral Density associated with frequency bands, specifically focusing on high frequency and low frequency. These frequency bands provide valuable information about sympathetic and parasympathetic activities [10].

FFS for Human Factor Studies

Due to the rarity of FFS, there is a limited body of literature that specifically addresses their utilization. Most studies, in fact, primarily focus on simulators that provide visual cues to pilots through screens but lack the comprehensive flight sensation that an FFS can deliver. In 2018, the European Union Aviation Safety Agency (EASA) released the latest specifications for Airplane Flight Simulation Training devices (CSFSTD-A), which classify flight simulators into four levels of qualification: A, B, C, and D. The D-level FFS are the most advanced and reliable. For instance, to achieve a D-level qualification, the FFS must include a real-time feedback tool that allows the instructor to monitor the training envelope and prevent the airplane's operating limits from being exceeded. In [11] it is reported that acute effects on HRV and anxiety during a real-time flight are not significantly different from those experienced in a simulator, indicating that the simulated task planning and design closely approximate real-world conditions; in this case, an operational F-5M by Indra Company flight simulator was used. It is also reported that future flight simulators should incorporate immersive virtual reality technology simulating G forces and vibration. Nevertheless, in today's context, D-level FFS can be used to do reliable research and prevent in real-life risky decisions. In essence, pilots must be conscious on which kind of decisions they have to take while flying, both in high and normal WL condition. Additionally, the study conducted in [12] employed the CESSNA Citation C560 XLS FFS. The main findings of the study demonstrated that WL levels can be effectively differentiated by analyzing various domains of HRV, including time, frequency, and non-linear measures. These results highlight the importance of HRV indexes in assessing WL, and suggest the potential development of real-time, non-invasive instruments for evaluating it. In a separate study [13], the application of an FFS was investigated within typical flight scenarios. The research collected pilots' objective and subjective metrics to establish an evaluation index system. Research has revealed that pilot's errors have become a significant obstacle, impeding the progress towards enhancing flight safety within the aviation industry. The study also found some deficiencies in the design layout of the cockpit as in the flight crew operation process that cause pilots to make mistakes easily. The authors proposed that *designing aircrafts suitable* for pilots

instead of *aircraft requiring pilots to adapt* can make the civil aircraft cockpit more humanized and highly automated. Also, the authors proposed a feasible method to analyze human factors (HF) in typical faults and incidents of transport category airplanes using comprehensive methods that combine subjective and objective measurements. In [14] it is investigated the correlation between subjective and objective indicators of fatigue, factors such as WL and work scheduling. It also examined whether the WL experienced by pilots during a simulator mission could serve as a moderator for increased fatigue after the mission. The study utilized a JAR STD 1A FFS. Results indicated that both subjective and objective measures of fatigue significantly rose during the three-hour experimental procedure. These findings suggest the presence of enduring effects from sleep deficit and propose a multifactorial model for assessing fatigue risks. In [15] two subjective WL measurements and three psychophysiological measurements were compared in both a simulator and a flight test. The comparisons were made across three flight scenarios using an ARJ21-700 FFS and a corresponding aircraft. Both flight scenarios and the flight environment significantly influenced NASA-TLX, eye blink rate, and HRV. Moreover, strong correlations were observed between the NASA-TLX and HRV, between the simulator and the flight test. These findings suggest that NASA-TLX and HRV can serve as consistent measures of WL in both FFS and real flight tests.

Conclusions

This short review aimed to highlight some subjective and objective metrics in order to understand the impact of stress on pilots' performance. The findings indicate that subjective and objective metrics play an important role for better understanding pilots' WL level. Furthermore, research involving FFS has shown promising results and benefits when compared to real flight experiences. Additionally, to emphasize the need for more studies is important. Despite current high safety standards, incidents related to HF still occur, highlighting the importance of ongoing investigation and improvement. By conducting more research and continuously improving understanding, pilot performance can be enhanced, risks can be mitigated, and safer aviation operations can be ensured for everyone involved.

Acknowledgment

This work was partially funded by the project "SAMOTHRACE" (Sicilian MicronanoTech Research And Innovation Center) – Funds: MUR, PNRR-M4C2, ECS_00000022, activity of Spoke 3 affiliated partner Kore University of Enna: WP3.4 SAfety MObility Sensors TESting Platform - SA.MO.S.TE.P.

References

- [1] Kharoufah, H., Murray, J., Baxter, G., & Wild, G. (2018). A review of human factors causations in commercial air transport accidents and incidents: From 2000–2016. *Progress in Aerospace Sciences*, 99, 1-13. <https://doi.org/10.1016/j.paerosci.2018.03.002>
- [2] Masi, G., Amprimo, G., Ferraris, C., & Priano, L. (2023). Stress and Workload Assessment in Aviation—A Narrative Review. *Sensors*, 23(7), 3556. <https://doi.org/10.3390/s23073556>
- [3] Mohanavelu, K., Poonguzhali, S., Ravi, D., Singh, P. K., Mahajabin, M., Ramachandran, K., & Jayaraman, S. (2020). Cognitive Workload Analysis of Fighter Aircraft Pilots in Flight Simulator Environment. *Defence Science Journal*, 70(2). <https://doi.org/10.14429/dsj.70.14539>
- [4] Kramer, A. F., & Parasuraman, R. (2007). Neuroergonomics: Applications of neuroscience to human factors.
- [5] Hart, S. G., & Staveland, L. E. (1988). Development of NASA-TLX (Task Load Index): Results of empirical and theoretical research. In *Advances in psychology* (Vol. 52, pp. 139-183). North-Holland. [https://doi.org/10.1016/S0166-4115\(08\)62386-9](https://doi.org/10.1016/S0166-4115(08)62386-9)

- [6] Reid, G. B., & Nygren, T. E. (1988). The subjective workload assessment technique: A scaling procedure for measuring mental workload. In *Advances in psychology* (Vol. 52, pp. 185-218). North-Holland. [https://doi.org/10.1016/S0166-4115\(08\)62387-0](https://doi.org/10.1016/S0166-4115(08)62387-0)
- [7] Oberhauser, M., & Dreyer, D. (2017). A virtual reality flight simulator for human factors engineering. *Cognition, Technology & Work*, 19, 263-277. <https://doi.org/10.1007/s10111-017-0421-7>
- [8] Iizuka, N., Awano, S., & Ansai, T. (2012). Salivary alpha-amylase activity and stress in Japan air self-defense force cargo pilots involved in Iraq reconstruction. *American Journal of Human Biology*, 24(4), 468-472. <https://doi.org/10.1002/ajhb.22247>
- [9] Watson, D. W. (2001, June). Physiological correlates of heart rate variability (HRV) and the subjective assessment of workload and fatigue in-flight crew: a practical study. In *2001 People in Control. The Second International Conference on Human Interfaces in Control Rooms, Cockpits and Command Centres* (pp. 159-163). IET. <https://doi.org/10.1049/cp:20010453>
- [10] Bilan, A., Witczak, A., Palusiński, R., Myśliński, W., & Hanzlik, J. (2005). Circadian rhythm of spectral indices of heart rate variability in healthy subjects. *Journal of electrocardiology*, 38(3), 239-243. <https://doi.org/10.1016/j.jelectrocard.2005.01.012>
- [11] Fuentes-García, J. P., Clemente-Suárez, V. J., Marazuela-Martínez, M. Á., Tornero-Aguilera, J. F., & Villafaina, S. (2021). Impact of real and simulated flights on psychophysiological response of military pilots. *International Journal of Environmental Research and Public Health*, 18(2), 787. <https://doi.org/10.3390/ijerph18020787>
- [12] Alaimo, A., Esposito, A., Faraci, P., Orlando, C., & Valenti, G. D. (2022). Human Heart-Related Indexes Behavior Study for Aircraft Pilots Allowable Workload Level Assessment. *IEEE Access*, 10, 16088-16100. <https://doi.org/10.1109/ACCESS.2022.3145043>
- [13] Xing, G., Sun, Y., He, F., Wei, P., Wu, S., Ren, H., & Chen, Z. (2023). Analysis of Human Factors in Typical Accident Tests of Certain Type Flight Simulator. *Sustainability*, 15(3), 2791. <https://doi.org/10.3390/su15032791>
- [14] Hörmann, H. J., Gontar, P., & Haslbeck, A. (2015). Effects of workload on measures of sustained attention during a flight simulator night mission.
- [15] Zheng, Y., Lu, Y., Jie, Y., & Fu, S. (2019). Predicting workload experienced in a flight test by measuring workload in a flight simulator. *Aerospace medicine and human performance*, 90(7), 618-623. <https://doi.org/10.3357/AMHP.5350.2019>

Applying an interior VR co-design approach for the medical deployment vehicle of the future

J. Herzig^{1,a}, F. Reimer^{1,b}, M. Lindlar^{2,c}, P. Weiland^{3,d}, J. Biedermann^{1,e},
F. Meller^{1,f}, B. Nagel^{1,g}

¹Institute of System Architectures in Aeronautics, Department Cabin and Payload Systems, German Aerospace Center e.V. (DLR), Hein-Saß-Weg 22, 21129 Hamburg, Germany

²Institute of Aerospace Medicine, Department Sleep and Human Factors Research, German Aerospace Center e.V. (DLR), Linder Höhe, 51147 Köln, Germany

³Institute of Flight Systems, Department Rotorcraft, German Aerospace Center e.V. (DLR), Lilienthalpl. 7, 38108 Braunschweig, Germany

^ajessica.herzig@dlr.de, ^bfabian.reimer@dlr.de, ^cmarkus.lindlar@dlr.de, ^dpeter.weiland@dlr.de, ^ejörn.biedermann@dlr.de, ^ffrank.meller@dlr.de, ^gbjörn.nagel@dlr.de

Keywords: VR, Co-Design, Cabin Design, User Centered

Introduction

The early arrival of qualified medical personnel at the scene of an accident is essential for a successful and effective first-aid treatment of emergency patients. Due to an increasing shortage of emergency medical personnel, as well as a decreasing hospital density in Germany, the continuity of medical care will be more challenging in the future. [1] [2]

According to a study by the Bertelsmann Foundation in the summer of 2019, the density of hospitals and clinics in Germany could be reduced from the current number of 1900 to 600. This immediately leads to the concentration of healthcare centers, making hospitals no longer equally accessible to the entire population. [3]

The resulting and extended time of arrival at the place of an accident immensely affects the adherence of the prehospital time and help time, which can seriously affect the health condition of the emergency patient. [1]

To ensure emergency medical care in the future, especially in structurally weak or densely populated regions, the DLR (German Aerospace Center) has set itself the goal of the "Rescue Helicopter 2030", to develop the aircraft of air rescue in Germany under the aspects of the future rescue service and to present new concepts.

Currently, research is being conducted on the concept of a medical deployment vehicle. This vehicle aims to transport medical professionals to the accident site in the shortest possible time to provide on-site initial care until the ambulance arrives for further transportation.

To maximize flight speed and range, this future rescue helicopter has been significantly reduced in size and weight.

The design of a tailored cabin concept for this purpose is characterized by high complexity in all aspects. In addition to the technical and mission-specific requirements of the helicopter system, new cabin designs must meet the individual needs to provide a high level of functionality and usability for all user groups. Furthermore, prototyping, planning, and conducting user tests are extremely time-consuming and costly, which increases the challenges in the development process [4]. To develop novel and highly complex cabin concepts that closely align with user requirements, the combination of user-centered design thinking methodology [5] and an immersive prototyping and feedback process has proven to be an effective approach [6] [7]

According to Burkett et. al., the concept of Co-design offers an approach that engages consumers and product users in the design process, aiming to foster enhancements and drive



innovation. [8]. Furthermore, co-creation is widely acknowledged as "practices where a design practice and one or more communities of practice participate in creating new desired futures" (Lee, 2018) [9]. Co-design involves the empowerment of individuals, granting them the opportunity to exert substantial influence over designs. User groups are regarded as central experts, uniquely positioned to contribute their expertise and insights throughout the entire process. [10]

The focus of this approach is on implementing a VR Co-Design process through the execution and evaluation of user workshops, with a particular emphasis on medical personnel and pilots with experience in air rescue.

Method

In the initial development phase, information regarding general experiences and challenges in air rescue were gathered from practicing pilots and emergency physicians. In addition to a subsequent description of the medical deployment vehicle concept, participants had the opportunity to familiarize themselves with the project and list initial requirements for the concept based on their own experiences. [10]

Participation in an online questionnaire and an initial engagement with the concept, as well as raising awareness about the topic, were fundamental prerequisites for attending a collaborative online workshop.

The following section will describe the structure of the study and the key findings of the second phase.

PARTICIPANTS

The online survey was completed by 25 participants from the air rescue sector,¹ including four pilots, six emergency medical technicians (HEMS TC), and 15 doctors. The age of the participants ranged from 22 to 60 years, with a mean age of 39.4 years.

After 37.5% of the online questionnaire respondents expressed interest in participating in a Co-Design workshop, a total of two workshops were conducted, each with three participants.

Special attention was given to the composition of the participants, aiming to bring together different user groups to combine diverse perspectives in the collaborative development process. The composition of the groups was as follows:

- Group 1: Person A (emergency physician), Person B (pilot), Person C (medical technician)
- Group 2: Person A (emergency physician), Person B (pilot), Person C (engineer)

PROCEDURE

At the beginning of the Co- Design workshop, the participants were presented with the requirements and mission scenario for the medical deployment vehicle. The interactive online tool *Conceptboard* was used for this purpose. Subsequently, all participants were asked to conceptually design an initial cabin layout based on their own requirements within ten minutes.

¹ The online survey was internally circulated among the employees of ADAC (Allgemeine Deutsche Automobil-Club e.V)

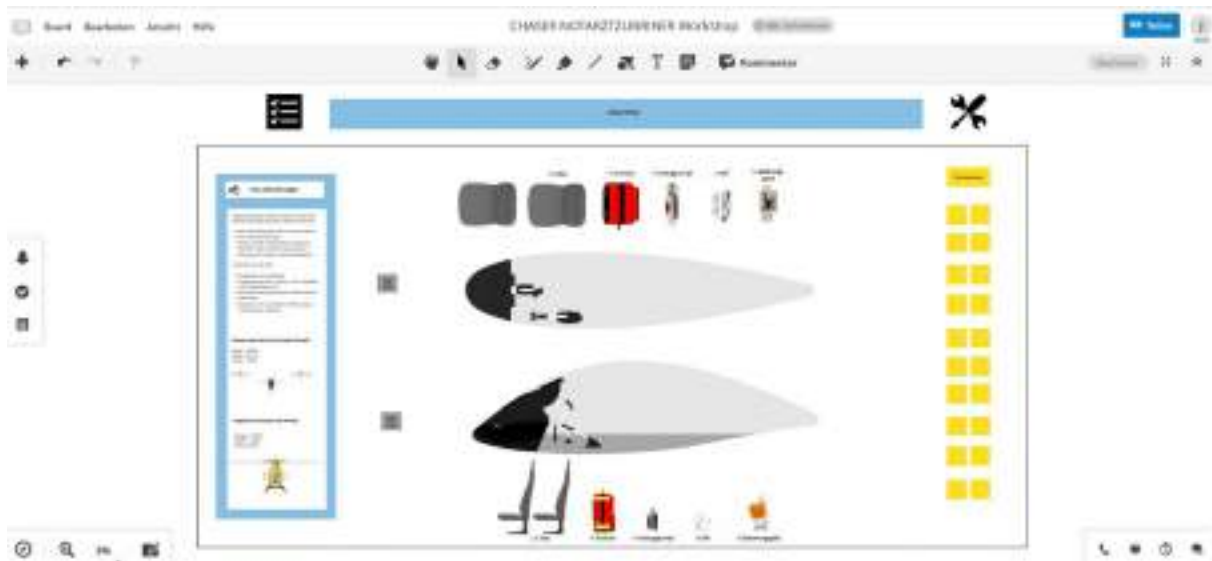


Figure 1: Example of the concept board work space for each participant including a description of the scenario, requirements and mission (left), the layout in two perspectives including interior parts and equipment (center) and notes for ideas (right)

Each participant received their own model where they could place objects on the helicopter floor plan. Additionally, there was an option to use post-it notes to add missing objects and include comments (see Figure 1). After presenting their concepts, the participants' designs were photographed and imported into the VR modeling program *Gravity Sketch*.

The 2D concepts created by the participants were placed in *Gravity Sketch* alongside the 3D model of the helicopter to provide an overview of the concepts and allow for a collaborative immersive incorporation of selected designs into the model.

A 3D cabin concept developed by the DLR cabin design team was positioned alongside as a comparative reference to the corresponding 2D solution approaches. Participation in the virtual reality session was facilitated through screen sharing of the collaboration app of *Gravity Sketch*.

After the participants were taken through the model via the shared screen, concept proposals could be expressed and implemented in real-time within the VR design model. With the aid of the newly gained spatial perspective, the concepts could be collectively reviewed, reevaluated, and optimized from the viewpoints of the three different professional groups regarding the usability of functions and positioning of modules (see Figure 2).



Figure 2: VR design concept as baseline for participants evaluation and further development process

Results

The workshop participants evaluated the Co-Design process of the medical deployment vehicle concept in virtual reality as an efficient and effective design method. The VR representation provided participants with an enhanced spatial awareness, making sizes, distances, and positions more comprehensible. This enabled immersive and rapid prototyping and efficient facilitated the evaluation of potential use cases.

The combination of the Co-Design process with immersive prototyping and optimization in virtual reality enables new and more effective design possibilities for user-centered and targeted cabin design.

This method allows for time and cost savings, as initial concepts can be developed in a short period. Additionally, it facilitates the direct implementation of experiences and requirements from different user groups into a virtual product, integrating the feedback and optimization process directly into the product. The findings of this paper provide a basis for adapting the method to other concepts with an expanded range of requirements. In addition to involving a higher number of participating stakeholder groups, direct integration into virtual reality is also conceivable.

References

- [1] ADAC Luftrettung GmbH, "Multikopter im Rettungsdienst," München, 2010.
- [2] S. M. A. u. H. D.Lauer, "Veränderungen und Entwicklungen in der präklinischen Notfallversorgung: Zentrale Herausforderungen für das Rettungsdienstmanagement," Bundesgesundheitsblatt-Gesundheitsforschung-Gesundheitsschutz, 2022.
- [3] J. Böken, "Neuordnung der Krankenhaus-Landschaft. Eine bessere Versorgung ist nur mit weniger Kliniken möglich," Bertelsmann Stiftung Nr.02, Gütersloh, 2019.
- [4] J. O. S.Ahmed, "Assessment of Types of Prototyping in Human-Centered Product Design," Assessment of Types of Prototyping in Human-Centered Product Design. In: Duffy, V.

- (eds) Digital Human Modeling. Applications in Health, Safety, Ergonomics, and Risk Management. DHM 2018. Lecture Notes in Computer Science(), vol 10917. Springer, 2018. https://doi.org/10.1007/978-3-319-91397-1_1
- [5] Hasso Plattner Institute of Design, "An Introduction in Design Thinking Process Guide," Hasso Plattner Institute of Design, Stanford, 2010.
 - [6] I. Moerland-Masic, "Advanced Air Mobility: The Cabin of the Future Rescue Helicopters,," AHFE2022, 2022. <https://doi.org/10.54941/ahfe1002492>
 - [7] S.Cornelje, "Mixing Realities: Combining Extended and Physical Reality in Co-Creative Design for the Galley of the Flying-V," TU Delft, Delft, Netherlands; Hamburg, Germany, 2023.
 - [8] Dr.I.Burkett, "Dr.I.Burkett, Co-designing for Social Good: The Role of Citizens in Designing and Delivering Social Services, Part One," University of NSW: Knode.
 - [9] M. A. T. R. a. M. J.J.Lee, "Design Choices Framework for Co-creation Projects," International Journal of Design, Helsinki/Singapore, 2018.
 - [10] F. Reimer, "Closing The Loop: The Immersiv and User Centered Co-Design Process for Future Rescue Helicopter Cabin Concepts," DLRK, 2023.
 - [11] T. u. F.S.Visser, "Lost in Co-X Interpretations of Co-Design and Co-Creation," T.Mattelmäki und F.S.Visser, Lost in Co-X Interpretations of Co-Design and Co-Creation, Aalto University School of Art and Design/Delft University of Technology: Proceedings of IASDR'11, 4th World Conference on Design Research, 2011.

Innovative ideas for the use of augmented reality devices in aerodrome control towers

Jürgen Teutsch

Royal Netherlands Aerospace Centre (NLR), Anthony Fokkerweg 2, 1059 CM Amsterdam, Netherlands

juergen.teutsch@nlr.nl

Keywords: Augmented Reality, Air Traffic Control, Aerodrome Control Tower, Attention Guidance, Human Machine Interface, SESAR, NARSIM

Abstract. In recent years Augmented Reality (AR) has become one of the major focus points of user interface development. With the rapidly increasing computing power and developments in software and hardware applications during the last two decades, it has moved from theoretical approaches towards industry-wide application and mass production. The Royal Netherlands Aerospace Centre, NLR, tested several devices in the past, but only recent developments made it possible to effectively use them in an Air Traffic Control (ATC) working environment for Aerodrome Control Towers. In 2021 NLR carried out innovative technology experiments on their high-fidelity real-time air traffic control simulation and validation platform, NARSIM. These experiments were part of the SESAR 2020 project Digital Technologies for Tower (DTT) and focused on advanced HMI interaction modes for aerodrome tower controllers. A proposed Attention Capturing and Guidance concept with an AR device was evaluated inside an aerodrome control tower environment for Amsterdam Airport Schiphol. This paper reflects on the technology development activities that took place at NLR during the last decade and describes the different steps taken to apply the technology in a conventional control tower environment. It is shown that the recent technology developments must be seen as a big step forward in practical application of AR devices for ATC. Furthermore, an outlook into the expected future use of AR devices in conventional control tower environments will be given that goes beyond abovementioned concept elements. This outlook considers additional developments for standardization of digitized airport information and communication between different stakeholders and general performance improvements for AR devices.

Introduction

The technology used for AR combines virtual objects or information generated by a computer with the real world. These computer-generated overlays enhance user perception of the physical environment and, with added sensory input technology, lead to an interactive and immersive user experience. The history of AR devices already dates back several decades, with the technology evolving and advancing over time in the areas of power supplies, display and sound elements, and gyros for orientation. Through this, a major step from a simple display of data towards the inclusion of 3D-images in the real-world view could be achieved [1].

Royal NLR has been actively exploring applications for the use of HMD devices in the aerodrome tower ATC environment for over a decade. Initial research began in 2010 when NLR tested the nVisor ST™ HMD from NVIS in the NARSIM Tower environment, the in-house developed platform for highly realistic real-time simulations of ATC tower operations. The HMD device served as a demonstrator, displaying basic flight strip information that could either be static or change depending on the controller's line of sight.

In 2016, NLR integrated a Google Glass™ device (now known as Glass™) into the NARSIM environment to showcase additional capabilities with improved comfort to a selected group of air



traffic controllers from ATC The Netherlands (LVNL). The device streamed video feeds from remote cameras. These feeds were then displayed on Google Glass and switched automatically based on the user's direction of view, which was continuously tracked. This demonstration aimed to illustrate how tower controllers could gain visibility into apron areas by looking beyond physical obstructions in the line of sight, such as buildings.

In late 2019, with the arrival of the Microsoft HoloLens 2™ in the AR device market, NLR acquired two of these units. Although NLR had previously used HoloLens devices between 2016 and 2019 for various purposes like aircraft maintenance training, simulation debriefings, and projecting simulation results onto aircraft components, the potential of AR devices in the context of air traffic management and control had not yet been explored [2].

Evaluation of an AR Device for Attention Capturing and Guidance

With abovementioned development steps in mind, NLR continued the goal of investigating the possibilities of AR devices for enhancing the effectiveness and efficiency of tower ATC operations. In 2020 NLR joined a consortium for carrying out a project that focused on advanced HMI interaction modes for aerodrome tower controllers. That project was part of SESAR 2020, the second Single European Sky Advanced Research Programme, and was called Digital Technologies for Tower, DTT [3].

While the display of weather-adaptive static information (buildings and outlines) and flight phase-adaptive traffic labels as well as air gestures to interact with the labels and the system was carried out by other partners of the consortium, NLR focused this activity on the evaluation of an Attention Capturing & Guidance (AC&G) concept [4].

The AC&G concept was demonstrated in 2021 based on visual and auditory cues displayed in the AR device to alert and guide controllers in case of critical events. In order to find relevant events that would trigger that process, two existing Schiphol runway controller alerting systems were considered, the Runway Incursion Alerting System (RIAS) and the Go-around Detection System (GARDS). Both systems were previously prototyped on NARSIM and thus available in the simulation environment.

Different cues for each type of event were designed within the HoloLens application with different types of symbols for information display and user guidance. Various shapes and colours were tested, but also different information content. Aircraft labels available from the NARSIM A-SMGCS servers were also visualized inside the HoloLens and were used as attention getters and guidance elements, increasing the SA of the tower controller.

The test programme consisted of different events and combinations of events that happened while two experienced tower controllers carried out routine work in the NARSIM environment for Schiphol airport. Pseudo-pilots were in control of aircraft movements and communicated with the tower controllers. Similar traffic scenarios were used to compare working with and without the HoloLens. Results were gathered in different ways, using questionnaires after each test run and performing debriefings and interviews [5].

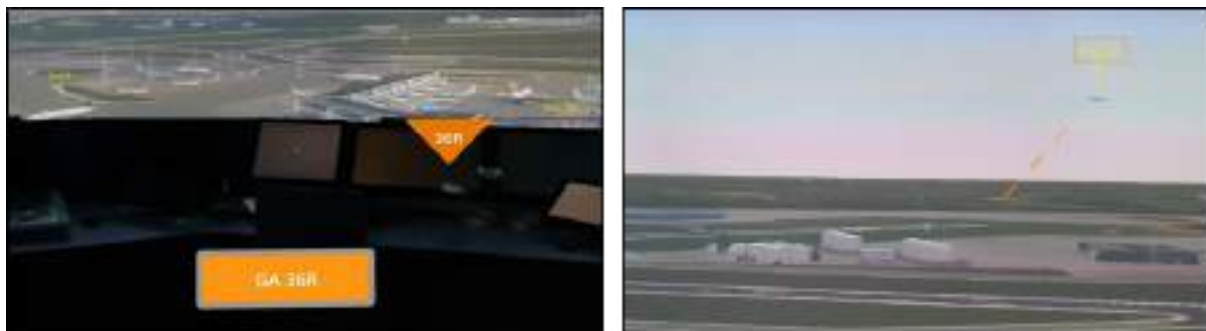


Fig. 1: Go-around Detection Alert as Seen through the AR Device

Based on the described evaluation experiment, it was determined that the AC&G operational concept for aerodrome tower controllers using an AR device is feasible and has potential. Although the experiment had a limited operational scope, and feedback was provided for improving certain aspects of the concept, the general outcome was positive. The feedback primarily focused on enhancing the symbology and timing of attention guidance cues. Overall, this result provided us with a solid foundation to further advance and refine the concept moving forward.

Additional Ideas about the Future Use of AR Devices in the Aerodrome Tower

Through discussions with the simulation participants, additional ideas emerged regarding potential future development steps and a vision for tower controller work with AR devices was developed. In the conventional context of improving existing visual operations within tower buildings, the inclusion of AR technology holds significant promise. AR presents the opportunity to enhance the outside view for controllers without the need to add further equipment to the working position and without forcing controllers to look down at the working position to acquire vital operational information. The latter means that head-up time is increased.

The augmentation of relevant information in the outside view including integrated 3D aural cues allows for several attention capturing and guidance capabilities that more effectively improve operations than non-AR technology. Intelligent virtual augmentation could include aspects, such as highlighted stop bars and their statuses, enhanced runway- and taxiway edges, indicated cleared routes for taxi operations, building contours and the outlines of other static obstacles or restricted areas. Such augmentation could be adapted automatically to the current visibility condition.

Traffic labels and their appearance and contents could be adapted to visibility conditions, the role of the controller, or the currently known flight status as well [6]. Taking it one step further, it could be investigated whether adaptation of what is shown or highlighted to support a controller could also take place in terms of the amount of traffic controlled or any signs of stress or high workload situations. This would mean that attention guidance would not only occur in case of a safety-relevant event already taking place, as in the case of safety net alerts being triggered, but much earlier in order to prevent such safety-critical situations in the first place.

Other technology additions may be considered as well, such as air gestures or automatic speech recognition. Air gestures generally would help in terms of system interaction, such as pulling up menus to change various settings, or system input operations, such as the selection of a route or a clearance limit as label information. Speech recognition, while generally meant to improve system input by itself, could be used together with AR to also highlight the labels of pilots calling in or, vice versa, callsigns being addressed by the controller, thus increasing SA and reducing workload once again.



Fig. 2: Innovative Use of AR Devices in the Aerodrome Tower (e.g. EFS, Adaptive Labelling)

Additionally, AR has the potential to redefine the roles and responsibilities of controllers, with the AR system being informed of the sequence of operations and actions required by each individual in the tower and guiding human actions in accordance with the expected procedures.

Naturally, such innovative arrangements would necessitate a high level of automation and a well-defined delegation of authority, particularly during system failures or contingencies. Nonetheless, a potential future milestone could involve a complete redefinition of all existing working arrangements in the pursuit of an optimal operation.

Conclusions

In summary, the potential of using AR devices in the aerodrome tower operational context is very promising but has not fully been investigated yet. Many innovative ideas and functions have not been addressed yet or even been conceived.

For the future, research with an exploratory character should be carried out to show the full potential of the functionalities sketched above, perhaps even from scratch, i.e. without being constrained by current working concepts and organisational structures. The focus of such research should be directed at the main capabilities of AR devices in terms of improvements in safety and operational efficiency, namely to augment controller vision by highlighting operationally relevant elements in an adaptive fashion inserting the most important information directly into the field-of-view. Other functionality exploiting the availability of different sensors (e.g. surveillance and video streams) or adding enhanced prediction capabilities on the basis of Artificial Intelligence [7] could be added to also guide controllers in carrying out operations using different kinds of visual and auditory cues with situation-adaptive information. Last but not least combinations of AR and automated system interaction and input technologies, such as speech recognition with Artificial Intelligence support, should be investigated further [8].

References

- [1] R.B. Wood, P.J. Howells, Head-up Display, in: C.R. Spitzer, U. Ferrell, T. Ferrell (Eds.), *Digital Avionics Handbook*, third edition, CRC Press, Taylor & Francis Group, Boca Raton (FL), 2015, pp. 17-1 to 17-27. <https://doi.org/10.1201/b17545>
- [2] S. Park, S. Bokijonov, Y. Choi, Review of Microsoft HoloLens Applications over the Past Five Years, *Applied Sciences*, 2021; 11(16):7259. <https://doi.org/10.3390/app11167259>
- [3] CORDIS EU Research Results, PJ05-W2 Digital Technologies for Tower, European Commission Website, Brussels, 2023. <https://doi.org/10.3030/874470>
- [4] J. Teutsch, T.J.J. Bos, G.D.R. Zon, Appendix A - Technological Validation Exercise 001 Report, in: SESAR 2020 PJ.05-W2 Sol. 97.1 and Sol. 97.2 TVALR, TRL4 Data Pack, Deliverable D3.1.050, SESAR-JU, Brussels, 2023. <https://doi.org/10.3030/874470>
- [5] J. Teutsch, T.J.J. Bos, M.C. van Apeldoorn and L. Camara, Attention Guidance for Tower ATC Using Augmented Reality Devices, 2022 Integrated Communication, Navigation and Surveillance Conference (ICNS), Dulles/Herndon, VA, USA, 2022, pp. 1-12. <https://doi.org/10.1109/ICNS54818.2022.9771479>
- [6] R. Santarelli, S. Bagassi, J. Teutsch, R. Garcia Lasheras et al., Towards a digital control tower: the use of augmented reality tools to innovate interaction modes, SESAR Innovation Days (SID) 2022, SESAR-JU, Brussels, 2022
- [7] P. Ortner, R. Steinhöfler, E. Leitgeb and H. Flühr, Augmented Air Traffic Control System - Artificial Intelligence as Digital Assistance System to Predict Air Traffic Conflicts, *AI Journal*, MDPI, 2022, 3(3), 623-644. <https://doi.org/10.3390/ai3030036>
- [8] European Aviation Artificial Intelligence High Level Group, The Fly AI Report - Demystifying and Accelerating AI in Aviation/ATM, EUROCONTROL, Brussels, 2020.

ADS-B driven implementation of an augmented reality airport control tower platform

Tommaso Fadda^{1,a*}, Sara Bagassi^{1,b} and Marzia Corsi^{1,c}

¹Department of Industrial Engineering, University of Bologna, Forlì, Italy

^atommaso.fadda2@unibo.it, ^bsara.bagassi@unibo.it, ^cmarzia.corsi2@unibo.it

Keywords: Augmented Reality, Air Traffic Control, ADS-B, Human Factors

Abstract. This paper describes a real-world implementation of the solutions developed within the SESAR DTT Solution 97.1-EXE-002 project, which tested in a simulated scenario the use of Augmented Reality (AR) to assist the airport control tower operators (TWR). Following a user-centred design methodology, the requirements of a real-world live AR platform join with design concepts validated in previous projects, namely the Tracking Labels, the weather interface, and a low-visibility overlay, all used to increase the TWR situational awareness, performance and reactivity while reducing the workload. The designed AR platform performs the live tracking and visualization of real aircraft and surveillance information in the airport traffic zone. It bases on three key processes: the transmission of an ADS-B data flow to a Microsoft™ HoloLens2, the registration process of the AR platform, and the rendering of a real-time tracking system and other surveillance overlays. The concept has been first validated with the help of a TWR, preceding a technical validation to ensure the repeatability and reproducibility of the results. The results allow for defining new guidelines for the deployment in a control tower environment.

Introduction

Being an airport control tower operator (TWR) implies overseeing the aircraft in the airport manoeuvring area and departing and arriving traffic, relying on the out-of-the-window (OTW) tower's view to provide separation and clearances. In this high-risk, high-concentration and time-critical job, controllers are concerned with keeping a smooth traffic flow while ensuring the overall safety of airport operations, with the sum of these tasks resulting in a heavy workload.

While performances are a priority in a worldwide ever-growing traffic scenario, the main upgrades in TWRs' job were due to the addition of visual interfaces, which are better suited to ensure an increase in safety, with a collateral increase in cognitive workload due also to the continuous shift of focus between the outside view (head-up position) and the head-down interfaces at the work position providing surveillance and traffic information [1].

In this scenario, Augmented/Mixed Reality (AR) is suitable for helping the TWR [2], moving the surveillance information from the head-down interfaces to a collinear vision within the OTW airport traffic, promising to solve the chronic safety over performance compromise. At the University of Bologna, Solution 97.1-EXE-002 of the SESAR's funded "Digital Technologies for Tower" (DTT) project [3,4,5] tested this possibility, using a system of virtual tracking labels to pinpoint each aircraft in the user's view, providing context-related flight information, tailored to different control roles (ground vs runway) and environmental conditions. TWRs could then keep the focus on the live traffic, with increased situational awareness and reduced workload, while improving the overall safety and efficiency (temporal and thus economical) of airport operations in every condition, especially high-traffic and low-visibility.

These studies were conducted in a simulated real-time airport scenario, focusing on developing the overall AR concept in a safe, non-critical, and fully controllable environment. This paper describes the subsequent implementation of the developed concepts into the real world, resulting in a live application tracking operative aircraft and acquiring their surveillance information. The



research addressed the tasks needed when dealing with a real-time physical world application. A new set of requirements have been defined, dealing with a global-coordinates registration process for AR and using live ADS-B data to retrieve the desired traffic information, as will be later described.

Methods

User-centred design (UCD) method is the obvious choice when dealing with a tricky task such as airport tower control. The design process is iterative, always considering the user needs before, during and after the development, ensuring that the final concept helps the TWR without relevant contraindications. This research aimed to increase the maturity of the solutions developed in a simulated environment, performing the critical steps to move up from a previous level 4 of the technology readiness scale, by transferring the concept into a relevant environment. For this purpose, some requirements were identified, joining outcomes of the lab validation campaign with new requirements for a real-world implementation. Table 1 summarizes all the requirements to implement and validate a real-time AR platform for the control tower.

Table 1. Summary of the design requirements

Solutions developed in previous projects	Requirements for real-world implementation
Use of Microsoft HoloLens2 as AR device	Real-time acquisition of accurate aircraft position
AR application developed with Unity3D	Accurate real-time tracking of aircraft in AR layer
Registration strategy using MRTK WLT	Management of multiple aircraft at the same time
Design of the tracking labels	Render tracking holograms minimizing latency
Definition of a runway overlay	Evaluate and counteract possible error sources
Design of the weather interface	Ensure reliability and precision of tracking system
Use of adaptive human-machine interface	Implement additional surveillance overlays
Ergonomic aspects	Validate

Design of the AR-based control tower platform

Starting from the requirements, a preliminary concept has been defined, using an ADS-B receiver to detect the aircraft in real-time and retransmitting the data stream to a HoloLens2 device using a user datagram protocol (UDP). The AR application in the device processes the data, identifying aircraft position and rendering the tracking labels. Figure 1 shows the architecture of the platform.

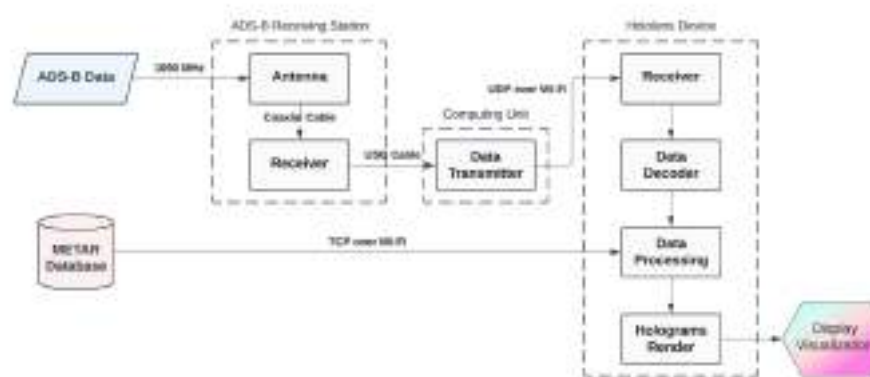


Figure 1. Architecture of the AR platform

ADS-B data flow. The vector state information is acquired from ADS-B data, which is constantly sent in real-time by every commercial aircraft. These data are read on a pc unit over serial communication and retransmitted over a UDP to the HoloLens, where they are used to constantly track the aircraft in the virtual world and provide surveillance information.

Calibration. A key aspect of AR applications is the registration process, meaning the continuous alignment of the virtual overlay over the intended elements in the physical world. Most AR technologies rely on a tracking system which can identify the user's position inside an environment and project the holographic overlay accordingly, with a real-time adaptation of the virtual elements' alignment over the physical world. This procedure is suited to position holograms with respect to a local frame of reference. Since aircraft positions are in global (geodetic) coordinates, a calibration procedure is required for the registration to occur. HoloLens2's applications can only fix the position of a virtual reference frame inside a room. Thus, a procedure was developed to identify the global position and orientation of this reference frame and then convert the relative position of aircraft with respect to the reference frame into cartesian coordinates using a conversion algorithm from geodetic coordinates to an East-North-Up (ENU) frame. Figure 2 shows the alignment of the reference frames and how the HoloLens 2 reference frame was positioned inside the environment. The virtual reference frame geodetic position is identified, and then the aircraft position is converted for an ENU frame with an origin coinciding with the virtual one. Finally, a rotation is applied to convert ENU coordinates into those of the virtual frame.

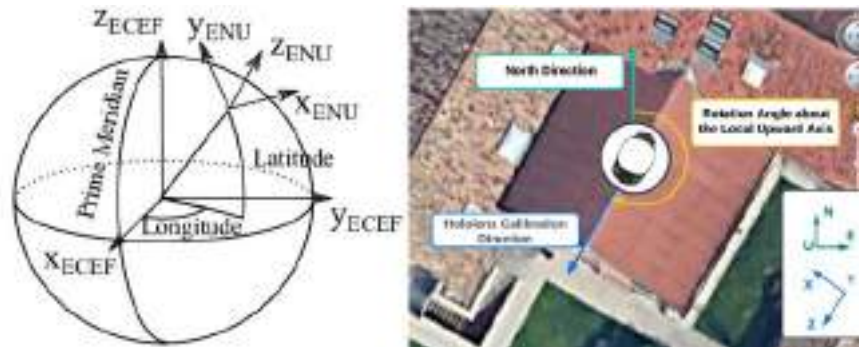


Figure 2. Calibration steps

Correction of position information. Some corrections had to be applied to the aircraft position data to obtain an adequate matching of the holograms. In particular, the altitude data comes from the pressure altimeter, with the uncorrected barometric altitude (H_{QNE}) - computed by the onboard barometer with respect to the standard sea-level value of 1013.25hPa - transmitted for collision avoidance purposes. The near-ground effect is also an issue at landings. Thus, the altitude was corrected considering the current sea-level pressure at the airport location (p_{QNH}), and a corrective term for landing gear height and ground effect (p_{LG}). The correction formula reports the height over ground (H_{QFE}) as the uncorrected altitude plus a corrective term for the different reference pressure, times a conversion term for the variation of pressure with altitude:

$$H_{QFE}(m) = H_{QNE}(m) + (p_{QNH} - (1013.25hPa - p_{LG})) \times 8,23m/hPa \quad (1)$$

Labels implementation. The tracking label design was retrieved from that already validated in the EXE-002 of Solution 97.1. The labels contain the aircraft height over ground (H_{QFE}), velocity, heading and callsign, with other information already computable or available, such as the distance from any point of the airport, the vertical rate, and H_{QNE} . The labels are positioned at a constant focal distance from the user, with a small sphere pinpointing the aircraft and a surmounting canvas containing the aircraft data. Colour coding is used for landing and departing traffic.

Real-time labels management. The whole purpose of the application is to track each detected aircraft keeping its position and information updated in real-time. The data processing chain starts with the ADS-B data being sent to the AR device as soon as they are detected. On the HoloLens2, the data are decoded and organized into a database containing the most updated information for

each aircraft, which is then used to calculate the holograms' position, update the label content, and render the holograms in a seamless cyclic loop run at least at 60Hz, which is the rendering frame frequency. Being HoloLens2 capable of tracking the user's position relative to the virtual reference frame, the holograms stay in place while both aircraft and users move.

Additional overlays. The application was completed with additional overlays helping the controller, in particular a weather interface, using real data from METAR, and a runway overlay for low-visibility conditions, triggered by the visibility distance indicated by the METAR.



Figure 3. Tracking Labels visualization with runway overlay, colour coding, and weather interface

Technical validation. As part of the UCD, a technical validation was needed to ensure the goodness of the design. After that, the fulfilment of all the requirements was verified in different environments to verify the repeatability and reproducibility of the configuration.

Conclusion

This paper presented an AR control tower application working in a real-world scenario. Real-time data were used, and the matching of real and virtual worlds was addressed.

Future development. Starting from this concept, it will be possible to improve the application by testing it in shadow mode in a control tower, while integrating other surveillance information and solutions coming from the SESAR programme.

References

- [1] Pinska, E., "An investigation of the head-up time at tower and ground control positions", Eurocontrol (2006).
- [2] R. Reisman, D. Brown, "Design of Augmented Reality Tools for Air Traffic Control Towers", 6th AIAA Aviation Technology, Integration and Operations Conference – ATIO (2006). <https://doi.org/10.2514/6.2006-7713>
- [3] S. Bagassi, F. De Crescenzo, S. Piastra, C.A. Persiani, M. Ellejmi, A.R. Groskreutz, J. Higuera, "Human-in-the-loop evaluation of an augmented reality based interface for the airport control tower", in *Computers in Industry*, Volume 123, article number 103291 (2020). <https://doi.org/10.1016/j.compind.2020.103291>
- [4] R. Santarelli, S. Bagassi, M. Corsi, J. Teutsch, R. Garcia Lasheras, M.A. Amaro Carmona, A.R. Groskreutz, "Towards a digital control tower: the use of augmented reality tools to innovate interaction modes", 12th SESAR Innovation Days, Budapest, Hungary, 5-8 December 2022.
- [5] Digital technologies for tower, <https://www.sesarju.eu/projects/dtt>. (2023).

Maturity-based taxonomy of extended reality technologies in aircraft lifecycle

Sara Bagassi^{1,a}, Marzia Corsi^{1,b*}, Francesca De Crescenzo^{1,c}, Martino Carlo Moruzzi^{1,d}, Sandhya Santhosh^{1,e}

¹Department of Industrial Engineering, University of Bologna, Forlì, Italy

^asara.bagassi@unibo.it, ^bmarzia.corsi2@unibo.it, ^cfrancesca.decrecenzio@unibo.it,

^dmartinocarlo.moruzzi2@unibo.it, ^esandhya.santhosh2@unibo.it

Keywords: Aircraft Lifecycle, Extended Reality, Aircraft Design, Aircraft Operations

Abstract. EXtended Reality (XR) is a fast growing and rapidly evolving technology. In the aeronautical sector, XR can be exploited for the entire aircraft lifecycle, however, different levels of maturity can be identified for applications in each one of the lifecycle's phases. This paper, by outlining the TRL of current XR applications over the aircraft lifecycle, aims to be a foundation to identify the possible future improvements and applications of immersive technologies in the aeronautical sector.

Introduction

EXtended Reality (XR) is a fast growing and rapidly evolving technology, a comprehensive term given to all computer-generated environments that either merge the physical and the virtual worlds or create an entirely immersive experience for the user. Even if XR technologies such as Virtual (VR) and Augmented Reality (AR) have already reached maturity as they are considered mainstream for a few domains of application, in the aeronautical sector this is not yet entirely true. XR can be exploited for the entire aircraft lifecycle, however, different levels of maturity can be identified for applications in each one of the lifecycle's phases (Figure 1).



Figure 1: Aircraft lifecycle's phases and Technology Readiness Level (TRL).

This paper, by outlining the TRL of current XR applications over the aircraft lifecycle, aims to be a foundation to identify the possible future improvements and applications of immersive technologies in the aeronautical sector.

Extended Reality in Aircraft Lifecycle

Extended Reality technologies can find a number of applications in aeronautics. Synthetic visualisation and multimodal interaction tools target almost all aircraft lifecycle phases. From design to manufacturing and maintenance, passing through training and operations [1] and since the early stages of industrialisation, the main aeronautical companies are relying on those technologies [2].



Figure 2: Industry-first concept based on Mixed Reality technologies for Cabin Customisation and Design for the A320 Family (courtesy of Airbus¹).

In the design and development phases, rather mature applications are established in the field of synthetic visualization which allow for a better understanding of the performance achieved by a certain design solution². Furthermore, XR has proven to be beneficial for collaborative design, design reviews and user assessment throughout the product development process [3]. This application is still in the early stages of research, begin now developed as a proof of concept [4]. One of the biggest opportunities provided by XR is the one of including user feedback in the design process, as proved in a study conducted to virtually test the comfort of newly conceived aircraft cabin designs. Not only the project exploited V/AR technology to validate the proposed design approach and strategy in the design of aircraft cabins, but it demonstrated how XR can be a useful tool, starting from the very early stages, to the entire process which results to be more open and flexible, time efficient and cost-effective [5]. As a matter of fact, early stages of design, when prototypes are still in the digital phase, are ideal for leveraging eXtended Reality technologies. Recent research^{3,4} [6], makes use of advanced VR technologies to enable the different stakeholders to experience and be immersed in the full scale design, allowing them to be involved in the process starting from the Inspiration and Ideation Phase [7-8].

In view of the production phase, a number of applications are developed within the framework of Industry 4.0 which aim at exploiting XR to make aircraft systems production and final assembly more efficient in terms of time, quality and dependability. In particular, if VR is mainly applied during the design phase, AR is mostly used in the production line. The usage of synthetic visualisation tools leading to early detection of non-conformities allows not only to avoid expensive corrections but also to improve the quality control process and reduce inspection time. Nevertheless, users' familiarity and training with the specific devices and technology are crucial aspects and must be considered to achieve the best possible results [9].

Airbus, among other companies such as Boeing and Embraer, foresaw the potential and applicability of digital technologies since the early 2000s, and in 2009 the European company collaborated to create an AR solution (*MiRA - Mixed Reality Application*) consisting of a tablet PC and related sensor pack to scan parts and detect errors. On the A380 MiRA allowed to check 80.000 brackets in the fuselage reducing the time needed from weeks to hours and the late discovery of mispositioned or damaged brackets by 40% [10]. Currently, Airbus is industrializing a first application to be deployed across various sites either to help with the drilling and fitting of brackets or to support quality control activities¹.

¹ <https://www.airbus.com/en/newsroom/stories/2023-06-mixed-reality-to-meet-future-challenges>

² <https://www.holoforge.io/en/project/safran-marketing/>

³ https://www.dlr.de/as/en/desktopdefault.aspx/tabid-18135/28809_read-74794/

⁴ <https://www.dlr.de/en/images/2020/1/indicad-fuselage-designs-for-the-future>

AR devices such as head-mounted displays, can be used not only to assist the assembly procedure, but also for communication purposes in human-autonomy system teams as proved by a recent research in which the hybrid team has to rivet stringers onto a fuselage [11]. Hazardous and physically demanding tasks were assigned to the mobile robotic system, while the human workers performed tasks requiring experience, knowledge and multi-sensory sensitivity.

The operational environment is benefiting a lot from the application of XR, both in training and real-life operations. One of the first applications of Augmented Reality is the cockpit head-up display (HUD), which enables the pilot to get synthetic information collimated with the real view (Figure 3). This is the only optical-based XR application that already reached complete maturity in the aeronautical sector.

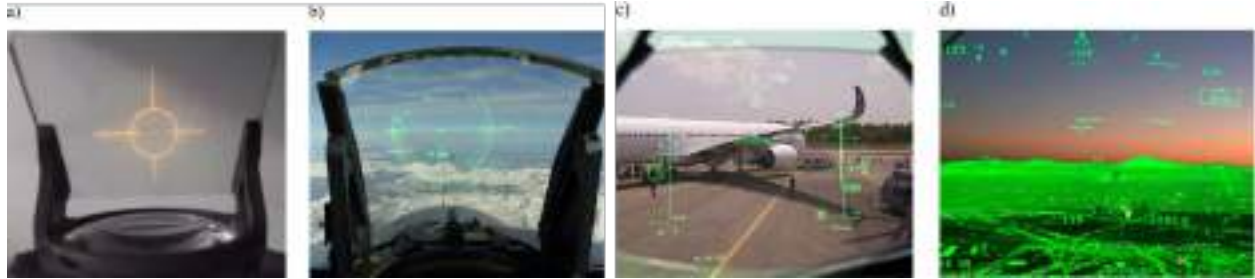


Figure 3: Technological advancement of the cockpit HUD [14].

More recently, different research projects explored a similar operational concept applied to airport control towers [12-13] reaching the development phase. The projects demonstrated how XR technologies in control towers are beneficial for the situational awareness of the controllers especially when the aerodrome is affected by low visibility conditions. The capability to make degraded visual information visible during low visibility and low-altitude operations given by XR can also enhance spatial awareness and safety during low visibility helicopters or ground operations [14-16]. Furthermore, ground operations are good candidates for technical solutions that make use of XR technologies.

Moving on to the support phase, a few quite mature applications of XR in maintenance, [17] inspection and repair operations are possible to identify. In 2015, Boeing adopted AR technology to reduce the impact of assembly harness errors. In 2017, General Electric used AR technology to communicate to mechanics whether they are properly tightening and sealing jet engine B-Nuts, and the working efficiency increased by 8-12% [18]. Maintenance is of paramount importance in the aviation industry therefore inspection and maintenance personnel have to be trained with appropriate tools. Training methods need to keep up with advanced technologies while ensuring safety and cost-effectiveness. Exploiting eXtended Reality as a training tool can overcome this issue providing a safe learning environment drastically reducing the risks that may occur during training with reduced costs, and improving labor efficiency [19].

The presented immersive technologies solutions are only a few of the numerous ones already available in the aeronautical sector. The proposed preliminary assessment of maturity-based taxonomy of XR technologies in aircraft lifecycle (Table 1) aims to serve as a base to identify the future possible improvements and applications of these technologies in the aircraft lifecycle. Furthermore, serves as a useful tool in understanding and addressing the number of challenges, ranging from technology to human factors, the aeronautical sector will face while maturing XR solutions in specific phases of aircraft lifecycle.

Table 1: Preliminary taxonomy assessment of XR technologies in aircraft lifecycle.

Lifecycle Phase		Taxonomy assessment		Reference
Design & Development	Scientific visualisation	Development	TRL 4-6	^{^2}
	Collaborative design	Research	TRL 1-3	[3-4]
	Human-centered design	Research	TRL 1-3	[5-8] - ^{^3-4}
Production	Assembly	Deployment Development	TRL 7-9 TRL 4-6	[9-10] ^{^1}
	Human-autonomy teaming	Research	TRL 1-3	[11]
Operation	Cockpit HUD	Deployment	TRL 7-9	[14]
	Airport Control Tower	Research	TRL 3	[12-13]
	Ground Operations	Development	TRL 4-6	[14-16]
Support	Maintenance	Deployment	TRL 7-9	[17-19]
	Digital Twin interaction	Research	TRL 1-3	[20]

Conclusions

As a matter of fact, most of the presented solutions may reach maturity in the next 20 years. The vision is that, in the future, XR will be an extension of the human senses necessary to understand, interact, control, and command complex systems belonging to the digital era.

In the context of aeronautics, a more advanced level of development would regard XR as a means to visualize and interact with digital twins throughout the entire aircraft lifecycle [20]. EXtended Reality will be the technical enabler to interact with such systems that will be more autonomous and enhanced by artificial intelligence. Nevertheless, a number of challenges and barriers are still limiting the evolution of such technology in aeronautics, making its development slower than expected. XR still relies on cumbersome equipment, previous attempts to overcome this obstacle have proven unsuccessful. Incremental improvements are being made to enhance the wearability of hardware. Additionally, more automated solutions are needed to fully exploit the potential of such technology. Whilst a few Mixed Reality devices are already mainstream, non-intrusive solutions are not mature enough. The cost of equipment along with some big company trends are also acting as barriers to the deployment of business solutions based on XR technology. Although Industry 4.0 was expected to boost XR growth, it has also introduced some standardization issues in a number of application domains. Lastly, human factors and user acceptance are considered among the main risks for eXtended Reality massive use in safety-critical environments.

A maturity-based taxonomy of immersive technologies aims to be a tool to understand and overcome the number of challenges, ranging from technology to human factors, the aeronautical sector will face while maturing XR solutions in specific phases of aircraft lifecycle.

References

- [1] Neretin, E. S., Kolokolnikov, P. A., & Mitrofanov, S. Y. (2021, June). Prospect for the application of augmented and virtual reality technologies in the design, production, operation of aircraft and training of aviation personnel. In *Journal of Physics: Conference Series* (Vol. 1958, No. 1, p. 012030). IOP Publishing. <https://doi.org/10.1088/1742-6596/1958/1/012030>

- [2] Frigo, M. A., da Silva, E. C., & Barbosa, G. F. (2016). Augmented reality in aerospace manufacturing: A review. *Journal of Industrial and Intelligent Information*, 4(2). <https://doi.org/10.18178/jiii.4.2.125-130>
- [3] S. Santhosh, and F. De Crescenzo, 2022. A Mixed Reality Application for Collaborative and Interactive Design Review and Usability Studies. In *Advances on Mechanics, Design Engineering and Manufacturing IV: Proceedings of the International Joint Conference on Mechanics, Design Engineering & Advanced Manufacturing, JCM 2022, June 1-3, 2022, Ischia, Italy* (pp. 1505-1515). Cham: Springer International Publishing. https://doi.org/10.1007/978-3-031-15928-2_131
- [4] M. Fuchs, F. Beckert, J. Biedermann and B. Nagel. Collaborative knowledge-based method for the interactive development of cabin systems in virtual reality. *Computers in Industry*, Vol. 136, 103590, ISSN 0166-3615, 2022. <https://doi.org/10.1016/j.compind.2021.103590>
- [5] F. De Crescenzo, S. Bagassi, S. Asfaux, N. Lawson (2019). Human centred design and evaluation of cabin interiors for business jet aircraft in virtual reality. *International Journal on Interactive Design and Manufacturing (IJIDeM)*, 13, 761-772. <https://doi.org/10.1007/s12008-019-00565-8>
- [6] I. Moerland-Masic, F. Reimer, T. M. Bock, F. Meller, & B. Nagel, (2021). Application of VR technology in the aircraft cabin design process. *CEAS Aeronautical Journal*, 1-10. <https://doi.org/10.1007/s13272-021-00559-x>
- [7] Schuchardt, B. I., Becker, D., Becker, R. G., End, A., Gerz, T., Meller, F., ... & Zhu, C. (2021). Urban air mobility research at the DLR German Aerospace Center—Getting the HorizonUAM project started. In *AIAA Aviation 2021 Forum* (p. 3197). <https://doi.org/10.2514/6.2021-3197>
- [8] Schuchardt, B. I. (2021, September). HorizonUAM Project Overview. In *HorizonUAM Symposium 2021*.
- [9] de Souza Cardoso, L. F., Mariano, F. C. M. Q., & Zorzal, E. R. (2020). Mobile augmented reality to support fuselage assembly. *Computers & Industrial Engineering*, 148, 106712. <https://doi.org/10.1016/j.cie.2020.106712>
- [10] Glockner, H., Jannek, K., Mahn, J., & Theis, B. (2014). Augmented reality in logistics: Changing the way we see logistics—a DHL perspective. *DHL Customer Solutions & Innovation*, 28.
- [11] Luxenburger, A., Mohr, J., Spieldenner, T., Merkel, D., Espinosa, F., Schwartz, T., ... & Stoyke, M. (2019, December). Augmented reality for human-robot cooperation in aircraft assembly. In *2019 IEEE International Conference on Artificial Intelligence and Virtual Reality (AIVR)* (pp. 263-2633). IEEE. <https://doi.org/10.1109/AIVR46125.2019.00061>
- [12] S. Bagassi, F. De Crescenzo, S. Piastra, C. A. Persiani, M. Ellejmi, A. R. Groskreutz, J. Higuera, Human-in-the-loop evaluation of an augmented reality based interface for the airport control tower, *Computers in Industry* 123 (2020) 103291. <https://doi.org/10.1016/j.compind.2020.103291>
- [13] R. Santarelli, S. Bagassi, M. Corsi, J. Teutsch, R. Garcia Lasheras, M. Angel Amaro Carmona, A. R. Groskreutz, Towards a digital control tower: the use of augmented reality tools to innovate interaction modes, in: *Sesar Innovation Days 2022*, 2022.
- [14] Stanton, N. A., Plant, K. L., Roberts, A. P., & Allison, C. K. (2019). Use of Highways in the Sky and a virtual pad for landing Head Up Display symbology to enable improved helicopter pilots situation awareness and workload in degraded visual conditions. *Ergonomics*, 62(2), 255-267. <https://doi.org/10.1080/00140139.2017.1414301>

- [15] Blundell, J., Collins, C., Sears, R., Plioutsias, A., Huddleston, J., Harris, D., ... & Lamb, P. (2022). Low-visibility commercial ground operations: An objective and subjective evaluation of a multimodal display. *The Aeronautical Journal*, In-press. <https://doi.org/10.1017/aer.2022.81>
- [16] Blundell, J., & Harris, D. (2023). Designing augmented reality for future commercial aviation: a user-requirement analysis with commercial aviation pilots. *Virtual Reality*, 1-15. <https://doi.org/10.1007/s10055-023-00798-9>
- [17] H. Eschen, T. Kötter, R. Rodeck, M. Harnisch, T. Schüppstuhl, (2018). Augmented and virtual reality for inspection and maintenance processes in the aviation industry. *Procedia manufacturing*, 19, 156-163. <https://doi.org/10.1016/j.promfg.2018.01.022>
- [18] Hongli, S., Qingmiao, W., Weixuan, Y., Yuan, L., Yihui, C., & Hongchao, W. (2021). Application of AR technology in aircraft maintenance manual. In *Journal of Physics: Conference Series* (Vol. 1738, No. 1, p. 012133). IOP Publishing. <https://doi.org/10.1088/1742-6596/1738/1/012133>
- [19] Wu, W. C., & Vu, V. H. (2022). Application of Virtual Reality Method in Aircraft Maintenance Service—Taking Dornier 228 as an Example. *Applied Sciences*, 12(14), 7283. <https://doi.org/10.3390/app12147283>
- [20] Albuquerque, G., Fischer, P. M., Azeem, S. M., Bernstein, A. C., Utzig, S., & Gerndt, A. (2023). Digital Twins as Foundation for Augmented Reality Applications in Aerospace. In *Springer Handbook of Augmented Reality* (pp. 881-900). Cham: Springer International Publishing. https://doi.org/10.1007/978-3-030-67822-7_35

Keyword Index

3D Elements	313	Aircraft Structures	381
3D Printing	325	Aircraft Systems	66
		Airport Noise	2
Acoustic Metamaterials	748	Airworthiness Requirements	399
Acoustic Resonators	254,740	Analytical Models	630
Acoustic	6	Anomaly Detection	625
Adaptive Finite Elements	313	Arbitrary Polygons	313
Adaptive Material	731	ArgoMoon	634
Adaptive Wing	349	Artemis-1	634
Additive Manufacturing	296,417,645	Asteroid	585
ADS-B	767	Astronauts Training	721
Advanced Air Mobility	426	Atmospheric Re-Entry	668
Aero Engine	6	Attention Guidance	763
Aeroacoustics	2,10,17	Attenuation	6
Aerocapture	522	Augmented Reality	763,767
Aerodrome Control Tower	763	Automated Fiber Placement	317
Aerodynamic Efficiency	337	Autonomous Proximity Operations	458
Aerodynamic Noise	21	Autonomous System	504,508
Aerodynamics	61,230,435	AWE	137
Aeroelastic Wind Tunnel Testing	48	Axial-Flux PMSM	89
Aeroelasticity	38		
Aeronautical History	84	Balanced Truncation	235
Aeronautics	249	Bar-and-Hinge	547
Aerospace Structures	291	Batch Filter	526
Aerospike Engine	695	Binary Models	390
Aerospike	675	Biodynamic Feedthrough	26
Aero-Thermo-Dynamic Loads	530	Boresight Pointing	611
Air Pollution	581	Boundary Element Method	341
Air Traffic Control	763,767	Boundary Layer Ingestion	17,61
Air Traffic	639	Break-Up	465,639
Aircraft Conceptual Design	431	Broadband	6
Aircraft Design	435,771	Buckling	349
Aircraft Electric Conversion	431	BWB	2
Aircraft Lifecycle	771		
Aircraft Noise	748	Cabin Design	758
Aircraft Operations	771	Capture Tool	508
		Carrera Unified Formulation	239,313,321,357,748

Casting Process	690	CubeSat	413,495,518
Cathode-Less Plasma Thrusters	679	CUF	141
Cavitation	197	Cumulative Distribution	513
Ceramic Matrix Composites	390	Curved Channel Flow	222
Certification by Analysis	399	Curved Composite Stiffened Panel	421
CFD	166,174,230		
CFRP	373	Damage Identification	146
Characteristic Velocity	664	Damage	386
Cis-Lunar	634	Damped Sinusoids	744
Clean Space	553	DART	634
Climatic Chamber	258	Data Fusion	70
Clothoids	104	Data Merging	713
CO2 Emission Standard	122	Debris	495
Co-Design	758	Deep Learning	368
Combined Loads	421	Deep Neural Networks	409
Combustion-Driven Facility	218	Deep Space	634
Composite Material	404	Defect Modeling	317
Composite Plate	146	Delamination Growth	373
Composite Structures	349,377,409	Deorbiting	553
Compressible	211	Deployable Booms	357
Computational Fluid Dynamics	61	Deployable Capsule	530
Computational Homogenization	341	Deployable Radiator	413
Computational Micro-Mechanics	341	Deployable Structure	572,547
Computer Vision	705	Design for Manufacturing	296
Conceptual Design	42,57	Deterministic Forces	736
Confined Aeroacoustics	21	Didymos	585,634
Conjugate Heat Transfer	206	Digital Twin Platform	249
Conjunction Analysis	526	Dilution of Precision (DOP)	108
Contact Mechanics	357	Dimorphos	634
Contingency	99	Discontinuous Galerkin Method	202,287
Continuum Damage Mechanics	390	Distributed Electric Propulsion	2
Correlation	499	Distributed Kalman Filter	94
Cover	725	Docking System	504
Crack Detection	308	Docking	518
Cryogenic	226	Doppler Observable	108
Cubesat Formation Flying	660	Double-Double	377
CubeSat Mission	483	Drag Modulation	522
CubeSat Swarms	590	Dust Mitigation	266

Dynamic Buckling	404	Fiber Optic Sensors	333
Dynamic Stall	156,161	Fibre Reinforced Composite	329
		Finite Element Analysis	421
e VTOL	80	Finite Element Method	239
Earth Monitoring	581	Flamelets	53
Earth Orbit Transfers	606	Flexible Spacecraft	368,487
Earth-Moon Transfers	596	Flight Data	530
EcosimPro Simulations	654	Flight Mechanics	137
Elastic Wave Propagation	304	Flight Path Control	634
Elastic Wedge	363	Floating Module	538
Elastoplastic Materials	394	Fluid-Structure Interaction	197,363
Electric Aircraft	448	Flutter Suppression	48
Electric General Aviation	431	Flutter	34,38,345
Electric Propulsion	431,679	Flux Homogeneity	700
Electrodynamics	534	Fly Your Satellite! Design Booster	495
Electromagnetic Microwave Propagation	469	Flying Test Bed	230
Electronics	601	Footprint	2
EMA	80	Formation Flying	621
Embedded Systems	444	Forward Swept Tailplane	435
Emitter	474	Fourier Transform Spectroscopy	270
Energy Efficiency	337	Fragmentation Testing	513
Energy Generation	381	Fragmentation	465
Enhanced Craig-Bampton	235	Frame-Dragging	563
Enveloped Sinusoids	744	Free-Floating Platforms	458
Environmental Sustainability	122	Freeze-Thaw Cycle	329
Epoxy Resin	333	Friction-Locking Devices	601
Eulerian Scheme	127	Front Door	725
EUSST	474	Fuel Cell	448
Event-Based Sensing	567	Fuel Gauging System	66
Experimental	675	Fuel System	66
Exploration	478	Full Flight Simulator	754
Extended Reality	426,771	Full-Electric Propulsion	89
		FWH	10
Fatigue	373	General Relativity	563
Feedback Guidance and Control	596,606	Generalized Curvilinear Coordinates	222
FEM	141	Genetic Algorithm	668
Fiber Bragg Gratings	417	Global Navigation Satellite Systems	108

Global Plasma Models	679	Hypersonic Vehicles	280
Green Aircraft	440	Hypersonic	170,218,230
Green Chemical Propulsion	645	Hypobaric Chamber	258
Gust Alleviation	133		
Gust Loads Alleviation	48	Ice Accretion	258
		Ice Crystals	127
Hardware in The Loop	70	Ice Tunnel	258
Harmonic Balance	10		
Helicopter Rotors	156	Image Processing	308
Helicopters	161	Immersive Technologies	426
Hera	585	Impact Detection	150
High Aspect Ratio Wing	34,42	Impact	585
High Flux Solar Simulator	700	Impingement	127
High-Order Accuracy	202	In Vacuo Material	731
High-Order Modelling	287	Inflatable Heat Shields	576
High-Order Structural Theories	300	In-Flight Calibration	542
High-Performance Polymers	266	In-Flight Icing	184
Hinge Moment	417	Inlet	6
HLLC Scheme	695	Innovative Design	118
Hopf Bifurcation	345	In-Orbit Servicing	508
Horizon Europe	576	Inspection	518
Human Factors	754,767	Interferometry	270
Human Machine Interface	426,763	Interior Penalty Coupling	353
Human Space Exploration	721	International Space Station	291
Humidity Absorption	329,333	IRIS	634
Hybrid Aircraft	76	Isogeometric Analysis	353
Hybrid Propulsion Systems	448	Isotropic Hardening	394
Hybrid Rocket Engine	660	ISRU	483
Hybrid Rockets	645,664		
Hybrid Schemes	170	J2 Effects	621
Hybrid Structures	296	Jacobian-Less Methods	30
Hydrodynamic Schrödinger Equation	174	Jet Propulsion	61
Hydrogen Peroxide	645,660	JUICE	558,725
Hydrogen	53	Jupiter	558
Hygrothermal Aging	333		
Hygrothermal Effects	329	Kane's Method	487
Hypersonic Aerodynamics	179	Kinematic Hardening	394
Hypersonic Flows	166	Kirchhoff-Love Shells	353

Lamb Waves	150	Lyapunov Characteristic Exponents	30
Laminar Separation Bubble	21,189		
Laminar-to-Turbulent Transition	166	Machine Learning	66,146,150,705
Laminates Optimization	377	Magnetorquers	611
Landing Gear	84	Manoeuvres	518
LARES 2	563	Mars Exploration	522
Large Constellation Design	108	Martian Atmosphere	211
Large Eddy Simulation (LES)	189,193	Mass Saving	377
Laser Ranging	563	MDAO	137
Lattice Boltzmann Method	174	Mechanics	547
Lattice Structures	296	Mesh Adaptation	184
Lattice-Boltzmann Method	21	Metallic Lattice Materials	386
Launchers	280	Metamaterial	325
Layer Wise (LW)	300	Metis	542
Leading Edge eXtension	435	Micromix Combustion	53
Level-Set Method	184	Microvibrations	235
LICIACube	634	Milani	585
Lifting Reentry	615	Mission Analysis	590
Light Curves	499	Modal Finite Element Analysis	601
Light Pollution	581	Model Based Systems Engineering	444
Limit Cycle Oscillation	38	Moon Surface Absorption	469
Linear Quadratic Estimation Method	274	Moon	266,483,634
Liner	6	MOR Techniques	235
Liquid Rocket Engine	206,654	MORE&LESS	57
Liquid Thrusters	645	Morphing Structure	572
Liquid-to-Liquid Heat Exchanger	76	Morphing Wings	133
Low Energy Transfers	596	Morphing	337
Low Friction Table	538	Multi Fluid Approach	679
Low Noise Technologies	2	Multibody Dynamics	30
Low Reynolds Number	211	Multibody Modelling	26
Low Thrust Propulsion	630	Multibody Spacecraft Dynamics	487
Low-By-Pass Turbofan	57	Multi-Disciplinary Optimization	440
Low-Thrust Maneuver Estimation	625	Multifunctional Materials	381,399
Low-Thrust Spacecraft	596,606	Multi-Functional Metamaterial	572
LOx/LCH4	654	Multilayered Shells	287
LPT	483	Multi-Object Tracking	567
LS-DYNA	363	Multi-Objective Optimization	337
Lunar Regolith	469	Multiscale Materials Modelling	341

Multi-Spectral	262	Orbit Perturbations	621
Multispectral/SAR Database	483	Orbit Propagation	621
Multi-Step	184	Orbital Maneuvers	660
		Ordinary State-Based Peridynamics	394
Nanofluid	76	Origami Structures	547
Nanosatellite	585	Oxy-Fueled Guns	218
NARSIM	763		
Navier Stokes Equations	174	Paraffin-Based Fuels	664
Navigation	634	Particle Migration	690
Neumann Boundary Conditions	304	Particle Swarm Optimization	596
Neural Networks	141,499	Particle-In-Cell	679
Neuromorphic Vision	567	Path Planning	104
Node- Dependent Kinematics	313	Pattern Recognition	161
Noise Control	740	Peridynamics	304
Noise Reduction	325	Pitching Airfoil	161
Noise Suppression	254	Planetary Geology	721
Non-Equilibrium	179	Planets: Mercury	717
Non-Holonomic Systems	345	Plasma Thrusters	679
Nonlinear Aeroelasticity	34	Plasma	179
Nonlinear Analysis	357	Plastic Detection from Space	483
Nonlinear Structural Behavior	287	Plug Nozzle	695
Novel	6	Pneumatic Tests	538
Nozzle Heat Transfer	664	Polycrystalline Materials	341
Nozzle	675	Polymer Composites	381
Numerical Simulation	465,534,679,690,695	Polymer Matrices	333
Numerical	675	Post-Buckling	421
Numerical-Experimental Correlation	84	Preliminary Design	80
		Preliminary Sizing	80
		Pressure Filter	197
Objective Methods	754	Probes	127
One-Dimensional Formulations	239	Process-Induced Deformations	321
OpenFOAM	690,695	Programmable Material	572
Optical Measurements	308	Propeller Aerodynamics	21
Optical Sensor	526	Proper Orthogonal Decomposition	161
Optimal Control	596		
Optimal Guidance	615	Qualification	558
Optimization	61,156,553	Quantum Computing	174
Orbit Determination	634		

Radar	474	Sensor Acquisition	713
Random Excitation	453	SESAR	763
Random Vibration Analysis	601	Shielding Effect	2
RANS	211	Shock Absorber	84
RC Airplane	150	Shock Response Spectrum	744
Reduced Attitude	611	Shock-Wave/Boundary Layer Interaction	222
Reduced Gravity	226	Simulation	89
Reduced Order Model	440	Sliding-Mode	615
Re-Entry Technology	576	Small Celestial Bodies	590
Refined Structural Model	453	Small Spacecraft	522
Regenerative Cooling Systems	206	Smoothed Particle Hydrodynamics	363
Regenerative Cooling	645,654	SMXB	373
Regional Aircraft	2	Solid Polymer Electrolyte (SPE)	381
Relative Navigation	458	Solid Rocket Motors	690
Relative Orbit Determination	526	Sound Absorption	254
Remote Sensing Instruments	717	Sounding Balloon Dynamics	274
Remote Sensing	262	Sounding Rocket	645
Requirements	249	Space Avionics	713
Residual Stresses	321	Space Collision Avoidance	630
Reynolds Averaged Navier Stokes (RANS)	189	Space Debris	291,465,474,513
Risk Analysis	114	Space Exploration	266
ROM	10	Space Flight Boundaries	114
Rosetta	709,725	Space Instrument	270,542,709
Rotor Noise	17	Space Mechanism	725
Rotorcraft-Pilot Coupling	26	Space Missions	717
RPAS Integration	99	Space Propulsion	679
RRT	104	Space Rider Observer Cube	504
		Space Rider	504
Safety at Sea	243	Space Robots	508
Satellite Design	563	Space Tethers	534
Satellite	262	Space Traffic Management	630
Satellites Break Up	513	Spacecraft Demise	668
Satellites Deorbiting	534	Spacecraft Re-Entry	639
Satellites Shields	291	Spacecraft Structures	601
Scientific Machine Learning	174	Spaceflight Mechanics	630
Semi-analytic Method	625	SPH	197
Sense and Avoid	70	Stability	30

Stability	611	Thermochemical Non-Equilibrium	170
STC	542	Thermo-Chemistry	179
Steady-State Thermo-Elasticity	341	Throttling	645
Stochastic Properties	390	Torsional Shape Memory Alloys	413
Stratospheric Balloon	280	Totimorphic	572
Structural Batteries	399	TRAC longerons	357
Structural Health Monitoring	308,368,409	Trajectory Reconstruction	274
Structural Theories	141	Transient Analysis	404
Structural Vibrational Response	736	Transient Nonlinear Analyses	239
Strut-Braced Wing	34,42	Transition Modelling	189
Subjective Methods	754	Transitional Configuration	118
Submersible Aircraft	118	Tunable Structured Fabric	731
Suborbital Flight	114,280,530	Tuneable Vibration Absorber	731
Subsonic	230	Turbulent Boundary Layer (TBL)	736
Supersonic Aircraft	57,122	Turbulent Compression Ramp	222
Supersonic Flows	193		
Supersonic Parachute	193	UAV Formation	94
Surface Node Method	304	UAV	89,104,133,243,258
Sustainability	325	Underwater Noise	740
Swarm Unmanned Vehicles	243	Unified Formulation	317
Synthesis	744	Unmanned Aerial Systems	426,444
System Characterization	258	Unmanned Aerial Vehicles	70
		Unsteady	193
Tank Self-Pressurization	226	Unstructured Grids	184
Target Localization	94	Urban Air Mobility	80,426
Telemetry	713	User Centered	758
Telescope	558,725	User Experience	249
Terminal Manoeuvring Area (TMA)	99	U-Space	426,444
Test of Satellite Hardware	700	USV	243
Test Validation	404	UUV	243
Testing	89		
Tether Deployment	553	Variable Angle Tow (VAT)	300
Thermal Bucklin	300	Variable Stiffness Composites	317
Thermal Control	413	Vegetation Index	262
Thermal Fluid-Structure Interaction	202	Vegetation Indices	581
Thermal Management System	76	Very-Large-Eddy-Simulation	21
Thermal Protection System	576	Vibration Test	146
Thermite	668	Vibro-acoustics	748

Virtual Element Method	386
Virtual Manufacturing	321
Virtual Testing	235
Visual Odometry	705
VOF	226
VR	758
Wall-Pressure Fluctuations (WPFs)	736
Wavelets	744
WENO	170
Whirl-Flutter	30
Wide Angle Camera	709
Wind Energy	137
Wind Tunnel Testing	417
Wind Turbines	161

